

UNIVERSITÀ
DEGLI STUDI
DI PADOVA

Head Office: Università degli Studi di Padova

Department of Industrial Engineering

Ph.D. COURSE in: Science and Engineering of Materials and Nanostructures (SIMN)

SERIES: XXXI

Electrode and Electrolyte Materials for the Development of High Voltage Lithium-ion Batteries and Secondary Batteries Based on Alkali and Alkaline-earth Ions

Thesis written with the financial contribution of “Centro Studi di Economia e Tecnica dell’Energia Giorgio Levi Cases” of the University of Padova

Coordinator: Ch.mo Prof. Giovanni Mattei

Supervisor: Ch.mo Prof. Vito Di Noto

Ph.D. student: Gioele Pagot

*“How many times in history has
the impossible of today become
the reality of tomorrow!”*

- Christian de Duve

Abstract

The research activity described in this thesis has been focused on the development and study of novel electrolyte and electrode materials for application in Lithium and Magnesium secondary batteries. The proposed materials belong to the “*beyond Li-ion*” class of compounds, where systems exceeding the energy density values of classic Li-ion batteries or completely innovative chemistries are presented.

Three different classes of electrolytes have been prepared and studied. A solid polymer electrolyte has been obtained by a lithium functionalization of a poly(vinyl alcohol-*co*-vinyl acetate), forming lithium alkoxide functional groups. In this way, the counter anion of Li⁺ was the overall polymer chain, giving rise to a single lithium ion conductivity. However, the room-temperature conductivity value observed for this material was quite low ($4.6 \cdot 10^{-10} \text{ S}\cdot\text{cm}^{-1}$). By ionic liquid (IL) doping of the solid polymer electrolyte, we have obtained a double effect: i) lithium cations have been exchanged by the cations of IL, enhancing the mobility of the active species; and ii) the flexibility of polymer chains has been increased by the plasticizing effect of the IL. Thus, a room temperature conductivity of $1.3 \cdot 10^{-5} \text{ S}\cdot\text{cm}^{-1}$ has been reached, maintaining a high value of Li transference number (0.59). By reacting glycerol with different quantities of lithium hydride, a new family of lithium-ion conducting electrolytes has been synthesized. In these electrolytes the lithium glycerolate component acts as a large and flexible macro-anion which is able to provide a single-ion conductivity to the material ($2.0 \cdot 10^{-4}$ at 30 °C and $1.6 \cdot 10^{-2} \text{ S}\cdot\text{cm}^{-1}$ at 150 °C). In the last class of electrolytes, ionic liquid-based materials for magnesium batteries, the cation and anion replacement effect on the structure, conductivity mechanism, and electrochemical performances has been studied. The proposed materials have exhibited a conductivity value between 10^{-3} and $10^{-4} \text{ S}\cdot\text{cm}^{-1}$, an overpotential in the magnesium deposition lower than 50 mV vs. Mg/Mg²⁺, an anodic stability up to +2.35 V vs. Mg/Mg²⁺, and a coulombic efficiency up to 99.94 %.

In the second part of this Ph.D. project, the improvement of the electrochemical features of various cathode materials has been studied. In the first case, it has been found that, by adding CuCO₃ to the precursors, segregated CuO particles have been formed. The presence of these particles has improved the charge-transfer kinetics during the charge/discharge processes of the cathode material. On the other hand, graphite addition to the precursors has been found to improve the

elasticity of the 3D structure of the cathode backbone. Thus, an increased structural flexibility that facilitates the percolation of lithium ions along the 1D channels of the cathode material has been observed. In the second approach, the improvement of the electron conductivity of a high-voltage cathode has been gauged by V, Nb, or Ta insertion within its olivine structure. This approach has allowed for an improved kinetic and reversibility of Li^+ insertion reaction. The specific capacity reached by these cathodes was equal to $149 \text{ mAh}\cdot\text{g}^{-1}$. The last cathode material has been implemented in a magnesium secondary battery device. A graphene oxide surface functionalization of vanadium-based nanoparticles has been obtained thanks to electrostatic interactions through ammonium bridges. This functionalization has allowed for the obtaining of a material able to: a) sustain extremely high current rates ($1000 \text{ mA}\cdot\text{g}^{-1}$, $1700 \text{ mW}\cdot\text{g}^{-1}$ of specific power); and b) give reasonable specific capacity values ($72 \text{ mAh}\cdot\text{g}^{-1}$).

Sommario (in italian)

L'attività di ricerca descritta in questa tesi è stata incentrata sullo sviluppo e studio di nuovi materiali elettrolitici ed elettrodici per l'applicazione in batterie secondarie al litio e magnesio. I materiali proposti appartengono alla classe di composti "*beyond Li-ion*", in cui sono presenti sistemi che superano i valori di densità energetica delle classiche batterie a ioni litio o chimiche completamente innovative.

In questo lavoro sono state preparate e studiate tre diverse classi di elettroliti. Un elettrolita polimerico di stato solido è stato ottenuto mediante la litiazione di un poli(vinil alcol-co-vinil acetato), formando gruppi funzionali di tipo litio alcossidico. In questo modo il contro anione del Li^+ era la catena polimerica stessa, dando così origine ad una conducibilità di singolo ione. Tuttavia, il valore di conducibilità a temperatura ambiente osservato per questo materiale era piuttosto basso ($4.6 \cdot 10^{-10} \text{ S} \cdot \text{cm}^{-1}$). Mediante il dopaggio dell'elettrolita polimerico di stato solido con un liquido ionico (IL) è stato ottenuto un duplice effetto: i) gli ioni litio sono stati scambiati dai cationi del liquido ionico, migliorando la mobilità delle specie attive; e ii) la flessibilità delle catene polimeriche è stata aumentata dall'effetto plastificante del liquido ionico. Pertanto, è stata raggiunta una conducibilità a temperatura ambiente di $1.3 \cdot 10^{-5} \text{ S} \cdot \text{cm}^{-1}$, mantenendo comunque un valore elevato di numero di trasporto (0.59). Facendo reagire il glicerolo con diverse quantità di idruro di litio, è stata sintetizzata una nuova famiglia di elettroliti conduttori di litio. In questi elettroliti il componente glicerolato di litio agiva come un macro-anione flessibile, in grado di fornire una conducibilità di singolo ione pari a $2.0 \cdot 10^{-4}$ a $30 \text{ }^\circ\text{C}$ e $1.6 \cdot 10^{-2} \text{ S} \cdot \text{cm}^{-1}$ a $150 \text{ }^\circ\text{C}$. Nell'ultima classe di elettroliti, materiali a base di liquidi ionici per batterie al magnesio, è stato studiato l'effetto di sostituzione del catione e dell'anione sulla struttura, sul meccanismo di conduzione e sulle prestazioni elettrochimiche degli elettroliti. I materiali proposti hanno mostrato valori di conducibilità compresi tra 10^{-3} e $10^{-4} \text{ S} \cdot \text{cm}^{-1}$, un sovrappotenziale nella deposizione di magnesio inferiore a 50 mV rispetto a Mg/Mg^{2+} , una stabilità anodica di +2.35 V rispetto a Mg/Mg^{2+} , ed una efficienza coulombica fino al 99.94%.

Nella seconda parte di questo progetto di dottorato, è stato studiato il miglioramento delle caratteristiche elettrochimiche di vari materiali catodici. Nel primo caso, è stato osservato che, aggiungendo CuCO_3 ai precursori, si sono formate particelle di CuO . La presenza di queste

particelle ha migliorato la cinetica di trasferimento di carica durante i processi di carica/scarica del catodo. L'aggiunta invece di grafite ai precursori, che si decompone durante la sintesi, ha invece migliorato l'elasticità della struttura catodica. Questo ha facilitato la percolazione di Li^+ lungo i canali dell'olivina durante i cicli di carica/scarica. Nel secondo approccio, la conducibilità elettronica di un catodo ad alto potenziale è stata migliorata mediante l'aggiunta di V, Nb o Ta all'interno della struttura. L'effetto che è stato osservato è un miglioramento della reazione di inserzione di Li^+ . La capacità specifica raggiunta da questi catodi è stata pari a $149 \text{ mAh}\cdot\text{g}^{-1}$. L'ultima proposta ha riguardato un catodo per batterie secondarie di magnesio. La funzionalizzazione superficiale con ossido di grafene di nanoparticelle a base di vanadio è stata ottenuta grazie all'interazione elettrostatica attraverso ponti ammonio. Questa funzionalizzazione ha consentito di ottenere un materiale in grado di: a) sostenere correnti estremamente elevate ($1000 \text{ mA}\cdot\text{g}^{-1}$, $1700 \text{ mW}\cdot\text{g}^{-1}$ di potenza specifica); e b) fornire discreti valori di capacità specifica ($72 \text{ mAh}\cdot\text{g}^{-1}$).

Acknowledgments

First of all, I would like to thank my grandpa, who always encouraged me to study. He always used to say that studying is never enough. Thanks to him, I understood the importance of learning, discovering, and achieving a proper education.

A special thank goes to my supervisor, Prof. Vito Di Noto, for giving me the opportunity to join his research group. He guided me throughout my Master, post Master, and PhD studies with a great support and kind advices. The scientific level of our fruitful discussions was of an inestimable value for my research preparation. I appreciated also the opportunity that he gave me to attend several conferences and meet so many interesting and important people. I would like also to thank the Centro Studi di Economia e Tecnica dell'Energia Giorgio Levi Cases of the University of Padova for the financial support.

I must express my gratitude to Dr. Federico Bertasi. He guided me from the beginning, since I joined this group six years ago. He taught me the main technical skills that I have now, with a lot of patience and enthusiasm. The first years passed together in the lab have been memorable. I am very thankful to Dr. Enrico Negro and Dr. Ketì Vezzù, I have never seen such an impressive hard work and generosity from anyone. Their assistance and expertise were essential for make me reaching all my objectives. Dear Ketì, I am deeply indebted with you for all the help you gave me with BES!

A lot of people came to our group, and I would like to particularly thank Dr. Giuseppe Pace, Dr. Graeme Nawn, Dr. Yannick Hervé Bang, Dr. Antoine Bach Delpèuch, and Dr. Angeloclaudio Nale. I spent a lot of time with you inside and outside the lab, I really appreciate your friendship. I am thankful to Dr. Chuanyu Sun, we shared the pain and pleasure of the PhD! Another thanks go to Dr. Nicola Boaretto, Dr. Arianna Adami, Dr. Jonas Rivetti, Dr. Agnieszka Zlotowicz, Dr. Sara Tonello, Dr. Edoardo Donà, and almost Dr. Marco Bandiera, we helped each other in a lot of occasions, I am really grateful.

I am deeply thankful to mum and dad, and to all of my family, for their love, support, and sacrifices. Without them, I would have never reached all the achievements I got till now, and I would not be

who I am. Thanks to the General NP, to all of my friends, and to GasGas, "*studying is never enough*", but it is not the only thing in the life! Thank you for all the adventures that we have shared.

I would like to express my appreciation to all of my past flat mates, and in particular to Dr. Federico Uliana and Dr. Alessandro Simonato. I will never forget every evening we spent together in our apartment and all the special dinners we had. I wish you all best in future.

This last word of acknowledgements I have saved for my dear Elisa, for her unconditional support during all the years we have spent together, and in particular in this last period. Thank you for the patience you had while I was working on this thesis and for proofreading. Thank you for all the things you might have missed for me, and for all the things I got from you.

Gioele Pagot

30th September 2018

Index

Abstract	v
Sommario (in italian)	vii
Acknowledgments	ix
List of Figures	xvii
List of Tables	xxv
List of Abbreviations	xxvii
1. Introduction	1
1.1 Battery Technology.....	1
1.1.1 Principal Battery Parameters.....	2
1.1.2 Conventional Secondary Batteries.....	4
1.1.3 “Beyond Lithium-ion” Batteries.....	7
1.2 Lithium Batteries.....	7
1.2.1 Electrolytes for Li Batteries.....	7
1.2.1.1 Liquid Electrolytes for LIBs.....	7
1.2.1.2 Solid-State Electrolytes for LIBs.....	10
1.2.1.3 Polymer Electrolytes for LIBs.....	13
1.2.1.4 Ionic Liquid-based Electrolytes for LIBs.....	16
1.2.2 Cathodes for Li Batteries.....	18
1.2.2.1 Chalcogenides.....	18
1.2.2.2 Vanadium Oxides and Derivatives.....	18
1.2.2.3 Lithium Cobalt Dioxide.....	19
1.2.2.4 Lithium Nickel Dioxide.....	20
1.2.2.5 Lithium Manganese Oxide.....	21
1.2.2.6 Lithium Manganese Dioxide.....	21
1.2.2.7 Lithium Nickel-Cobalt Dioxide.....	22
1.2.2.8 Lithium Manganese-Cobalt Dioxide.....	22
1.2.2.9 Lithium Manganese-Nickel Dioxide.....	22
1.2.2.10 Lithium Nickel-Manganese-Cobalt Dioxide (NMC).....	23
1.2.2.11 Lithium Nickel-Cobalt-Aluminum Dioxide (NCA).....	23
1.2.2.12 Lithium Nickel Phosphate.....	23
1.2.2.13 Lithium Cobalt Phosphate.....	24
1.2.2.14 Lithium Iron Phosphate.....	24
1.3 Magnesium Batteries.....	25

1.3.1	Electrolytes for Mg Batteries.....	27
1.3.1.1	Liquid Electrolytes for Mg Batteries.....	27
1.3.1.2	Solid-State Electrolytes for Magnesium Batteries	28
1.3.1.3	Polymer Electrolytes for Magnesium Batteries	29
1.3.1.4	Ionic Liquid-based Electrolytes for Magnesium Batteries	30
1.3.2	Cathodes for Mg Batteries	31
1.3.2.1	Metal Sulfides	31
1.3.2.2	Metal Oxides	31
1.3.2.3	Metal Silicates	32
1.3.2.4	Sulfur and Selenium.....	33
1.3.2.5	Oxygen.....	33
1.3.2.6	Halides.....	33
2.	Summary and Aims of the Thesis	35
3.	Instruments and Methods.....	37
3.1	General Characterization Approach.....	37
3.2	Dry box and Vacuum-Inert Atmosphere Line	38
3.3	ICP-AES.....	40
3.4	Thermal Measurements	40
3.4.1	Thermogravimetry Analysis (TGA)	40
3.4.1.1	Sample Preparation	41
3.4.2	Differential Scanning Calorimetry (DSC).....	41
3.4.2.1	Sample Preparation	42
3.5	Vibrational Spectroscopy.....	42
3.5.1	Infrared Spectroscopy (FT-IR).....	42
3.5.1.1	Sample Preparation	43
3.5.2	Raman Spectroscopy.....	43
3.5.2.1	Sample Preparation	44
3.6	Electrochemical Techniques	44
3.6.1	Potentiostat/Galvanostat.....	44
3.6.2	Battery Cycling	45
3.7	Broadband Electrical Spectroscopy	45
3.7.1	Sample preparation	48
4.	Lithium Single Ion Conducting Solid Polyelectrolytes Based on Poly(vinyl alcohol)....	49
4.1	Experimental Section.....	49

4.1.1	Reagents.....	49
4.1.2	Synthesis.....	50
4.1.2.1	PVA Lithiation.....	50
4.1.2.2	PVA and Li_PVA Membrane Preparation.....	50
4.1.2.3	Li_PVA Plasticization.....	50
4.2	Results and Discussion.....	51
4.2.1	Composition and Thermal Behavior.....	51
4.2.2	Vibrational Analyses.....	54
4.2.3	Lithium Transference Number.....	60
4.2.4	Broadband Electrical Spectroscopy Studies.....	60
4.2.4.1	Polarization Phenomena.....	62
4.2.4.2	Dielectric Relaxation Events.....	65
4.2.4.3	Activation Energies.....	65
4.3	Conclusions.....	67
5.	Lithium Glycerolate: a New Glass-forming Electrolyte.....	69
5.1	Experimental Section.....	69
5.1.1	Reagents.....	69
5.1.2	Synthesis.....	69
5.2	Results and Discussion.....	70
5.2.1	Chemical Composition.....	70
5.2.2	Vibrational Spectroscopy Studies.....	71
5.2.2.1	Glycerol Conformations.....	71
5.2.2.2	Fourier-Transform Infrared Spectroscopy.....	73
5.2.2.3	Micro-Raman Spectroscopy.....	80
5.2.3	Thermal Studies.....	83
5.2.3.1	Thermo-Gravimetric Analyses.....	83
5.2.3.2	Modulated Differential Scanning Calorimetry Studies.....	84
5.2.4	Broadband Electrical Spectroscopy Studies.....	86
5.2.4.1	Polarization Phenomena.....	89
5.2.4.2	Dielectric Relaxation Events.....	92
5.2.4.3	Activation Energies.....	95
5.2.4.4	Diffusion Coefficients and Average Charge Migration Distance.....	97
5.2.4.5	Conductivity Mechanism.....	100
5.3	Conclusions.....	102

6. Structural Elasticity Modification of a High Voltage Cathode for Lithium Batteries ...	105
6.1 Experimental Section.....	105
6.1.1 Reagents.....	105
6.1.2 Synthesis.....	106
6.2 Results and Discussion	106
6.2.1 Preface: Structure and Electrochemistry	106
6.2.1.1 Powder X-Ray Diffraction.....	106
6.2.1.2 Vibrational Studies.....	107
6.2.1.3 Battery Test.....	108
6.2.2 Broadband Electrical Spectroscopy Studies.....	110
6.3 Conclusions.....	112
7. Effect of High Valence Transition Metal Insertion in High Voltage Olivine Cathodes for Lithium Secondary Batteries	115
7.1 Experimental Section.....	115
7.1.1 Reagents.....	115
7.1.2 Synthesis.....	116
7.1.2.1 Oxidizing Solid State Synthesis	116
7.1.2.2 Partially Reducing Solid State Synthesis.....	116
7.1.2.3 Reducing Solid State Synthesis	116
7.2 Results and Discussion	117
7.2.1 Thermal Stability	117
7.2.2 Morphology.....	119
7.2.2.1 Scanning Electron Microscopy	119
7.2.2.2 High-Resolution Transmission Electron Microscopy	121
7.2.3 X-ray Photoelectron Spectroscopy.....	122
7.2.4 Powder X-ray Diffraction	126
7.2.5 Vibrational Spectroscopy.....	131
7.2.6 Electrochemical Analyses	134
7.2.6.1 Cyclic Voltammetry.....	134
7.2.6.2 Electrochemical Impedance Spectroscopy	138
7.2.7 Battery Test	142
7.3 Conclusions.....	147
8. Exploit BCl₄⁻ Structural Probe Ability to Unfold the Coordination Network Structure of Ionic Liquids Electrolytes	149
8.1 Experimental Section.....	149

8.1.1	Reagents.....	149
8.1.2	Synthesis.....	150
8.2	Results and Discussion	151
8.2.1	Thermal Behavior	151
8.2.1.1	Thermogravimetric Analyses	151
8.2.1.2	Differential Scanning Calorimetry	153
8.2.2	DFT Calculations and Molecular Modeling.....	154
8.2.3	Fourier Transform Infrared Spectroscopy	158
8.2.4	Broadband Electrical Spectroscopy Studies.....	164
8.2.4.1	Polarization Phenomena	166
8.2.4.2	Dielectric Relaxation Events	170
8.2.4.3	Activation Energies.....	172
8.2.4.4	Diffusion Coefficient and Average Migration Distance	173
8.2.4.5	Conductivity Mechanism	176
8.3	Conclusions.....	177
9.	A Novel Halotitanate Ionic Liquid for Magnesium Secondary Batteries	179
9.1	Experimental Section.....	179
9.1.1	Reagents.....	179
9.1.2	Synthesis.....	180
9.2	Results and Discussion	180
9.2.1	Thermal Behavior	180
9.2.2	DFT Calculations.....	182
9.2.3	Vibrational Studies	183
9.2.3.1	Fourier-Transform Infrared Spectroscopy	183
9.2.4	Broadband Electrical Spectroscopy Studies.....	191
9.2.4.1	Polarization Phenomena	193
9.2.4.2	Dielectric Relaxation Events	196
9.2.4.3	Activation Energy	198
9.2.5	Electrochemical Studies	201
9.3	Conclusions.....	204
10.	Beyond Mg Electrolyte Limits: High Performing Ionic Liquid Electrolyte for Magnesium Secondary Batteries Based on Pyr₁₄Cl, AlCl₃, and δ-MgCl₂.....	207
10.1	Experimental Section.....	208
10.1.1	Reagents.....	208

10.1.2	Synthesis	208
10.2	Results and Discussion	208
10.2.1	Thermal Behavior	208
10.2.2	Vibrational Studies	210
10.2.3	Broadband Electrical Spectroscopy Studies.....	216
10.2.3.1	Polarization Phenomena	217
10.2.3.2	Dielectric Relaxation Events	219
10.2.3.3	Activation Energies.....	221
10.2.3.4	Charge Migration Distances	222
10.2.4	Electrochemical Characterization	223
10.2.5	Battery Test	226
10.3	Conclusions.....	228
11.	Graphene Oxide Decorated Vanadium Nanoparticles: a High Power Cathode for Magnesium Batteries.....	229
11.1	Experimental Section.....	229
11.1.1	Reagents.....	229
11.1.2	Electrochemical Activation of Vanadium Species	230
11.1.3	GO@V Synthesis.....	230
11.2	Results and Discussion	230
11.2.1	Composition.....	230
11.2.2	Thermal Behavior	231
11.2.3	Morphology and Structure	232
11.2.3.1	Electron Microscopy.....	232
11.2.3.2	Vibrational Analyses.....	233
11.2.4	Electrochemical Characterization	235
11.2.5	Battery Test	237
11.3	Conclusions.....	238
12.	Conclusions.....	239
	References.....	243

List of Figures

Figure 1.1. Scheme summarizing the main battery components [9].....	2
Figure 1.2. Timeline of battery evolution [10].....	2
Figure 1.3. Recent accidents regarding lithium battery explosions reported in the newspapers... 8	
Figure 1.4. Temperature dependence of the conductivity of various solid-state inorganic electrolytes (a). Magnification of the conductivities at near ambient temperature (b) [31].	11
Figure 1.5. Crystal structure of LiV_2O_5 and LiV_3O_8 . Intercalated lithium ions are represented in green [76].....	19
Figure 1.6. $\alpha\text{-LiCoO}_2$ structure, lithium ions are represented in green, CoO_6 in light blue [79].	20
Figure 1.7. LiMnO_2 structure. Oxygen ions are represented in white, large black atoms correspond to manganese ions, and lithium is represented as small black atoms [88].	22
Figure 1.8. Olivine structure of LiNiPO_4 , analogous to that of LiFePO_4 and LiCoPO_4 [98].	24
Figure 1.9. Crystal cell of LiFePO_4 (a) and overall olivine structure where it can be observed the lithium ion conductivity channels (b) [103].	25
Figure 3.1. Dry- box used: homemade on the left and commercial model on the right.	39
Figure 3.2. Scheme of a simplified vacuum-inert atmosphere line.	39
Figure 3.3. TGA 2950 of TA Instruments.	41
Figure 3.4. DSC instrument.	42
Figure 3.5. Principle of the electric measurements. The sample is placed between two electrodes and a potential $U(t)$ is applied (a); the output current $I(t)$ is out of phase by an angle φ with respect to the applied voltage (b).	46
Figure 3.6. BES measuring system including the analyzer, temperature control system, the cryostat, the sample holder cell, and the vacuum pump (hidden), and electronic data management.	47
Figure 4.1. Preparation of Li_PVA , Li_PVA+IL , and $\text{Li_PVA+IL}_{\text{soak}}$ samples (a). Steps I, II, and III are reported. Mechanism of reaction between MeOLi and carbonyl side groups (b).	50
Figure 4.2. HR-TGA profiles of pristine PVA, IL, and PVA-based PEs.	52
Figure 4.3. DSC profiles of PVA-based and IL samples; T_m indicates the melting event of EMImTFSI , while T_g corresponds to the glass transition of the PVA domain. Measurements are collected cooling the samples from $+160$ to -150 °C.	54
Figure 4.4. Docked Mid-ATR and Far-FTIR spectra of pristine PVA, IL, and PVA-based polymer electrolytes.	55
Figure 4.5. Magnification of selected spectral regions of FT-IR measurements for Li_PVA+IL , $\text{Li_PVA+IL}_{\text{soak}}$, and IL samples.	56
Figure 4.6. Structural and interaction features of PVA, Li_PVA , and Li_PVA+IL or $\text{Li_PVA+IL}_{\text{soak}}$ materials.	59

Figure 4.7. 3D- <i>tan delta</i> surfaces of pristine IL and PVA-based materials.....	61
Figure 4.8. Dependence on T^{-1} of the σ_k conductivity values (a), and of the f_j dielectric relaxation frequencies (b) for pristine IL and PVA-based materials. Temperature regions are indicated as I, II, and III.....	62
Figure 4.9. Dependence on T^{-1} of the overall conductivity ($\sigma_T = \sum_{i=1}^4 \sigma_{IP,i} + \sigma_{EP}$) of investigated materials.....	64
Figure 4.10. Correlation map of activation energies of measured conductivities (E_{a,σ_i}) and dielectric relaxation events (E_{a,f_j}) of different samples in various temperature regions.....	66
Figure 5.1. The α , β , and γ conformations of glycerol (a). Most probable conformations assumed by the glycerol molecule, $\alpha\alpha$ and $\alpha\gamma$. Color legend: C (grey), O (red), H (white), oxygen electron pair (pink). Hydrogen bonds are highlighted with a dotted line (b). Glycerol inter-molecular structure in the liquid phase (c).....	71
Figure 5.2. Coordination geometries assumed by glycerol molecules upon coordination of Li^+ cations. Color legend: C (grey), O (red), H (white), Li (violet). Li-O interactions are highlighted with a dotted line. g1 coordination geometry, with four monodentate glycerol ligands (a). g2.1 coordination geometry, with two monodentate glycerol ligands and one bidentate glycerol ligand (b). g2.2 coordination geometry, with two bidentate glycerol ligands (c). g3 coordination geometry, with one monodentate glycerol ligand and one tridentate glycerol ligand (d).....	72
Figure 5.3. ATR FT-IR spectra of $GlyLi_x$ electrolytes.....	73
Figure 5.4. FT-IR differential spectra. Glycerol FT-IR spectrum is subtracted from the spectrum of each $GlyLi_x$ sample.	75
Figure 5.5. Intensity and wavenumber behavior of $\nu(OH)$, $\nu^{g^3}(C-C-O)$, and $\nu^{g^1}(C-C-O)$ FT-IR vibrations at different x values.....	76
Figure 5.6. Gaussian fitting of the FT-IR spectra of: pristine glycerol, Gly ($x = 0$) in the $2500 \div 3700$ cm^{-1} region (a). Lithium glycerolate, $GlyLi$ ($x = 1.000$) in the $2500 \div 3700$ cm^{-1} region (b). Pure glycerol, Gly ($x = 0$) in the $770 \div 1150$ cm^{-1} region (c). Lithium glycerolate, $GlyLi$ ($x = 1.000$) in the $770 \div 1150$ cm^{-1} region (d).....	77
Figure 5.7. Semi-quantitative analysis of the peaks centered at <i>ca.</i> 3386, 3267, 3149, and 3071 cm^{-1} as a function of x.....	78
Figure 5.8. Semi-quantitative analysis of the peaks in the range $770 \div 1150$ cm^{-1} as a function of x.	79
Figure 5.9. Normalized micro-Raman spectra of $GlyLi_x$ samples.....	81
Figure 5.10. Lorentzian fitting of the micro-Raman spectrum of pristine glycerol ($x = 0$) in the $2600 \div 3100$ cm^{-1} region.	81
Figure 5.11. Areal behavior of the micro-Raman peaks as a function of x.....	82
Figure 5.12. Thermo-gravimetric analyses of $GlyLi_x$	83
Figure 5.13. MDSC profiles of $GlyLi_x$	85

Figure 5.14. MDSC results of pristine glycerol, Gly ($x = 0$) and lithium glycerolate, GlyLi ($x = 1.000$) samples. The reversible and non-reversible heat flow contributions are distinguished in the two graphs.	85
Figure 5.15. 3D $\tan\delta$ surfaces of GlyLi $_x$ samples, with $0 \leq x \leq 1.000$	88
Figure 5.16. Complete analysis of the electric response of GlyLi $_{0.250}$ sample in terms of ϵ' , ϵ'' , σ' , and $-\sigma''$	89
Figure 5.17. Log σ_k vs. T^{-1} curves of all the polarizations for every sample. Region I and II are divided by the T_g of the sample.	90
Figure 5.18. Log σ_T vs. T^{-1} curves for the various groups of GlyLi $_x$ samples. Region A: $x \leq 0.090$; region B: $0.170 \leq x \leq 0.450$; region C: $0.780 \leq x \leq 1.000$	91
Figure 5.19. Representation of glycerol α , β , and γ dielectric relaxations; μ indicates the dipole moment.	93
Figure 5.20. Log f_j vs. T^{-1} curves of each dielectric relaxation event for every sample. Region I and II are divided by the T_g of the sample.	94
Figure 5.21. $\Delta\epsilon_j$ vs. T^{-1} curves of each dielectric relaxation event for every sample. Region I and Region II are divided by the T_g of the sample.	94
Figure 5.22. Activation energies calculated for each polarization phenomenon and relaxation event of every sample. The plot is divided into a low-temperature region (Region I, $T < T_g$) and a high-temperature region (Region II, $T > T_g$).	95
Figure 5.23. Diffusion coefficient calculated for each polarization (σ_{EP} , $\sigma_{IP,1}$, and $\sigma_{IP,2}$ rows), as a function of the dielectric relaxation frequencies (f_γ , f_β , and f_α , columns). Dotted lines represent the ideal glycerol diffusion coefficient.	98
Figure 5.24. Average migration distance as a function of the temperature for σ_{EP} , $\sigma_{IP,1}$, $\sigma_{IP,2}$, and $\sigma_{IP,3}$	99
Figure 5.25. Proposed conduction mechanism for: $\sigma_{IP,1}$ (a), $\sigma_{IP,2}$ (b), and $\sigma_{IP,3}$ (c); overall proposed conduction mechanism (d). The delocalization body (DB) is highlighted with a red dotted line.	102
Figure 6.1. X-ray diffraction. WAXD spectra of LFNCP/Cu (red line) and LFNCP/Cu+C (black line); Miller indices are reported above the peaks. Every different phase is indicated with a different marker (●LiMPO $_4$, ■Fe $_2$ O $_3$, ►CuO, and ▲NiO).	107
Figure 6.2. Vibrational analyses. FT-MIR and FT-FIR spectra of LFNCP/Cu (red dotted line) and LFNCP/Cu+C (black solid line). The inset shows a magnification of the spectra in the 200-700 cm^{-1} range; the two curves are superimposed to highlight the differences in absorbance intensities after normalization on the peak at 641 cm^{-1}	108
Figure 6.3. Battery tests. Galvanostatic charge/discharge profiles of LFNCP/Cu (red line) and LFNCP/Cu+C (black line) during cycle number 1 (solid line) and cycle number 150 (dashed line) (a). Discharge cycling performances of LFNCP/Cu (●), and LFNCP/Cu+C (▲), and cycling stability of LFNCP/Cu (◆) and LFNCP/Cu+C (■). The difference in maximum discharge capacity of LFNCP/Cu and LFNCP/Cu+C is highlighted with a dashed-dot circle (b).	109

Figure 6.4. BES results. ϵ'' vs. frequency for LFNCVP (blue), LFNCVP/Cu (red), and LFNCVP/Cu+C (black) from -80 to 150 °C. α and β dielectric relaxations are highlighted with an arrow.....	110
Figure 6.5. LFNCVP (blue), LFNCVP/Cu (red), and LFNCVP/Cu+C (black) log f vs. 1/T plot.	111
Figure 7.1. Thermogravimetric analyses of the proposed cathode materials under a nitrogen atmosphere.....	118
Figure 7.2. SEM images of LFNCVP (a); LFNCVP/C (b); LFNCVP/H (c); LFNCNP (d); and LFNCPTP (e) at different magnifications.	119
Figure 7.3. EDX maps of LFNCVP (a); LFNCVP/C (b); LFNCVP/H (c); LFNCNP (d); and LFNCPTP (e). Different elements are highlighted with different colors.	120
Figure 7.4. TEM (a), HR-TEM (b), STEM (c) images, FFT of HR-TEM (d), and SAD (e) of LFNCVP material.....	121
Figure 7.5. XPS spectra of LFNCVP (a); LFNCVP/C (b); LFNCVP/H (c); LFNCNP (d); and LFNCPTP (e).	125
Figure 7.6. Powder X-ray diffraction spectra of all the cathode materials. Miller indices are reported above the peaks. Every different phase is indicated with a different marker (●LiMPO ₄ , ◆Li ₃ PO ₄ , ■Fe ₂ O ₃ , ▲LiMP ₂ O ₇ , and ▼Ta ₂ O ₅).....	127
Figure 7.7. Rietveld refinement for LFNCVP sample.....	128
Figure 7.8. Docked FT-MIR and FT-FIR measurements in the 200÷1300 cm ⁻¹ range of all the samples.	131
Figure 7.9. Comparison of ν_4 peak separation in the different samples with respect to the reference material (LFNCVP).....	133
Figure 7.10. Cyclic voltammetry experiments at different scan rates of the proposed materials. Lithium ribbons are used as counter and reference electrodes, the working electrode consists of platinum. The electrolyte is 1.0 M LiPF ₆ in EC/DMC 1:1.....	135
Figure 7.11. Current peak vs. square root of the scan rate for all the samples. Data are obtained from CV experiments.	137
Figure 7.12. Electrochemical impedance spectroscopy results of all the samples (a-e). Fitting curve is highlighted in red. The equivalent circuit used for the fitting of Nyquist plots is represented in (f).	139
Figure 7.13. Log(D _{Li}) values for each sample evaluated with both CV and EIS techniques.	141
Figure 7.14. Galvanostatic battery cycling test performed at C/5 for LFNCVP (a); LFNCVP/C (c); LFNCVP/H (e); LFNCNP (g); and LFNCPTP (i) at different cycle numbers. Durability test during the first 150 cycles for LFNCVP (b); LFNCVP/C (d); LFNCVP/H (f); LFNCNP (h); and LFNCPTP (j). ...	143
Figure 7.15. Comparison between the maximum discharge specific capacity of all the proposed materials.....	144
Figure 7.16. Rate capability test comparing different synthetic routes (a), different dopant ion (b), and with respect to the reference (c). In (c) 100 % corresponds to the discharge capacity of the first cycle.	147
Figure 8.1. Schematic representation and real synthesis apparatus.....	150

Figure 8.2. HR-TGA profiles of the proposed IL-based electrolytes at different salt concentrations.	151
Figure 8.3. Thermal decomposition temperature at different magnesium contents (x). T _{Ila} is the temperature at which this event starts, while T _{Iib} is the temperature where the maximum of the decomposition rate takes place.	152
Figure 8.4. DSC profiles for [Pyr ₁₄ Cl/(BCl ₃) _{0.5}]/(δ-MgCl ₂) _x samples.	153
Figure 8.5. Phase diagram of [Pyr ₁₄ Cl/(BCl ₃) _{0.25}]/(δ-MgCl ₂) _x electrolytes.	154
Figure 8.6. Coordination geometries of the different complexes present into the IL-based electrolytes. Color legend: C (black); H (white); N (blue); B (pink); Cl (light green); and Mg (green). BCl ₄ ···MgCl ₂ coordination is highlighted in red.	155
Figure 8.7. Molecular modeling results of Pyr ₁₄ Cl/(BCl ₃) _{0.25} (a) and [Pyr ₁₄ Cl/(BCl ₃) _{0.25}]/(δ-MgCl ₂) _{0.095} (b). The composition of each cluster is reflecting the real concentration of species resulting from ICP-AES measurements.	156
Figure 8.8. Detail of the cation domain in the sample with x=0 (a) and x=0.095 (b) in the IL context. The cation helix extracted from the context for x=0 (c) and x=0.095 (d).	157
Figure 8.9. X-ray and neutron scattering simulated spectra of the sample with x=0 and x=0.095.	158
Figure 8.10. Docked FT-IR spectra in the mid and far regions of [Pyr ₁₄ Cl/(BCl ₃) _{0.25}]/(δ-MgCl ₂) _x electrolytes.	159
Figure 8.11. Gaussian decomposition of Pyr ₁₄ Cl/(BCl ₃) _{0.25} (a) and [Pyr ₁₄ Cl/(BCl ₃) _{0.25}]/(δ-MgCl ₂) _{0.095} (b) compounds. Circle markers are the experimental curves, black lines correspond to the fitting results, red points are the residues (difference between experimental and fitting data), and red lines represent each vibrational peak.	162
Figure 8.12. Peak intensity behavior vs. x curves of [Pyr ₁₄ Cl/(BCl ₃) _{0.25}]/(δ-MgCl ₂) _x electrolytes. Peaks considered for this graph are those attributed to the ν _a (B-Cl) and ν _a (Mg-Cl-B) peaking at 687 and 352 cm ⁻¹ , respectively.	163
Figure 8.13. Graphical sketch of the different coordination geometries forming in each magnesium concentration region. Color legend: B (pink); Cl (light green); and Mg (green).	163
Figure 8.14. 3D imaginary permittivity spectra as a function of frequency and temperature for [Pyr ₁₄ Cl/(BCl ₃) _{0.25}]/(δ-MgCl ₂) _x samples, with x=0, 0.020, 0.041, and 0.071.	165
Figure 8.15. Log σ _k vs. T ⁻¹ curves of each polarization for every sample. Temperature regions (I-IV) are divided by the transition temperatures of each sample detected with DSC measurements.	167
Figure 8.16. Contribution of each polarization (φ _k) to the overall conductivity as a function of temperature. Temperature regions (I-IV) are divided by the transition temperatures of each sample detected with DSC measurements.	168
Figure 8.17. Log σ _{TOT} vs. T ⁻¹ curves for the various [Pyr ₁₄ Cl/(BCl ₃) _{0.25}]/(δ-MgCl ₂) _x electrolytes divided in the different Mg concentration regions (A, B, and C).	169

Figure 8.18. Log f_j vs. T^{-1} curves of each dielectric relaxation event for every sample. Temperature regions (I-IV) are divided by the transition temperatures of each sample detected with DSC measurements.....	171
Figure 8.19. Representative cartoon of the dielectric relaxation events detected for these materials.....	172
Figure 8.20. Activation energies calculated for each polarization phenomenon and relaxation event of every sample in the various temperature regions.	173
Figure 8.21. Diffusion coefficient calculated for each polarization (σ_{EP} , and $\sigma_{IP,1}$ rows), as a function of the dielectric relaxation frequencies ($f_{\alpha 1}$, $f_{\alpha 2}$, and $f_{\beta 1}$, columns). Dotted lines represent the ideal IL diffusion coefficient.	174
Figure 8.22. Average migration distance as a function of the temperature for σ_{EP} , $\sigma_{IP,1}$, σ_{IP2} , and $\sigma_{IP,3}$	175
Figure 9.1. Modulated Differential Scanning Calorimetry profiles of $[\text{EMImCl}/(\text{TiCl}_4)_{1.4}]/(\delta\text{-MgCl}_2)_x$. The glass transition temperature (T_g) is indicated.	181
Figure 9.2. Thermal reorganization of the complexes after glass transition temperature.....	181
Figure 9.3. Optimized geometries of the electrolyte complexes determined at the B3LYP/6-311G** level of theory. $\text{EMIm}^+[\text{TiCl}_6]^{2-}$ (a); $\text{EMIm}^+[\text{TiCl}_6\text{MgCl}_2]^{2-}$ (b); $\text{EMIm}^+[\text{TiCl}_6\text{MgCl}_2\text{MgCl}_2]^{2-}$ (c); $\text{EMIm}^+[\text{Ti}_2\text{Cl}_9]^-$ (d); $\text{EMIm}^+[\text{Ti}_2\text{Cl}_9\text{MgCl}_2]^-$ (e); $\text{EMIm}^+[\text{Ti}_2\text{Cl}_9\text{MgCl}_2\text{MgCl}_2]^-$ (f). Color code: H atoms, white; N atoms, blue; C atoms, black; Cl atoms, green; Ti atoms, grey; Mg atoms, yellow. H...Cl distances, in angstroms, are reported.	182
Figure 9.4. Mid-IR spectra of $[\text{EMImCl}/(\text{TiCl}_4)_{1.4}]/(\delta\text{-MgCl}_2)_x$ electrolytes.....	184
Figure 9.5. Far infrared spectra and vibrational assignment of $[\text{EMImCl}/(\text{TiCl}_4)_{1.4}]/(\delta\text{-MgCl}_2)_x$ samples in the range $150\div 500\text{ cm}^{-1}$; ν = stretching, δ = bending, γ = out-of-plane, def = deformation (a). Gaussian decomposition of the far-IR spectra in the region $150\div 500\text{ cm}^{-1}$. The band corresponding to the ν (Mg-Cl) is highlighted in green. Colored circles represent the experimental data and black lines are the fitting curves (b).....	186
Figure 9.6. Raman spectra of $[\text{EMImCl}/(\text{TiCl}_4)_{1.4}]/(\delta\text{-MgCl}_2)_x$ electrolytes in the full range of analysis.....	188
Figure 9.7. Raman spectra and vibrational assignment of $[\text{EMImCl}/(\text{TiCl}_4)_{1.4}]/(\delta\text{-MgCl}_2)_x$ samples in the range $50\div 550\text{ cm}^{-1}$; ν = stretching, δ = bending, def = deformation (a). Lorentzian decomposition of the Raman spectra in the region $260\div 490\text{ cm}^{-1}$. The peak of the antisymmetrical stretching (ν_a) of TiCl_6^{2-} is highlighted in blue. The band of the bridging stretching (ν_{bridg}) of Ti_2Cl_9^- is highlighted in red. Colored circles represent the experimental data and black lines are the fitting curves (b).	190
Figure 9.8. Φ molar ratio on x of $[\text{EMImCl}/(\text{TiCl}_4)_{1.4}]/(\delta\text{-MgCl}_2)_x$ electrolytes.	191
Figure 9.9. 3D $\tan \delta$ surfaces of $[\text{EMImCl}/(\text{TiCl}_4)_{1.4}]/(\delta\text{-MgCl}_2)_x$ samples.	192
Figure 9.10. Dependence on T^{-1} of the conductivity values (σ_k) of $[\text{EMImCl}/(\text{TiCl}_4)_{1.4}]/(\delta\text{-MgCl}_2)_x$ samples.	194
Figure 9.11. Contribution of each polarization (φ_k) to the total conductivity as a function of temperature.	195

Figure 9.12. σ_T vs. T^{-1} profiles of [EMImCl/(TiCl ₄) _{1.4}]/(δ -MgCl ₂) _x electrolytes.....	196
Figure 9.13. Relaxation modes (f_j , with $1 \leq j \leq 4$) of the imidazolium cation EMIm ⁺	197
Figure 9.14. Dependence on T^{-1} of the dielectric relaxation frequencies (f_j) of [EMImCl/(TiCl ₄) _{1.4}]/(δ -MgCl ₂) _x samples.....	198
Figure 9.15. Activation energies of measured conductivities (E_{a,σ_k}) and dielectric relaxation events (E_{a,f_j}) on x	199
Figure 9.16. Dielectric relaxations (f_j , with $1 \leq j \leq 4$) of EMIm ⁺ cations (a). Conductivity mechanisms of the electrolytes below and above the glass transition temperature (b). Conductivity mechanism occurring by exchange events of magnesium-chlorotitanate complexes through different cationic and anionic nanodomains (delocalization bodies, DBs) at room temperature (c).	200
Figure 9.17. Cyclic voltammograms of [EMImCl/(TiCl ₄) _{1.4}]/(δ -MgCl ₂) _x : on x , with $x \geq 0.05$, at a scan rate of 10 mV·s ⁻¹ (a); at $x = 0.10$ at different scan rates (b). The inset shows the electrochemical stability window of [EMImCl/(TiCl ₄) _{1.4}]/(δ -MgCl ₂) ₀ vs. C we (black line), [EMImCl/(TiCl ₄) _{1.4}]/(δ -MgCl ₂) ₀ vs. Pt we (red line), and [EMImCl/(TiCl ₄) _{1.4}]/(δ -MgCl ₂) _{0.10} vs. C we (blue line). Average coulombic efficiency evaluation for [EMImCl/(TiCl ₄) _{1.4}]/(δ -MgCl ₂) _{0.10} (c).....	201
Figure 9.18. Cyclic voltammograms of [EMImCl/(TiCl ₄) _{1.4}]/(δ -MgCl ₂) _{0.10} at a scan rate of 10 mV·s ⁻¹ for the freshly assembled cell (red solid line) and after a 6 hours stop (blue dashed line).....	203
Figure 10.1. DSC profiles for [Pyr ₁₄ Cl/(AlCl ₃) _{1.5}]/(δ -MgCl ₂) _x	209
Figure 10.2. Phase diagram of [Pyr ₁₄ Cl/(AlCl ₃) _{1.5}]/(δ -MgCl ₂) _x electrolytes.	210
Figure 10.3. Raman spectra of [Pyr ₁₄ Cl/(AlCl ₃) _{1.5}]/(δ -MgCl ₂) _x electrolytes.....	211
Figure 10.4. Raman spectra decomposition (a) and ratio (Φ) between the area of the Al ₂ Cl ₇ ⁻ and AlCl ₄ ⁻ bands vs. x (b).	213
Figure 10.5. Concentration equilibrium of the two forms of chloroaluminate complexes increasing the δ -MgCl ₂ salt concentration.....	214
Figure 10.6. FT-FIR spectra (a) and spectral decomposition (b) for [Pyr ₁₄ Cl/(AlCl ₃) _{1.5}]/(δ -MgCl ₂) _x electrolytes. Peaks attributed to the vibrations of δ -MgCl ₂ are highlighted in green.....	214
Figure 10.7. 3D conductivity spectra as a function of frequency and temperature (a). Counter plot of the conductivity (b). Both the figures are related to [Pyr ₁₄ Cl/(AlCl ₃) _{1.5}]/(δ -MgCl ₂) _{0.091} sample.	216
Figure 10.8. Log σ_k vs. T^{-1} curves of each polarization for every sample. Temperature regions are divided by the transition temperatures of each sample detected with MDSC measurements.....	217
Figure 10.9. Log σ_T vs. T^{-1} curves for the various [Pyr ₁₄ Cl/(AlCl ₃) _{1.5}]/(δ -MgCl ₂) _x electrolytes. ..	218
Figure 10.10. Contribution of each polarization (φ_k) to the total conductivity as a function of temperature.	219
Figure 10.11. Log f_j vs. T^{-1} curves of each dielectric relaxation event for every sample. Temperature regions are divided by the transition temperatures of each sample detected with MDSC measurements.....	220

Figure 10.12. Representative cartoon of the dielectric relaxation events detected for these materials.....	221
Figure 10.13. Activation energies calculated for each polarization phenomenon and relaxation event of every sample in the various temperature regions.	221
Figure 10.14. Average charge migration distances vs. T^{-1} for $[\text{Pyr}_{14}\text{Cl}/(\text{AlCl}_3)_{1.5}]/(\delta\text{-MgCl}_2)_x$ samples.	222
Figure 10.15. CV deposition/stripping measurements of $[\text{Pyr}_{14}\text{Cl}/(\text{AlCl}_3)_{1.5}]/(\delta\text{-MgCl}_2)_{0.056}$ (a) and $[\text{Pyr}_{14}\text{Cl}/(\text{AlCl}_3)_{1.5}]/(\delta\text{-MgCl}_2)_{0.146}$ (b) at different scan rates on a platinum working electrode. ESW of $[\text{Pyr}_{14}\text{Cl}/(\text{AlCl}_3)_{1.5}]/(\delta\text{-MgCl}_2)_{0.056}$ at $5 \text{ mV}\cdot\text{s}^{-1}$ (c).....	224
Figure 10.16. Average coulombic efficiency evaluation for $[\text{Pyr}_{14}\text{Cl}/(\text{AlCl}_3)_{1.5}]/(\delta\text{-MgCl}_2)_{0.056}$ electrolyte.	225
Figure 10.17. SEM images of the electrodeposited layer.	226
Figure 10.18. Cycling performances of a $\text{Mg} [\text{Pyr}_{14}\text{Cl}/(\text{AlCl}_3)_{1.5}]/(\delta\text{-MgCl}_2)_{0.056} \text{V}_2\text{O}_5$ battery at different current rates (a) and long-term cycling at $350 \text{ mA}\cdot\text{h}\cdot\text{g}^{-1}$ (b).	227
Figure 11.1. Representative sketch of the GO@V architecture. It can be observed how the positively-charged ammonium “shell” is able to coordinate the negatively-charged vanadium active species nanoparticles to the graphene oxide nanoflakes.	231
Figure 11.2. HR-TGA profiles of GO@V sample obtained under a N_2 atmosphere.	231
Figure 11.3. SEM micrographs of GO@V material at different magnifications.....	233
Figure 11.4. Micro-Raman (blue) and ATR-FTIR (black) vibrational spectra of GO@V sample.	233
Figure 11.5. CV tests at different scan rates (a); peak current of the different redox events as function of the square root of the scan rate (b).....	236
Figure 11.6. Cycling performances of GO@V sample, cycled at a current rate of <i>ca.</i> 12.5 C ($1000 \text{ mA}\cdot\text{g}^{-1}$).....	237

List of Tables

Table 1.1. Main technical characteristics of conventional secondary batteries [11].	4
Table 1.2. Main operational characteristics of conventional secondary batteries [11].	5
Table 1.3. Conventional solvents for liquid electrolytes [25].	9
Table 1.4. Conventional salts for liquid electrolytes [25].	10
Table 1.5. Numerical comparison between physical properties of several low reduction potential metals.	26
Table 1.6. Economic data for lithium and magnesium.	26
Table 2.1. Summary of the proposed and studied electrolyte and electrode materials described in this thesis.	36
Table 4.1. Compositional data of PVA-based materials.	51
Table 4.2. Mid- Far-IR vibrational frequencies assignment for PVA-based membranes.	57
Table 5.1. Composition of the obtained GlyLi _x samples.	70
Table 5.2. FT-IR and Raman correlational assignments of glycerol (Gly) and lithium glycerolate (GlyLi) samples.	74
Table 5.3. Coordination geometries results of Gly and GlyLi _x electrolytes.	80
Table 5.4. Thermal results of Gly and GlyLi _x electrolytes.	84
Table 5.5. Activation energies calculated for each polarization phenomenon.	96
Table 5.6. Activation energies calculated for each relaxation event.	96
Table 6.1. Activation energies (kJ·mol ⁻¹) of LFNCVP, LFNCVP/Cu, and LFNCVP/Cu+C dielectric relaxations.	112
Table 7.1. Composition of the synthesized cathode materials.	117
Table 7.2. Sample surface composition evaluated from XPS analyses.	126
Table 7.3. Assignment of principal peaks detected in LFNCVP sample.	129
Table 7.4. Cell parameters calculated from Rietveld refinement for all the samples and the reference olivine material.	130
Table 7.5. FT-IR correlational assignments of LFNCVP sample.	132
Table 7.6. Peak positions of M-O and Li-O vibrations.	134
Table 7.7. Lithium ion diffusion coefficients (D _{Li} in cm ² ·s ⁻¹) for cathode materials at different scan rate, calculated from CV experiment.	138
Table 7.8. Charge transfer resistance and exchange current density values calculated by fitting of the Nyquist plots of Figure 7.12.	140
Table 7.9. Lithium ion diffusion coefficients calculated from EIS experiments and comparison with the average D _{Li} evaluated from CV measurements.	141

Table 7.10. Maximum specific capacity and energy values for the obtained materials and the reference cathode.....	144
Table 8.1. Composition of $[\text{Pyr}_{14}\text{Cl}/(\text{BCl}_3)_{0.25}]/(\delta\text{-MgCl}_2)_x$ electrolytes.....	151
Table 8.2. Experimental and calculated vibrational frequencies with relative assignment for the samples with $x=0$ and 0.095	161
Table 9.1. Composition of $[\text{EMImCl}/(\text{TiCl}_4)_{1.4}]/(\delta\text{-MgCl}_2)_x$ electrolytes.....	180
Table 9.2. Mid-IR vibrational frequencies assignment for $[\text{EMImCl}/(\text{TiCl}_4)_{1.4}]/(\delta\text{-MgCl}_2)_x$ electrolytes.....	185
Table 9.3. Far-IR vibrational frequencies assignment for $[\text{EMImCl}/(\text{TiCl}_4)_{1.4}]/(\delta\text{-MgCl}_2)_x$ electrolytes.....	187
Table 9.4. Raman vibrational frequencies assignment for $[\text{EMImCl}/(\text{TiCl}_4)_{1.4}]/(\delta\text{-MgCl}_2)_x$ electrolytes.....	189
Table 10.1. Composition of $[\text{Pyr}_{14}\text{Cl}/(\text{AlCl}_3)_{1.5}]/(\delta\text{-MgCl}_2)_x$ electrolytes.....	208
Table 10.2. Correlative assignment of $[\text{Pyr}_{14}\text{Cl}/(\text{AlCl}_3)_{1.5}]/(\delta\text{-MgCl}_2)_x$ electrolytes Raman vibrations.....	212
Table 10.3. Correlative assignment of $[\text{Pyr}_{14}\text{Cl}/(\text{AlCl}_3)_{1.5}]/(\delta\text{-MgCl}_2)_x$ electrolytes FT-FIR vibrations.....	215
Table 11.1. Correlative assignment of FT-FIR and micro-Raman vibrations for GO@V sample.....	234

List of Abbreviations

3D-HION-APEs	3 Dimensional-Hybrid Inorganic Organic Networks-As Polymer Electrolytes
Al-ion	Aluminum-ion battery
APC	All Phenyl Complex
ATR	Attenuated Total Reflectance
BC	Butylene Carbonate
BE	Binding Energy
BES	Broadband Electrical Spectroscopy
γ BL	γ -Butyrolactone
CA	Chrono-Amperometry
CP	Chevrel Phase
CV	Cyclic Voltammetry
DB	Delocalization Body
DEC	Diethyl Carbonate
DFT	Density Functional Theory
DMC	Dimethyl Carbonate
DOE	Department of Energy
EA	Ethyl Acetate
EB	Ethyl Butyrate
EC	Ethylene Carbonate
EIS	Electrochemical Impedance Spectroscopy
EMC	Ethyl Methyl Carbonate
EMIm ⁺	1-ethyl-3-methylimidazolium
ESW	Electrochemical Stability Window
EVs	Electric Vehicle
FT-FIR	Fourier Transform Far Infrared
FT-MIR	Fourier Transform Medium Infrared
GO	Graphene Oxide
G-PE	Gel-Polymer Electrolyte
HGE	Hybrid Gel Electrolyte
HIO-PE	Hybrid Inorganic Organic-Polymer Electrolyte

ICP-AES	Inductively Coupled Plasma Atomic Emission Spectroscopy
IC-P	Ion Conducting Polyelectrolyte
IL	Ionic Liquid
IR-PEs	Ionic Rubber-Polymer Electrolyte
Li-air	Lithium-air battery
LIB	Lithium battery
Li-ion	Lithium-ion battery
Li-S	Lithium-sulfur battery
MACC	Magnesium Aluminum Chloride Complex
MB	Methyl Butyrate
MDSC	Modulated Differential Scanning Calorimetry
MeOLi	Lithium methoxide
MePrPi ⁺	N-methyl-N-propilpyridinium
MePrPp ⁺	N-methyl-N-propilpyperidinium
Mg-ion	Magnesium-ion battery
MM	Molecular Modeling
Na-S	Sodium-Sulfur battery
NASICON	Na Super Ionic Conductor
NCA	Lithium Nickel-Cobalt-Aluminum Dioxide
Ni-Cd	Nickel-Cadmium battery
Ni-MH	Nickel-Metal hydride battery
NMC	Lithium Nickel-Manganese-Cobalt Dioxide
NMO	N-Methyl Oxazolidinone
NMR	Nuclear Magnetic Resonance
Pb-acid	Lead-acid battery
PC	Propylene Carbonate
PE	Polymer Electrolyte
PEO	Polyethylene Oxide
PHEV	Plug-in Hybrid Electric Vehicle
P-PE	Plasticized-Polymer Electrolyte
PrMeImCl	Propyl, methylimidazolium chloride
PVA	Poly(vinyl alcohol)
Pyr ₁₄	1-methyl-1-butylpyrrolidinium

RTIL	Room Temperature Ionic Liquid
SEI	Solid-Electrolyte Interphase
SLI	Starting, Lighting, and Ignition
SPE	Solid Polymer Electrolyte
SSE	Solid-State Electrolyte
T_g	Glass Transition
TFSI-	N,N-bis(trifluorometan)sulfonyl imide
TGA	Thermogravimetric Analyses
THF	Tetrahydrofuran
t_{Li^+}	Lithium Ion Transference Number
TMePrA ⁺	Trimetilpropilammonio
γ VL	γ -Valerolactone
VTF	Vogel-Tamman-Fulcher
XRD	X-Ray Diffraction
Z-IOPE	Zeolitic-Inorganic Organic Polymer Electrolyte
Zn-air	Zinc-air battery

1. Introduction

1.1 Battery Technology

The growing of the environmental pollution and the progressive fossil fuel consumption have prompt the global shift from a carbon economy to more sustainable, environmental friendly, and renewable electrical energy sources, such as wind, solar, and wave [1-3]. The increasing interest in renewable electrical energy technologies is reflected by the huge amount of money that governments, such as USA through the Department of Energy (DOE) [4], are investing to research, develop, and deploy breakthroughs able to provide sustainable transportation and energy with high efficiency. However, the intermittence of these electrical energy suppliers and the non-constant electrical power profile during the 24 h period, constrain to couple renewable electrical energy sources with storage, power regulation, and load-leveling systems [5-8]. Within this panorama, electrochemical energy storage systems, and in particular secondary batteries, play a pivotal role for the current and next generation energy applications [5].

Batteries are electrochemical devices able to convert chemical energy into electrical energy, and *vice versa*. The assembly consists of a cathode and an anode electrode that are typically electrical insulated by the interposing of a separator and an electrolyte. The latter allows ions to flow from one electrode to the other. During the discharge of the battery, oxidation reactions occur at the anode side with the consequent production of electrons. Concurrently, at the cathode, electro-active species are reduced as soon as the electrons reach the electrode surface. The generated flux of electrons through the external circuit gives rise to the production of electrical energy, as shown in Figure 1.1. Furthermore, if the reactions are reversible, the battery can be recharged by applying an external voltage across the electrodes. The operation of a battery is based on the difference between the anode and the cathode active material chemical potentials.

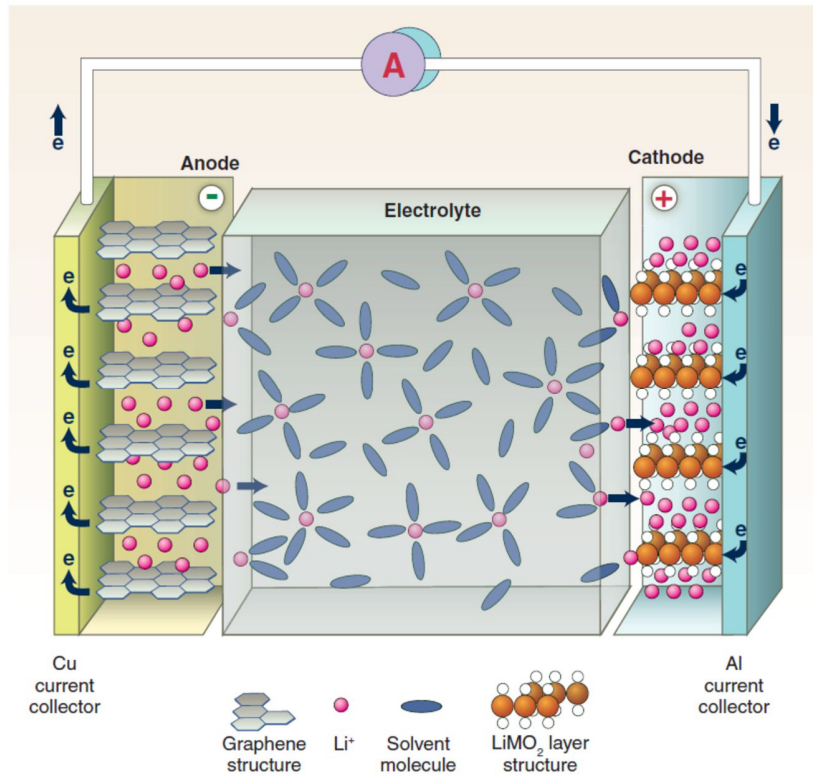


Figure 1.1. Scheme summarizing the main battery components [9].

The history of batteries has started in 1800 (Figure 1.2), when the Italian physicist Prof. Alessandro Volta built the first electrochemical device that was able to produce electrical current. Since then, great efforts have been done, and several milestones have been achieved, giving rise to the development of lithium batteries, the most performing secondary batteries up to now.

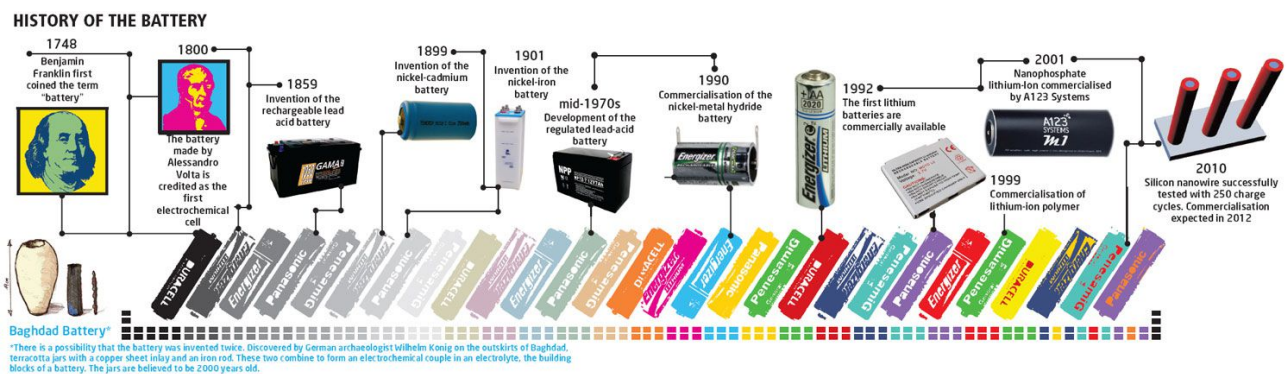


Figure 1.2. Timeline of battery evolution [10].

1.1.1 Principal Battery Parameters

Several operating conditions can be modulated during the charge and discharge processes of a battery, and its performances can be described by different parameters:

- **Operating Voltage:** it is the voltage window in which the battery is running. Typically, by convention, the potential of the anode (*e.g.* Li^+/Li^0 , or $\text{Mg}^{2+}/\text{Mg}^0$) is set to 0.00 V. As a consequence, the standard potential of the cathode active material will rule the operating voltage of the assembled battery device. Obviously, the anode and the cathode active materials should be selected in order to maximize their redox potential difference. Indeed, the highest is the operating voltage of the battery, and the highest value of energy (see later) can be achieved. Nevertheless, when selecting the proper electrode materials, it must be kept in mind that the operating voltage of the battery must be within the Electrochemical Stability Window (ESW) of the used electrolyte, in order to avoid its electrochemical degradation.
- **Specific Capacity:** it describes the total amount of current that can be drained/given from/to a battery in order to fully discharge/charge the device. The standard unit is milliampere hour per gram [$\text{mAh}\cdot\text{g}^{-1}$]. The theoretical specific capacity can be calculated as the product between the total moles of the ions that are oxidized/reduced, the electrons that are exchanged in each redox reaction, and F , the Faraday constant. Then, this value has to be divided by 3.6 and the molecular mass of the active material. For example, LiFePO_4 , a well-known cathode for lithium batteries, has a theoretical specific capacity of: $(1\cdot 1\cdot 96485)/(3.6\cdot 157.76) = 169.89 \text{ mAh}\cdot\text{g}^{-1}$.
- **Specific Power and Power Density:** it is the power (electric current multiplied by voltage, $i\cdot V$) generated by the battery, normalized by the mass (specific), or the volume (density). Its standard unit is typically expressed as milliwatt per gram [$\text{mW}\cdot\text{g}^{-1}$], or milliwatt per cubic centimeter [$\text{mW}\cdot\text{cm}^{-3}$].
- **Specific Energy and Energy Density:** it is calculated by multiplying the given power by the discharge time, normalized by the mass (specific), or the volume (density). It describes the total energy that can be drawn at a certain current per mass unit or volume unit. Its standard unit is typically expressed as milliwatt hour per gram [$\text{mWh}\cdot\text{g}^{-1}$], or milliwatt hour per cubic centimeter [$\text{mWh}\cdot\text{cm}^{-3}$].
- **Columbic Efficiency:** it is the ratio between the discharge capacity and the prior charge capacity, in percentage. It describes the reversibility of the systems, and, in particular, how many electrons can be extracted during the discharge process with respect to how many electrons have been given during the previous charge.

- **Energy Efficiency:** it is calculated as the ratio between the energy that can be released during the discharge and the energy that has been given during the charge. With respect to the coulombic efficiency, this parameter reveals the presence of any overpotential (see later), and so if there is a potential difference between the discharge and the charge processes.
- **Cell Overpotential:** it is the potential difference between the thermodynamic value of an electrode equilibrium potential and the potential at which the redox event is experimentally detected. It is due to the presence of resistances and it gives rise to a loss of energy, released as heat.
- **Rate Capability:** it describes the ability of a battery device to be cycled at different current rates. Typically, the current rate is expressed in term of $x \cdot C$, where C is the current needed to fully discharge the battery in one hour, and x is a number usually comprise between 10 and 0.01.
- **Cyclic Stability:** it shows how the performances of the battery decay among cycling. Typically, specific capacity, specific energy, and coulombic efficiency values are reported vs. the number of cycles.
- **Daily self-discharge:** it describes how much capacity, in percentage, is lost when the battery device is in rest and no current is drained.

1.1.2 Conventional Secondary Batteries

On the basis of the above described battery parameters, a general comparison between the conventional secondary battery technologies can be done, and the results are summarized in Table 1.1 and Table 1.2 [11].

Table 1.1. Main technical characteristics of conventional secondary batteries [11].

Battery type	Operating temperature (°C)	Operating voltage (V)	Cycling times	Specific power (W·kg ⁻¹)	Specific energy (Wh·kg ⁻¹)	Energy capital cost (\$·kWh ⁻¹)
Pb-acid	-5÷40	2.0	200÷2000	180	30÷50	200÷400
Ni-Cd	-40÷50	1.2	1500÷3000	140÷180	35÷60	800÷1500
Ni-MH	-40÷50	1.2	1200÷1800	220	50÷75	200÷730
Na-S	300÷350	2.0	1500÷5000	150÷240	120	300÷500
Li-ion	-30÷60	3.7	3000÷10000	500÷2000	100÷200	600÷2500

Table 1.2. Main operational characteristics of conventional secondary batteries [11].

Battery type	Daily self-discharge (%)	Lifetime (years)	Energy efficiency (%)	Suitable storage duration	Autonomy at power rating	Application field
Pb-acid	0.1÷0.2	5÷15	85÷90	min÷day	s÷h	Distributed power quality support, starting/lighting/ignition services
Ni-Cd	0.1÷0.2	10÷20	60÷90	min÷day	s÷h	Distributed power quality support, automotive support
Ni-MH	5÷20	2÷15	50÷80	-	-	Distributed power quality support, automotive support
Na-S	ca. 0	10÷15	89÷92	s÷h	s÷h	Decentralized power quality support, centralized energy management
Li-ion	0.03	5÷15	ca. 100	min÷day	min÷h	Portable devices, future PHEVs and EVs

Lead-acid (Pb-acid) batteries are the oldest type of secondary electrochemical devices, and are widely used in transport vehicles for engine Starting, Lighting, and Ignition (SLI) and energy storage. Moreover, they find application also as stationary batteries for storage in backup power supplies, thanks their ability to supply high inrush current because of their large specific power. Nevertheless, even if they are very cheap, with a low energy capital cost, the sulfuric acid safety issues and lead toxicity limit the usage of Pb-acid batteries in a wide range of applications.

Nickel-cadmium (Ni-Cd) and Nickel-Metal hydride (Ni-MH) are a widely used battery technology based on the exploit of nickel oxide-hydroxide at the cathode electrode. They belong to the alkaline battery category, and are able to provide an operating voltage of 1.2 V. Ni-Cd and Ni-MH batteries deliver higher specific energy and longer cycling times with respect to Pb-acid, even if they are more expensive. Unfortunately, nickel-based batteries suffer from the so-called “*memory effect*”, thus they need to be completely discharge before charging, in order not to definitely lose their capacity. When Ni-MH batteries have been proposed, using a hydrogen adsorbing alloy instead of the toxic cadmium, Ni-Cd technology rapidly lost market share, thanks also to Ni-MH higher specific energy and lower price. Nevertheless, Ni-MH shows a lower cyclability, lower energy efficiency, and a higher self-discharge with respect to Ni-Cd. Nowadays, nickel-based batteries still have a big slice of the battery market because of their competitive specific energy, cost, lifetime, and, furthermore, wide thermal usage window.

Sodium-sulfur (Na-S) batteries are very attracting because they provide high values of operating voltage, specific power, specific energy, lifetime, energy efficiency, and a low self-discharge, maintaining a quite low energy capital cost. Na-S battery consists of a sodium anode, a sulfur cathode, and a beta-alumina solid electrolyte. It works at high temperatures, between 300 and 350 °C, in order to melt both sodium and sulfur, while the electrolyte remains solid and allows Na⁺ ions to pass through it without allowing anode and cathode to be in contact. Despite the very good performances of Na-S batteries, the high working temperature and the related safety issues make these batteries not so much fascinating, and limit their usage mainly into public transportation and stationary applications.

Lithium-ion (Li-ion) batteries take advantage of the excellent features of lithium [12], such as: i) low redox potential (-3.07 V), that allows to obtain high voltage batteries; ii) a very high theoretical specific capacity (3862 mAh·g⁻¹ for lithium metal and 372 mAh·g⁻¹ for graphite, the mostly used anode in Li-ion batteries); iii) low atomic weight and specific density; iv) low ionic radius which enhances its mobility in the solid state; and v) the formation of a protecting and Li⁺-conducting Solid-Electrolyte Interphase (SEI) on the anode surface, that prevents further undesired decomposition of the electrolyte, which would consume Li ions [13]. Depending on the cathode material used in the battery, devices based on Li-ion technology are able to supply more than 200 Wh·kg⁻¹, for more than 10000 cycles, with a very low daily self-discharge. Thus, Li-ion batteries are the best choice to feed mobile electronic equipment (smartphones, tablets, and laptops) and electric vehicles. Despite all of these described features, lithium batteries bring forth several issues that need to be solved, such as: i) Li-intercalating cathodic materials typically contain toxic, rare, and expensive heavy metals; ii) commercial electrolytes are based on organic carbonates, which are volatile and flammable; iii) practically, Li-metal anode cannot be used due to dendrite formations and safety issue if exposed to moisture; and iv) lithium has a low natural abundance, is present in a few number of countries, and it has a high cost, that will further increase since the depleting of worldwide lithium reserves. Therefore, an urgent need for the development of new materials and new technologies that overcome all of these issues is attracting many scientists, prompting the research towards this topic.

1.1.3 “Beyond Lithium-ion” Batteries

The growth in terms of energy densities, especially gravimetric, of lithium-ion batteries is quite limited. Thus, the development of a new alternative battery chemistry with the potential for higher performances than Li-ion is needed. Examples are Zn-air [14], Li-air [15], Li-S [16], or other multivalent metals, such as Mg-ion [17] and Al-ion [18]. Li-ion devices with dramatically innovative electrolytes and electrodes (*e.g.* solid-state polymer or inorganic electrolytes, Li-metal anodes, or high-voltage cathodes) belong to the so called “*beyond Li-ion*” category too [19].

In order to exceed the limitations of the old generation of Li-ion batteries, the aim of this Ph.D. project has been focused on the development of new materials belonging to the class of “*beyond Li-ion*” batteries, such as: i) solid polymer electrolytes (SPEs) stable against lithium metal anode [20]; ii) glass-forming ion conducting electrolytes for Li batteries [21]; iii) high-voltage cathodes for Li-ion batteries [22]; iv) ionic liquid (IL)-based electrolytes for Mg-ion batteries [23]; and v) graphene oxide-based high power cathode for Mg-ion batteries. All the proposed materials exhibit several interesting features that overcome the issues of the state of the art electrolytes and electrodes for lithium and magnesium secondary batteries, as described in details in the following chapters.

1.2 Lithium Batteries

In this section a detailed overview on the state of the art materials implemented in classic lithium secondary batteries is given. The focus is set to highlight the limits that characterize the electrolytes and electrode materials used in lithium batteries up to date.

1.2.1 Electrolytes for Li Batteries

Electrolytes are typically classified according to their physical state at operating conditions. Thus, liquid, gel, glassy, solid (ceramic and polymeric), and hybrid electrolytes can be found. In order to be appealing, an electrolyte should show suitable features, such as: i) high ionic and negligible electronic conductivities; ii) high thermal stability, low flammability and low vapor pressure; iii) easy of processing and low cost; iv) wide electrochemical stability window and low deposition/stripping overpotentials; and v) high stability in contact with the electrodes.

1.2.1.1 Liquid Electrolytes for LIBs

The liquid electrolyte used in lithium-ion devices generally consists of a lithium salt (LiX) and a non-aqueous solvent. Water is avoided because: a) it reacts violently with lithiated graphite

(anode) producing explosive hydrogen gas; b) it has a low electrochemical stability window ($0 \div 1.23$ V); and c) it can be used only within a narrow thermal window ($5 \div 80$ °C). Typically, a mixture of organic carbonates such as ethylene carbonate (EC) or dimethyl carbonate (DMC) is used as solvent, and lithium hexafluorophosphate (LiPF_6) or lithium perchlorate (LiClO_4) salts are dissolved in it to provide the lithium ion source. The salt concentration depends on the device application (*e.g.* low temperature batteries require a low viscosity electrolyte; thus, a low salt concentration is preferred). Despite liquid electrolytes show high conductivity values ($> 10^{-3} \text{ S}\cdot\text{cm}^{-1}$), they are volatile, flammable, they react with lithium metal anode creating a passivating Solid-Electrolyte Interphase (SEI), they are electrochemically stable up to only *ca.* 4.5 V vs. Li/Li^+ , and salts are not highly stable and hydrolyze in presence of traces of water [24, 25]. In particular, the flammability of the electrolyte is the mainstream concern for lithium batteries, and several accidents have been reported in the last years, as shown in Figure 1.3.



Figure 1.3. Recent accidents regarding lithium battery explosions reported in the newspapers.

Furthermore, several issues related to the leakage and corrosion of the battery case need to be solved and, more importantly, the use of classic liquid electrolyte in high temperature applications cannot be realized. The conventional solvents and salt used in liquid electrolytes for lithium batteries, together with their physico-chemical characteristics, are summarized in Table 1.3 and Table 1.4.

Table 1.3. Conventional solvents for liquid electrolytes [25].

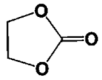
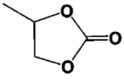
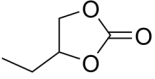
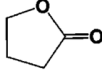
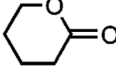
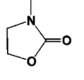
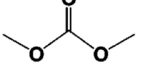
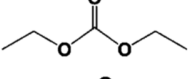
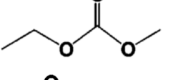
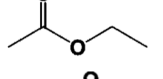
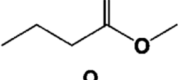
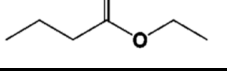
Solvent	Structure	MW / g·mol ⁻¹	T _m / °C	T _b / °C	η / cP (25 °C)	ε (25 °C)	Dipole Moment / D	d / g·cm ⁻³ (25 °C)
EC		88	36.4	248	1.90	89.78	4.61	1.321
PC		102	-48.8	242	2.53	64.92	4.81	1.200
BC		116	-53	240	3.2	53	-	-
γBL		86	-43.5	204	1.73	39	4.23	1.199
γVL		100	-31	208	2.0	34	4.29	1.057
NMO		101	15	270	2.5	78	4.52	1.17
DMC		90	4.6	91	0.59	3.108	0.76	1.063
DEC		118	-74.3	126	0.75	2.805	0.96	0.969
EMC		104	-53	110	0.65	2.958	0.89	1.006
EA		88	-84	77	0.45	6.02	-	0.902
MB		102	-84	102	0.6	-	-	0.898
EB		116	-93	120	0.71	-	-	0.878

Table 1.4. Conventional salts for liquid electrolytes [25].

Salt	MW / g·mol ⁻¹	T _m / °C	T _{dec.} / °C (in solution)	Al-corrosion	σ / S·cm ⁻¹ (1.0 M, 25 °C)	
					in PC	in EC/DMC
LiBF ₄	93.9	293	>100	N	3.4·10 ⁻³	4.9·10 ⁻³
LiPF ₆	151.9	200	ca. 80	N	5.8·10 ⁻³	1.07·10 ⁻²
LiAsF ₆	195.9	340	>100	N	5.7·10 ⁻³	1.11·10 ⁻²
LiClO ₄	106.4	236	>100	N	5.6·10 ⁻³	8.4·10 ⁻³
Li Triflate	155.9	>300	>100	Y	1.7·10 ⁻³	-
Li Imide	286.9	234	>100	Y	5.1·10 ⁻³	9.0·10 ⁻³

1.2.1.2 Solid-State Electrolytes for LIBs

Several disadvantages of the liquid electrolyte can be overcome using solid-state electrolytes (SSEs) [26]. Indeed, they show: i) high thermal stability; ii) they do not require systems for liquid containment; iii) wide electrochemical stability window; iv) they can be easily processed in several geometries, depending on the application; and v) they do not require the use of separators, reducing the cost of the battery and lowering the number interface resistances. Thus, the use of SSEs is regarded as a fundamental solution to the safety issues. Furthermore, by suppressing the growth of dendrites, lithium metal anode can be used, resulting in an increased energy density secondary battery [27]. However, there are still many challenges to be addressed before the development of a practical SSE, such as its low ionic conductivity, high cost, inefficient electrolyte-electrode interface, and oversensitivity [28-30]. In SSEs the conductivity mechanism generally occurs by hopping of the mobile ions through the vacancies. Thus, these SSEs are usually used at high temperature. Nevertheless, recent advancements demonstrated that a high conductivity (> 10⁻² S·cm⁻¹) can be achieved even at low temperatures, as shown in Figure 1.4 [31].

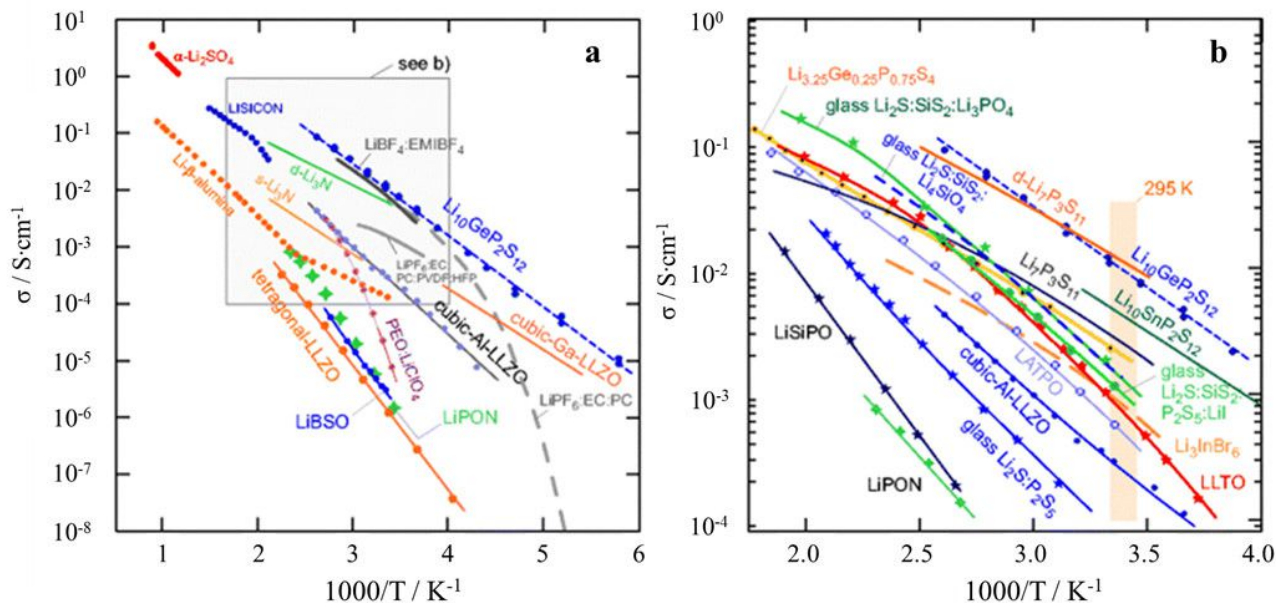


Figure 1.4. Temperature dependence of the conductivity of various solid-state inorganic electrolytes (a). Magnification of the conductivities at near ambient temperature (b) [31].

Up to date, several families of SSEs have been proposed because of their potential application for next-generation batteries. Representative examples have been selected and an overview on their characteristics is given.

NASICON-Type SSEs

Na super ionic conductor (NASICON)-type has a general formula $NaA_2^{IV}(PO_4)_3$, with $A^{IV} = Ge, Ti, \text{ or } Zr$, and is typically obtained through a high-temperature solid-state reaction. This electrolyte has been firstly proposed by Goodenough and co-workers in 1976 [32]. NASICON structure consists of MO_6 octahedra and PO_4 tetrahedra units that share a corner, forming a 3D coordination framework [33]. Na^+ ions are hosted within the interstitial sites and percolate along the c -axis of the NASICON structure. A Li^+ conductor NASICON-type SSE can be easily obtained by substitution of sodium ions with lithium ions, maintaining its original structure. The conductivity mechanism occurring in this material is ruled by two different aspects: the site percolation and the bottleneck size. The lithium ion conduction activation energy generally decreases linearly with the bottleneck size. Thus, the optimization of the dimension of the diffusion channels for Li^+ conduction is the principal interest to obtain a high conductivity value. The typical room-temperature conductivity of these SSEs ranges between 10^{-9} and $10^{-3} S \cdot cm^{-1}$. The main drawback of these materials is related to the easy

reduction of the A^{IV} metal by the metallic lithium, limiting their possible usage only to Li-ion batteries.

Garnet-Type SSEs

Garnet-type SSEs are characterized by a $Li_3M_2(LaO_4)_3$ general formula, with $M = Zr, Ta, \text{ or } Nb$. Each metal (*i.e.* Li, M, and La) is hosted in an eight, six, and four oxygen coordinated cation site, respectively [34]. The synthesis consists of a high-temperature solid-state reaction, where the sintering temperature seems to be directly correlated to ionic conductivity of the obtained SSE [35]. The high conductivity demonstrated by these electrolytes is originated by the static repulsion between lithium ions hosted in the octahedral sites arising by a short Li-Li distance [36]. The conductivity values reached by Garnet-type SSEs are up to $10^{-3} \text{ S}\cdot\text{cm}^{-1}$, that, together with the chemical stability towards lithium metal and the wide electrochemical stability window (6 V vs. Li/Li⁺), makes these materials one of the most promising SSE. Nevertheless, they are highly reactive against adsorbed H₂O and CO₂ [37]. Thus, there is still space for improvements.

LISICON-Type SSEs

Both Li super ionic conductor (LISICON)-type and thio-LISICON-type SSE have an analogous crystalline structure to that of $\gamma\text{-Li}_3\text{PO}_4$ compound, where all the cations are in a tetrahedral coordination [38]. In general, LISICON compounds have a low conductivity at room temperature ($10^{-6} \text{ S}\cdot\text{cm}^{-1}$) and are also very reactive toward metallic lithium and CO₂. The replacement of O²⁻ ions with S²⁻, proposed by Kanno *et al.* in 2011 [39], gives rise to an extremely high Li⁺ room-temperature conductivity ($1.2\cdot 10^{-2} \text{ S}\cdot\text{cm}^{-1}$). This remarkable conductivity is the result of a weakened binding between Li ions and the host framework, together with an enlargement of the ion-transport channels.

Perovskite-Type SSEs

Perovskite-type SSEs have a general formula ABO_3 ($A = La, Sr, \text{ or } Ca$, and $B = Al \text{ or } Ti$) and have been proposed by Takahashi and Iwahara in 1971 [40]. Lithium ions can substitute part of the A atoms, creating a $Li_{3x}A_{(2/3)-x}BO_3$ system; the structure is cubic, where the octahedrally coordinated B atoms occupy the corner of the cube, while the A site in the center of the cube hosts either a A^{2+} ion, a Li⁺ ion, or is left vacant [41]. The conductivity values showed by these electrolytes is determined by

the concentration of lithium ions, vacancies, and the interactions between each other. Despite the high conductivity reached by this type of materials ($10^{-3} \text{ S}\cdot\text{cm}^{-1}$, [41]), the reduction of Ti^{4+} to Ti^{3+} when the SSE is faced against lithium metal largely limits their applications.

Sulfide SSEs

Sulfide SSEs are typically in the glass state, and are obtained following a low temperature heat treatment of glassy powders [27]. They are composed by three different components: i) lattice-forming species, such as SiO_2 and P_2S_5 ; ii) lattice-modifying species, such as Li_2O or Li_2S ; and iii) a lithium salt. The first component forms macromolecular chains through intra-chain bonds. The lattice-modifying species are able to interact with the inorganic network created by the lattice-forming species, breaking the M-O or M-S bonds and thus introducing ionic bonds. The temperature dependent conductivity behavior of these materials follows the Arrhenius law in the whole temperature range, showing values comprised between 10^{-2} and $10^{-5} \text{ S}\cdot\text{cm}^{-1}$ [42]. The main drawback of these SSEs is its chemical instability in air and the consequent evolution of the dangerous H_2S gas [43].

Antiperovskites-Type SSEs

In 2015 a novel family of lithium-conducting antiperovskites SSEs has been proposed by Deng and co-workers, with a general formula Li_3OX ($\text{X} = \text{Cl}$, or Br) [44]. In these materials oxygen atoms occupy the octahedral cavities, while the halogen ions, or a mixture of them, are hosted in the dodecahedral centers [45]. A typical synthesis consists of a solid-state reaction where precursors are in the molten state. It is demonstrated that lithium ion vacancies and the anion sublattice disorder are the two main driving forces for an enhanced conductivity mechanism [46]. Furthermore, the antiperovskites crystalline structure can be easily modulated by halogen chemical substitution, inducing an improved ionic conductivity. These materials show a good mechanical strength, a high stability when faced to a lithium metal anode, and a high conductivity (10^{-5} – $10^{-8} \text{ S}\cdot\text{cm}^{-1}$). Nevertheless, the sensitivity of these materials toward the presence of moisture has to be improved.

1.2.1.3 Polymer Electrolytes for LIBs

Since in SSEs the counterions of the active species are blocked in the crystalline structure, SSEs are essentially single-ion conductors. Thus, ceramic and glassy solid-state electrolytes have a clear

advantage with respect to classic polymer electrolytes. Nevertheless, the bad contact at the interface between the electrolyte and the electrodes, and the low resistance to mechanical stresses, together with the chemical instability, are the main issues that limit the application of ceramic and glassy SSEs in commercial devices. On the other hand, Polymer Electrolytes (PEs), and in particular high molecular weight PEs, seem to be the optimal candidates for the realization of a full solid-state room temperature secondary battery device. Indeed, their plastic characteristics allow for an intimate contact between the electrolyte layer and the electrode surface, maintaining a constant connection during the electrochemical testing. Furthermore, even if they show a conductivity 100 or 1000 times lower than that of ceramic electrolytes, PEs can be obtained as very thin-layer films, reducing the resistance of the material.

The family of PEs includes several classes of materials, which are distinguished by the nature of the system [47]: i) classic *Polymer Electrolytes* (PEs) – solid or liquid macromolecular systems capable to dissolve suitable salts; ii) *Gel Polymer Electrolytes* (G-PEs) – an inert polymer matrix impregnated of a solution consisting of a salt dissolved into a polar liquid; iii) *Plasticized Polymer Electrolytes* (P-PEs) – polymer electrolytes doped with small amounts of a solvent characterized by a high dielectric constant or an ionic liquid; iv) *Ionic Rubber Polymer Electrolytes* (IR-PEs) - high molecular weight polymer mixed with a liquid electrolyte; v) *Ion Conducting Polyelectrolytes* (IC-P) - polymer electrolytes in which the counter ions of the active species (anions or cations) are covalently bonded to the polymer backbone; and vi) *Hybrid Inorganic–Organic Polymer Electrolytes* (HIO-PEs) – electrolytes where inorganic atoms are introduced in the polymer matrix of hybrid PEs [48]. The latter class of compounds is in turn divided into three subgroups: a) *three-Dimensional Hybrid Inorganic–Organic Networks As Polymer Electrolytes* (3D-HION-APEs) – three dimensional ion-conducting materials, where metal or nonmetal atoms act as bridges between macromolecules [49]; b) *Zeolitic Inorganic–Organic Polymer Electrolytes* (Z-IOPEs) – where inorganic clusters, formed by the aggregation of two or more inorganic coordination complexes, are bridged by organic macromolecules [50, 51]; and c) *Hybrid Gel Electrolytes* (HGEs) – obtained from inorganic or organometallic precursors bearing an ion-conducting cation and low molecular or macromolecular liquids [52].

In PEs the temperature dependent conductivity behavior generally follows the Vogel-Tamman-Fulcher law instead of the Arrhenius law. However, depending on the characteristics of the PE,

different trends can be often observed: i) VTF behavior at high temperatures and Arrhenius behavior at low temperatures; ii) two Arrhenius trends with different slopes delimited by the glass transition (T_g) of the material; and iii) VTF behavior at low temperatures ($T < T_g$) and Arrhenius behavior at high temperatures. This variability can be assigned to the fact that the coordination of lithium ions to the polymer has to be broken to allow the conductivity mechanism to occur. This event is assisted by the segmental motions of the polymer chains, which contribute to the overall migration process of cations where empty spaces are so formed. Thus, Li^+ ions can be exchanged under the effect of an electric field. When these kinds of processes occur, the conductivity mechanism is no longer a pure hopping of lithium ions between coordination sites, but the polymer relaxations have a pivotal role on the long-range charge migration process. Furthermore, in plasticized PEs, the presence of dopant domains can increase the number of percolation pathways for the diffusion of cations, improving the conductivity of the electrolyte.

The most studied polymer for electrochemical applications is polyethylene oxide (PEO). In this material lithium cations are coordinated by the oxygen functionalities of the ethereal chains, and they can be exchanged along and between different polymer chains through a hopping process. The first report on the alkali metal ionic conductivity in PEO-based polymer electrolytes has been proposed by Wright in 1975 [53]. PEs with oxygen functionalities seem to be the right choice to obtain an efficient complexation and dissociation of Li^+ , due to the presence of a partially amorphous phase and an optimal distance between oxygen atoms, allowing the creation of a coordinating cage around the cation [54]. The main drawbacks of classic PEs are the low room temperature conductivity (*ca.* 10^{-5} – 10^{-6} $\text{S}\cdot\text{cm}^{-1}$) and quite low transference number (*ca.* 0.2–0.3). The best way to increase the lithium ion transference number (t_{Li^+}) in PEs is to block the Li^+ coordinating ion (*e.g.* O^{2-}) through a direct covalent bond to the polymer backbone [55] or to increase the size of the anion in order to reduce its conductivity, due to a higher steric hindrance. In these ways, a single-ion conductor polyelectrolyte can be obtained, and the measured conductivities are completely attributed to the exchange of only lithium cations. Unfortunately, polyelectrolytes typically have lower conductivities with respect to classic PEs. Indeed, in polyelectrolytes the strong dipole moments of the side chains can approach each other because of the dipole–dipole electrostatic interactions, which are stronger than those of van der Waals

interactions. These dipole–dipole interactions act to localize the free ions, reducing their conductivity [56].

1.2.1.4 Ionic Liquid-based Electrolytes for LIBs

Ionic Liquids (ILs) are salts with a melting temperature lower than 100 °C. Furthermore, if they are in the liquid state even at room temperature, they are classified as Room-Temperature Ionic Liquids (RTILs). ILs typically show: i) a very low volatility, high thermal stability, and a very low flammability; ii) high electrochemical stability up to 6.0 V; iii) high conductivity and high ion concentration; iv) easiness and modulation of synthesis, which allow to obtain the desired functionalities in the cation and anion molecule; and v) scalability of the synthesis and high price reduction when high amounts of IL are synthesized [57]. Probably, the low vapor pressure and low flammability are the main interesting features that make these compounds appealing for the production of highly safe and durable devices.

Depending on their chemical composition, ILs can be distinguished into three different classes: protic, aprotic, and zwitterionic [58]. Aprotic ionic liquids generally have a low melting point, due to a low efficiency in packing large and irregular organic cations with small inorganic anions. Typically, ILs can be used for applications in batteries, IL-based fuel cell, and supercapacitors, respectively.

The generally low melting temperature of all ionic liquids is the result of a weak interaction between anions and cations, due to the high steric hindrance of the cations and the great charge delocalization in the anions. The prototype of the ILs is obtained by the combination of an imidazolium cation (*e.g.* 1-ethyl-3-methylimidazolium, EMIm⁺) and a N,N-bis(trifluoromethanesulfonyl)imide (TFSI⁻) anion [59]. A liquid with a conductivity similar to that of classic liquid electrolytes and a thermal stability up to 350 °C can be obtained, thanks to the presence of two strongly electron attractor groups (CF₃SO₂) bonded together through a S–N–S bond.

Several ILs have been synthesized and proposed in the last years, and are now available with high degrees of purity [60]. Generally, the most used cations are in the type of: i) aromatic cyclic amines such as pyridinium and imidazolium; ii) saturated cyclic amines like piperidinium and pyrrolidinium; iii) quaternary ammonium salts R₄N⁺; and iv) sulfonium and phosphonium (R₃S⁺

and R_4P^+). Coordinated to these cations, there are commonly found: i) TFSI⁻; ii) BF₄⁻; and iii) PF₆⁻ anions. Small anions such as halides (Cl⁻, I⁻, F⁻) give rise to ionic liquids with typically high melting temperatures, due to their little size and symmetric charge distribution. Nevertheless, propyl, methylimidazole chloride (PrMeImCl) is one of the few exceptions. On the contrary, BF₄⁻ anion is able to generally form RTILs with both imidazolium and pyrrolidinium cations. The same ability is shown by TFSI⁻, which is able to form RTILs with all cations except with the spherical R₄N⁺. ILs typically have a density greater than that of water, but within the range 1.2÷1.5 g·mL⁻¹. The viscosity of this class of compounds is higher than water too (at 25 °C $\eta_{H_2O} = 0.89$ cP, $\eta_{RTILs} = 30-50$ cP).

ILs show a room temperature conductivity in the range between 10⁻² and 10⁻⁴ S·cm⁻¹, that is *ca.* two orders of magnitude lower than the values exhibit by liquid aqueous electrolytes (KOH, H₂SO₄, and NH₄Cl) used in alkaline, lead-acid, and Leclanché batteries, respectively. Nevertheless, if compared to conductivities typical of lithium salts dissolved in organic carbonate solvents, IL-based electrolytes are one order of magnitude better than them. As described before, in lithium conducting PEs the conductivity mechanism occurs by cation hopping between coordination sites, assisted by polymer chains segmental motions. When an ionic liquid is added to the PE, new conductivity mechanisms are possible [61]. Indeed, the IL molecules can influence the migration process, either by Li⁺ complexation favoring the intrachain charge exchange, or by direct assisting the hopping mechanism with its relaxation motions. These two latter events can be also observed in pure ionic liquid-based electrolytes: IL macroaggregates can behave like a polymer unit, and Li⁺ ions, that are delocalize within the macroaggregate, are exchanged between neighborhood domains. This conductivity mechanism is assisted by both the relaxation motions of the single IL molecules and the fluctuations of the macroaggregates.

The electrochemical stability window (ESW) is the difference between the cathodic and anodic stability limit. In IL, the anodic limit is due to the oxidation of the anion, while the cathodic limit is typically related to the reduction of the organic cation. Ionic liquids generally show a wide ESW, that ranges from *ca.* 2 to 6 V. The lower is typical of halogen ions (*e.g.* F⁻, Br⁻), while anions like TFSI⁻ are generally oxidized at a higher potential. Thus, the ESW can be easily modulated by changing the characteristics of the anion and the cation that make up the IL.

Thanks to the high concentration of ions and their high mobility, together with the high conductivity values, ILs are used as electrolytes in a wide range of application, such as rechargeable batteries, fuel cells, solar cells, and capacitors [62, 63]. In particular, IL based on 1-ethyl-3-methylimidazolium (EMIm⁺), trimetilpropilammonio (TMePrA⁺), N-methyl-N-propylpyridinio (MePrPi⁺), and N-methyl-N-propylpyperidinium (MePrPp⁺) cations and TFSI⁻ anion have been used in secondary batteries applications [64, 65]. Full cell secondary battery devices have been obtained such as Li₄Ti₅O₁₂|EMImBF₄-LiBF₄|LiCoO₂, that works at 2.0 V [66], and Li|MePrPpTFSI-LiTFSI|LiCoO₂, with a working potential of *ca.* 3.9 V [67]. Even if in the both cases a liquid electrolyte is used, the IL-based electrolytes have the advantage of being a completely non-volatile compound with a high electrochemical stability. Thus, safer secondary battery devices have been obtained if compared to those based on conventional organic carbonate solvents.

1.2.2 Cathodes for Li Batteries

1.2.2.1 Chalcogenides

During the seventies, an important discovery about the ability of layer-structured dicalcogenides to intercalate small molecules and ions has been presented [68]. Among all the studied materials, titanium disulfide is the most interesting, because of its low density and the high lithium diffusivity within its structure. Moreover, this cathode material allows to intercalate up to one mole of lithium ions *per* mole of material (from TiS₂ to LiTiS₂) in a reversible way, without structural variations, and therefore without energy losses due to rearrangements or crystalline nucleation [69]. Another important chalcogenide studied for these applications is niobium triselenide, which is able to intercalate up to three lithium moles *per* mole of material, forming Li₃NbSe₃ [70]. Unfortunately, both the chalcogenides compounds work at a quite low potential, *ca.* 2.0 V, giving rise to very low specific energies.

1.2.2.2 Vanadium Oxides and Derivatives

Vanadium oxides have been the first examples of layered oxides designed for lithium batteries. The main advantage of these materials is the possibility to reduce vanadium by three oxidation states, from V⁵⁺ to V²⁺, thus leading to a hypothetical greater capacity. However, it has been demonstrated that the structural variations occurring in the material during these events are a great issue. Indeed, V₂O₅ allows for a reversible intercalation of one mole lithium ions, with a phase transition from α to δ , between 3.5 and 2.5 V; the subsequent intercalation, where other two moles of lithium

ions are hosted within the structure, occurs at 1.5 V, which, however, gives rise to the irreversible formation of the γ phase [71]. Several studies have been carried out on thin deposits of vanadium oxide in order to reveal its performances as the structure changes; films can be obtained by laser pulsed deposition, vacuum deposition, induced plasma, anodic, and thermal metal oxidation [72]. The variation in performances as a function of the thickness of the deposited layer is significant, reaching a maximum specific capacity of $450 \text{ mAh}\cdot\text{g}^{-1}$ [73]. In the family of vanadium oxides, lithium trivanadate (LiV_3O_8) has also been studied for lithium intercalation. This material is able to intercalate up to 4.5 moles of lithium ions for each mole of cathode, with a specific capacity of $419 \text{ mAh}\cdot\text{g}^{-1}$ [74]. Finally, the $\text{Li}_3\text{V}_2(\text{PO}_4)_3$ compound has been proposed; lithium vanadium phosphate has a monoclinic structure and intercalates up to three moles of lithium ions, at a potential between 3.5 and 4.5 V, with a specific capacity of $160 \text{ mAh}\cdot\text{g}^{-1}$ [75]. Some of the vanadium-based cathode materials here described are represented in Figure 1.5.

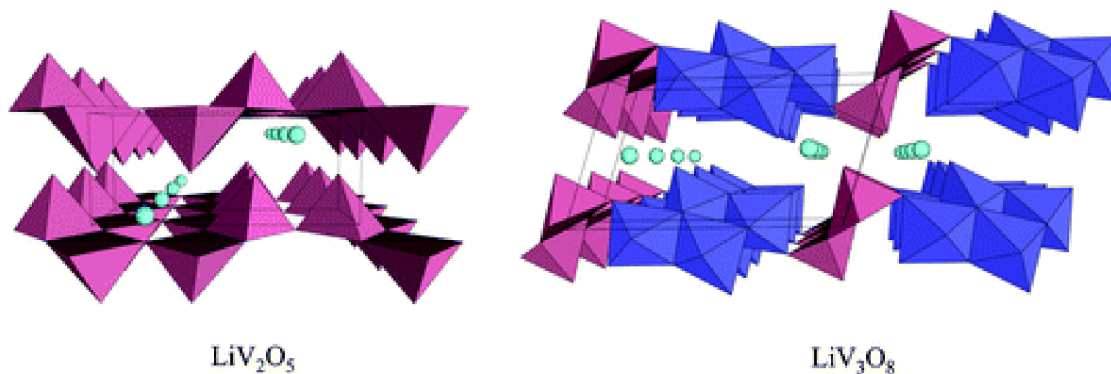


Figure 1.5. Crystal structure of LiV_2O_5 and LiV_3O_8 . Intercalated lithium ions are represented in green [76].

1.2.2.3 Lithium Cobalt Dioxide

The LiCoO_2 compound has a layered structure that allows the extraction and reinsertion of the lithium ions within the crystal, during its operation as a cathode. The structure is a cubic close-packed (ccp) (see Figure 1.6), which rearranges in hexagonal close-packed (hcp) after the complete extraction of lithium ions [77, 78]. Several structural phases with different levels of reticulation distortion are obtained during the lithium extraction reaction.

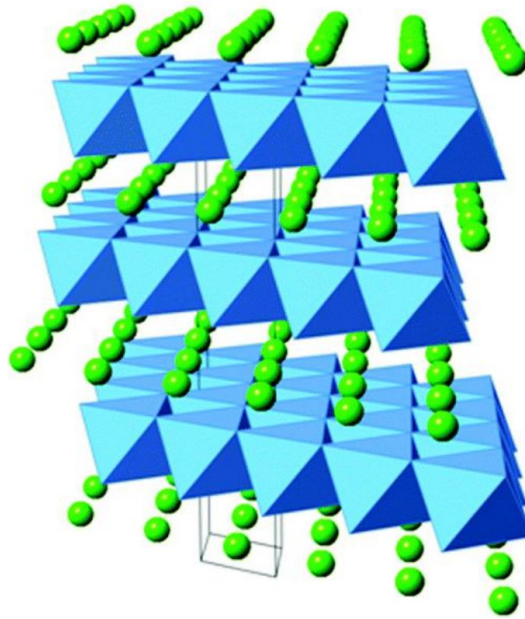
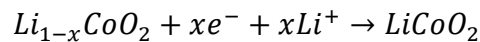


Figure 1.6. α -LiCoO₂ structure, lithium ions are represented in green, CoO₆ in light blue [79].

During the discharge the reaction that takes place is:



The complete removal of lithium ions corresponds to a theoretical specific capacity of 274 mAh·g⁻¹. Structural restrictions do not allow for an extraction of more than 0.5 moles of lithium ions per mole of cathode, giving rise to a practical specific capacity of 120-140 mAh·g⁻¹, in a potential range of 3.0÷4.0 V [80]. This material has been used as cathode by Sony in the first commercialized secondary lithium battery in 1990. Since then, it is one of the most used cathode for portable electronic applications [81]. Several improvements can be obtained by increasing the pyrolyzing temperature up to 850 °C, or by covering the surface with Al₂O₃ particles. The high-temperature synthesis gives rise to a material with a specific capacity of 150 mAh·g⁻¹ [82], while alumina coating results in a specific capacity of 174 mAh·g⁻¹, unfortunately for a low number of cycles (*ca.* 50), in a wide potential range of 2.75÷4.40 V [83]. The main issues of this material, that prompt the research towards the proposal of new materials, is the low abundance, high cost, and high toxicity of cobalt [84], especially in the case of high demanding large batteries like those for the automotive [85].

1.2.2.4 Lithium Nickel Dioxide

LiNiO₂ has the same structure of lithium cobalt oxide, but it has not the same widespread usage like LiCoO₂. The real composition is not known, even if the hypothesis of a nickel-rich compound

($\text{Li}_{1-y}\text{Ni}_{1+y}\text{O}_2$) is the most reliable, where nickel ions are occupying lithium sites in between the layers of the cathode. Thus, the lithium ion diffusion coefficient is quenched, and so do the battery performances. Furthermore, when lithium ions are extracted, the material becomes instable in contact with organic solvents, which are composing the electrolyte. A second mole of lithium ions can be hosted by this material, reaching a $\text{Li}_{1.8-y}\text{Ni}_{1+y}\text{O}_2$ composition, which is a mixture of LiNiO_2 and Li_2NiO_2 [86].

1.2.2.5 *Lithium Manganese Oxide*

This compound has a molecular formula LiMn_2O_4 and a spinel structure, with oxygen atoms in a ccp configuration, and metal ions hosted in the octahedral and tetrahedral cavities. It shows two different plateaus during discharge, at 4.0 and 3.0 V. Its low cost and high stability make it a fascinating cathode for electric vehicles. Nevertheless, the main issue of this material is the high solubility of manganese ions in the electrolyte, especially at high temperatures, which reduces the capacity of the cathode during time [87].

1.2.2.6 *Lithium Manganese Dioxide*

The low toxicity and low cost of this material (Figure 1.7) have attracted the attention of scientists. Unfortunately, this cathode is not stable at the typical high temperatures needed for the synthesis, thus it has to be obtained by ion exchange from NaMnO_2 [88], or following a low-temperature hydrothermal synthesis [89]. The principal problem of this material, which limits its usage in secondary batteries, is the conversion, at 150 °C or among cycling, to the more stable LiMn_2O_4 compound. The doping with several ions has been studied to stabilize its initial form and to limit the conversion reaction [90].

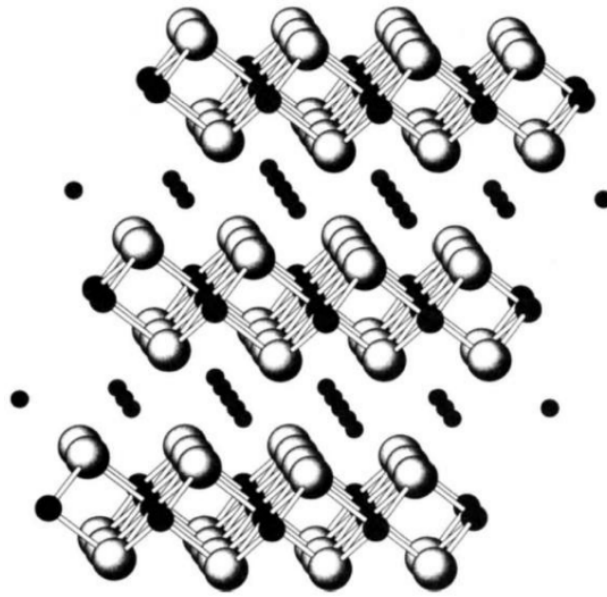


Figure 1.7. LiMnO_2 structure. Oxygen ions are represented in white, large black atoms correspond to manganese ions, and lithium is represented as small black atoms [88].

1.2.2.7 *Lithium Nickel-Cobalt Dioxide*

Compounds at different Ni/Co molar ratios can be obtained, and changes in these values result in modification of the cathode electrochemical properties, such as stability and ability to reversible insert lithium ions. In particular, in $\text{LiNi}_{1-y}\text{Co}_y\text{O}_2$, the presence of nickel ions in the lithium sites is reduced by the addition of cobalt, and can be neglected for $y > 0.3$. Thus, higher values of lithium ion diffusivity can be obtained by cobalt doping [84].

1.2.2.8 *Lithium Manganese-Cobalt Dioxide*

Several compounds where manganese and cobalt ions coexist within the same oxide structure, with a formula $\text{LiMn}_{1-y}\text{Co}_y\text{O}_2$ ($0 \leq y \leq 0.5$), have been reported in literature. They have the same structure of $\alpha\text{-NaFeO}_2$, and they tend to convert to the spinel structure during cycling. These materials can be synthesized by ion exchange between sodium and lithium, starting from sodium compounds with the desired cobalt-manganese ratio. A specific capacity of $200 \text{ mAh}\cdot\text{g}^{-1}$ can be obtained during the first 20 cycles, in a working potential range of $2.8\div 4.8 \text{ V}$ [91, 92].

1.2.2.9 *Lithium Manganese-Nickel Dioxide*

Different ratios between manganese and nickel have been studied to obtain the best performances, reaching a specific capacity of $150 \text{ mAh}\cdot\text{g}^{-1}$. The typical deterioration of manganese is diminished by synthesizing the materials at high temperatures, between $700 \text{ }^\circ\text{C}$ and $1000 \text{ }^\circ\text{C}$ [84].

1.2.2.10 Lithium Nickel-Manganese-Cobalt Dioxide (NMC)

Up to now, the most performing cathode materials for lithium battery applications are the mixed nickel-manganese-cobalt compounds (NMC). In these cathodes, nickel gives a high specific capacity to the material, due to the oxidation from 2+ to 4+, together with the cobalt ion which is oxidized from 3+ to 4+. Manganese ions, on the other hand, do not participate in the electrochemical events, but give stability to the structure [93, 94]. Thus, a high percentage of nickel increases the specific capacity of the material (*i.e.* 160 mAh·g⁻¹ for NMC-111, LiNi_{0.33}Mn_{0.33}Co_{0.33}O₂, and grows to more than 200 mAh·g⁻¹ for NMC-811, LiNi_{0.80}Mn_{0.10}Co_{0.10}O₂). The working potential for these cathodes is *ca.* 3.7 V vs. metallic lithium [94]. NMC are the leading materials in the field of lithium battery cathodes, and they are currently used in the electric vehicles available on the market [95]. Recent studies have demonstrated that these materials can be lithium- and manganese-enriched (LMR-NMC), showing capacities up to 300 mAh·g⁻¹ at 3.4 V. Nevertheless, they suffer from important instability problems, which lower their cycle life and durability [94].

1.2.2.11 Lithium Nickel-Cobalt-Aluminum Dioxide (NCA)

The last widely studied layered metal oxide material is the nickel-cobalt-aluminum oxide, NCA (LiNi_{0.80}Co_{0.15}Al_{0.05}O₂). It shares analogies with NMC by offering high specific energy, reasonably good specific power, and a long lifespan. Less impressive characteristics are the safety and the cost of these cathodes. A specific capacity of 200 mAh·g⁻¹ [94] and cyclability up to 1000-1500 cycles are demonstrated [95]. They are actually the first choice after NMC in the automotive field [95].

1.2.2.12 Lithium Nickel Phosphate

This cathode (LiNiPO₄) belongs to the olivine family, together with LiFePO₄ e LiCoPO₄ (see Figure 1.8). The main advantages of this material are the low cost, environmental friendliness, the stability, and safety. These characteristics are given by the stable olivine structure, which do not show any structural transition during the charge and discharge of the material. Unfortunately, this cathode has a low electrical conductivity, that forces to add high amounts of graphite in the cathodic mixture, and reduces the rate capability. Furthermore, the Ni³⁺/Ni²⁺ redox events occur at 5.1 V vs. lithium, which is beyond the stability of the common electrolyte for lithium batteries. Thus, its application in commercial devices is far from being made. Up to now, the extraction and reinsertion reactions of Li⁺ are partially reversible, and a practical capacity of only 50 mAh·g⁻¹ has been demonstrated [96, 97].

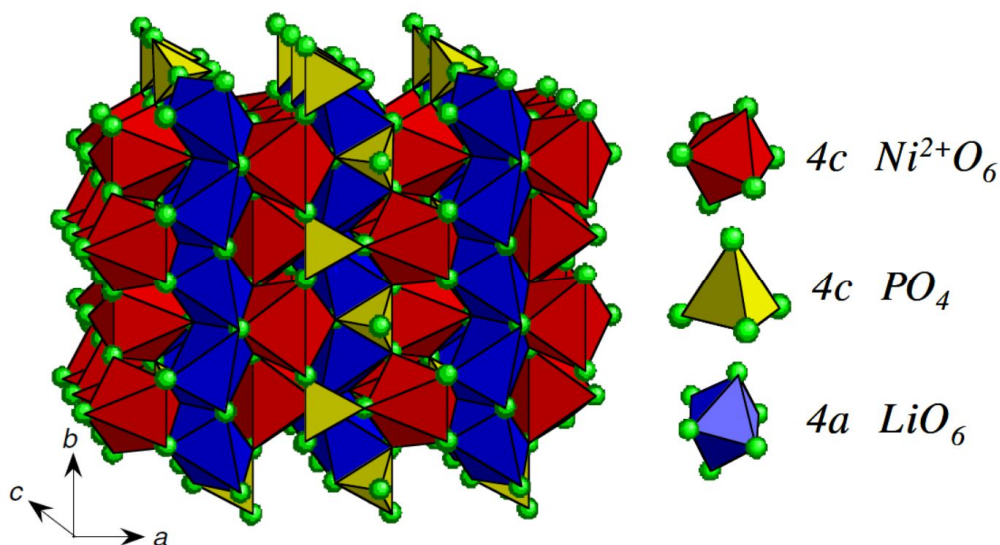


Figure 1.8. Olivine structure of LiNiPO_4 , analogous to that of LiFePO_4 and LiCoPO_4 [98].

1.2.2.13 Lithium Cobalt Phosphate

This material shows a high working potential (4.8 V vs. metallic lithium) and a high theoretical specific capacity of $167 \text{ mAh}\cdot\text{g}^{-1}$ [99]. The high potential is given by the strong covalent character of the Co-O bond, which is able to stabilize the $\text{Co}^{2+}/\text{Co}^{3+}$ anti-bond through an inductive effect of the Co-O-P coordination [100]. Similar to LiNiPO_4 , it shows a low stability, and the capacity decreases from $92 \text{ mAh}\cdot\text{g}^{-1}$ to $54 \text{ mAh}\cdot\text{g}^{-1}$ in ten cycles [101]. Improvements have been achieved by substituting part of the cobalt ions with iron. Indeed, $\text{Li}_{0.98}\text{Co}_{0.8}\text{Fe}_{0.2}\text{PO}_4$ material is able to provide $120 \text{ mAh}\cdot\text{g}^{-1}$ for almost 500 cycles, between 2.5 and 5.3 V at $17 \text{ mA}\cdot\text{g}^{-1}$ [102].

1.2.2.14 Lithium Iron Phosphate

The search for more stable cathode materials, especially when fully charged, has resulted in the proposal of LiFePO_4 cathode material. This compound has an olivine structure, is cheap, is non-toxic, and has an excellent thermal and cycling stability. Like all the other olivine materials, the main issues are the low electrical conductivity ($10^{-9}\div 10^{-10} \text{ S}\cdot\text{cm}^{-1}$) and the low lithium ion diffusion coefficient within the material ($10^{-11}\div 10^{-13} \text{ cm}^2\cdot\text{s}^{-1}$). Several solutions have been proposed, such as the graphite coating, and the reduction of the particle size [103]. Currently, specific capacities of $167 \text{ mAh}\cdot\text{g}^{-1}$ can be reached (the theoretical capacity of the material is $170 \text{ mAh}\cdot\text{g}^{-1}$) [104] and it finds applications in portable electronics and electric vehicles [95].

The olivine structure (see Figure 1.9) has an orthorhombic unit cell, with a spatial group $Pnma$. The lattice parameters for the LiFePO_4 are $a = 10.3320 \text{ \AA}$, $b = 6.0100 \text{ \AA}$ and $c = 4.6920 \text{ \AA}$. Lithium atoms occupy the octahedral sites created by the oxygen atoms of the phosphate groups, which instead have a tetrahedral structure with the phosphorus ion in the center. Each FeO_6 octahedron shares an edge with two LiO_6 octahedra, and the other with a PO_4 tetrahedron. This structure forms "channels" that allow the lithium ions to be inserted and extracted from the lattice during the operation of the device [105].

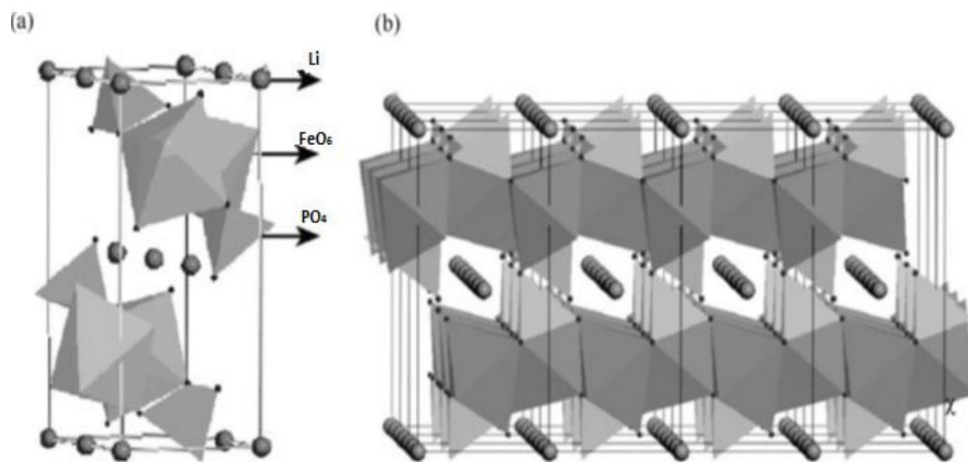


Figure 1.9. Crystal cell of LiFePO_4 (a) and overall olivine structure where it can be observed the lithium ion conductivity channels (b) [103].

1.3 Magnesium Batteries

Magnesium-based power sources seem to be a valid alternative to the well consolidated lithium technology, due to several intrinsic advantages of Mg metal. Despite a higher reduction potential (-3.04 V for Li and -2.37 V for Mg) and a lower specific capacity ($3862 \text{ Ah}\cdot\text{kg}^{-1}$ for Li and $2205 \text{ Ah}\cdot\text{kg}^{-1}$ for Mg), magnesium is more abundant in the Earth's crust, is cheaper, safer, the cost of waste treatment is lower, and it has a higher volumetric capacity (3832 vs. $2062 \text{ Ah}\cdot\text{dm}^{-3}$) with respect to lithium [106]. In addition, batteries based on magnesium have an excellent cyclability, higher capacity retention, and a wide temperature operation range. A comparison between the physical properties of magnesium, lithium, and other appealing metals for application in secondary batteries is reported in Table 1.5.

Table 1.5. Numerical comparison between physical properties of several low reduction potential metals.

Metal	Z	M / g·mol ⁻¹	Reduction Reaction	E / V vs. SHE	Specific density / g·cm ⁻³	Theoretical specific charge / Ah·kg ⁻¹	Theoretical volumetric capacity / Ah·dm ⁻³
Li	3	6.93	Li ⁺ +e ⁻ ↔ Li	-3.04	0.53	3862	2062
Na	11	22.99	Na ⁺ +e ⁻ ↔ Na	-2.71	0.97	1160	1120
Mg	12	24.31	Mg ²⁺ +2e ⁻ ↔ Mg	-2.37	1.75	2205	3832
Al	13	26.98	Al ³⁺ +3e ⁻ ↔ Al	-1.66	2.70	2980	8046
Ca	20	40.08	Ca ²⁺ +2e ⁻ ↔ Ca	-2.87	1.55	1340	2060

There are no doubts that lithium is the most performing element between alkali and alkaline earth metals, considering all the physical parameters. Nevertheless, keeping in mind the lower costs of magnesium with respect to lithium (see Table 1.6), and the quite good electrochemical properties, Mg is still an attractive substitute for Li able to produce very cheap and high performing secondary batteries.

Table 1.6. Economic data for lithium and magnesium.

Metal	Earth's crust abundance / ppm	Annual production / ton in 2016	Price / \$·ton ⁻¹
Li	17	35'000	64'800
Mg	29'000	1'010'000	2'700

The research in the magnesium secondary battery field has been carried out all around the world with increasing interest, as demonstrated by the growing number of publications. However, compared to the state of the art LIBs, magnesium secondary battery devices are still in their youthful stage. The major problems that limit the commercialization of Mg batteries is the development of: i) a high performing and high stable electrolyte material; and ii) cathode materials able to host and redistribute the high charge density of Mg²⁺ ions, when they are inserted into the structure [107]. Here below a detailed summary of the state of the art electrolyte and cathode materials for magnesium secondary battery applications is reported. Thus, a contextualization of the materials obtained in this Ph.D. project is given, with respect to the more advanced compounds present in literature.

1.3.1 Electrolytes for Mg Batteries

A standout snag to obtain suitable Mg-based rechargeable batteries is the improvement of the electrolyte, making it able to exchange effectively magnesium species without being decomposed, and to be stable with the electrodes (*e.g.* the magnesium metal anode, aluminum- and stainless steel-based battery case, metal-based cathodes, *etc.*) [108].

1.3.1.1 Liquid Electrolytes for Mg Batteries

The first attempt on magnesium metal deposition is attributed to Jolibois that, in 1912, has demonstrated how a Mg layer can be obtained by using a solution of diethylmagnesium (Et_2Mg) and magnesium iodide (MgI_2) dissolved in diethyl ether (Et_2O) [109]. This pioneering work has opened the door to the development of suitable electrolyte solutions capable to reversibly deposit and dissolve magnesium. Nevertheless, we have to wait almost 80 years to see the birth of the idea of a magnesium battery when, in 1990, Gregory *et al.* have reported the first paper on a magnesium electrolyte for direct use in a battery device [110].

It seems that simple halide salts cannot be used in liquid electrolytes in order to obtain a magnesium reversible deposition. This is due to a poor dissociation ability of classic solvents, such as THF. Nevertheless, Soeda *et al.* have demonstrated that it is possible to plate and dissolve magnesium using a MgI_2 /non-ethereal solvent electrolyte, with low current density values, but with a high efficiency and a low overpotential [111]. Similarly, Connor, Shiraga, and Sheha have shown that a magnesium deposition can be obtained with a MgBr_2 solution in Me-THF or DMSO [112-114].

The solubility of the magnesium salt can be improved using a complex analogous of salts used in LIBs, such as BF_4^- , PF_6^- , AsF_6^- , and ClO_4^- . Unfortunately, these salts form a thick passivating layer on magnesium metal anode that inhibits Mg^{2+} transport.

By reacting an alkyl magnesium compound ($\text{R}'_2\text{Mg}$) with two molecules of alkyl metal ($\text{R}''_3\text{B}$ or $\text{R}''_3\text{Al}$), new salts of the type $\text{Mg}(\text{R}'\text{R}''_3(\text{B},\text{Al}))_2$ can be obtained. These salts are stable and non-corrosive, due to the elimination of halide ions. Gregory has been the first author to propose several of these salts like $\text{Mg}(\text{BBu}_4)_2$ and $\text{Mg}(\text{BBu}_3\text{Ph})_2$ that, dissolved in THF:DME, show a conductivity of $1.0 \cdot 10^{-3}$ and $2.3 \cdot 10^{-3} \text{ S} \cdot \text{cm}^{-1}$ [110]. In this class of materials, the solubility, conductivity, and electrochemical stability depend only on the anion ligands. The introduction of

aryl-based ligands, proposed by Muldoon *et al.*, has yielded to the obtaining of an electrolyte with a superior salt solubility ($> 1 \text{ M}$) and high stability towards oxidation ($> 4.0 \text{ V vs. Mg/Mg}^{2+}$) [115, 116]. Nevertheless, the overpotential in the magnesium deposition shown by these electrolytes is still quite high.

The last class of magnesium salts developed for liquid electrolytes is the one where a dimer is obtained by coordinating two Mg ions with three halides cations and six solvent molecules (*e.g.* THF). The solubility of these compounds, and the magnesium transference number, are increased. However, the stability is quite low, and MgCl_2 species are product as a result of the decomposition. Several examples are present in literature, and the most performing are “*All Phenyl Complex*” (APC) from Aurbach *et al.* [117] and the “*Magnesium Aluminum Chloride Complex*” (MACC) by Doe *et al.* [118]. APC is synthesized by reacting two moles of phenylmagnesium chloride with one of aluminum chloride, and the resulting salt is dissolved into THF. The obtained electrolyte shows a Mg deposition overpotential of *ca.* 200 mV, a Coulombic Efficiency close to 100 % (evaluated by CV experiment), quite high current density values (on the order of $10^1 \text{ mA}\cdot\text{cm}^{-2}$), and an electrochemical stability up to *ca.* 3.0 V vs. Mg/Mg^{2+} . MACC is synthesized by mixing MgCl_2 with AlCl_3 (2:1), and the resulting mixture is dissolved in 1,2-dimethoxyethane. The performances of this electrolyte are: i) Mg deposition overpotential of *ca.* 500 mV; ii) coulombic efficiency of 99 %; iii) current density values on the order of $10^0 \text{ mA}\cdot\text{cm}^{-2}$; and iv) an electrochemical stability up to *ca.* 3.1 V vs. Mg/Mg^{2+} .

Typically, all the liquid electrolytes demonstrate nice Mg reversible plating performances, a good coulombic efficiency, and few of them also show a high stability toward oxidation. Their major disadvantage is related to their safety, because they use ethereal-based solvents which have a high vapor pressure and flammability, that restrain their application in commercial devices.

1.3.1.2 Solid-State Electrolytes for Magnesium Batteries

The best way to solve the high flammability issues of liquid electrolytes is to move towards solid-state electrolytes. Furthermore, this class of materials prevent the degradations at the interface between the electrolyte and the electrodes, and could offer a magnesium transference number close to one. Several attempts have been done to develop such an electrolyte, but unfortunately conductivities on the order of only $10^{-6} \text{ S}\cdot\text{cm}^{-1}$ are obtained, at temperatures in the range of $150\div 800 \text{ }^\circ\text{C}$ [119, 120]. Great improvements have been obtained by Aubrey *et al.* impregnating

different metal-organic frameworks (MOF) with several liquid electrolytes. In this way, conductivities between $7.9 \cdot 10^{-9}$ and $2.5 \cdot 10^{-4} \text{ S} \cdot \text{cm}^{-1}$ can be obtained [121].

1.3.1.3 Polymer Electrolytes for Magnesium Batteries

As already explained for lithium, PEs have the advantage of adaptability to the irregular electrodes surface, and they can usually be stretched. The conductivity values are lower than those of liquid electrolytes, but higher than those of SSEs, and, with respect to liquid, they typically have a very low flammability. The first reported polymer electrolyte exhibiting a Mg^{2+} conductivity is a magnesium perchlorate/magnesium chloride-polyethylene oxide blends in 1986 [122, 123]. The conductivity of these PEs is comprised between 10^{-9} and $10^{-6} \text{ S} \cdot \text{cm}^{-1}$, very far from practical applications. Only ten years later, Di Noto *et al.* have been able to increase the conductivity up to $10^{-5} \text{ S} \cdot \text{cm}^{-1}$, thanks to the extremely high reactivity of the magnesium salt used in their electrolytes [17, 124]. In their work, they have used the δ form of MgCl_2 , a salt characterized by a high crystallographic disorder that increases its solubility in solvents and its reactivity [125]. Its structure consists of magnesium chloride repeated units that form a sort of polymer chain, in which the different units are connected through covalent bonds. Unfortunately, the polymer used in these electrolytes is not compatible with magnesium metal, making these pioneering studies not suitable for practical applications. Nevertheless, thanks to these works, several insights on the structures, coordinations, and conductivity mechanism occurring in these electrolytes have been revealed, opening the doors to a deeper and more detailed comprehension of the interactions established between the hosting polymer matrix and the magnesium salt. In 1999 a cross-linked polyethylene glycol diacrylate compound, in which magnesium trifluoromethanesulfonate salt is dissolved, has been developed, exhibiting a room-temperature conductivity of $2 \cdot 10^{-4} \text{ S} \cdot \text{cm}^{-1}$ [126]. By using the same salt, dissolved in polyacrylonitrile and plasticized with propylene carbonate and ethylene carbonate, a gel polymer electrolyte with a room-temperature conductivity of $1.8 \cdot 10^{-3} \text{ S} \cdot \text{cm}^{-1}$ has been obtained [127]. In 2004 Aurbach *et al.* have assembled a rechargeable battery using a magnesium metal anode, a molybdenum sulfide cathode, and a polymer electrolyte synthesized with a mixture of butyl magnesium and aluminum diethyl chloride, dissolved in polyvinylidene fluoride, and plasticized with tetraglyme [128]. Nevertheless, the addition of these solvents, that allows for a higher conductivity, has brought back all the safety issues that polymer electrolytes are supposed to overcome with respect to liquid electrolytes. Thus, these solutions are not suitable for practical applications.

1.3.1.4 Ionic Liquid-based Electrolytes for Magnesium Batteries

The first IL-based electrolyte for magnesium batteries has been proposed by NuLi *et al.* in 2005 [129, 130]: a reversible deposition and dissolution of magnesium at low currents ($0.1 \text{ mA}\cdot\text{cm}^{-2}$) for more than 150 cycles can be obtained by dissolving magnesium trifluoromethanesulfonate salt into a 1-butyl-3-methylimidazolium tetrafluoroborate. Binary ionic liquid-polymer systems of the type 1-ethyl-3-methylimidazolium bis(trifluoromethylsulfonyl)imide-polyethylene oxide/polymethyl acrylate, where magnesium bis(trifluoromethylsulfonyl)imide is dissolved, show a room-temperature conductivity value of $1\cdot 10^{-4} \text{ S}\cdot\text{cm}^{-1}$. However, no magnesium deposition/dissolution can be obtained using these electrolytes [131]. By using a mixture of THF, a Grignard complex, and N,N-diethyl-N-methyl-N-(2-methoxyethyl) ammonium-bis(trifluoromethanesulfonyl)imide ionic liquid, Yoshimoto *et al.* demonstrate that a room-temperature conductivity of $7.4\cdot 10^{-3} \text{ S}\cdot\text{cm}^{-1}$ and a reversible magnesium deposition can be reached [132]. Nevertheless, the introduction of THF in the electrolyte, results in a flammable material. In 2015 Bertasi *et al.* have reported that an IL-based magnesium electrolyte can be obtained by dissolving $\delta\text{-MgCl}_2$ or $\delta\text{-MgI}_2$ in 1-ethyl-3-methylimidazolium tetrafluoroborate, 1-ethyl-3-methylimidazolium chloride/aluminum trichloride, or 1-ethyl-3-methylimidazolium iodide/aluminum triiodide [57, 133, 134]. They have demonstrated a room-temperature conductivity in the range $3.0\cdot 10^{-4}\div 7\cdot 10^{-3} \text{ S}\cdot\text{cm}^{-1}$, a very low overpotential in the magnesium deposition ($< 100 \text{ mV}$), a high coulombic efficiency (99.94 %), and a current density on the order of $10^1 \text{ mA}\cdot\text{cm}^{-2}$. Furthermore, for the first time, a rechargeable battery has been obtained by using a pure ionic liquid-based electrolyte [57]. In the same period, also Kar *et al.* have reported the reversible magnesium plating/stripping using a pure N-ethyl-2-(2-methoxyethoxy)-N,N-bis(2-(2-methoxyethoxy)ethyl)-ethan-1-aminium bis(trifluoromethyl-sulfonyl)imide ionic liquid with magnesium boron hydride salt [135].

Ionic liquids allow to solve several of the issues that emerge with liquid, solid, and polymer electrolytes, maintaining high values of conductivity, reversibility, and stability. Nevertheless, a lot of key points remain to be solved, and the understanding of how the conductivity mechanism and the coordination of active species occur within these systems would give rise to the realization of a commercial magnesium rechargeable battery.

1.3.2 Cathodes for Mg Batteries

In the last decades, great efforts have been done to obtain a high performing electrolyte for Mg reversible deposition. Meanwhile, the research on the development of a cathode material that exhibits a high energy density, good cyclability, and nice rate capability, is still not satisfying. Cathodes for Mg secondary batteries can be divided into two different categories, depending on the type of reaction occurring during the charge/discharge processes: i) intercalation cathodes, where Mg-ion species are hosted within their crystal structure (*e.g.* metal sulfides, metal oxides, metal phosphates); and ii) conversion cathodes, which directly react with magnesium, forming a new compound (*e.g.* sulfur, selenium, oxygen, and halides). The former has a lower capacity with respect to conversion cathodes, due to a limited number of magnesium hosting sites; however, the cycle life and stability are better, because of a crystal structure that does not change substantially during the electrochemical processes. On the contrary, conversion cathodes show higher capacities and lower stability than intercalation electrodes.

1.3.2.1 Metal Sulfides

The most used cathode for magnesium batteries is the well-known Chevrel phase (CP) molybdenum sulfide (Mo_6S_8) proposed by Aurbach *et al.* in 2000 [136]. The working potential of this cathode is *ca.* 1.1 V vs. Mg/Mg²⁺, with a specific capacity of *ca.* 100 mAh·g⁻¹. Despite the outstanding performances, especially for the time at which this cathode was proposed, such a low working potential is not compatible for practical applications. The working potential can be increased by using MoS₂ or WSe₂ cathodes, which show capacities of *ca.* 175 and 140 mAh·g⁻¹, and working potentials of 1.8 and 1.5 V vs. Mg/Mg²⁺, respectively [137, 138]. The cycle life of the reported batteries is very low, even if it could be addressed to the low stability of the electrolytes used in these works.

1.3.2.2 Metal Oxides

Due to the strong nature of Mg-O interactions, many metal oxides intercalate magnesium in an irreversible way, making them unsuitable for the application in secondary batteries. Nevertheless, manganese oxide demonstrates an interesting specific capacity (280 mAh·g⁻¹) at *ca.* 1.5 V vs. Mg/Mg²⁺, that unfortunately drops to 80 mAh·g⁻¹ after only six cycles, indicating a poor stability [139]. Furthermore, this cathode is cycled at a very low current, *i.e.* 0.015 C or 4.2 mA·g⁻¹, that is not fitting the requirements for a commercial device. Vanadium oxide (V₂O₅) is probably the most

studied cathode for magnesium secondary batteries. In 1993 Novák and Desilvestro have demonstrated that Mg^{2+} intercalation can occur in a vanadium oxide cathode material through a CV experiment [140]. Unfortunately, very low specific capacities (*ca.* $25 \text{ mAh}\cdot\text{g}^{-1}$) can be obtained if no water is added into the device. Several examples of Mg^{2+} intercalation evaluated in CV tests with a three-electrodes cell are present in literature; on the contrary, the first battery assembled with a vanadium-based cathode appears only in 2005, when Jiao *et al.* have shown that, using a device obtained by assembling a Mg metal anode and vanadium oxide nanotubes-based cathode, a capacity of $75 \text{ mAh}\cdot\text{g}^{-1}$ can be reached at a current rate of $5 \text{ mA}\cdot\text{g}^{-1}$ [141]. The rate capability of this material is very low; indeed, the specific capacity drops to $50 \text{ mAh}\cdot\text{g}^{-1}$ if the current is increased up to $10 \text{ mA}\cdot\text{g}^{-1}$. By functionalizing V_2O_5 with graphene oxide (GO), higher capacities can be obtained ($178 \text{ mAh}\cdot\text{g}^{-1}$), even if, in this case, the device is cycled at quite low current rates ($35 \text{ mA}\cdot\text{g}^{-1}$) [142]. An initial capacity of $75 \text{ mAh}\cdot\text{g}^{-1}$ has been reached by Bertasi *et al.*, when they have discharged their battery at a current rate of $35 \text{ mA}\cdot\text{g}^{-1}$ [57]. Other oxide materials, used as cathode for magnesium batteries, are present in literature, such as Co_3O_4 [143] and RuO_2 [144]. The former exhibits a specific capacity of $74 \text{ mAh}\cdot\text{g}^{-1}$ when cycled at $25 \text{ mA}\cdot\text{g}^{-1}$, while the latter demonstrates $74 \text{ mAh}\cdot\text{g}^{-1}$ at $35 \text{ mA}\cdot\text{g}^{-1}$. In both cases the performances are evaluated using a CV test and not assembling a real battery device.

1.3.2.3 Metal Silicates

The last principal family of intercalation cathodes used in magnesium secondary batteries consists of silicates polyanion. With respect to oxides, they are more chemically stable due to a decreased energy level of oxygen p-orbital given by an induction effect. The charge neutrality during Mg^{2+} intercalation and release is balanced by the redox activity of the metal center, typically a 3d transition metal. Metal silicates for magnesium reversible insertion have a general formula of the type MgMSiO_4 , where M is a metal able to undergo to an oxidation from $2+$ to $4+$, after magnesium removal. The first olivine-like cathode using a manganese metal center has appeared in literature in 2008, when Feng *et al.* have shown the possibility of Mg^{2+} to be inserted in MgMnSiO_4 , with a specific capacity of $244 \text{ mAh}\cdot\text{g}^{-1}$ at $1.6 \text{ V vs. Mg/Mg}^{2+}$ [145]. However, these incredible performances, reached at $3.1 \text{ mA}\cdot\text{g}^{-1}$, rapidly drop down to $76 \text{ mAh}\cdot\text{g}^{-1}$ when the current is increased up to only $15.7 \text{ mA}\cdot\text{g}^{-1}$. The substitution of Mn with Fe, Ni, or Co results in a modulation of the obtained specific capacity, ranging from 125 to $70 \text{ mAh}\cdot\text{g}^{-1}$ (Fe \rightarrow Co) at modest current rates (*ca.* $10 \text{ mA}\cdot\text{g}^{-1}$) [146-148].

1.3.2.4 Sulfur and Selenium

Kim *et al.* have proposed the first device involving a sulfur cathode, and have successfully obtained a discharge specific capacity of $1200 \text{ mAh}\cdot\text{g}^{-1}$ [149]. Nevertheless, the capacity fade due to magnesium polysulfides dissolution makes this battery impossible to be used in practical devices. 20 charge/discharge cycles with a Mg-S battery have been reported by Yu *et al.*, with a specific capacity of $800 \text{ mAh}\cdot\text{g}^{-1}$ at a current rate of *ca.* $80 \text{ mA}\cdot\text{g}^{-1}$ [150]. Slightly better results have been shown by Zhang and co-workers in 2017 [151]. Furthermore, they have also demonstrated that a selenium cathode can be used in a magnesium battery, showing a specific capacity of *ca.* $500 \text{ mAh}\cdot\text{g}^{-1}$, for 200 cycles, at a current rate of *ca.* $50 \text{ mA}\cdot\text{g}^{-1}$ [151].

1.3.2.5 Oxygen

Prompted by the very high theoretical electrochemical performances of a Mg-air battery, research on developing a device able to provide electrical energy from a magnesium metal anode and an oxygen cathode has been done. Unfortunately, due to a high chemical stability and very low conductivity of the produced MgO, this goal is difficult to be reached. Shiga *et al.* have demonstrated that a rechargeable Mg-O₂ battery can be obtained by the addition of iodine, that is an electro-active additive able to dissolve and decompose magnesium oxide [152].

1.3.2.6 Halides

Halides, such as iodine and bromine, are able to reversibly react with magnesium ions producing MgX₂ compounds, with interesting capacities and operating voltages higher than 2.0 V vs. Mg/Mg²⁺. One example has been a Mg/I₂ battery, with a carbon matrix cathode impregnated with iodine. The assembled device has shown a specific capacity higher than $200 \text{ mAh}\cdot\text{g}^{-1}$, at a current rate of *ca.* $100 \text{ mA}\cdot\text{g}^{-1}$ [153]. Unfortunately, the intrinsic reactivity and volatility of iodine, make this cathode difficult to be confined. Similar to I₂, a proof of concept cell with Br₂ active species has shown a specific capacity of $275 \text{ mAh}\cdot\text{g}^{-1}$, at a current rate of *ca.* $100 \text{ mA}\cdot\text{g}^{-1}$ [154]. Nevertheless, this work only shows a new way for a low cost and high capacity technology, but it is still very far from practical applications.

Thus, the development of high performing cathodes for magnesium rechargeable batteries still remains a huge challenge in the beyond lithium-ion battery technology. Furthermore, cathodes able to sustain high demands of current are desired, due to the exponentially increased production of electric vehicles.

2. Summary and Aims of the Thesis

Following the scientific panorama described in the Introduction chapter, the research activity conducted in this Ph.D. project has been mainly focused on the development, synthesis, and characterization of novel electrolyte and electrode (cathode) compounds for application in lithium and magnesium secondary batteries, belonging to the “*beyond Li-ion*” class of materials.

Typically, the electrolytes have been obtained with different concentrations of the active metal (either Li^+ or Mg^{2+}), in order to study the effect of the cation concentration on the structural, coordination, and thermal properties of the materials. Furthermore, the complexation of the cations and their effects on the long-range charge transfer migration at the different contents have been carefully studied by vibrational spectroscopy and Broadband Electrical Spectroscopy (BES). Three different classes of electrolytes have been prepared and studied: i) single lithium ion conducting solid polymer electrolytes and IL doped solid polymer electrolytes; ii) viscous glass forming Li-ion conducting electrolyte materials; and iii) ionic liquid-based electrolytes for magnesium conduction.

The improvement of the electrochemical features of various cathode materials has been achieved following three different approaches: i) addition, during the synthesis, of carbon and/or copper sources to modify the olivine structure increasing the elasticity of the coordination network; ii) substitution, in the structure, of divalent cobalt ions with higher valence vanadium, niobium or tantalum atoms to exploit the electron compensation effect that gives rise to an enhanced electron conductivity; and iii) modification of a vanadium-based cathode architecture by surface functionalization, gauged through the addition of highly conductive graphene oxide. The performances of all the proposed cathode materials have been evaluated testing them with classical electrochemical techniques (*e.g.* cyclic voltammetry, electrochemical impedance spectroscopy, etc.), and amperostatic cycling of full cell prototypes.

All the materials have been obtained following different synthetic routes, such as inert atmosphere procedures, high temperature solid state syntheses under oxidizing or reducing environments, or hydrothermal protocols. The characterization analyses have ranged from elemental characterizations, *e.g.* CHNS-O and Inductively Coupled Plasma Atomic Emission Spectroscopy (ICP-AES), to thermal analyses, *e.g.* Thermogravimetric Analyses (TGA) and Modulated Differential

Scanning Calorimetry (MDSC), Density Functional Theory (DFT) and Molecular Modeling (MM), vibrational spectroscopies, such as Fourier Transform Medium and Far Infrared (FT-MIR and FT-FIR) and micro-Raman, powder X-Ray Diffraction (XRD), several electrochemical techniques (CV, CA, EIS), Broadband Electrical Spectroscopy (BES), and amperostatic battery cell cycling.

All the proposed materials, electrolytes and cathodes, are summarized in Table 2.1.

Table 2.1. Summary of the proposed and studied electrolyte and electrode materials described in this thesis.

Acronym	Composition	Description	Conductivity / S·cm ⁻¹	Sp. Capacity / mAh·g ⁻¹	Ref.
Li_PVA	(PVA) ₄₇₀ - (Li_PVA) ₃₀ +EMImTFSI y%wt (0 ≤ y ≤ 23)	Li solid polymer electrolytes	1.29·10 ⁻⁵	-	[20, 155]
GlyLi _x	C ₃ H ₅ (OH) _{3-x} (OLi) _x (0 ≤ x ≤ 1)	Glass forming electrolytes for LIBs	1.99·10 ⁻⁴	-	[21]
LFNCP	LiFe _{1/3} Ni _{1/3} Co _{1/3} PO ₄	Olivine-based high voltage Li-ion cathodes	-	101	[22]
LFNCMP	LiFe _{0.33} Ni _{0.07} Co _{0.55} M _{0.05} PO ₄ (M= V,Nb,Ta)	Olivine-based high voltage Li-ion cathodes	-	149	-
Pyr ₁₄ Cl/(BCl ₃) _{0.25} / (δ-MgCl ₂) _x	Pyr ₁₄ Cl/(BCl ₃) _{0.25} /(δ-MgCl ₂) _x (0 ≤ x ≤ 0.095)	IL-based Mg electrolytes	1.43·10 ⁻⁴	-	[156, 157]
EMImCl/(TiCl ₄) _{1.4} / (δ-MgCl ₂) _x	EMIm/(TiCl ₄) _{1.4} /(δ-MgCl ₂) _x (0 ≤ x ≤ 0.23)	IL-based Mg electrolytes	2.15·10 ⁻⁴	-	[23, 158, 159]
Pyr ₁₄ Cl/(AlCl ₃) _{1.5} / (δ-MgCl ₂) _x	Pyr ₁₄ Cl/(AlCl ₃) _{1.5} /(δ-MgCl ₂) _x (0 ≤ x ≤ 0.146)	IL-based Mg electrolytes	2.07·10 ⁻³	-	-
GO@V	GO/NH ₄ VO ₂ HSO ₄ Cl	High power Mg-ion cathode	-	72	[160]

3. Instruments and Methods

In this chapter the main techniques and instruments used to synthesize and characterize the proposed materials are briefly summarized. An introduction is given for each technique, followed by the description of the samples preparation. Further experimental details are given in the discussion sections for each case.

3.1 General Characterization Approach

First, each material is characterized by elemental chemical analyses, in particular by microanalysis and/or inductively-coupled plasma atomic emission spectroscopy. On the basis of compositional results, the stoichiometry of the materials can be calculated and subsequently some important molar ratios such as Li/O, Mg/Ionic Liquid etc. can be obtained. Indeed, after this evaluation, the mechanisms of the reactions involved in the synthesis can be better understood.

Then, thermal stability and transitions of the materials are measured by high resolution thermogravimetric analysis (HR-TGA) and modulated differential calorimetry (MDSC) techniques, obtaining information on the structure and coordinations.

Subsequently, SEM, TEM, and EDX measurements are performed in order to investigate the morphology and the homogeneity of the materials, thus confirming the compositions obtained from the elemental analyses.

For highly crystalline materials, XRD measurements allow to reveal and calculate the structure and structural changes present in the synthesized samples, in order to correlate the structural behavior to all of the material characteristics. Then, the far-infrared vibrational spectroscopy provides information on metal-ligand interactions such as Li-O, Mg-O, etc. Hence, the compositional information and the metal-ligand vibrational modes enable to carry out preliminary hypotheses or to confirm the coordinations occurring in the studied materials. Mid-infrared and Raman spectroscopies allow to obtain detailed structural information. The vibrational modes are assigned on the basis of literature, starting from the inorganic components and subsequently to the organic moieties, observing the interactions between the two. In some cases, the vibrational modes attribution is assisted by DFT calculations.

BES measurements, after the evaluation of the coordinations and structures that are formed within the materials, allow to determine the conductivity mechanism occurring in the proposed electrolytes and the structural flexibility specific of the cathode material. In particular, the temperature and the active species concentration (*i.e.* Li and Mg) modulations on the conductivity mechanism occurring in the proposed electrolytes are revealed.

Electrochemical analyses (cyclic voltammetry, electrochemical impedance spectroscopy, linear sweep voltammetry, etc.) are taken under consideration to reveal the redox events taking place, the kinetics of electrochemical reactions, and stability of the materials. Finally, the most performing materials are used to assemble full cell devices (CR2032 coin cell, Swagelok, or EL-CELL), which are characterized under operating conditions and at long term.

3.2 Dry box and Vacuum-Inert Atmosphere Line

Every manipulation of air sensitive reactants and products must take place under inert atmosphere, in order to obtain H₂O and O₂ free materials. This is achieved by using a N₂/Ar Schlenk line and Ar-filled gloveboxes [161].

Since metallic Li and Mg metals are highly reactive, and part of the used reagents are highly hygroscopic, all the common operations of synthesis, washing, transferring, storage, spectroscopic characterizations *etc.* are carried out using two gloveboxes (Figure 3.1). The first one is a homemade glovebox, build on the base of a Braun MB 150-B-4-II, and works under Ar. There are two antechambers of 2.5 and 50 L of volume, connected to a rotary vacuum pump Vacuubrand RD4, enabling the access to the main chamber. The introduction or extraction of objects from the glovebox is performed only after a series of 4 cycles of rotary vacuum of 15 minutes each, in order to avoid contamination of the main chamber. An open jar containing phosphorus pentoxide is present inside the main chamber, with the function of removing residual traces of H₂O. The second glovebox, with twice the volume with respect to the homemade one, is a commercial MBRAUN Unilab filled with argon. It is able to ensure concentrations of H₂O and O₂ below 1 ppm through a system of filters.



Figure 3.1. Dry- box used: homemade on the left and commercial model on the right.

In addition to the gloveboxes, a Schlenk line is used for syntheses (Figure 3.2), connected with a rotary pump Alcatel 8063, and Ar and N₂ gas tanks. The Schlenk line consists of two main branches of distribution: one is connected to the vacuum system, while the other is connected to the line of the highly pure argon and nitrogen gases. A further purification of nitrogen occurs by the interposition of two traps filled with molecular sieves and cooled with liquid nitrogen. Completing the system, a mercury pressure-release bubbler is present.

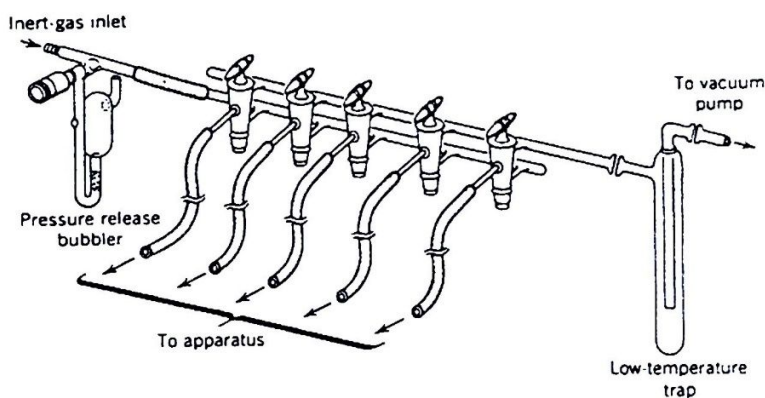


Figure 3.2. Scheme of a simplified vacuum-inert atmosphere line.

When using the Schlenk line, all the glassware is made of Pyrex® glass, which best suits to withstand the mechanical and thermal stress. Furthermore, all the connections with the equipment are realized by means of Tygon® tubing specific for vacuum. Finally, the connections between the glassware are covered with a thin layer of silicone grease, in order to obtain the best compromise between grip and risk of pollution of the reactants as well as products. Three cycles of vacuum-argon in the inner volume of the reaction equipment are systematically performed to avoid oxygen

and moisture contamination. Moreover, the empty equipment is always assembled inside the argon-filled glovebox, before to the connection with the Schlenk line.

3.3 ICP-AES

The elemental composition of the samples is determined by inductively-coupled plasma atomic emission spectroscopy (ICP-AES). The instrument is a Spectro Arcos EOP equipped with an end-on plasma torch. Depending on the required sensitivity, a conventional Meinhard nebulizer or a Cyclonic nebulized are used. Before measuring, samples are digested following suitable procedures, depending on the characteristics of the materials.

3.4 Thermal Measurements

Thermal analyses are intended to determine the physico-chemical properties of a substance as a function of temperature or time. The sample undergoes a controlled temperature program that may have phases of heating, cooling, constant temperature maintenance, or a combination of temperature and time. The obtained graph is called thermogram. In the analysis of the proposed materials, two methods are taken under consideration, *i.e.* thermogravimetric analysis (TGA) and modulated differential scanning calorimetry (MDSC). Both TGA and DSC instruments need a preliminary calibration to correct any temperature bias. In the case of DSC, an indium reference is used (m.p. 156.61 °C). In addition, in the case quantitative measurements of specific heats, another calibration using a sample with a known heat capacity (C_p) is necessary. Indium reference is used also for heat capacity calibration.

3.4.1 Thermogravimetry Analysis (TGA)

In thermogravimetric measurements the mass of a sample, subjected to a controlled atmosphere (Air or N₂), is continuously recorded as a function of temperature, which is typically increased linearly. A thermal profile, in which is possible to detect decomposition and oxidation events of the sample, as well as physical processes such as evaporation, sublimation, or desorption, can be obtained.

A classic TGA system is composed by: i) an analytical balance; ii) a furnace operating in a wide temperature range (from room temperature to 1200 °C in our case) with a programmable gradient; iii) a system of gas to maintain an inert atmosphere in the oven (or reactive) and to cool the outside part of the oven to exclude heat transfers to the balance; iv) a computer for component

management and data processing; and v) a sample holder (platinum in our case). In this work a high resolution thermobalance 2950 (TA Instruments, Figure 3.3), with a resolution equal to 1 μg , is used. Differently from a standard thermobalance, this apparatus has the ability to vary the rate of heating depending on the first derivative of the weight loss of the sample. Thus, a considerable reduction in the analysis time when no decomposition events are occurring, and an improvement in the resolution in those temperatures where a weight loss is present, are obtained.



Figure 3.3. TGA 2950 of TA Instruments.

3.4.1.1 Sample Preparation

TGA measurements are carried out by placing a suitable amount of material (*ca.* 10 mg) onto a platinum pan, previously cleaned by several passages on a Bunsen burner and, when necessary, into an acid solution. The measurements are executed under a flux of nitrogen in a temperature range from 30 to 950 °C. To ensure an inert atmosphere, the instrument is placed inside a nitrogen-filled polyethylene glove-bag, and the sample, already loaded onto the pan, is transferred from the glovebox to the glove-bag by using a sealed container.

3.4.2 Differential Scanning Calorimetry (DSC)

In this technique the heat flow difference between a sample and a reference is measured as a function of temperature or time, during a heating or cooling procedure. The parts composing the instrument are: i) a measure cell; ii) a system for heating and cooling; and iii) a gas flushing system (typically helium). The heat reaches the sample and the reference capsules through a constantan heated platform, which is able to accommodate two hermetic aluminum pans for the sample and the reference. The heat flow difference between the two capsules is measured by using two thermocouples of Chromel/Constantan, while the temperature is measured with a

Chromel/Alumel junction located in correspondence of the measurement cell. The difference in the heat flows between the sample and the reference is directly proportional to the difference between the output signals of the two thermocouples. Measurements are typically performed from -150 °C to 250 °C, with a heating/cooling rate comprise between 3 and 10 °C·min⁻¹. This range depends on the thermal stability and on the location of thermal transitions and/or structural changes of the materials, which generally occur in a very broad temperature range. To perform the measurements, a system able to heat or cool the cell is needed. Indeed, in our case a TA Instrument LNCS operating with liquid nitrogen is used. The instrument used in this work is reported in Figure 3.4.



Figure 3.4. DSC instrument.

3.4.2.1 Sample Preparation

The samples, liquids or solids, are placed into a hermetic aluminum pan sealable using a special tool. The entire operation is carried out inside the argon-filled glovebox. Generally, 10 mg of material are used. The reference is an empty hermetic aluminum pan sealed inside the glovebox.

3.5 Vibrational Spectroscopy

Vibrational spectroscopy allows to investigate the structure, as well as bonds and interactions of the functional groups in the materials. In this work, both FT-IR and microRaman spectroscopies are taken under consideration to reveal the structural and coordination network that is formed within the studied materials.

3.5.1 Infrared Spectroscopy (FT-IR)

Infrared radiation has a low energy, so only the transitions from the fundamental vibrational state to an excited vibrational state can occur. In order to produce a vibrational transition, in addition

to energy conservation, the electromagnetic radiation must be able to induce a transition from the v state to the $v \pm 1$ state, with a concurrent variation of the electric dipole moment of the molecule. While the variation of the electric dipole moment during the molecular motion is an essential selection rule that must be respected to observe an absorption in the IR, the $\Delta v = \pm 1$ rule is only applied in the harmonic approximation. Indeed, it is also possible to observe transitions with $\Delta v = \pm 2, 3, 4$, since the potentials of the nuclear motions are anharmonic. The infrared spectroscopy used to characterize the proposed materials operates with the Fourier Transform methodology. Thus, the application of an interferometer allows for the detection of all the frequencies present in the IR radiation emitted by the sample, without the necessity of using a prism to disperse the beam in each wavelength.

The used spectrometer is a Nicolet Nexus FT-IR, equipped with a Globar lamp source in silicon carbide, with a length of 55 mm and a diameter of 5 mm, which is heated to a temperature between 1330 and 1500 K. The detector consists of a pyroelectric material based on triglycin sulfate (TGS). The instrument has also a conditioning system capable of purifying and eliminating water and carbon dioxide from the air. In the medium infrared region, the beamsplitter is potassium bromide with a germanium coating, while in the far IR region a silicon coated silica beamsplitter is used, in order to avoid any absorption in the studied region.

3.5.1.1 *Sample Preparation*

The spectra collected in the medium IR, *i.e.* from 400 to 4000 cm^{-1} , are obtained in ATR mode, using a SPECAC® Golden Gate single reflection diamond. The sample holder is loaded inside the glovebox so that the measurements are performed under anhydrous and O_2 -free conditions. In the far IR region, *i.e.* from 600 to 50 cm^{-1} , the spectra are acquired in transmission. A small amount of the sample is placed between two polyethylene discs, which are hermetically sealed in a special sample holder inside the glovebox.

3.5.2 **Raman Spectroscopy**

Raman spectroscopy, similar to IR spectroscopy, allows to investigate the structure and chemical bonds present in the materials, exploiting the vibro-rotational transitions occurring in the material after the exposure to an irradiating beam. IR and Raman spectroscopies are complementary techniques, since the selection rule for Raman-allowed transitions is the variation in the polarizability of the molecule. This implies that vibrations not visible in IR spectroscopy could be

Raman active, and *vice versa*. This technique involves the study of the radiation diffused by the sample after the absorption of a monochromatic radiation. A small percentage of photons is reflected with the same wavelength of the incident radiation, while a minor part is coupled with the vibrational modes of the molecules gaining or losing energy. Thus, reflected photons at a shorter or longer wavelength are generated. Photons scattered with the same energy give rise to the Rayleigh scattering, while those with a different energy correspond to the anti-Stokes and Stokes scattering, respectively. The energy difference between the incident and the emitted photon is related to the energy of the vibration to which it is coupled. Thus, by scanning all the wavelengths of the emitted photons, a Raman spectrum in cm^{-1} can be obtained. Indeed, the instrument sends a monochromatic radiation to the sample and collects its scattered radiation. After removing the Rayleigh scattering by using a filter, the light is divided into its components by a diffraction grating and sent to a CCD (Charge-Coupled Device) type detector, which measures the intensity of the radiation at different wavelength. When this technique is coupled to an optical microscope, in order to focus the incident beam only on a small surface area of the sample and controlling also the sampling depth, it is called microRaman.

Raman spectroscopy measurements are obtained using a Thermo Scientific DXR Raman Microscope with a solid-layer laser of 532 nm (green) wavelength, with a power value from 0 to 10 mW and a microscope with 10X magnification. The instrument allows to obtain a spectrum from 50 to 3550 cm^{-1} , with a spectral resolution of *ca.* 5 cm^{-1} . The parameters (*e.g.* exposure time, number of scans, laser intensity, *etc.*) are optimized for each sample.

3.5.2.1 Sample Preparation

Sensitive samples are placed in a sealed glass vial inside the glovebox, and measurements are carried out by focusing the laser beyond the glass surface. Samples stable to moisture and oxygen exposure are directly loaded onto a microscope slide window.

3.6 Electrochemical Techniques

3.6.1 Potentiostat/Galvanostat

The electrochemical characterizations of the materials (CV, CA, electrochemical stability window, exchange current density measurement, electrochemical impedance spectroscopy, *etc.*) are carried out using a multichannel VSP potentiostat/galvanostat (Biologic). The configuration and the

nature of the electrodes depend on the specific measurement and are described in each section. In the case of working electrode (WE), counter electrode (CE), or reference electrode (RE), they can be composed of reactive metals, such as magnesium or lithium, or by inert material, like platinum or glassy carbon. The measurement cells are homemade. Furthermore, the experiment temperature can be chosen and it remains constant along the whole measurement by using a thermostatic bath system.

3.6.2 Battery Cycling

The battery prototype testing is performed using a Maccor 4300 instrument. Specific galvanostatic or potentiostatic procedures, including parameters such as charge/discharge cutoff voltage, current *etc.*, are used depending on the material implemented into the battery and are described in each section. CR2032 coin cell, Swagelok cell, or EL-CELL configurations are used, and devices are assembled inside the glovebox by sealing them using a specific tool. A thermostatic oven allows for the maintaining of the temperature along the battery tests.

3.7 Broadband Electrical Spectroscopy

Broadband electrical spectroscopy (BES) allows to study the interactions between the materials and the electromagnetic field in a wide range of frequencies, between 10^{-7} and 10^{12} Hz. From 10^{-2} to 10^7 Hz the interactions between matter and the electromagnetic field give rise to the macroscopic polarization due to three different types of phenomena: i) the orientation of dipoles present in the material (dielectric relaxations); ii) free charges motion (ionic conduction); and iii) interdomain polarizations (interdomain conductivity).

For the preliminary analysis of the spectra, several representations (*e.g.* imaginary permittivity, real permittivity, imaginary conductivity, real conductivity, or tan delta) are taken into consideration to determine the type of events occurring in the material. The data are then interpolated by using the appropriate empirical equation (described in the BES section of each material, see for example section 4.2.4), which allows to calculate the conductivity, dielectric strength and relaxation time values of all the detected phenomena. In dielectric polymeric materials, BES technique typically reveals the presence of molecular relaxations associated with local or collective fluctuations of molecular dipole moments. The conductive materials present a spectrum in which both the molecular (dielectric) relaxation and the mesoscopic phenomena can

be detected, typically at different permittivity values. In the first case there is a reorientation of the dipole moments, which results in low permittivity values (usually less than 100); the mesoscopic phenomena, which are associated with the collective movement of charges, give a much more intense electrical responses [162].

In these electric measurements, an oscillating voltage $U(t)$ is applied to the electrodes of the cell, and the output current $I(t)$ is detected (Figure 3.5).

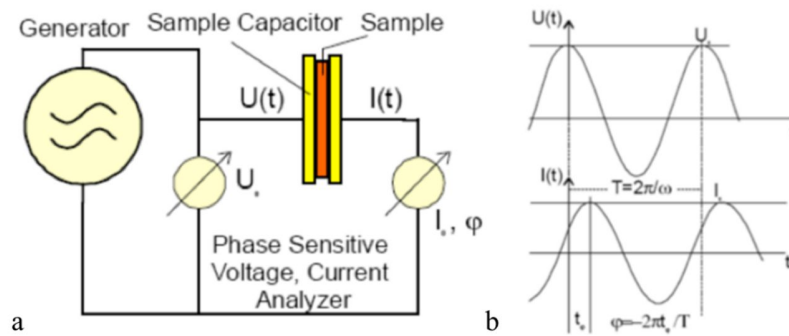


Figure 3.5. Principle of the electric measurements. The sample is placed between two electrodes and a potential $U(t)$ is applied (a); the output current $I(t)$ is out of phase by an angle φ with respect to the applied voltage (b).

The output current $I(t)$ is out of phase with respect to the applied voltage $U(t)$ by an angle φ

$$I(t) = I_0 \cos(\omega t + \varphi)$$

This measurement is repeated at different ω values, typically in the frequency range from μHz to MHz . The instrumentation detects the current $I(t)$ value at each frequency, and then the complex current $I^*(\omega)$ value is calculated by using the Fourier transform equation:

$$I^*(\omega) = \frac{2}{nT} \int_0^{nT} I(t) \exp(i\omega t) dt = I' + i I''$$

Several parameters can now be obtained. For example, the complex impedance $Z^*(\omega)$ is calculated by dividing U_0 to $I^*(\omega)$, while the complex conductivity $\sigma^*(\omega)$ is obtained using the equation:

$$\sigma^* = \sigma' - i\sigma'' = \frac{1}{Z^*(\omega)} \frac{d}{A}$$

where A is the area of the electrode and d is the distance between the two electrodes. Furthermore, the electric response can also be expressed in terms of complex permittivity, calculated as:

$$\varepsilon^*(\omega) = \varepsilon'(\omega) + i\varepsilon''(\omega) = \frac{\sigma^*(\omega)}{i\omega\varepsilon_0}$$

Thus, with one measurement, it is possible to reveal the electric response of the material in terms of complex (real and imaginary component) conductivity, permittivity, impedance *etc.* The best representation that allows for a good interpretation of the electric phenomena depends on the characteristics of the material.

The BES measurements of all the materials studied in this thesis are collected in the frequency range 10^{-2} - 10^7 Hz using a Novocontrol Alpha-A impedance analyzer. This instrument is joint with a temperature control system, comprising a cryostat able to heat and cool the chamber where the measuring cell is present with a N_2 gas jet (see Figure 3.6).



Figure 3.6. BES measuring system including the analyzer, temperature control system, the cryostat, the sample holder cell, and the vacuum pump (hidden), and electronic data management.

In a first step, the analyzer measures the complex impedance $Z^*(\omega)$ of the sample over the selected frequency range, and then it transforms the obtained values in terms of complex permittivity and

conductivity, $\varepsilon^*(\omega)$ and $\sigma^*(\omega)$. The electrical experimental parameters, the data collection, storage, and display are ensured by using the *Novocontrol WinDETA* software.

The efficient control of the temperature plays a pivotal role in order to ensure: i) the correct temperature at which the sample is exposed, especially when it is close to a thermal transition; and ii) the reduction of the measuring time, because oscillations in the temperature during low frequency measurements (< 0.1 Hz) would result in an exponential elongation of the sampling time, affecting the overall measurement. The microprocessor which control the temperature system has four independent channels, controlling in parallel the sample and gas temperature (gas heater), the temperature of liquid nitrogen, and the pressure in the dewar. Inside the dewar, a resistance heats the liquid nitrogen to a set point pressure, allowing the cold gas flow to reach the heating module. At this step, the gas is heated to the set point temperature, and finally arrives to the cryostat, where the cell containing the sample is present. The connection line between the dewar and the heating module, and the cryostat, are isolated by an external vacuum chamber. The instrument temperature limits are in the range $-160\div 450$ °C.

3.7.1 Sample preparation

Solid membranes are prepared by cutting the material in a disk of 13 mm of diameter. Solid powders are sintered in a pellet press of 13 mm of diameter. The thickness of the samples is measured by using a mechanical micrometer, and then the samples are placed between two platinum electrodes inside a hermetical cell. Liquid samples are directly added in the measuring cell, between the two Pt electrodes, and three optical fibers with a known thickness are used as spacers in order to avoid short-circuits. Finally, the closed cell is placed inside the BES instrument. Moisture and oxygen contaminations are avoided by conducting all the operations inside an Ar-filled glovebox. Even if the measuring cell is hermetically closed, the inert atmosphere during the measurement is also ensured by the nitrogen gas fluxed inside the cryostat.

4. Lithium Single Ion Conducting Solid Polyelectrolytes Based on Poly(vinyl alcohol)

In this chapter, we report the synthesis and the study of a solid membrane polyelectrolyte for secondary lithium batteries based on poly(vinyl alcohol) (PVA). The single-ion conducting material is synthesized through a direct lithiation of poly(vinyl alcohol-co-vinyl acetate), forming a lithium-poly(vinyl alkoxide) macromolecular salt. In a second step, the obtained polymer is plasticized by doping with 1-ethyl-3-methylimidazolium bis(trifluoromethylsulfonyl)imide (EMImTFSI) ionic liquid, in order to improve the conductivity. High resolution thermogravimetric analyses reveal a thermal stability higher than 215 °C, and allow to calculate the IL content in the obtained plasticized membranes. Differential scanning calorimetry studies demonstrate a melting transition related to the ionic liquid domains and a polymer associated glass transition event present at *ca.* -40 and +80 °C, respectively. Fourier-transform infrared spectroscopy shows that, after lithiation, a growth of the amorphicity of the polymer backbone is obtained, and that, after IL addition, a successful coordination between Li⁺ ions and TFSI⁻ anions of the ionic liquid is reached. Broadband electrical spectroscopy investigations demonstrate that these materials are characterized by the presence of different polarization phenomena and several dielectric relaxation events. After analyzing BES results, a reasonable conductivity mechanism is proposed. Furthermore, the IL-doped solid membrane polyelectrolyte reveals an ionic conductivity of $1.29 \cdot 10^{-5}$ and $1.92 \cdot 10^{-3}$ S·cm⁻¹ at 30 and 80 °C, respectively. Thus, these materials appear to be very promising for application in electrochemical devices.

4.1 Experimental Section

4.1.1 Reagents

Poly(vinyl alcohol-co-vinyl acetate) is provided by INEOS Technologies Italia Srl. The polymerization degree (defined as the sum of vinyl acetate (m) and vinyl alcohol repeat units (n), see Figure 4.1) is equal to 500, the hydrolysis degree ($n/(n+m)$) is 0.88, and the polymer average molecular weight is 25 kDa. Ethanol, methanol, 1-ethyl-3-methylimidazolium bis(trifluoromethylsulfonyl)imide (EMImTFSI), and lithium metal are obtained from Sigma-Aldrich.

4.1.2 Synthesis

4.1.2.1 PVA Lithiation

Poly(vinyl alcohol-co-vinyl lithium alkoxide), namely lithiated poly(vinyl alcohol) (Li_PVA), is synthesized by mixing 5.003 g of PVA and 8.611 g of lithium methoxide (MeOLi) in 75 mL of methanol (see Figure 4.1a, I). This reaction is performed into a Teflon autoclave, heated up to 85 °C for 20 h. The MeOLi precursor is obtained by direct reaction between lithium metal and dry methanol. Li_PVA is recovered by centrifuge precipitation, and washed 5 times with 30 mL of ethanol. The powder of the co-polymer is then dried under vacuum at 80 °C for 48 h, and finally stored into an argon filled glove-box.

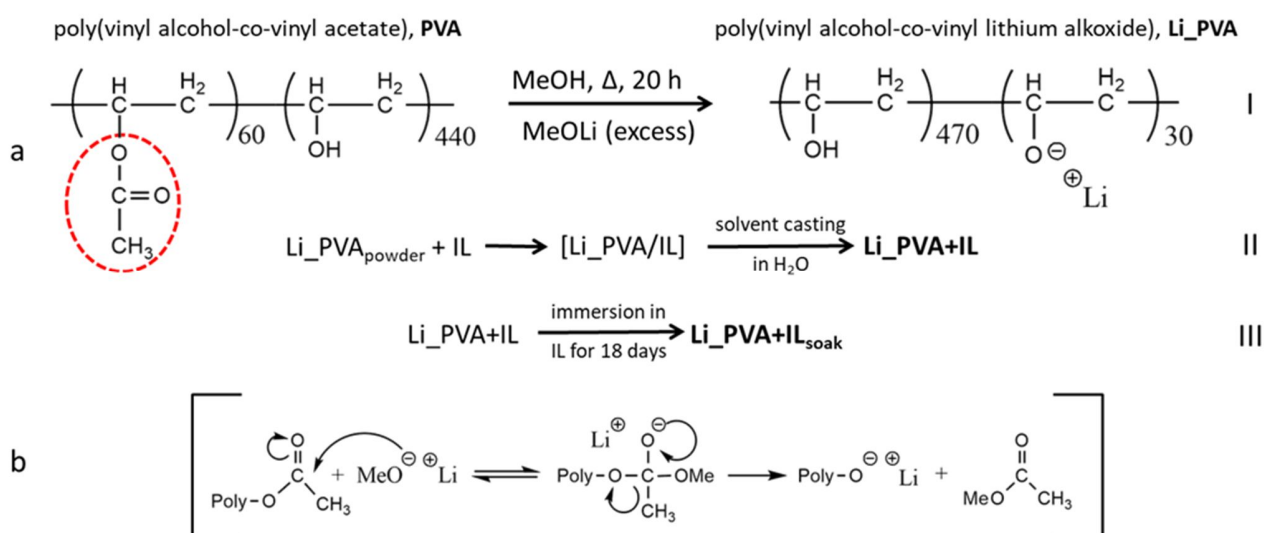


Figure 4.1. Preparation of Li_PVA, Li_PVA+IL, and Li_PVA+IL_{soak} samples (a). Steps I, II, and III are reported. Mechanism of reaction between MeOLi and carbonyl side groups (b).

4.1.2.2 PVA and Li_PVA Membrane Preparation

The two polymer powders (PVA and Li_PVA) are firstly dissolved in bidistilled water (*ca.* 5 % by weight), and then casted in a Teflon Petri dish at 80 °C. In this way, membranes with a thickness of the order of 60 μm are obtained

4.1.2.3 Li_PVA Plasticization

The ionic liquid-doped sample (Li_PVA+IL) is obtained by mixing 0.070 g of EMImTFSI with 0.288 g of Li_PVA powder. Then, 4 mL of bidistilled water are added to the mixture and kept stirred at 85 °C for 10 minutes. Finally, after the addition of methanol (7 mL), the overall suspension is casted in order to obtain a membrane (see step II of Figure 4.1a). A higher level of doping is gauged by

soaking Li_PVA+IL membrane directly into the ionic liquid at 70 °C for 18 days (see step III of Figure 4.1a).

Summarizing, four solid membrane are synthesized: i) pristine partially hydrolyzed poly(vinyl alcohol) (PVA); ii) lithiated PVA (Li_PVA); iii) moderately plasticized Li_PVA (Li_PVA+IL); and iv) strongly IL doped Li_PVA+IL membrane (Li_PVA+IL_{soak}).

4.2 Results and Discussion

4.2.1 Composition and Thermal Behavior

The lithiation reaction consists of a nucleophilic attack of methoxide on the side carbonyl functionality, as described in Figure 4.1b. HR-TGA and ATR-FTIR analyses confirm the complete elimination of the acetate groups of pristine PVA, together with the formation of lithium alkoxide functionalities. The degree of lithiation is determined by ICP-AES measurements, while the IL uptake is evaluated by CHNS and HR-TGA measurements. Results are reported in Table 4.1.

Table 4.1. Compositional data of PVA-based materials.

Sample	m ^a	n ^b	x ^c	IL _{EA} (wt%) ^d	IL _{TGA} (wt%) ^e
PVA	60	440	-	-	-
Li_PVA	-	469.40	30.60	-	-
Li_PVA+IL	-	469.64	30.36	14.89	15.92
Li_PVA+IL _{soak}	-	469.75	30.25	22.15	22.93

^am is the number of vinyl acetate units belonging to each polymer chain; ^bn is the number of vinyl alcohol units belonging to each polymer chain; ^cx is the number of lithium alkoxide units belonging to each polymer chain, evaluated by ICP analysis; ^dionic liquid content calculated from CHNS elemental analysis; ^eionic liquid content extrapolated from HR-TGA analysis.

After lithiation, Li_PVA sample owns *ca.* 30 lithium alkoxide units *per* polymer repeat unit, while all the acetate functionalities are selectively eliminated during the reaction reported in Figure 4.1b. Thus, a single lithium ion conducting polyelectrolyte is obtained, where Li⁺ are neutralizing R-O⁻ oxygen functionalities directly bonded to the polymer backbone. Indeed, since the anions are confined to the whole large macromolecular polymer chain, with a conductivity close to zero, lithium cations are the only mobile species.

The thermal behaviors characterizing the proposed materials are studied by HR-TGA, and the results are reported in Figure 4.2.

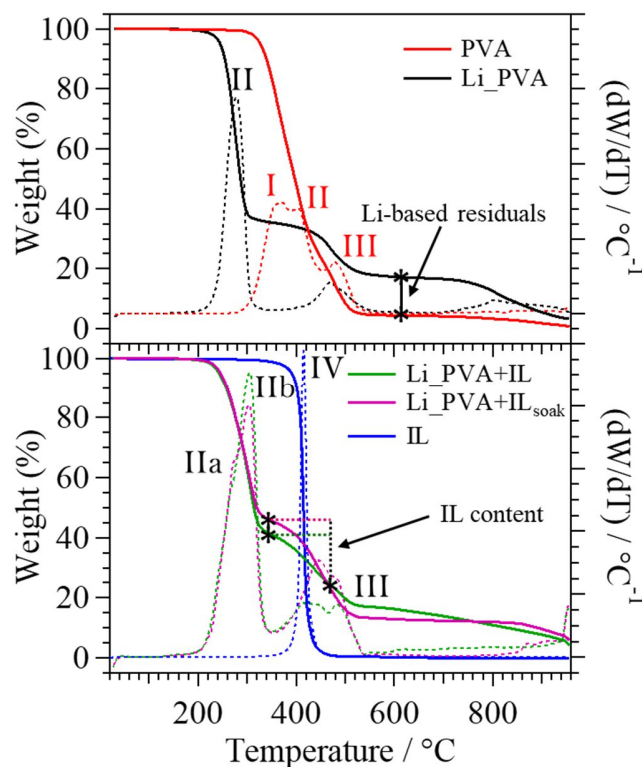


Figure 4.2. HR-TGA profiles of pristine PVA, IL, and PVA-based PEs.

In accordance with literature, PVA presents the typical thermal behavior of a poly(vinyl alcohol-co-vinyl acetate) compound [163]. Event I appears at *ca.* 300 °C, and is attributed to the thermal decomposition of the carbonyl functionalities which produce acetic acid. The second event (II), revealed at *ca.* 390 °C, corresponds to the crosslinking process of PVA fragments. Indeed, during this process, water molecules are released, with a consequent weight loss. Event III is detected at *ca.* 455 °C, and is attributed to the thermal degradation of the polymer backbone, where C-, H-, and O-based volatile species evolve. During the latter described event, different reactions are occurring, such as Diels-Alder reaction, intramolecular cyclization, and radical reactions, which lead to the formation of several volatile species, *e.g.* aldehydes, ketones, and others [163, 164].

For the lithiated polymer (Li_PVA), no peak attributed to the acetic acid elimination (I) is detected, confirming the complete elimination of acetate groups. Event II is observed to take place at a lower temperature with respect to the pristine polymer, starting at *ca.* 215 °C. Thus, the presence of Li⁺O⁻R functional groups catalyzes the crosslinking process of polymer chains, decreasing the temperature at which it occurs. Nevertheless, Li_PVA demonstrates a thermal stability higher than

215 °C. At high temperatures ($T > 600$ °C), the presence of a residual weight is observed, which is attributed to the remaining of high-stability lithium-based inorganic species.

In Li_PVA+IL and Li_PVA+IL_{soak} samples, thermal event II splits into two different sub-events, demonstrating the presence of different types of domains in the material. Indeed, the doping with EMImTFSI ionic liquid allows to generate a stabilized PVA domain, due to the interactions between the IL and the polymer matrix. The sub-event attributed to the degradation of these stabilized domains is labeled as IIb and occurs at higher temperatures (with a maximum in the derivative weight loss at *ca.* 305 °C). On the contrary, event IIa, that corresponds the degradation of those domains where no coordination between the polymer and the ionic liquid occurs, appears at temperatures more similar to the pure Li_PVA sample (starting at *ca.* 215 °C). In the doped membranes, the thermal degradation of the ionic liquid, event IV, is detected at 17 °C higher than in the pure EMImTFSI (*ca.* 345 °C). The synergistic interactions between the IL and the polymer give rise to a stabilizing effect on the ionic liquid in the plasticized membranes. The ionic liquid uptake in the membranes is evaluated by determining the weight loss between the two minima of the derivative curves, before and after IL decomposition. Li_PVA+IL sample is composed by the 15.92 %_{wt} of EMImTFSI, while the IL uptake in Li_PVA+IL_{soak} is 22.93 %_{wt} (see Table 4.1). These values are similar to those obtained from the elemental analysis, showing a good agreement between the two measuring techniques.

In this kind of materials is very important to study the thermal transitions occurring when the temperature is changed. Indeed, thermal transitions can affect and modify the conductivity mechanism. Following this, DSC measurements on the proposed materials are conducted in the temperature range 160÷-150 °C, and the results are presented in Figure 4.3.

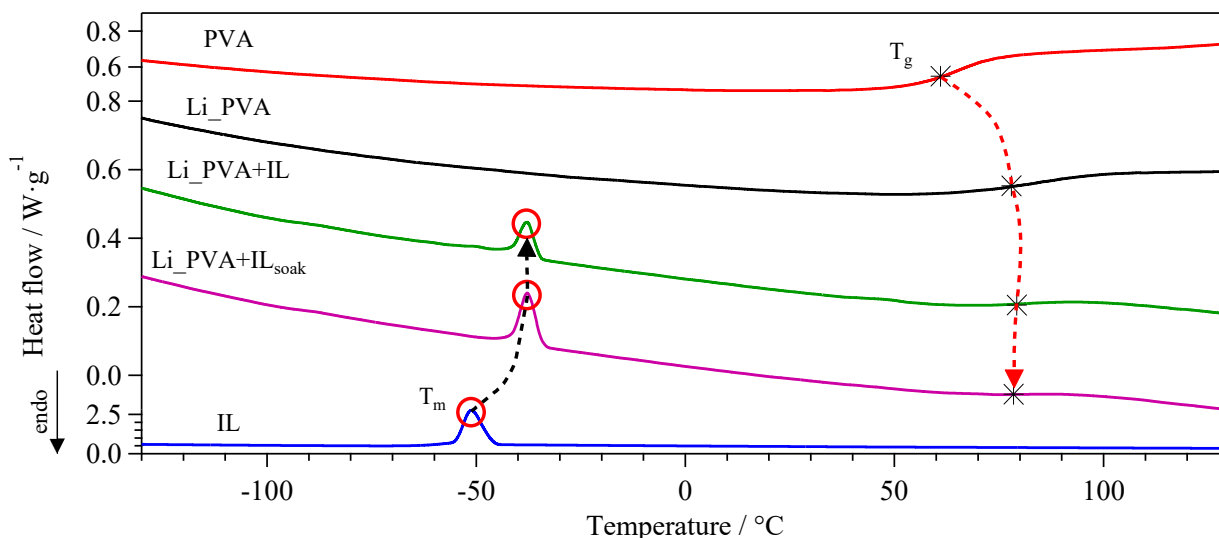


Figure 4.3. DSC profiles of PVA-based and IL samples; T_m indicates the melting event of EMImTFSI, while T_g corresponds to the glass transition of the PVA domain. Measurements are collected cooling the samples from +160 to -150 °C.

The pristine co-polymer (PVA sample) shows only one transition at *ca.* 64 °C, attributed to a glass transition (T_g) where an order/disorder modification of the amorphous polymer domains occurs. Upon lithiation, in Li_PVA, the glass transition is observed to shift at higher temperatures, at *ca.* 84 °C, indicating that lithium alkoxide functionalities hinder the flexibility of the polymer matrix, creating a sort of inter-chain dynamic crosslinks. After doping the polymer with the ionic liquid (Li_PVA+IL and Li_PVA+IL_{soak}), a slight decrease in the T_g is detected, which occurs at *ca.* 81 and 80 °C, respectively. This is the result of the plasticizing effect of the EMImTFSI on the polymer matrix, due to the nano-swelling events occurring in the materials. In this environment, polymer chains are solvated by IL molecules, and IL nano-clusters are created, which are incapsulated in the polymer matrix. The formation of the ionic liquid clusters is responsible for the increase of the EMImTFSI melting transition (T_m), that is detected, in PEs, at *ca.* -38 °C. This is a further proof of the effectiveness of the interactions occurring in the IL doped electrolyte membranes.

4.2.2 Vibrational Analyses

Vibrational analyses, carried out by ATR FT-IR measurements in the medium and far infrared regions, are a valid tool to investigate the structure and interactions occurring in the proposed materials. Figure 4.4 reports the results of vibrational measurements. PVA and Li_PVA spectra are normalized with respect to the band at 2910 cm^{-1} , while Li_PVA+IL, Li_PVA+IL_{soak}, and IL spectra are normalized with respect to the band at 1347 cm^{-1} .

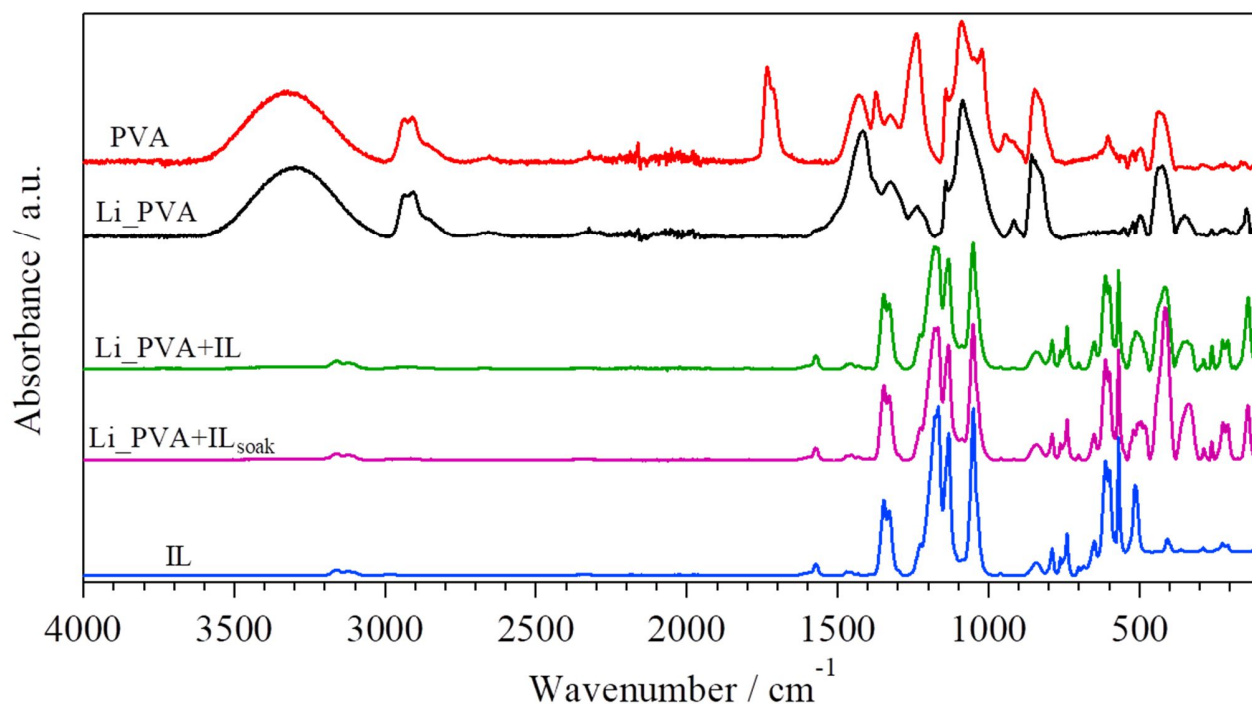


Figure 4.4. Docked Mid-ATR and Far-FTIR spectra of pristine PVA, IL, and PVA-based polymer electrolytes.

PVA and Li_PVA Mid-ATR and Far- FTIR spectra show the typical vibrations of a poly(vinyl alcohol) material. In particular, the $\nu(\text{OH})$ stretching mode of the hydroxyl groups of alcohol functionalities is detected at *ca.* 3318 cm^{-1} [165, 166]. At *ca.* 2939 , 2910 , and 2858 cm^{-1} , the antisymmetrical and symmetrical stretching modes of CH_2 ($\nu_a(\text{CH}_2)$ and $\nu_s(\text{CH}_2)$), and the symmetrical stretching vibration of CH_3 peak ($\nu_s(\text{CH}_3)$) are observed, respectively [165-167]. The two bands at *ca.* 1733 and 1714 cm^{-1} are attributed to the “free” and “H-bonded” $\nu(\text{C}=\text{O})$ stretching modes of the acetate groups in PVA sample [163, 167, 168]. On the contrary, Li_PVA spectrum do not show any peak in this region, indicating the absence of the acetate groups. Thus, their complete elimination during the lithiation reaction is confirmed. In the $820 \div 1430 \text{ cm}^{-1}$ spectral region the stretching, bending, twisting, rocking, and wagging vibrational modes of C-H and C-O are detected [165-167]. The peak at *ca.* 607 cm^{-1} corresponds to the wagging vibration of OH groups [166]. The *in phase* $\delta(\text{C}-\text{CH}_2)$ bending vibration is detected at *ca.* 551 cm^{-1} [167]; at *ca.* 521 cm^{-1} the $\delta(\text{C}-\text{C}-\text{O})$ bending is observed [169]. The $\delta(\text{C}-\text{O})$ bending, *out of phase* $\delta(\text{C}-\text{H})$ bending, and $\omega(\text{C}-\text{O})$ wagging are assigned to the peaks centered at *ca.* 496 and 484 , 440 , and 422 cm^{-1} , respectively [166, 167]. Finally, in Li_PVA sample, new peaks are detected at *ca.* 391 , 363 , and 260 cm^{-1} , which correspond to the $\text{Li}^+\text{-O}^-$ stretching vibrations [170, 171]. Thus, the successful lithiation of PVA polymer is confirmed.

In the ATR-FTIR profiles of Li_PVA+IL and Li_PVA+IL_{soak} it is observed that the vibrational modes of the IL dominate the spectra, thus neglecting the PVA component. Nevertheless, the vibrations attributed to the polymer matrix can be detected by expanding appropriate spectral regions of Figure 4.4. Results are reported in Figure 4.5.

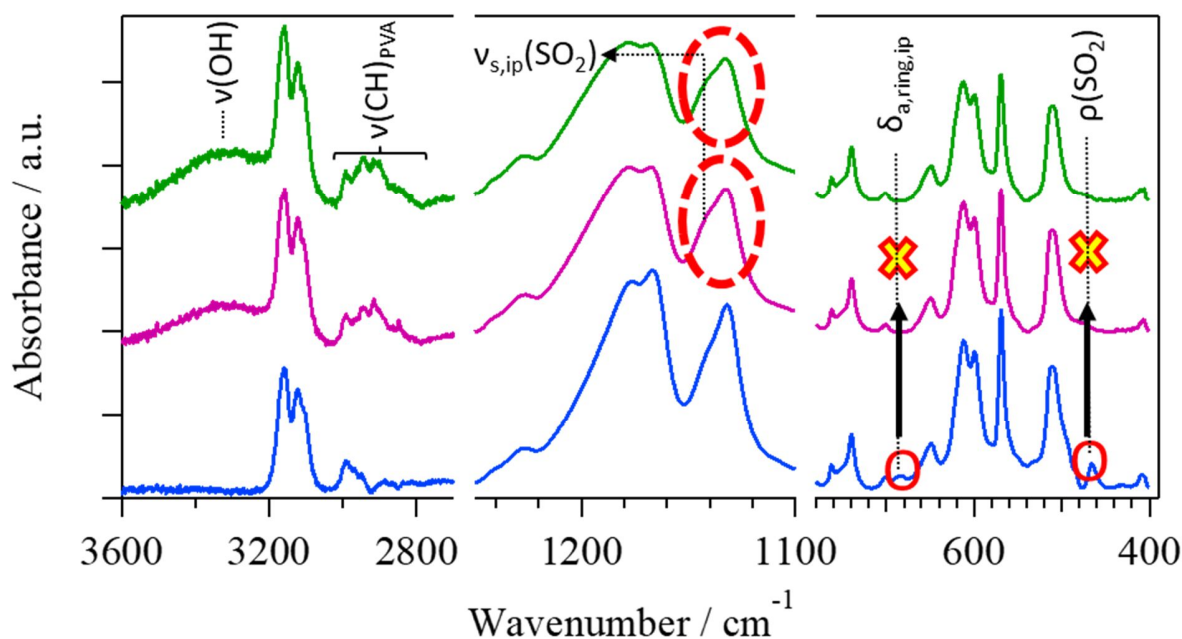


Figure 4.5. Magnification of selected spectral regions of FT-IR measurements for Li_PVA+IL, Li_PVA+IL_{soak}, and IL samples.

In the following list all the peaks attributed to the EMImTFSI ionic liquid are assigned to the relative vibrational mode: i) between 3160 and 2950 cm^{-1} , the symmetrical and antisymmetrical $\nu(\text{C-H})$ stretching vibrations of the imidazolium ring [172]; ii) the symmetrical and antisymmetrical $\delta(\text{C-N})$ bending and $\nu(\text{C-H})$ stretching of the imidazolium ring are observed in the range 1575÷1450 cm^{-1} [172]; iii) between 1180 and 1130 cm^{-1} , the vibrations related to the SO_2 and CF_3 of the TFSI anion are detected [172]; iv) from 850 to 550 cm^{-1} , different overlapped modes corresponding to both the imidazolium cation and TFSI⁻ anion are revealed [172]; and v) the vibration at *ca.* 513 cm^{-1} and the series of peaks at *ca.* 287, 225, and 207 cm^{-1} are attributed to the antisymmetrical bending and rocking modes of CF_3 , respectively [172, 173].

All the vibrational assignments are summarized in Table 4.2.

Table 4.2. Mid- Far-IR vibrational frequencies assignment for PVA-based membranes.

PVA	Experimental frequencies (cm ⁻¹) ^a				Assignment ^b	Ref.
	Li_PVA	Li_PVA+IL	Li_PVA+IL _{soak}	IL		
3318 (m)	3299 (m)	3320 (vw)	3312 (vw)		$\nu(\text{OH})$	[165, 166]
		3158 (vw)	3158 (vw)	3158 (vw)	$\nu_s(\text{HCCH})_{\text{ring}}+\nu_{s,\text{ip}}(\text{ring})$	[172]
		3122 (vw)	3122 (vw)	3122 (vw)	$\nu_s(\text{NC(H)NCH})_{\text{ring}}$	[172]
		2992 (vw)	2992 (vw)	2992 (vw)	$\nu_a(\text{CH}_3(\text{N})\text{HCH})_{\text{ring}}$	[172]
				2952 (vw)	$\nu_a(\text{CH}_3\text{HCH})_{\text{terminal}}$	[172]
2939 (m)	2936 (m)	2944 (vw)	2944 (vw)		$\nu_a(\text{CH}_2)$	[166, 167]
2910 (m)	2909 (m)	2916 (vw)	2916 (vw)		$\nu_s(\text{CH}_2)$	[165-167]
2858 (w,sh)	2858 (w,sh)	2849 (vw)	2849 (vw)		$\nu_s(\text{CH}_3)$	[166, 167]
2655 (vw)	2658 (vw)					
1733 (s)					$\nu(\text{C}=\text{O})$ "free"	[163, 167, 168]
1714 (m,sh)					$\nu(\text{C}=\text{O})$ "H-bonded"	[163, 168]
		1573 (vw)	1575 (vw)	1574 (vw)	$\nu_{a,s,\text{ip}}(\text{ring})+\nu(\text{CH}_3(\text{N}))+$ $\nu(\text{CH}_2(\text{N}))+\nu_s(\text{CN})$	[172]
		1471 (vw)	1471 (vw)	1471 (vw)	$\nu_{a,\text{ip}}(\text{ring})+\nu(\text{CH}_3(\text{N}))$	[172]
		1455 (vw)	1455 (vw)	1456 (vw)	$\delta_s(\text{CCH HCC})+\delta_s(\text{CH}_3(\text{N})\text{HCH})+$ $\delta_a(\text{CH}_3\text{HCH})_{\text{terminal}}$	[172]
1430 (m)	1420 (s)	1431 (vw)	1432 (vw)	1432 (vw)	$\delta_a(\text{CH}_2)$	[166, 167]
1373 (m)	1377 (m,sh)	1394 (vw)	1394 (vw)	1393 (vw)	$\omega(\text{CH})$	[166]
		1347 (m)	1347 (m)	1347 (m)	$\nu_a(\text{SO}_2)$	[172]
		1330 (m)	1329 (m)	1330 (m)	$\nu_a(\text{SO}_2)+\nu_{s,\text{ip}}(\text{ring})+\nu(\text{CC})+$ $\nu(\text{CH}_2(\text{N}))+\nu(\text{CH}_3(\text{N})\text{CN})$	[172]
1324 (m)	1326 (m)				$\delta(\text{H-C-OH})$	[165, 166]
1238 (vs)	1237 (w)				$\omega(\text{CH})$	[166]
		1227 (w,sh)	1227 (w,sh)	1227 (w,sh)	$\tau(\text{CH}_2)+\rho(\text{CH}_2)$	[172]
		1178 (s)	1177 (s)	1176 (s)	$\nu_a(\text{CF}_3)$	[172]
		1168 (s)	1168 (s)	1167 (s)	$\nu_{s,\text{ip}}(\text{SO}_2)$	[172]
1142 (m)	1141 (m)				$\nu(\text{C-O})$	[166, 167]
		1142 (s,sh)	1142 (s,sh)	1142 (s,sh)	$\nu_{s,\text{oop}}(\text{SO}_2)$	[172]
		1132 (s)	1132 (s)	1132 (s)	$\nu_{s,\text{ip}}(\text{SO}_2)$	[172]
1089 (vs)	1086 (vs)				$\nu(\text{C-O})$	[166, 167]
		1051 (s)	1051 (s)	1050 (s)	$\nu_{a,\text{ip}}(\text{ring})+\nu(\text{CC})+\nu_a(\text{SNS})+\tau(\text{NCH}_3)$	[172]
1047 (s,sh)					$\omega(\text{CH}_2)$	[167]
1022 (s)	1021 (m,sh)				$\tau(\text{CH}_2)$	[167]
947 (w)					$\omega(\text{CH}_3)$	[167]
914 (w,sh)	916 (w)				$\rho(\text{CH}_2)$	[166]
847 (m)	857 (m)				$\nu(\text{C-C})$	[166]
		844 (w)	843 (w)	843 (w)	$\delta_{\text{ring}}(\text{NC(H)N})+\delta(\text{CCH})$	[172]

826 (m,sh)	825 (m,sh)				$\delta_{ip}(C-O)$	[167]
		789 (w)	789 (w)	789 (w)	$\delta_{a,ring}(HCCH)+v(CS)$	[172]
		763 (w,sh)	763 (w,sh)	763 (w,sh)	$v(CF)+v(SN)v(CS)$	[172]
		740 (w)	740 (w)	740 (w)	$\delta(CH_3(N))+\delta(CH_2(N))+\delta_s(CF_3)+\delta_{ring,ip}+v(SNS)$	[172]
		701 (vw)	701 (vw)	701 (vw)	$\delta_{a,ring,ip}+v(CH_2(N))+v(CH_3(N)CN)$	[172]
				685 (w)	$\delta_{a,ring,ip}$	[172]
		649 (w)	649 (w)	649 (w)	$\delta_{a,ring,oop}+\delta(SNS)$	[172]
		612 (s)	612 (s)	612 (s)	$\delta_{a,ring,oop}+\delta_a(SO_2)+v(CH_3(N)CN)$	[172]
607 (w)					$\omega(OH)$	[166]
		599 (s)	600 (s)	600 (s)	$\delta_{s,ring,ip}+\delta_a(SO_2)+v(CH_3(N)CN)$	[172]
		569 (s)	569 (s)	569 (s)	$\delta_{s,ring,ip}+\delta_a(CF_3)$	[172]
551 (w)	553 (w)				$\delta_{ip}(C-CH_2)$	[167]
521 (w)	521 (w)	521 (w)	520 (w)	515 (m)	$\delta(C-C-O)$	[169]
		513 (w)	502 (w)		$\delta_a(CF_3)$	[172]
496 (w)	498 (w)	493 (w)	494 (w)		$\delta(CO)$	[166]
484 (w)	489 (w)	481 (w)	481 (w)		$\delta(CO)$	[166]
440 (m)	436 (m)	438 (m)	439 (m,sh)		$\delta_{oop}(CH)$	[167]
422 (m)	423 (m)	414 (m)	415 (m)	407 (w)	$\omega(CO)$	[166]
	391 (w,sh)	396 (w,sh)	397 (w,sh)		$v(Li-O)$	[171]
	363 (w)	361 (w)	358 (w)		$v(Li-O)$	[171]
	332 (w)	332 (w)	336 (w)		$\delta_{oop}(C-CH_2)$	[167]
		287 (w)	287 (w)	287 (vw)	$\rho(CF_3)$	[173]
	260 (vw)	260 (w)	260 (w)		LiO ₆ within cages	[170]
		225 (w)	224 (w)	226 (vw)	$\rho(CF_3)$	[173]
		207 (w)	207 (w)	206 (vw)	$\rho(CF_3)$	[173]
	146 (w)	140 (m)	141 (w)		C-C torsion	[167]

^aIntensities are reported in brackets: v= very strong; s=strong; m=medium; w=weak; vw=very weak; sh=shoulder. ^bv stretching; δ bending; ω = wagging, ρ = rocking, τ = twisting, ip = in phase, oop = out of phase, a = antisymmetrical, s = symmetrical.

ATR-FTIR spectra are useful to evaluate the degree of crystallinity of the polymer matrix before and after lithiation, as reported in literature [174, 175]. Indeed, the ratio between the intensities of the peaks centered at *ca.* 1142 and 1430 cm⁻¹ ($\rho = I_{1142}/I_{1430}$), attributed to the $v(C-O-C)$ and $\delta_a(CH_2)$ of PVA, is an index of the crystalline domain density concentration in the co-polymer. It is observed that, after lithiation, ρ decreases, indicating that the lithium alkoxide functional groups interrupt the crystallinity of the polymer increasing the amorphicity of PVA. This effect is also confirmed by the decreasing intensities of the $\omega(CH)$ wagging vibrations at *ca.* 1373 and 1238 cm⁻¹, and that of the $\tau(CH_2)$ twisting vibration at *ca.* 1202 cm⁻¹ [169]. Lithium cations are coordinated by both alkoxide side groups of polymer chains and by the oxygens of TFSI⁻ anions. Insights on

these coordination geometries can be obtained by vibrational analyses. The shoulder intensity present at *ca.* 1142 cm^{-1} , attributed to the *out of phase* symmetrical bending of the SO_2 group, increases: i) in the order pristine IL < Li_PVA+IL < Li_PVA+IL_{soak}; and ii) as the concentration of LiTFSI in lithiated PEs increases [176]. Furthermore, the effective interactions occurring between IL and PVA are confirmed by the disappearance of the peak assigned to the antisymmetrical *in phase* bending mode of the imidazolium ring of EMImTFSI at *ca.* 685 cm^{-1} . Finally, the peak centered at *ca.* 260 cm^{-1} , attributed to the Li-O stretching vibration, indicates that Li^+ is coordinated by six oxygen ligands in a hexacoordination geometry [170]. Indeed, it is probable that these six oxygen atoms come from: i) one hydroxyl and one alkoxide functional groups of the polymer matrix; and ii) two different TFSI⁻ anions, each one contributing with two oxygen atoms.

All the information gained by HR-TGA, DSC, and ATR FT-IR studies about the structure and interactions occurring in the proposed solid membrane polyelectrolytes can be summarized by the following representation (Figure 4.6).

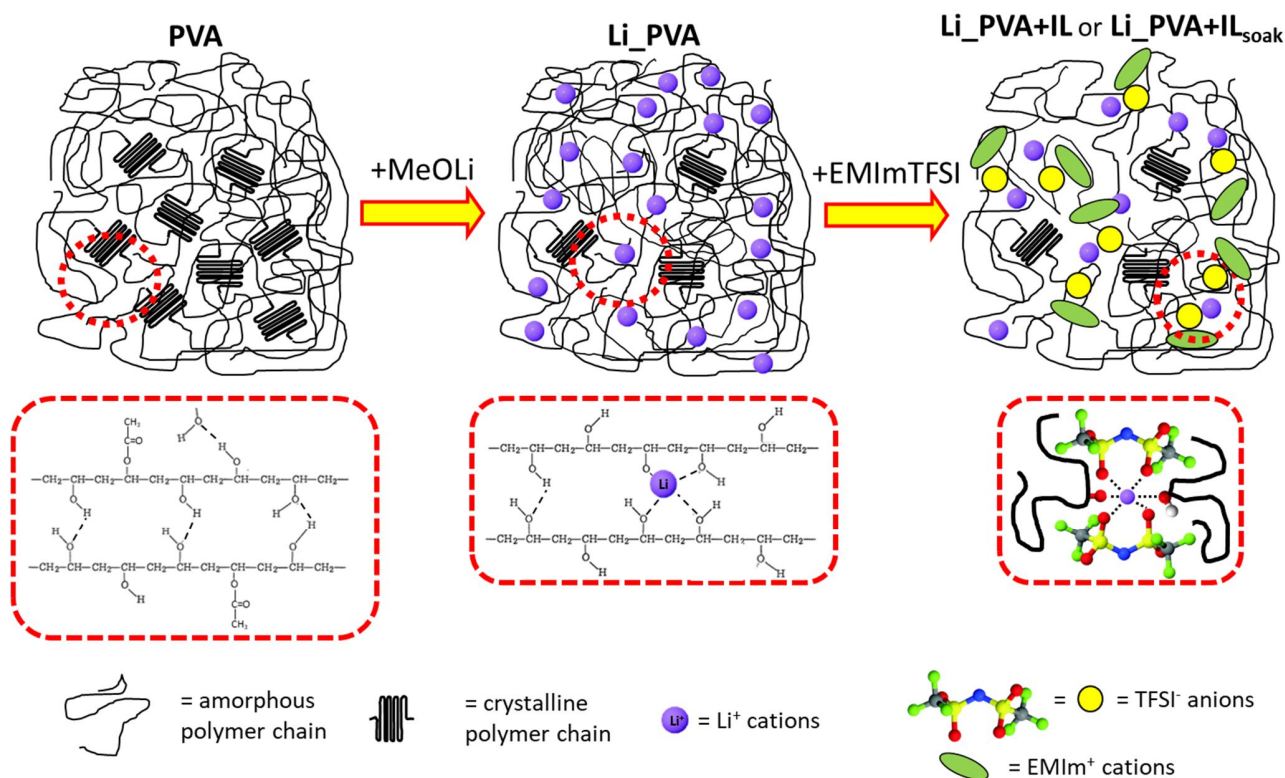


Figure 4.6. Structural and interaction features of PVA, Li_PVA, and Li_PVA+IL or Li_PVA+IL_{soak} materials.

Pristine poly(vinyl alcohol-co-vinyl acetate) is composed by both amorphous and crystalline domains. Upon lithiation, Li_PVA exhibits an increased amorphicity, due to the coordination of lithium cations by the oxygen ligands of polymer chains in a distorted tetrahedral geometry [177, 178]. The doping of Li_PVA sample with EMImTFSI ionic liquid results in three different effects: i) swelling and plasticization of the polymer matrix, with a consequent increase in the flexibility and mobility of polymer chains; ii) $\text{Li}^+ \leftrightarrow \text{EMIm}^+$ ion exchange in alkoxide functionalities, that further improves the mobility of lithium cations; and iii) coordination of lithium cations by TFSI⁻ anions, improving the mobility of Li^+ ions. Furthermore, this interaction induces a modification of the coordination geometry from a distorted tetrahedral in Li_PVA to an octahedral distorted geometry in Li_PVA+IL and Li_PVA+IL_{soak}. In the doped membranes, the latter two events act together to completely delocalize Li^+ cations, thus improving the lithium conductivity in bulk materials.

4.2.3 Lithium Transference Number

The lithium transference number, t_{Li^+} , for Li_PVA+IL_{soak} membrane is measured according to the Bruce and Vincent method [179]. The sample is left at 80 °C for 24 h after assembling the cell, in order to allow a stable SEI to be formed on the surfaces. The t_{Li^+} for this sample is equal to 0.59. Indeed, this value is the result of two concurring effects: i) the single-ion conductivity of pure Li_PVA; and ii) the ion exchange that occurs between Li^+ and EMIm^+ when IL is added, with the consequent coordination of lithium ions to TFSI⁻ anions. As expected, the lithium transference number decreases from 1 (Li_PVA) upon plasticization due to the introduction of new mobile ionic species, *i.e.* those of EMImTFSI ionic liquid. Nevertheless, t_{Li^+} for Li_PVA+IL_{soak} membrane results to be an interesting value in this class of materials, and it is in line with values reported in literature for similar plasticized PEs [180, 181].

4.2.4 Broadband Electrical Spectroscopy Studies

The electric response of materials is investigated by broadband electrical spectroscopy studies from 150 to -130 °C, and in the frequency range $10^{-2} \div 10^7$ Hz. The obtained results indicate that the electric response is characterized by the overlap of different polarization (σ_k) and several dielectric relaxation (f_j) events. The 3D-*tan delta* surfaces, with $\tan \delta = \epsilon''/\epsilon'$ (ϵ'' and ϵ' are the imaginary and the real components of the complex permittivity), of each material are plotted as a function of temperature (T) and frequency (f) in Figure 4.7.

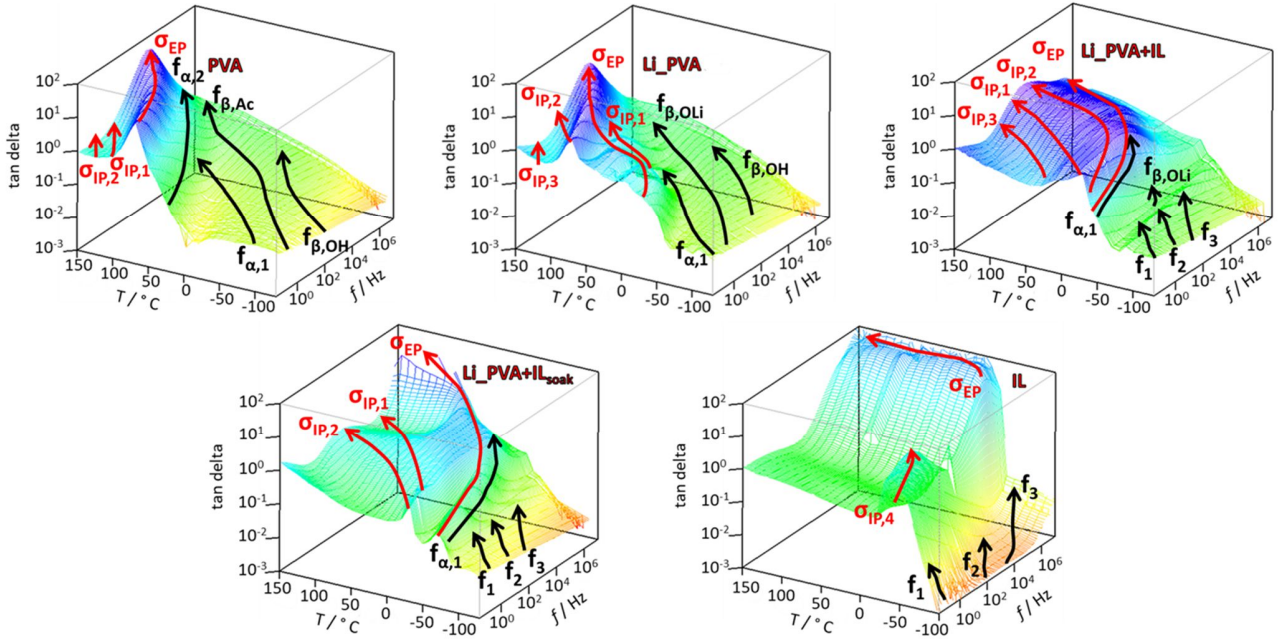


Figure 4.7. 3D-*tan delta* surfaces of pristine IL and PVA-based materials.

The electric response, in terms of both the imaginary and real components of the conductivity and permittivity, are analyzed with a suitable model, described by the following equation [52, 162]:

$$\varepsilon_m^*(\omega) = -i \left(\frac{\sigma_0}{\omega \varepsilon_0} \right)^N + \frac{\sigma_{EP}(i\omega\tau_{EP})^{\gamma_{EP}}}{i\omega\varepsilon_0[1+(i\omega\tau_{EP})^{\gamma_{EP}}]} + \sum_{k=1}^n \frac{\sigma_{IP,k}(i\omega\tau_{IP,k})^{\gamma_{IP,k}}}{i\omega\varepsilon_0[1+(i\omega\tau_{IP,k})^{\gamma_{IP,k}}]} + \sum_{j=1}^m \frac{\Delta\varepsilon_j}{[1+(i\omega\tau_j)^{\alpha_j}]^{\beta_j}} + \varepsilon_\infty \quad (4.1)$$

where $\varepsilon^*(\omega) = \varepsilon'(\omega) - i\varepsilon''(\omega)$, and $\sigma^*(\omega) = i\omega\varepsilon_0\varepsilon^*(\omega)$. The first term of the equation describes the material conductivity at zero frequency. ε_∞ accounts for the permittivity of the material at infinite frequency (electronic contribution). The second term is associated with electrode polarization, while the third describes the interdomain polarizations. σ_k and τ_k are the conductivity and the relaxation times, respectively, associated with the k^{th} electrical event. γ_k is associated with the broadening of the k^{th} polarization peak. The third term accounts for the dielectric relaxation described by the Havriliak-Negami theory [162, 182]. $\Delta\varepsilon$, τ_j , α_j , and β_j are the dielectric strength, relaxation time, symmetric and antisymmetric shape parameter of each j^{th} relaxation event, respectively. The analysis of the electric response of the samples is considered of high quality only if the experimental profiles, in terms of all the physical quantities (ε' , ε'' , σ' , σ'' , and *tan delta* vs. frequency), are perfectly interpolated by the here described Equation at all the temperatures.

4.2.4.1 Polarization Phenomena

The results in terms of conductivity parameters, obtained by interpolation of experimental data with Equation 4.1, are plotted as $\log(\sigma_k)$ vs. T^{-1} in Figure 4.8a. These data are fitted with a suitable model, *i.e.* Vogel-Tammann-Fulcher (VTF) [183] or Arrhenius (A) equation [162] to determine the activation energy of the polarization phenomena.

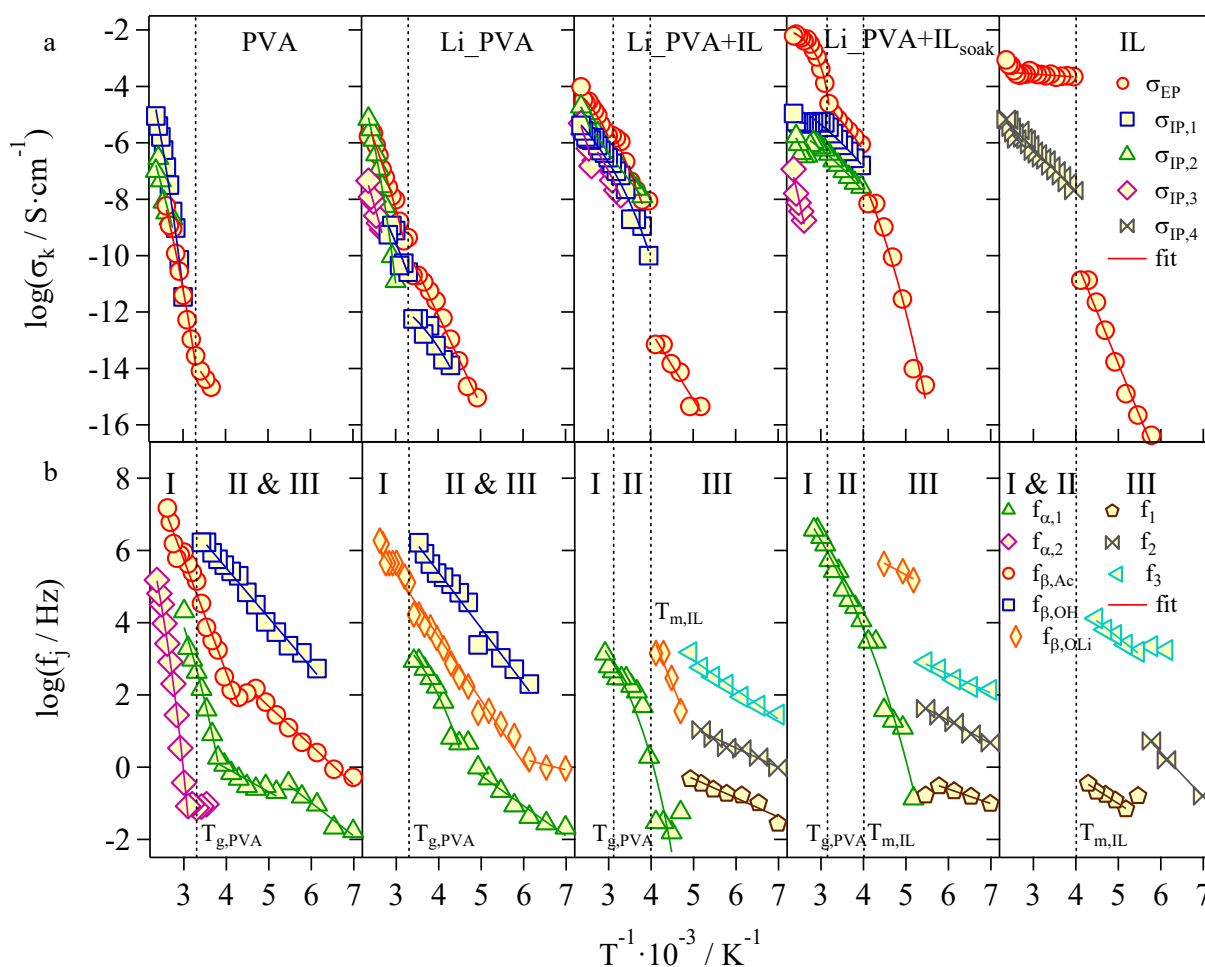


Figure 4.8. Dependence on T^{-1} of the σ_k conductivity values (a), and of the f_j dielectric relaxation frequencies (b) for pristine IL and PVA-based materials. Temperature regions are indicated as I, II, and III.

Three different temperature regions are detected, which are delimited by the thermal transitions observed in DSC measurements. At $T > T_{g,PVA}$, it is possible to observe four different σ_k polarization phenomena, which correspond to four different conductivity pathways in the polymer electrolytes. In particular, σ_{EP} is attributed to the accumulation of charges at the interface between the electrolyte and the Pt electrodes of the sampling cell, and corresponds to the electrode polarization

event [162]. Furthermore, when $\sum_{i=1}^3 \sigma_{IP,i} \ll \sigma_{EP}$, σ_{EP} coincide to the bulk conductivity of the material. The presence of the interdomain polarizations ($\sigma_{IP,i}$, with $1 \leq i \leq 3$), that correspond to the accumulation of charges at the interface between domains with different permittivity, allows to say that the proposed solid polymer electrolytes are heterogeneous at the mesoscale and consist of nanodomains [162]. Thus, these systems are determined to be composed by polymeric domains with different crystallinity. It is clear from Figure 4.8a that the nanomorphology of the materials is significantly modified by IL addition. Indeed, the doping of Li_PVA with EMImTFSI results in a split and a shift of $\sigma_{IP,i}$ vs. T^{-1} profiles with respect to Li_PVA sample. In this temperature range all the σ_k vs. T^{-1} curves show a Vogel-Tammann-Fulcher (VTF) trend, suggesting that the segmental motion of polymeric matrix is playing a crucial role in assisting the long-range charge migration events in these solid polymer electrolytes. Furthermore, it is observed that the plasticizing and cation exchange effects of IL doping results in a great improvement of the segmental motion of polymer backbone chains, and consequently in the conductivity value of σ_k .

At temperatures lower than the glass transition of PVA matrix, σ_{EP} event is the only detected polarization phenomena, with conductivity values lower than 10^{-12} S·cm⁻¹. Only Li_PVA+IL_{soak} sample shows a value higher than 10^{-9} S·cm⁻¹ at temperatures close to $T_{g,PVA}$. These evidences indicate that, in this temperature region, the ions mobility is hindered and that σ_{EP} is the only available conductivity pathway for the long-range charge migration phenomena.

The overall conductivity (σ_T) of the proposed electrolytes is calculated as the sum of all the conductivities that contribute to this value. The dependence of σ_T on T^{-1} is reported in Figure 4.9.

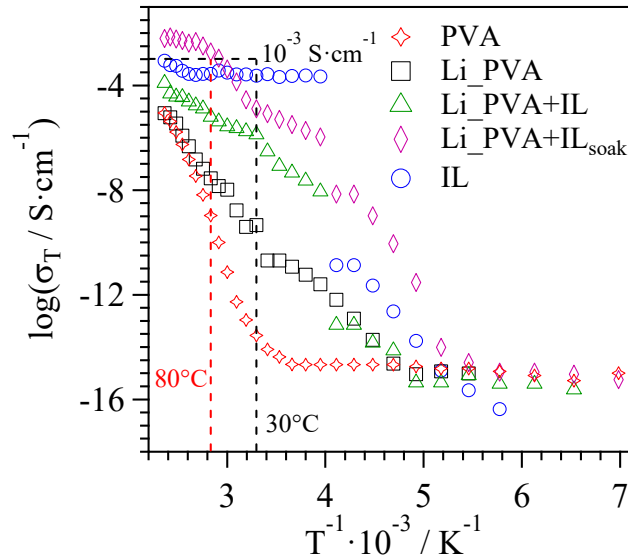


Figure 4.9. Dependence on T^{-1} of the overall conductivity ($\sigma_T = \sum_{i=1}^4 \sigma_{IP,i} + \sigma_{EP}$) of investigated materials.

PVA membrane shows a room-temperature conductivity of $2.82 \cdot 10^{-14} \text{ S}\cdot\text{cm}^{-1}$, indicating that, as expected, there are no species exchanged in this material. After lithiation (Li_PVA), σ_T increases by four orders of magnitude, reaching a value of *ca.* $4.58 \cdot 10^{-10} \text{ S}\cdot\text{cm}^{-1}$. Even if the conductivity is quite low, Li_PVA solid membrane polyelectrolyte is a lithium single ion conducting material. The IL doping of the polymer has a great effect on the electrolyte overall conductivity. Indeed, σ_T is improved by five orders of magnitude: the highest value is obtained with Li_PVA+IL_{soak} sample, which shows a room-temperature conductivity of *ca.* $1.29 \cdot 10^{-5} \text{ S}\cdot\text{cm}^{-1}$. This indicates that Li_PVA+IL_{soak} membrane is a very promising electrolyte with respect to the state of the art solid polymer electrolytes. Moreover, the Li_PVA+IL_{soak} total conductivity measured at medium temperatures (80 °C) is equal to $1.92 \cdot 10^{-3} \text{ S cm}^{-1}$, which is more than one order of magnitude higher than that of pure EMImTFSI ($2.76 \cdot 10^{-4} \text{ S}\cdot\text{cm}^{-1}$). Summarizing, after IL doping, the strength of the Li⁺-O-R coordination bonds is weakened by the formation of the distorted octahedral coordination geometry of Li⁺ cations by both TFSI⁻ anions and oxygen ligands of polymer matrix. This facilitates the Li⁺ exchange processes between adjacent coordination sites and, at room-temperature, the delocalization of the cations and the conductivity of the polymer electrolyte is improved. Concluding, it should be highlighted that, if we compare the conductivity of Li_PVA+IL_{soak} with that of other solid state polymer electrolytes recently reported in the literature [184], the proposed material is a very promising electrolyte for electrochemical device applications.

4.2.4.2 Dielectric Relaxation Events

At $T < T_{g,PVA}$, eight dielectric relaxation events are found in the electric response of the studied materials (see Figure 4.8b). These relaxations are attributed to the polymer ($f_{\alpha,1}, f_{\alpha,2}, f_{\beta,Ac}, f_{\beta,OH}, f_{\beta,OLi}$) and EMImTFSI ionic liquid (f_j , with $1 \leq j \leq 3$) components. The $f_{\alpha,1}$ and $f_{\alpha,2}$ modes are assigned to the diffusion of conformational states along polymer chains (segmental motions) of poly(vinyl alcohol) and poly(vinyl acetate) domains, respectively. The $f_{\beta,Ac}$, $f_{\beta,OH}$, and $f_{\beta,OLi}$ are beta relaxations attributed to the local fluctuations of the dipole moments of acetate, hydroxyl, and lithium alkoxide side groups. For the ionic liquid component, f_1 and f_2 dielectric relaxation modes are associated with the rotational motions around the short and long axes of spheroidal EMIm⁺ cations, respectively. Finally, f_3 is a relaxation event assigned to the inter-ion motion between the EMIm⁺ ring and TFSI⁻ ions. All of these dielectric relaxation events are in accordance with those of other PVA-based materials [185-188] and EMIm-based ionic liquids [23, 57, 133, 134, 189] reported in literature. It can be observed that, after lithiation, $f_{\alpha,1}$ shifts to slightly lower frequencies. In accordance with DSC measurements, this can be explained by the hinderance of the segmental motions in Li_PVA with respect to the pristine PVA polymer matrix, due to the formation of a sort of inter-chain dynamic crosslinks. With the addition of the IL, the typical relaxation events of EMImTFSI are clearly observed, which occur concurrently with those of the polymer matrix. In Li_PVA+IL_{soak}, $f_{\alpha,1}$ of pristine Li_PVA is shifted to higher frequencies, thus indicating that the IL effectively interacts with the PVA acting as an optimum plasticizer in enhancing the segmental motions of polymer matrix.

At $T > T_{g,PVA}$, the only detected dielectric relaxation is $f_{\beta,OLi}$, just for Li_PVA sample. Indeed, in this temperature range the electric response of the electrolytes is dominated by the higher intense polarization phenomena.

4.2.4.3 Activation Energies

The ultimate tool to unveil the conductivity mechanism that is occurring in the proposed solid membrane polyelectrolyte materials, is the calculation of the activation energies (E_a) of each polarization phenomena and dielectric relaxation events reported into Figure 4.8. This can be obtained by fitting, in all the temperature regions, the curves with a VTF-, VTFH-, or an Arrhenius-like equation. The calculated E_a values, for all the samples and at each temperature region, are plotted in Figure 4.10.

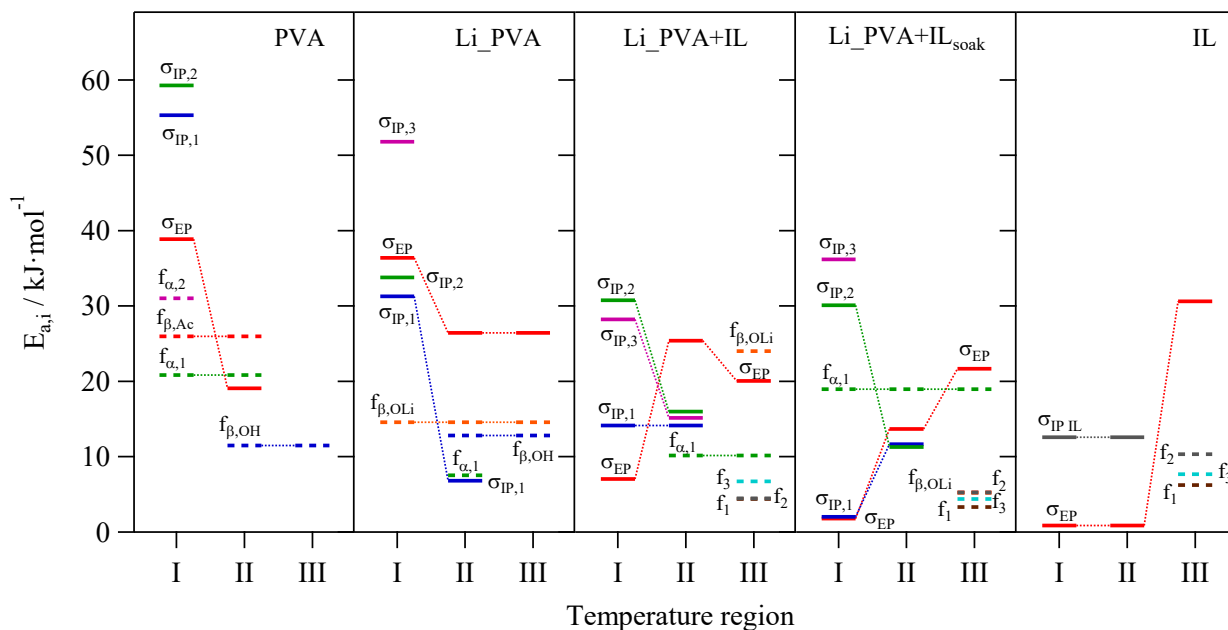


Figure 4.10. Correlation map of activation energies of measured conductivities (E_{a,σ_i}) and dielectric relaxation events (E_{a,f_j}) of different samples in various temperature regions.

This graph is very useful to understand the relationships existing between the polarization, and so the conductivity, and the dielectric relaxation events. In Li_PVA, σ_{EP} seems to not be correlated to any of the dielectric relaxation of the polymer matrix, indicating that PVA relaxations do not modulate the lithium ion conductivity mechanism. Nevertheless, at high temperatures (region I) the $f_{\alpha,1}$ dielectric event is neglected by the polarization signals. Thus, it is difficult to exclude its involvement in the overall conductivity of the electrolyte. At medium temperatures, in region II, it is observed that the $\sigma_{IP,1}$ interdomain polarization activation energy is very similar to that of $f_{\alpha,1}$ mode, indicating that this relaxation is assisting the long-range charge migration events along $IP,1$ conductivity pathway. The presence in bulk polymer of EMImTFSI, in Li_PVA+IL, decreases the E_a of σ_{EP} in the whole temperature range. Again, in region I, it is difficult to detect the dielectric relaxations and to correlate their activation energy values to those of polarization phenomena, thus evaluating if any correlation between the two events is present. At low temperatures, region III, the local fluctuations of the dipole moments of $-\text{RO}-\text{Li}^+$ side groups play a crucial role in assisting the overall conductivity mechanism of the samples. Moreover, in region II, it can be observed that the segmental motions of PVA fragments ($f_{\alpha,i}$) are modulating the conductivity mechanisms occurring along conductivity pathways measured by interdomain polarization events ($\sigma_{IP,i}$, $1 \leq i \leq 3$). Finally, Li_PVA+IL_{soak} membrane shows the lowest values of σ_{EP} activation energy (*ca.* 13.7

$\text{kJ}\cdot\text{mol}^{-1}$ at room-temperature). This outcome reveals that the presence of EMImTFSI clusters at the interfaces between PVA domains allows for a very low threshold of conductivity mechanism initiation.

4.3 Conclusions

In this chapter, a new set of PVA-based solid polymer electrolyte membranes is presented. The materials are synthesized by direct lithiation of poly(vinyl alcohol-co-vinyl acetate), which occurs selectively thanks to the direct nucleophilic attack of acetate groups by lithium methoxide. The obtained PEs are thermal stable up to more than $215\text{ }^{\circ}\text{C}$, and reveal the presence of a glass transition in the temperature range of $60\div 80\text{ }^{\circ}\text{C}$. FT-IR ATR studies show that: i) the lithiation reaction eliminates the acetate groups from pristine PVA; ii) lithium functionalization increases the amorphicity of the polymer, due to the coordination of lithium cations by the oxygen ligands of polymer chains in a distorted tetrahedral geometry; iii) after ionic liquid addition, the lithium coordination is shifted towards the formation of octahedral coordination cages, thanks to the participation of the oxygen functionalities of TFSI⁻ anions; and iv) a cation exchange occurs between EMIm⁺ and Li⁺. BES studies reveal the presence of one electrode polarization, three interdomain polarizations, and eight dielectric relaxations. Between the dielectric relaxations, five of them are related to the polymer matrix (two α - relaxations and three β relaxations), and the remaining three are associated with the IL domains. These relaxation events are playing a crucial role in modulating the long-range conductivity mechanism of ionic species. At $30\text{ }^{\circ}\text{C}$ the ionic conductivity of Li_PVA sample is at least four orders of magnitude higher than that of PVA pristine copolymer ($4.58\cdot 10^{-10}\text{ S}\cdot\text{cm}^{-1}$ vs. $2.82\cdot 10^{-14}\text{ S}\cdot\text{cm}^{-1}$). Doping of Li_PVA with IL further increases the ionic conductivity ($1.29\cdot 10^{-5}\text{ S}\cdot\text{cm}^{-1}$ for Li_PVA+IL_{soak} at $30\text{ }^{\circ}\text{C}$). Finally, at $80\text{ }^{\circ}\text{C}$, Li_PVA+IL_{soak} exhibits a value of ionic conductivity of $1.92\cdot 10^{-3}\text{ S}\cdot\text{cm}^{-1}$, together with a very low activation energy of the long-range charge migration process ($1.8\text{ kJ}\cdot\text{mol}^{-1}$).

5. Lithium Glycerolate: a New Glass-forming Electrolyte

In this work, a detailed study of the relations occurring between the physicochemical properties and the conductivity mechanism in a family of lithium glycerolate electrolytes is described. Glycerol is an interesting cheap, colorless, odorless, viscous, and non-toxic organic low-molecular-weight component endowed with a glass transition (T_g) at -80 °C, and a melting event at 18 °C [190]. Furthermore, this material is characterized by a glass-forming behavior, a high flexibility of the backbone, and an efficient lithium ions coordination ability. Thus, it can be considered an attracting ion-conducting medium for the obtaining of a new lithium electrolyte. Here, the preparation and the extensive characterization of a set of eleven electrolytes based on lithium glycerolate is proposed. The electrolytes show a general formula $C_3H_5(OH)_{3-x}(OLi)_x$, where $0 \leq x \leq 1$, (GlyLi_x). The composition of these materials is gauged by inductively-coupled plasma atomic emission spectroscopy. The evolution of the interactions and the structures assumed by lithium glycerolate molecules at different x values is evaluated by vibrational spectroscopies (FT-IR and micro-Raman). The thermal behavior is studied by both modulated differential scanning calorimetry and thermogravimetric analysis. Finally, broadband electrical spectroscopy measurements allow to investigate the long-range charge migration mechanism and glycerol relaxation events. Results demonstrate that in these electrolytes glycerolate molecule acts as a large and flexible macro-anion, bestowing to the material single-ion conductivity ($1.99 \cdot 10^{-4} \text{ S} \cdot \text{cm}^{-1}$ at 30 °C and $1.55 \cdot 10^{-2} \text{ S} \cdot \text{cm}^{-1}$ at 150 °C, for $x = 0.250$).

5.1 Experimental Section

5.1.1 Reagents

Glycerol ($\geq 99\%$) is obtained from Carlo Erba, lithium hydride (LiH, $\geq 99\%$) is purchased from Sigma-Aldrich.

5.1.2 Synthesis

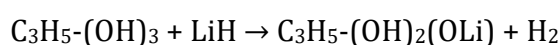
Before using, glycerol is dried under vacuum at 60 °C for 8 days, and then stored inside an Argon-filled glove-box. Then, in a 100 mL round flask 30 mL of dried glycerol are inserted, and 1.000 g of lithium hydride is gradually added to the solution. The obtained solution is stirred under vacuum at 50 °C, and lithium glycerolate (GlyLi) is obtained. The remaining 9 samples are obtained by

different dilutions of GlyLi with pristine dry glycerol. Thus, eleven compounds with a general formula GlyLi_x with 0 ≤ x ≤ 1 are obtained.

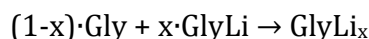
5.2 Results and Discussion

5.2.1 Chemical Composition

During the synthesis of lithium glycerolate, each glycerol molecules exchanges one H⁺ with one Li⁺. Thus, lithium glycerolate, with a formula C₃H₅-(OH)₂(OLi), is obtained; this compound is indicated as GlyLi. The formation reaction of GlyLi proceeds as follow:



As described in the synthesis section, the remaining GlyLi_x electrolytes are obtained by proportional dilution of GlyLi with pristine Gly:



The lithium content in the different samples is evaluated by ICP-AES measurements. The composition of the eleven GlyLi_x electrolytes is reported in Table 5.1.

Table 5.1. Composition of the obtained GlyLi_x samples.

Sample	Li / wt%	n _{Li} / mol·kg ⁻¹	n _{glycerol} / mol·kg ⁻¹	r = n _{Li} /n _o ^a	x = n _{Li} /n _{glycerol} ^b	y = n _{Gly} /n _{GlyLi} ^c
1	7.14	10.00	10.8	0.33	1.000	0
2	6.30	9.67	10.2	0.30	0.890	0.12
3	5.55	8.47	10.3	0.26	0.780	0.28
4	3.30	4.92	10.5	0.15	0.450	1.22
5	1.83	2.69	10.7	0.082	0.250	3.00
6	1.23	1.79	10.7	0.055	0.170	4.88
7	0.68	0.99	10.8	0.030	0.090	10.1
8	0.36	0.52	10.8	0.016	0.048	19.8
9	0.08	0.11	10.8	0.0033	0.010	99.0
10	0.04	0.06	10.8	0.0018	0.005	200
11	0	0	10.9	0	0	∞

^ar describes the fraction of lithium ions that are coordinated by each oxygen atom. ^bx represents the average lithium molar content in each glycerol molecule. ^cy defines the number of glycerol molecules that are solvating each lithium glycerolate.

5.2.2 Vibrational Spectroscopy Studies

5.2.2.1 Glycerol Conformations

In literature it is reported that glycerol consists of a mixture of molecules with several conformations. Typically, three structural arrangements of CH₂OH and OH groups are possible, namely α , β , and γ [191]. This is due to possibility of CH₂OH and OH groups to rotate around the C-C covalent bond in the backbone. The α conformation shows a C-C-O angle (φ) equal to 71°, and the terminal oxygen atom of the CH₂OH group in *trans* position with respect to the carbon atom of the CHOH group. On the contrary, in the β conformation the two oxygen atoms of CH₂OH and CHOH groups are in *trans* position. In the third conformation, γ , φ is equal to 71°, and the terminal oxygen atom of the CH₂OH group is in *trans* position with respect to the hydrogen atom of the CHOH group. The three different conformations are represented in Figure 5.1a.

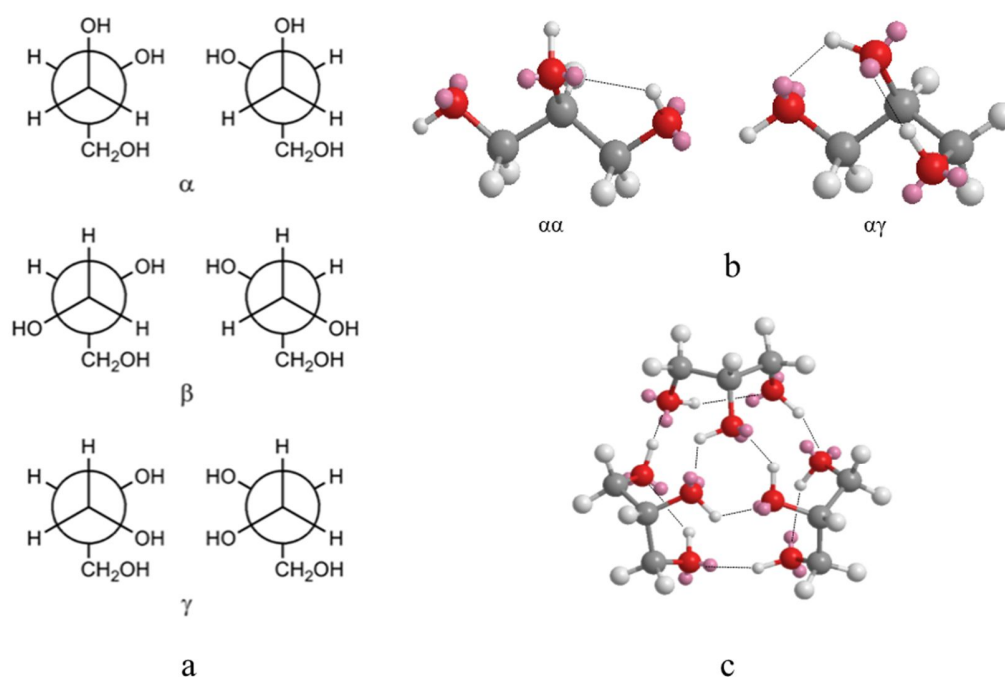


Figure 5.1. The α , β , and γ conformations of glycerol (a). Most probable conformations assumed by the glycerol molecule, $\alpha\alpha$ and $\alpha\gamma$. Color legend: C (grey), O (red), H (white), oxygen electron pair (pink). Hydrogen bonds are highlighted with a dotted line (b). Glycerol inter-molecular structure in the liquid phase (c).

The only conformation present into crystalline glycerol is the $\alpha\alpha$, while, when glycerol is liquid, both the $\alpha\alpha$ and $\alpha\gamma$ conformers can be observed (Figure 5.1b) [192]. The conformation $\gamma\gamma$ is very difficult to observe, due to the low probability of formation. Furthermore, dynamic mechanical

studies reveal that several coordination geometries are possible through intra- and inter-molecular H-bonds (Figure 5.1c). In particular, five-member atoms rings in the α and $\alpha\gamma$ conformers, and a six-atom ring coordination in the $\gamma\gamma$ conformer, are found [52, 193, 194]. Assuming that: i) Li^+ cations typically assume a tetrahedral coordination geometry [195]; and ii) each lithium cation is coordinated by one $-\text{O}^-$ and three electron pairs of the oxygen of different $-\text{OH}$ groups, it is possible, for glycerol, to assume four different coordination geometries. Resulting coordinations are described as follows: a) g1: glycerol is in the $\alpha\alpha$ conformation, and each Li^+ is coordinated by four glycerol molecules through four monodentate bonds (Figure 5.2a); b) g2.1: glycerol assumes an $\alpha\alpha$ conformation, where one glycerol molecule coordinates a lithium cation as a bidentate ligand, while two more glycerol molecules coordinate the lithium cation as monodentate ligands (Figure 5.2b); c) g2.2: glycerol is characterized by an $\alpha\alpha$ conformation, and two glycerol molecules coordinate Li^+ as bidentate ligands (Figure 5.2c); and d) g3: glycerol exhibits a $\gamma\gamma$ conformation, in which one glycerol molecule coordinates Li^+ as a monodentate ligand, while another glycerol molecule coordinates Li^+ as a tridentate ligand (Figure 5.2d). In the studied material all of these conformations are present, and FT-IR and micro-Raman studies will allow to detect which coordination geometry is preferentially assumed at each $n_{\text{Li}}/n_{\text{gly}}$ ratio (x).

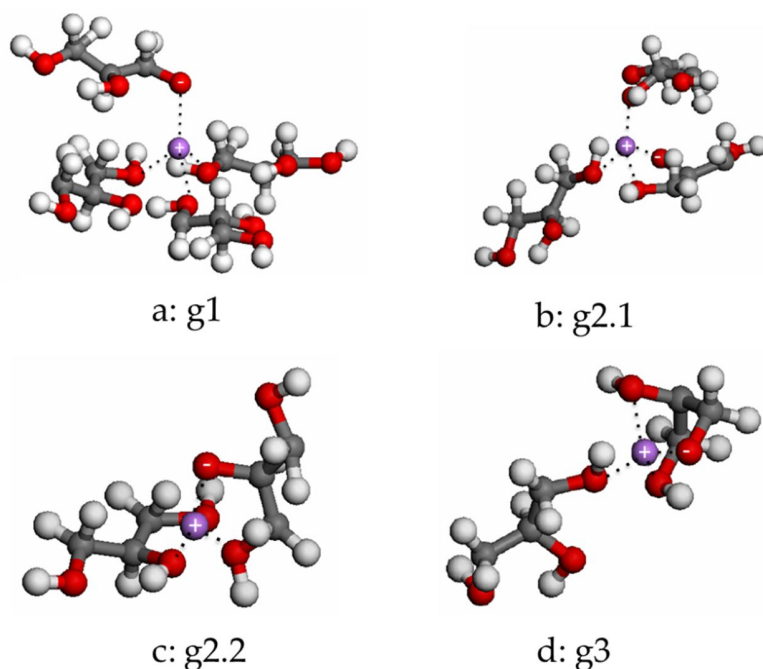


Figure 5.2. Coordination geometries assumed by glycerol molecules upon coordination of Li^+ cations. Color legend: C (grey), O (red), H (white), Li (violet). Li-O interactions are highlighted with a dotted line. g1 coordination geometry, with four monodentate

glycerol ligands (a). g2.1 coordination geometry, with two monodentate glycerol ligands and one bidentate glycerol ligand (b). g2.2 coordination geometry, with two bidentate glycerol ligands (c). g3 coordination geometry, with one monodentate glycerol ligand and one tridentate glycerol ligand (d).

5.2.2.2 Fourier-Transform Infrared Spectroscopy

As reported above, vibrational spectroscopy studies are an important instrument to reveal which of the glycerol coordination geometry is preferentially assumed by the compound at different lithium content. FT-IR spectra are presented in Figure 5.3. Both FT-IR and micro-Raman spectra are baseline subtracted and normalized with respect to the peaks centered at 1323 cm^{-1} (FT-IR) and 1253 cm^{-1} (micro-Raman), attributed to the superposition of the *in-plane* OH bending and CH wagging, respectively.

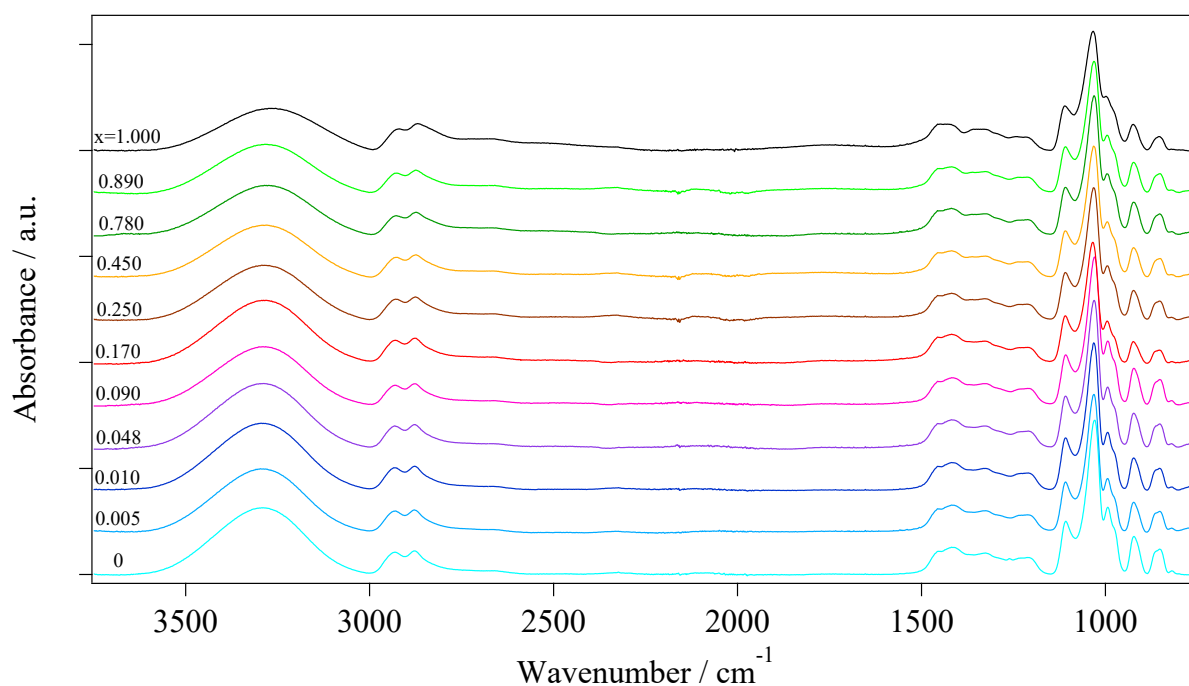


Figure 5.3. ATR FT-IR spectra of GlyLi_x electrolytes.

The vibrational spectra can be divided into three different regions: i) in the high wavenumber region ($\tilde{\nu} > 3000\text{ cm}^{-1}$), the typical OH stretching vibrations (ν_{OH}) are observed [52, 196, 197]; ii) in the region $2700\div 3000\text{ cm}^{-1}$, the CH stretching vibrations (ν_{CH}) of the glycerol backbone are revealed [52, 196, 197]; and iii) in the wavenumber range between 480 and 1500 cm^{-1} , the CH₂ scissoring (sr), OH in-plane bending (δ_{ip}), CO stretching (ν_{CO}), CO bending (δ_{CO}), CC internal rotations (φ_{CC}), and CO rocking (ρ_{CO}) vibrations are detected [52, 196-199]. Li-O vibrational modes

cannot be detected in this spectral region, because they appear at lower wavenumbers (*ca.* 426 cm^{-1} [52]), in the Far-IR. In Table 5.2 the correlative assignment of vibrational modes of GlyLi_x samples is reported.

Table 5.2. FT-IR and Raman correlational assignments of glycerol (Gly) and lithium glycerolate (GlyLi) samples.

Glycerol, Gly ($x = 0$)		Lithium glycerolate, GlyLi ($x = 1.000$)		Assignment ^b	Ref.
$\omega_{\text{IR}}^a / \text{cm}^{-1}$	$\omega_{\text{Raman}} / \text{cm}^{-1}$	$\omega_{\text{IR}} / \text{cm}^{-1}$	$\omega_{\text{Raman}} / \text{cm}^{-1}$		
3422 (s)	-	3386 (s)	-	$\nu^f(\text{OH})$	[52, 196, 197]
3286 (vs)	3350 (s)	3267 (vs)	3350 (s)	$\nu^{\text{Hy}}(\text{OH})$	[52, 196, 197]
-	-	3149 (m)	-	$\nu_{\text{g}^3\text{Li}}(\text{OH})$	[this work]
-	-	3071 (w)	-	$\nu_{\text{g}^2\text{Li}}(\text{OH})$	[this work]
-	2966 (wv)	-	2967 (w)	$\nu_{\text{g}^2,\text{a}}(\text{CH})$	[this work]
2931 (m)	2945 (vs)	2929 (m)	2945 (vs)	$\nu_{\text{g}^1,\text{a}}(\text{CH})$	[52, 196, 197]
-	2909 (w)	-	2909 (s)	$\nu_{\text{g}^2,\text{s}}(\text{CH})$	[this work]
-	2885 (vs)	-	2885 (vs)	$\nu_{\text{g}^1,\text{s}}(\text{CH})$	[52, 196, 197]
2879 (m)	2874 (m)	2878 (m)	2876 (m)	$\nu_{\text{g}^3,\text{a}}(\text{CH})$	[52, 196, 197]
-	-	2867 (m)	-	$\nu_{\text{g}^3,\text{a}}(\text{CH})$	[this work]
2844 (m)	2831 (s)	2842 (w)	-	$\nu_{\text{g}^3,\text{s}}(\text{CH})$	[this work]
2800 (w)	-	-	-	$\nu_{\text{g}^3,\text{s}}(\text{CH})$	[this work]
2754 (vw)	2741 (vw)	2695 (vw)	2736 (w)	$\nu^s(\text{CH of C}_2)$	[52, 196, 197]
2727 (vw)	-	-	-	$\nu^s(\text{CH of C}_2)$	[this work]
-	-	2504 (vw)	-	$\nu(\text{CH})$	[this work]
-	1465 (s)	-	1464 (s)	$\nu^s(\text{CH}_2)$	[52, 196, 197]
1416 (s)	-	1435 (s)	-	$\delta_{\text{ip}}(\text{OH}), \omega(\text{CH}_2)$	[52, 196, 197]
1323 (m)	1313 (vw)	1336 (m)	1313 (vw)	$\delta_{\text{ip}}(\text{OH}), \omega(\text{CH})$	[52, 196, 197]
1210 (w)	1253 (v)	1225 (vs)	1253 (v)	$\delta_{\text{ip}}(\text{OH}), \omega(\text{CH})$	[52, 196, 197]
1108 (vs)	1112 (s)	1111 (m)	1112 (s)	$\nu_{\text{g}^3,\text{sec}}(\text{C-C-O})$	[52, 196, 197]
1088 (w)	-	1091 (w)	-	$\nu_{\text{g}^1,\text{sec}}(\text{C-C-O})$	[this work]
1075 (w)	-	1073 (w)	-	$\nu_{\text{g}^2,\text{sec}}(\text{C-C-O})$	[this work]
1054 (m)	-	1054 (m)	-	$\nu_{\text{g}^3,\text{pri}}(\text{C-C-O})$	[this work]
1029(vs)	1055 (s)	1034 (vs)	1055 (s)	$\nu_{\text{g}^1,\text{pri}}(\text{C-C-O})$	[52, 196, 197]
995 (s)	975 (w)	998 (sh)	975 (w)	$\nu^a(\text{CO}), \text{T}$	[52, 196, 197]
977 (s)	-	980 (s)	-	$\nu^s(\text{CO}), \text{T}$	[this work]
924 (m)	922 (m)	925 (m)	922 (m)	$\nu^a(\text{CO}), \text{G}$	[52, 196, 197]
908 (vw)	-	909 (vw)	-	$\nu^s(\text{CO}), \text{G}$	[this work]
866 (w)	-	867 (w)	-	$\nu^a,\text{pri}(\text{C-C-C})$	[this work]
849 (m)	850 (s)	850 (m)	850 (s)	$\nu^s,\text{pri}(\text{C-C-C})$	[52, 196, 197]
819 (vw)	820 (m)	820 (vw)	820 (m)	$\nu^{\text{pri}}(\text{C-C-C})$	[52, 196, 197]
639 (m,sh)	673 (w)	630 (m,sh)	673 (w)	$\delta(\text{C-C-O})$	[52, 196, 197]
550 (s)	548 (w)	563 (w)	548 (w)	$\varphi(\text{C-C})$	[52, 198]
488 (s)	484 (m)	493 (m)	484 (m)	$\rho(\text{C-C-O})$	[52, 198]
	413 (m)		413 (m)	$\rho(\text{C-C-O})$	[52, 198]
	327 (vw)		327 (vw)	$\varphi(\text{C-C}), \delta(\text{C-C-O})$	[52]

^aRelative intensities are shown in parentheses: vs: very strong; s: strong; m: medium; w: weak; vw: very weak; sh: shoulder. ^b ν : stretching; δ : bending; sr: scissoring; ω : wagging; φ : internal rotations; ρ : rocking a: antisymmetric mode; s: symmetric mode; f: free; Hy: involved in a hydrogen bonding; Li: coordinate to lithium; g1: g1 coordination geometry; g2: g2 coordination geometry; g3: g3 coordination geometry; ip: in-plane; pri: primary alcohol; sec: secondary alcohol; T: *trans*; G: *gauche*.

It is observed that the most affected vibrations by the different concentration of Li^+ are the OH stretching vibration, centered at *ca.* 3300 cm^{-1} , and the CO stretching vibrations of primary and secondary alcohols, peaking in the range $1000\div 1100\text{ cm}^{-1}$. This effect is even more clear from the differential spectra reported in Figure 5.4, where the glycerol spectrum is subtracted from all the other spectra.

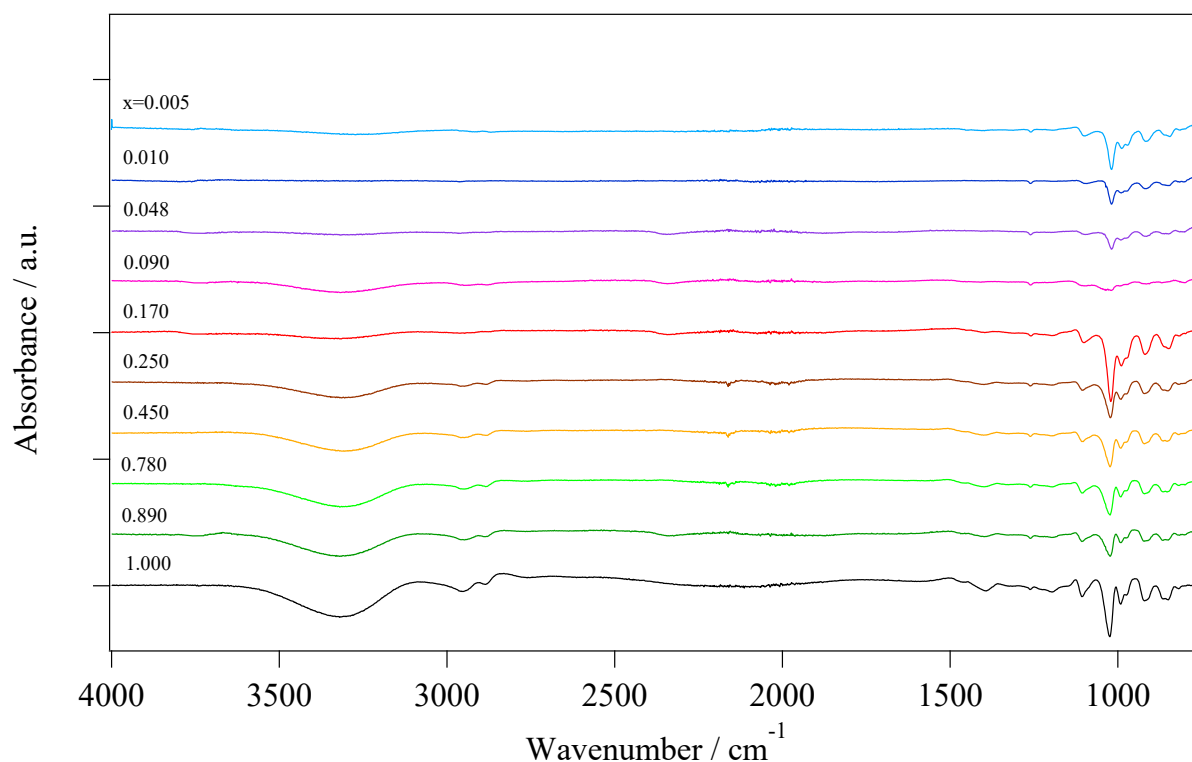


Figure 5.4. FT-IR differential spectra. Glycerol FT-IR spectrum is subtracted from the spectrum of each GlyLi_x sample.

With x , the $\nu(\text{OH})$ vibration shifts to lower wavenumbers, and its intensity is concurrently reduced. The trend can be explained considering that the OH stretching vibrations are involved in the dynamic formation of hydrogen bonds, whose number decreases upon the addition of Li^+ [200]. Moreover, the weakening of the hydrogen-oxygen bond strength in glycerol results in the downshift in wavenumber of $\nu(\text{OH})$ [200]. The vibrations peaking at *ca.* 1034 and 1111 cm^{-1} , which are attributed to the CO stretching of a g1 and g3 conformation geometry, respectively, are the

second FT-IR peaks that are strongly affected by the concentration of Li^+ . It can be seen that, as x increases, the intensity of these peaks decrease. Nevertheless, g3 vibration intensity decreases with a lower magnitude with respect to that of g1 , indicating that, probably, the increase concentration of Li^+ results in a stabilization of the g3 conformation geometry. This behavior is reported in Figure 5.5. Summarizing, the introduction of Li^+ destabilizes the typical conformation geometry of pristine glycerol, altering the hydrogen-oxygen interactions.

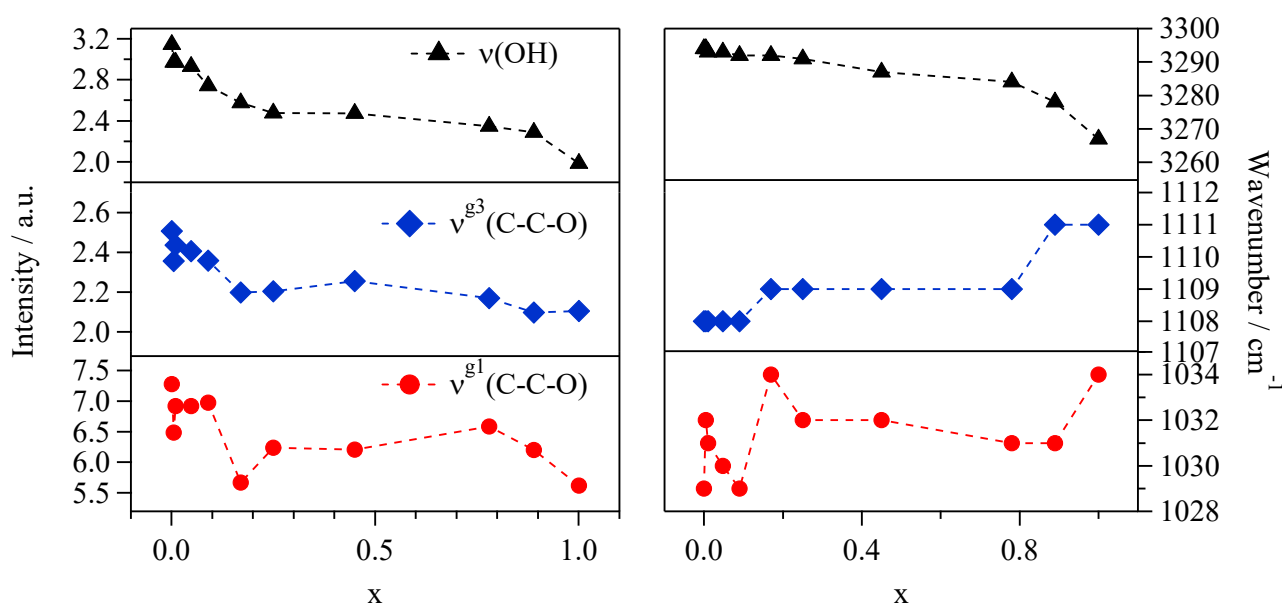


Figure 5.5. Intensity and wavenumber behavior of $\nu(\text{OH})$, $\nu^{\text{g}3}(\text{C-C-O})$, and $\nu^{\text{g}1}(\text{C-C-O})$ FT-IR vibrations at different x values.

Gaussian decomposition of the peaks in the $2500\div 3700$ and $770\div 1150$ cm^{-1} regions is used to obtain further insights on the glycerol conformation geometries at different concentrations of Li^+ . For brevity, only the fitting results obtained from pristine glycerol, Gly ($x = 0$) and lithium glycerolate, GlyLi ($x = 1.000$) are reported in Figure 5.6.

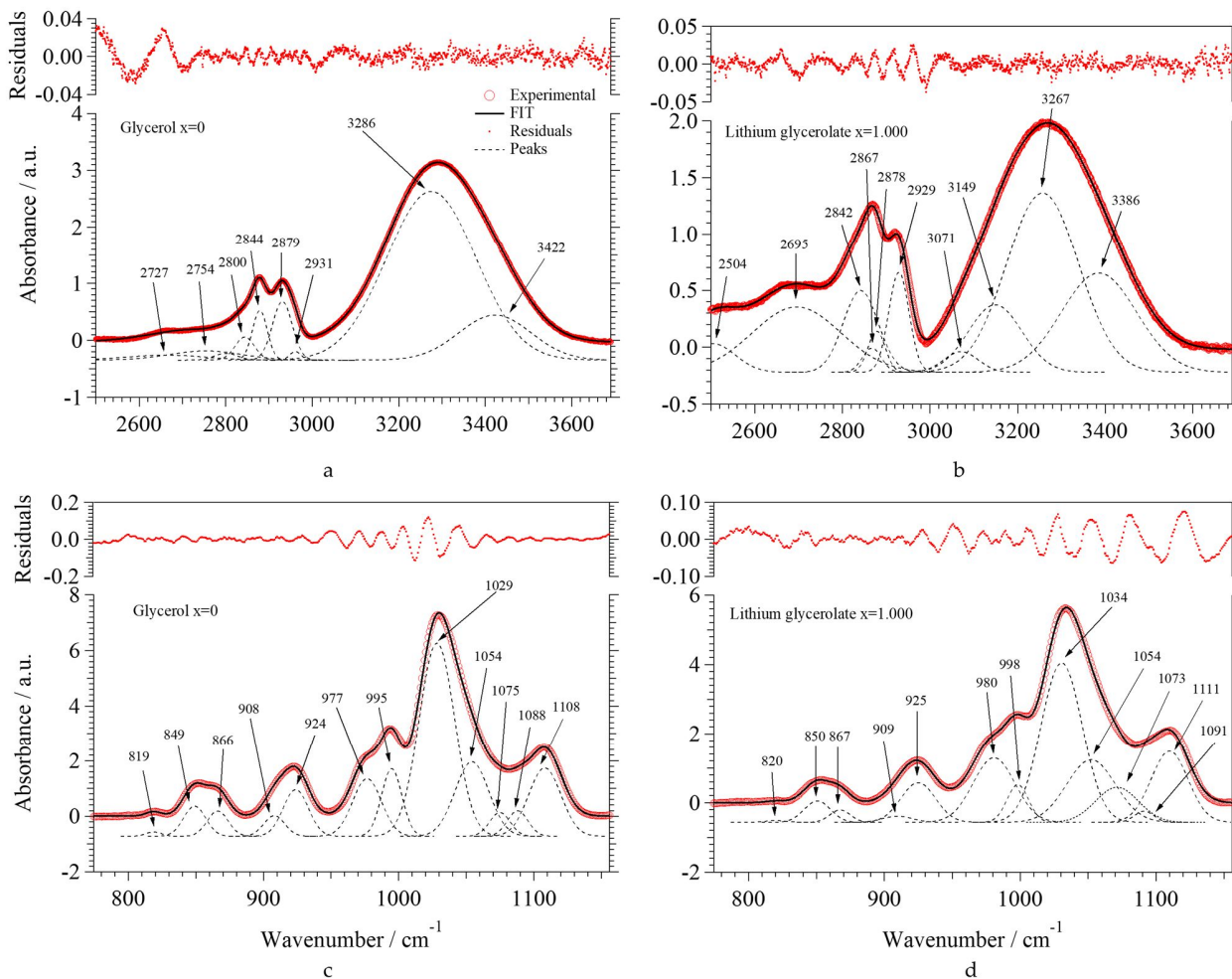


Figure 5.6. Gaussian fitting of the FT-IR spectra of: pristine glycerol, Gly ($x = 0$) in the 2500÷3700 cm^{-1} region (a). Lithium glycerolate, GlyLi ($x = 1.000$) in the 2500÷3700 cm^{-1} region (b). Pure glycerol, Gly ($x = 0$) in the 770÷1150 cm^{-1} region (c). Lithium glycerolate, GlyLi ($x = 1.000$) in the 770÷1150 cm^{-1} region (d).

In the spectra of both GlyLi and GlyLi_x (with $x \geq 0.170$), two new peaks at *ca.* 3071 and 3149 cm^{-1} appear, with respect to pristine glycerol. They are attributed to the $\nu(\text{OH})$ g2 and g3 coordination geometries of the glycerol molecules, respectively. Fitting results allow to carry out a semi-quantitative analysis on the areas of the peaks centered at *ca.* 3386, 3267, 3149, and 3071 cm^{-1} . The areal percentage of each peak is calculated as follow:

$$A_n \% = \frac{A_n}{\sum_{i=1}^m A_i} \cdot 100 \quad (5.1)$$

where $A_n\%$ is the areal percentage of each n^{th} peak, A_n is the calculated area of the n^{th} peak, and the sum is calculated adding all the areas of the peaks centered at *ca.* 3386, 3267, 3149, and 3071 cm^{-1} . Results are reported in Figure 5.7.

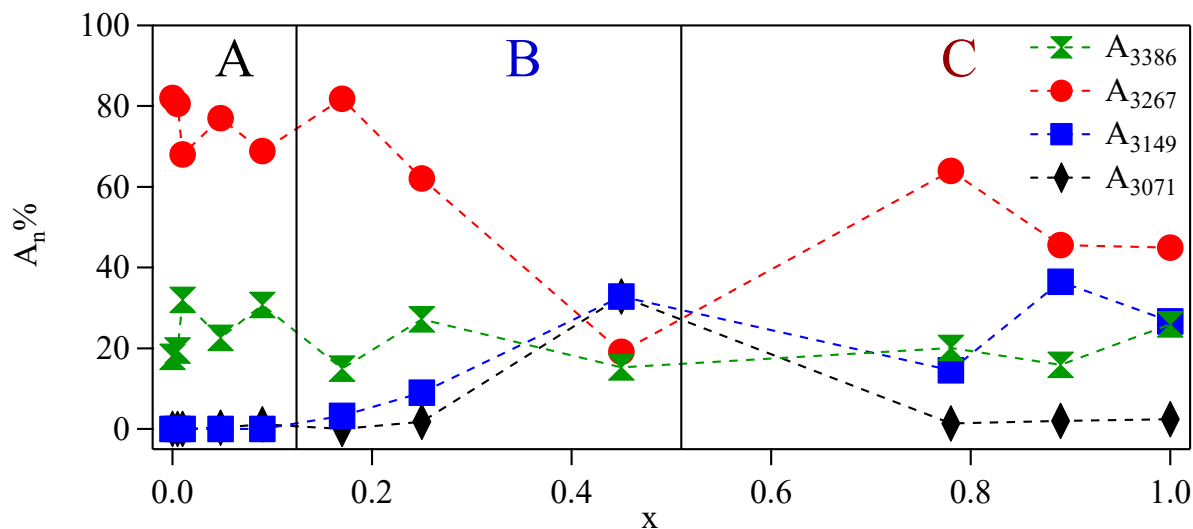


Figure 5.7. Semi-quantitative analysis of the peaks centered at *ca.* 3386, 3267, 3149, and 3071 cm^{-1} as a function of x .

From this graph, it is clear that the proposed electrolytes can be divided into three different lithium concentration regions:

- Region A: at low lithium concentrations ($x \leq 0.090$), the intensity of the peaks associated with $\nu^f(\text{OH})$ (3386 cm^{-1}) and $\nu^{\text{Hy}}(\text{OH})$ (3267 cm^{-1}) remains almost constant, with a variation of no more than 5%. The areal percentage of the peaks centered at *ca.* 3149 and 3071 cm^{-1} , attributed to the $\nu_{\text{g}^3\text{Li}}(\text{OH})$ and $\nu_{\text{g}^2\text{Li}}(\text{OH})$ modes, is equal to 0. Thus, at low x values, a huge number of intra- and inter-molecular hydrogen bonds are present. The coordination geometry assumed by glycerol molecules is similar to that of pristine glycerol. Indeed, g1 allows for a higher number of hydrogen bonds with respect to g2 and g3 coordination geometries.
- Region B: at medium Li^+ concentrations ($0.170 \leq x \leq 0.450$), A_{3386} remains almost constant while A_{3267} is decreased by *ca.* 63 %, indicating a lower number of hydrogen bonds. The peaks centered at *ca.* 3149 and 3071 cm^{-1} start to appear, reaching a value of *ca.* 30 %. This decreased number of hydrogen bonds is ascribed to the diminishing number of oxygen atoms involved in the coordination of Li^+ , as highlighted by the increased intensities of the

peaks attributed to the $\nu_{g^{3Li}}(\text{OH})$ and $\nu_{g^{2Li}}(\text{OH})$. In this concentration region, the coordination geometries expected for glycerol molecules are preferentially g2.1 and g2.2, due to a lower number of hydrogen bonds and to the formation of lithium coordination by oxygen functionalities.

- Region C: at high lithium concentrations ($x \geq 0.780$), A_{3386} remains almost constant, while A_{3267} increases to medium values of areal percentage (up to 64 %). Furthermore, the areas attributed to $\nu_{g^{3Li}}(\text{OH})$ and $\nu_{g^{2Li}}(\text{OH})$ vibrational modes are not overlapped anymore, with the former larger than the latter. These outcomes reveal that the prevalent coordination geometry at these lithium concentrations is g3. This geometry ensures for a higher number of hydrogen bonds with respect to g2, with a high number of oxygen atoms is coordinating Li^+ .

The same areal percentage equation is used to evaluate the behavior of peaks area at different Li^+ concentration in the range $770\div 1150\text{ cm}^{-1}$. Results are reported in Figure 5.8.

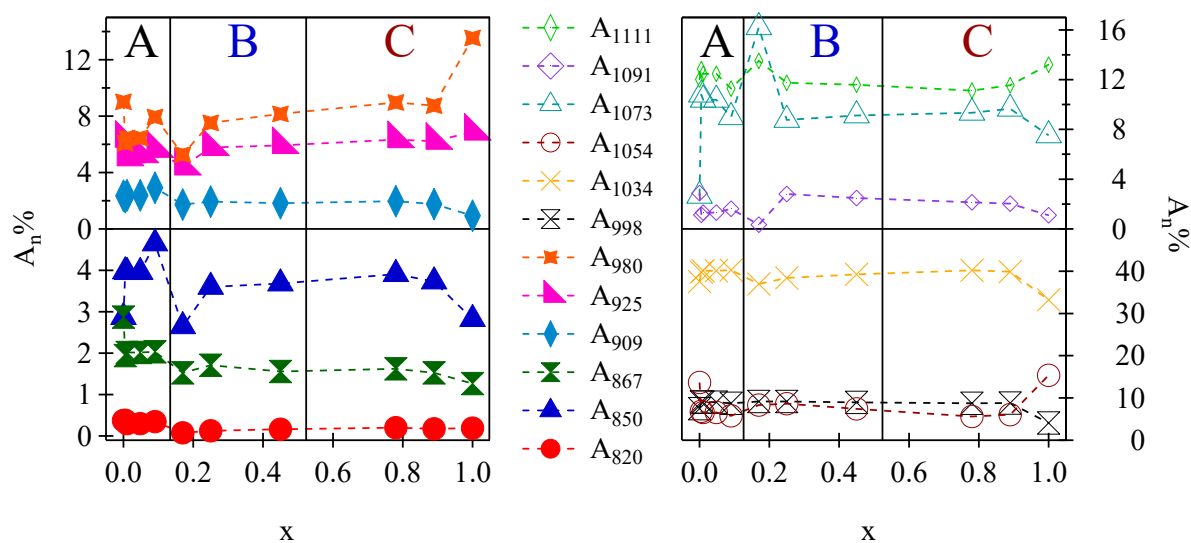


Figure 5.8. Semi-quantitative analysis of the peaks in the range $770\div 1150\text{ cm}^{-1}$ as a function of x .

The most indicative peaks for the attribution of glycerol coordination geometry are those centered at *ca.* 1034, 1054, 1073, 1091, and 1111 cm^{-1} , attributed to $\nu_{g^{1,pri}}(\text{C-C-O})$, $\nu_{g^{3,pri}}(\text{C-C-O})$, $\nu_{g^{2,sec}}(\text{C-C-O})$, $\nu_{g^{1,sec}}(\text{C-C-O})$, and $\nu_{g^{3,sec}}(\text{C-C-O})$, respectively. The same lithium concentration regions observed in Figure 5.7 are revealed also in Figure 5.8.

- Region A: at low Li⁺ concentrations ($x \leq 0.090$), the $\nu^{g1,pri}(C-C-O)$ vibration is the most intense peak, revealing that the majority of Li⁺ is coordinated by the oxygen functionalities of primary alcohols in the g1 coordination geometry.
- Region B: at medium lithium concentrations ($0.170 \leq x \leq 0.450$), the area of the peak attributed to $\nu^{g1,pri}(C-C-O)$ vibration decreases, in parallel to an increase of both A₁₀₇₃ and A₁₁₁₁. This is explained considering that in this lithium concentration region the main coordination geometries taken by glycerol molecules are g2.1 and g2.2, with secondary alcohol hydroxyl groups coordinating Li⁺.
- Region C: at high Li⁺ concentrations ($x \geq 0.780$), the peak areas of $\nu^{g1,pri}(C-C-O)$, $\nu^{g3,pri}(C-C-O)$, and $\nu^{g3,sec}(C-C-O)$ increase. On the opposite, the areas of the peaks associated with $\nu^{g2,sec}(C-C-O)$ and $\nu^{g1,sec}(C-C-O)$ show a minimum for $x = 1.000$. This indicates that, at a high concentration of Li⁺, the dominating coordination geometry for glycerol molecules is g3.

The results obtained from the fitting of the 2500÷3700 cm⁻¹ region are in good agreement with these, arising from the fitting of the 770÷1150 cm⁻¹ region. All the coordination geometry attributions are summarized in Table 5.3.

Table 5.3. Coordination geometries results of Gly and GlyLi_x electrolytes.

x	Group	Coordination Geometry ^a
0	A	g1
0.005	A	g1
0.010	A	g1
0.048	A	g1
0.090	A	g1
0.170	B	g2.1 and g.2.2
0.250	B	g2.1 and g.2.2
0.450	B	g2.1 and g.2.2
0.780	C	g3
0.890	C	g3
1.000	C	g3

^aResults obtained from the fitting of FT-IR and micro-Raman spectra.

5.2.2.3 Micro-Raman Spectroscopy

Micro-Raman spectroscopy measurements result to be more sensitive to CH vibrational modes with respect to FT-IR. Thus, further information on the coordination geometries assumed by

glycerol as a function of the concentration of Li^+ can be gauged from the micro-Raman spectra decomposition of the peaks detected in Figure 5.9.

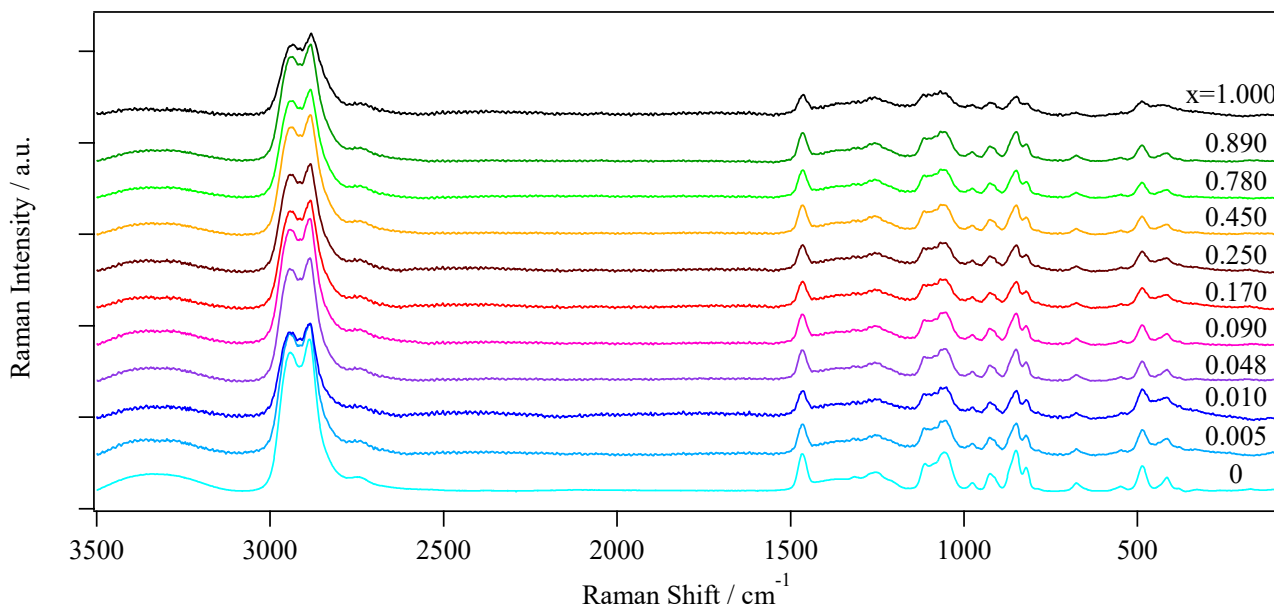


Figure 5.9. Normalized micro-Raman spectra of GlyLi_x samples.

For the sake of clarity, the Lorentzian fitting of the spectra of pristine glycerol in the $2600\div 3100\text{ cm}^{-1}$ range is reported in Figure 5.10.

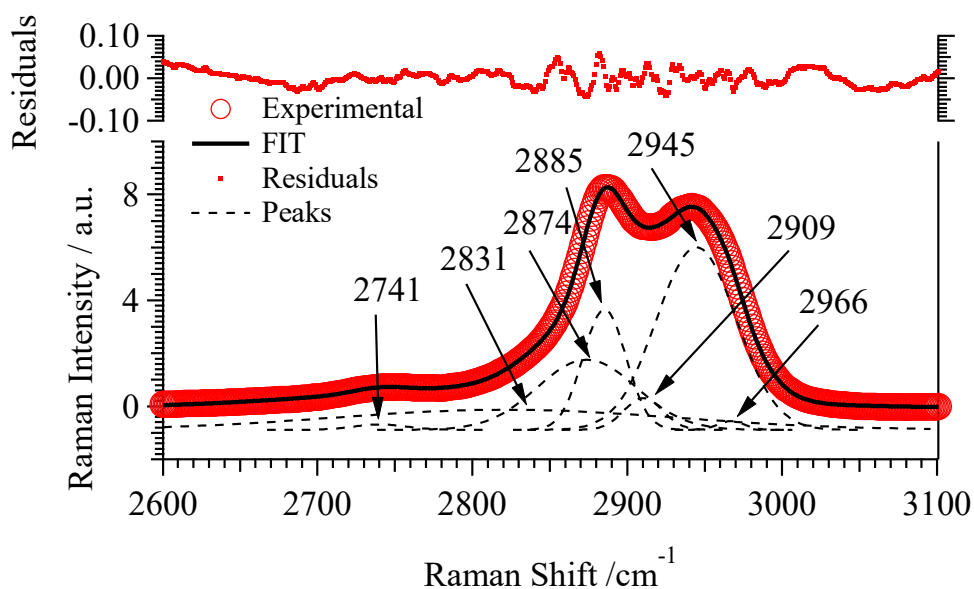


Figure 5.10. Lorentzian fitting of the micro-Raman spectrum of pristine glycerol ($x = 0$) in the $2600\div 3100\text{ cm}^{-1}$ region.

The areal behavior of the peaks as a function of x are reported in Figure 5.11.

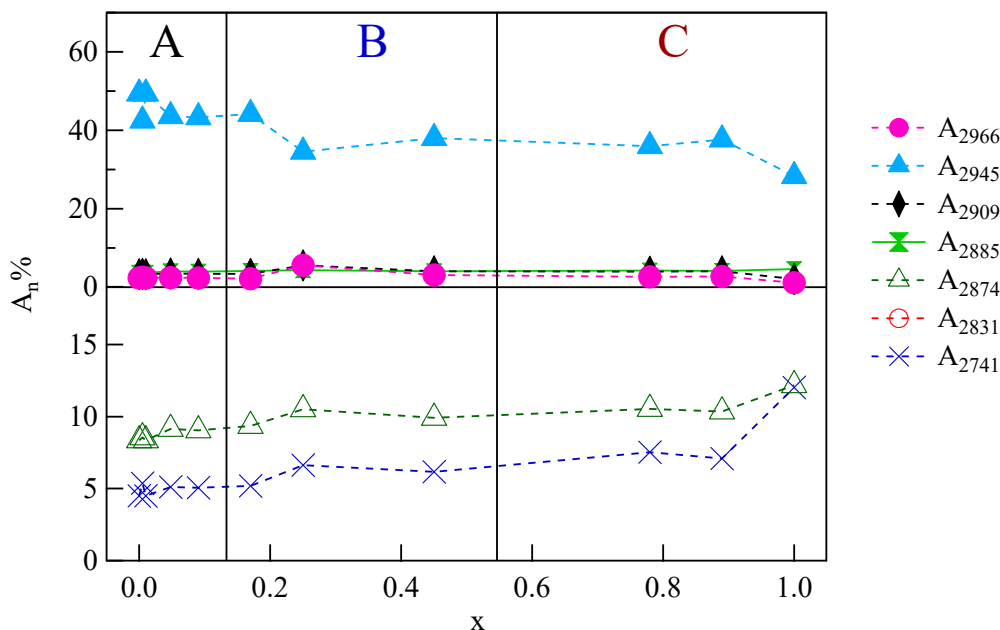


Figure 5.11. Areal behavior of the micro-Raman peaks as a function of x .

In accordance with FT-IR results, in micro-Raman spectra the same three lithium concentration regions are revealed:

- Region A: at low lithium concentrations ($x \leq 0.090$), the areal percentage of the peak centered at *ca.* 2945 cm^{-1} , attributed to the $\nu^{\text{g}1,\text{a}}(\text{CH})$ vibration, shows the highest value among all the other peaks. The g1 coordination geometry is confirmed at these Li^+ concentrations.
- Region B: at medium Li^+ concentrations ($0.170 \leq x \leq 0.450$), it is shown that the area attributed to the CH stretching of g1 conformation decreases. In parallel, an increase in the areal percentage of A_{2966} and A_{2909} is observed. The latter are attributed to $\nu^{\text{g}2,\text{a}}(\text{CH})$ and $\nu^{\text{g}2,\text{s}}(\text{CH})$, respectively, with a maximum for the sample with $x = 0.250$. In this concentration region, g2.1 and g2.2 coordination geometries are the most probable for glycerol molecules.
- Region C: at high lithium concentrations ($x \geq 0.780$), a decrease in the area attributed to $\nu^{\text{g}1,\text{a}}(\text{CH})$ vibration is observed. Furthermore, a significant increase of A_{2831} , attributed to $\nu^{\text{g}3,\text{s}}(\text{CH})$, is detected. This reveals that, in this concentration range of Li^+ , the number of glycerol molecules taking g3 coordination geometry is increased.

Concluding, FT-IR analysis is useful to evaluate how OH and CO stretching vibrations are affected by the different concentrations of Li^+ . Differently, micro-Raman spectroscopy allows to study the changes in coordination geometry by analyzing the CH stretching modifications. A clear division into three groups of samples with a different concentration of Li^+ is observed in all of the measurements: at low Li^+ content ($x \leq 0.090$) glycerol molecules prefer the g1 coordination geometry, while at medium concentrations of Li^+ ($0.170 \leq x \leq 0.450$) the prevalent coordination geometry is g2. Finally, at high lithium contents ($x \geq 0.780$), g3 conformation for glycerol molecules starts to be significantly observed.

5.2.3 Thermal Studies

5.2.3.1 Thermo-Gravimetric Analyses

The thermal stability and the effects of the presence of Li^+ on the decomposition temperature of GlyLi_x electrolytes are evaluated by thermo-gravimetric analyses. Figure 5.12 and Table 5.4 summarize the results of these measurements.

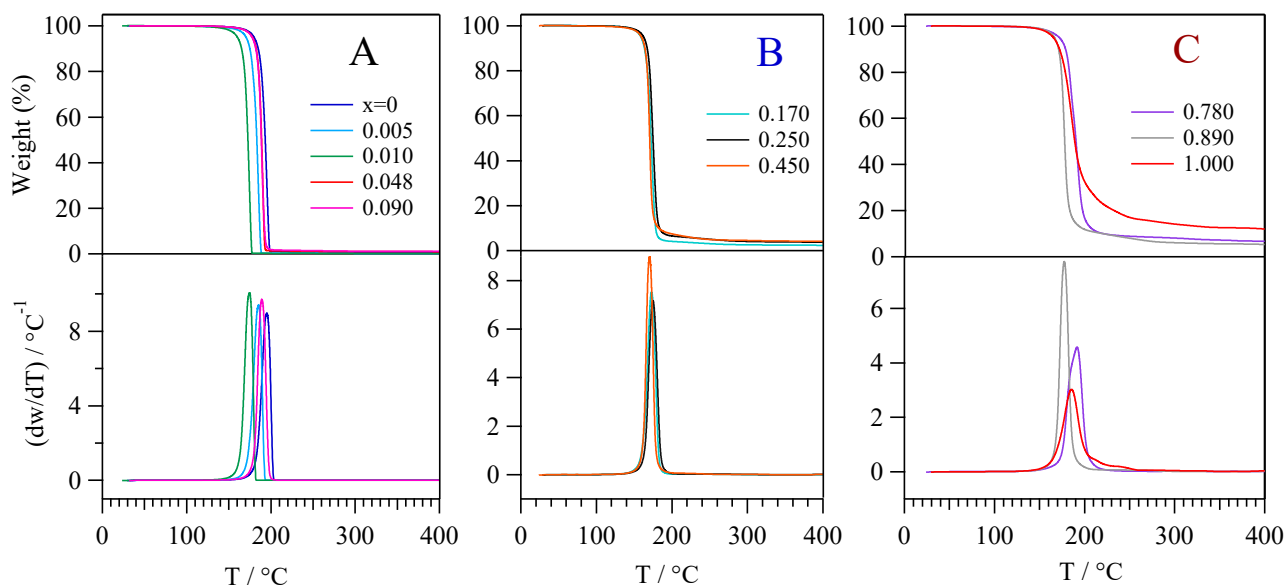


Figure 5.12. Thermo-gravimetric analyses of GlyLi_x .

Table 5.4. Thermal results of Gly and GlyLi_x electrolytes.

x	Group	T _{dec.} ^a / °C	T _g ^b / °C	ΔH _{er} ^c / J·g ⁻¹
0	A	195.09	-78.51	-2.476
0.005	A	195.03	-78.22	-2.267
0.010	A	190.38	-78.53	-2.521
0.048	A	190.19	-76.18	-1.877
0.090	A	188.95	-76.17	-2.057
0.170	B	172.77	-72.35	-2.096
0.250	B	174.79	-69.07	-2.077
0.450	B	170.14	-66.15	-1.84
0.780	C	191.34	-64.93	-1.637
0.890	C	177.09	-63.04	-3.483
1.000	C	185.42	-42.95	-3.29

^aDecomposition temperature obtained from TGA measurements. ^bGlass-transition temperatures are evaluated from MDSC measurements. ^cRelaxation enthalpies are calculated from MDSC measurements.

Pristine glycerol exhibits the highest thermal stability (T_{dec.}) among all the electrolytes, that correspond to 195.09 °C, with no high-temperature residual weight [201]. The addition of lithium ions results in the formation of a high-temperature residue, whose magnitude increases with x. This corresponds to the production of lithium oxide (Li₂O), which can be formed under a nitrogen atmosphere thanks to the degradation of the glycerol matrix. The decomposition temperature behavior as a function of x reveals the same division in three different lithium concentration regions observed in the vibrational studies. In region A all the samples show a T_{dec.} similar to that of pristine glycerol. At x ≥ 0.170, a drop of more than 16 °C in the thermal stability is detected. In region C, the decomposition temperature goes back to high values. Thus, it is inferred that: i) the injection of lithium ions decreases the thermal stability of the compounds, endorsing the decomposition of glycerol; and ii) T_{dec.} is highly affected by the coordination geometry taken by the glycerol molecules. Indeed, the diminished stability could arise from the reduction of the number of hydrogen bonds [202].

5.2.3.2 Modulated Differential Scanning Calorimetry Studies

MDSC results of the synthesized materials are reported in Figure 5.13.

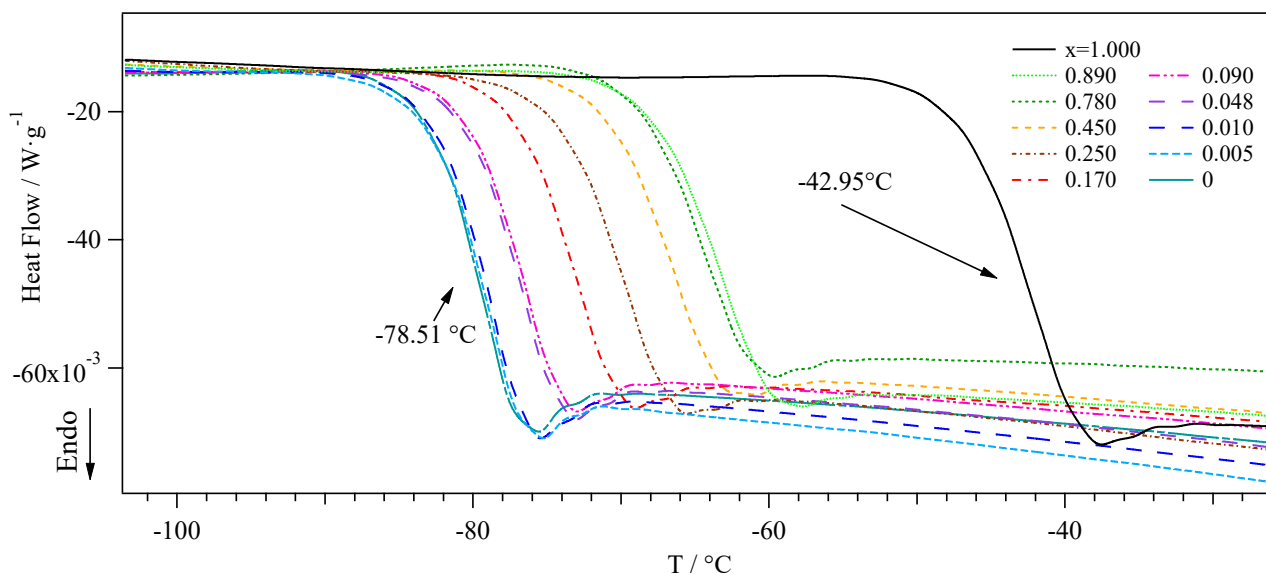


Figure 5.13. MDSC profiles of GlyLi_x.

All the samples show the presence of two different contributions, that can be easily decoupled by the modulated option of the DSC instrument. The separation of reversible and non-reversible heat flow components for pristine glycerol ($x = 0$) and GlyLi ($x=1.000$) is shown in Figure 5.14.

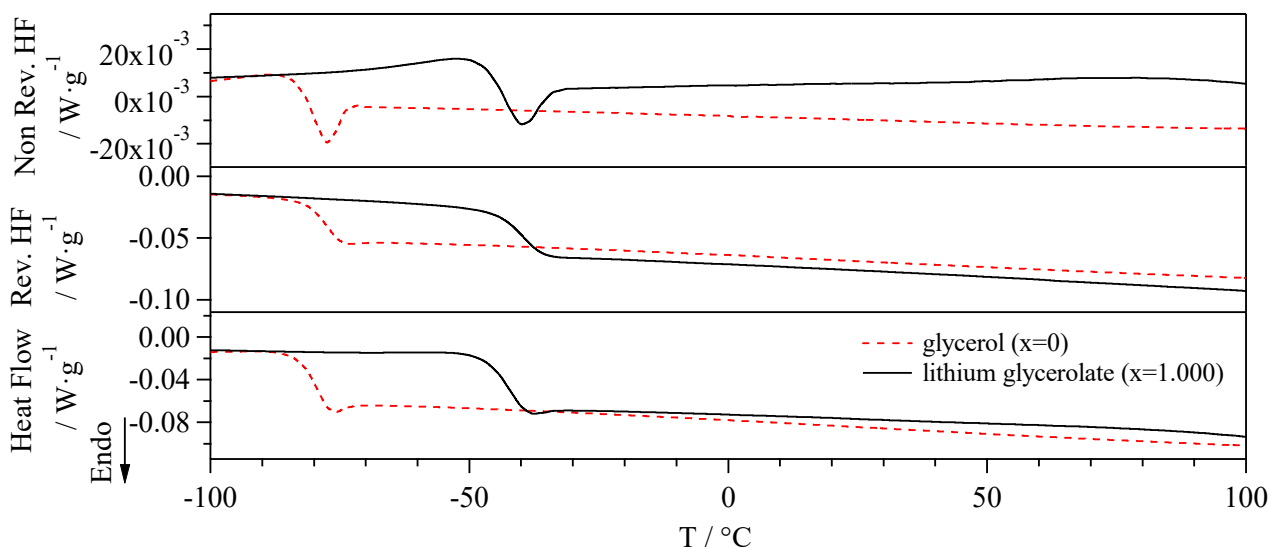


Figure 5.14. MDSC results of pristine glycerol, Gly ($x = 0$) and lithium glycerolate, GlyLi ($x = 1.000$) samples. The reversible and non-reversible heat flow contributions are distinguished in the two graphs.

The reversible contribution to the total heat flow is assigned to a glass transition (T_g) of the glycerol matrix, while the non-reversible element is attributed to an enthalpic relaxation (ΔH_{er}) associated

with T_g . Modulated differential scanning calorimetry measurements show that the T_g of the electrolytes increases with x (see Table 5.4 and Figure 5.13), with a growth of more than 35 °C between pure glycerol ($T_g = -78.51$ °C, similar to that reported in the literature [203]) and GlyLi ($T_g = -42.95$ °C). Thus, the addition of Li^+ results in the formation of a coordination network that increases the energy needed for the structural reorganization of the electrolyte occurring during the T_g . The enthalpic relaxation value measured for pristine glycerol, -2.476 J·g⁻¹, is similar to that reported in literature [204]. In all the electrolytes the ΔH_{er} has a negative value, revealing that this transition is endothermic. The coordination geometries assumed by the glycerol molecules influence the enthalpy associated with the glass transition. In region A the enthalpy values are low, due to the high number of hydrogen bonds occurring in the materials. In region B, with the increasing content of lithium ions and the reduced number of hydrogen bonds, ΔH_{er} values are raised. Finally, in region C, the negative trend of ΔH_{er} as x increases is explained by the formation of several tetrahedral coordination geometries due to the presence of a high concentration of Li^+ .

5.2.4 Broadband Electrical Spectroscopy Studies

GlyLi_x electrolytes are extensively characterized by Broadband Electrical Spectroscopy (BES) technique with the aim of revealing the interplay between the structure, relaxations, and conductivity mechanism of the proposed electrolytes as a function of the concentration of Li^+ . BES measurements are conducted from 100 mHz to 10 MHz, in the temperature range $-130 \div 150$ °C. The spectra of the complex permittivity vs. temperature and frequency are fitted with the following empirical equation [162]:

$$\varepsilon^*(\omega) = i \left(\frac{\sigma_0}{\varepsilon_0 \omega} \right)^N + \sum_{k=1}^n \frac{\sigma_k (i\omega\tau_k)^{\gamma_k}}{i\omega\varepsilon_0 [1 + (i\omega\tau_k)^{\gamma_k}]} + \sum_{j=1}^m \frac{\Delta\varepsilon_j}{i\omega [1 + (i\omega\tau_j)^{\alpha_j}]^{\beta_j}} + \varepsilon_\infty \quad (5.2)$$

where $\varepsilon^*(\omega) = \varepsilon'(\omega) - i\varepsilon''(\omega)$ ($\sigma^*(\omega) = i\omega\varepsilon_0\varepsilon^*(\omega)$). The first term of the Equation is assigned to the conductivity of the electrolyte at zero frequency (the residual conductivity of the sample). ε_∞ accounts for the permittivity of the electrolyte at infinite frequency (electronic contribution). The second term is related to the electrode ($k = 1$) and interdomain ($k \geq 2$) polarization phenomena. τ_k and σ_k correspond to the relaxation times and the conductivity, respectively, associated with the k^{th} polarization. γ_k is a pre-exponential factor that varies from 0.5 to 1.0. The third term, attributed to the dielectric relaxation, is described by the Havriliak-Negami theory [162, 182]. $\Delta\varepsilon$, τ_j , α_j , and β_j

correspond to the dielectric strength, relaxation time, symmetric and antisymmetric shape parameters of each j^{th} relaxation event, respectively.

The analysis of the three-dimensional $\tan\delta$ ($\tan\delta = \varepsilon''/\varepsilon'$) surfaces is a useful tool to detect the polarization and relaxation phenomena occurring in the electrolytes. All the results, in terms of $\tan\delta$, are reported in Figure 5.15. In Figure 5.16 a complete analysis of the electric response of GlyLi_{0.250} sample, the electrolyte with the highest conductivity, in terms of ε' , ε'' , σ' , and $-\sigma''$, is shown.

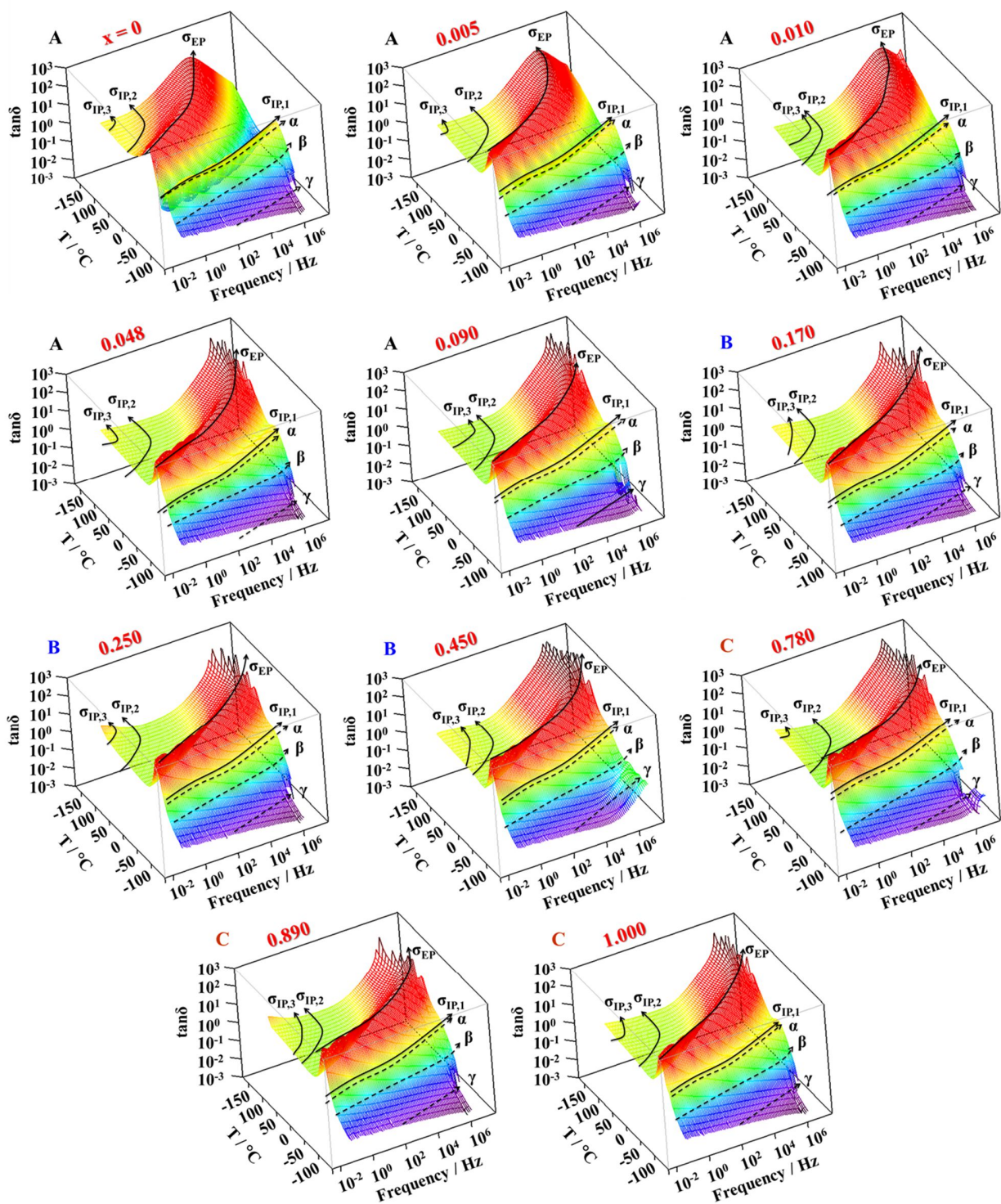


Figure 5.15. 3D $\tan\delta$ surfaces of GlyLi_x samples, with $0 \leq x \leq 1.000$.

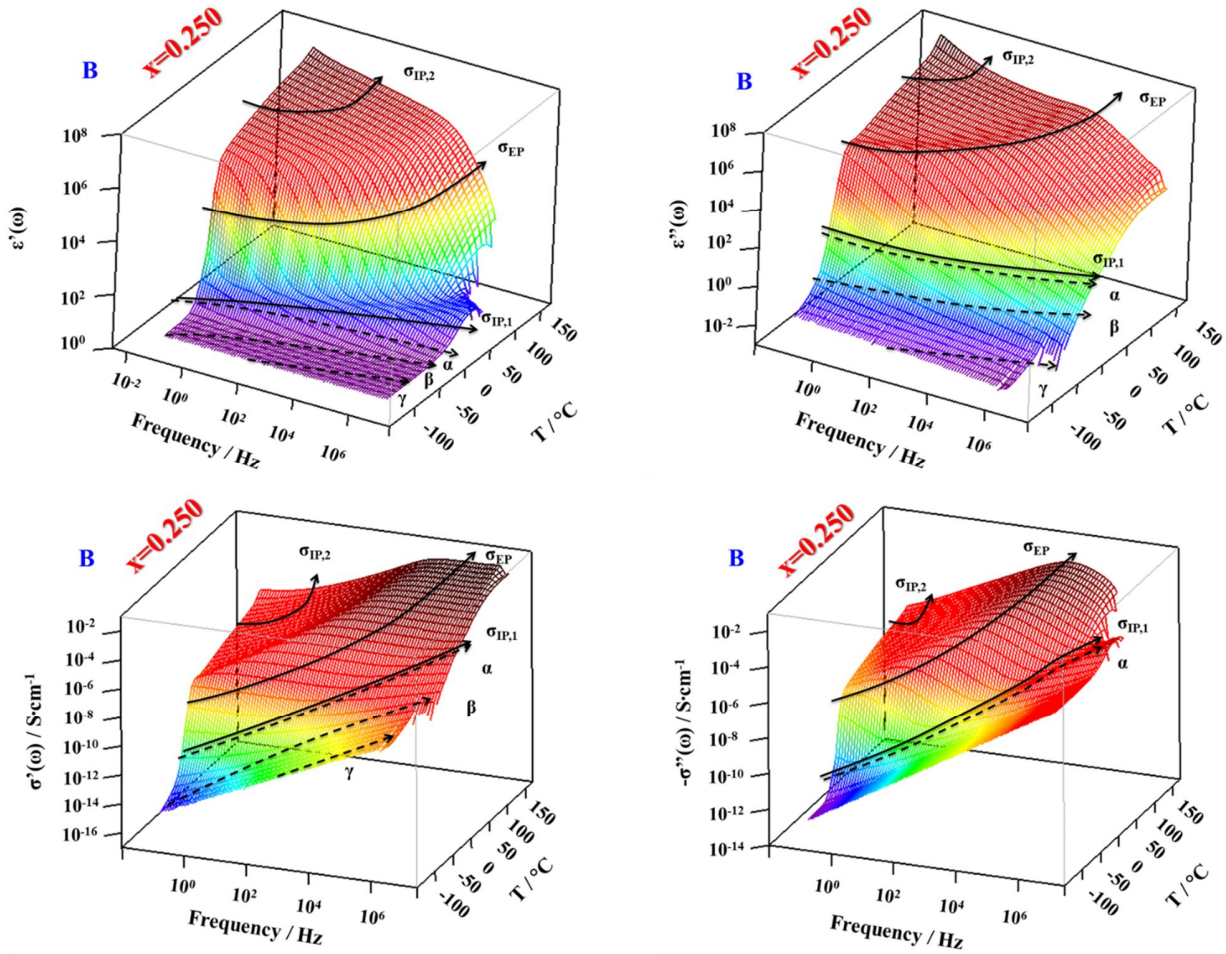


Figure 5.16. Complete analysis of the electric response of GlyLi_{0.250} sample in terms of ϵ' , ϵ'' , σ' , and $-\sigma''$.

5.2.4.1 Polarization Phenomena

Four different polarization phenomena are detected in the samples: i) the electrode polarization event (σ_{EP}), that can be seen at $T > -60$ °C and that is attributed to the accumulation of charge at the interface between the sample and the platinum blocking electrodes [162]; and ii) three different interdomain polarizations at $-70 \div 10$ °C ($\sigma_{IP,1}$), $0 \div 150$ °C ($\sigma_{IP,2}$), and above 60 °C ($\sigma_{IP,3}$). The presence of these latter polarizations, that are assigned to the accumulation of charge at the interface between domains with different permittivity [162], demonstrates that the proposed electrolytes are heterogeneous at the mesoscale, and glycerol molecules tend to aggregate forming nano-domains. The conductivity values of each σ , obtained from the fitting parameter associated with the detected events, are plotted vs. T^{-1} . Each curve is fitted with a suitable model, *i.e.* Vogel-

Tammann-Fulcher (VTF) [183] or Arrhenius (A) equation [162]. Results are reported in Figure 5.17.

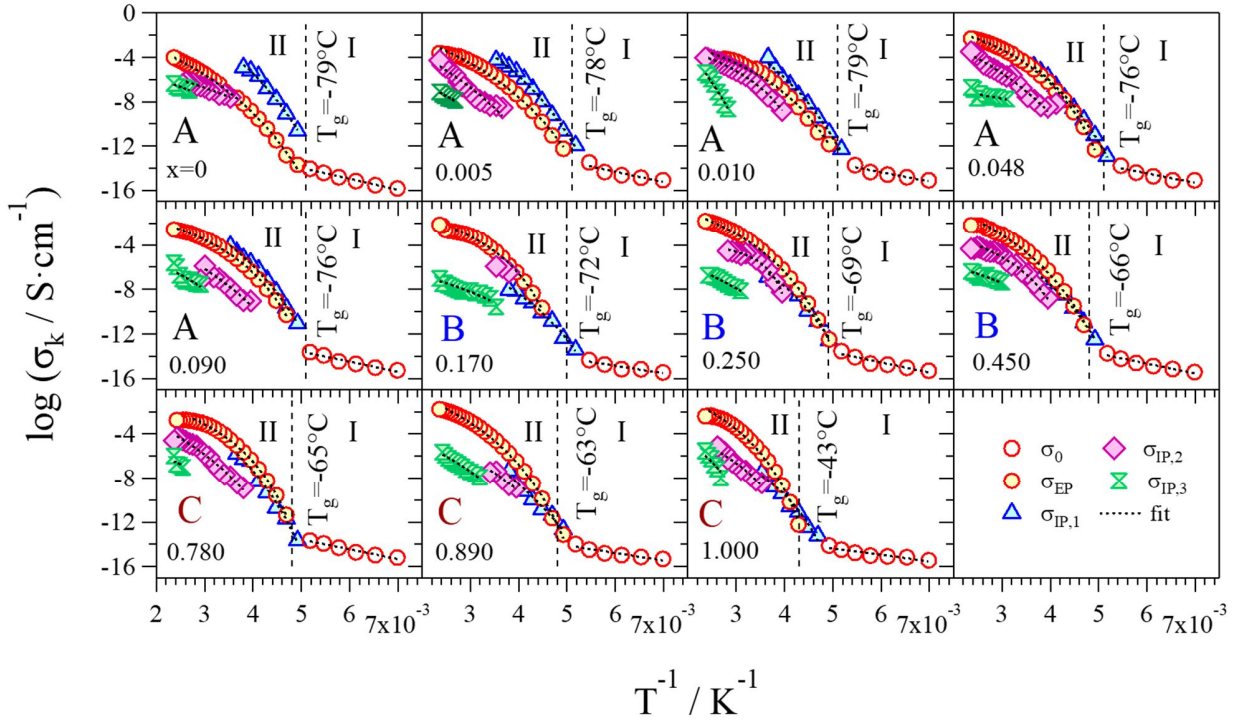


Figure 5.17. Log σ_k vs. T^{-1} curves of all the polarizations for every sample. Region I and II are divided by the T_g of the sample.

Two different temperature regions are detected, which are delimited by the T_g of glycerol. At $T < T_g$, *i.e.* *ca.* -60°C (Region I), only σ_0 contribution to the overall conductivity is observed, and it shows an Arrhenius behavior. This indicates that, at these temperatures, charge migration occurs through hopping events between different domains. At $T > T_g$ (Region II), all σ_k reveal a VTF-like behavior, witnessing that the conductivity mechanism is assisted by the segmental motion of the cluster aggregates. The overall conductivity is equal to the sum of the single conductivities of each polarization occurring in the electrolyte [205]:

$$\sigma_T = \sigma_0 + \sum_{k=1}^n \sigma_k = \sigma_0 + \sigma_{EP} + \sigma_{IP,1} + \sigma_{IP,2} + \sigma_{IP,3} \quad (5.3)$$

In Figure 5.18 the logarithm of the overall conductivity as a function of T^{-1} is shown; the GlyLi_x samples are divided into the three Li^+ concentration regions.

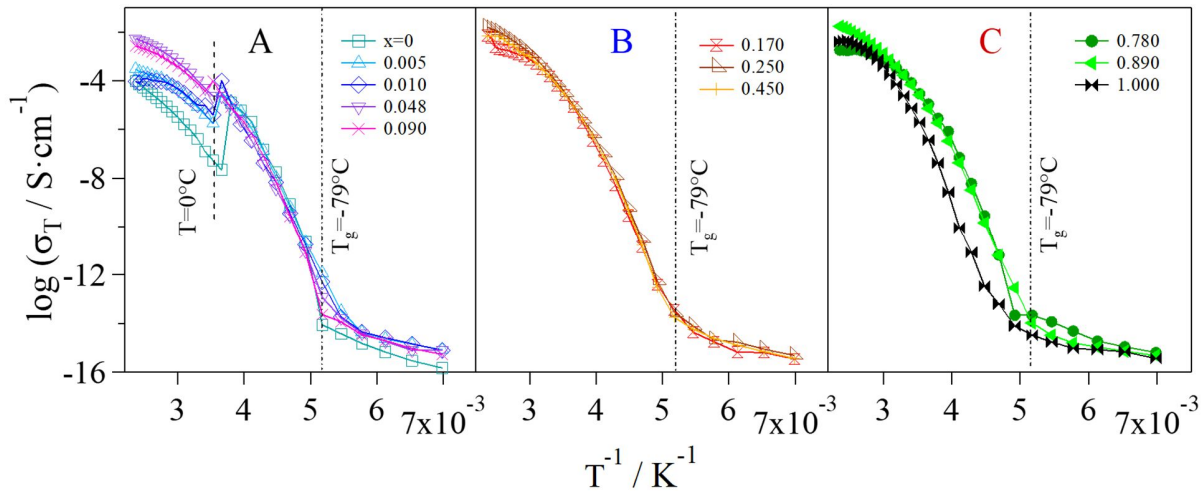


Figure 5.18. Log σ_T vs. T^{-1} curves for the various groups of GlyLi_x samples. Region A: $x \leq 0.090$; region B: $0.170 \leq x \leq 0.450$; region C: $0.780 \leq x \leq 1.000$.

Region A: the lowest values of the total conductivity are shown by glycerol and samples with low Li⁺ concentration ($x \leq 0.090$). In this region glycerol molecules are in the α conformation and coordinate Li⁺ through the g1 geometry, with the highest number of intra- and inter-molecular hydrogen bonds. Thus, the glycerol structure arising from the presence of all of these interactions hinders the migration of Li⁺. A drop of conductivity at *ca.* 0 °C is observed, even if MDSC measurements do not reveal any thermal transition. A possible explanation is that, at these concentrations of Li⁺ and in this particular temperature range ($T_g \leq T \leq 0$ °C), the coordination network created in glycerol aggregates is facilitating the $\sigma_{IP,1}$ polarization, making it the most contributing component to the overall conductivity, and perturbing the log σ_T vs. T^{-1} curve. This effect lowers as the Li⁺ content is increased. At temperatures higher than 0 °C the main contribution to the overall conductivity becomes the electrode polarization.

Region B: the electrolytes belonging to this lithium concentration region reveal the highest values of the total conductivity. In particular, GlyLi_{0.250} sample demonstrates the highest lithium single-ion room-temperature conductivity value, *i.e.* $1.99 \cdot 10^{-4}$ at 30 °C. The achieved value is in line with those present in the literature for lithium ion-conducting polymer electrolytes. Thus, the proposed electrolytes are extremely interesting for application in Li-ion batteries [52, 206]. Moreover, this sample shows: i) an exceptional high-temperature conductivity of $1.55 \cdot 10^{-2}$ S·cm⁻¹ at 150 °C; and ii) an impressive low-temperature conductivity, that is higher than 10^{-6} S·cm⁻¹ at -10 °C, thanks to the glass-forming behavior of the glycerol matrix. At these lithium concentrations, glycerol

molecules assume a g2 conformation geometry, which do not facilitate the $\sigma_{IP,1}$ polarization. Thus, i) the conductivity of this event strongly decreases; ii) at $T > T_g$, σ_{EP} starts to be the most contributing component to the overall conductivity; and iii) the conductivity drop at 0 °C is no longer observed.

Region C: high values of room-temperature conductivity are still demonstrated ($\sigma_T > 10^{-4} \text{ S}\cdot\text{cm}^{-1}$) by these electrolytes. Nevertheless, GlyLi exhibits a not impressive conductivity, especially at $T_g \leq T \leq 30 \text{ °C}$. Reasonably, this is the result of three concurring effects: i) the high content of Li^+ renders the structure of the glycerol matrix more rigid, inhibiting the migration process of Li^+ , as already demonstrated by MDSC results; ii) the g3 conformation geometry taken by glycerol molecules in this concentration region strongly decreases the $\sigma_{IP,1}$ polarization contribution, thus lowering the total conductivity; and iii) the presence of a huge number of lithium cations increases the probability of blocking Li^+ into the tetrahedral coordination structures, assumed by glycerol molecules.

Summarizing, at $T \leq T_g$ (ca. -60 °C), the only contribution to the total conductivity is provided by σ_0 , and lithium cations are exchanged through a hopping process. At medium temperatures ($T_g \leq T \leq 10 \text{ °C}$) and at a low Li^+ concentration ($x \leq 0.090$), the main contribution to the total conductivity is given by $\sigma_{IP,1}$. The contribution of this polarization decreases as the content of Li^+ is raised, while σ_{EP} becomes more and more important, thus providing the largest contribution to the total conductivity. Finally, at high temperatures ($T > 10 \text{ °C}$), σ_{EP} is the main contribution to the total conductivity and the migration of Li^+ active species is assisted by the segmental motions of the glycerol aggregates.

5.2.4.2 Dielectric Relaxation Events

At low temperatures ($T < 10 \text{ °C}$), the presence of three different dielectric relaxation events is detected. These relaxations are attributed to pristine glycerol and GlyLi_x samples. At high frequency ($>10^2 \text{ Hz}$), and at temperatures lower than -70 °C, a dielectric relaxation attributed to a γ relaxation is observed. γ is associated with the rapid local fluctuations of the dipole moments of glycerol hydroxyl terminal functionalities (Figure 5.19) [207]. At frequencies lower than those shown by γ , and in -100÷-20 °C temperature range, a β dielectric relaxation is detected. This relaxation is assigned to an internal modification in the molecular conformation of glycerol, and it is typically referred to as a “ β mode of glass-forming materials” [208, 209]. In particular, it is

attributed to the local fluctuations of the dipole moments of glycerol molecules that are coordinating protons or lithium cations through the hydrogen bonds (Figure 5.19) [205]. At the lowest values of the frequency, and at temperatures up to 30 °C, the observed relaxation is assigned to an α dielectric relaxation mode. This kind of relaxation is a dynamic process that involves the diffusion of conformational states along the polymer chains or molecules aggregates, as in this case, and it is known as a “segmental motion” (Figure 5.19) [208].

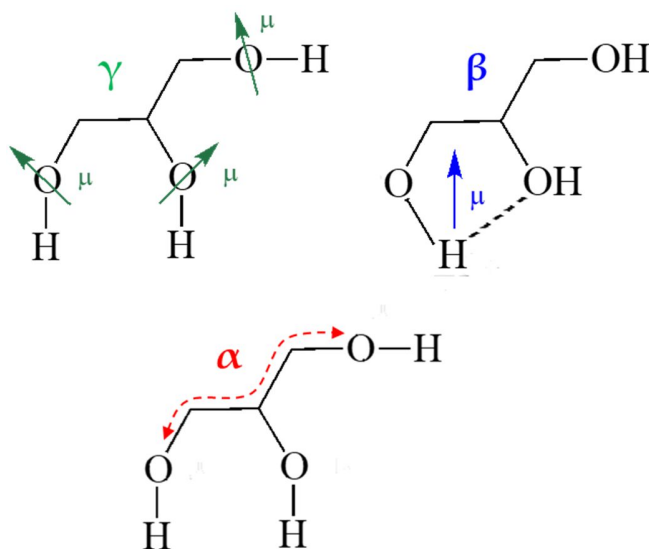


Figure 5.19. Representation of glycerol α , β , and γ dielectric relaxations; μ indicates the dipole moment.

The results of 3D surfaces fitting using the Equation described above, allows for the determination of the dielectric relaxation frequency (f_j) and dielectric strength ($\Delta\epsilon_j$) values for each event. These values are plotted as a function of temperature (T^{-1}) and are reported in Figure 5.20 and Figure 5.21, respectively. All the curves reported in Figure 5.20 are fitted with a Vogel-Tammann-Fulcher-Hesse (VTFH) [210] or an Arrhenius-like [210] equation.

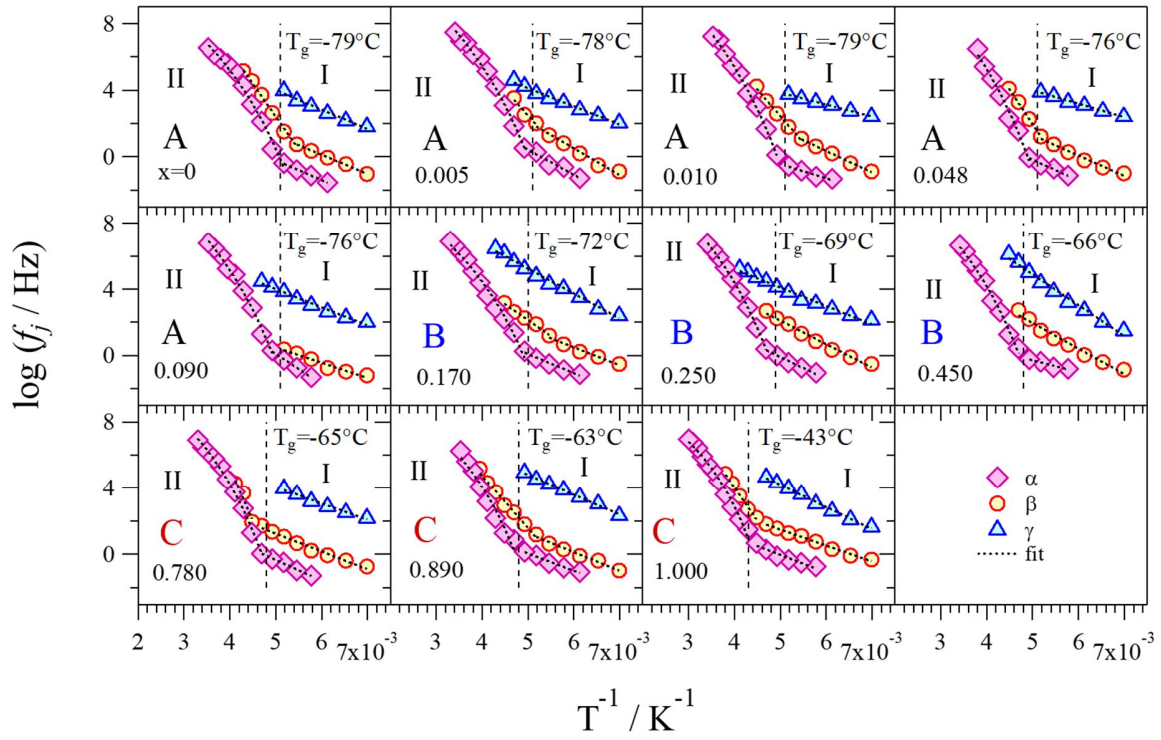


Figure 5.20. $\log f_j$ vs. T^{-1} curves of each dielectric relaxation event for every sample. Region I and II are divided by the T_g of the sample.

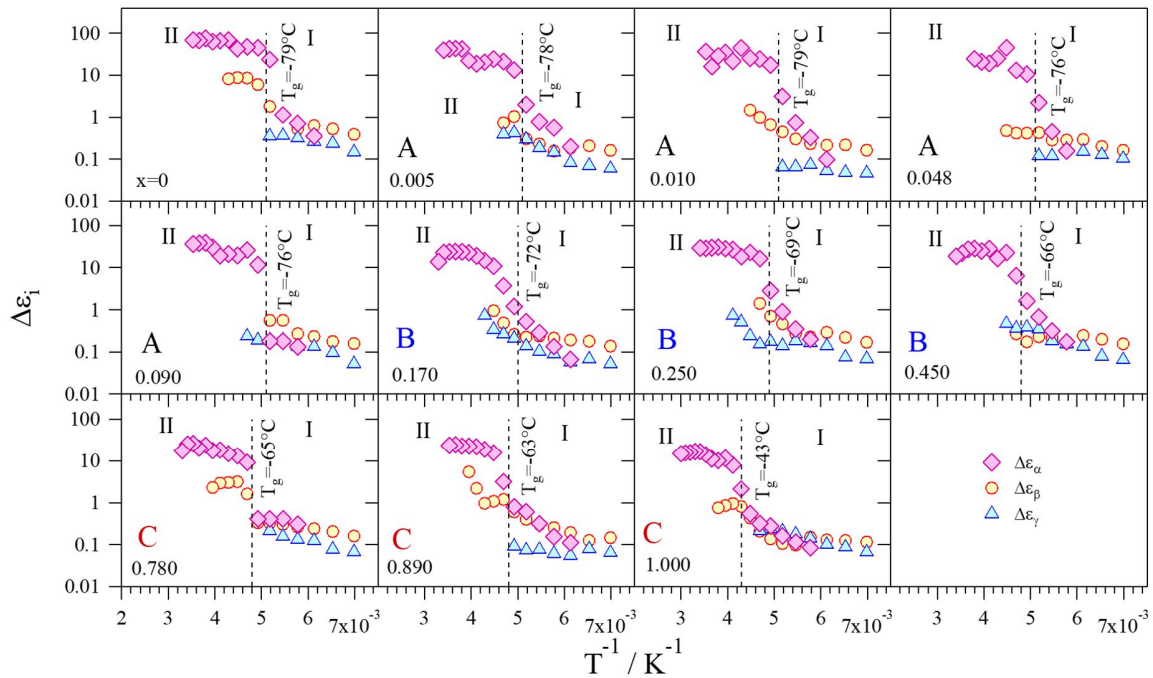


Figure 5.21. $\Delta\epsilon_i$ vs. T^{-1} curves of each dielectric relaxation event for every sample. Region I and Region II are divided by the T_g of the sample.

The α dielectric relaxation is detected in both Region I, with an Arrhenius-like behavior, and Region II, with a VTFH behavior, at all the lithium concentrations. Furthermore, at $T > T_g$, $\Delta\epsilon_\alpha$ is the only dielectric strength that reaches values higher than 10, demonstrating a lower interaction between α dipole moments [52]. As elsewhere described [162], β relaxation shows an Arrhenius-like behavior in the whole temperature range, indicating that this relaxation is responsible for the migration of lithium cations through hopping events between different glycerol molecules. The dielectric strength of the β relaxation is observed to be lower than that of the α event. Finally, γ dielectric relaxation mode is detected only at temperatures lower than the T_g , and it demonstrates an Arrhenius-like dependence to T^{-1} , similarly to β . The corresponding dielectric strength values ($\Delta\epsilon_\gamma$) shows the lowest values among all the observed relaxations.

5.2.4.3 Activation Energies

The values of the activation energy (E_a) related to each conductivity pathway are obtained by fitting the conductivity and dielectric relaxation frequency curves vs. T^{-1} shown in Figure 5.17 and Figure 5.20, respectively. Results are summarized in Figure 5.22, Table 5.5, and Table 5.6.

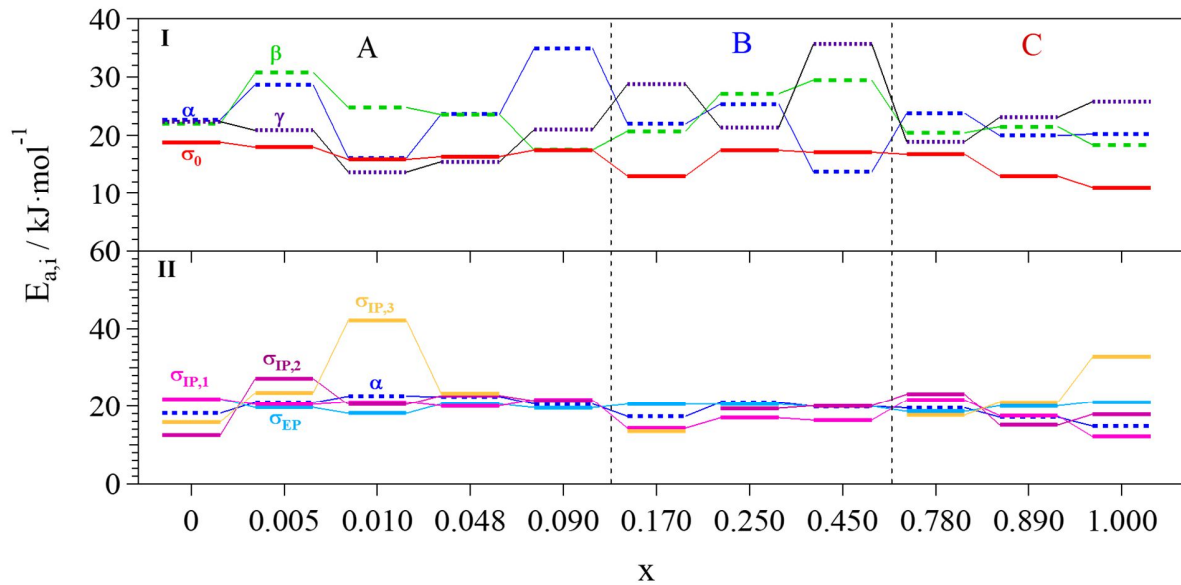


Figure 5.22. Activation energies calculated for each polarization phenomenon and relaxation event of every sample. The plot is divided into a low-temperature region (Region I, $T < T_g$) and a high-temperature region (Region II, $T > T_g$).

Table 5.5. Activation energies calculated for each polarization phenomenon.

x	Group	Polarizations ^a				
		σ_0	σ_{EP}	$\sigma_{IP,1}$	$\sigma_{IP,2}$	$\sigma_{IP,3}$
		$E_a / \text{kJ}\cdot\text{mol}^{-1}$	$E_a / \text{kJ}\cdot\text{mol}^{-1}$	$E_a / \text{kJ}\cdot\text{mol}^{-1}$	$E_a / \text{kJ}\cdot\text{mol}^{-1}$	$E_a / \text{kJ}\cdot\text{mol}^{-1}$
	I	II	II	II	II	
0	A	18±1	21.9±0.2	21.9±0.7	12.5±0.6	16±2
0.005	A	18±2	19.6±0.4	20.4±0.5	27±2	24±2
0.010	A	16±2	18.1±0.6	21.1±0.8	20.4±0.5	42.2±0.3
0.048	A	16±2	20.5±0.4	21.1±0.3	22.8±0.8	23.4±0.9
0.090	A	18±2	19.6±0.4	21.6±0.4	21±1	23±2
0.170	B	13±1	20.5±0.7	14.3±0.5	-	14±1
0.250	B	17±1	20.5±0.2	17.0±0.8	19±2	18.8±0.7
0.450	B	17±1	20.0±0.4	16.4±0.6	20.1±0.8	13.0±0.1
0.780	C	17±1	18.6±0.7	22±1	23.1±0.7	17.7±0.1
0.890	C	13±1	20.1±0.3	17.5±0.1	15.1±0.6	21.0±0.9
1.000	C	11±2	21.2±0.2	12±1	18±1	32.8±0.1

^aResults are obtained from the fitting of polarization curves of Figure 5.17.

Table 5.6. Activation energies calculated for each relaxation event.

x	Group	Relaxations ^a				
		α		β		γ
		$E_a / \text{kJ}\cdot\text{mol}^{-1}$		$E_a / \text{kJ}\cdot\text{mol}^{-1}$		$E_a / \text{kJ}\cdot\text{mol}^{-1}$
	I	II	I	II	I	
0	A	23±1	18.1±0.7	22.0±0.5	75±3	22±2
0.005	A	29±2	20.9±0.5	31±2	59±5	20.9±0.9
0.010	A	16±1	22.7±0.5	24.8±0.8	61±3	13.7±0.4
0.048	A	23±2	23±1	24±2	80±1	16.5±0.6
0.090	A	35±2	20.57±0.06	18±2	-	21±1
0.170	B	22±2	17.3±0.7	20±2	36.63±0.03	29±1
0.250	B	25±2	20.0±0.2	27±1	-	21±1
0.450	B	14±1	19.9±0.7	30±2	-	36±2
0.780	C	24±1	19.6±0.4	20±1	120±10	18.0±0.7
0.890	C	20±2	17±1	22±1	60±3	23.1±0.7
1.000	C	20±3	14.8±0.6	18.378±0.004	77±4	25.8±0.7

^aResults are obtained from the fitting of relaxation curves of Figure 5.20.

At $T < T_g$ (region I) and at low concentrations of Li^+ ($0.005 \leq x \leq 0.090$), it is observed that E_a of σ_0 is very similar to the activation energy of the γ dielectric relaxation. Thus, in these cases, the local fluctuations of the dipole moments of glycerol terminal hydroxyl functionalities are playing a

crucial role in the overall conductivity. Increasing the lithium content ($x \geq 0.170$), it seems that a correlation between the activation energy of σ_0 and that of any relaxation does not exist, indicating that in region I the glycerol relaxations are not assisting the migration process of lithium cations. In the temperature region II, the activation energy value of σ_k , and in particular E_a of σ_{EP} , is very similar to the activation energy of α dielectric relaxation at all x values with a difference of no more than $4 \text{ kJ}\cdot\text{mol}^{-1}$. Hence, independently from which is the coordination geometry assumed by glycerol molecules, the diffusion of conformational states between glycerol cluster aggregates is ruling the overall lithium ion conductivity mechanism. Furthermore, E_a of this relaxation is very low, always lower than $23 \text{ kJ}\cdot\text{mol}^{-1}$, showing that the formation and dissolution mechanism of hydrogen bonds in clusters of glycerol molecules, required for the initiation of α relaxation, is very efficient in long range charge migration events.

5.2.4.4 Diffusion Coefficients and Average Charge Migration Distance

Definitive insights on the conductivity mechanism and the charge transfer processes occurring in the proposed materials are obtained by evaluating the temperature dependence of the diffusion coefficient (D_{σ_k}) and the average charge migration distance ($\langle r_k \rangle$). D_{σ_k} is calculated with the Nernst-Einstein equation [49]:

$$D_{\sigma_k}(T_i) = \frac{RT_i\sigma_k}{Z_k^2 C_k F^2} \quad (5.4)$$

where R is the gas constant, T_i is the temperature at which D is calculated, σ_k is the conductivity of the k^{th} polarization, Z_k and C_k are the charge and concentration of the k^{th} species exchanged during the σ_k polarization, and F is the Faraday constant. The correlation between the diffusion coefficient D , associated with each polarization, and the dielectric relaxation events, is derived from the Stokes-Einstein equation. The result is:

$$D_{\sigma_k}(T_i, \tau_j) = \frac{(k_b T_i)^{2/3}}{6\pi^{2/3} \tau_j^{1/3} \eta_i^{2/3}} \quad (5.5)$$

where k_b is the Boltzmann constant, τ_j is the relaxation time of the j^{th} dielectric relaxation, and η is the viscosity of the system. The viscosity is approximated with the temperature-dependent viscosity of glycerol found in literature [211], even if it should slightly increase by increasing the

lithium content. The analysis of this latter equation reveals that a linear correlation between $\log(D_{\sigma k})$ and $\log(f_j)$ is present. Results are reported in Figure 5.23.

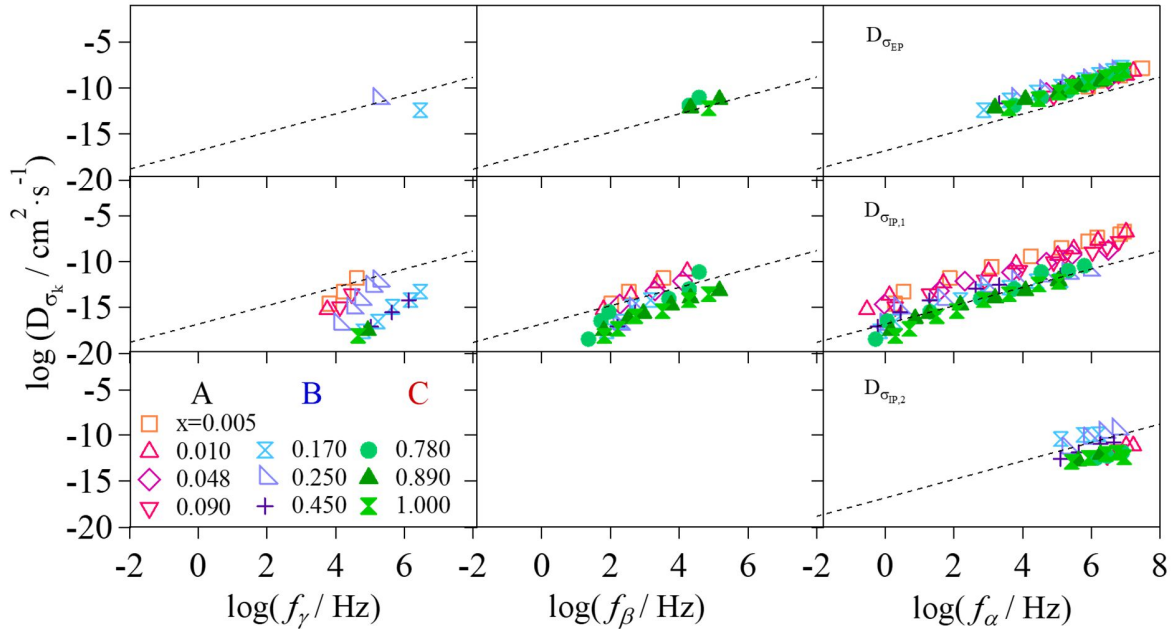


Figure 5.23. Diffusion coefficient calculated for each polarization (σ_{EP} , $\sigma_{IP,1}$, and $\sigma_{IP,2}$ rows), as a function of the dielectric relaxation frequencies (f_γ , f_β , and f_α , columns). Dotted lines represent the ideal glycerol diffusion coefficient.

The correlation existing between $D_{\sigma k}$ and the relaxation frequencies at different temperatures and lithium concentrations permits for the determination of the relationships between polarization phenomena and dielectric relaxation events. Two concurring events appear to declare the fruitful relationship between the two phenomena: i) a linear dependence of the logarithm of the diffusion coefficient on the logarithm of the dielectric relaxation frequency; and ii) this linear dependence has to be superimposable to the ideal viscosity of the material (dotted lines in Figure 5.23). It is shown that all the polarizations are influenced by α dielectric relaxation, while β is correlated only to σ_{EP} and $\sigma_{IP,1}$. On the contrary, γ dielectric relaxation is not influencing any migration process. Experimental data of electrolytes belonging to lithium concentration region A fit very well the ideal one, for both α and β dielectric relaxations. Increasing lithium content in the electrolyte (region B), the overlap between experimental and ideal data is even better, especially for the α relaxation. Thus, a high migration efficiency is detected, and a higher conductivity is expected. Finally, in region C ($x \geq 0.780$) a good correlation between $D_{\sigma_{EP}}$, $D_{\sigma_{IP,1}}$, $D_{\sigma_{IP,2}}$, and both α and β dielectric relaxations is observed, even if $D_{\sigma_{IP,1}}$ and $D_{\sigma_{IP,2}}$ are a few $\text{cm}^2\cdot\text{s}^{-1}$ lower than the ideal values.

The average charge migration distance ($\langle r_k \rangle$) values, as a function of temperature, of the different percolation pathways is obtained using the Einstein-Smoluchowski equation:

$$\langle r_k \rangle(T_i) = \sqrt{6D_{\sigma_k} \tau_k} = \sqrt{\frac{6RT_i \sigma_k \tau_k}{Z_k^2 C_k F^2}} \quad (5.6)$$

where τ_k is the relaxation time of the σ_k polarization. Results are shown in Figure 5.24.

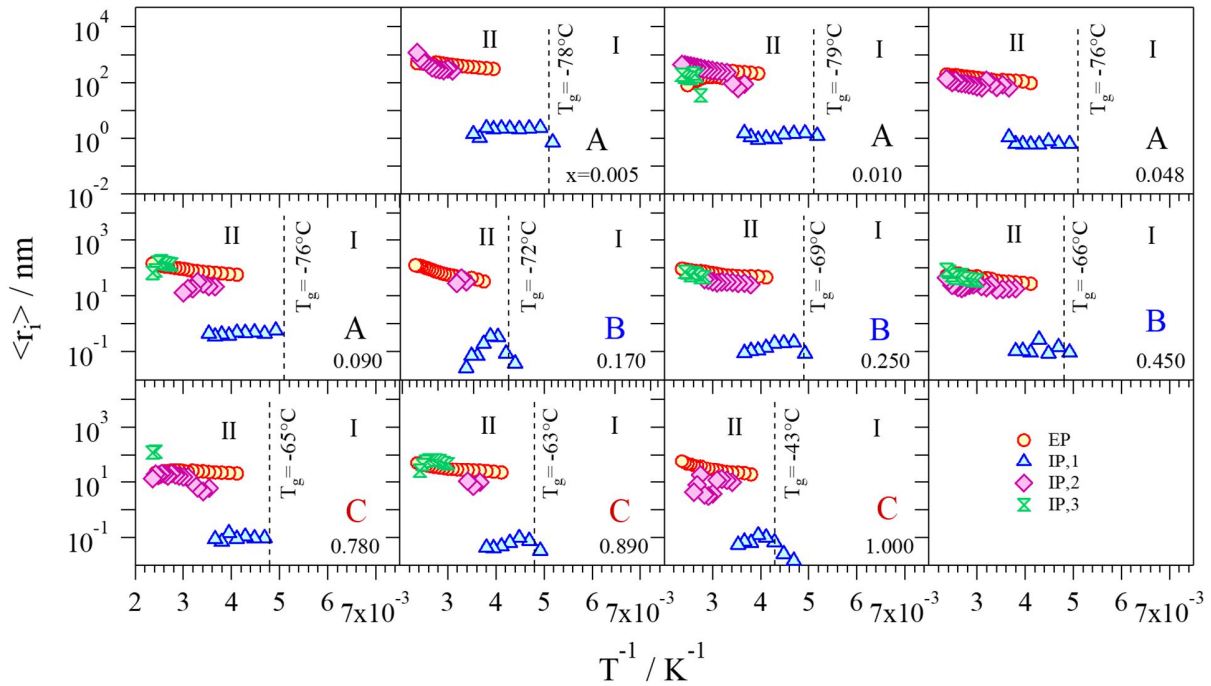


Figure 5.24. Average migration distance as a function of the temperature for σ_{EP} , $\sigma_{IP,1}$, $\sigma_{IP,2}$, and $\sigma_{IP,3}$.

It is demonstrated that the average migration distance increases as the temperature is raised. At $T < T_g$ (temperature region I), $\langle r_k \rangle$ is not present. Indeed, Li^+ are strongly coordinated by glycerol molecules, and high values of energy are needed in order to activate the relaxation processes of the cluster aggregates and allow lithium ions to be exchanged. Above the T_g (temperature region II), the average migration distance behavior as a function of temperature is almost constant for all the polarizations. On the contrary, the different concentrations of Li^+ in the electrolytes highly affect the migration distance values. Indeed, a decrease of one order of magnitude is observed going from the samples with $x = 0.005$ to $x = 1.000$. Thus, the higher the number of Li^+ able to be exchanged is present in the electrolyte, and the smaller the dimension of the domains is. It is observed that the $\langle r_{EP} \rangle$ values range from 10^2 to 10^1 nm, with $\langle r_{EP} \rangle$ responsible for the long-range

migration. Differently from $\langle r_{EP} \rangle$, $\langle r_{IP,1} \rangle$ shows the lowest values among all the polarizations, demonstrating that this phenomenon is responsible for the short-range migration. Furthermore, this distance is equivalent to 1 nm, that is similar to the distance between two adjacent glycerol molecules. Thus, it is reasonable to attribute IP,1 to the exchange of lithium ions between neighboring glycerol molecules. Finally, $\langle r_{IP,2} \rangle$ and $\langle r_{IP,3} \rangle$ show values similar to $\langle r_{EP} \rangle$, indicating that they also account for the long-range charge migration processes, contributing with a higher intensity in the electrolytes with a low concentration of Li⁺. Moreover, $\langle r_k \rangle$ reflects the dimensions of the domains among which lithium ions are exchanged: thus, IP,2 and IP,3 domains are more far with respect to the domains involved in the IP,1 percolation pathways.

5.2.4.5 Conductivity Mechanism

BES studies highlight that: i) three different interdomain polarizations, related to three Li⁺ conduction pathways, are present; and ii) three kind of nanodomains with different permittivities (ϵ_1 , ϵ_2 , and ϵ_3) exist within the materials. At $T > T_g$, all the conductivities show a VTF behavior, demonstrating that they are all assisted by the dielectric relaxation events of the glycerol aggregates, with particular reference to α relaxation. Each domain is composed by glycerol molecules coordinated through different geometries, g_1 , $g_{2,1}$, $g_{2,2}$, and g_3 , that affect its permittivity value. Nanodomains 2 and 3 are mostly present into high lithium concentration electrolytes ($x \geq 0.170$), where $\sigma_{IP,2}$ and $\sigma_{IP,3}$ ensure an important contribution to the long-range migration.

$\sigma_{IP,1}$ polarization phenomenon: it is detected at $T_g \leq T \leq 10$ °C, and is responsible for a short-range migration process IP,1 (*ca.* 1 nm). At these temperatures, the domains related to $\sigma_{IP,1}$ are dominant and are composed by large aggregates of crystalline glycerol molecules (“*type 1 domains*”) that: i) expose the negatively charged -O⁻ functionalities on their external surface; and ii) adopt an ordered structure that permits the exchange of Li⁺ between neighboring molecules. The presence of type 1 nanodomains explains the short-range migration pathways of lithium cations and the manifestation of this polarization at low temperatures and high frequencies. Type 1 domains are rigid. Thus, the diffusion of conformational states along the glycerol aggregates is inhibited. Indeed, the conductivity of the electrolyte along these pathways is low. A representative sketch that clarifies $\sigma_{IP,1}$ polarization phenomenon is reported in Figure 5.25a.

$\sigma_{IP,2}$ polarization phenomenon: it appears at $T > 10$ °C, and at frequencies lower than those exhibited by $\sigma_{IP,1}$. $\sigma_{IP,2}$ allows for a long-range charge migration process of Li^+ , reaching distances of *ca.* 1 μm . The nanodomains correlated to $\sigma_{IP,2}$ (“*type 2 domains*”) are described by the presence of a distribution of ordered aggregates with smaller sizes with respect to those associated with type 1 domains. Indeed, $\sigma_{IP,2}$ is observed at temperatures higher than $\sigma_{IP,1}$. In $\sigma_{IP,2}$ polarization phenomenon, lithium cations are exchanged between neighboring type 2 nanodomains, reaching a longer average charge migration distance with respect to $\sigma_{IP,1}$. Furthermore, type 2 nanodomains exhibit a more flexible structure if compared to that of type 1 nanodomains, improving the diffusion of conformational states within glycerol aggregates (α mode) and facilitating the Li^+ migration process. The percolation of lithium cations following $\sigma_{IP,2}$ is represented in Figure 5.25b.

$\sigma_{IP,3}$ polarization phenomenon: is detected at $T > 60$ °C and at lower frequencies with respect to $\sigma_{IP,1}$ and $\sigma_{IP,2}$. Similarly to $IP,2$, $IP,3$ allows for a long-range migration process (*ca.* 1 μm). However, it contributes with a lower magnitude to the total conductivity if compared to $IP,2$. “*Type 3 domains*”, that are related to $\sigma_{IP,3}$, are constituted by amorphous glycerol molecules aggregates with a distribution of coordination geometries falling between those observed in type 1 and type 2 domains. Indeed, only at temperatures higher than 60 °C it is possible to detect this polarization. Type 3 domains have a very flexible structure. Thus, the long-range charge migration of Li^+ is modulated by the diffusion of conformational states along glycerol molecule aggregates. The conductivity mechanism along $\sigma_{IP,3}$ pathways is graphically described in Figure 5.25c.

σ_{EP} polarization phenomenon: gives the dominant contribution to the total conductivity at $T > 10$ °C in all the electrolytes. The presence of nanodomains in the materials helps the long-range Li^+ transfer, which occurs through the exchange between different delocalization bodies (DBs) of the material [212]. A delocalization body consists of a portion of the electrolyte with a defined volume that includes type 1, type 2, and type 3 nanodomains. Li^+ ions can be considered delocalized in each DB, thanks to the fast lithium exchange occurring between the coordination sites present in each DB. Thus, in the proposed materials the long-range charge migration occurs as Li^+ are exchanged between different DBs as they come into contact owing to conformational changes caused by the diffusion of conformational states of the glycerol molecules.

The total conductivity mechanism occurring in the $GlyLi_x$ electrolytes, revealed by the analysis of the polarization phenomena and dielectric relaxation events, is reported in Figure 5.25d. In this

mechanism, all the four polarizations (σ_{EP} , $\sigma_{IP,1}$, $\sigma_{IP,2}$, and $\sigma_{IP,3}$) concur to the diffusion of the Li^+ ions through different percolation pathways within the materials.

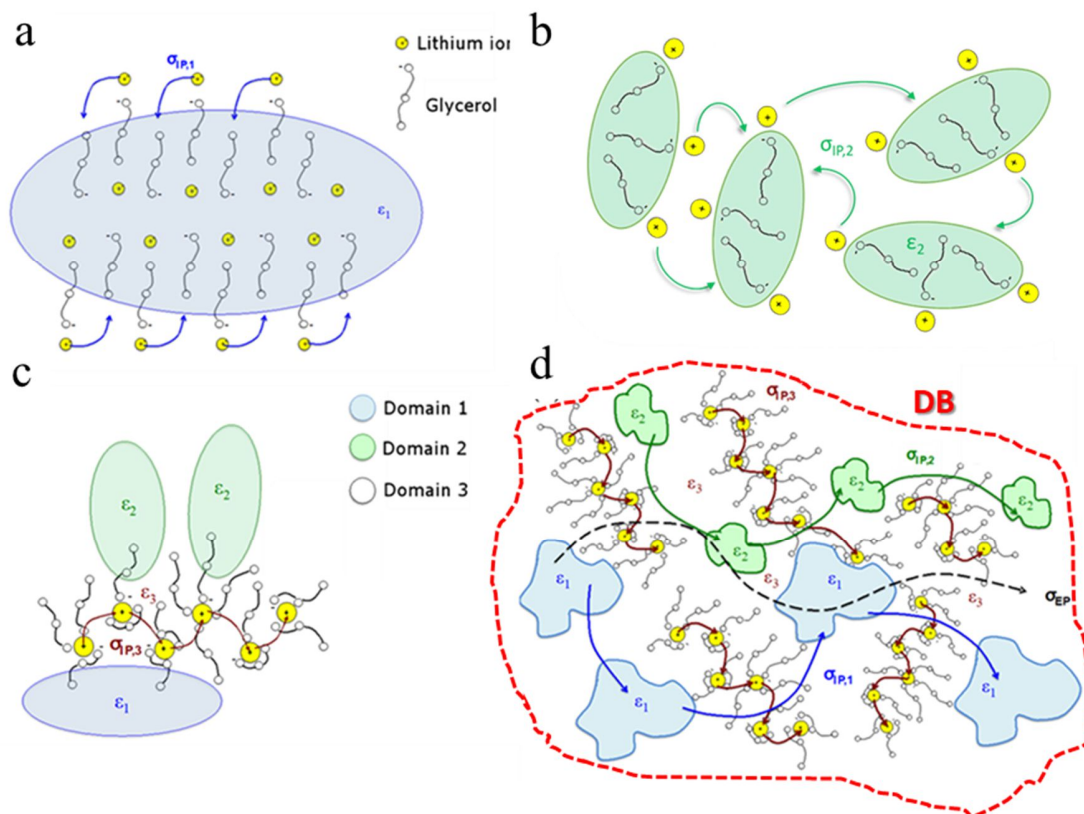


Figure 5.25. Proposed conduction mechanism for: $\sigma_{IP,1}$ (a), $\sigma_{IP,2}$ (b), and $\sigma_{IP,3}$ (c); overall proposed conduction mechanism (d). The delocalization body (DB) is highlighted with a red dotted line.

5.3 Conclusions

In this work, a set of new electrolytes for lithium conduction is proposed. Vibrational studies (*i.e.* FT-IR and micro-Raman) allow for the understanding of the coordination geometries assumed by glycerol molecules as a function of lithium concentration. High-resolution thermogravimetric analyses highlight that the proposed materials are thermally stable up to 170 °C, while modulated differential scanning calorimetry measurements demonstrate that, as the content of Li^+ is increased, the T_g shifts to higher temperatures (from -78.51 °C of pristine glycerol to -42.95 °C of lithium glycerolate, GlyLi). The thermal behavior of the proposed electrolytes is well explained considering the coordination geometries, revealed by vibrational results, assumed by glycerol molecules. Finally, broadband electrical spectroscopies show that the highest conductivity values

are reached by GlyLi_{0.25} electrolyte: higher than 10^{-6} S·cm⁻¹ at -10 °C, $1.99 \cdot 10^{-4}$ at 30 °C, and $1.55 \cdot 10^{-2}$ S·cm⁻¹ at 150 °C. Furthermore, a deep study of BES results allows to propose a reasonable conductivity mechanism for lithium ions. In particular, it appears that Li⁺ ions are exchanged between crystalline and amorphous domains, thanks to the diffusion of conformational states of glycerol molecule aggregates. At $T < T_g$, the conductivity mechanism occurs through “hopping” processes between neighboring glycerol molecules. At higher temperatures, new polarization phenomena appear, such as $\sigma_{IP,1}$, which is the dominant event between T_g and 10 °C. At $T > 10$ °C, the electrode polarization σ_{EP} becomes the principal contribution to the total conductivity. σ_{EP} involves the exchange of Li⁺ between different delocalization bodies (DBs), that results in a long-range charge migration process. In this temperature range the contribution of $\sigma_{IP,2}$ polarization becomes important, and the flexibility of glycerol molecules improves the conductivity of the proposed electrolytes. The best conductivity values showed by the proposed electrolytes are of a clear importance if compared with the state-of-the-art polymer electrolytes for application in Li-ion batteries.

6. Structural Elasticity Modification of a High Voltage Cathode for Lithium Batteries

There are no doubts that, nowadays, lithium secondary batteries are the most performing energy storage system, thanks to their specific energy, high efficiency and long service lifetime. A lot of different combinations of lithium metal oxides and phosphates are present in literature as cathode materials for LIBs. Furthermore, it is demonstrated that the properties of the resulting material can be modulated by the selection and concentration of metals inserted into them. In particular, lithium-mixed metal-phosphates exhibit very interesting electrochemical properties, like a high working potential, a good specific capacity, and very good specific energy values, thanks to their olivine structure. The unveiling of the lithium-ion conductivity mechanism within the cathode crystal structure is very useful in order to obtain materials with the desired characteristics that enhance the Li^+ diffusion coefficient in the bulk. To do this, broadband electrical spectroscopy studies are a valid technique, because of their ability to investigate how the structural motions are involved in the lithium percolation process. In this work, three different cathode materials are synthesized and studied: i) $\text{LiFe}_{1/3}\text{Ni}_{1/3}\text{Co}_{1/3}\text{PO}_4$ [LFNCP]; ii) $\text{LiFe}_{1/3}\text{Ni}_{1/3}\text{Co}_{1/3}\text{PO}_4$ with a copper precursor added during the synthesis [LFNCP/Cu]; and iii) $\text{LiFe}_{1/3}\text{Ni}_{1/3}\text{Co}_{1/3}\text{PO}_4$ with a copper precursor and graphite added during the synthesis [LFNCP/Cu+C]. The electric response of the proposed materials is analyzed in order to elucidate how the copper precursor and graphite additions to the reactants can modify the resulting structural flexibility of the olivine system. The addition of copper precursor is selected because of the well-known beneficial role of metal oxides in improving the charge-transfer kinetics at the cathode/electrolyte interface.

6.1 Experimental Section

6.1.1 Reagents

Lithium carbonate (99 %) is provided from British Drug Houses (BDH). Ammonium phosphate dibasic (99 %) is purchased from Riedel-de Haën. Iron(III) oxide from Baker, cobalt(II) carbonate (50.5 % Co assay), nickel(II) oxide (97 %), and copper(II) carbonate (56.0 % Cu assay) are obtained from Carlo Erba, while graphite from TIMCAL.

6.1.2 Synthesis

The materials are synthesized as follows: Li_2CO_3 (1.000 g), $(\text{NH}_4)_2\text{HPO}_4$ (3.575 g), Fe_2O_3 (0.721 g), NiO (0.675 g), and $2\text{CoCO}_3 \cdot 2\text{Co}(\text{OH})_2 \cdot n\text{H}_2\text{O}$ (1.053 g) are mixed together, obtaining a mixture with a molar ratio Li:P:Fe:Ni:Co of 1.00:1.00:0.33:0.33:0.33. The mixture is ground in a planetary ball-mill for 2 hours at 500 rpm in an agate jar. Copper (II) carbonate (0.667 g, 8.6 wt.%) is added to the mixture, which is further ground for 2 hours at 500 rpm. The product is divided into two parts, labeled (I) and (II). Graphite (0.204 g, 5.0 wt.%) is added to (II); the resulting powders are ground for 2 hours at 500 rpm. From both (I) and (II) a pellet is obtained and subsequently pyrolyzed at 700 °C in air for 24 h, giving LFNCP/Cu and LFNCP/Cu+C samples, respectively. Finally, each pellet is ground using a planetary ball mill in order to obtain fine powders. LFNCP material is obtained following the same procedure, without the addition of both copper (II) carbonate and graphite.

6.2 Results and Discussion

6.2.1 Preface: Structure and Electrochemistry

In a previous study, the structure and the electrochemical performances of these materials have been studied by powder X-ray diffraction, ATR-FT-IR, and battery test measurements [22].

6.2.1.1 Powder X-Ray Diffraction

An olivine structure is revealed from the XRD diffractogram (Figure 6.1), with a $Pbnm$ (D_{2h}^{16}) space group belonging to the orthorhombic lattice system. All the metal ions (*i.e.* Fe, Ni, and Co) result to be vicariant in the octahedral sites, and are coordinated by six oxygen ions of the phosphate groups. Lithium ions are located in the octahedral cavities formed by phosphate tetrahedra. The olivine structure reveals no remarkable structural variations in LFNCP/Cu and LFNCP/Cu+C with respect to undoped LFNCP material. Thus, it suggests that the very small differences in the “free” volume of the channels in LFNCP/Cu and LFNCP/Cu+C cathodes will only slightly modulate the Li^+ diffusion within the bulk 3D-material during the charge/discharge processes. Rietveld analysis demonstrates that Cu is not vicariant within the olivine-like structure, but it aggregates in a segregated phase of copper(II) oxide. Likely, the Jahn-Teller distortion, exhibited by elements with a d^9 electronic configuration such as that of Cu(II), makes these ions unsuitable for metal substitution in octahedral coordination sites of the olivine crystal structure. In LFNCP/Cu and LFNCP/Cu+C, copper(II) oxide phase adopt a monoclinic $C 1 2/c 1$ space group [213].

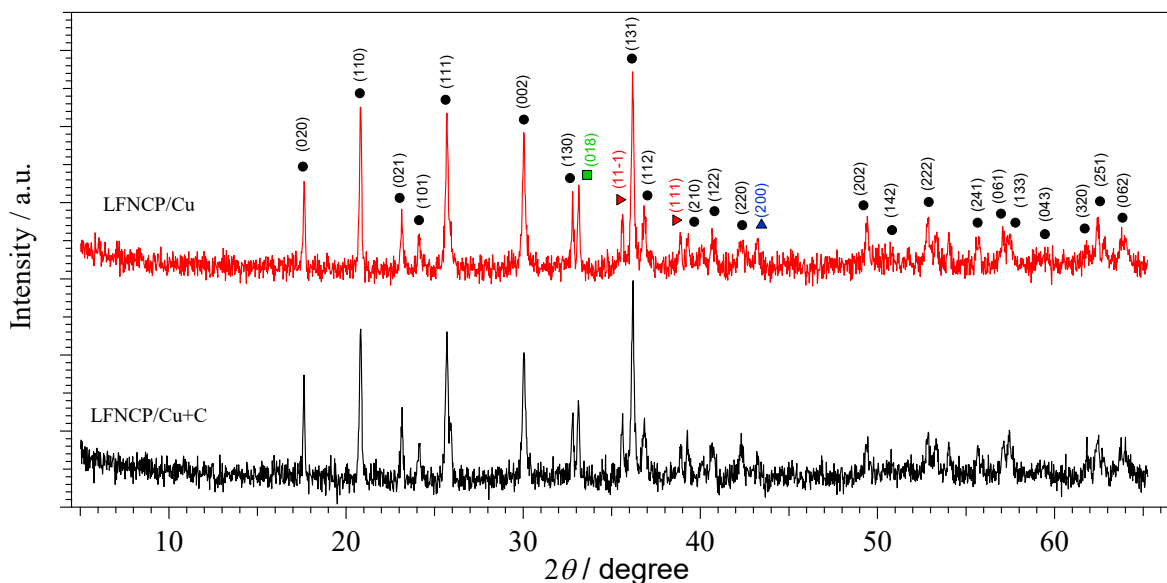


Figure 6.1. X-ray diffraction. WAXD spectra of LFNCP/Cu (red line) and LFNCP/Cu+C (black line); Miller indices are reported above the peaks. Every different phase is indicated with a different marker (●LiMPO₄, ■Fe₂O₃, ▲CuO, and ▲NiO).

6.2.1.2 Vibrational Studies

The spectral region between 1300 and 200 cm^{-1} of Figure 6.2 is diagnostic of the crystallinity of LFNCP/Cu and LFNCP/Cu+C materials. Indeed, for both the samples well-resolved peaks can be observed, which confirm that these materials are characterized by a very ordered and defined structure [98]. In the region above 500 cm^{-1} , the peaks associated with the internal vibrational modes of the tetrahedral $[\text{PO}]_4^{3-}$ group are detected. In particular, symmetric (ν_s) and antisymmetric (ν_a) stretching modes, and the symmetric (δ_s) and antisymmetric (δ_a) bending modes, show a split owing to factor group effects in solid state. In detail, factor group splitting of $[\text{PO}]_4^{3-}$ vibrational modes appears when $[\text{PO}]_4^{3-}$ units are located in specific equivalent positions within the unit cell of the crystal; this effect is also known as the *correlation effect* [98]. Below 500 cm^{-1} , the presence of the typical M-O and Li-O stretching vibrations is observed, confirming the existence of the olivine structure, and the vicariant behavior of the metal within the crystal cell. The intensities of these latter vibrations are higher in LFNCP/Cu with respect to LFNCP/Cu+C, indicating that the density of defects in the sample where graphite is added during the synthesis is higher. Thus, a higher flexibility of the structure for LFNCP/Cu+C cathode is expected. The higher magnitude of structural defects occurs when CO_2 is formed in materials as a consequence of the oxidation of graphite precursor during the pyrolysis process. Indeed, this process augments the

free volume in materials and creates a local reducing environment at the interface between nanoparticles, which lowers the density of interparticle crosslinks. Taken all together, with respect to LFNCP/Cu, Li⁺ mobility in the bulk LFNCP/Cu+C structure is improved thanks to a weaker and reduced number of Li-O coordination interactions (confirmed also by impedance spectroscopy measurements).

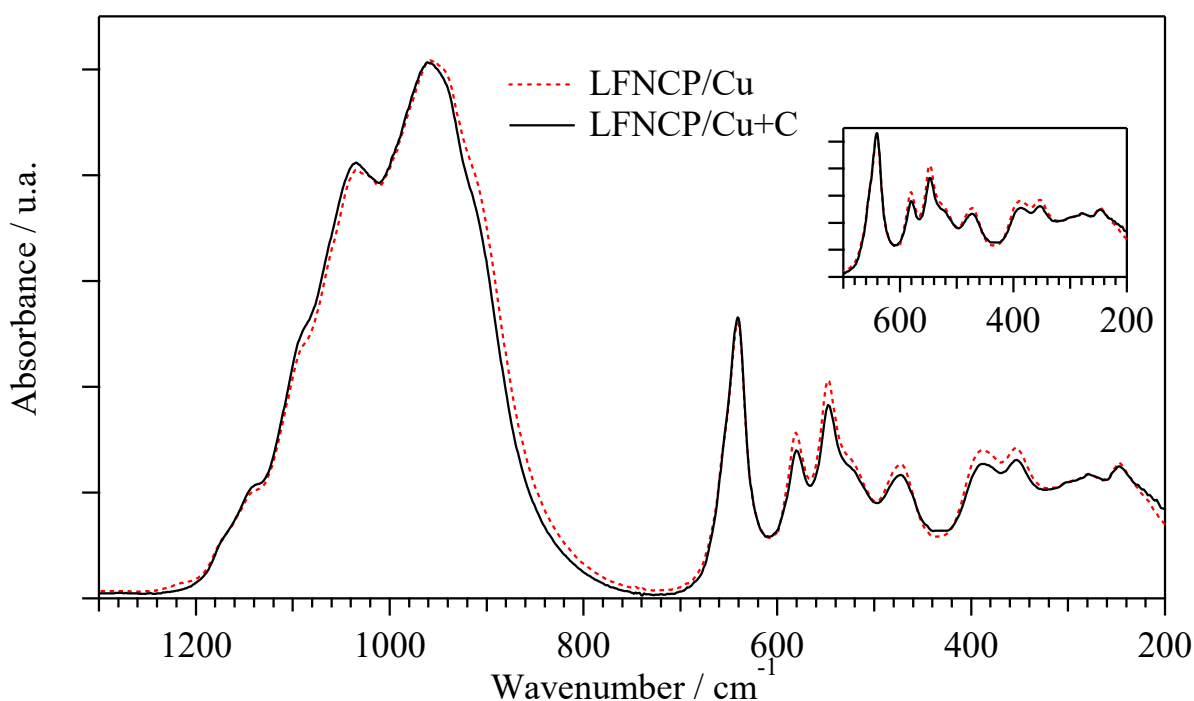


Figure 6.2. Vibrational analyses. FT-MIR and FT-FIR spectra of LFNCP/Cu (red dotted line) and LFNCP/Cu+C (black solid line). The inset shows a magnification of the spectra in the 200-700 cm⁻¹ range; the two curves are superimposed to highlight the differences in absorbance intensities after normalization on the peak at 641 cm⁻¹.

6.2.1.3 Battery Test

The proposed cathode materials are tested under galvanostatic cycling in order to demonstrate their ability to provide a good specific capacity at high voltage, thus supply high energy values. In particular, a lithium metal anode, 1.0 M LiPF₆ in EC/DMC electrolyte, and LFNCP/Cu+C or LFNCP/Cu cathode are assembled to obtain a full cell device. Batteries are cycled between 3.5 and 5.0 V at a constant current of *ca.* 100 mA·g⁻¹. Results are shown in Figure 6.3.

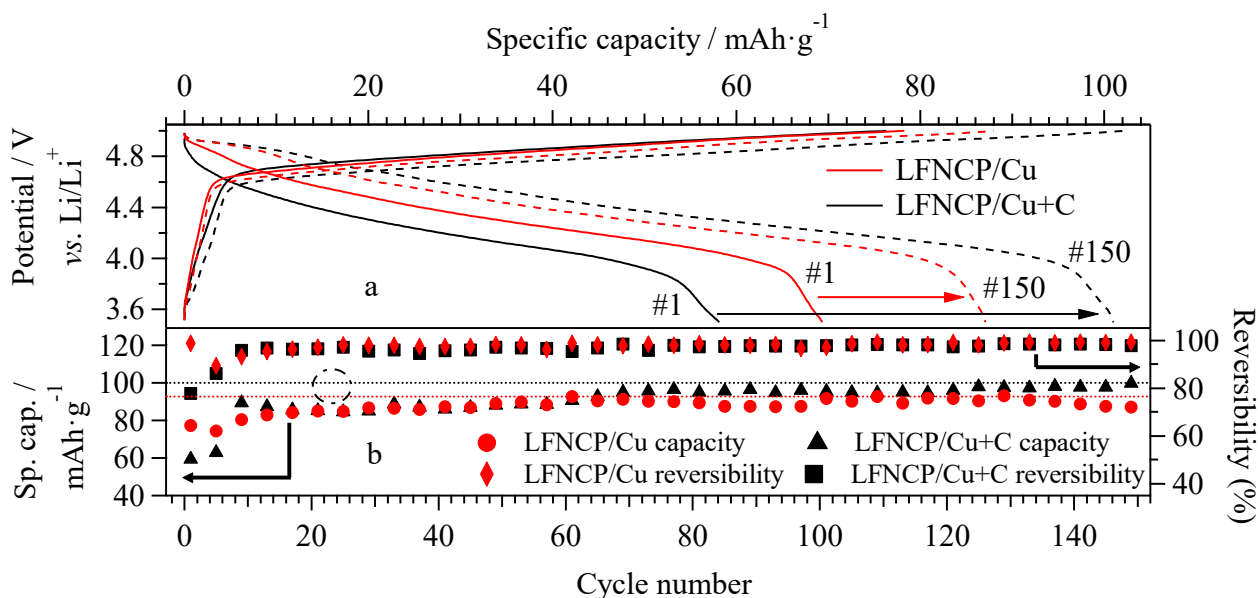


Figure 6.3. Battery tests. Galvanostatic charge/discharge profiles of LFNCP/Cu (red line) and LFNCP/Cu+C (black line) during cycle number 1 (solid line) and cycle number 150 (dashed line) (a). Discharge cycling performances of LFNCP/Cu (●), and LFNCP/Cu+C (▲), and cycling stability of LFNCP/Cu (◆) and LFNCP/Cu+C (■). The difference in maximum discharge capacity of LFNCP/Cu and LFNCP/Cu+C is highlighted with a dashed-dot circle (b).

In Figure 6.3, it can be observed that, after few stabilization cycles, both LFNCP/Cu and LFNCP/Cu+C materials achieve 100 % of reversibility, which is maintained constant for at least 150 cycles. LFNCP/Cu+C cathode reaches a maximum specific capacity of 101 mAh·g⁻¹, corresponding to a specific energy of 455 mWh·g⁻¹ at 1.0 C (102 mA·g⁻¹). The reported performances is similar with that typical of commercial cathodes based on LiCoO₂ (ca. 520 mWh·g⁻¹) [80] and with other electrode materials with an analogous composition (405-560 mWh·g⁻¹) [214]. On cycling, LFNCP/Cu+C shows a performance increase during the first 70 cycles, indicating the gradual activation of the cathode material. These results reveal that the lithium ion insertion\de-insertion reactions, the reversibility, and the kinetics of migration of Li⁺ within the channels of 1D olivine-like structure of LFNCP/Cu+C cathode are significantly affected by the flexibility of the material structure during the charge and discharge phenomena.

The cycling test results of LFNCP/Cu demonstrate: i) inferior electrochemical outcomes with respect to LFNCP/Cu+C, as expected from the spectroscopic and diffraction studies; and ii) a maximum specific capacity of ca. 93 mAh·g⁻¹ (420 mWh·g⁻¹ of specific energy). Pristine LFNCP material [214], the cathode with no copper or graphite addition during the synthesis, is able to provide a maximum specific capacity of 100 mAh·g⁻¹, a reversibility of ca. 100%, and a low capacity

fade during the first 150 cycles. Summarizing, with respect to pristine LFNCP: i) LFNCP/Cu cathode shows a lower performance in battery cycling; and ii) LFNCP/Cu+C material exhibits a slightly better specific capacity and an improved cycling life. Further studies will need be conducted in order to study the effect of the only addition of carbon to the precursors, without the presence of a copper source (LFNCP/C).

6.2.2 Broadband Electrical Spectroscopy Studies

The exotic concept of olivine structural flexibility, that is only hinted by vibrational studies, is definitely confirmed by BES studies. The use of this technique to evaluate the elasticity of a crystal structure is an innovative concept that is highly helpful and that leaves no room for doubts about the flexibility of cathode materials.

The electric response of LFNCP-based cathode materials, in terms of structural relaxations and polarization phenomena, is studied by BES in the frequency and temperature ranges of 10^{-2} ÷ 10^7 Hz and -80 ÷ 150 °C, respectively. The spectra of imaginary component of permittivity ($\epsilon''(\omega)$ vs. f , where f is the frequency in Hz and $\omega = 2\pi f$) are reported in Figure 6.4.

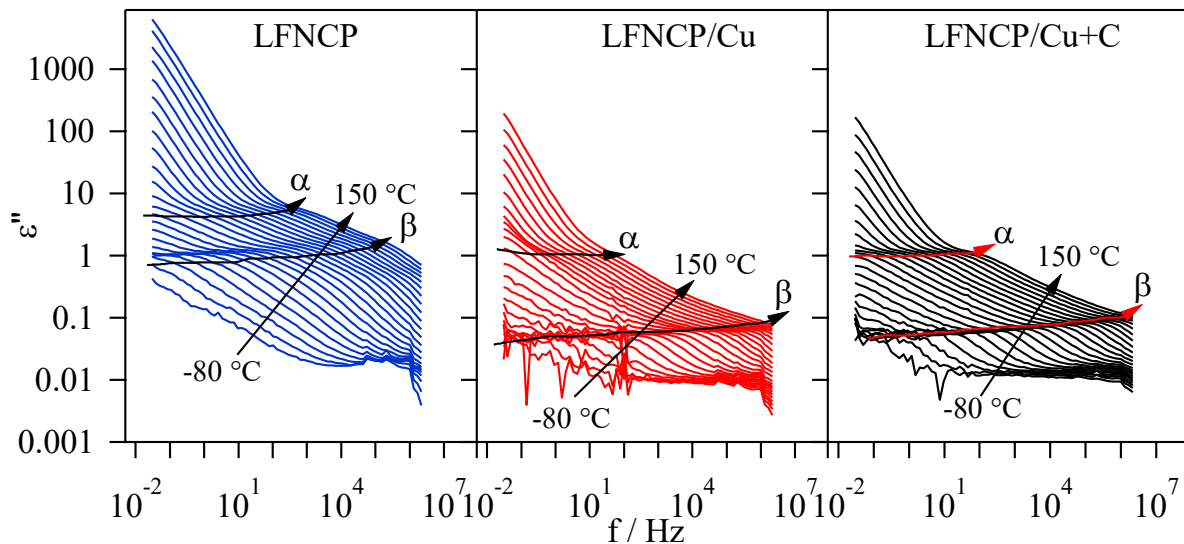


Figure 6.4. BES results. ϵ'' vs. frequency for LFNCP (blue), LFNCP/Cu (red), and LFNCP/Cu+C (black) from -80 to 150 °C. α and β dielectric relaxations are highlighted with an arrow.

It is revealed that the electric response of LFNCP-based cathode materials is composed by: i) two different dielectric relaxation events detected in the medium (α) and high frequency region (β) of the spectra; and ii) a polarization phenomenon, attributed to the lithium ion dc conductivity of

materials, measured in the low frequency wing of $\varepsilon''(\omega)$ profiles. α and β modes are assigned to the dynamics of host olivine matrices. In details, α -mode is related to the diffusion of conformational states along phosphate repeat units in the 3D-network of LFNCP-based materials. Thus, α -mode, which describes the coupled motion of phosphate dipole moments, is an analogous of the typical segmental motion observed in polymer materials. β dielectric relaxation is ascribed to the local fluctuation of the dipole moments associated with distorted octahedral repeat units that are coordinating the transition metals. The occurrence of these relaxation modes demonstrates that the olivine backbone structure of the proposed LFNCP-based cathode materials is flexible. The dependence on temperature of relaxation frequencies of the α and β modes of LFNCP, LFNCP/Cu, and LFNCP/Cu+C cathodes is reported in Figure 6.5.

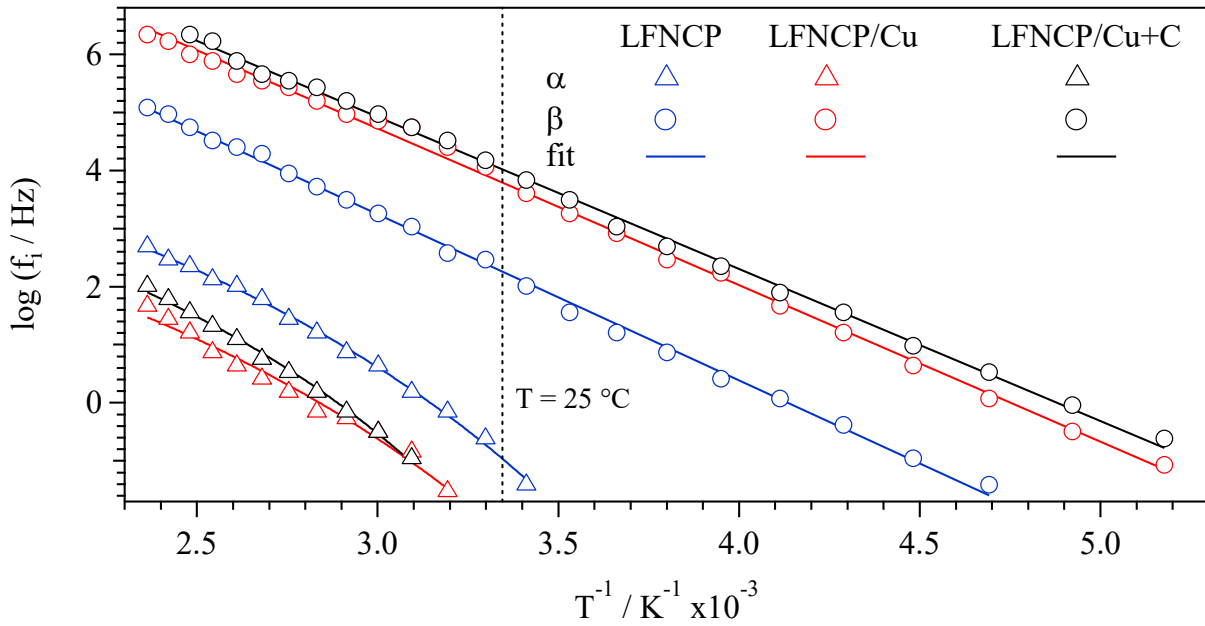


Figure 6.5. LFNCP (blue), LFNCP/Cu (red), and LFNCP/Cu+C (black) $\log f$ vs. $1/T$ plot.

It appears that β relaxations exhibit an Arrhenius-like [210] (A) profile, while α modes follow the typical Vogel–Tammann–Fulcher–Hesse [210] (VTFH) behavior. The activation energies of α and β relaxations, recapped in Table 6.1, are calculated by fitting the data of Figure 6.5 using the following VTFH or A equations [210]:

$$f = A_f \cdot \exp\left(-\frac{E_a}{R \cdot (T - T_0)}\right) \quad (\text{VTFH}) \quad (6.1) \quad A_f \cdot \exp\left(-\frac{E_a}{R \cdot T}\right) \quad (\text{A}) \quad (6.2)$$

where A_f is the pre-exponential term, which is associated with the density of charge carriers. R is the universal gas constant. E_a is the activation energy value, and T_0 is the thermodynamic ideal glass transition temperature, that is the temperature at which the configurational entropy of material becomes zero. Results highlight that the split between α and β relaxations increases moving from pristine LFNCP toward LFNCP/Cu and LFNCP/Cu+C samples, shifting the β -mode to higher frequencies. This indicates that the treatment with Cu and Cu+C during the synthesis allows to obtain LFNCP/Cu and LFNCP/Cu+C cathodes which, differently from the pristine LFNCP, show: i) an increased decoupling of the dynamics of the α and β dielectric relaxation modes; and ii) a very fast β relaxation, which is responsible of the improved kinetics of Li^+ exchange between coordination sites along the 1D channels of olivine materials.

The values of activation energy, summarized in Table 6.1, clearly show that, with respect to pristine LFNCP, the dynamics of both α and β modes of the here proposed cathode materials are promoted, increasing in the order: LFNCP < LFNCP/Cu < LFNCP/Cu+C. Thus, the precursors treatments are very valid to improve the structural flexibility of proposed olivine systems. Indeed, for β relaxation the E_a values of LFNCP, LFNCP/Cu, and LFNCP/Cu+C decrease in the order 54.79 ± 0.53 , 51.59 ± 0.51 and 50.09 ± 0.16 $\text{kJ} \cdot \text{mol}^{-1}$, respectively.

Table 6.1. Activation energies ($\text{kJ} \cdot \text{mol}^{-1}$) of LFNCP, LFNCP/Cu, and LFNCP/Cu+C dielectric relaxations.

$E_a / \text{kJ} \cdot \text{mol}^{-1}$	LFNCP	LFNCP/Cu	LFNCP/Cu+C
α^{VTFH}	16.75 ± 0.23	16.64 ± 0.13	15.32 ± 0.06
β^{A}	54.79 ± 0.53	51.59 ± 0.51	50.09 ± 0.16

^AArrhenius fit. ^{VTFH}Vogel–Tammann–Fulcher–Hesse fit.

Concluding, it should be pointed out that both α and β modes modulate the overall “channel flexibility” of materials, which is: i) directly associated with the mobility of lithium cations in materials; and ii) a crucial event able to modulate the Li^+ migration processes along the insertion channels of the olivine structure.

6.3 Conclusions

In this chapter, the application of broadband electrical spectroscopy technique is proposed in order to evaluate the structural flexibility of a cathode material. In the studied materials, BES measurements confirm vibrational and X-ray diffraction studies, demonstrating that the addition

of graphite during the synthesis gives more elasticity and flexibility to the backbone structure. Moreover, a more facilitated de-insertion/insertion process of Li^+ during the charge/discharge events of battery cycling is revealed in LFNCP/Cu+C with respect to LFNCP/Cu. This is the result of the higher charge-transfer kinetics of these processes given by the presence of segregated CuO nanoparticles in the cathode material. Summarizing, BES measurements are demonstrated to be a useful tool to predict the ability of cathode materials to host and release metal ions, such as Li^+ , K^+ , Mg^{2+} , Ca^{2+} , *etc.*, during the cycling of a full cell device, as highlighted by this work.

7. Effect of High Valence Transition Metal Insertion in High Voltage Olivine Cathodes for Lithium Secondary Batteries

In this work, two ways for the improvement of an olivine cathode material for high-voltage secondary lithium batteries are investigated: i) the reductive power formed during the synthesis; and ii) the introduction in the olivine structure of different metals belonging to the same group (*i.e.* group V). Transition metals of the V group (*i.e.* V, Nb, and Ta) are selected due to their typical higher valence with respect to that of iron, nickel and cobalt present in the classic olivine structure. The charge difference influences the overall electronic structure introducing a “*charge compensation*” mechanism, which rises, as a result, the electron conductivity of the cathode. Higher electron conductivities are expected to improve the rate capability during battery tests. The bulk and surface compositions of the proposed materials are characterized by ICP-AES and XPS analyses, respectively, while thermal stability is gauged with HR-TGA measurements. The morphology of the samples is studied by both SEM and HR-TEM microscopies. The structure of the obtained materials is solved by Rietveld calculations on XRD measurements. The coordination of metals within the olivine structure is determined by FT-IR spectroscopies. The electrochemistry of the cathode is studied by CV and EIS techniques, which allow also for the evaluation of the lithium ion diffusion coefficient within the cathode particles. Finally, the here proposed materials are used to assembled lithium secondary batteries, which are galvanostatic cycled under different conditions, in order to evaluate their applicability in high-voltage and high-energy demanding applications.

7.1 Experimental Section

7.1.1 Reagents

Lithium metal, polyvinyl difluoride (PVDF), 1-methyl-2-pyrrolidone (99.5%, anhydrous), 1.0 M lithium hexafluorophosphate (LiPF_6) solution in ethylene carbonate/dimethyl carbonate 1:1, vanadium(V) oxide, and tantalum(V) oxide are purchased from Sigma-Aldrich. Lithium carbonate (99%) is obtained from BDH, ammonium phosphate dibasic (99%) from Riedel-de Haën, iron(III) oxide from Baker, nickel(II) oxide (97%) and cobalt(II) carbonate (50.5% assay) from Carlo Erba, and graphite (type SK6) from TIMCAL. Niobium(V) oxide is purchased from Fluka, and graphite (type XC72R) from Carbocrom.

7.1.2 Synthesis

In the first part of this work, three different synthetic routes for the production of a vanadium-doped cathode materials are compared (*i.e.* oxidizing solid state synthesis, partially reducing solid state synthesis, and reducing solid state synthesis). After the evaluation of which protocol gives rise to the best material in terms of battery performances (see Section 7.2.7), niobium- and tantalum-doped cathode materials are obtained following the best synthesis.

7.1.2.1 Oxidizing Solid State Synthesis

The reagents are weighed with an exact stoichiometry, in order to obtain a Li:Fe:Ni:Co:(V/Nb/Ta):PO₄ molar ratio of 1:0.33:0.07:0.55:0.05:1. Powders are preliminarily homogenized in an agate mortar and then ball milled in planetary ball miller, 2 h at 500 rpm. The obtained mixture is sintered in a 20 mm diameter pellet, under a pressure of 4 tons. The pellets are then pyrolyzed in a muffle oven in air at 700 °C for 24 h, before being allowed to cool slowly. Finally, pellets are ground again in a planetary ball miller (2 h, 500 rpm) giving rise to LFNCVP, LFNCNP, and LFNCTP cathode materials (containing as dopant V, Nb, and Ta, respectively).

7.1.2.2 Partially Reducing Solid State Synthesis

An amount of 5 % by weight of graphite (type XC72R) is added to the precursors mixture before the first ball milling process. All the subsequent steps are the same of those described in Section 7.1.2.1, giving rise to LFNCVP/C cathode material.

7.1.2.3 Reducing Solid State Synthesis

The preparation of reactants pellet is equivalent of the one reported in Section 7.1.2.1. Once the pellet is obtained, it is placed inside a quartz tube, closed on the top by a double tap cap. Argon gas is fluxed for 30 minutes in order to eliminate all the oxygen and moisture present inside the quartz tube. Then, a H₂/N₂ (10:90 % by volume) gas mixture is fluxed at *ca.* 0.5 L·min⁻¹, and the quartz tube is heated at 700 °C for 24 h. After the pyrolysis, the product is slowly cooled down to ambient temperature under an Argon flow. Finally, the pellet is ground in a planetary ball miller (2 h, 500 rpm), giving rise to LFNCVP/H cathode material.

The composition of the obtained cathodes is evaluated by ICP-AES measurements and results are reported in Table 7.1.

Table 7.1. Composition of the synthesized cathode materials.

Sample	Formula ^a
LFNCVP	$\text{Li}_{1.09}\text{Fe}_{0.33}\text{Ni}_{0.07}\text{Co}_{0.55}\text{V}_{0.04}(\text{PO}_4)_{0.93}$
LFNCVP/C	$\text{Li}_{1.00}\text{Fe}_{0.34}\text{Ni}_{0.07}\text{Co}_{0.57}\text{V}_{0.04}(\text{PO}_4)_{0.98}$
LFNCVP/H	$\text{Li}_{1.06}\text{Fe}_{0.33}\text{Ni}_{0.07}\text{Co}_{0.55}\text{V}_{0.04}(\text{PO}_4)_{0.95}$
LFNCNP	$\text{Li}_{0.99}\text{Fe}_{0.34}\text{Ni}_{0.07}\text{Co}_{0.57}\text{Nb}_{0.04}(\text{PO}_4)_{0.94}$
LFNCTP	$\text{Li}_{0.98}\text{Fe}_{0.35}\text{Ni}_{0.07}\text{Co}_{0.58}\text{Ta}_{0.04}(\text{PO}_4)_{0.97}$

^aCalculated from ICP-AES analyses.

7.2 Results and Discussion

7.2.1 Thermal Stability

The thermal stability of cathode materials is studied by HR-TGA measurements, from 30 to 900 °C under a nitrogen atmosphere. Results are reported in Figure 7.1.

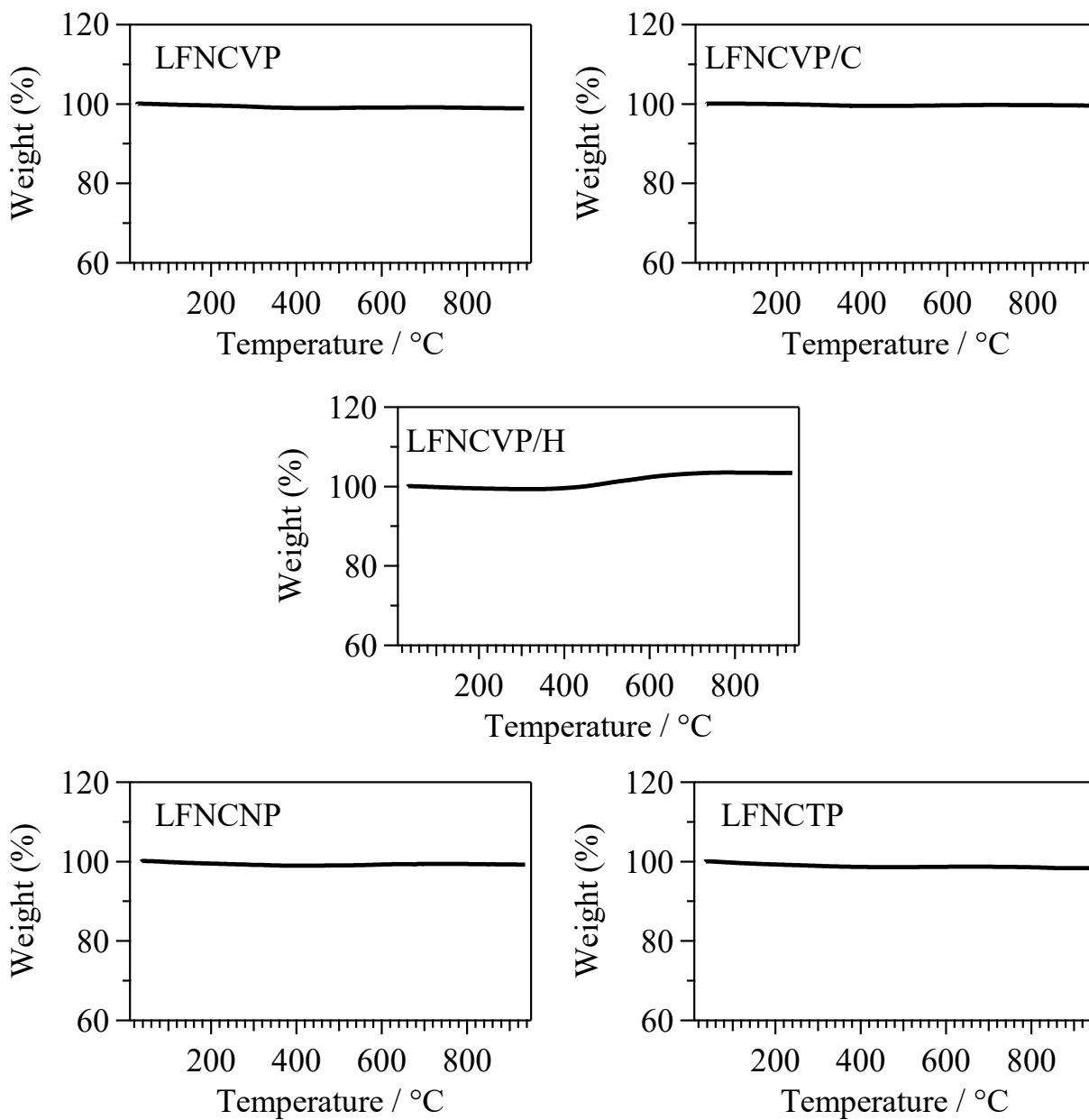


Figure 7.1. Thermogravimetric analyses of the proposed cathode materials under a nitrogen atmosphere.

It can be observed that no significant variations in the sample weight within the analyzed temperature range are present. Indeed, this high thermal stability is typical of the olivine-like cathodes, and devices assembled using these materials are safer in case of fire.

7.2.2 Morphology

7.2.2.1 Scanning Electron Microscopy

In order to study the morphology of the synthesized materials and their local elemental composition, the SEM images (Figure 7.2) and EDX maps (Figure 7.3) are collected. A Jeol JSM 5600 LV instrument is used, equipped with an Oxford Instruments 6587 EDX micro-analyzer, acceleration voltage of 20 kV. All the samples are gilded by ion-sputtering to avoid excessive accumulation of surface charges.

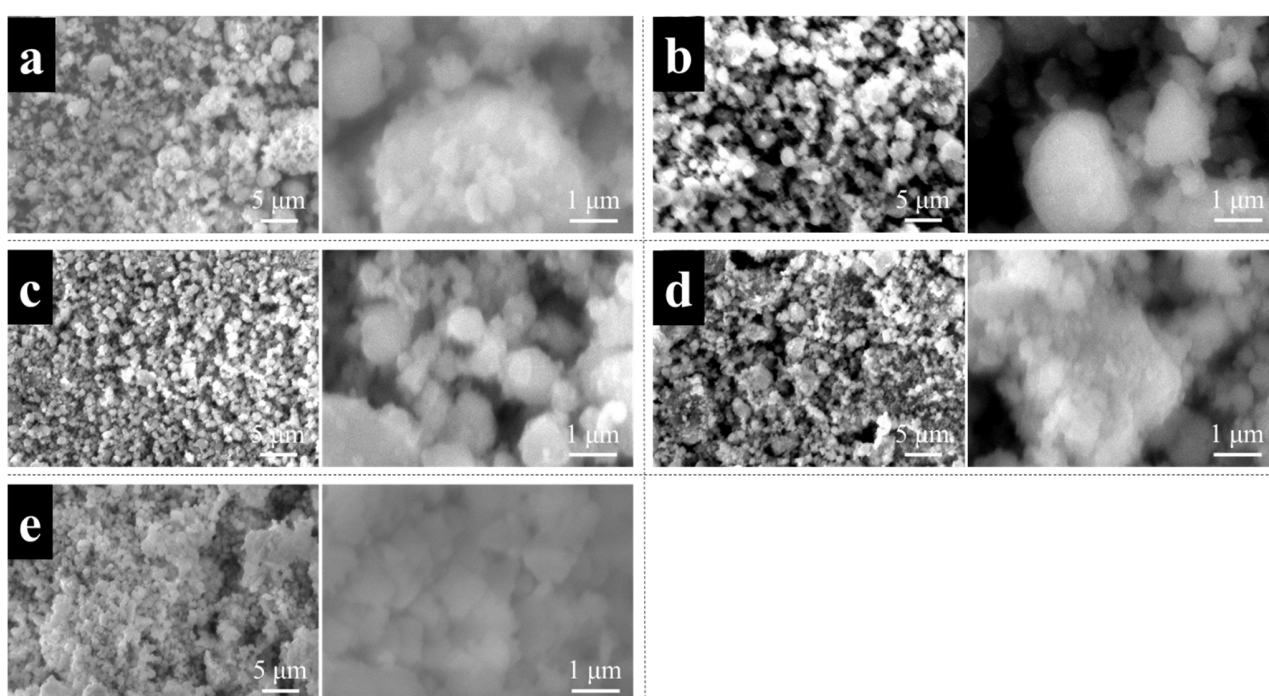


Figure 7.2. SEM images of LFNCVP (a); LFNCVP/C (b); LFNCVP/H (c); LFNCNP (d); and LFNCTP (e) at different magnifications.

From SEM images it is possible to observe how the three synthetic routes lead to a different dimensional distribution of the products. In details, all the materials show a bi-modal distribution, with particles of few hundred nanometers diameter supported on the surface of bigger particles, with a size of few micrometers. Similar results are reported in literature for analogous cathode materials [22, 214]. The synthesis in reducing environment (LFNCVP/H) gives rise to a cathode composed by particles with a diameter of no more than one micrometer, and a more homogeneous size distribution. This reveals how the choice of the synthetic route not only influences the composition of the cathode, but also its morphology. The samples LFNCNP and LFNCTP show a

similar morphology to that of LFNCVP material, demonstrating that the variation of the dopant ion (*i.e.* V, Nb, or Ta) does not influence the dimensionality of the cathode particles.

In Figure 7.3 the EDX maps of all the samples are reported.

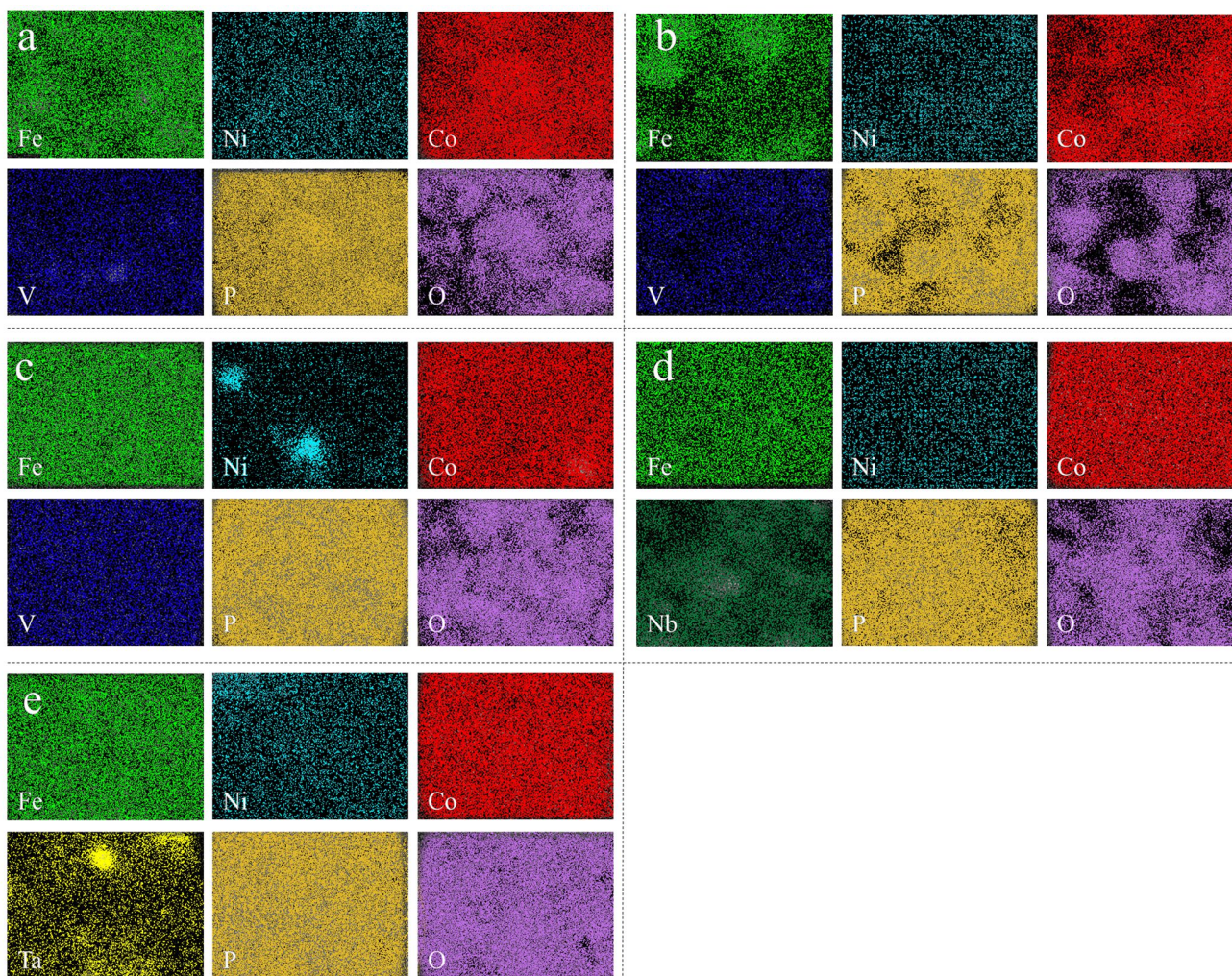


Figure 7.3. EDX maps of LFNCVP (a); LFNCVP/C (b); LFNCVP/H (c); LFNCNP (d); and LFNCTP (e). Different elements are highlighted with different colors.

EDX maps allow to estimate the homogeneity of the elements distribution in the various samples. It can be observed that the samples show a good uniformity, excluding nickel in LFNCVP/H sample and tantalum in LFNCTP material. Regarding nickel, this could be assigned to the formation of more Ni-rich olivine areas. On the contrary, the presence of segregated tantalum-based particles is due to the existence of unreacted tantalum oxide residues, whose presence is confirmed by XRD analysis (see Section 7.2.4). The homogeneity in the cathode composition is an indication of a

successful synthesis, with a quite high conversion of the reagents into products. The atomic percentages of the elements in the different compounds, obtained from the EDX measurements, are in good agreement with those calculated from ICP-AES analyses.

7.2.2.2 High-Resolution Transmission Electron Microscopy

HR-TEM microscopy allows for a better comprehension of the morphology of the obtained samples and for the determination of the crystallinity of the materials. Results for LFNCVP cathode are shown in Figure 7.4. The other samples show a similar behavior.

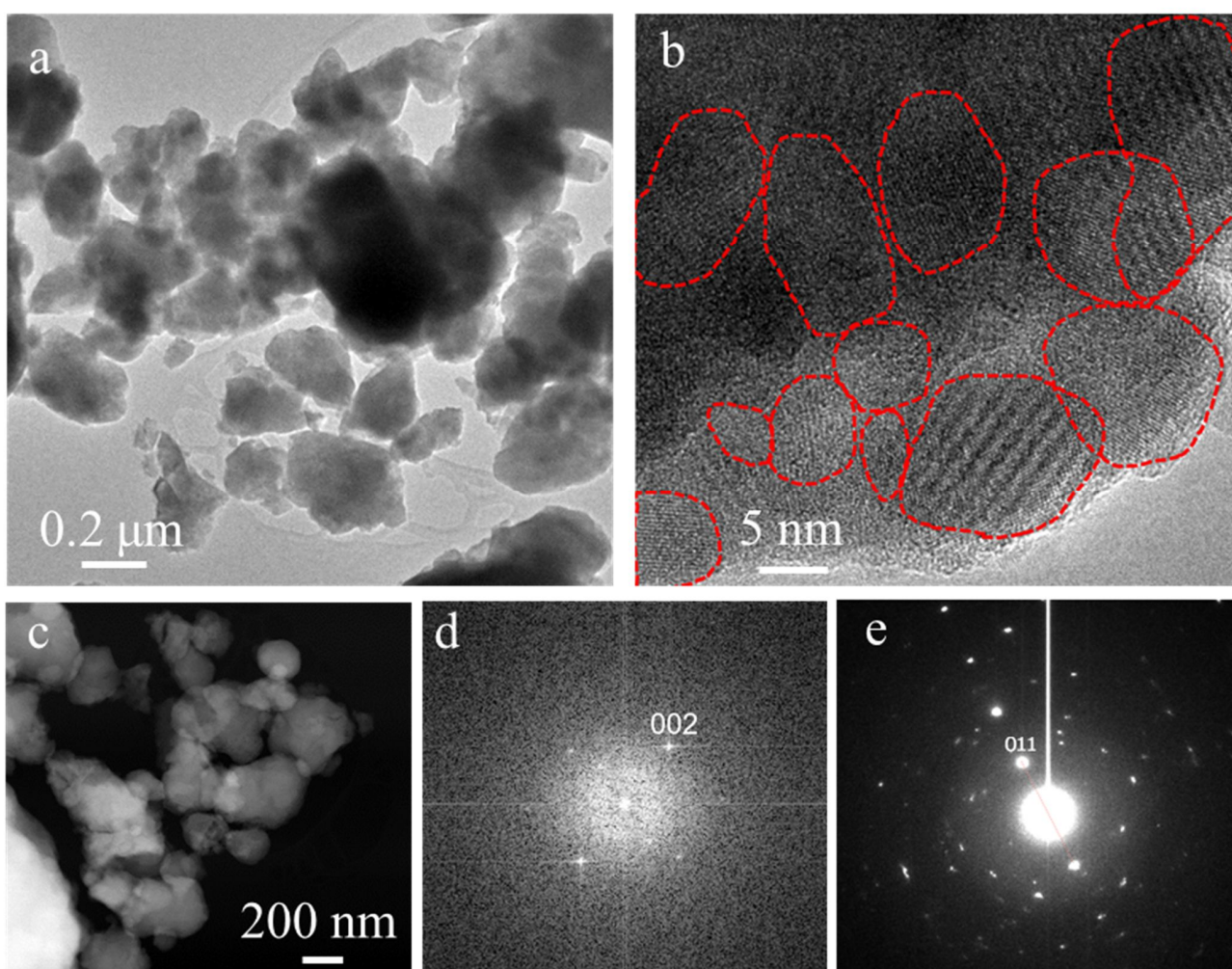


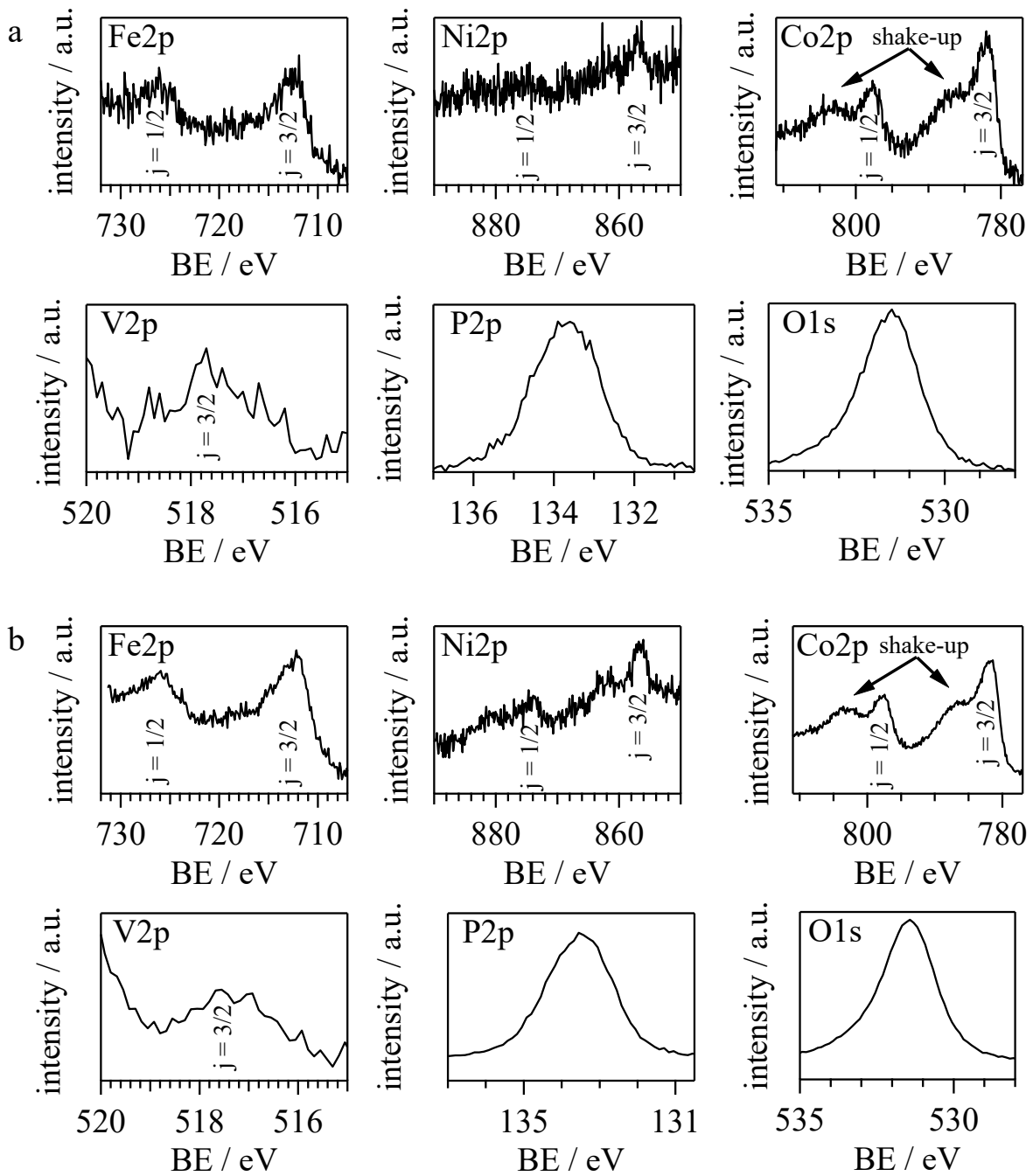
Figure 7.4. TEM (a), HR-TEM (b), STEM (c) images, FFT of HR-TEM (d), and SAD (e) of LFNCVP material.

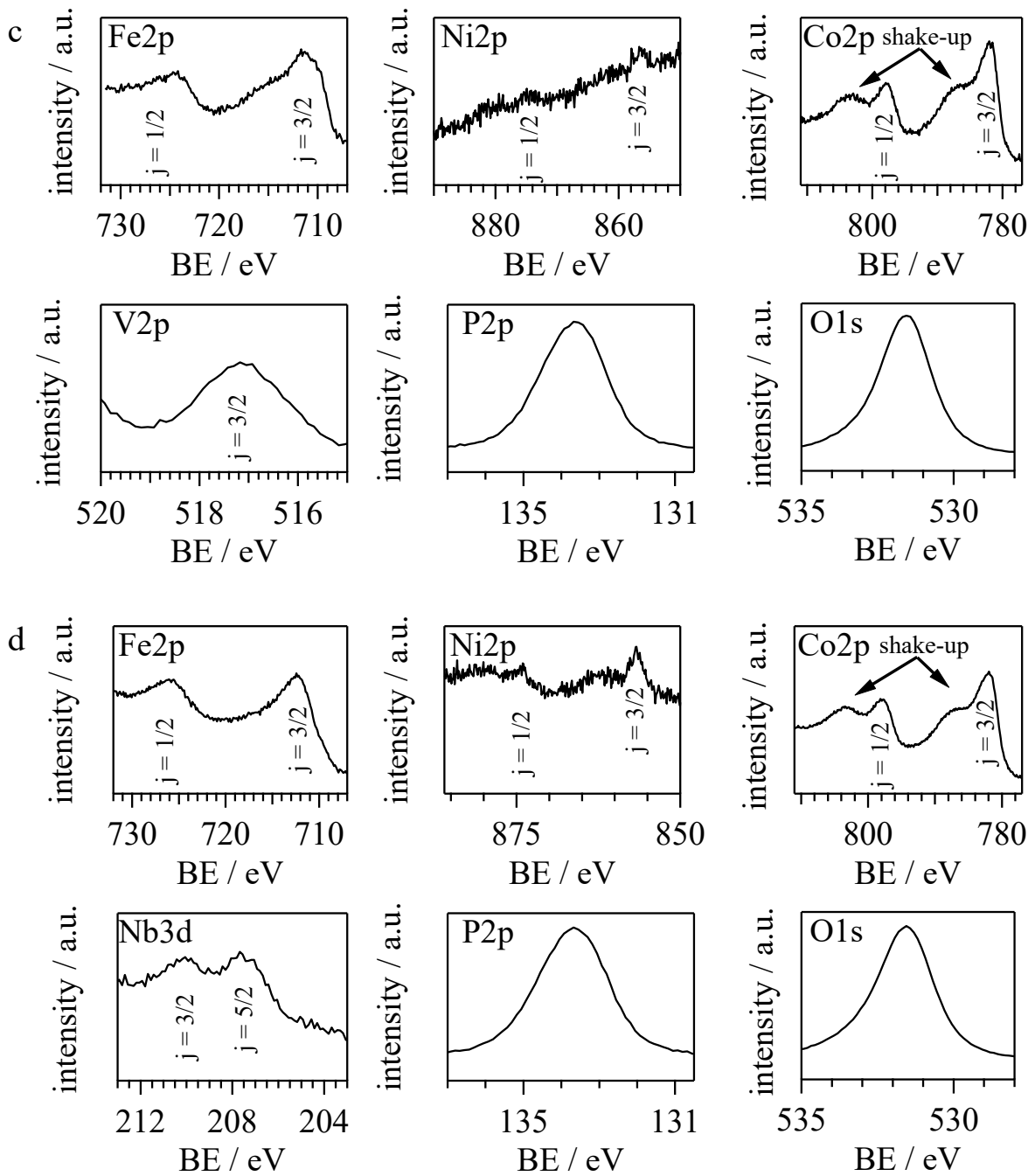
A similar size distribution detected by SEM microscopy is confirmed by TEM. The HR-TEM image reveals the presence of very well define atomic planes, indicating a high crystallinity of the cathodes. It is interesting to observe that, within each particle, several coalescent crystal domains

are present, with different orientations. Probably, the presence of high valence ions, whose more thermodynamic stable structure does not correspond to an olivine, hinders the growth of single crystals. Indeed, in olivine cathodes obtained without the addition of these dopants (*i.e.* V, Nb, and Ta), larger crystal domains are present into each particle [214]. Thanks to the fast Fourier transform (FFT) of HR-TEM images, which is able to reveal the fringe periodicity by applying the Fourier transform function on the frequency distribution of the pixels intensities in the HR-TEM images, the exact reflections and Miller indices can be attributed to the observed planes. In particular, the crystalline planes observed in Figure 7.4b are attributed to the 002 olivine plane, corresponding to a d-spacing of 0.24 nm. The presence of a very crystalline olivine material is confirmed by selected area diffraction (SAD) images, which reveal the presence of the 011 reflection. Several interplanar distances are revealed by FFT and SAD images for the other samples, all belonging to an olivine structure. Only FFT image of LFNCVP/C sample determines the presence of hematite, together with the 011 and 111 planes of the olivine.

7.2.3 X-ray Photoelectron Spectroscopy

The XPS spectra of all the five materials are collected with the purpose of evaluating each element oxidation states and the surface atomic composition. The measurements are carried out with a Perkin Elmer spectrometer Φ 5600ci at a pressure lower than 10^{-8} bar, using the non-monochromatized radiation Mg-K α ($h\nu = 1253.6$ eV) as the excitation source. The samples are loaded on a support consisting of a double-sided carbon-based adhesive. In a first step, a complete scan of the Binding Energy (BE) is performed in order to evaluate the position of the peaks of the different elements (survey). Subsequently, the measurement is performed at each BE window for every element recognized during the survey, with a resolution of 0.125 eV \cdot step $^{-1}$, 50 s of accumulation *per* step, and Pass Energy of 50.70 eV. Spectra are corrected by assigning to the 1s carbon line a BE of 284.8 eV. In Figure 7.5 the XPS spectra of each element for the different samples are reported.





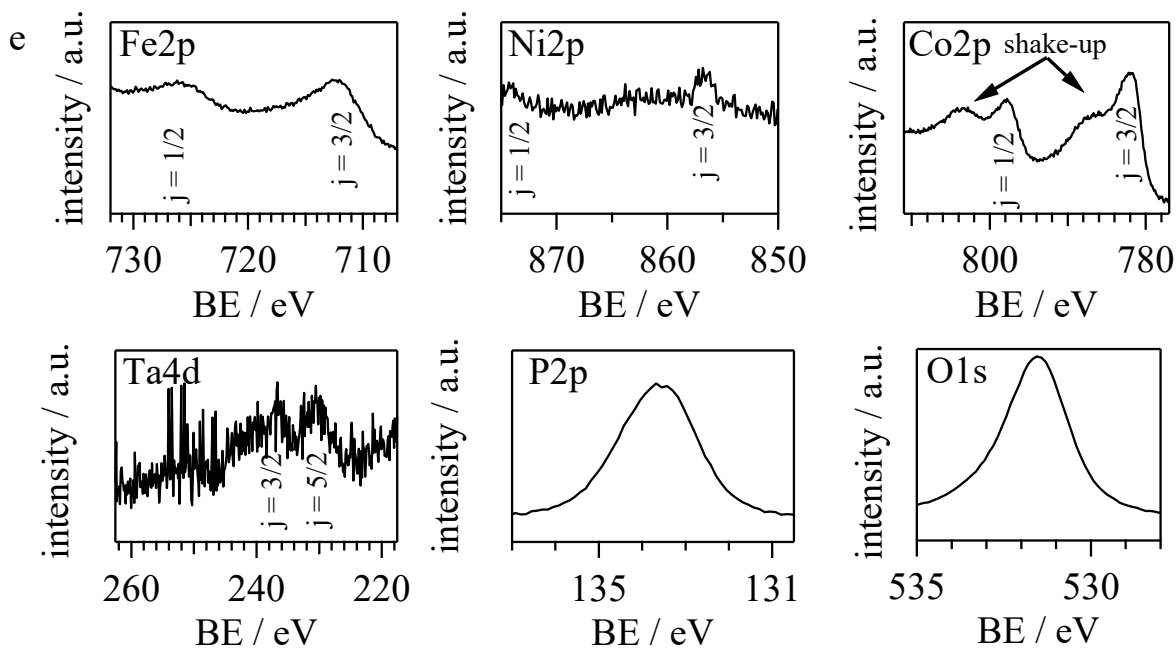


Figure 7.5. XPS spectra of LFNCVP (a); LFNCVP/C (b); LFNCVP/H (c); LFNCNP (d); and LFNCVP (e).

The XPS peaks are in agreement with the BE values reported in literature for each element [215]. For all the samples the peaks attributed to iron are observed at 512 and 525 eV, with no satellite peaks, as typically observed for Fe^{2+} ions belonging to an olivine structure [216, 217]. Small traces of Fe^{3+} , remaining from the synthesis (*i.e.* Fe_2O_3), cannot be excluded due to the similarities between the peaks [218, 219]. Even if the peaks attributed to nickel have a low intensity, they can still be detected at the correct BE values [214]. All the cathode materials show the presence of two peaks centered at 782 and 798 eV, with the relative shake-up peaks, belonging to Co^{2+} in olivine materials [214, 220, 221]. One interesting feature arising from XPS analyses is the broadening of the peak attributed to $\text{V}2p_{3/2}$ at 517 eV. Indeed, V^{5+} in V_2O_5 appears at 518 eV, while V^{4+} in VO_2 is typically found at 517 eV. The broadening of the peak found in the experimental results indicate the possible coexistence of the two vanadium oxidation states [222, 223]. Furthermore, increasing the reducing environment of the synthesis (LFNCVP \rightarrow LFNCVP/C \rightarrow LFNCVP/H), the peak attributed to vanadium shifts to lower BE, indicating the major presence of V^{4+} . In any case, all the synthetic routes give rise to the insertion of $\text{V}(\text{IV})$ in the olivine structure, as reported in literature [216]. Niobium ions in LFNCNP sample exhibit the typical BE values of Nb^{5+} belonging to an olivine structure [224]. The $\text{Ta}4f_{7/2}$ and $\text{Ta}4f_{5/2}$ peaks of tantalum(V), centered at 26 and 29 eV, respectively, are hidden by the more intense $\text{O}2s$ oxygen peak. Thus, only a shoulder attributed to

Ta4f_{7/2} can be detected, and the Ta atomic ratio has to be calculated considering the low intensity Ta4d peak at *ca.* 230 eV [215, 225]. Finally, traces of carbon are highlighted by the appearance of C1s peak, attributed to non-completely reacted carbonates on the surface of LFNCVP/C, LFNCVP/H, LFNCNP, and LFNCTP samples.

Table 7.2 reports the surface atomic composition calculated from XPS analyses.

Table 7.2. Sample surface composition evaluated from XPS analyses.

	LFNCVP ^a	LFNCVP/C ^a	LFNCVP/H ^a	LFNCNP ^a	LFNCTP ^a
Fe	0.18	0.11	0.16	0.19	0.17
Ni	0.07	0.08	0.02	0.07	0.05
Co	0.56	0.51	0.41	0.62	0.57
V	0.02	0.02	0.07	0.00	0.00
Nb	0.00	0.00	0.00	0.04	0.00
Ta	0.00	0.00	0.00	0.00	0.01
P	1.00	1.00	1.00	1.00	1.00
O	4.07	4.44	4.22	5.02	4.83

^aNormalized on phosphorous concentration.

It can be observed that the surface composition of the samples is different with respect to the stoichiometric composition of the bulk (Table 7.1). In details, the oxygen/phosphorus ratio on the surface is slightly higher than four in all samples. This can be explained by considering the presence of some oxide residues on the surface of the particles, due to the non-complete consumption of the reactants (see Section 7.2.4). Furthermore, iron content does not correspond to the theoretical one, indicating that, on the surface, the olivine phase is poorer in Fe.

7.2.4 Powder X-ray Diffraction

The X-ray diffraction spectra (XRD) of the five samples are collected in order to investigate in details the crystalline phases present in the synthesized materials as the composition changes. Measurements are collected in transmission with a Bragg–Brentano θ - 2θ configuration, Cu-K α 1 ($\lambda=1.5406$ Å) source radiation, $5\div 65^\circ$ 2θ range, every 0.02° . The diffractograms of the five samples are shown in Figure 7.6.

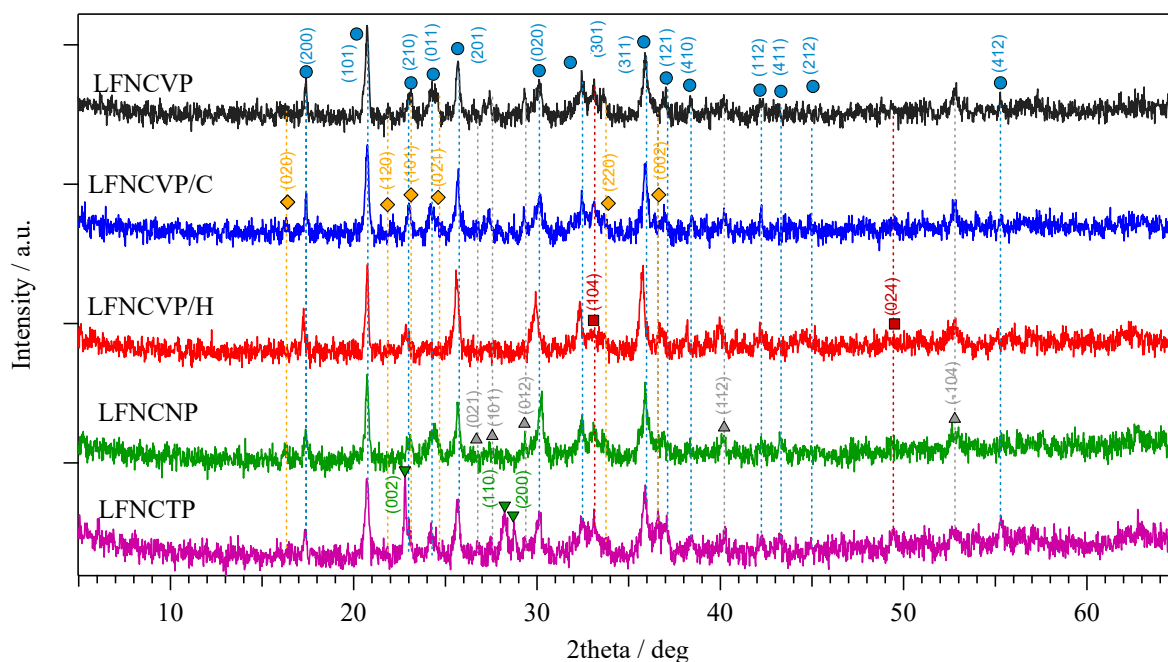


Figure 7.6. Powder X-ray diffraction spectra of all the cathode materials. Miller indices are reported above the peaks. Every different phase is indicated with a different marker (●LiMPO₄, ◆Li₃PO₄, ■Fe₂O₃, ▲LiMP₂O₇, and ▼Ta₂O₅).

The typical peaks of an olivine structure dominate all the diffractograms. Traces of byproducts and unreacted reagents are also detected. Moreover, the peaks exhibited by the different samples are similar in terms of both intensity and position, apart from: i) LFNCVP/H, that shows a slight shift in peaks position; and ii) LFNCTP, where new intense peaks arise. The analysis of the XRD measurements consists of two steps: i) spectra are studied using Match! software [226], in order to determine all the crystal phases composing the materials; and ii) curves are analyzed using Maud software [227], to solve the crystal structure calculating all the cell parameters for the synthesized materials with the Rietveld method.

Five phases are recognized:

Principal

- LiMPO₄: this is the principal phase composing the samples, with an orthorhombic olivine-like crystal system, *Pnma* space group [228]. In this structure, the phosphate tetrahedra are sharing the oxygen vertices, forming a three-dimensional structure where the metals, both lithium and transition metals, occupy the octahedral sites and are coordinated by the oxygen ions [229].

Traces

- LiMP_2O_7 : monoclinic, $P12_11$ space group [230]. In this phase, metal ions form MO_6 octahedra that share the vertices with the PO_4 tetrahedra. Lithium occupies the tetrahedral sites in the crystal [231].
- Fe_2O_3 : trigonal, $R-3c$ space group. Iron ions are hosted inside distorted octahedral sites [232].
- Li_3PO_4 : orthorhombic crystal system, $Pcmn$ space group [233].
- Ta_2O_5 : orthorhombic crystal system, $Pccm$ space group [234].

A detectable presence of NiO , V_2O_5 , and Nb_2O_5 phases is excluded due the absence of the corresponding typical peaks. For Rietveld refinement, the metal occupancy in the olivine phase is modified according to ICP calculations. For the sake of brevity, only the refinement result for LFNCVP sample is reported in Figure 7.7.

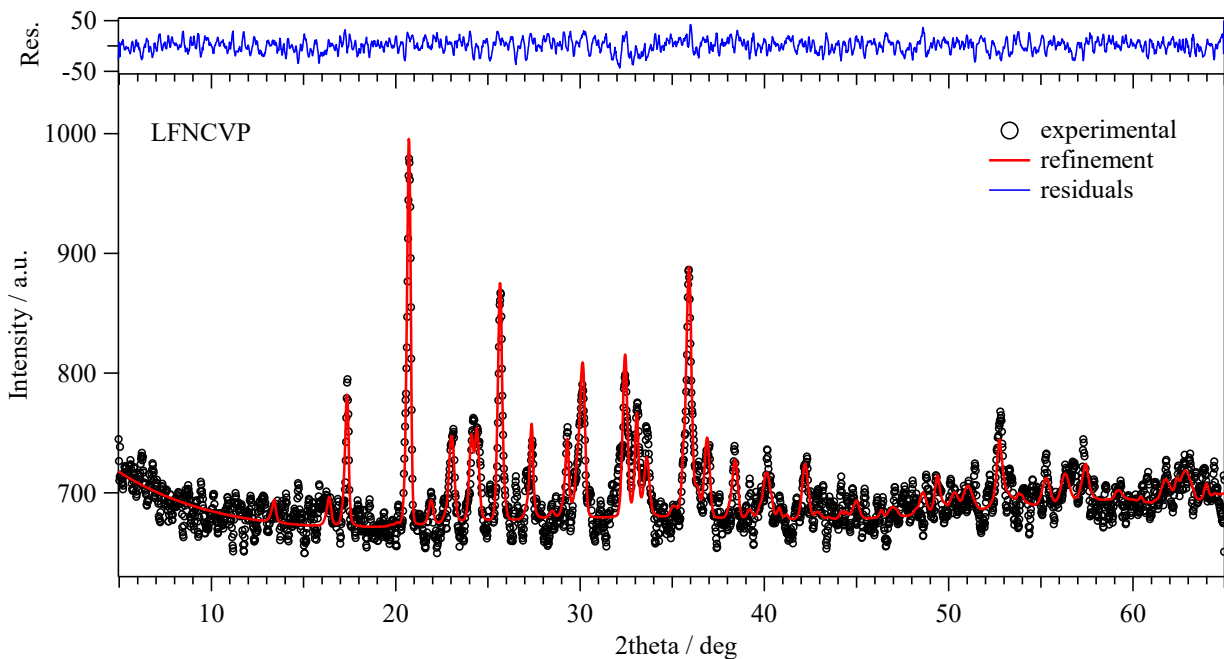


Figure 7.7. Rietveld refinement for LFNCVP sample.

Rietveld refinements confirm that the main phase present into the samples is the olivine LMPO_4 , indicating that all three synthetic routes led to the main formation of the desired material. It is also observed that, increasing the reducing environment during the synthesis ($\text{LFNCVP} \rightarrow \text{LFNCVP/C} \rightarrow \text{LFNCVP/H}$), the content of byproducts and unreacted reagents is decreased. In Table 7.3 the

assignment of experimental peaks to the correct *hkl* indices of the various phases for LFNCVP sample is reported.

Table 7.3. Assignment of principal peaks detected in LFNCVP sample.

2theta / °	<i>hkl</i>	$d_{hkl} / \text{Å}^a$	phase	ref.
13.44	001	6.5836	LiMP ₂ O ₇	[230]
16.37	020	5.4106	Li ₃ PO ₄	[233]
17.40	200	5.0936	LFNCVP	[228]
17.52	011	5.0593	LiMP ₂ O ₇	[230]
20.76	101	4.2747	LFNCVP	[228]
21.91	120	4.0535	Li ₃ PO ₄	[233]
23.02	210	3.8597	LFNCVP	[228]
23.04	-111	3.8575	LiMP ₂ O ₇	[230]
23.18	101	3.8347	Li ₃ PO ₄	[233]
24.14	011	3.6843	LFNCVP	[228]
24.43	021	3.6403	Li ₃ PO ₄	[233]
25.69	111	3.4647	LFNCVP	[228]
25.74	201	3.4579	LFNCVP	[228]
26.27	021	3.3892	LiMP ₂ O ₇	[230]
27.38	101	3.2543	LiMP ₂ O ₇	[230]
29.37	012	3.0389	LiMP ₂ O ₇	[230]
29.91	211	2.9852	LFNCVP	[228]
30.11	120	2.9653	LiMP ₂ O ₇	[230]
30.19	020	2.9576	LFNCVP	[228]
32.48	301	2.7544	LFNCVP	[228]
33.07	104	2.7067	Fe ₂ O ₃	[232]
33.62	220	2.6634	Li ₃ PO ₄	[233]
35.57	110	2.5218	Fe ₂ O ₃	[232]
35.94	311	2.4969	LFNCVP	[228]
36.49	002	2.4602	Li ₃ PO ₄	[233]
36.93	121	2.4322	LFNCVP	[228]
38.45	410	2.3392	LFNCVP	[228]
40.43	112	2.2291	LiMP ₂ O ₇	[230]
42.22	112	2.1389	LFNCVP	[228]
49.35	024	1.8451	Fe ₂ O ₃	[232]
52.74	-104	1.7343	LiMP ₂ O ₇	[230]
52.80	222	1.7323	LFNCVP	[228]
52.91	402	1.7289	LFNCVP	[228]

^aResulting from Rietveld refinement.

Iron, nickel, and cobalt ions are confirmed to be vicariant within the olivine structure [214]. Moreover, this work allows to determine the vicariant behavior of vanadium, niobium, and tantalum, at low concentrations (*i.e.* ≤ 0.05 molar). The insertion of different ions in the crystal structure results in the increase or decrease of the lattice parameters, with a concurrent volume variation of the cell. In Table 7.4 the resulting parameters for all the samples are summarized.

Table 7.4. Cell parameters calculated from Rietveld refinement for all the samples and the reference olivine material.

sample	a / Å	b / Å	c / Å	V / Å ³	R _{wp} ^a / %
LFNCVP	10.187	5.915	4.709	283.776	1.78
LFNCVP/C	10.191	5.924	4.719	284.934	1.76
LFNCVP/H	10.266	5.965	4.706	288.194	1.83
LFNCNP	10.199	5.912	4.711	284.066	1.81
LFNCTP	10.187	5.925	4.707	284.098	2.13
LFNCP ^b	10.183	5.923	4.710	284.056	-

^aR_{wp} is a discrepancy index between the experimental and fitting data which defined the Rietveld error; this value is calculated as $R^2_{wp} = \frac{\sum_i w_i (\gamma_{C,i} - \gamma_{O,i})^2}{\sum_i w_i (\gamma_{O,i})^2}$, with w_i the weights, γ_i the intensity, C is referred to the computed values and O stands for observed values [235]. ^bLFNCP has a molecular formula of $\text{LiFe}_{0.33}\text{Ni}_{0.07}\text{Co}_{0.61}\text{PO}_4$, and is used as reference for comparisons.

By comparing the cell parameters, and in particular the volumes, it can be observed how an increasing reducing environment during the synthesis leads to a progressive growth in the cell volume. One possible explanation is that the reduced quantity of byproducts enriches the iron content in the olivine structure. It is well known that iron leads to an enlargement of the cell volume, being the largest among metal ions present in the compound [214]. On the contrary, the substitution of the dopant ion, *i.e.* V, Nb, and Ta, results in not appreciable variations of the channel volumes. Thus, lithium-ion diffusion within the bulk 3D-material is expected to be only slightly modulated during the charge/discharge processes by the small differences in the “free” volume of the channels in the olivine materials.

In conclusion, XRD analyses allow to determine that the predominant phase in the obtained cathode materials is an olivine-type structure. All the transition metals are found to be vicariant within the crystal at these concentrations. The increased reducing environment leads to: i) a diminished formation of byproducts; ii) a greater consumption of the reagents; and iii) a slight increase in the cell volume. Finally, it is determined that just small variations in channel volumes are obtained by substituting vanadium with niobium or tantalum.

7.2.5 Vibrational Spectroscopy

Fourier transform infrared spectroscopy is a useful tool to evaluate the crystallinity of the materials and to highlight the coordination strength of M-O and Li-O groups. Results in the 1300÷200 cm^{-1} range are reported in Figure 7.8. Curves are baseline subtracted and normalized with respect to the peak at 957 cm^{-1} . Table 7.5 summarizes the vibrational assignments of all the peaks observed in FT-IR spectra for LFNCVP sample.

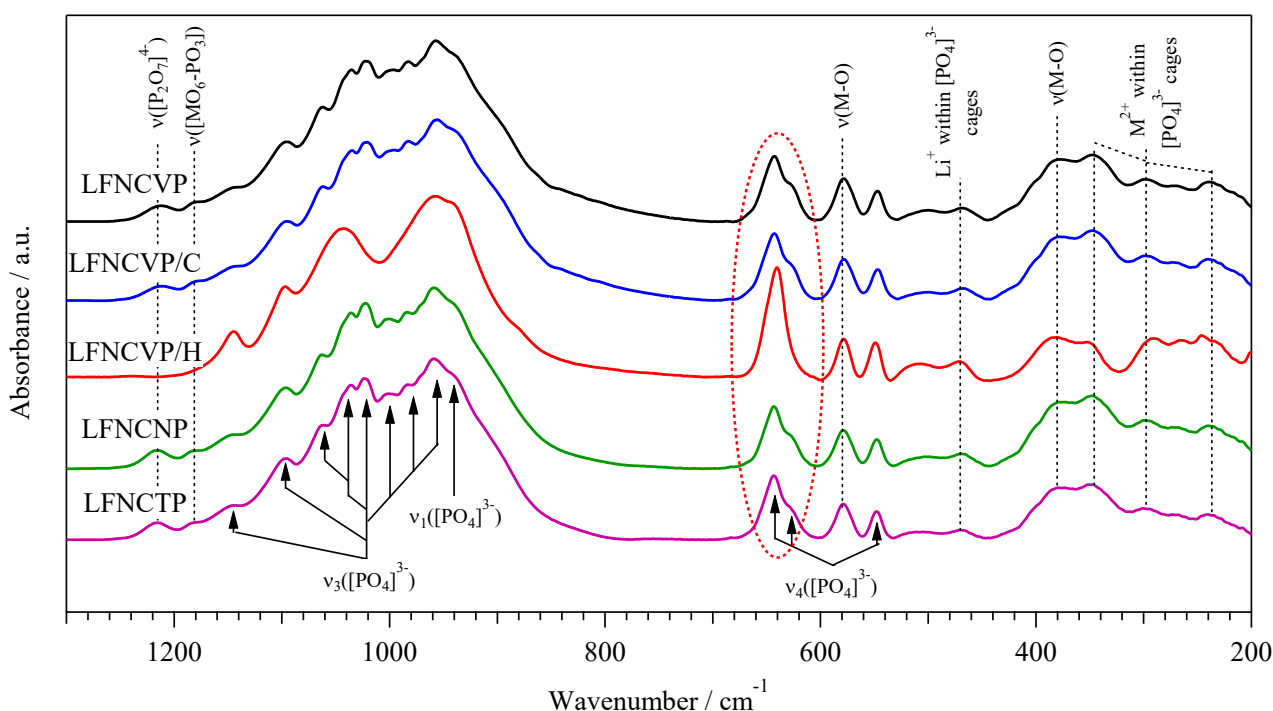


Figure 7.8. Docked FT-MIR and FT-FIR measurements in the 200÷1300 cm^{-1} range of all the samples.

Above 1300 cm^{-1} spectra do not show the presence of any peaks, demonstrating the almost complete consumption of the reagents, with particular reference to the ammonium and carbonate functional groups. In the 500÷1300 cm^{-1} range all the principal peaks are attributed to the vibrations of $[\text{PO}_4]^{3-}$ tetrahedral groups. The peak centered at *ca.* 1212 cm^{-1} is attributed to the presence of the diphosphate ion [100, 236], which is absent in the LFNCVP/H sample, as already demonstrated by XRD analyses. Below 500 cm^{-1} , the peaks associated to the metal-oxygen and lithium-oxygen vibrational modes are detected [237, 238].

Phosphate ions are characterized by the presence of four vibrational modes: ν_1 singlet (A_1) at 938 cm^{-1} related to the symmetric stretching of P-O bond, triple degenerate ν_3 (F_2) at 1027 cm^{-1}

associate with the asymmetric stretching of P-O bond, ν_2 doublet (E) at 465 cm^{-1} related to the symmetric bending of O-P-O bond, and triple degenerate ν_4 (F_2) at 567 cm^{-1} associate with the asymmetric bending of O-P-O bond [98].

Table 7.5. FT-IR correlational assignments of LFNCVP sample.

wavenumber ^a / cm^{-1}	assignment ^b	ref.
1212 (w)	$\nu([\text{P}_2\text{O}_7]^{4-})$	[100, 236]
1181 (w)	$\nu(\text{MO}_6\text{-PO}_3)$	[236]
1144 (w)	$\nu_3([\text{PO}_4]^{3-})$	[237]
1095 (s)	$\nu_3([\text{PO}_4]^{3-})$	[237]
1062 (s)	$\nu_3([\text{PO}_4]^{3-})$	[237, 238]
1035 (s)	$\nu_3([\text{PO}_4]^{3-})$	[236]
1022 (s)	$\nu_3([\text{PO}_4]^{3-})$	[236, 238]
997 (s,sh)	$\nu_3([\text{PO}_4]^{3-})$	[238]
982 (s)	$\nu_3([\text{PO}_4]^{3-})$	[238]
957 (s)	$\nu_3([\text{PO}_4]^{3-})$	[237]
940 (s,sh)	$\nu_1([\text{PO}_4]^{3-})$	[98, 236, 237]
643 (m)	$\nu_4([\text{PO}_4]^{3-})$	[237]
630 (m,sh)	$\nu_4([\text{PO}_4]^{3-})$	[236]
579 (m)	$\nu(\text{M-O})$	[98, 100]
547 (m)	$\nu_4([\text{PO}_4]^{3-})$	[236, 237]
469 (vw)	Li^+ within $[\text{PO}_4]^{3-}$ cages	[98, 237]
427 (vw,sh)	$\nu_2([\text{PO}_4]^{3-})$	[236]
378 (m)	$\nu(\text{M-O})$	[98]
347 (m)	M^{2+} within $[\text{PO}_4]^{3-}$ cages	[237]
299 (w)	M^{2+} within $[\text{PO}_4]^{3-}$ cages	[237, 238]
272 (vw)	rotation of $[\text{PO}_4]^{3-}$ -group+ M^{2+} transition	[238]
242 (w)	M^{2+} within $[\text{PO}_4]^{3-}$ cages	[237, 238]

^aRelative intensities are reported in brackets; s: strong, m: medium, w: weak, vw: very weak, sh: shoulder. ^b ν_1 is the symmetric stretching of the phosphate group. ν_2 is the symmetric bending of the phosphate group. ν_3 is the anti-symmetric stretching of the phosphate group. ν_4 is the anti-symmetric bending of the phosphate group.

In solid state the presence of more than one molecular group in the crystal cell, *i.e.* the presence of the metal octahedra in the lattice, gives rise to the so-called “*correlation effect*”, which leads to the separation of the IR bands in the spectrum. Moreover, the strong intensity and the well-defined separation of the bands are a signal of the high crystallinity of the materials [98]. The intensity of the peak separation is correlated to the ionization energy of the element present in the octahedral

site: the higher is the energy, the greater will be the splitting [100]. Furthermore, it is reported in literature that the separation of the band peaking at *ca.* 640 cm^{-1} is attributed to the insertion into the structure of a metal with a higher ionization energy [214]. Therefore, it is expected that the substitution of Co^{2+} (with a second ionization energy of 17.083 eV [239]) with V^{4+} (fourth ionization energy of 46.709 eV [239]), Nb^{5+} (fifth ionization energy of 50.55 eV [239]), or the Ta^{5+} (fifth ionization energy of 45 eV [240]), gives rise to a greater separation in the band, even if the percentage of doping is quite small. This phenomenon is confirmed in Figure 7.9, where it is possible to observe that, compared to the reference sample (LFNCVP, no high valence metal doping) synthesized following the same methodology of LFNCVP, LFNCNP, and LFNCTP, the shoulder arising from the separation of the peaks is more pronounced.

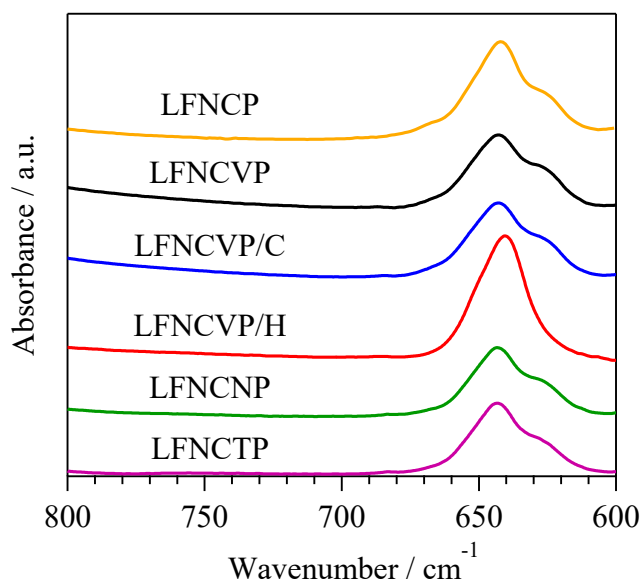


Figure 7.9. Comparison of ν_4 peak separation in the different samples with respect to the reference material (LFNCVP).

Moreover, it is detected that, for all the samples, the spectra are essentially similar in intensity and in number of peaks related to the phosphate ion vibrations, with the exception of the LFNCVP/H sample. Indeed, LFNCVP/H sample shows a lower separation of the phosphate peaks in the whole spectral range. The broadening of these peaks is a proof of a decrease in the lifetime of the phonons and therefore of the existence of structural defects that break the periodicity of the lattice inside the olivine crystallite. Thus, as a consequence of the presence of structural defects, lower electrochemical performances are expected for this sample [241].

Finally, a redshift is observed towards lower wavenumbers of the peak position of the M-O and Li-O vibrational modes, with respect to the reference cathode (LFNCP) [214]. Results are summarized in Table 7.6.

Table 7.6. Peak positions of M-O and Li-O vibrations.

sample	ν (M-O) / cm^{-1}	Li ⁺ within [PO ₄] ³⁻ cages / cm^{-1}	ν (M-O) / cm^{-1}	M ²⁺ within [PO ₄] ³⁻ cages / cm^{-1}	M ²⁺ within [PO ₄] ³⁻ cages / cm^{-1}	M ²⁺ within [PO ₄] ³⁻ cages / cm^{-1}
LFNCP ^a	580	474	384	355	303	249
LFNCVP	579	469	378	347	299	242
LFNCVP/C	579	468	378	347	300	240
LFNCVP/H	579	472	381	352	301	247
LFNCNP	579	469	378	348	300	240
LFNCTP	579	471	379	348	300	241

^aLFNCP is the reference cathode obtained under an oxidizing atmosphere without the addition of the high valence metals.

The redshift is the result of the insertion of a high valence ion (*i.e.* V(IV), Nb(V), and Ta(V)) that destabilizes the metal- and lithium-oxygen coordination, decreasing the strength of this bond. Thus, the weaker Li-O coordination is expected to enhance and facilitate the kinetics of Li⁺ insertion/de-insertion during discharge and charge of the battery device. Since LFNCVP/H exhibits stronger Li-O bonds (lower shift in the wavenumber), the electrochemical performances will not be strongly improved.

7.2.6 Electrochemical Analyses

7.2.6.1 Cyclic Voltammetry

The electrochemical performances of the obtained materials is studied by the cyclic voltammetry technique, in the 3.5÷5.0 V vs. Li/Li⁺ potential range, using a three-electrodes cell. Two lithium ribbons are used as counter and reference electrodes, while a Pt wire covered with the active material (mixed with a PVDF binder and conductive carbon) is used as working electrode. The electrolyte consists of a 1.0 molar solution of LiPF₆ in EC/DMC 1:1 by volume. Results are shown in Figure 7.10.

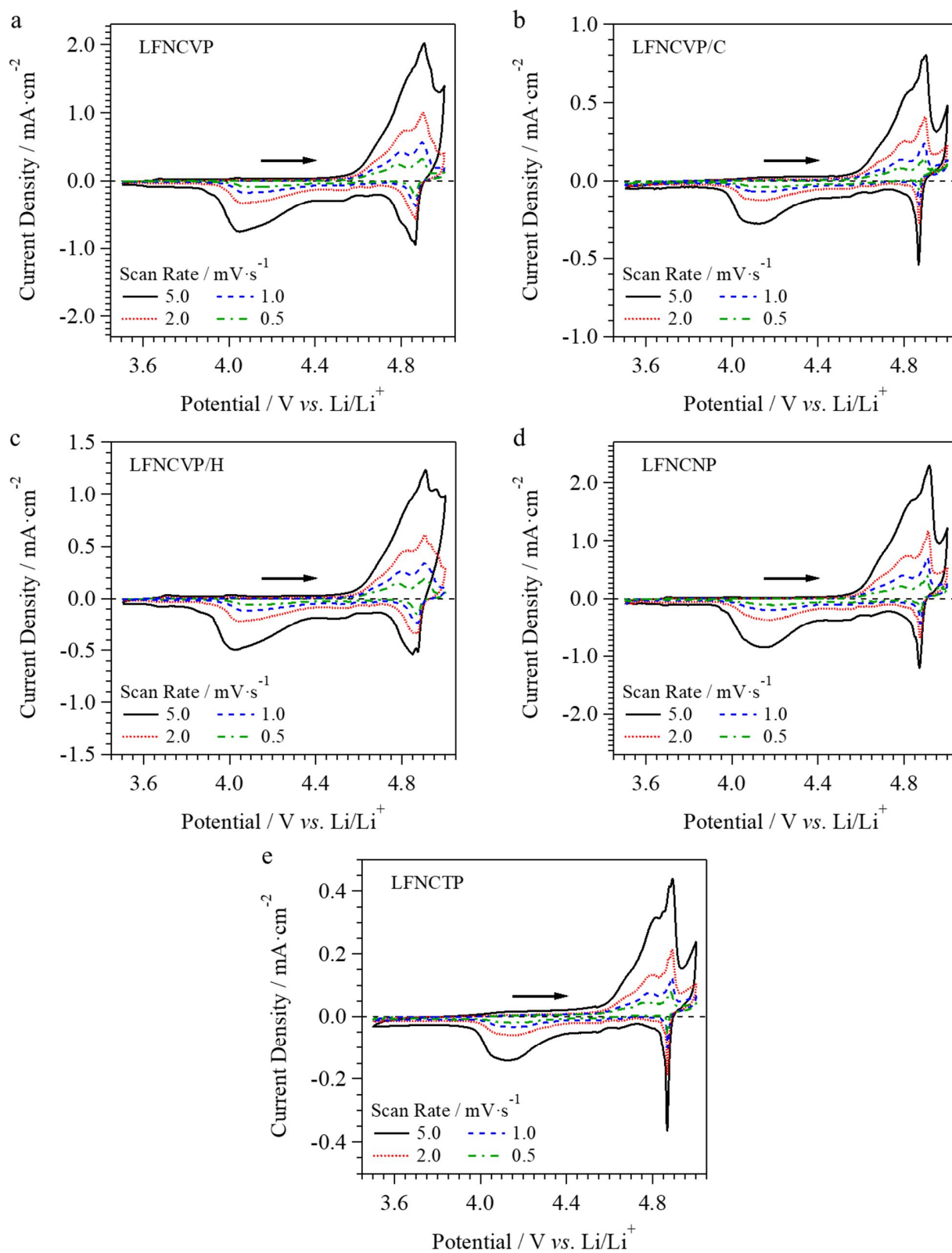
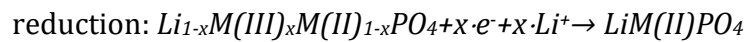
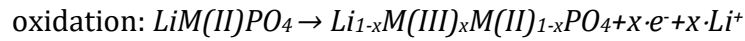


Figure 7.10. Cyclic voltammometry experiments at different scan rates of the proposed materials. Lithium ribbons are used as counter and reference electrodes, the working electrode consists of platinum. The electrolyte is 1.0 M LiPF₆ in EC/DMC 1:1.

During the oxidation process, occurring between 4.6 and 4.9 V vs. Li/Li⁺, the extraction of lithium ions from the olivine structure takes place. In the back scan, Li⁺ are re-inserted inside the crystalline structure. A scheme of the reactions occurring during the oxidation and reduction events are here reported:



For all the samples, it is observed that the transition metal oxidation event takes place in a narrow potential window (*ca.* 4.60÷4.95), with a shoulder at a lower potential. This effect is clearer at low scan rates. On the contrary, the reduction occurs in a broad potential range, with two main peaks at *ca.* 4.2 and 4.9 V vs. Li/Li⁺. This non-symmetrical behavior of the redox events is attributed to the presence of a solid state electronic orbital originated from concurring contributions by all four transition metals (*i.e.* Fe, Ni, Co, and V/Nb/Ta) [214]. Thus, the redox events are not localized to a specific ion center, but they could be assigned to an overall channel electrochemical behavior, modulated by the distribution of all the vicariant transition metal complexes present [214]. Interestingly, the Fe(II/III) redox couple, that typically appears at +3.5 V for similar systems [242], and the redox events attributed to the crystalline phase Li₃V₂(PO₄)₃, which are usually detected at 3.6, 3.7, 4.1, and 4.6 V [243], are not observed in the proposed materials. Thus, it is a further confirmation that the doping transition metals are vicariant within the olivine structure, and they do not form segregated single-metal LiMPO₄ phases.

The different current densities obtained for the samples is attributed to a different reactivity of the materials. Nevertheless, differences in the thickness of the cathodic layer painted onto the platinum working electrode could contribute to affect the real quantity of electroactive species. The current peaks vs. the square root of the scan rate curves are reported in Figure 7.11.

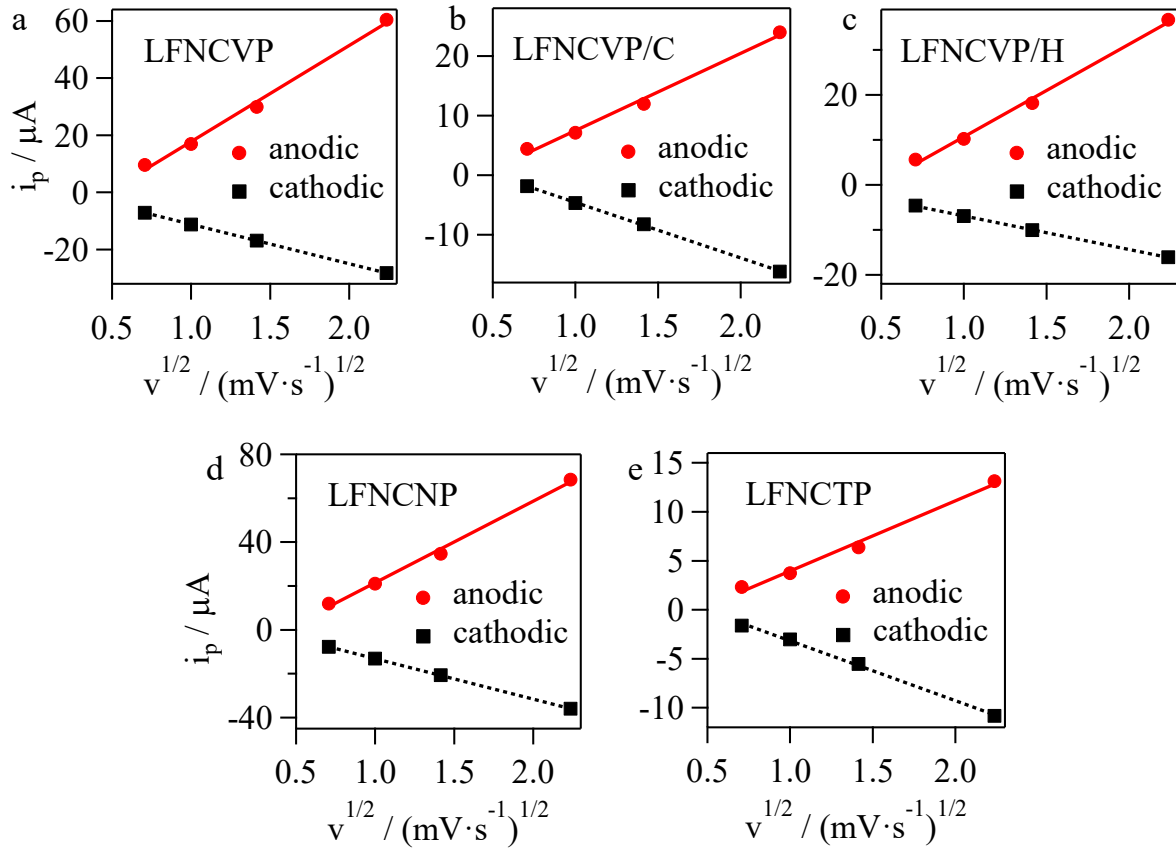


Figure 7.11. Current peak vs. square root of the scan rate for all the samples. Data are obtained from CV experiments.

All the samples display a linear behavior of the curves, indicating a very high reversibility of the insertion/de-insertion reactions of lithium ions within the olivine channels [244]. The linear dependence is defined by the following Equation, which allows to calculate the lithium ion diffusion coefficient at each scan rate [244]:

$$i_p = 0.4463 \left(\frac{F^3}{RT} \right)^{\frac{1}{2}} \cdot n^{3/2} \cdot A \cdot D_0^{\frac{1}{2}} \cdot C_0^* \cdot v^{\frac{1}{2}} \quad (7.1)$$

where i_p is the current peak, F is the Faraday constant, R the gas constant, and T the temperature. n is the number of electron exchanged during each redox process (*i.e.* 1), A the electrode active surface in cm^2 , D_0 the lithium ions diffusion coefficient in $\text{cm}^2 \cdot \text{s}^{-1}$, C_0^* the lithium ion concentration in $\text{mol} \cdot \text{cm}^{-3}$, and v is the scan rate. In Table 7.7 the obtained lithium ion diffusion coefficients calculated using CV experiments are reported.

Table 7.7. Lithium ion diffusion coefficients (D_{Li} in $\text{cm}^2\cdot\text{s}^{-1}$) for cathode materials at different scan rate, calculated from CV experiment.

sample	cathodic ^a				anodic ^b			
	$D_{Li,5.0\text{ mV}\cdot\text{s}^{-1}}$ / $\text{cm}^2\cdot\text{s}^{-1}$	$D_{Li,2.0\text{ mV}\cdot\text{s}^{-1}}$ / $\text{cm}^2\cdot\text{s}^{-1}$	$D_{Li,1.0\text{ mV}\cdot\text{s}^{-1}}$ / $\text{cm}^2\cdot\text{s}^{-1}$	$D_{Li,0.5\text{ mV}\cdot\text{s}^{-1}}$ / $\text{cm}^2\cdot\text{s}^{-1}$	$D_{Li,5.0\text{ mV}\cdot\text{s}^{-1}}$ / $\text{cm}^2\cdot\text{s}^{-1}$	$D_{Li,2.0\text{ mV}\cdot\text{s}^{-1}}$ / $\text{cm}^2\cdot\text{s}^{-1}$	$D_{Li,1.0\text{ mV}\cdot\text{s}^{-1}}$ / $\text{cm}^2\cdot\text{s}^{-1}$	$D_{Li,0.5\text{ mV}\cdot\text{s}^{-1}}$ / $\text{cm}^2\cdot\text{s}^{-1}$
LFNCVP	$4.13\cdot 10^{-12}$	$3.72\cdot 10^{-12}$	$3.27\cdot 10^{-12}$	$2.63\cdot 10^{-12}$	$1.89\cdot 10^{-11}$	$1.16\cdot 10^{-11}$	$7.45\cdot 10^{-12}$	$4.80\cdot 10^{-12}$
LFNCVP/C	$1.53\cdot 10^{-12}$	$9.97\cdot 10^{-13}$	$6.46\cdot 10^{-13}$	$1.98\cdot 10^{-13}$	$3.38\cdot 10^{-12}$	$2.11\cdot 10^{-12}$	$1.49\cdot 10^{-12}$	$1.16\cdot 10^{-12}$
LFNCVP/H	$1.92\cdot 10^{-12}$	$1.89\cdot 10^{-12}$	$1.79\cdot 10^{-12}$	$1.57\cdot 10^{-12}$	$1.00\cdot 10^{-11}$	$6.14\cdot 10^{-12}$	$3.89\cdot 10^{-12}$	$2.35\cdot 10^{-12}$
LFNCNP	$7.98\cdot 10^{-12}$	$6.62\cdot 10^{-12}$	$5.33\cdot 10^{-12}$	$3.73\cdot 10^{-12}$	$2.90\cdot 10^{-11}$	$1.86\cdot 10^{-11}$	$1.38\cdot 10^{-11}$	$8.90\cdot 10^{-12}$
LFNCTP	$1.83\cdot 10^{-12}$	$1.19\cdot 10^{-12}$	$7.08\cdot 10^{-13}$	$4.06\cdot 10^{-13}$	$2.68\cdot 10^{-12}$	$1.58\cdot 10^{-12}$	$1.09\cdot 10^{-12}$	$8.47\cdot 10^{-13}$

^aDuring reduction processes. ^bDuring oxidation processes.

The calculated lithium ion diffusion coefficients are coherent with the values reported in literature for similar olivine materials [22], even if they are slightly lower. This could be the result of the presence of very small crystalline domains within each cathodic particle, which interrupt the Li^+ diffusion within the nanoparticle. Once lithium ions reach the nanodomain border, they need to be exchanged towards the neighboring domain, slowing the overall diffusion process. The highest D_{Li} values are obtained with LFNCVP and LFNCNP materials, thus highest performances in the battery tests are expected for these materials.

7.2.6.2 Electrochemical Impedance Spectroscopy

The lithium ion migration mechanism of the obtained cathode materials is investigated by electrochemical impedance spectroscopy (EIS), adopting a Li|electrolyte|sample cell configuration, with 1.0 M LiPF_6 solution in EC/DMC (1:1 vol) used as electrolyte, in an EL-CELL device. In order to reduce the effect of the interface resistance on the electrochemical response of the cell, AC impedance measures are collected after ten galvanostatic cycles. Thus, a well formed SEI is obtained and a correct electrolyte flooding in the interstitial free volume between cathode nanoparticles is reached. Figure 7.12 reports the measured Nyquist plots for the proposed materials.

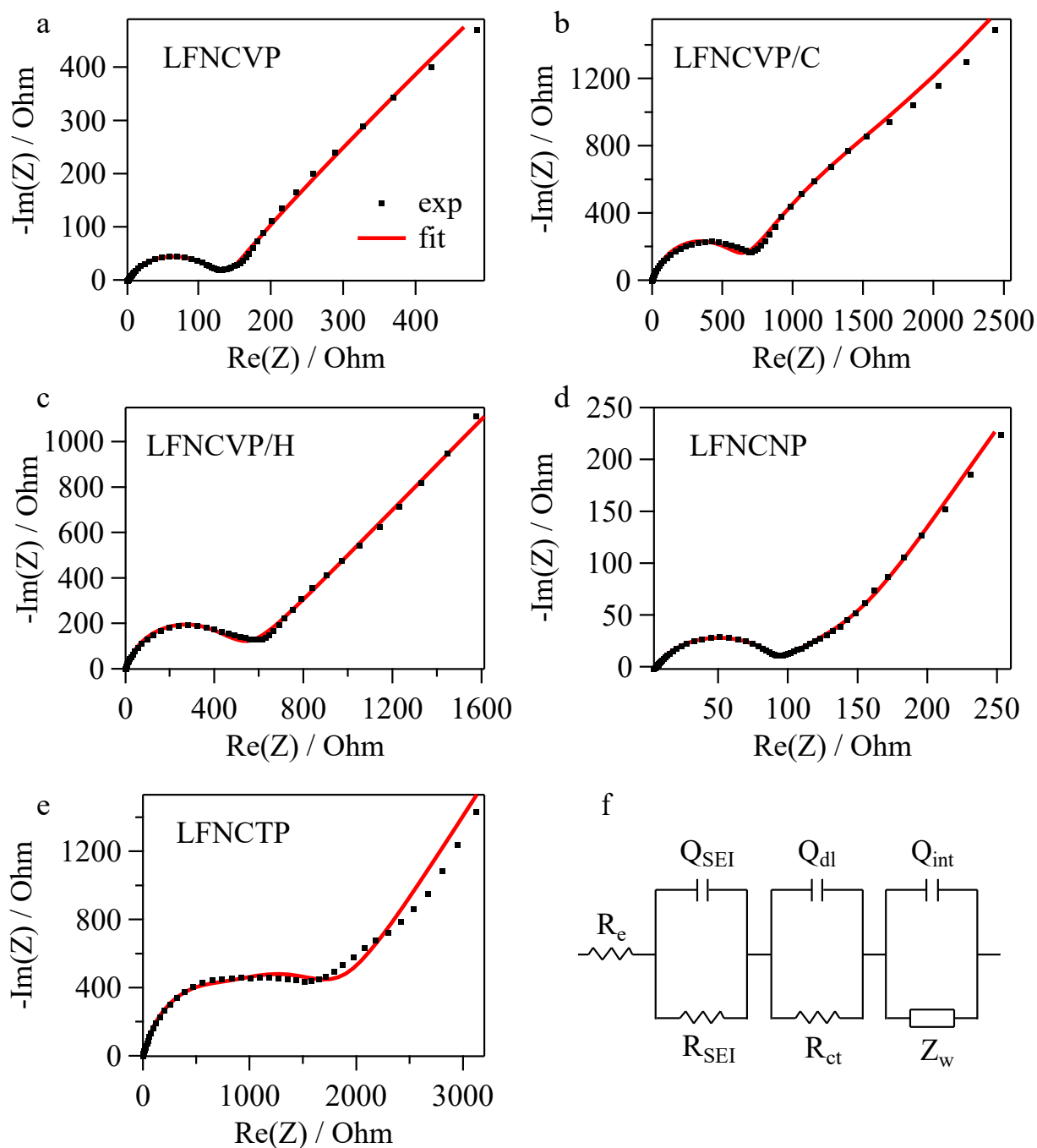


Figure 7.12. Electrochemical impedance spectroscopy results of all the samples (a-e). Fitting curve is highlighted in red. The equivalent circuit used for the fitting of Nyquist plots is represented in (f).

The equivalent circuit used for the fitting of Nyquist plots (Figure 7.12f) is hypothesized after the evaluation of the possible electrical events occurring in the proposed materials, and is coherent with other present in literature [245]. R_e element is related to the ohmic resistance of the

electrolyte, while Q_{SEI} and R_{SEI} express the SEI capacitance and resistance, respectively. R_{ct} and Q_{dl} are the charge transfer resistance and the double layer capacitance at the interface of SEI/LiMPO₄, while Z_w and C_{int} are attributed to the Warburg impedance and intercalation capacitance of lithium ions in olivine materials.

The exchange current density values (i_0) are calculated using R_{ct} (charge-transfer resistance) values and the following Equation [244]:

$$i_0 = \frac{R \cdot T}{n \cdot F \cdot R_{ct}} \quad (7.2)$$

where R is the universal gas constant, T is the absolute temperature, n is the number of the electrons exchanged during each electrochemical process (1), and F is the Faraday constant. A summary of charge-transfer resistance and exchange current density values is reported in Table 7.8.

Table 7.8. Charge transfer resistance and exchange current density values calculated by fitting of the Nyquist plots of Figure 7.12.

sample	R_{ct} / Ohm	i_0^a / mA·cm ⁻²
LFNCVP	122.60	0.37
LFNCVP/C	593.20	0.09
LFNCVP/H	445.60	0.12
LFNCNP	87.50	0.52
LFNCTP	857.30	0.06

^aThe area used for the calculation of current density values is approximated to the geometrical area of the cathode materials.

Similar to the results of lithium ion diffusion coefficients calculated by CV experiments, LFNCVP and LFNCNP materials seem to be the best materials in terms of electrochemical performances. Indeed, they show the lowest values of charge transfer resistance. The formation of a reducing environment during the synthesis results in an increased value of R_{ct} (see LFNCVP/C and LFNCVP/H samples). This indicates that, probably, the presence of traces of by-products on the surface of active olivine materials (*e.g.* metal oxides) could help the charge transfer processes at the interface between the electrolyte and the nanoparticles of the proposed materials [22].

EIS spectroscopy is a useful technique in order to estimate the lithium ion diffusion coefficient (D_{Li}) within the olivine particles [22, 246-248]. D_{Li} values are calculated with the following Equation [247-249]:

$$D_{Li} = \frac{1}{2} \left[\left(\frac{V_m}{F \cdot S \cdot \sigma} \right) \left(\frac{dE}{dx} \right) \right]^2 \quad (7.3)$$

V_m corresponds to the molar volume of the olivine material, F is the Faraday constant, S is the surface area of the electrode, σ describes the Warburg factor obtained from the fitting of EIS measurements, dE/dx corresponds to the slope of the electrode potential (E) vs. composition and can be calculated from the galvanostatic curves. Obtained D_{Li} values for the proposed samples are summarized in Table 7.9.

Table 7.9. Lithium ion diffusion coefficients calculated from EIS experiments and comparison with the average D_{Li} evaluated from CV measurements.

sample	$Z_w / \text{Ohm} \cdot \text{s}^{-1/2}$	$D_{Li,EIS}^a / \text{cm}^2 \cdot \text{s}^{-1}$	$D_{Li,CV}^b / \text{cm}^2 \cdot \text{s}^{-1}$
LFNCVP	377.20	$1.97 \cdot 10^{-12}$	$3.44 \cdot 10^{-12}$
LFNCVP/C	767.60	$8.68 \cdot 10^{-13}$	$8.44 \cdot 10^{-13}$
LFNCVP/H	576.30	$1.92 \cdot 10^{-12}$	$1.80 \cdot 10^{-12}$
LFNCNP	248.20	$4.53 \cdot 10^{-12}$	$5.92 \cdot 10^{-12}$
LFNCTP	787.20	$1.31 \cdot 10^{-12}$	$1.03 \cdot 10^{-12}$

^aCalculated from EIS experiments. ^bCalculated from CV measurements and correspond to the average of the cathodic D_{Li} values obtained at different rates (Table 7.7).

D_{Li} values, obtained with the two different techniques (*i.e.* EIS and CV), are really similar to each other (see Figure 7.13). Thus, the agreement between the two measurements determines the quality of both the results, and the optimal modeling of the equivalent circuit used to fit EIS results. Furthermore, they lead to the same conclusions: i) an oxidizing atmosphere during the synthesis is more desirable; and ii) the obtained lithium ion diffusivity increases in the order $Ta < V < Nb$. Thus, the best performances in galvanostatic cell cycling tests are expected for LFNCNP material.

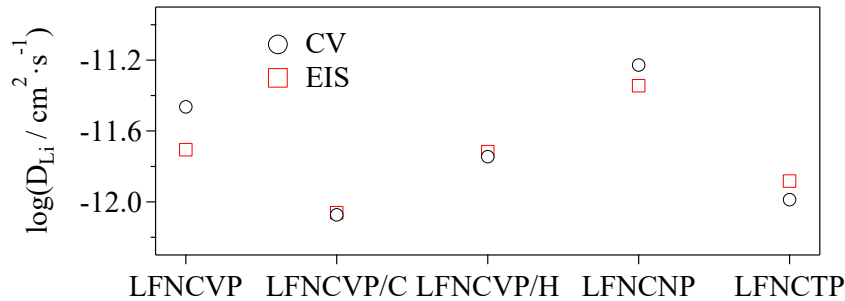
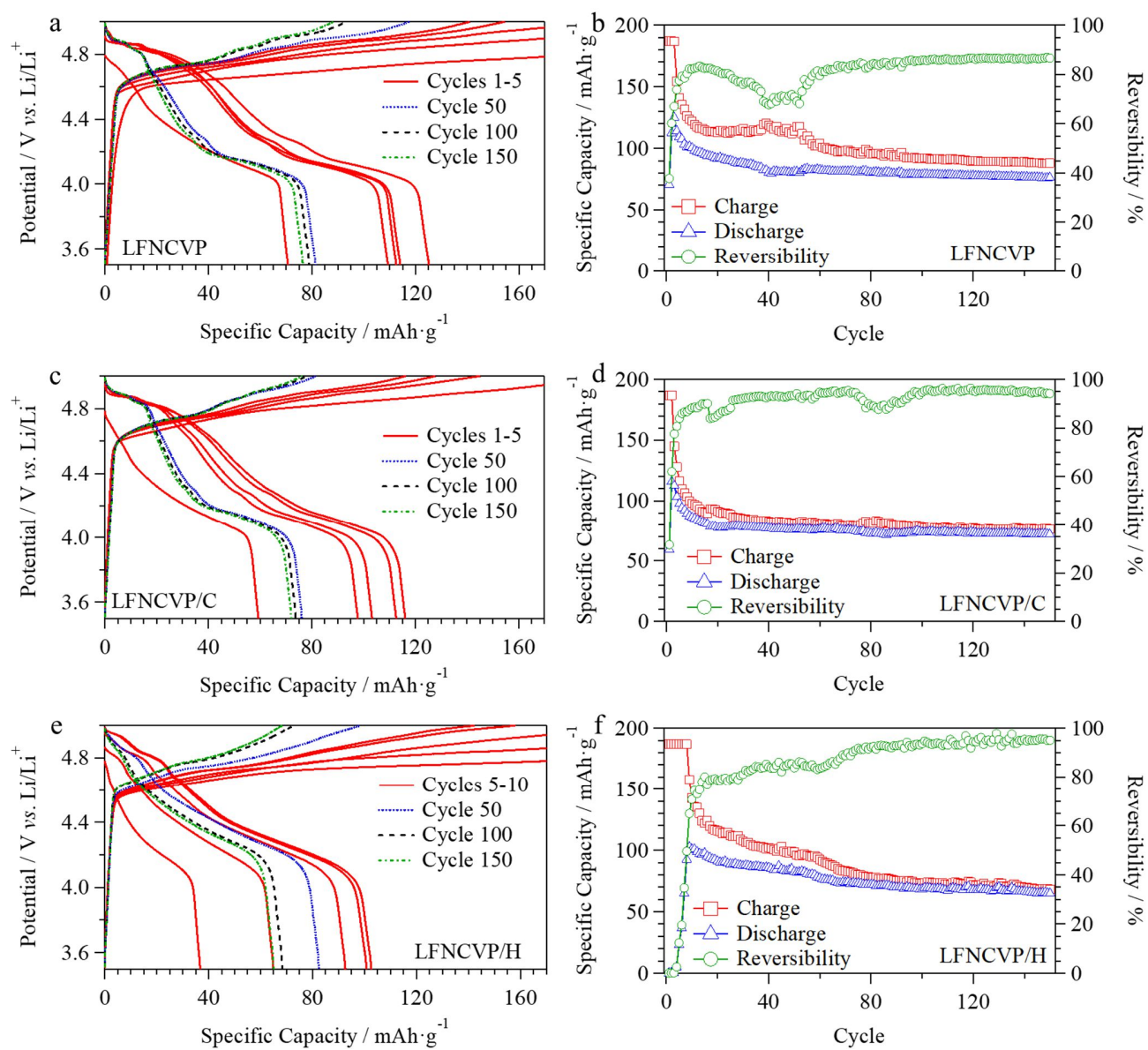


Figure 7.13. Log(D_{Li}) values for each sample evaluated with both CV and EIS techniques.

7.2.7 Battery Test

All the proposed materials are coupled with a lithium metal anode in a CR2032 coin cell device and tested under galvanostatic conditions, to evaluate their electrochemical performances as cathode for Li secondary batteries. Cells are charged and discharged between 3.5 and 5.0 V, at C/5 rate (34 mA·g⁻¹) for the durability tests, and at different rates (*i.e.* C/5→C/2→C→2C→C/5) for the rate capability tests. 1.0 M LiPF₆ solution in EC/DMC (1:1 vol) is used as electrolyte. Durability results are shown in Figure 7.14.



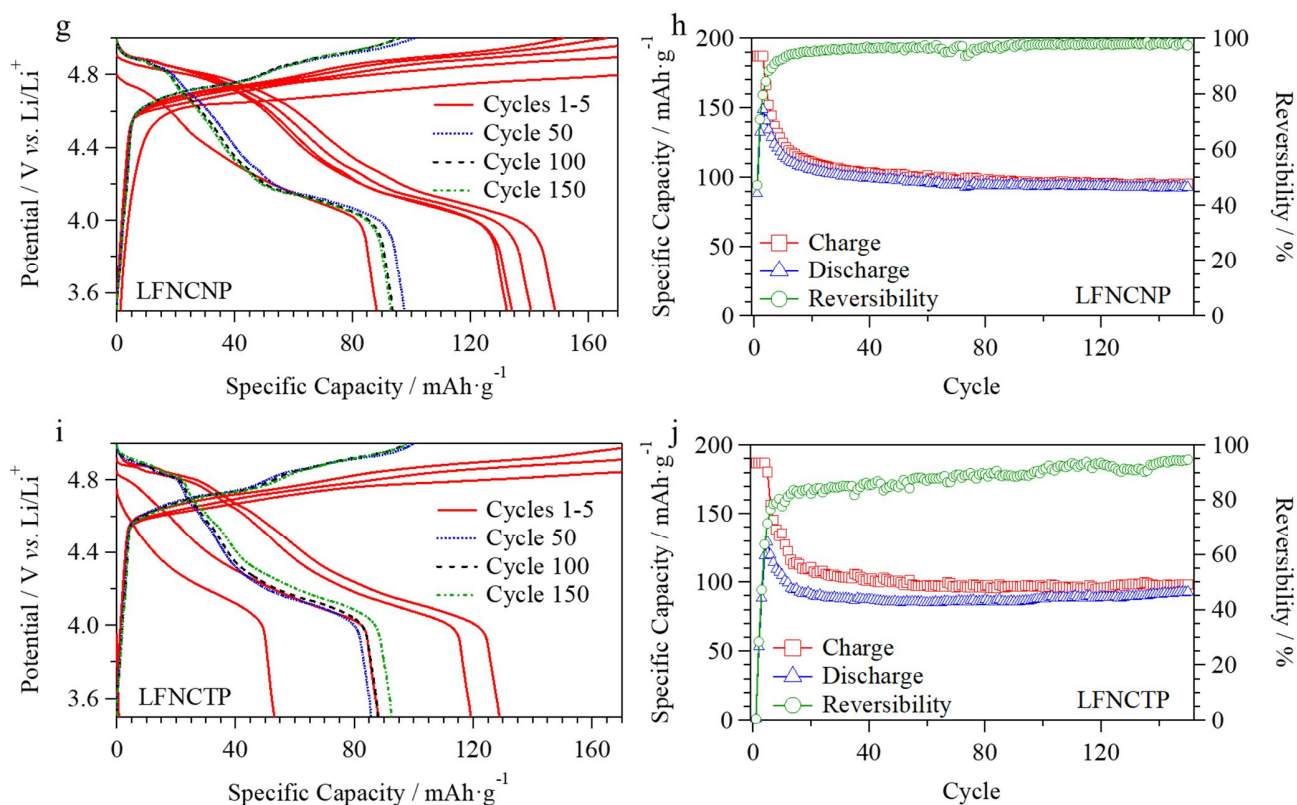


Figure 7.14. Galvanostatic battery cycling test performed at C/5 for LFNCVP (a); LFNCVP/C (c); LFNCVP/H (e); LFNCNP (g); and LFNCNP (i) at different cycle numbers. Durability test during the first 150 cycles for LFNCVP (b); LFNCVP/C (d); LFNCVP/H (f); LFNCNP (h); and LFNCNP (j).

All the materials need an activation process consisting of a couple of charge/discharge cycles before starting to show discrete capacities, with the exception of LFNCVP/H sample that requires six charge/discharge cycles to be activated. The peaks observed in CV measurements are confirmed as plateau in galvanostatic tests. No remarkable variations in the working potential are observed: i) with respect to the reference LFNCNP material; ii) increasing the reductive environment during the synthesis; and iii) substituting V with Nb or Ta. Thus, the potential at which the charge and discharge processes settle is ruled by the dominant metal present into the olivine structure (*i.e.* cobalt) and not by any dopant addition or selected synthetic route. The obtained materials show a slight capacity decay over cycling, that stabilizes after *ca.* 40 cycles. This could be addressed to a lower structural stability of the olivine, due to the increased flexibility given by the insertion of a high valence metal. Nevertheless, the decomposition of the electrolyte, which occurs starting from 4.6 V, could affect the starting cycles, forming a protective passivating layer on the surface of

the cathode particles, thus decreasing the capacity of the material. In Figure 7.15 the best discharge cycle for each material is reported, and the obtained capacity values are summarized in Table 7.10.

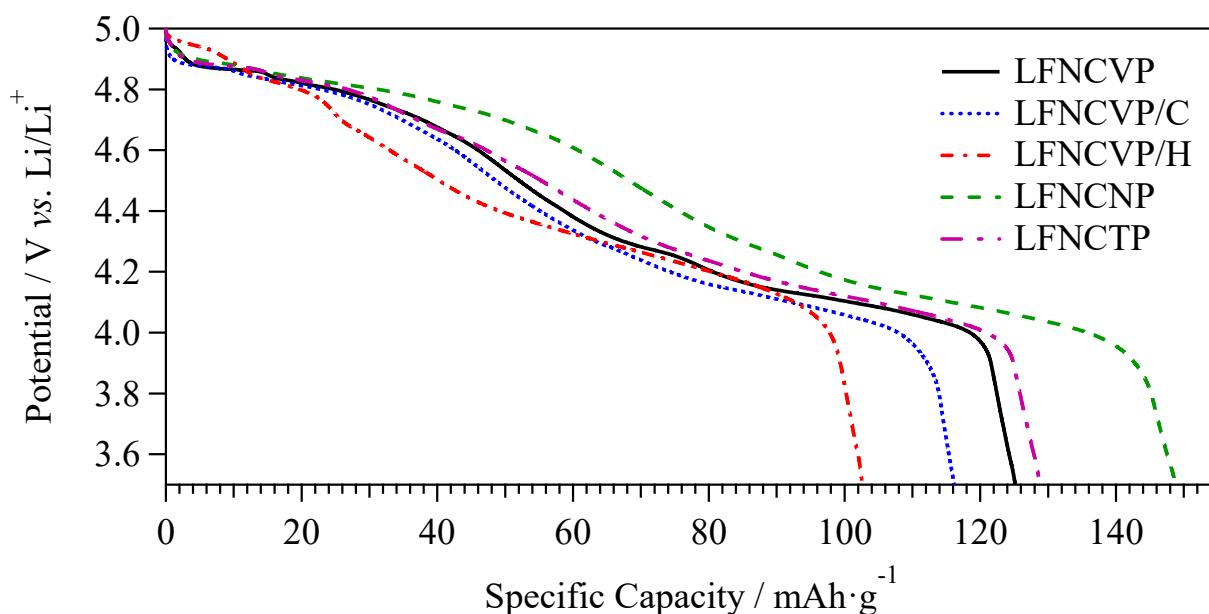


Figure 7.15. Comparison between the maximum discharge specific capacity of all the proposed materials.

Table 7.10. Maximum specific capacity and energy values for the obtained materials and the reference cathode.

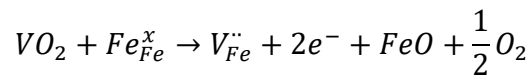
sample	specific capacity / mAh·g ⁻¹	specific energy / mWh·g ⁻¹
LFNCVP	125	550
LFNCVP/C	116	512
LFNCVP/H	103	455
LFNCNP	149	656
LFNCTP	129	568
LFNCP ^a	125	560

^aLFNCP is the reference cathode obtained using an oxidizing atmosphere and without the addition of V, Nb, or Ta.

The synthetic protocol that gives rise to the best performances, both in terms of highest discharge specific capacity and retained discharge specific capacity after 150 cycles, is that one realized under an oxidizing atmosphere. Indeed, LFNCVP material shows a maximum discharge specific capacity of 125 mAh·g⁻¹, of which more than 60 % is retained after 150 cycles. On the contrary, LFNCVP/C and LFNCVP/H samples show a maximum discharge specific capacity of 116 and 103 mAh·g⁻¹, which decreases down to 72 and 65 mAh·g⁻¹, respectively. It is interesting to notice how, even if XRD and HR-TEM analyses demonstrates a lower content of residues and by-products in LFNCVP/C and LFNCVP/H samples with respect to LFNCVP material, this does not give rise to

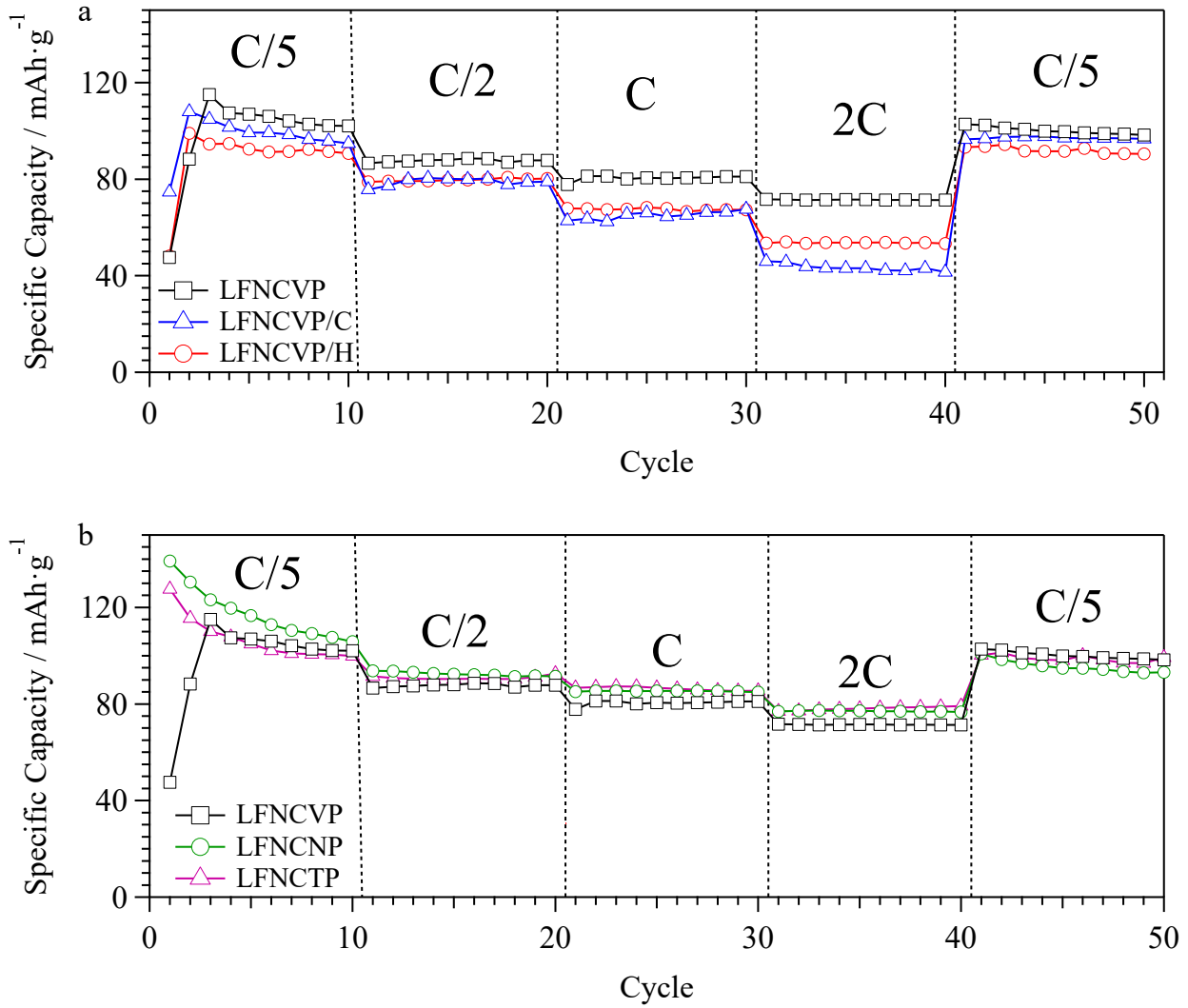
better performances in electrochemical tests. On the contrary, the presence of traces of residual reactants and by-products in LFNCVP could acts as a protective layer able to improve the cycling performances of the cathode. Concerning the differences between cathodes containing different high valence ions, it is observed that the addition of niobium leads to the best cathode material obtained in this work. Indeed, by substituting vanadium with niobium, a maximum specific discharge capacity of 149 mAh·g⁻¹ can be reached (656 mWh·g⁻¹ of specific energy), which, after 150 cycles, decreases to 93 mAh·g⁻¹. Furthermore, a reversibility (coulombic efficiency) close to 100 % is shown for all the 150 cycles. The sample containing tantalum, LFNCTP, demonstrates lower performance (maximum specific discharge capacity of 129 mAh·g⁻¹) with respect to LFNCNP material, but still higher than those obtained with the vanadium-doped and the undoped reference cathodes (125 mAh·g⁻¹ for both). These electrochemical performances are greater than those reported for commercial cathode for lithium secondary batteries, especially in terms of specific energy. Indeed, LiCoO₂ exhibits a specific energy value of *ca.* 520 mWh·g⁻¹ [80], while LiFePO₄ of *ca.* 620 mWh·g⁻¹ [104]. If compared with the specific energy provided by NMC (Lithium Nickel-Manganese-Cobalt Oxide) cathodes, *i.e.* *ca.* 740 mWh·g⁻¹ [94], it is slightly lower. Nevertheless, working at almost 1.0 V higher, the proposed materials are able to supply higher specific power with respect to NMC, making them more suitable for automotive applications.

In addition to these impressive performances, the ability of the obtained material to sustain high currents without losing too much capacity (rate capability) is studied. Indeed, the reason why we decide to doped the olivine with a high valence ion, such as V(IV), Nb(V), or Ta(V), is to take advantage of the so called “*charge compensation effect*”. It is demonstrated that the presence of a high valence ion within LiMPO₄ cathode materials allows for an improved electron conductivity [216, 250, 251]. This mechanism implies that the charge difference between M₁(IV or V) and M₂(II) could be balanced by electrons. In the case of vanadium and iron, the incorporation mechanism might be represented by the following defect equation:



This type of charge compensation is demonstrated to be favorable to improve the bulk electrical conductivity of the olivine cathode. In particular, with the increase in the doping amount of

vanadium, the electrical conductivity increases linearly [216]. Results of the rate capability tests are reported in Figure 7.16.



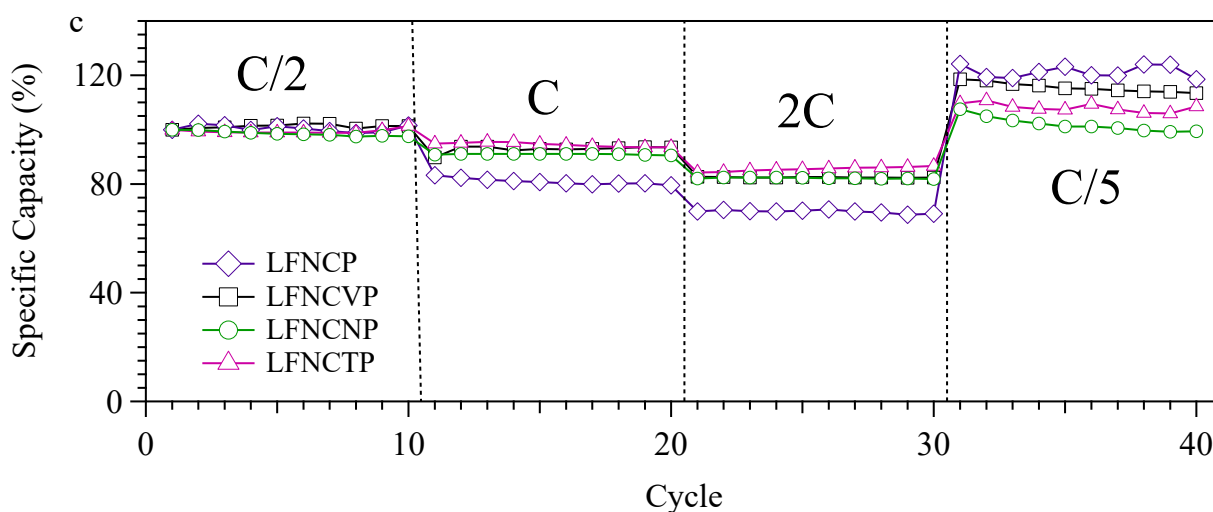


Figure 7.16. Rate capability test comparing different synthetic routes (a), different dopant ion (b), and with respect to the reference (c). In (c) 100 % corresponds to the discharge capacity of the first cycle.

It is determined that, increasing the current rate, the difference between the oxidizing and reducing atmosphere during the synthesis is emphasized. Indeed, while LFNCVP material shows a good specific discharge capacity even at quite high rates, the specific discharge capacity of LFNCVP/C and LFNCVP/H at high rates decreases with a more elevated magnitude (Figure 7.16a). On the contrary, substituting vanadium with niobium or tantalum does not change the rate capability of the material (Figure 7.16b). The great improvement with the state of the art cathode is observed in Figure 7.16c: with respect to the reference LFNCVP sample, the materials where a high valence ion is inserted show a clear improved specific discharge capacity retention increasing the current rate. Thus, the electron charge compensation effect plays an important role in improving the ability of the proposed cathode materials to sustain high current demands, limiting the capacity lost to low values. Indeed, this characteristic is very important in secondary batteries that are used in the electric vehicles field, where batteries are subjected to high amount of current drains.

7.3 Conclusions

In this chapter two concepts for the improvement of a cathode material are investigated: i) the effects of the oxidative/reductive environment during the synthesis on the resulting materials; and ii) the result of introducing in the olivine structure different high valence metals belonging to the

same group (*i.e.* group V). It is observed that in all the cases the morphology and crystal structure are very similar. Nevertheless, with respect to the reference undoped LFNCNP material, the cathode nanoparticles are composed by a higher number of coalescent olivine nanodomains with different orientations. XRD measurements reveal that, increasing the reductive power of the synthesis, fewer by-products and unreacted reagents are found. Vibrational analyses demonstrate a high level of crystallinity, and a weaker coordination of lithium ions within the hosting cavities, with respect to LFNCNP material. Furthermore, it is found that this strength is decreased by increasing the oxidizing power of the synthesis. Cyclic voltammetry experiments allow to study the electrochemical reactions occurring in the material during the insertion and extraction of lithium ions. Moreover, they lead to the calculation of the lithium ion diffusion coefficients, which: i) are in line with literature; ii) are very similar to those obtained with the electrochemical spectroscopy technique; and iii) demonstrate that the highest D_{Li} value is reached by LFNCNP sample; and iv) materials obtained using a reductive synthesis (in hydrogen and with the addition of graphite) show lower D_{Li} values. Finally, secondary lithium batteries are assembled using the proposed materials as cathode. The increasing of the reducing character of the synthesis results in a decrease of the specific capacity. Indeed, LFNCVP, LFNCVP/C, and LFNCVP/H provide 125, 116, and 103 $\text{mAh}\cdot\text{g}^{-1}$ of maximum discharge specific capacity, respectively. As expected, the best performances in terms of maximum specific capacity and cyclability are obtained with the cathode where niobium ions are inserted into the olivine structure (maximum of 149 $\text{mAh}\cdot\text{g}^{-1}$, 93 $\text{mAh}\cdot\text{g}^{-1}$ after 150 cycles, and a coulombic efficiency close to 100 %). Thus, an improvement by more than 19 % (with respect to LFNCNP reference) of specific capacity can be obtained by doping the material with a high valence ion (*i.e.* Nb(V)). Furthermore, thanks to the electron charge compensation effect, the rate capability of the proposed materials is greatly improved, giving rise to cathodes that are able to sustain high currents rates without loose high amounts of capacity. Summarizing, the obtained materials here described are extremely appealing in comparison with the state of the art cathodes for lithium batteries, due to: i) the high working potential (between 4.0 and 5.0 V) which allows to obtain high specific energy values ($656 \text{ mWh}\cdot\text{g}^{-1}$); ii) the high discharge specific capacity; and iii) fascinating rate capabilities. All of these characteristics fit very well with the demand of the electric vehicles industry.

8. Exploit BCl_4^- Structural Probe Ability to Unfold the Coordination Network Structure of Ionic Liquids Electrolytes

The aim of this work is the study of a new family of pyrrolidinium-based ionic liquids for applications as electrolytes in magnesium secondary batteries. These innovative materials are obtained by reacting 1-butyl-1-methylpyrrolidinium chloride (Pyr_{14}Cl) with boron trichloride; subsequently, different amounts of $\delta\text{-MgCl}_2$, a highly reactive phase of magnesium chloride salt, are dissolved in the IL, yielding eight samples at various salt concentrations with a general formula $[\text{Pyr}_{14}\text{Cl}/(\text{BCl}_3)_{0.25}]/(\delta\text{-MgCl}_2)_x$, with $0 \leq x \leq 0.095$. The boron trichloride anion is selected because, once reacted with chloride ions, it forms BCl_4^- species, which are excellent "*structural probe*" anions. Indeed, the spectroscopic properties of this anion are diagnostic of the surrounding structure and the coordination network that is formed within the proposed materials. Thus, studying the structure of BCl_4^- we will be able to reveal how molecules aggregate and change their coordination as a function of temperature and magnesium concentration.

The obtained electrolytes are characterized structurally, chemically, and electrically by: i) ICP-AES, to evaluate the chemical composition; ii) DFT and molecular modeling, to understand the structure of the aggregates that are formed in the material; iii) TGA and DSC, to study its stability and thermal behavior; iv) medium and far infrared (FT-IR) and micro-Raman spectroscopy, to study the structure and coordination of the various units within the materials; and finally v) by BES, to reveal the conductivity mechanisms that occur in these innovative electrolytes.

8.1 Experimental Section

8.1.1 Reagents

Pyr_{14}Cl is supplied from io·li·tec. Metallic magnesium (50 mesh), 1.0 M boron trichloride solution in toluene, and 1-chlorobutane are Aldrich reagents grade. The ionic liquid is dried under vacuum at 105 °C for 7 days, while 1-chlorobutane is further purified by standard methods and stored under Argon on 4A molecular sieves to prevent moisture contamination. All transfer and handling operations are performed under a strictly argon atmosphere, either inside an argon-filled glove-box or using a Schlenk line.

8.1.2 Synthesis

Anhydrous δ -MgCl₂ is obtained by direct reaction of metallic magnesium with 1-chlorobutane under a strictly anhydrous atmosphere, as described elsewhere [17]. The Pyr₁₄Cl/(BCl₃)_{0.25} ionic liquid is synthesized by boron trichloride distillation over the pure IL. In particular, 100 mL of the boron trichloride solution are inserted in a three-neck distilling flask, while 12 g of Pyr₁₃Cl are introduced in the receiving flask. BCl₃ gas (b.p. 12.6 °C) is distilled by heating toluene (b.p. 110.6 °C) at 90 °C, and condensing the gas at -10 °C. In this way, liquid boron trichloride is added drop by drop to the cold Pyr₁₄Cl, forming the Pyr₁₄Cl/(BCl₃)_{0.25} desired ionic liquid. Toluene evaporation is limited by cooling vapors with a column refrigerator, before the condenser, cooled at 25 °C. The distillation is carried on for 3 h. The apparatus is assembled inside an Ar-filled glove box, and the argon atmosphere is maintained during the reaction by fluxing Ar from the distilling flask. The synthesized ionic liquid (*ca.* 10 g) is collected and stored inside the glove box. The apparatus is represented in Figure 8.1.

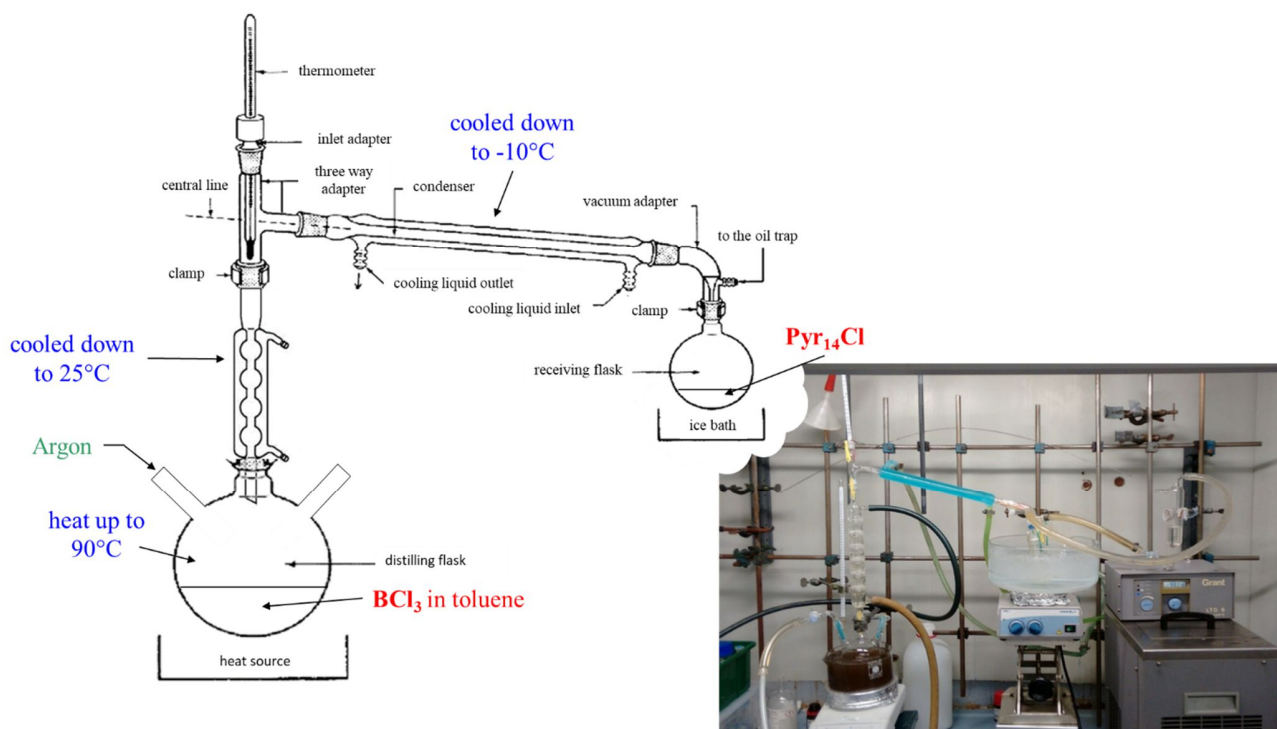


Figure 8.1. Schematic representation and real synthesis apparatus.

The most concentrated sample ([Pyr₁₄Cl/(BCl₃)_{0.25}]/(δ -MgCl₂)_{0.095}) is obtained by dissolving the 3.99 wt% of the magnesium salt (δ -MgCl₂) into the pure ionic liquid. Further dilutions with Pyr₁₄Cl/(BCl₃)_{0.25} yield the [Pyr₁₄Cl/(BCl₃)_{0.25}]/(δ -MgCl₂)_x electrolytes, thus obtaining a family of

compounds with x ranging from 0 to 0.095. The composition of the obtained electrolytes is evaluated by ICP-AES measurements and results are reported in Table 8.1.

Table 8.1. Composition of $[\text{Pyr}_{14}\text{Cl}/(\text{BCl}_3)_{0.25}]/(\delta\text{-MgCl}_2)_x$ electrolytes.

Sample	wt% $\delta\text{-MgCl}_2$	$x = n_{\text{Mg}}/n_{\text{IL}}^{\text{a}}$	$y = n_{\text{Mg}}/n_{\text{B}}^{\text{a}}$	concentration region
IL	0	0	0	A
1	0.56	0.012	0.048	A
2	0.95	0.020	0.080	A
3	1.46	0.032	0.128	B
4	1.87	0.041	0.164	B
5	2.52	0.056	0.224	B
6	3.15	0.071	0.284	C
7	3.99	0.095	0.380	C

^a n_{Mg} , and n_{IL} are the moles of $\delta\text{-MgCl}_2$ and $[\text{Pyr}_{14}\text{Cl}/(\text{BCl}_3)_{0.25}]$, respectively, determined by ICP-AES spectroscopy.

8.2 Results and Discussion

8.2.1 Thermal Behavior

8.2.1.1 Thermogravimetric Analyses

The thermal behaviors of the proposed materials are studied by HR-TGA, and the results are reported in Figure 8.2.

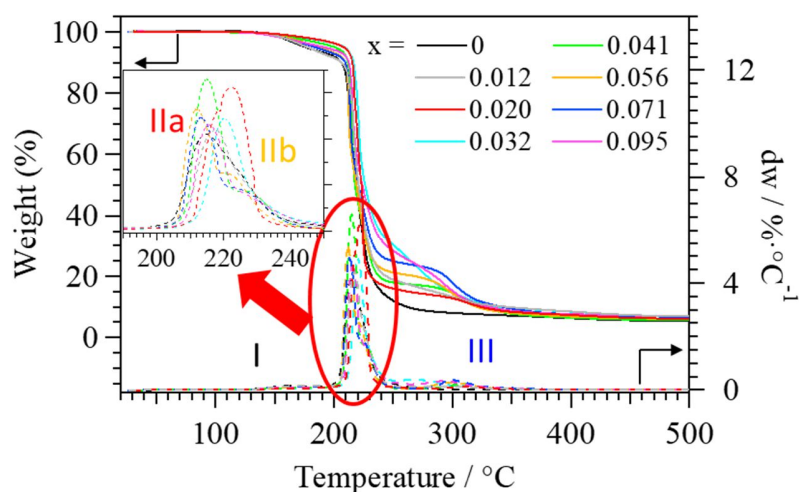


Figure 8.2. HR-TGA profiles of the proposed IL-based electrolytes at different salt concentrations.

It is observed the presence of three main thermal decomposition events. The first event (event I) starts at *ca.* 130 °C, and can be assigned to the elimination of BCl₃, which is formed from the BCl₄⁻ thermal decomposition. The second event (event II) is observed starting from *ca.* 200 °C, and is attributed to the main thermal degradation of the ionic liquid. After the addition of δ-MgCl₂ salt, this thermal decomposition event clearly splits into two different sub-events, IIa and IIb. Finally, the third degradation event (event III), absent in the sample with x = 0, is observed to occur between 260 and 280 °C. This last thermal decomposition can be reasonably assigned to the degradation of organo-Mg species that are formed during the previous events (IIa and IIb).

The behavior of the decomposition temperatures of each event as a function of x is represented in Figure 8.3. A clear separation in three different magnesium concentration regions (A, B, and C) is detected. Thus, the formation of different coordination compounds is present, and they concur to the thermal stabilization or destabilization of the system.

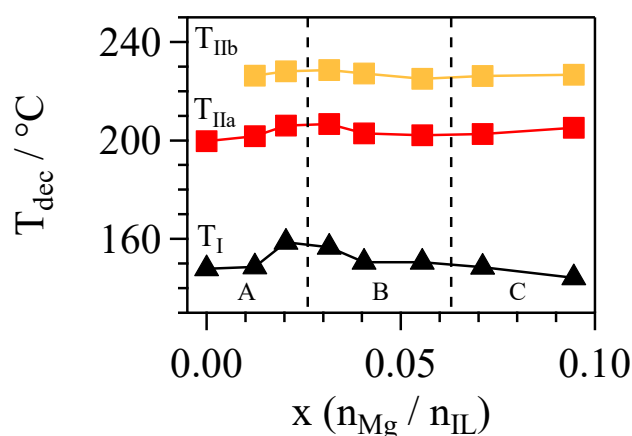


Figure 8.3. Thermal decomposition temperature at different magnesium contents (x). T_{IIa} is the temperature at which this event starts, while T_{IIb} is the temperature where the maximum of the decomposition rate takes place.

In region A, event I seems to be stabilized by δ-MgCl₂ salt addition, probably due to the formation of a coordination between BCl₄⁻ and MgCl₂ units, which gives rise to the [BCl₄MgCl₂]⁻ dimers. After this initial stabilization, further additions of magnesium salt (region B and C) result in a weakening of the thermal stability of the system. Indeed, a higher concentration of Mg²⁺ ions can catalyze the decomposition reaction. A similar behavior is observed for T_{IIa} and T_{IIb} where, after an initial increase, a plateau is reached. The split of event II in two sub-events, which starts to be clearer in sample with x=0.032, is the consequence of the formation of [BCl₄MgCl₂]⁻ dimers, which are able to improve the overall IL thermal stability due to the formation of a strong coordination network.

8.2.1.2 Differential Scanning Calorimetry

The phase and thermal transitions of the ionic liquids are studied by differential scanning calorimetry (DSC) between -100 and 100 °C. Results are shown in Figure 8.4.

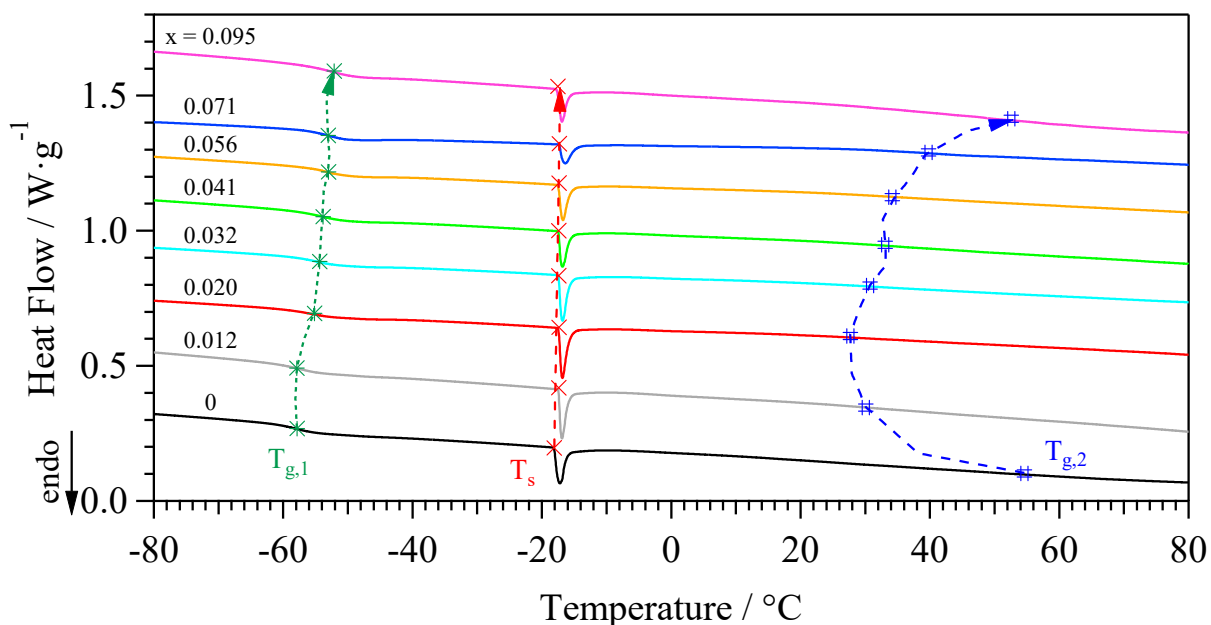


Figure 8.4. DSC profiles for $[\text{Pyr}_{14}\text{Cl}/(\text{BCL}_3)_{0.5}]/(\delta\text{-MgCl}_2)_x$ samples.

The materials show the presence of a glass transition ($T_{g,1}$) in a temperature range $-58\div-52$ °C, attributed to a structural order-disorder event where Pyr_{14}^+ cation and chloroaluminate anion stacks are reorganizing in a "zig-zag" arrangement [133]. A solid-state transition (T_s) appears at *ca.* -18 °C, and is associated with a transition event between phases with different rotational order that are gradually formed during heating [252-255]. In particular, it is hypothesized that some BCL_4^- units can be hosted between the butyl chains of adjacent cation stacks. Finally, a very broad glass transition ($T_{g,2}$) is highlighted between 28 and 55 °C by the change in the slope of DSC profiles. This transition corresponds to the formation of a viscous fluid that, for samples at medium magnesium concentrations ($0.012 \leq x \leq 0.056$), occurs at room temperature.

The phase diagram at different salt additions (see Figure 8.5) allows for the determination of how the thermal transitions of the electrolytes are dependent from x .

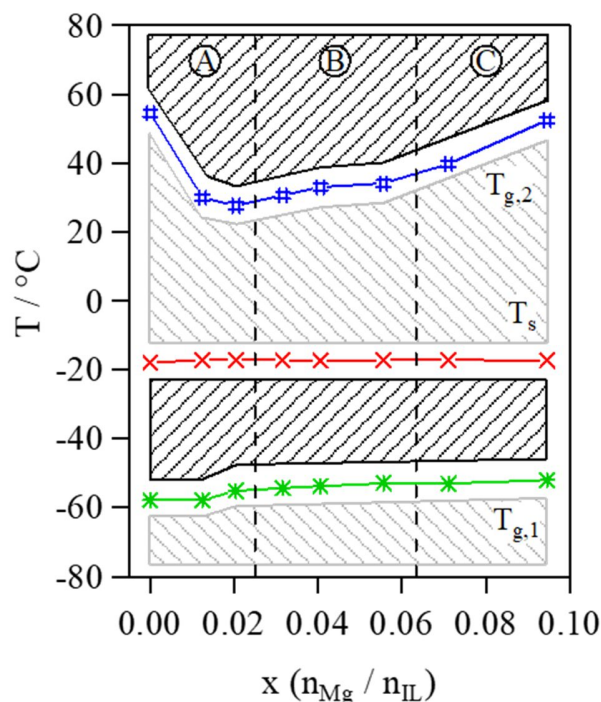


Figure 8.5. Phase diagram of $[\text{Pyr}_{14}\text{Cl}/(\text{BCl}_3)_{0.25}]/(\delta\text{-MgCl}_2)_x$ electrolytes.

The addition of magnesium salt ($x > 0$) corresponds to a slight increase of $T_{g,1}$, due to the formation of a more complex network of concatenated $[\text{BCl}_4\text{MgCl}_2]^-$ dimers. On the contrary, T_s is not affected by the addition of $\delta\text{-MgCl}_2$, and the temperature at which this event occurs remains almost constant for all the samples. The second glass transition ($T_{g,2}$), shows a particular trend on x . In details, the addition of the salt leads to the formation of agglomerates with an increased rotational disorder, in which the planes of the complexes can slide between each other. In concentration region C, the widespread complex network of concatenated $[\text{BCl}_4\text{MgCl}_2]^-$ dimers that is formed, and the growth in viscosity, result in the increase of the temperature at which this event occurs.

8.2.2 DFT Calculations and Molecular Modeling

In a first step, the geometry of the model compounds composing the ionic liquid samples is optimized using Materials Studio 2016 software, DMol3 package, GGA basis set, and BLYP functional. Results are reported in Figure 8.6.

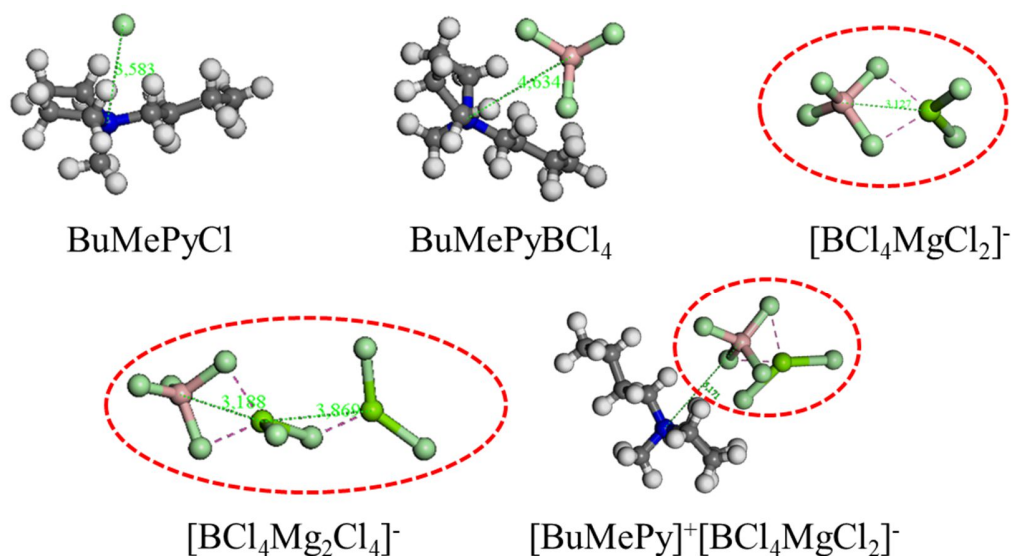


Figure 8.6. Coordination geometries of the different complexes present in the IL-based electrolytes. Color legend: C (black); H (white); N (blue); B (pink); Cl (light green); and Mg (green). BCl₄...MgCl₂ coordination is highlighted in red.

Results reveal that the butyl group of Pyr₁₄⁺ cation is inclined with respect to the pyrrolidinium plane, and that chloride and boron tetrachloride anions preferentially coordinate the nitrogen atom at the opposite position with respect to the methyl group. The most interesting outcome is that, as already demonstrated in other studies [23, 57, 133], magnesium chloride units are coordinated by the anion of the ionic liquid. Thus, the Mg²⁺ conductivity will occur by the exchange of anionic species. Furthermore, results of calculations reveal that more than one MgCl₂ unit can be coordinated to each BCl₄⁻, forming the typical chain-like structure of the δ form of magnesium chloride.

The energy of a cluster (*ca.* 105 Å³) composed by 512 ionic liquid molecules, resulting from DFT optimization calculations, is minimized, in order to simulate the structure and coordination occurring in the sample with no magnesium chloride ($x=0$) and in that with the highest amount of the salt ($x=0.095$). Molecular modeling calculations are done using Materials Studio 2016 software, Forcite package. This is done using an iterative process in which the atomic coordinates, and possibly also the cell parameters, are adjusted by applying an external electric field to the cluster, and leaving them the possibility to reorganize until the total energy of the structure is minimized. Therefore, the optimized structure corresponds to a minimum in the potential energy surface. This model is based on reducing the order of magnitude of the calculated forces and stresses, until they become smaller than a defined convergence value. The composition of the two clusters reflects the

concentration of ionic species in each sample ($x=0$ and $x=0.095$) given by ICP-AES measurements. Results are shown in Figure 8.7.

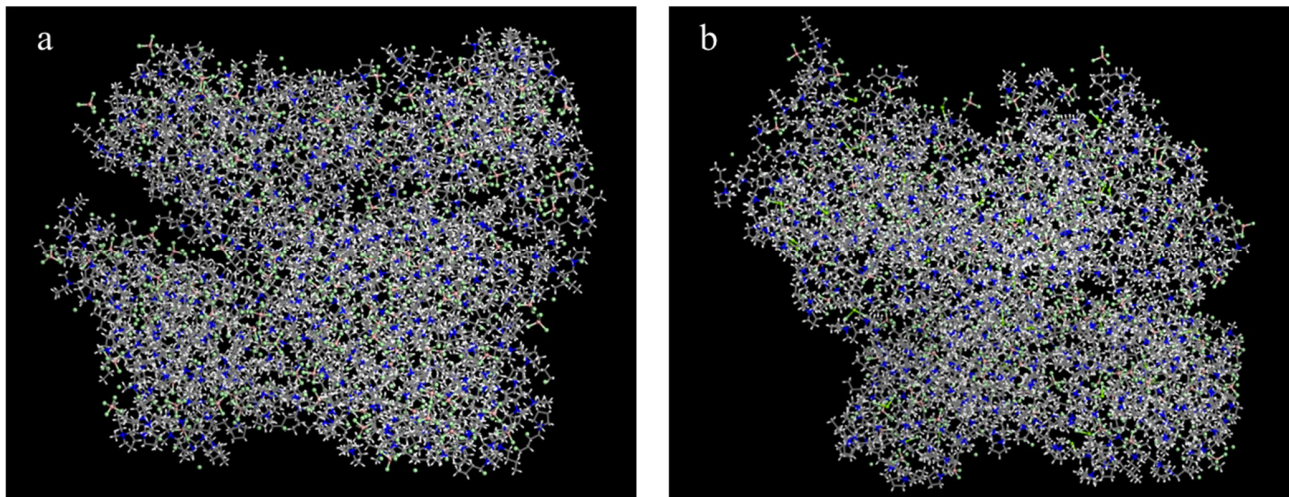
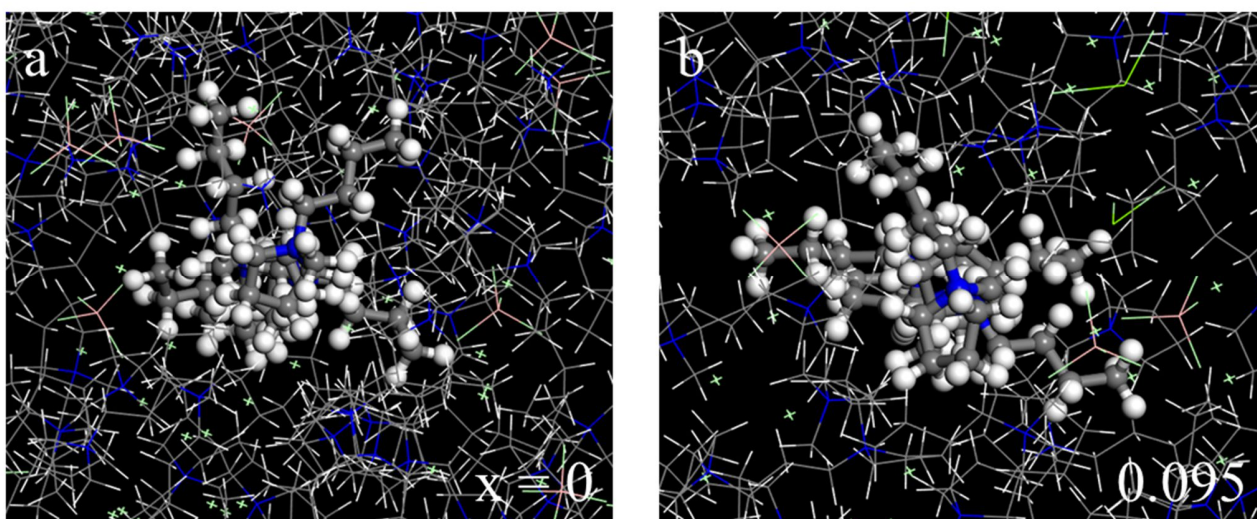


Figure 8.7. Molecular modeling results of $\text{Pyr}_{14}\text{Cl}/(\text{BCl}_3)_{0.25}$ (a) and $[\text{Pyr}_{14}\text{Cl}/(\text{BCl}_3)_{0.25}]/(\delta\text{-MgCl}_2)_{0.095}$ (b). The composition of each cluster is reflecting the real concentration of species resulting from ICP-AES measurements.

In order to highlight the geometry of the aggregation compounds present into the IL electrolytes, a region of Figure 8.7a and Figure 8.7b, respectively, is enlarged and reported in Figure 8.8a and Figure 8.8b. The geometries assumed by one single cation aggregate extracted from the IL context is shown in Figure 8.8c and Figure 8.8d.



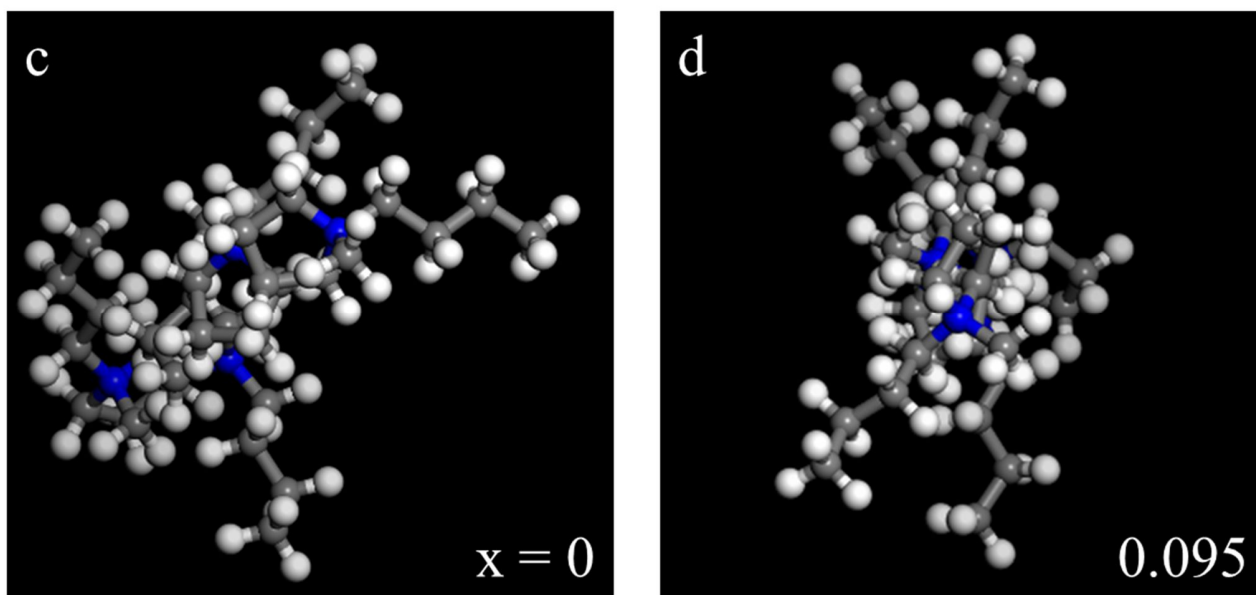


Figure 8.8. Detail of the cation domain in the sample with $x=0$ (a) and $x=0.095$ (b) in the IL context. The cation helix extracted from the context for $x=0$ (c) and $x=0.095$ (d).

The result of the calculations shows the presence of anionic and cationic domains. In particular, cations assume a helix structure, where four pyrrolidinium molecules are needed to complete a helix turn. The cations are slightly inclined with respect to the stacking plane, and the distance between two neighborhood pyrrolidinium ion is about 8 Å. Butyl chains protrude from the helix, while the BCl_4^- anions form a spiral around the helices, even when they coordinate the $\delta\text{-MgCl}_2$ units. It can be observed that the boron tetrachloride compounds tend to interact with each other, forming anion domains. Indeed, these latter aggregates form the percolation pathways where the magnesium ion conduction takes place (see BES Section 8.2.4).

The X-ray and neutron scattering simulated spectra of the obtained aggregates is calculated, and results are reported in Figure 8.9.

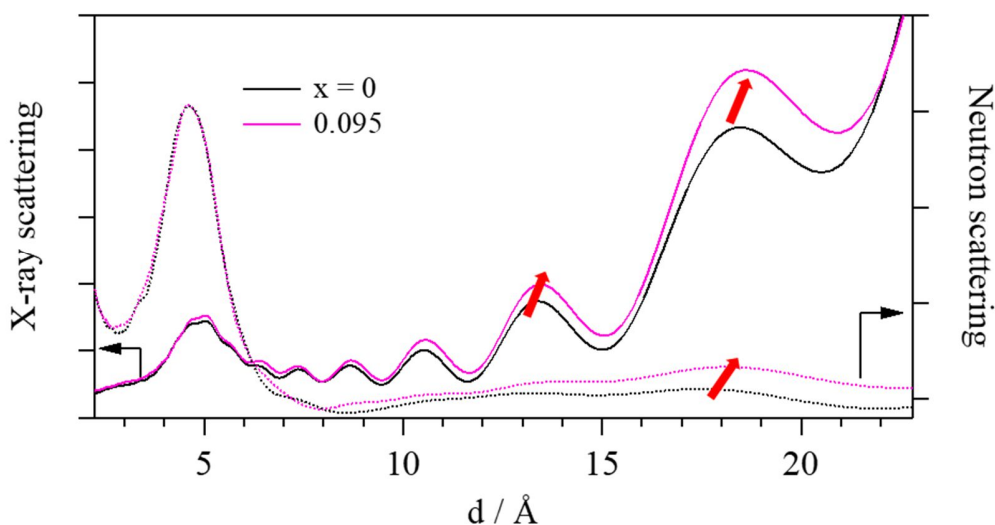


Figure 8.9. X-ray and neutron scattering simulated spectra of the sample with $x=0$ and $x=0.095$.

In all the diffractograms a periodicity in the structure can be recognized, indicating the presence of ordered domains. Moreover, with the addition of magnesium salt, an increase in the long-range atomic distances is observed. Thus, an increase in the disorder and in the distance between the helices is obtained by inserting units of δ -MgCl₂.

8.2.3 Fourier Transform Infrared Spectroscopy

Further insights on the structure and coordination network occurring in the obtained electrolytes can be gauged by infrared spectroscopy measurements. In details, the evolution of these features at different amounts of δ -MgCl₂ additions is studied. As anticipated, the choice of using BCl₄⁻ anion is done because of its ability to be an excellent probe to study the structural interactions and reorganization of the surrounding environment by modifications of its own structure. FT-IR spectra are represented in Figure 8.10. Curves are baseline subtracted and normalized with respect to the peak centered at *ca.* 2963 cm⁻¹, corresponding to the antisymmetric stretching $\nu_a(\text{CH}_3, \text{CH}_2)$ of butyl group.

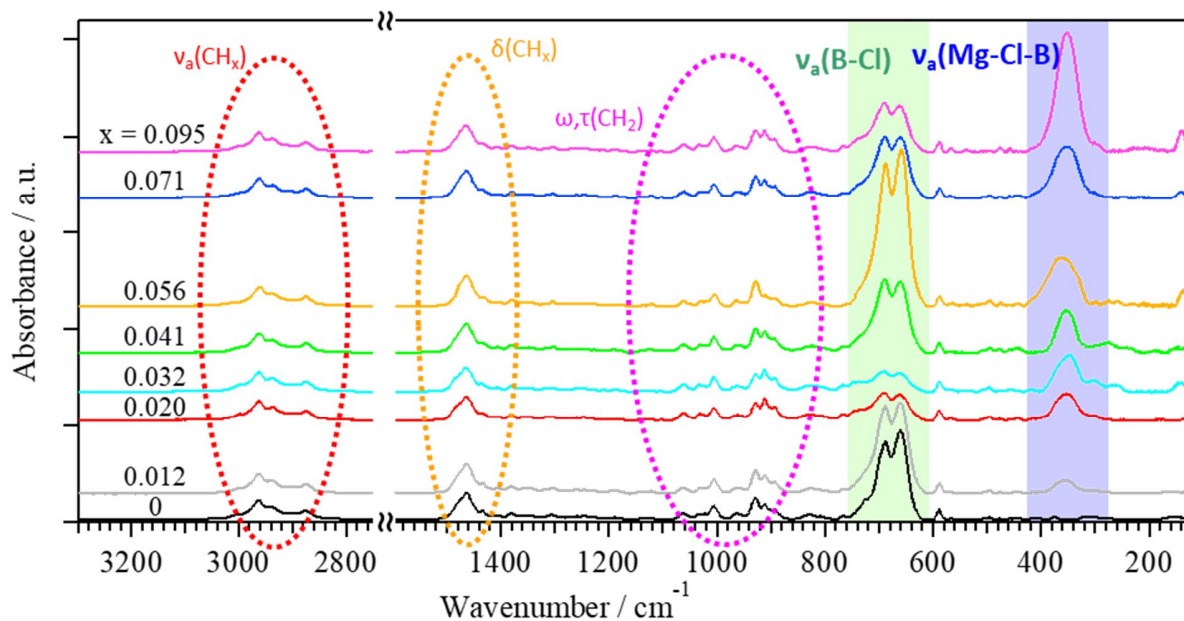


Figure 8.10. Docked FT-IR spectra in the mid and far regions of $[\text{Pyr}_{14}\text{Cl}]/(\text{BCl}_3)_{0.25}]/(\delta\text{-MgCl}_2)_x$ electrolytes.

At high wavenumbers, between 3010 and 2800 cm^{-1} , the peaks of the typical pyrrolidinium cation vibrations are observed, such as stretching $\nu_a(\text{CH}_3, \text{CH}_2)$ of butyl group at 3001, 2963, 2941, 2876 cm^{-1} [256-258].

In the medium region, from 1500 to 750 cm^{-1} , the peaks attributed to the bending $\delta(\text{CH}_2)$ of the ring, and to the $\delta(\text{CH}_2, \text{CH}_3)$ of the butyl group are observed at 1478 and 1380, and 1463 cm^{-1} , respectively [256, 258]. The out of plane (CH_3) scissoring is detected at 1434 cm^{-1} [259]. The wagging $\omega(\text{CH}_2)(\text{N})$ at 1405 cm^{-1} , $\omega(\text{CH}_2)$ at 1259, 1189, 1005, and 929 cm^{-1} , the $\omega(\text{CH}_2)$ of the ring at 1246, 1229, and 1034 cm^{-1} , and finally the $\omega(\text{CH}_2)$ of the butyl groups at 1104, and 743 cm^{-1} are detected [256-258, 260, 261]. At 1350 and 1313 cm^{-1} the twisting $\tau(\text{CH}_2)$ of butyl groups, at 1307 cm^{-1} those of the ring, and at 1138 cm^{-1} general $\tau(\text{CH}_2)$ vibrations are observed [256-258, 262]. At lower wavenumbers, 1122, 1062, and 911, and 964 cm^{-1} , the typical C-C and C-N stretching vibrations are detected [256, 257, 260]. Finally, the symmetric ring breath and rocking $\rho(\text{CH}_2)$ vibrations are observed at 893, and 829 and 765 cm^{-1} , respectively [256, 257].

In the lower region, below 750 cm^{-1} , the typical boron chloride and magnesium chloride vibrational modes can be detected. In particular, the peaks centered at 725, 687, 588, and 566 cm^{-1} are attributed to the antisymmetric stretching $\nu_a(\text{B-Cl})$ vibration [261-263]. Some vibrations attributed to the cation are still detected at 702, 634, 539, 456, 415, 376, 302, and 154 cm^{-1} , and

are all attributed to some deformation modes [256, 258, 259]. The superposition of the stretching and bending vibrations of the B-Cl groups are detected at 659 and 496 cm^{-1} [261, 262]. The antisymmetric stretching $\nu_a(\text{Mg-Cl})$ vibration is observed at 473 and 352 cm^{-1} , assigned thanks to the results of DFT calculations. Finally, the symmetric stretching $\nu_s(\text{B-Cl})$, the superposition $\nu_a+\nu_s(\text{B-Cl})$, and antisymmetric bending $\delta_a(\text{B-Cl})$ vibrations are assigned to the peaks centered at 404, 315, and 274 cm^{-1} , respectively [262, 264, 265].

The complete assignment of vibrational modes detected in Figure 8.10 are summarized in Table 8.2. Calculated and experimental results are in good agreement, confirming that the geometries resulting from DFT calculations reflects the real structures assumed by the ionic complexes.

Table 8.2. Experimental and calculated vibrational frequencies with relative assignment for the samples with x=0 and 0.095.

Experimental ^a / cm ⁻¹		Calculated at GGA/BLYP / cm ⁻¹				Assignment ^b	Ref.
x = 0	x = 0.095	BuMePyCl	BuMePyBCl ₄	[BCl ₄ MgCl ₂] ⁻	[BCl ₄ Mg ₂ Cl ₄] ⁻		
3001 (m,sh)	3001 (m,sh)		3021			v _a (CH ₃)(Bu)	[256-258]
2963 (vs)	2963 (vs)	2974	2986			v _a (CH ₂)(Bu)	[256-258]
2941 (s,sh)	2937 (s,sh)	2938	2946			v _a (CH ₂)(Bu)	[256-258]
2876 (s)	2876 (s)	2890				v _a (CH ₂)(Bu)	[256-258]
2661 (vww)	2662 (vww)					overtones	[257]
2340 (vww)	2346 (vww)					overtones	[257]
1762 (vww)	1768 (vww)					overtones	[257]
1478 (s,sh)	1478 (s,sh)	1492	1492			δ(CH ₂)(ring)	[258]
1463 (vs)	1465 (vs)	1483	1486			δ(CH ₂ ,CH ₃)(Bu)	[258]
1434 (m)	1435 (m)	1441	1416			sc(CH ₃) oop	[259]
1405 (w)	1407 (w)	1409	1404			ω(CH ₂)(N)	[260]
1380 (m)	1380 (m)	1379	1366			δ _s (CH ₂)(ring)	[256]
1350 (w)	1350 (w)	1355	1355			τ(CH ₂)(Bu)	[256-258]
1313 (w,sh)	1315 (w,sh)	1312	1316			τ(CH ₂)(Bu)	[256-258]
1307 (w)	1304 (w)	1297	1306			τ(CH ₂)(ring)	[256-258]
1259 (w)	1260 (w)	1260	1260			ω(CH ₂)	[261]
1246 (w)	1246 (w)	1241	1241			ω(CH ₂)(ring)	[257]
1229 (w)	1229 (w,sh)	1228	1216			ω(CH ₂)(ring)	[257]
1189 (vw)	1192 (vw)	1185	1182			ω(CH ₂)	[257]
1138 (vw)	1135 (vw)	1158	1157			τ(CH ₂)	[256, 262]
1122 (vw)	1122 (vw)	1131	1126			v(C-C)	[260]
1104 (vw)	1103 (vww)	1101	1100			ω(CH ₂)(Bu)	[258]
1062 (m)	1062 (m)	1071	1069			v _a (C-C)(ring)	[256, 257]
1034 (m)	1032 (m)	1031				ω(CH ₂)(ring)	[256]
1005 (s)	1006 (s)	1001	1010			ω(CH ₂)	[256]
964 (m)	964 (m)	964	957			v _a (C-N)(ring)	[256]
929 (vs)	929 (vs)	945	939			ω(CH ₂)	[256, 257]
911 (s)	912 (vs)	913	916			v _a (C-C)	[256]
893 (m)	893 (s)	883	894			s ring breath	[256, 257]
829 (w)	829 (w)	842	852			ρ(CH ₂)	[256]
765 (w)	767 (w)	756	773			ρ(CH ₂)	This work
743 (w)	747 (w)	737	740			ω(CH ₂)(Bu)	This work
725 (s,sh)	735 (s,sh)			782	747	v _a (B ¹⁰ -Cl)	[262]
702 (vvs,sh)	706 (vvs,sh)	683	698			ω(CH ₂) oop	[259]
687 (vvs)	690 (vvs)		702	698		v _a (B ¹¹ -Cl)	[261-263]
659 (vvs)	660 (vvs)					v _s +δ _a (B-Cl)	[261, 262]
634 (vww)	627 (vww)	636	637			ip ring def	[256]
588 (w)	588 (w)		587	603	623	v _a (B-Cl)	This work
566 (w)	563 (w)		578			v _a (B-Cl)	This work
	539 (vw)					ring def	[256]
496 (vw)	497 (vw)				501	v _a +δ _s (B-Cl)	[262]
	473 (w)				483	v _a (Mg-Cl)	This work
456 (vw)	458 (w)	454	455			ip def	This work
415 (vw)		431	425			γ ring def	This work
404 (vw)			367	393		v _s (B-Cl)	[262, 264]
376 (vw)		383	386			γ def	This work
	352 (vvs)			376	368	v _a (Mg-Cl-B)	This work
315 (vw)				291	353	v _a +v _s (B-Cl)	[262]
302 (vw)	301 (w)	294	279			γ ring def	[258]
274 (vw)			260	262	275	δ _a (B-Cl)	[262, 264, 265]
154 (vw)	140 (vw)	155	144			γ def	This work

^aIntensities are reported in brackets: vs=very strong; s=strong; m=medium; w=weak; vw=very weak; vww=very very weak;

sh=shoulder. ^bv stretching; δ bending; τ twisting; sc scissoring; ω wagging; γ out of plane; ip in plane; def deformation; s symmetric; a anti-symmetric.

The spectra reported in Figure 8.10 reveal that the intensity and position of vibrations attributed to the cation are not affected by the variation of the concentration of magnesium salt. Thus, in these cation domains, pyrrolidinium structural geometry does not change on x . On the contrary, as expected, the intensity of the peaks assigned to the boron- and magnesium-chloride groups changes by adding δ -MgCl₂. In order to quantify the intensity contribution of the single $\nu(\text{B-Cl})$ vibration peaking at 687 cm⁻¹, the spectrum of each sample is Gaussian decomposed in the region ranging from 610 to 785 cm⁻¹. For clarity, an example of the decomposition of the spectra of Pyr₁₄Cl/(BCl₃)_{0.25} and [Pyr₁₄Cl/(BCl₃)_{0.25}]/(δ -MgCl₂)_{0.095} compounds are shown in Figure 8.11. Since $\nu(\text{Mg-Cl})$ vibration at 352 cm⁻¹ is not superimposed to any other peak, the intensity of this peak is detected without any decomposition. As a result, the interactions present between BCl₄⁻ and the δ -MgCl₂ can be elucidated.

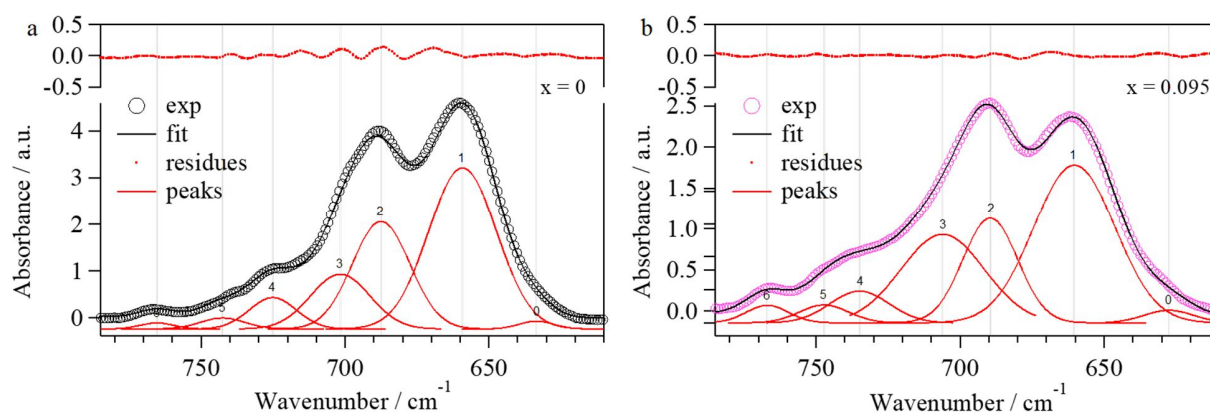


Figure 8.11. Gaussian decomposition of Pyr₁₄Cl/(BCl₃)_{0.25} (a) and [Pyr₁₄Cl/(BCl₃)_{0.25}]/(δ -MgCl₂)_{0.095} (b) compounds. Circle markers are the experimental curves, black lines correspond to the fitting results, red points are the residues (difference between experimental and fitting data), and red lines represent each vibrational peak.

Peak intensity behavior vs. x ($n_{\text{Mg}}/n_{\text{IL}}$) curves are reported in Figure 8.12, and a representative sketch of the coordination reactions occurring during δ -MgCl₂ additions is summarized in Figure 8.13.

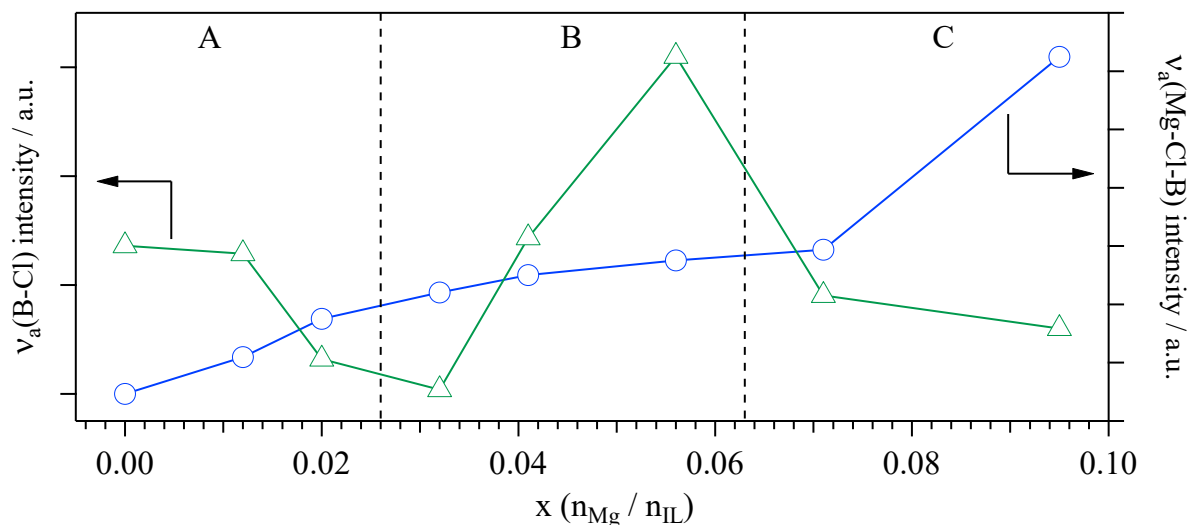


Figure 8.12. Peak intensity behavior vs. x curves of $[\text{Pyr}_{14}\text{Cl}/(\text{BCl}_3)_{0.25}]/(\delta\text{-MgCl}_2)_x$ electrolytes. Peaks consider for this graph are those attributed to the $\nu_a(\text{B-Cl})$ and $\nu_a(\text{Mg-Cl-B})$ peaking at 687 and 352 cm^{-1} , respectively.

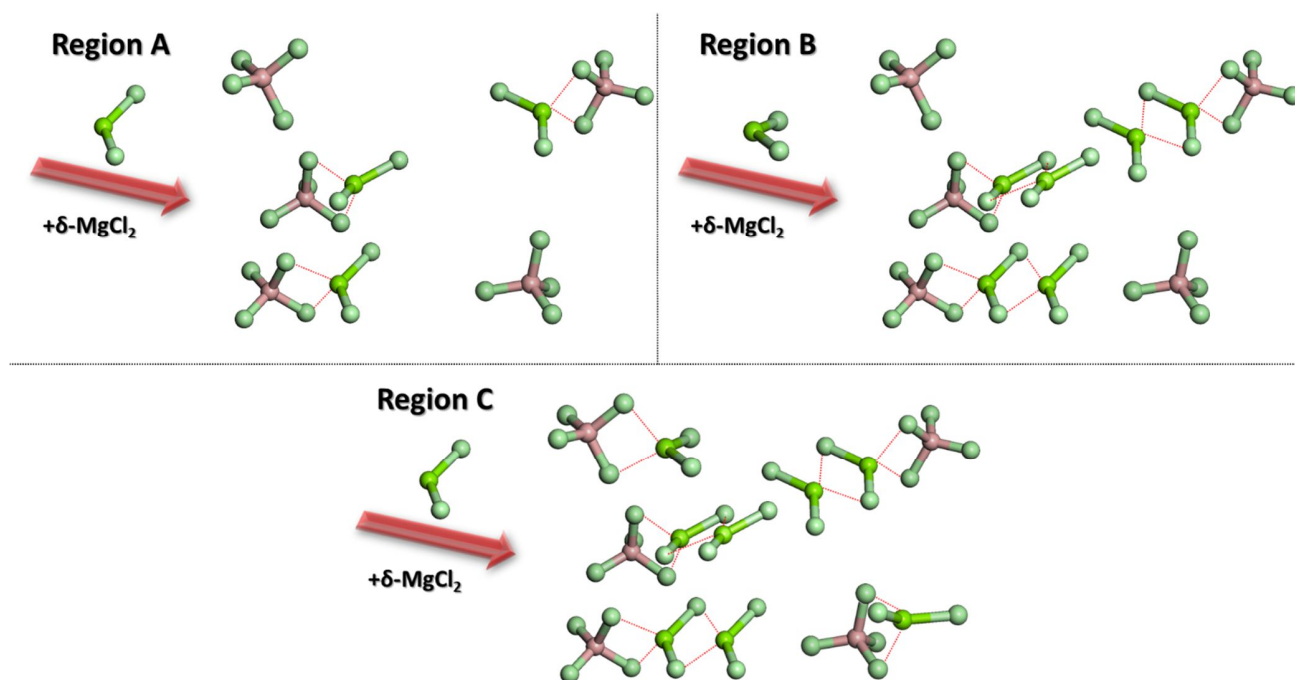


Figure 8.13. Graphical sketch of the different coordination geometries forming in each magnesium concentration region. Color legend: B (pink); Cl (light green); and Mg (green).

First of all, it is interesting to observe that the $\nu_a(\text{Mg-Cl-B})$ peak at 352 cm^{-1} arises only when MgCl_2 units are coordinated by BCl_4^- groups, otherwise the typical $\nu(\text{Mg-Cl})$ occurs at 243 cm^{-1} [17]. As already observed in the thermal analyses, samples can be divided into three different Mg concentration regions. In region A ($x < 0.032$), an increase of the intensity of the $\nu_a(\text{Mg-Cl-B})$ band

is detected, due to the addition of δ -MgCl₂ and the formation of Mg-Cl-B bonds. In parallel, as a consequence of the formation of the [BCl₄···MgCl₂]⁻ dimers, the number of B-Cl bonds “free” to vibrate is decreased, with a resulting decrease in the intensity of the peak (see Figure 8.13, region A). At medium concentrations of the salt ($0.032 \leq x \leq 0.056$, region B), further additions of the magnesium salt result in the coordination of the freshly added MgCl₂ units to those already coordinated to BCl₄⁻ anions. Thus, the formation of the typical “chain like” structure of δ -MgCl₂ (see Figure 8.13, region B) is detected. Indeed, a plateau of the peak attributed to $\nu_a(\text{Mg-Cl-B})$ vibration is reached, because new dimers are not formed anymore. Furthermore, the formation of these chains increases the distance and the disorder between neighboring cation helices, explaining the trend of $T_{g,2}$ in DSC measurements. On the contrary, the intensity of $\nu(\text{B-Cl})$ increases. This can be explained taking into consideration that, as already demonstrated by DSC measurements and explained here, in the medium concentration region the disorder of ionic aggregates is increased ($T_{g,2}$ decreases), and the cation-anion interactions become weaker. Thus, the number of B-Cl bonds “free” to vibrate increases, with a concurrent growth of the intensity of the related peak. Finally, in region C ($x > 0.056$), the solubility of the δ -MgCl₂ chains reaches the maximum. Thus, the formation of magnesium chloride chains is blocked, and the equilibrium shifts back towards the formation of new [BCl₄···MgCl₂]⁻ dimers, with a consequent increase of the $\nu_a(\text{Mg-Cl-B})$ peak. As explained for region A, the formation of dimers results in a decrease of $\nu(\text{B-Cl})$ peak intensity (see Figure 8.13, region C).

8.2.4 Broadband Electrical Spectroscopy Studies

[Pyr₁₄Cl]/(BCl₃)_{0.25}]/(δ -MgCl₂)_x samples are widely studied by Broadband Electrical Spectroscopy (BES) technique with the aim of: i) reveal the conductivity mechanisms which give rise to the long-range charge migration process; ii) detect the correlation occurring between the coordination network of the ionic aggregates and the charge transfer mechanisms; and iii) study the effects of the δ -MgCl₂ addition on the overall conductivity of the IL-based electrolytes. BES measurements are carried out in the frequency range $3 \cdot 10^{-2} \div 10^7$ Hz, from -100 to 100 °C. The overall electric response in terms of imaginary permittivity as a function of temperature and frequency for the compounds with $x = 0, 0.020, 0.041, \text{ and } 0.071$ are reported, as an example, in Figure 8.14.

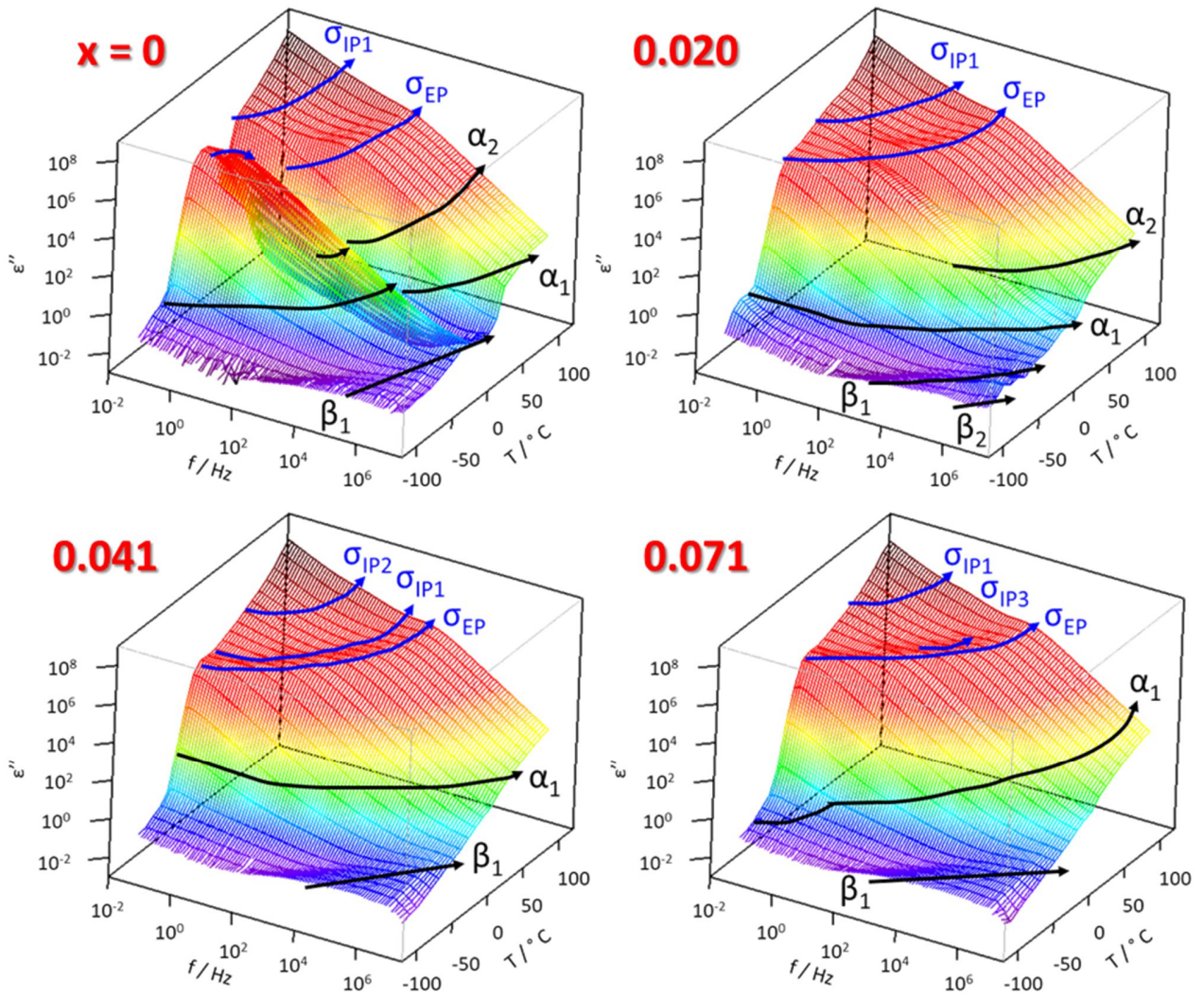


Figure 8.14. 3D imaginary permittivity spectra as a function of frequency and temperature for $[\text{Pyr}_{14}\text{Cl}]/(\text{BCl}_3)_{0.25}]/(\delta\text{-MgCl}_2)_x$ samples, with $x=0, 0.020, 0.041,$ and 0.071 .

The electric response, in terms of both the imaginary and real components of the conductivity and permittivity, are analysed with a suitable model, described by the following equation [52, 162]:

$$\varepsilon_m^*(\omega) = -i \left(\frac{\sigma_0}{\omega \varepsilon_0} \right)^N + \frac{\sigma_{EP}(i\omega\tau_{EP})^{Y_{EP}}}{i\omega\varepsilon_0[1+(i\omega\tau_{EP})^{Y_{EP}}]} + \sum_{k=1}^n \frac{\sigma_{IP,k}(i\omega\tau_{IP,k})^{Y_{IP,k}}}{i\omega\varepsilon_0[1+(i\omega\tau_{IP,k})^{Y_{IP,k}}]} + \sum_{j=1}^m \frac{\Delta\varepsilon_j}{[1+(i\omega\tau_j)^{a_j}]^{b_j}} + \varepsilon_\infty \quad (8.1)$$

where $\varepsilon^*(\omega) = \varepsilon'(\omega) - i\varepsilon''(\omega)$, and $\sigma^*(\omega) = i\omega\varepsilon_0\varepsilon^*(\omega)$. The first term of the equation describes the material conductivity at zero frequency. ε_∞ accounts for the permittivity of the material at infinite frequency (electronic contribution). The second term is associated with electrode polarization, while the third describes the interdomain polarizations. σ_k and τ_k are the conductivity and the

relaxation times, respectively, associated with the k^{th} electrical event. γ_k is associated with the broadening of the k^{th} polarization peak. The third term accounts for the dielectric relaxation described by the Havriliak-Negami theory [162, 182]. $\Delta\varepsilon$, τ_j , α_j , and β_j are the dielectric strength, relaxation time, symmetric and antisymmetric shape parameter of each j^{th} relaxation event, respectively.

8.2.4.1 Polarization Phenomena

The conductivity vs. T^{-1} curves of all the polarization events, obtained by fitting BES measurement results with Equation 8.1, are shown in Figure 8.15. These data are fitted with a suitable model, *i.e.* Vogel-Tammann-Fulcher (VTF) [183] or Arrhenius (A) equation [162] to determine the activation energy of the polarization phenomena.

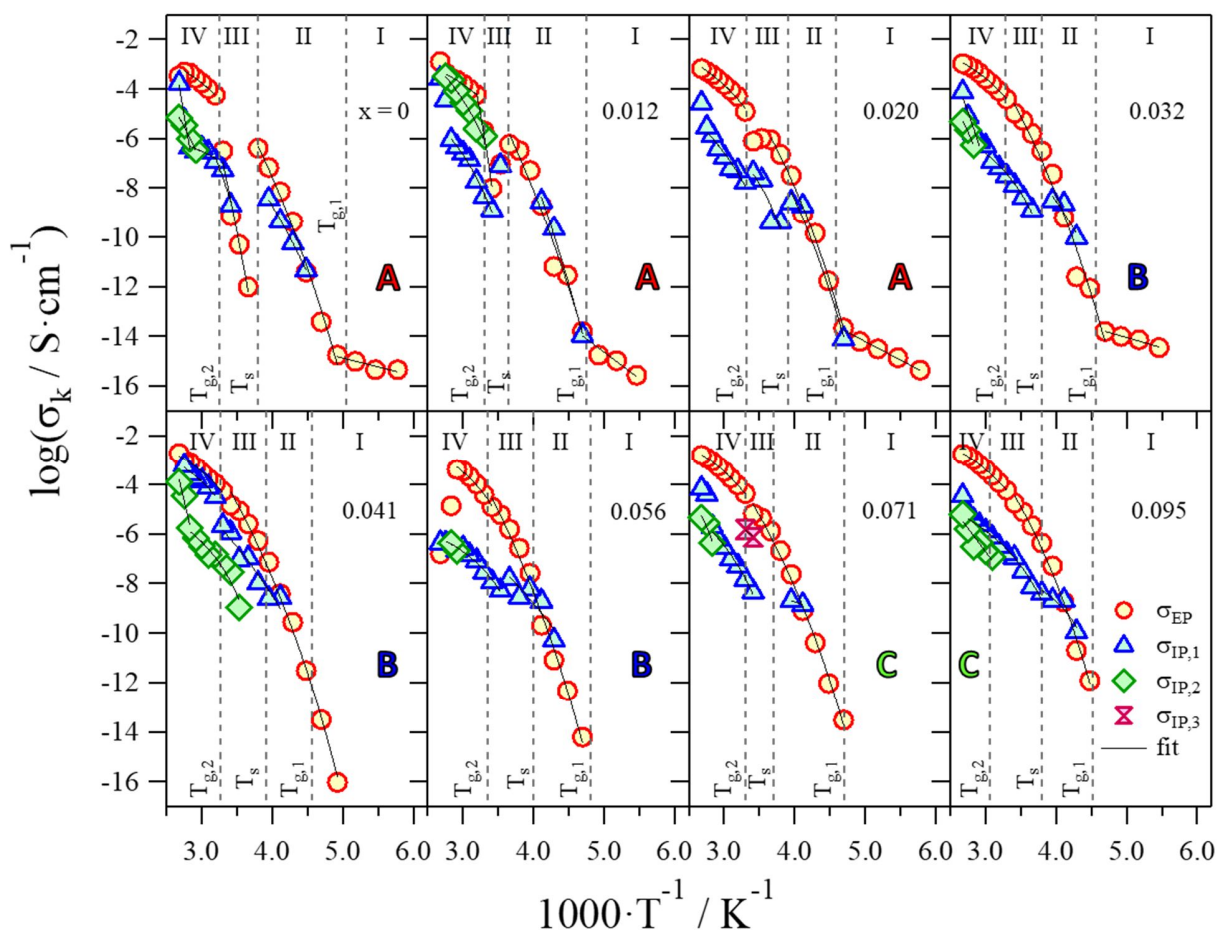


Figure 8.15. Log σ_k vs. T^{-1} curves of each polarization for every sample. Temperature regions (I-IV) are divided by the transition temperatures of each sample detected with DSC measurements.

Four different temperature regions are detected, delimited by the thermal transitions determined with DSC measurements. At temperatures higher than $T_{g,1}$ four polarization phenomena can be observed: i) σ_{EP} , electrode polarization, attributed to the accumulation of charge at the interfaces between the sample and the electrodes of the measuring cell [162]; and ii) three different interdomain polarizations (σ_{IP_i} with $1 \leq i \leq 3$), assigned to the charge accumulation at the interfaces between nano domains with different permittivity [162]. The presence of σ_{IP_i} confirms the heterogeneity, at the mesoscale, of the proposed materials. In particular, as demonstrated by DFT, MM, and FT-IR measurements, samples consist of pyrrolidinium-based cation aggregates coordinated to chloroborate anion nanodomains. In this temperature range all σ_k show a VTF-like behavior, demonstrating that the conductivity mechanism along these conductivity pathways is assisted by the relaxations of the IL aggregates.

At $T < T_{g,1}$ the electrode polarization is the only detectable phenomenon, contributing with a very low conductivity ($<10^{-13} \text{ S}\cdot\text{cm}^{-1}$). Indeed, at these temperatures the mobility of ionic species is limited, due to the low thermal activation energy available for an effective conductivity process. Furthermore, an Arrhenius behavior is observed for σ_{EP} , witnessing that, in this temperature region, charge migration occurs through hopping events between different domains, without the assistance of the dielectric relaxation events.

The contribution of each polarization to the overall conductivity ($\phi_k = \sigma_k / \Sigma \sigma_k$), as a function of temperature, is shown in Figure 8.16.

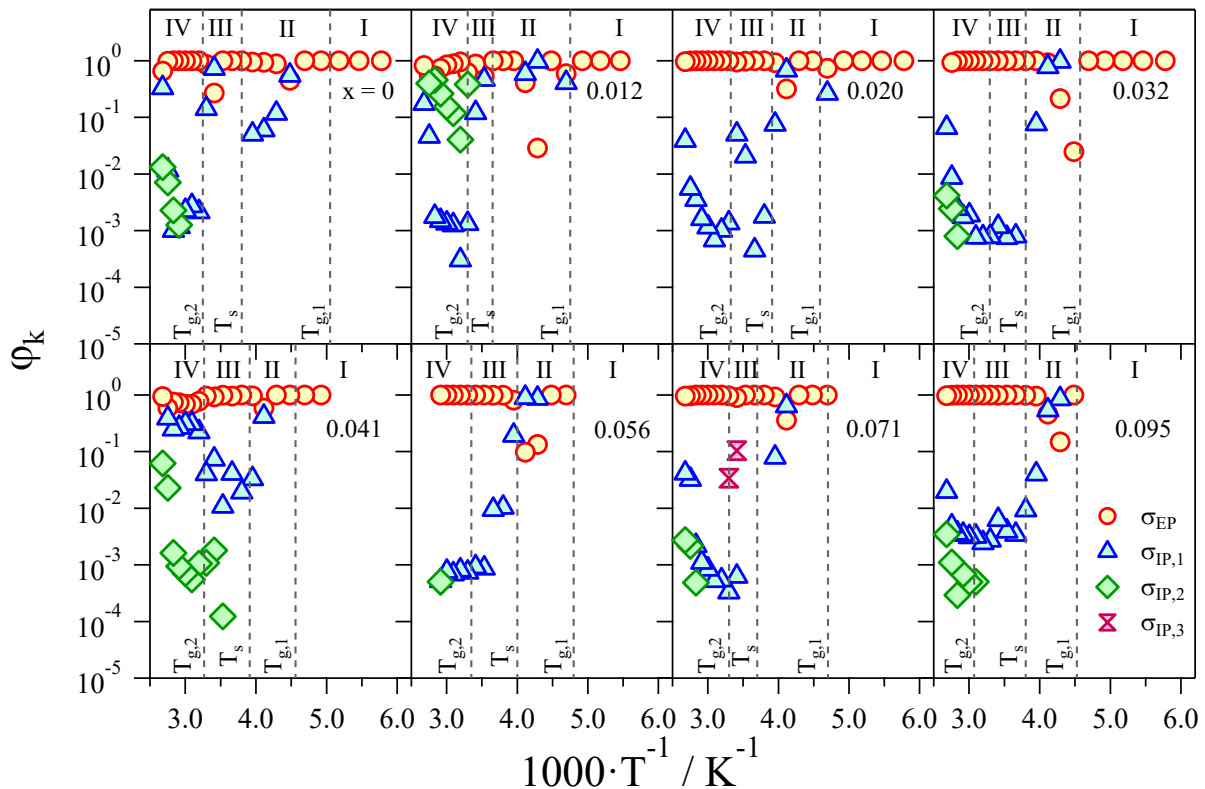


Figure 8.16. Contribution of each polarization (ϕ_k) to the overall conductivity as a function of temperature. Temperature regions (I-IV) are divided by the transition temperatures of each sample detected with DSC measurements.

The electrode polarization gives the dominant contribution to the overall conductivity for all the samples in almost the whole studied temperature range. Only $\sigma_{IP,1}$, for some temperatures (*e.g.* between $T_{g,1}$ and T_s , Region II), reaches values comparable to those shown by σ_{EP} .

The total conductivity (σ_{TOT}) is obtained as the sum of the single conductivities of each polarization[205], and takes into consideration all the mobile ions present in the electrolytes (*i.e.* $[\text{Pyr}_{14}]^+$, $[\text{BCl}_4]^-$, and $[\text{BCl}_4\text{MgCl}_2]^-$):

$$\sigma_{TOT} = \sum_{k=1}^n \sigma_k = \sigma_{EP} + \sigma_{IP,1} + \sigma_{IP,2} + \sigma_{IP,3} \quad (8.2)$$

In Figure 8.17 the logarithm of the total conductivity as a function of T^{-1} is reported.

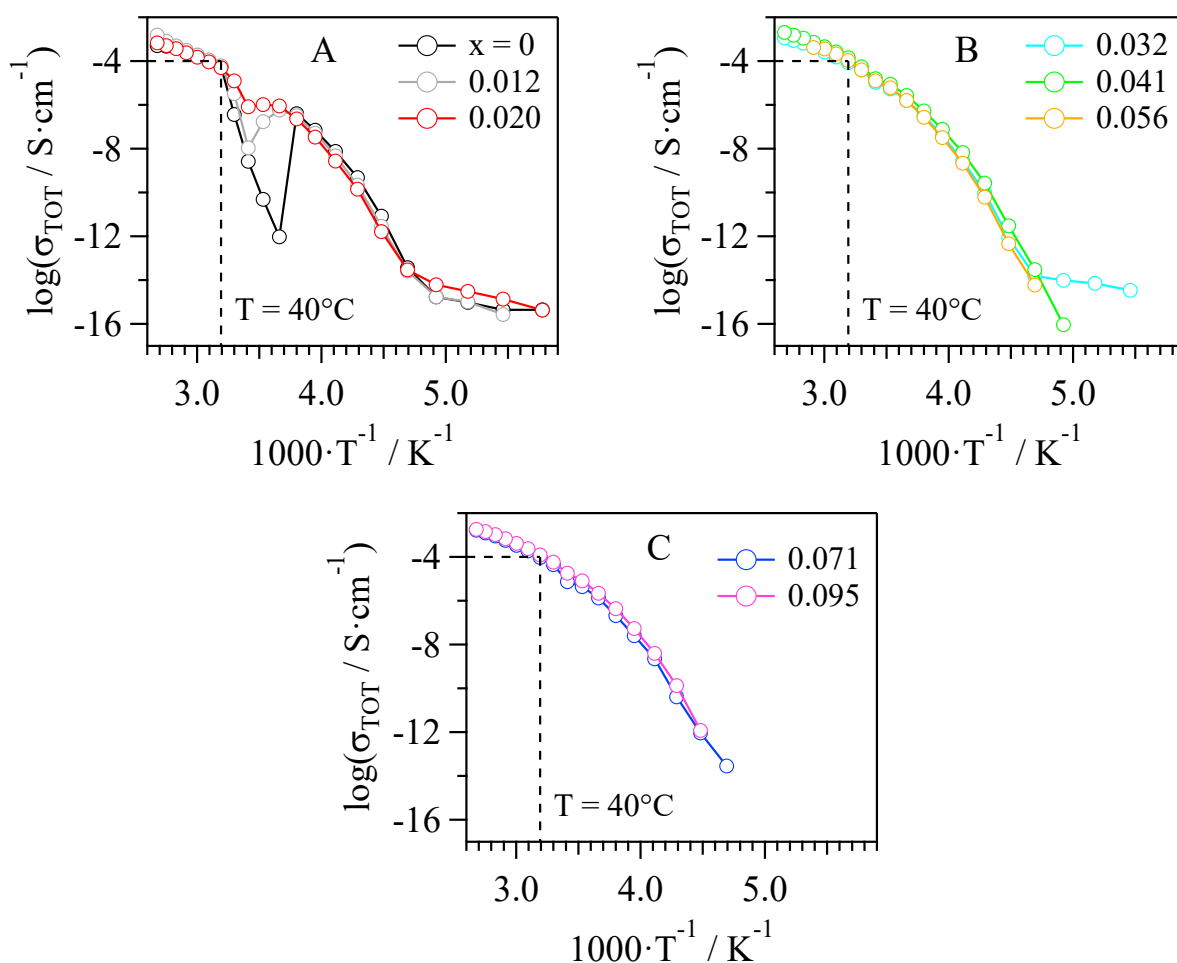


Figure 8.17. Log σ_{TOT} vs. T^{-1} curves for the various $[\text{Pyr}_{14}\text{Cl}/(\text{BCl}_3)_{0.25}]/(\delta\text{-MgCl}_2)_x$ electrolytes divided in the different Mg concentration regions (A, B, and C).

Pure ionic liquid and samples with a low concentration of magnesium (region A) show a drop in conductivity at $T_s \leq T \leq T_{g,2}$, which is gradually inhibited as the salt concentration increases. This event can be assigned to the structural reorganization that occurs during T_s . Indeed, as previously hypothesized (see DSC measurements, Section 8.2.1.2), at T_s BCl_4^- units can be hosted between the

butyl chains of adjacent cation stacks. Thus, an interruption of some conductivity pathways along the anion aggregates, and the inhibition of the conductivity, occur at this temperature. By increasing the Mg concentration, this effect is attenuated, due to the increased disorder and spacing between the adjacent cation helices, which results in the formation of larger and continuative pathways even after T_s transition. In this region, the lowest values of σ_{TOT} are obtained (*i.e.* up to $6.08 \cdot 10^{-5} \text{ S} \cdot \text{cm}^{-1}$ at $40 \text{ }^\circ\text{C}$).

In region B, the drop in σ_{TOT} is only barely appreciated, thus confirming that the increased disorder given by magnesium salt additions, and the enlargement of anion conduction channels created by $\delta\text{-MgCl}_2$ chains formation, inhibit the total conductivity diminution. The $[\text{Pyr}_{14}\text{Cl}/(\text{BCl}_3)_{0.25}]/(\delta\text{-MgCl}_2)_{0.041}$ electrolyte, which belongs to concentration region B, shows the highest total conductivity at $40 \text{ }^\circ\text{C}$, which corresponds to $1.43 \cdot 10^{-4} \text{ S} \cdot \text{cm}^{-1}$.

Finally, the samples with the highest magnesium salt concentration (region C) show still high values of σ_{TOT} , even if the viscosity and the charge concentration are increased with respect to samples present in region B. At $40 \text{ }^\circ\text{C}$, $[\text{Pyr}_{14}\text{Cl}/(\text{BCl}_3)_{0.25}]/(\delta\text{-MgCl}_2)_{0.095}$ sample exhibits a total conductivity of $1.24 \cdot 10^{-4} \text{ S} \cdot \text{cm}^{-1}$.

8.2.4.2 Dielectric Relaxation Events

The contribution of dielectric relaxation events to the electric response of the electrolytes is determined using the Equation 8.1, and dielectric relaxation frequency (f_j) values are so obtained. The f_j vs. T^{-1} curves and the relative fitting with Vogel-Tammann-Fulcher-Hesse (VTFH) or Arrhenius-like (A) equations [162] are shown in Figure 8.18.

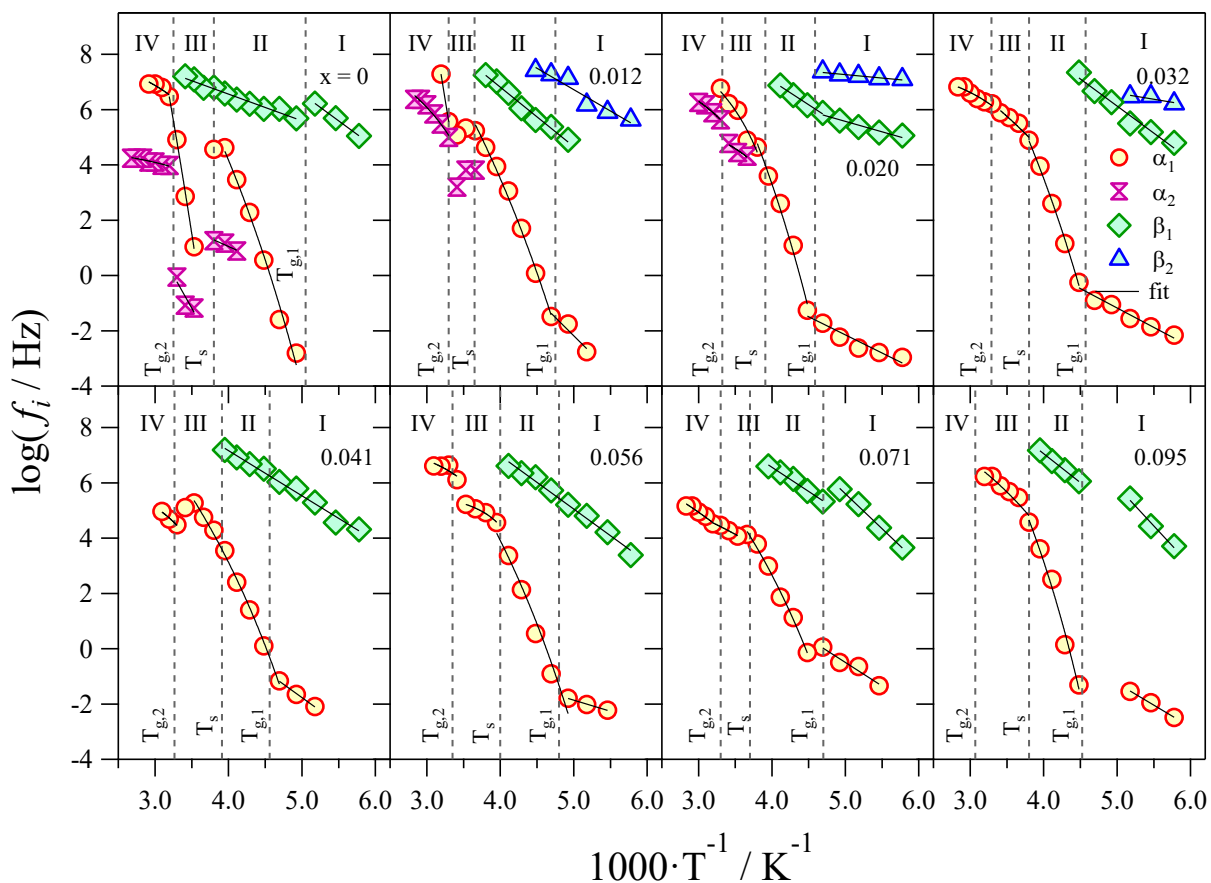


Figure 8.18. Log f_j vs. T^{-1} curves of each dielectric relaxation event for every sample. Temperature regions (I-IV) are divided by the transition temperatures of each sample detected with DSC measurements.

The same temperature regions observed for the polarization phenomena are detected also in Figure 8.18. The presence of four different dielectric relaxation events (f_j , with $1 \leq j \leq 4$) is determined. They consist of two α - and two β -mode relaxations. The α_1 dielectric relaxation is associated with the diffusion of rotational states along the main stacking axis of the cation pillars (Figure 8.19), while α_2 is attributed to the diffusion of conformational states along the direction of interacting butyl chains of nearby helices (Figure 8.19). The β_1 and β_2 relaxations are associated with the rotational motion around the short and the long axis of Pyr_{14}^+ (Figure 8.19), respectively. With respect to β_2 , β_1 takes place at a lower frequency due to the higher steric hindrance of the ordered butyl chains.

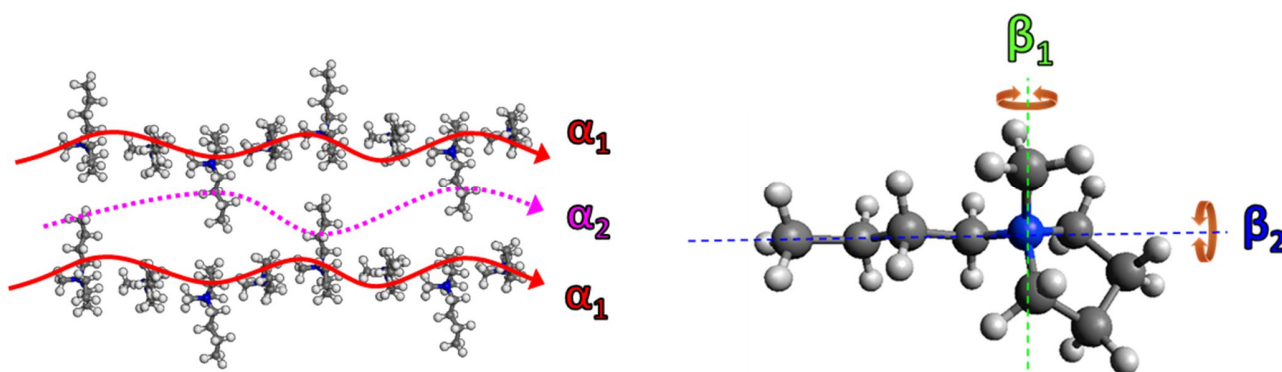


Figure 8.19. Representative cartoon of the dielectric relaxation events detected for these materials.

α_1 shows an Arrhenius trend at $T < T_{g,1}$ and a VTF trend at $T > T_{g,1}$, suggesting a modulation of the aggregate nanostructure. At $x \geq 0.032$, α_2 shifts to higher frequencies, exceeding the experimental range, indicating that the presence of $\delta\text{-MgCl}_2$ units raises the disorder between different aggregates and expand the volume of each domain. This is in line with the coordination network described by all the other characterizations, indicating that different measurements lead to the same hypothesized panorama. β relaxations show an Arrhenius trend over the entire temperature range, typical of the fluctuation of side chains.

8.2.4.3 Activation Energies

The values of the activation energy (E_a) associated with each polarization phenomenon and relaxation event, calculated by fitting the curves reported in Figure 8.15 and Figure 8.18 with a suitable model (*i.e.* Vogel-Tammann-Fulcher (VTF) [183], Vogel-Tammann-Fulcher-Hesse (VTFH) [162], or Arrhenius (A) equation [162]), are reported in Figure 8.20.

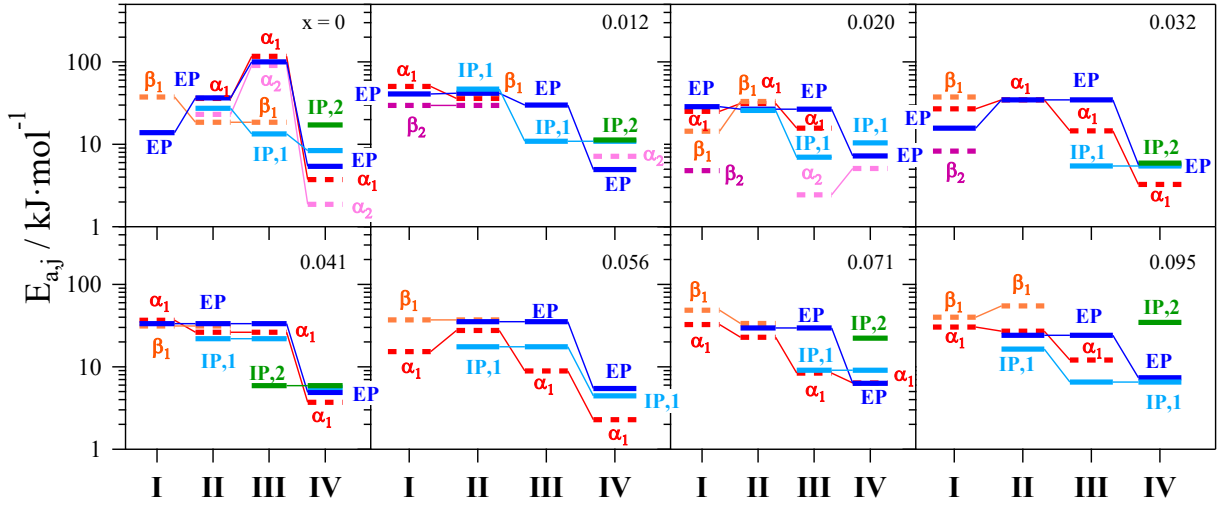


Figure 8.20. Activation energies calculated for each polarization phenomenon and relaxation event of every sample in the various temperature regions.

It is observed that σ_{EP} , the dominant contribution to the total conductivity, is predominantly correlated to α_1 dielectric relaxation in all the temperature regions and for all the samples. A correlation between σ_{EP} and α_2 is also observed for $x < 0.032$. Finally, it is determined that α_1 rules the conductivity along $\sigma_{IP,1}$ pathway, due to a similar E_a value for the two events, especially for samples with $x \geq 0.032$. The relaxation involving the rotational motions around the short axis of rod-like BuMePy⁺ cations (β_1) seems to contribute in the modulation of the long-range charge migration process at medium-low temperatures ($T_{g,1} \leq T \leq T_s$).

8.2.4.4 Diffusion Coefficient and Average Migration Distance

Final findings on the conductivity mechanism and the charge transfer processes occurring in the proposed electrolytes are given by assessing the temperature dependence of the diffusion coefficient (D_{σ_k}) and the average charge migration distance ($\langle r_k \rangle$). D_{σ_k} is calculated by using the Nernst-Einstein equation [49]:

$$D_{\sigma_k}(T_i) = \frac{RT_i \sigma_k}{Z_k^2 C_k F^2} \quad (8.3)$$

where R is the gas constant, T_i is each temperature at which D is evaluated, σ_k is the conductivity of the k^{th} polarization, Z_k and C_k correspond to the charge and concentration of the k^{th} species exchanged during the σ_k polarization, and F is the Faraday constant. The correlation between the

diffusion coefficient D_{σ_k} of each polarization, and the dielectric relaxation events, is derived from the Stokes-Einstein equation:

$$D_{\sigma_k}(T_i, \tau_j) = \frac{(k_b T_i)^{2/3}}{6\pi^{2/3} \tau_j^{1/3} \eta_i^{2/3}} \quad (8.4)$$

where k_b is the Boltzmann constant, τ_j is associated with the relaxation time of the j^{th} dielectric relaxation, and η is the viscosity of the system. Thus, if a polarization is in a relationship with a dielectric relaxation, a linear correlation between $\log(D_{\sigma_k})$ and $\log(f_j)$ is present. Results are shown in Figure 8.21.

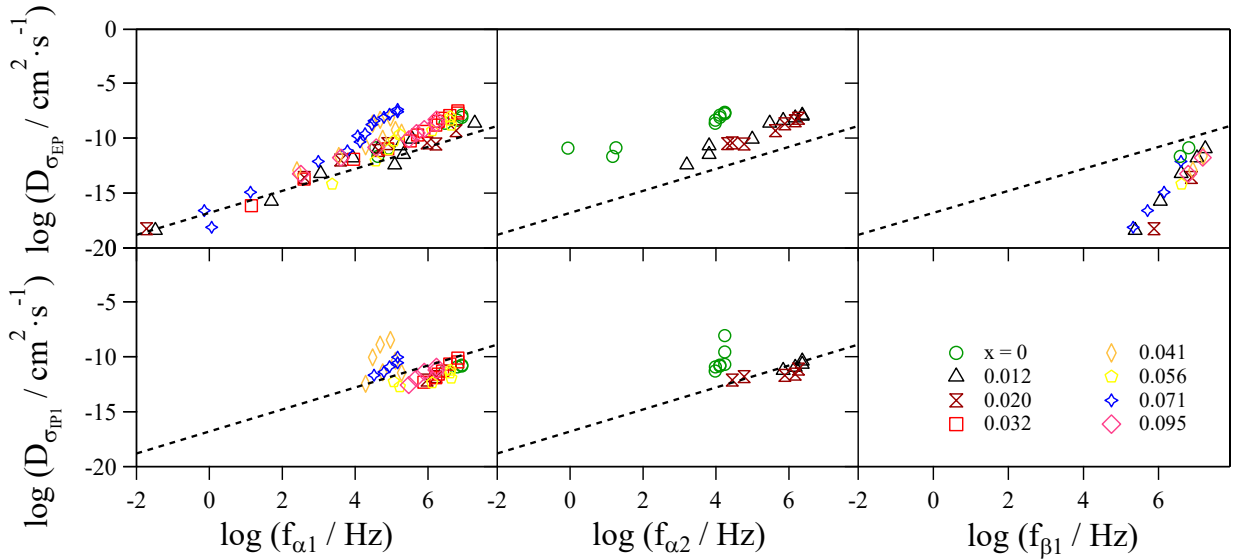


Figure 8.21. Diffusion coefficient calculated for each polarization (σ_{EP} , and $\sigma_{IP,1}$ rows), as a function of the dielectric relaxation frequencies ($f_{\alpha 1}$, $f_{\alpha 2}$, and $f_{\beta 1}$, columns). Dotted lines represent the ideal IL diffusion coefficient.

It is observed that both σ_{EP} and $\sigma_{IP,1}$ polarization phenomena are influenced by α_1 dielectric relaxation, while α_2 is correlated only to σ_{EP} . Thus, as already perceived, the segmental motions along the two directions (*i.e.* stacking axis, and butyl pendent groups) are essential to modulate the overall conductivity mechanism. On the contrary, β_1 dielectric relaxation is just slightly influencing the migration along σ_{EP} conductivity pathway.

The Einstein-Smoluchowski equation allows for the calculation of the average charge migration distance ($\langle r_k \rangle$) values:

$$\langle r_k \rangle(T_i) = \sqrt{6D_{\sigma_k} \tau_k} = \sqrt{\frac{6RT_i \sigma_k \tau_k}{Z_k^2 C_k F^2}} \quad (8.5)$$

where τ_k is the relaxation time of the σ_k polarization. Results are shown in Figure 8.22.

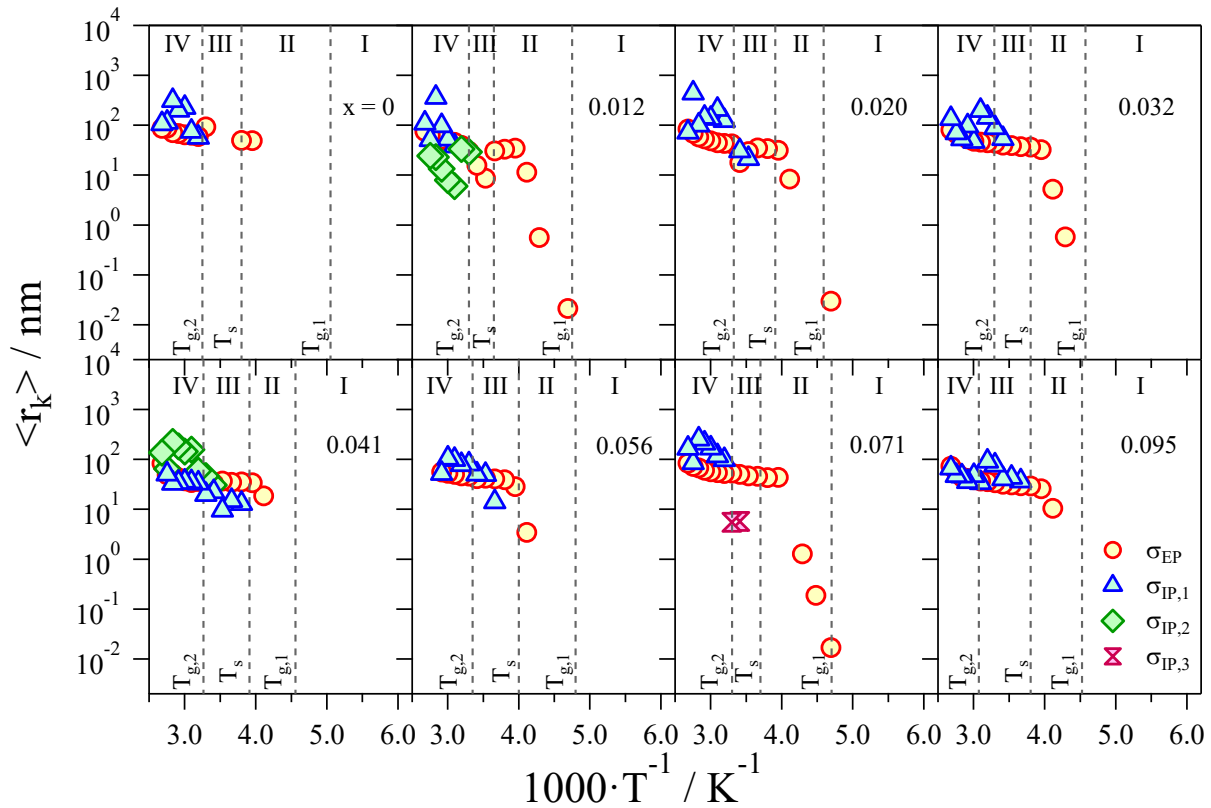


Figure 8.22. Average migration distance as a function of the temperature for σ_{EP} , $\sigma_{IP,1}$, $\sigma_{IP,2}$, and $\sigma_{IP,3}$.

It is demonstrated that the average migration distance increases as the temperature is raised. In region I ($T \leq -60 \text{ }^\circ\text{C}$) almost no conduction is detected, thus it is impossible to calculate the migration distance. In region II ($-60 \leq T \leq -15 \text{ }^\circ\text{C}$) the migration distance associated with the electrode polarization increases by almost four orders of magnitude (from 0.01 nm to 100 nm) as a function of temperature. Indeed, as mentioned above, a greater thermal energy allows for a more facilitated migration of ions. At these temperatures, $\langle r \rangle$ is not affected by the different magnesium concentrations. In region III ($-15 \leq T \leq 30 \text{ }^\circ\text{C}$) the migration distance values along the different percolation pathways (*i.e.* EP, IP,1, IP,2, and IP,3) are similar. A slight growth of $\langle r_k \rangle$ with increasing x is detected, in accordance with the higher disorder given by MgCl_2 units additions. At high temperatures ($T \geq 30 \text{ }^\circ\text{C}$, region IV), the highest migration distances are reached, since the exchange process of the ions is more facilitated in the liquid form of the ionic liquid.

8.2.4.5 Conductivity Mechanism

The BES measurements provide sufficient hints to describe in details the conductivity mechanism occurring in the proposed electrolyte, as a function of temperature and magnesium salt concentration. At low temperatures (region I), due to the absence of interdomain polarizations and to the presence of an Arrhenius behavior of σ_{EP} , the only possible conductivity mechanism is the “hopping” of anion species $[\text{BCl}_4\text{MgCl}_2]^-$ between different coordination sites. The migration distance cannot be calculated, but it is likely to be very small, indicating that, at these temperatures, the exchange of active species only happens in a short range. At the medium-low temperatures (region II), the interdomain polarization 1 starts to contribute to the total conductivity. The presence of the latter phenomenon confirms the formation of domains with different permittivity (*i.e.* cation and anion domains), as demonstrated by DFT and MM calculations, and FT-IR measurements. The conductivity along σ_{EP} pathway is modulated by α_1 and α_2 dielectric relaxations, while that along $\sigma_{IP,1}$ pathway is assisted by the α_1 dielectric relaxation. α_1 causes modifications of the helices conformational states, stimulating the exchange of the active species between different domains. In this temperature range, a rapid increase in the migration distance of $[\text{BCl}_4\text{MgCl}_2]^-$ dimeric species is observed, covering distances up to 90 nm. The exchange of active species within the various domains is so rapid that magnesium ions can be considered delocalized. Those domains where active species are delocalized are named Delocalization Bodies (DBs) [134]. At medium-high temperatures (region III), a drop in the conductivity is observed for the samples at low magnesium salt concentration, which is attributed to the structural reorganization that occurs after T_s thermal transition. Indeed, the new structure chokes the anion conductivity channels, inhibiting the exchange of active species. Nevertheless, by adding further amounts of δ - MgCl_2 , these channels are enlarged by the presence of long chain $(\text{MgCl}_2)_n$ complexes, preventing the obstructions arising from T_s thermal transition. The conductivity mechanism is similar to that occurring in region II, nevertheless the distances reached by active species is longer (*ca.* 90 nm). Finally, at high temperatures (region IV), the transition of the ionic liquid from solid to a viscous liquid promotes a more facile conductivity mechanism. Greater distances, up to 500 nm, are achieved, and long-range migration process is assisted by α_1 and α_2 dielectric relaxations, as demonstrated by the similar E_a values and the linear behavior of the diffusion coefficients. Moreover, the activation energy values in this temperature region are the very low (*ca.* 6 $\text{kJ}\cdot\text{mol}^{-1}$), denoting an efficient long-range charge migration event.

8.3 Conclusions

In this chapter the ability of BCl_4^- anions to reveal the structure of the surrounding network is exploited to study a family of new electrolytes for magnesium conduction, based on 1-butyl-1-methylpyrrolidinium chloride ionic liquid. Eight samples are obtained at different $\delta\text{-MgCl}_2$ salt concentrations, from $x = 0$ to $x = 0.095$ (with $x = n_{\text{Mg}}/n_{\text{IL}}$). The elemental composition is confirmed by ICP-AES analyses, while the thermal behavior is studied by HR-TGA and DSC measurements. Three different thermal events are detected (*i.e.* $T_{g,1}$, T_s , and $T_{g,2}$), which correspond to an increasing rotational disorder of the ion aggregates. It is found that $T_{g,2}$ is highly affected by the different additions of the magnesium salt. DFT and MM calculations: i) allow to obtain the optimized geometries of the complexes composing the electrolytes; ii) demonstrate that MgCl_2 units are coordinated to the anion of the ionic liquid; iii) cation and anion domains are present, and in particular cations are stacked one on the other forming helices; and iv) the addition of magnesium salt results in an increase of the distance between neighboring helices. FT-IR measurements reveal the presence of three different concentration regions: i) at low Mg concentration ($x < 0.032$), region A, as soon as the salt is added, MgCl_2 units are coordinated to BCl_4^- anions, forming $[\text{BCl}_4 \cdots \text{MgCl}_2]$ - dimers; ii) for $0.032 \leq x \leq 0.056$, region B, the new MgCl_2 added units are coordinated by those already bonded to the anions, forming the typical “*chain-like polymeric structure*” of $\delta\text{-MgCl}_2$; and iii) at high Mg concentrations ($x > 0.056$), region C, the maximum solubility of magnesium chloride chains is reached, thus the equilibrium shifts towards the formation of new dimers. Finally, BES studies: i) show that $[\text{BuMePyCl}/(\text{BCl}_3)_{0.25}]/(\delta\text{-MgCl}_2)_{0.041}$ sample exhibits the best total conductivity, with a value of $1.43 \cdot 10^{-4} \text{ S} \cdot \text{cm}^{-1}$ at 40°C ; ii) reveal that the electric response of $[\text{BuMePyCl}/(\text{BCl}_3)_{0.25}]/(\delta\text{-MgCl}_2)_x$ is modulated by four dielectric events (α_1 , α_2 , β_1 , and β_2) and four polarization phenomena (σ_{EP} , $\sigma_{\text{IP},1}$, $\sigma_{\text{IP},2}$, and $\sigma_{\text{IP},3}$); iii) demonstrate that the interdomain polarizations and the IL nanostructure are correlated; and iv) allow for the proposal of a reasonable conductivity mechanism, in which the diffusion of rotational states along the aggregation axis of Pyr_{14}^+ pillars (α_1) predominantly plays a crucial role in assisting the long-range exchange of Mg species between different aggregates.

9.A Novel Halotitanate Ionic Liquid for Magnesium Secondary Batteries

In this chapter, a set of new ionic liquid electrolytes based on $[\text{EMImCl}/(\text{TiCl}_4)_{1.4}]/(\delta\text{-MgCl}_2)_x$ are proposed for electrochemical applications. Here, the effects of the substitution of the metal, with respect to a similar family of electrolytes [57], are thoroughly studied. The electrolytes are synthesized by a direct reaction of 1-ethyl-3-methylimidazolium chloride (EMImCl) with titanium(IV) chloride (TiCl_4), followed by increasing additions of $\delta\text{-MgCl}_2$. The only detected thermal transition, a T_g at *ca.* $-36\text{ }^\circ\text{C}$, corresponds to a structural reorganization of the cation and anion aggregates. Vibrational studies demonstrate that, in the proposed materials, the anionic domains consist of large monomeric and dimeric 3D-catenated halotitanate aggregates. Magnesium chloride units are coordinated to Ti species, and the equilibrium concentration between the two species (monomer and dimer) is modulated by the different contents of the magnesium salt. Density functional theory (DFT) calculations allow to reveal the structural and coordination features occurring in Mg-chlorometallates species. In particular, vibrational analyses and DFT calculations agree in confirming: i) the presence of both the monomer and dimer species; and ii) the effective coordination of magnesium to halotitanate compounds. Broadband electrical spectroscopy (BES) measurements reveal that the electric response of these electrolytes consists of several polarization and different dielectric relaxation events. These measurements demonstrate the relationship existent between the conductivity mechanisms and the dielectric relaxation of the host matrix of the electrolytes. The best material, $[\text{EMImCl}/(\text{TiCl}_4)_{1.4}]/(\delta\text{-MgCl}_2)_{0.23}$, shows an ion conductivity of $2.15 \cdot 10^{-4}\text{ S cm}^{-1}$ at $40\text{ }^\circ\text{C}$. Finally, preliminary electrochemical tests reveal that the proposed electrolytes are able to deposit and strip a Mg-Ti alloy with high reversibility, high average coulombic efficiency (99.3 %), and a low overvoltage (10 mV).

9.1 Experimental Section

9.1.1 Reagents

1-ethyl-3-methylimidazolium chloride, EMImCl, is supplied from io·li·tec. Metallic magnesium (50 mesh), titanium tetrachloride, and 1-chlorobutane are purchased from Aldrich. The pristine ionic liquid is dried under vacuum at $105\text{ }^\circ\text{C}$ for 140 h, while 1-chlorobutane is further purified following

standard methods and stored under Argon on 4A molecular sieves to prevent moisture contamination. All transfer and handling operations are performed under a strictly argon atmosphere, either inside an argon-filled glove-box or by using a Schlenk line.

9.1.2 Synthesis

Anhydrous δ -MgCl₂ is obtained by direct reaction of metallic magnesium with 1-chlorobutane under a strictly anhydrous atmosphere, as described elsewhere [17]. The ionic liquid EMImCl/(TiCl₄)_{1.4} is obtained by slow drop by drop additions of titanium tetrachloride on EMImCl. The most concentrated sample ([EMImCl/(TiCl₄)_{1.4}]/(δ -MgCl₂)_{0.23}) is obtained by dissolving the 5.00 %wt of the magnesium salt into the pure ionic liquid (EMImCl/(TiCl₄)_{1.4}). Further dilutions with EMImCl/(TiCl₄)_{1.4} yield the [EMImCl/(TiCl₄)_{1.4}]/(δ -MgCl₂)_x electrolytes, thus obtaining a family of compounds with x ranging from 0 to 0.23. The composition of the obtained electrolytes is evaluated by ICP-AES measurements and results are reported in Table 9.1.

Table 9.1. Composition of [EMImCl/(TiCl₄)_{1.4}]/(δ -MgCl₂)_x electrolytes.

Sample	%wt IL	%wt δ -MgCl ₂	$x = n_{Mg}/n_{IL}^a$
0	100	0	0
1	98.9	1.1	0.05
2	97.8	2.2	0.10
3	95.0	5.0	0.23

^ax is defined as the ratio between the moles of magnesium (n_{Mg}) and the moles of the Ionic Liquid (n_{IL}), (EMImCl/(TiCl₄)_{1.4}).

9.2 Results and Discussion

9.2.1 Thermal Behavior

The thermal transitions of [EMImCl/(TiCl₄)_{1.4}]/(δ -MgCl₂)_x are detected by MDSC measurements and results are shown in Figure 9.1.

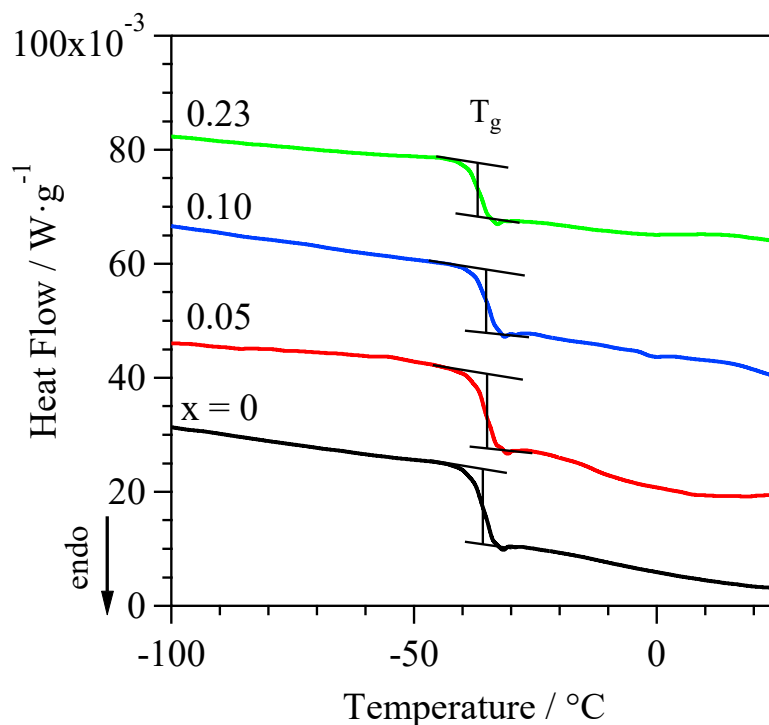


Figure 9.1. Modulated Differential Scanning Calorimetry profiles of $[\text{EMImCl}/(\text{TiCl}_4)_{1.4}]/(\delta\text{-MgCl}_2)_x$. The glass transition temperature (T_g) is indicated.

The MDSC curves reveal the presence of a T_g at *ca.* -36 °C, which is only slightly affected by the different $\delta\text{-MgCl}_2$ concentrations present into the materials. It is demonstrated in literature that similar systems show an analogous thermal behavior, where the T_g event is attributed to an order-disorder transition involving ordered cation pillars and anion aggregates [57, 266, 267], as represented in Figure 9.2.

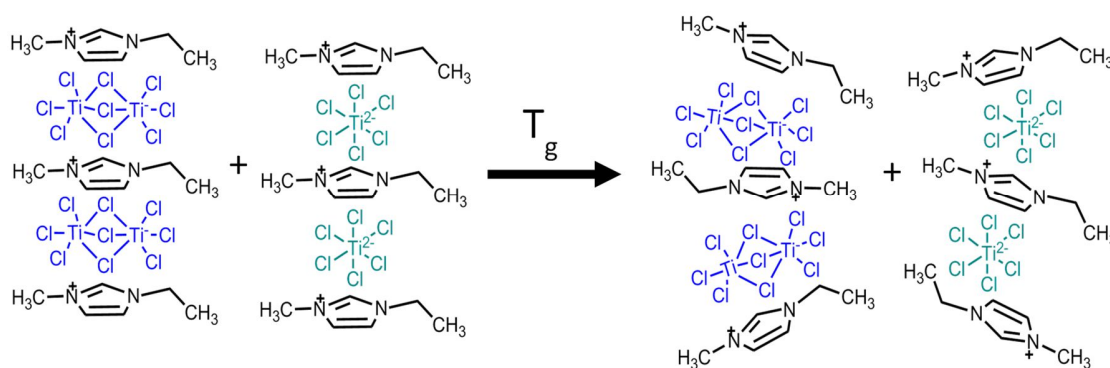


Figure 9.2. Thermal reorganization of the complexes after glass transition temperature.

Indeed, at $T < T_g$, $[\text{EMImCl}/(\text{TiCl}_4)_{1.4}]/(\delta\text{-MgCl}_2)_x$ electrolytes are characterized by an alternate cation-anion stacking sequence. At $T > T_g$, the anions and cations are reorganized into large

disordered aggregates [57]. Furthermore, the $[\text{EMImCl}/(\text{TiCl}_4)_{1.4}]/(\delta\text{-MgCl}_2)_x$ samples reveal that, increasing x , the extension of 3D-catenated network is augmented, due to the formation of anionic domains with a larger size and a higher charge delocalization. This phenomenon acts to improve the structural disorder of the electrolytes and to inhibit crystallization and melting transitions, that are not observed in the proposed materials.

9.2.2 DFT Calculations

Joining high-level density functional theory calculations with vibrational and electrical spectroscopic studies is crucial in understanding the structural features, host dynamics, and long-range charge transfer processes in the obtained electrolytes. In accordance with literature, DFT results reveal that in IL-based electrolytes the halotitanate complexes are present in two different forms: the monomer TiCl_6^{2-} , and the dimer Ti_2Cl_9^- [268]. Using these structures as a starting point, the ionic cluster geometries are optimized both before, and after $\delta\text{-MgCl}_2$ addition (Figure 9.3).

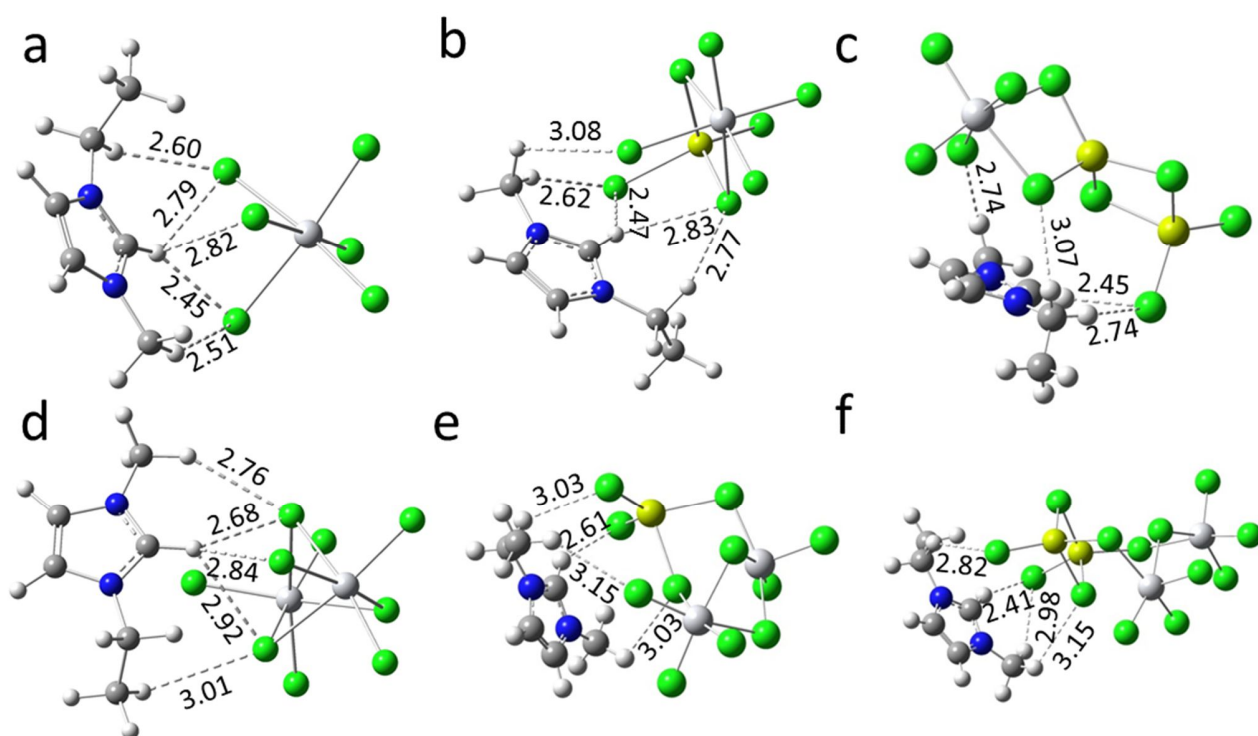


Figure 9.3. Optimized geometries of the electrolyte complexes determined at the B3LYP/6-311G** level of theory. $\text{EMIm}^+[\text{TiCl}_6]^{2-}$ (a); $\text{EMIm}^+[\text{TiCl}_6\text{MgCl}_2]^{2-}$ (b); $\text{EMIm}^+[\text{TiCl}_6\text{MgCl}_2\text{MgCl}_2]^{2-}$ (c); $\text{EMIm}^+[\text{Ti}_2\text{Cl}_9]^-$ (d); $\text{EMIm}^+[\text{Ti}_2\text{Cl}_9\text{MgCl}_2]^-$ (e);

EMIm⁺[Ti₂Cl₉MgCl₂MgCl₂]⁻ (f). Color code: H atoms, white; N atoms, blue; C atoms, black; Cl atoms, green; Ti atoms, grey; Mg atoms, yellow. H...Cl distances, in angstroms, are reported.

Both the monomeric and the dimeric titanium-based anions are preferentially coordinated to the imidazolium cation through Cl...H bonding at the (2) position of the [EMIm]⁺ ring, rather than at the (4) or (5) positions. The addition of one or two units of δ -MgCl₂ to [EMImCl/(TiCl₄)] compound results in the formation of large 3D-catenated halotitanate anionic clusters, in which magnesium chloride is coordinated to Ti species. The calculated vibrational frequencies of the EMIm⁺[TiCl₆MgCl₂MgCl₂]²⁻ and EMIm⁺[Ti₂Cl₉MgCl₂MgCl₂]⁻ complexes, where two δ -MgCl₂ units are present, are in better agreement with the experimental results than those calculated using the complexes that contain only one equivalent of δ -MgCl₂ (see section 9.2.3). These results support the hypothesis that the catenated structures of pristine δ -MgCl₂ and TiCl₄ [269, 270] are kept even when part of the anionic complexes of the electrolyte materials. The comparisons between the experimental and computed vibrational frequencies in the Far-IR and Raman spectral regions are reported in section 9.2.3.

9.2.3 Vibrational Studies

The medium FT-IR, far FT-IR, and Raman spectra are used in together with DFT calculations to recognize the structure and coordination of the ionic species occurring in the [EMImCl/(TiCl₄)_{1.4}]/(δ -MgCl₂)_x electrolytes. FT-MIR spectra are normalized with the peak centered at *ca.* 3144 cm⁻¹, FT-FIR with the one at *ca.* 596 cm⁻¹, and micro-Raman with the peak detected at *ca.* 3168 cm⁻¹.

9.2.3.1 Fourier-Transform Infrared Spectroscopy

In the medium FT-IR region the diagnostic bands of the EMIm⁺ cation can be found. The spectra are shown in Figure 9.4.

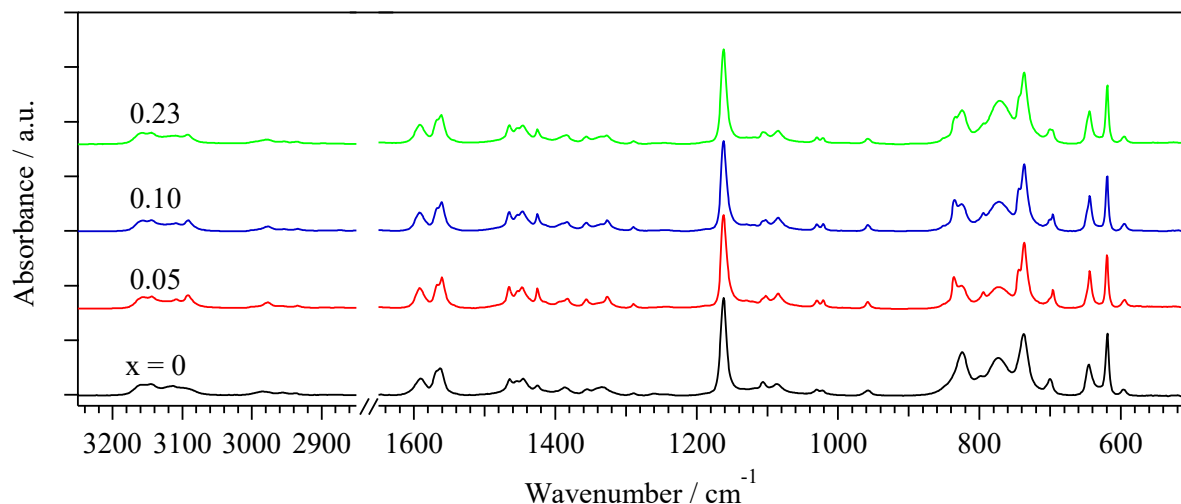


Figure 9.4. Mid-IR spectra of $[\text{EMImCl}/(\text{TiCl}_4)_{1.4}/(\delta\text{-MgCl}_2)_x$ electrolytes.

When EMIm^+ cations are isolated, the ring C-H stretching modes (C(2)-H, C(4)-H, and C(5)-H) are all degenerate, and should be centered at *ca.* 3170 cm^{-1} [271]. When they are coordinated to the anion, the degeneracy is lost, and a shift of the C(2)-H band towards lower wavenumbers is observed (at *ca.* 3099 cm^{-1}) [271]. The C(4)-H and C(5)-H *in-phase* and *out-of-phase* stretching bands are detected at 3158 cm^{-1} and 3144 cm^{-1} , respectively. The shift in the C(2)-H stretching band is revealing of the hydrogen-bonding interactions occurring between the cation and the anion [271]. The addition of magnesium chloride results in a further shift of the C(2)-H band to 3091 cm^{-1} , whilst the C-H stretching bands of C(4)-H and C(5)-H remain unaffected. This change demonstrates that the doping with the magnesium salt alters the hydrogen-bonding network in which the C(2) hydrogen atom is involved [271]. Indeed, this is supported by the DFT calculations. The C-H stretching modes (ν) of ethyl and methyl groups of EMIm^+ cations are assigned as follows: i) the antisymmetrical stretching of the methyl group centered at *ca.* 2977 cm^{-1} ; ii) the antisymmetrical stretching of the CH_3 of the ethyl group peaking at *ca.* 2955 cm^{-1} ; and iii) the symmetrical CH_2 stretching of the ethyl group detected at *ca.* 2935 cm^{-1} [271-274]. The complete assignment of the vibrations detected in the mid FT-IR is summarized in Table 9.2.

Table 9.2. Mid-IR vibrational frequencies assignment for [EMImCl/(TiCl₄)_{1.4}]/(δ-MgCl₂)_x electrolytes.

x = 0 ^a	Experimental frequencies / cm ⁻¹			Assignment ^b	Ref.
	0.05 ^a	0.10 ^a	0.23 ^a		
3158 (w)	3156 (w)	3157 (w)	3158 (w)	v(C4-H), v(C5-H) (in phase)	[271, 274]
3145 (w)	3144 (w)	3144 (w)	3144 (w)	v(C4-H), v(C5-H) (out of phase)	[271, 274]
3099 (w,sh)	3091 (w)	3091 (w)	3092 (w)	v(C2-H)	[271, 273, 274]
3009 (vw,sh)	2999 (vw,sh)	3000 (vw,sh)	2996 (vw,sh)	v _a (CH ₃),v(CH ₂)	[271, 274]
2985 (vw)	2982 (vw,sh)	2980 (vw,sh)		v _a (CH ₃),v(CH ₂)	[271, 274]
2979 (vw,sh)	2977 (vw)	2977 (vw)	2979 (vw)	v _a (CH ₃) (Me)	[271, 274]
2955 (vw)	2956 (vw,sh)	2955 (vw,sh)	2954 (vw,sh)	v _a (CH ₃) (Et)	[271, 274]
2937 (vw)	2934 (vw)	2934 (vw)	2935 (vw)	v _s (CH ₂)	[271, 274]
1590 (m)	1592 (m)	1592 (m)	1591 (m)	v _{a,ring} (N-CH ₂),v _{a,ring} (N-CH ₃ CN),(in phase)	[272]
1568 (m,sh)	1567 (m)	1567 (m,sh)	1567 (m,sh)	v C=C	[271, 274]
1563 (m)	1560 (m)	1561 (m)	1561 (m)	v _a (N1C2N3),v(C2H)	[271, 274]
1465 (m)	1466 (m)	1466 (m)	1465 (m)	δ _a (CH ₃) (Et)	[271, 274]
1454 (w)	1453 (w,sh)	1453 (m,sh)	1453 (m,sh)	δ _a (CH ₃) (Me)	[271, 274]
1445 (m)	1447 (m)	1446 (m)	1445 (m)	δ _a (CH ₃) (Et)	[271, 274]
1425 (w)	1425 (m)	1425 (m)	1425 (m)	δ _s (CH ₃)	[271, 274]
1414 (vw,sh)	1414 (vw,sh)	1414 (vw,sh)	1416 (vw,sh)	δ(CH ₂),v(ring)	[271, 274]
1398 (vw,sh)	1393 (vw,sh)	1393 (vw,sh)	1390 (vw,sh)	δ _s (CH ₃) (Et),ω(CH ₂)	[271, 274]
1387 (w)	1383 (w)	1384 (w)	1384 (w)	v _a (C2N1C5),δ _s (CH ₃) (Et)	[271, 274]
1355 (vw)	1357 (w)	1356 (w)	1356 (w)	ω(CH ₂)	[271, 274]
1334 (w)	1327 (w)	1326 (w)	1327 (w)	v(N-Et),v(N-Me),breathing	[271, 274]
1289 (vw)	1289 (vw)	1289 (vw)	1289 (vw)	ρ(C4-H),ρ(C5-H),τ(CH ₂)	[271, 274]
1244 (vw)	1240 (vw)	1247 (vw)	1243 (vw)	ρ(C2-H)	[271, 274]
1162 (vs)	1162 (vs)	1162 (vs)	1162 (vs)	ρ(C2-H),ρ(C4-H),v(N-Et),v(N-Me)	[271, 274]
	1129 (w)	1130 (vw)	1129 (w)	ρ(CH ₂),ρ(CH ₃) (Et)	[271, 274]
1118 (w,sh)	1121 (w)	1121 (vw)	1121 (vw)	ρ(CH ₃)	[271, 274]
1106 (w)	1107 (w,sh)	1106 (w,sh)	1106 (w)	ρ(CH ₃)	[271, 274]
1086 (w)	1084 (w)	1085 (w)	1085 (w)	ρ(CH ₃)	[271, 274]
1030 (vw)	1030 (vw)	1030 (vw)	1030 (vw)	δ(ring)	[271]
1022 (vw)	1021 (vw)	1021 (vw)	1021 (vw)	v(N-Et),v(N-Me),breathing	[271, 274]
958 (vw)	958 (vw)	958 (vw)	958 (vw)	v(C-C) (Et)	[271, 274]
	851 (vw,sh)	851 (vw,sh)	851 (vw,sh)	γ(CH)	[271]
	836 (s)	836 (m)	834 (m)	δ _{a,ring} (HCCH)	[272]
824 (s)	825 (m)	825 (m)	824 (s)	δ(CC)	[272]
798 (m,sh)	795 (w)	795 (w)	795 (m)	ρ(CH ₂),ρ(CH ₃) (Et)	[271, 274]
738 (s)	737 (vs)	737 (vs)	737 (vs)	δ _{s,ring} (HCCH)	[272]
700 (m)	701 (w,sh)	700 (w,sh)	700 (w)	v(N-Et),v(N-Me)	[271, 274]
	696 (m)	696 (w)	696 (w)	v(N-Et),v(N-Me)	[271, 274]
645 (m)	644 (s)	644 (m)	644 (m)	γ(N-Et),γ(N-Me),ring puckering	[271, 274]
619 (s)	620 (s)	619 (s)	619 (vs)	γ(N-Me),ring puckering	[271, 274]
596 (vw)	595 (vw)	595 (vw)	595 (vw)	v(N-Et),v(n-Me)	[271, 274]

^avs = very strong, s = strong, m = medium, w = weak, vw = very weak, sh = shoulder. ^bv = stretching, δ = bending, ω = wagging, ρ = rocking, τ = twisting, γ = out-of-plane, a = antisymmetrical, s = symmetrical.

The bands diagnostic of the structural features of the halotitanate anions of [EMImCl/(TiCl₄)_{1.4}]/(δ-MgCl₂)_x samples appear in the far FT-IR (Figure 9.5).

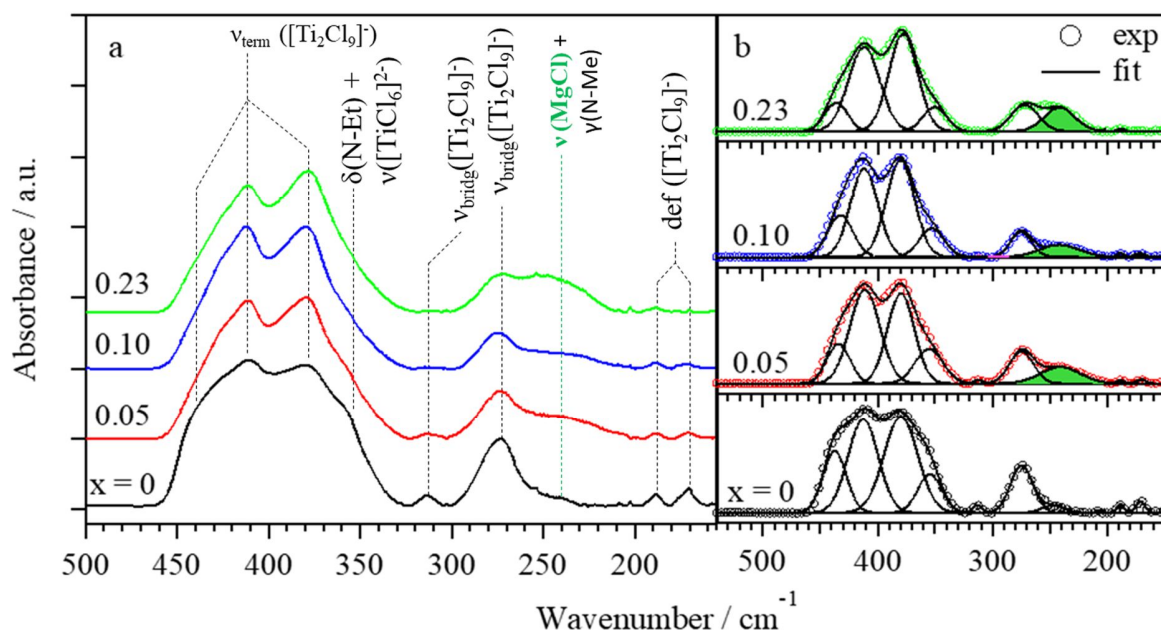


Figure 9.5. Far infrared spectra and vibrational assignment of $[\text{EMImCl}/(\text{TiCl}_4)_{1.4}]/(\delta\text{-MgCl}_2)_x$ samples in the range $150\div 500\text{ cm}^{-1}$; ν = stretching, δ = bending, γ = out-of-plane, def = deformation (a). Gaussian decomposition of the far-IR spectra in the region $150\div 500\text{ cm}^{-1}$. The band corresponding to the $\nu(\text{Mg-Cl})$ is highlighted in green. Colored circles represent the experimental data and black lines are the fitting curves (b).

The terminal Ti-Cl stretching modes of the dimeric Ti_2Cl_9^- anion ($\nu_{\text{term}}[\text{Ti}_2\text{Cl}_9^-]$) are detected in the range $380\div 450\text{ cm}^{-1}$. The Ti-Cl stretching vibrations of the chloride bridge in the dimer ($\nu_{\text{bridg}}[\text{Ti}_2\text{Cl}_9^-]$) are observed at *ca.* 312 and 275 cm^{-1} , while the deformation modes of the terminal and bridging Ti-Cl groups ($\delta[\text{Ti}_2\text{Cl}_9^-]$) are found at *ca.* 189 and 171 cm^{-1} , respectively [275]. The decrease in the intensity of these four peaks increasing the $\delta\text{-MgCl}_2$ concentration reveals that, at each x , there is shift in the equilibrium between the dimeric and the monomeric forms of the halotitanate complexes. At low $\delta\text{-MgCl}_2$ concentration, this equilibrium leans toward the formation of dimeric Ti_2Cl_9^- species, while at high x the monomeric TiCl_6^{2-} species are preferentially formed. Centered at *ca.* 242 cm^{-1} , the out-of-plane $\gamma(\text{N-Me})$ and the ring puckering vibrational modes overlap with the Mg-Cl stretching mode ($\nu(\text{Mg-Cl})$) [17, 271, 274]. Since the $\gamma(\text{N-Me})$ contribution remains constant, the growth in the intensity of this band on x reveals the increased magnitude of the $\nu(\text{Mg-Cl})$ contribution, and therefore the increasing density of magnesium-chloride covalent bonds within materials [276]. Moreover, the calculated stretching frequencies of $\nu(\text{Mg-Cl})$ for the complexes where two units of $\delta\text{-MgCl}_2$ per complex species are present, are in better agreement with the experimental results than those where only one unit of $\delta\text{-MgCl}_2$ is added. Thus, the

magnesium chloride in anionic aggregates is not present as a monomeric species, but it maintains the polymeric structure of $[\text{MgCl}_2]_n$ chains. The complete assignments of the calculated and experimental FT-FIR vibrational modes are summarized in Table 9.3.

Table 9.3. Far-IR vibrational frequencies assignment for $[\text{EMImCl}/(\text{TiCl}_4)_{1.4}]/(\delta\text{-MgCl}_2)_x$ electrolytes.

$x = 0^a$	Experimental frequencies / cm^{-1}			Calculated frequencies / cm^{-1} at B3LYP/6-31G**		Assignment ^d	Ref.
	0.05 ^a	0.10 ^a	0.23 ^a	IL ^b	IL+ δMgCl_2^c		
596 (vw)	595 (vw)	596 (vw)	596 (vw)			$\nu(\text{N-Et}), \nu(\text{n-Me})$	[271, 274]
437 (s,sh)	434 (s,sh)	432 (s,sh)	436 (s,sh)	432	442	$\nu_{\text{a,terminal}}(\text{Cl-Ti})$ ($[\text{Ti}_2\text{Cl}_9]^-$)	[275, 277]
413 (vs)	411 (vs)	412 (vs)	412 (vs)	418	413	$\nu_{\text{s,terminal}}(\text{Cl-Ti})$ ($[\text{Ti}_2\text{Cl}_9]^-$)	[277]
380 (vs)	380 (vs)	380 (vs)	378 (vs)	380	383	$\nu_{\text{terminal}}(\text{Cl-Ti})$ ($[\text{Ti}_2\text{Cl}_9]^-$)	[277]
355 (s,sh)	355 (s,sh)	353 (m,sh)	351 (m,sh)	354	354	$\delta(\text{N-Et}) + \nu(\text{Cl-Ti})$ ($[\text{TiCl}_6]^{2-}$)	[271, 274]
313 (m)	312 (m)	312 (w)	310 (vw)	280	316	$\nu_{\text{bridging}}(\text{Cl-Ti})$ ($[\text{Ti}_2\text{Cl}_9]^-$)	[277]
275 (s)	275 (m)	275 (m)	272 (m)	263	275	$\nu_{\text{bridging}}(\text{Cl-Ti})$ ($[\text{Ti}_2\text{Cl}_9]^-$)	[275, 277]
247 (m)	241 (m)	242 (m)	242 (m)	234	247	$\gamma(\text{N-Me}), \text{ring}$ puckering+ $\nu(\text{Mg-Cl})$	[17, 271, 274]
189 (vw)	188 (vw)	189 (vw)	188 (vw)	188	181	deformation (Ti-Cl) ($[\text{Ti}_2\text{Cl}_9]^-$)	[275]
171(vw)	171 (vw)	172 (vw)	175 (vw)	178	174	deformation (Ti-Cl) ($[\text{Ti}_2\text{Cl}_9]^-$)	[275]

^avs = very strong, s = strong, m = medium, w = weak, vw = very weak, sh = shoulder. ^b ν = stretching, δ = bending, ω = wagging, ρ = rocking, τ = twisting, γ = out-of-plane, a = antisymmetrical, s = symmetrical.

In Figure 9.6 the confocal Raman spectra of the $[\text{EMImCl}/(\text{TiCl}_4)_{1.4}]/(\delta\text{-MgCl}_2)_x$ electrolytes are shown.

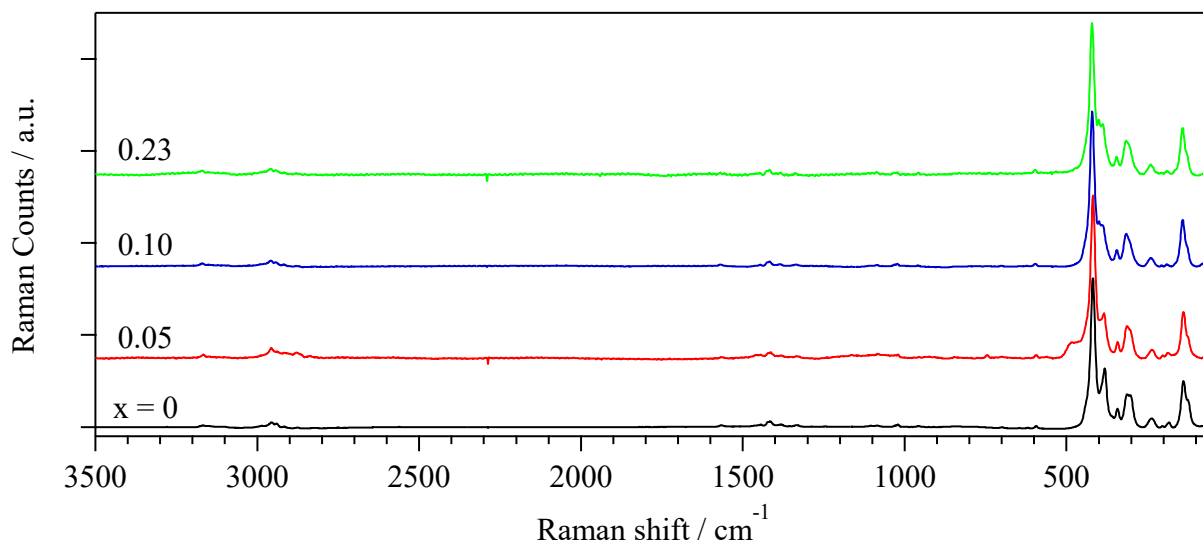


Figure 9.6. Raman spectra of $[\text{EMImCl}/(\text{TiCl}_4)_{1.4}/(\delta\text{-MgCl}_2)_x$ electrolytes in the full range of analysis.

The vibrations assigned to both the monomeric (TiCl_6^{2-}) and dimeric (Ti_2Cl_9^-) species, as suggested by DFT calculations, are clearly detected. For the monomer, the antisymmetrical stretching ($\nu_a[\text{TiCl}_6]^{2-}$) and bending ($\delta_a[\text{TiCl}_6]^{2-}$) vibrational modes appear at *ca.* 317 and 189 cm^{-1} [277-279]. The dimer reveals the presence of several bands, associated with the different stretching and bending vibrational modes: i) Ti-Cl terminal stretching modes ($\nu_{\text{term}}[\text{Ti}_2\text{Cl}_9]^-$) at *ca.* 421, 400, and 388 cm^{-1} ; ii) Ti-Cl bridging stretching mode ($\nu_{\text{bridg}}[\text{Ti}_2\text{Cl}_9]^-$) at *ca.* 305 and 206 cm^{-1} ; and iii) the deformation $\delta([\text{Ti}_2\text{Cl}_9]^-)$, at *ca.* 141 and 128 cm^{-1} . Peaks observed above 500 cm^{-1} are all assigned to the imidazolium (EMIm^+) vibrational modes. A complete assignment of the Raman bands is reported in Table 9.4.

Table 9.4. Raman vibrational frequencies assignment for [EMImCl/(TiCl₄)_{1.4}]/(δ-MgCl₂)_x electrolytes.

x = 0 ^a	Experimental frequencies / cm ⁻¹			Calculated frequencies / cm ⁻¹ at B3LYP/6-31G**		Assignment ^d	Ref.
	0.05 ^a	0.10 ^a	0.23 ^a	IL ^b	IL+δMgCl ₂ ^c		
3168 (vw)	3166 (vw)	3170 (vw)	3170 (vw)			v(C4-H), v(C5-H) (in phase)	[271, 274]
2986 (vw)		2990 (vw,sh)				v _a (CH ₃ ,CH ₂)	[271, 274]
2956 (vw)	2957 (vw)	2958 (vw)	2957 (vw)			v _a (CH ₃) (Me)	[271, 274]
2940 (vw)	2939 (vw)	2942 (vw)	2942 (vw)			v _a (CH ₃) (Et)	[271, 274]
2916 (vw)	2917 (vw)	2918 (vw)	2916 (vw)			v _s (CH ₂)	[271, 274]
2876 (vw)	2878 (vw)	2880 (vw)	2876 (vw)			v _s (CH ₃) (Et)	[271, 274]
1567 (vw)	1567 (vw)	1569 (vw)	1568 (vw)			v _a (N1C2N3),v(C2H)	[271, 274]
1462 (vw,sh)	1462 (vw,sh)	1462 (vw,sh)	1462 (vw,sh)			δ _a (CH ₃) (Et)	[271, 274]
1445 (vw)	1445 (vw)	1447 (vw)	1448 (vw)			δ _a (CH ₃) (Et)	[271, 274]
1423 (vw,sh)	1421 (vw,sh)	1423 (vw,sh)	1426 (vw,sh)			δ _s (CH ₃)	[271, 274]
1415 (vw)	1414 (vw)	1417 (vw)	1417 (vw)			δ(CH ₂),v ring	[271, 274]
	1396 (vw)	1399 (vw)	1399 (vw)			δ _s (CH ₃) (Et),ω(CH ₂)	[271, 274]
1382 (vw)	1381 (vw)	1384 (vw)	1383 (vw)			v _a (C2N1C5),δ _s (CH ₃) (Et)	[271, 274]
1354 (vw,sh)	1352 (vw)					ω(CH ₂)	[271, 274]
1331 (vw)	1334 (vw)	1337 (vw)	1339 (vw)			v(N-Et),v(N-Me),breathing	[271, 274]
1288 (vw)	1288 (vw)	1287 (vw)	1285 (vw)			ρ(C4-H),ρ(C5-H),τ(CH ₂)	[271, 274]
1244 (vw)	1242 (vw)	1244 (vw)	1241 (vw)			ρ(C2-H)	[271, 274]
1162 (vw)	1163 (vw)	1165 (vw)	1165 (vw)			ρ(C2-H),ρ(C4-H),v(N-Et),v(N-Me)	[271, 274]
1105 (vw)	1106 (vw)	1107 (vw)	1109 (vw)			ρ(CH ₃)	[271, 274]
1085 (vw)	1082 (vw)	1086 (vw)	1087 (vw)			ρ(CH ₃)	[271, 274]
1028 (vw,sh)	1030 (vw,sh)	1031 (vw,sh)	1032 (vw)			δ(ring)	[271]
1021 (vw)	1020 (vw)	1023 (vw)	1023 (vw)			v(N-Et),v(N-Me),breathing	[271, 274]
956 (vw)	955 (vw)	959 (vw)	956 (vw)			v(C-C) (Et)	[271, 274]
	485 (m,sh)					v _s +δ _s ([Ti ₂ Cl ₉] ⁻)	[275]
426 (m)	424 (m)	426 (m)	426 (m)	432	442	v _{terminal} (Cl-Ti) ([Ti ₂ Cl ₉] ⁻)	[275, 277]
417 (vs)	418 (vs)	421 (vs)	421 (vs)	418	413	v _{terminal} (Cl-Ti) ([Ti ₂ Cl ₉] ⁻)	[277]
390 (m,sh)	394 (m,sh)	400 (m)	400 (m)	391	392	v _{terminal} (Cl-Ti) ([Ti ₂ Cl ₉] ⁻)	[277]
382 (m)	383 (m)	388 (m)	386 (m)	380	383	v _{terminal} (Cl-Ti) ([Ti ₂ Cl ₉] ⁻)	[277]
343 (w)	342 (w)	345 (w)	345 (w)	338	354	δ(N-Et)+v(Cl-Ti) ([TiCl ₆] ²⁻)	[271, 274]
314 (m)	314 (m)	317 (m)	317 (m)	332	321	v _a (Cl-Ti) ([TiCl ₆] ²⁻)	[277-279]
301 (m)	302 (m,sh)	304 (m,sh)	305 (m,sh)	280	315	v _{bridging} (Cl-Ti) ([Ti ₂ Cl ₉] ⁻)	[275, 277]
237 (w)	236 (w)	238 (w)	239 (w)	234	237	γ(N-Me)+v(Mg-Cl)	[17, 271, 274]
204 (vw)	203 (vw)	206 (vw)	207 (vw)	206	217	v _{bridging} (Cl-Ti) ([Ti ₂ Cl ₉] ⁻)	[275]
185 (w)	186 (vw)	190 (vw)	190 (vw)	181	177	δ _a ([TiCl ₆] ²⁻)	[277-279]
139 (m)	139 (m)	141 (m)	141 (m)	138	134	deformation (Ti-Cl) ([Ti ₂ Cl ₉] ⁻)	[275]
124 (m,sh)	124 (m,sh)	127 (w,sh)	127 (w,sh)	124	123	deformation (Ti-Cl) ([Ti ₂ Cl ₉] ⁻)	[275]

^avs = very strong, s = strong, m = medium, w = weak, vw = very weak, sh = shoulder. ^bCalculated frequencies at B3LYP/6-31G** for [EMImCl]/(TiCl₄)_{1.4}/(δ -MgCl₂)₀ sample. ^cCalculated frequencies at B3LYP/6-31G** for [EMImCl]/(TiCl₄)_{1.4}/(δ -MgCl₂)_x (0.05 \leq x \leq 0.23) samples. ^dv = stretching, δ = bending, γ = out-of-plane, a = antisymmetrical.

The vibration peaking at *ca.* 317 cm⁻¹, assigned to the Ti-Cl antisymmetrical stretching mode of the dimer, and the peak centered at *ca.* 305 cm⁻¹, attributed to the stretching mode of the Ti-Cl bridge in the dimer, can be used to evaluate the relative abundance of each species at each x value. Indeed, as x increases, it can be observed a shift in the monomer-dimer equilibrium toward the formation of the monomer (Figure 9.7).

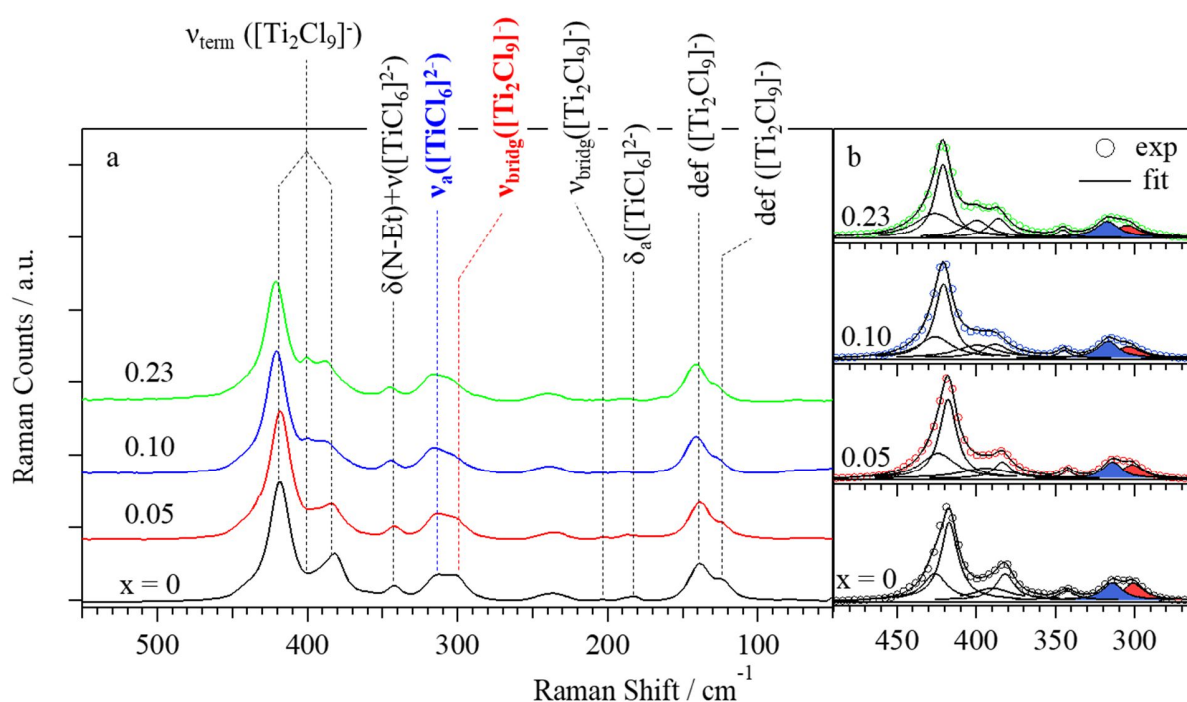


Figure 9.7. Raman spectra and vibrational assignment of [EMImCl]/(TiCl₄)_{1.4}/(δ -MgCl₂)_x samples in the range 50–550 cm⁻¹; ν = stretching, δ = bending, def = deformation (a). Lorentzian decomposition of the Raman spectra in the region 260–490 cm⁻¹. The peak of the antisymmetrical stretching (ν_a) of TiCl₆²⁻ is highlighted in blue. The band of the bridging stretching (ν_{bridge}) of Ti₂Cl₉⁻ is highlighted in red. Colored circles represent the experimental data and black lines are the fitting curves (b).

Raman spectroscopy results are in good agreement with those of infrared spectroscopy. In order to perform a semi-quantitative analysis of the ratio between the monomer and dimer species at each x value, the Raman curves of Figure 9.7a are decomposed with Lorentzian peaks (see Figure 9.7b). The fraction of dimers, Φ , with $\Phi = A_{\text{Ti}_2\text{Cl}_9^-} / (A_{\text{Ti}_2\text{Cl}_9^-} + A_{\text{TiCl}_6^{2-}})$, where $A_{\text{Ti}_2\text{Cl}_9^-}$ corresponds to the area of the peak related to the vibrational mode of Ti₂Cl₉⁻, and $A_{\text{TiCl}_6^{2-}}$ is the area of the peak associated with the TiCl₆²⁻ vibrational mode, is plotted vs. x in Figure 9.8. Results demonstrate that

the addition of $\delta\text{-MgCl}_2$ salt shifts the equilibrium of anionic species towards the formation of the monomeric TiCl_6^{2-} , thus diminishing the concentration of the dimeric Ti_2Cl_9^- halotitanate species. This result agrees with studies carried out in analogous IL-halometallate- $\delta\text{-MgX}_2$ electrolytes [57, 133].

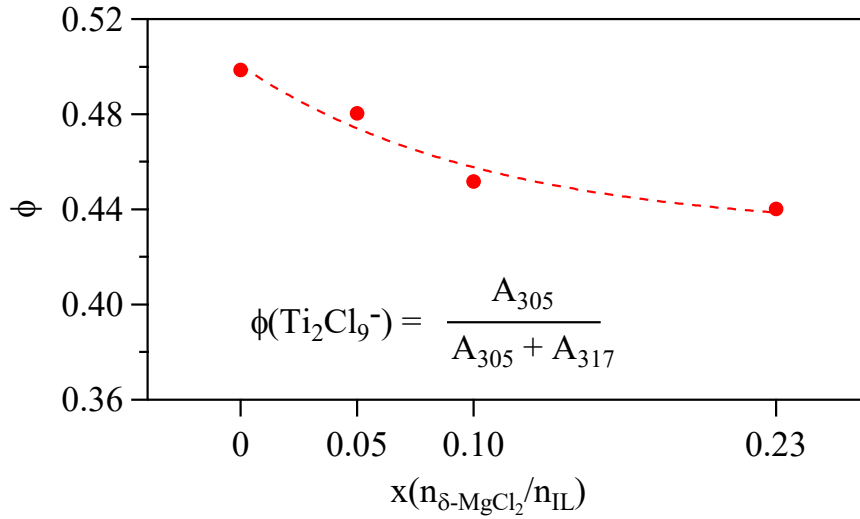


Figure 9.8. Φ molar ratio on x of $[\text{EMImCl}/(\text{TiCl}_4)_{1.4}]/(\delta\text{-MgCl}_2)_x$ electrolytes.

9.2.4 Broadband Electrical Spectroscopy Studies

The electric response of the electrolytes, in terms of polarization and relaxation phenomena, is studied by broadband electrical spectroscopy (BES). Particular interest is devoted to the understanding of the interplay between the conductivity mechanism and the IL nanostructure, thus revealing important insights into the long-range charge migration process.

Measurements are collected from -130 to 100 °C and in the frequency range of 10^{-2} to 10^7 Hz. The spectra of the complex permittivity vs. T and f are fitted with the following empirical equation:

$$\varepsilon^*(\omega) = i \left(\frac{\sigma_0}{\varepsilon_0 \omega} \right)^N + \sum_{k=1}^4 \frac{\sigma_k (i\omega\tau_k)^{\gamma_k}}{i\omega\varepsilon_0 [1 + (i\omega\tau_k)^{\gamma_k}]} + \sum_{j=1}^4 \frac{\Delta\varepsilon_j}{i\omega [1 + (i\omega\tau_j)^{\alpha_j}]^{\beta_j}} + \varepsilon_\infty \quad (9.1)$$

where $\varepsilon^*(\omega) = \varepsilon'(\omega) - i\varepsilon''(\omega)$ ($\sigma^*(\omega) = i\omega\varepsilon_0\varepsilon^*(\omega)$). The first term of eq. 1 is related to the material conductivity at zero frequency (outside the measurement frequency region). ε_∞ defines the permittivity of the material at infinite frequency (electronic contribution). The second term is correlated with the electrode ($k = 1$) and interdomain ($k \geq 2$) polarization. σ_k and τ_k are the conductivity and the relaxation times, respectively, associated with the k^{th} electrical event. γ_k is

associated with the broadening of the k^{th} polarization peak. The third term accounts for the dielectric relaxation described by the Havriliak-Negami theory [162, 182]. $\Delta\epsilon$, τ_j , α_j , and β_j are the dielectric strength, relaxation time, symmetric and antisymmetric shape parameter of each j^{th} relaxation event, respectively.

The 3D $\tan\delta$ (with $\tan\delta = \epsilon''/\epsilon'$) profiles allows for the easily identification of the polarization and relaxation phenomena, as shown in Figure 9.9.

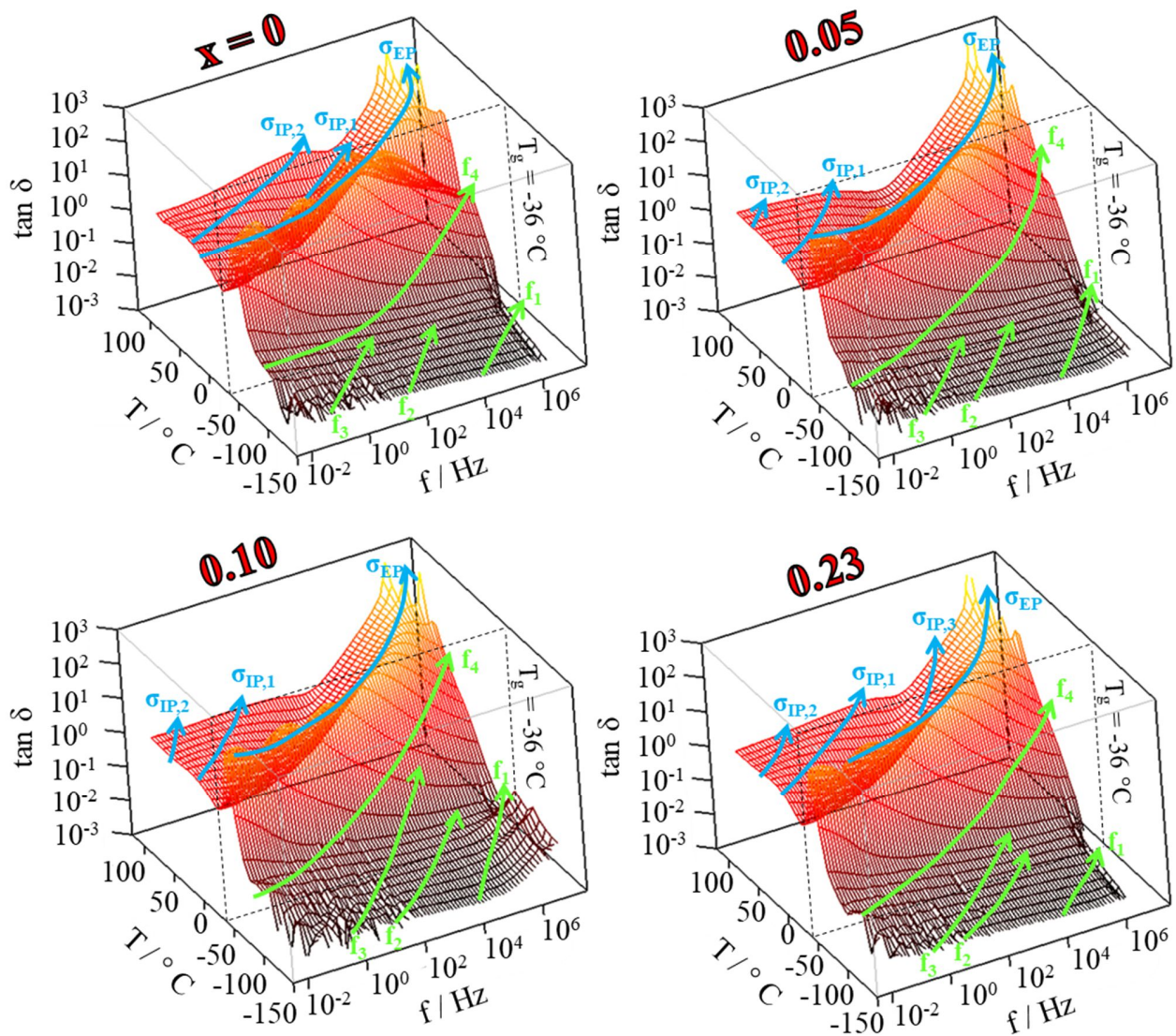


Figure 9.9. 3D $\tan\delta$ surfaces of $[\text{EMImCl}/(\text{TiCl}_4)_{1.4}]/(\delta\text{-MgCl}_2)_x$ samples.

9.2.4.1 Polarization Phenomena

Four different conductivity regions (I, II, III and IV) are detected. T_g separates region II from region III. At $T > T_g$, four different polarization phenomena are detected: one electrode polarization (σ_{EP}), and three different interdomain polarizations ($\sigma_{IP,i}$, with $1 \leq i \leq 3$). The electrode polarization event (σ_{EP}) is correlated to the charge accumulation at the interface between the sample and the Pt blocking electrodes of the measurement cell [162]. Whilst, the presence of several interdomain polarizations at $f < 10^5$ Hz ($\sigma_{IP,i}$, with $1 \leq i \leq 3$) reveals that the charge accumulation takes place at the interfaces between domains with different permittivity [162]. This demonstrates that the electrolytes are heterogeneous at the mesoscale, and are composed by imidazolium-based cation nanodomains, neutralized by the chlorotitanate anion nanodomains, in agreement with vibrational spectroscopy.

At $T < T_g$, the materials demonstrate a very low conductivity ($< 10^{-12}$ S cm⁻¹) and the only visible polarization phenomena is the electrode polarization (σ_{EP}). This is consistent with the low mobility of ionic species at these temperatures, which is due to the low thermal energy available under these conditions for an effective charge migration phenomenon.

The conductivity values of all the polarizations, obtained by fitting the observed events in BES measurements, are plotted vs. T^{-1} . Each curve is fitted with a suitable model, *i.e.* Vogel-Tammann-Fulcher (VTF) [183] or Arrhenius (A) equation [162]. Results are reported in Figure 9.10.

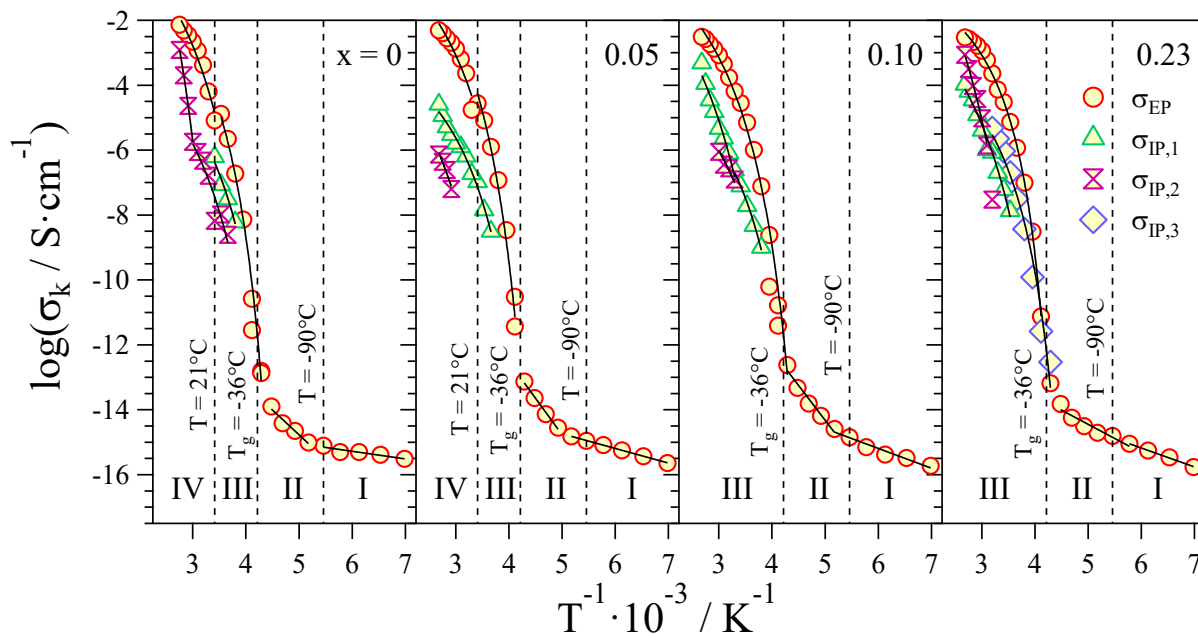


Figure 9.10. Dependence on T^{-1} of the conductivity values (σ_k) of $[\text{EMImCl}/(\text{TiCl}_4)_{1.4}]/(\delta\text{-MgCl}_2)_x$ samples.

The Arrhenius-like behaviour of σ_{EP} vs. T^{-1} in regions I and II reveals that a long range charge transfer process occurs due to charge hopping events between different anionic nanodomains [280]. At $T > T_g$, σ_{EP} and $\sigma_{IP,i}$ ($1 \leq i \leq 3$) show a Vogel-Tamman-Fulcher (VTF) trend. Thus, in regions III and IV, it is suggested that the fluctuation of cation and anion aggregates (segmental motion) promotes the long-range charge transfer processes. This is easily explained considering that, in the proposed electrolytes, cation aggregates, neutralized by anionic concatenated nanodomains, create a well-defined volume, in which the charge carriers can be considered delocalized (delocalization bodies, DBs) due to the fast ion exchange within them (see also Figure 9.16) [57, 133, 134].

The contribution of each polarization ($\varphi_k = \sigma_k / \sigma_T$) to the total conductivity (σ_T) as a function of temperature is shown in Figure 9.11.

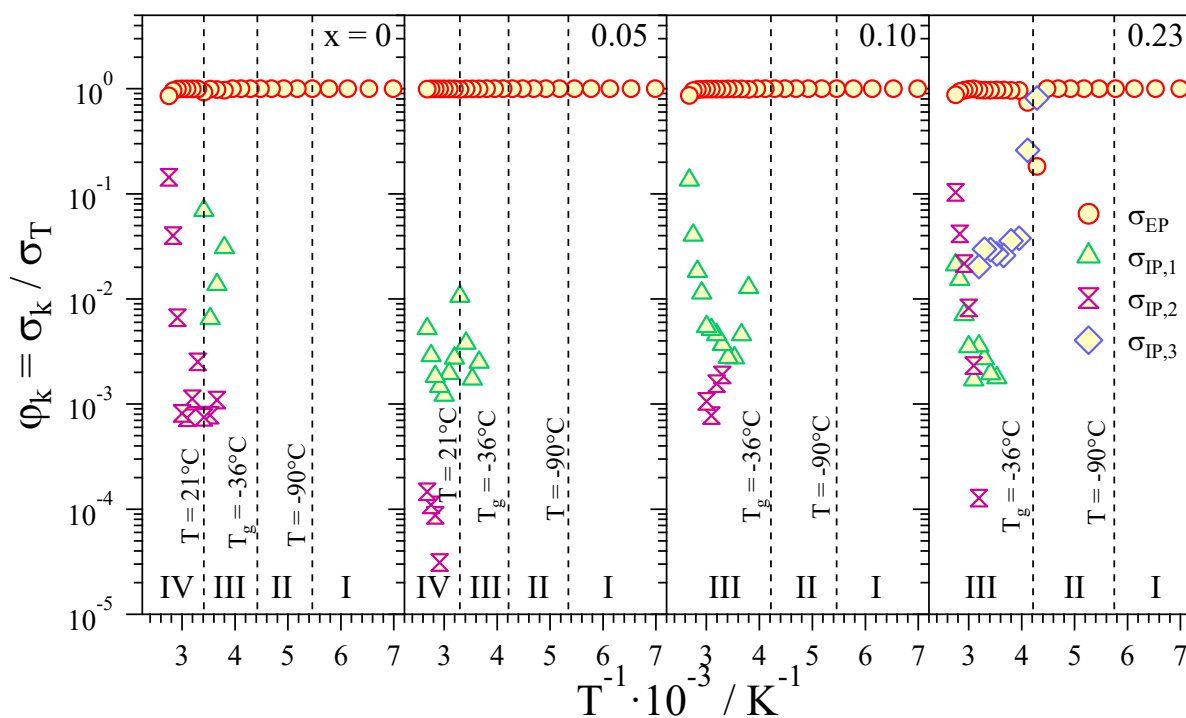


Figure 9.11. Contribution of each polarization (ϕ_k) to the total conductivity as a function of temperature.

The electrode polarization is the dominant contribution to the overall conductivity for all the samples and in the whole studied temperature range, as it can be observed. Only $\sigma_{IP,3}$, for $[EMImCl]/(TiCl_4)_{1.4}/(\delta-MgCl_2)_{0.23}$ sample around the T_g , reaches values comparable to those of σ_{EP} .

The dependence of the total conductivity ($\sigma_T = \sum_{i=1}^4 \sigma_k$, where σ_k are the conductivity values associated with all the detected percolation pathways) on T^{-1} is reported in Figure 9.12. Figure 9.12 reveals that the conductivity of $[EMImCl]/(TiCl_4)_{1.4}/(\delta-MgCl_2)_x$ electrolytes at $T = 40^\circ C$ is greater than $10^{-4} S cm^{-1}$, but falls near $25^\circ C$, as observed in other imidazolium-based ionic liquids [133]. The drop in conductivity is the consequence of an order/disorder transition of the EMIm⁺ stacks, which is hindered as the density and strength of the 3D catenated bonds in the magnesium-halotitanate networks increases.

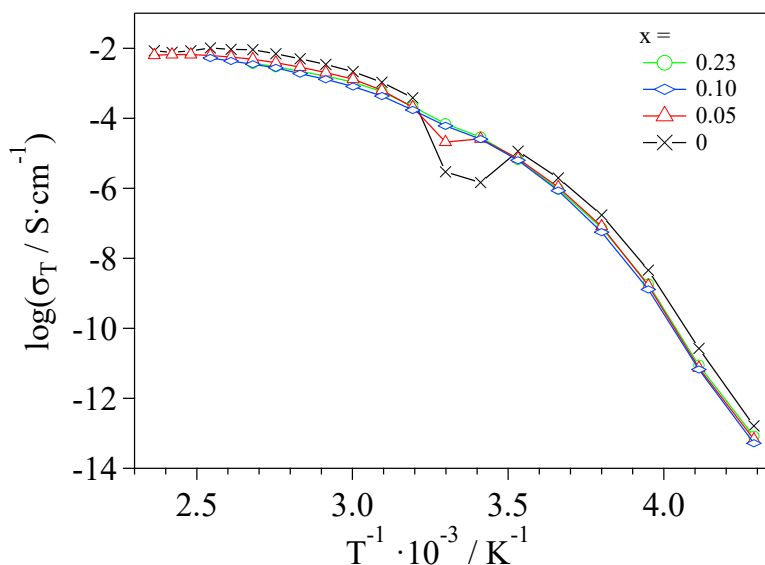


Figure 9.12. σ_T vs. T^{-1} profiles of $[\text{EMImCl}/[(\text{TiCl}_4)_{1.4}]/(\delta\text{-MgCl}_2)_x]$ electrolytes.

9.2.4.2 Dielectric Relaxation Events

At $T < T_g$, four different dielectric relaxation events (f_j , with $1 \leq j \leq 4$) are observed. These relaxations are assigned to the fluctuation of the imidazolium cation, which has a permanent dipole moment. In details, f_1 and f_2 , which are detected at higher frequencies, are related to two different relaxation modes associated to the motion of the inter-ion dipole moment exists between the EMIm^+ and TiCl_6^{2-} or Ti_2Cl_9^- ionic species, respectively. f_3 is attributed to the rotational motion around the long axis of spheroidal EMIm^+ cations, while f_4 is associated with the rotation around the short axis of the spheroidal EMIm^+ cation. All of these phenomena are in accordance with other similar compounds reported in the literature [134, 189], and are graphically represented in Figure 9.13. The relaxation frequencies vs. T^{-1} curves (see Figure 9.14) show an Arrhenius-like behaviour in these temperature regions. This suggests that no coupling between the relaxation events of stacks of EMIm^+ species (segmental motion) and magnesium exchange processes is present under these conditions.

Above the T_g , the polarization phenomena dominate the overall permittivity of the samples, thus neglecting the dielectric relaxations events contribution. Indeed, the only measurable relaxation is f_4 at all the $\delta\text{-MgCl}_2$ concentrations. In these temperature regions, the relaxation frequency curves follow a VTFH trend, suggesting that, in accordance with the results of Figure 9.10, the diffusion of conformational states of cationic aggregates (segmental motion) contributes to the long-range

charge migration phenomena. It is also shown that, in $[\text{EMImCl}/(\text{TiCl}_4)_{1.4}]/(\delta\text{-MgCl}_2)_x$, the f_1 and f_2 values shift to higher frequencies. This result is consistent with the reduction of the density and strength of the cation-anion interactions as the size of the 3D catenated network increases. In summary, the formation of Mg catenated chlorotitanate anionic complexes reduces the interactions between the anionic domains and EMIm^+ aggregates, facilitating the migration of charge.

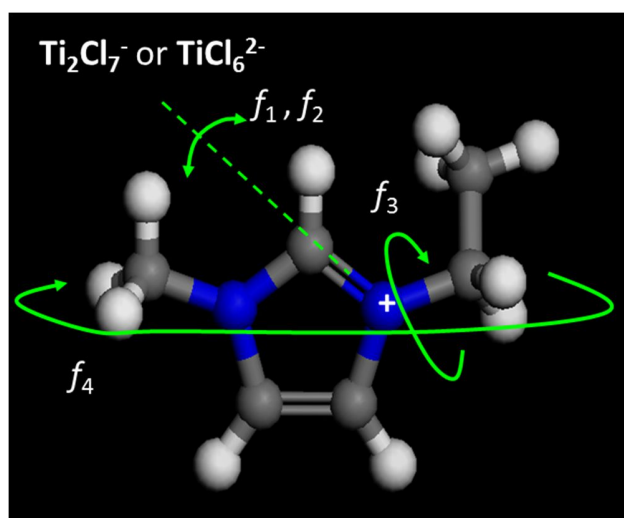


Figure 9.13. Relaxation modes (f_j , with $1 \leq j \leq 4$) of the imidazolium cation EMIm^+ .

The $\log f_j$ vs. T^{-1} curves for $[\text{EMImCl}/(\text{TiCl}_4)_{1.4}]/(\delta\text{-MgCl}_2)_x$ electrolytes are shown in Figure 9.14.

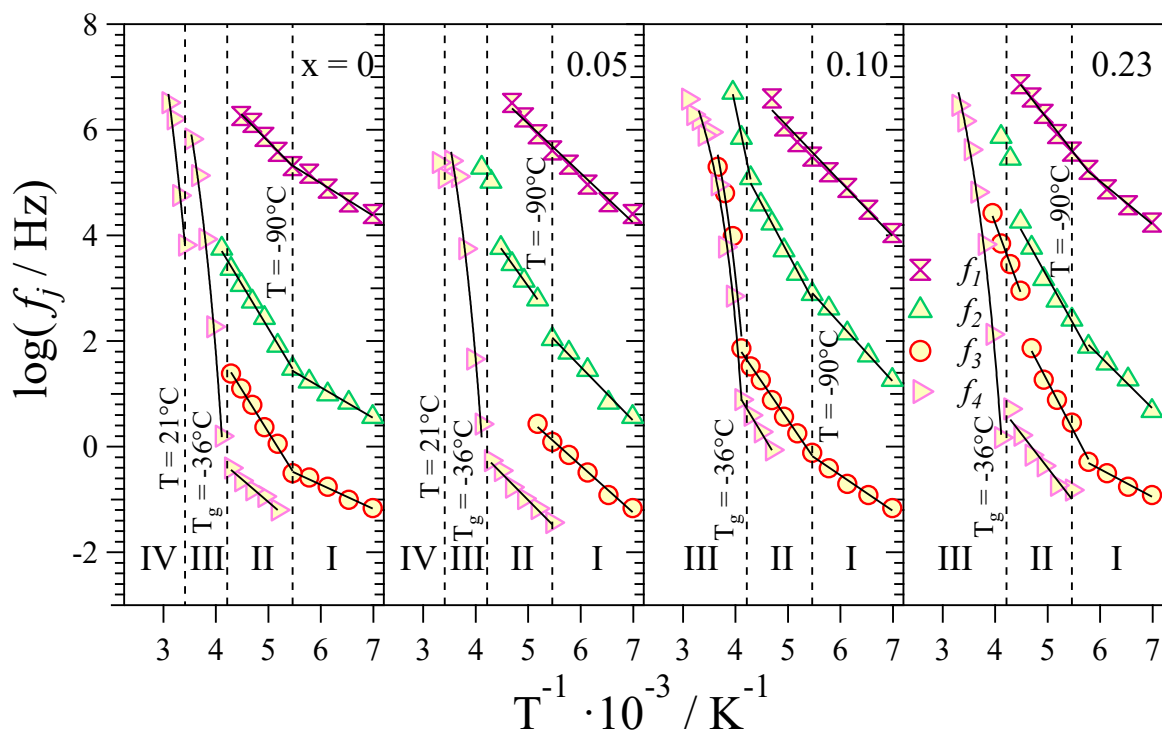


Figure 9.14. Dependence on T^{-1} of the dielectric relaxation frequencies (f_j) of $[\text{EMImCl}/(\text{TiCl}_4)_{1.4}]/(\delta\text{-MgCl}_2)_x$ samples.

9.2.4.3 Activation Energy

Further information on the conductivity mechanism is obtained by calculating the activation energy of the polarization and dielectric relaxation events by fitting the profiles shown in Figure 9.10 and Figure 9.14 with a VTF-, VTFH-, or Arrhenius-like equation. Results are reported in Figure 9.15.

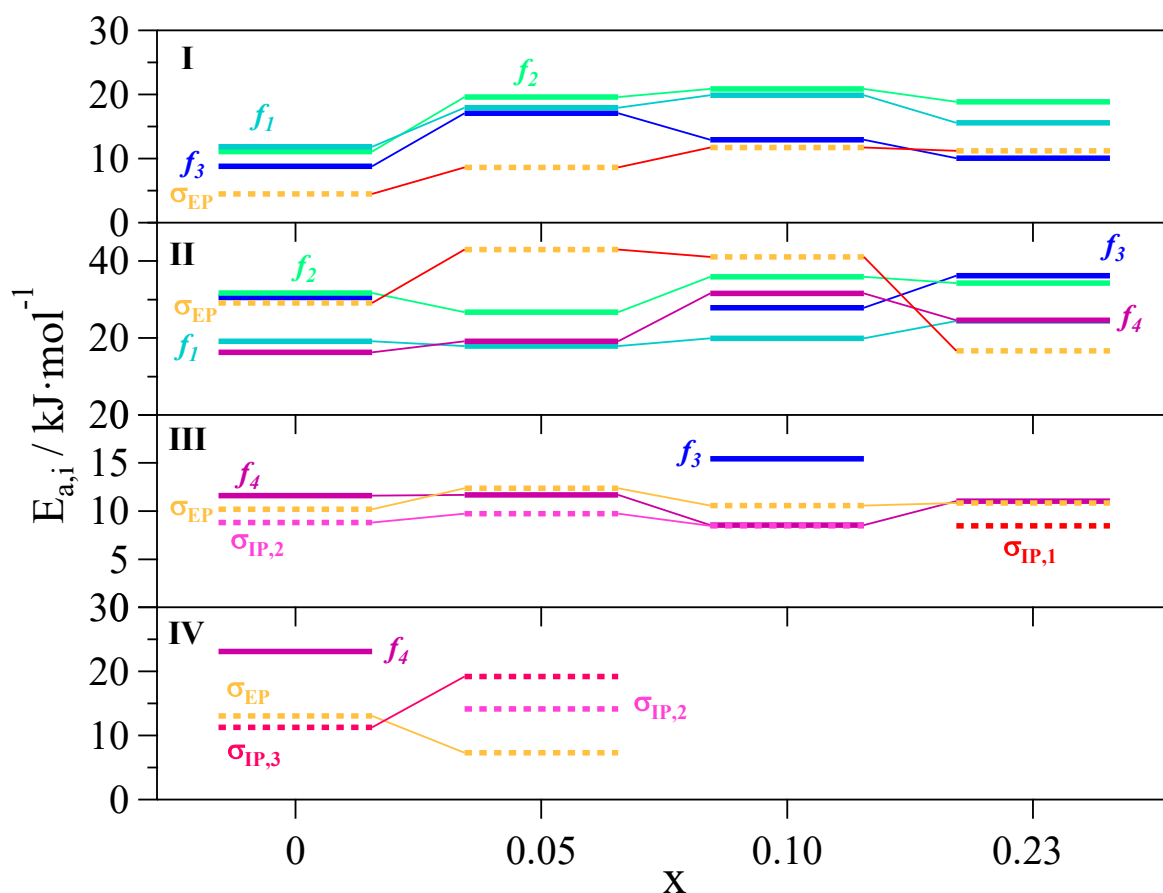


Figure 9.15. Activation energies of measured conductivities ($E_{a,\sigma k}$) and dielectric relaxation events ($E_{a,\beta}$) on x .

It can be seen that at $T < T_g$ (regions I and II) the activation energy of σ_{EP} is very similar to that of the f_3 dielectric relaxation, especially at low magnesium concentrations. This demonstrates that the long-range charge migration, in these temperature regions, is mostly assisted by the fluctuation of the imidazolium cations along their long axis (f_3). In agreement with the DSC results, this relaxation is accountable for the fluctuation of the whole imidazolium/chlorotitanate alternate pillar structure, which is expected to be determinant in modulating the overall conductivity. The gradual increase of $E_a(\sigma_{EP})$ on x reveals that the dynamics of charge aggregates is hindered, further confirming that δ -MgCl₂ units are involved in a more strongly bonded 3D catenated network.

At $T > T_g$ (regions III and IV), σ_{EP} is associated to the fluctuation of the imidazolium cations along their short axis (f_4), as demonstrated by their very close activation energy values. Thus, the fluctuation of cationic aggregates of different sizes is responsible for an efficient long-range charge migration mechanism. It should be observed that $E_a(f_1)$ and $E_a(f_2)$ are always different from $E_a(\sigma_{EP})$.

This observation declares that cation-anion interactions only play a minor role in modulating the overall conductivity.

Concluding, considering the presence of the delocalization bodies, the long-range migration process occurs when negatively-charged magnesium-chlorotitanate complexes are exchanged at the interface between different DBs. These phenomena are significantly affected by the segmental motion of the EMIm⁺ clusters (f_3 and f_4), and, marginally, by the local fluctuation of cation-anion dipole moments (f_1 and f_2) [57, 212]. The trends of both σ_{EP} and $\sigma_{IP,i}$ curves as a function of T^{-1} suggest further proofs of the influence of the segmental motions of EMIm⁺ aggregates on the dynamics of the anionic domains. These latter events are strongly correlated with the long-range charge migration process, which gives rise to the ion conductivity of electrolytes. The interacting cation and anion aggregate domains are crucial in forming the number and the type of pathways contributing to the overall conductivity of the proposed systems. Below the T_g , the addition of δ -MgCl₂ increases the conductivity. A representative summary of the hypothesized conductivity mechanism is schematically represented in Figure 9.16.

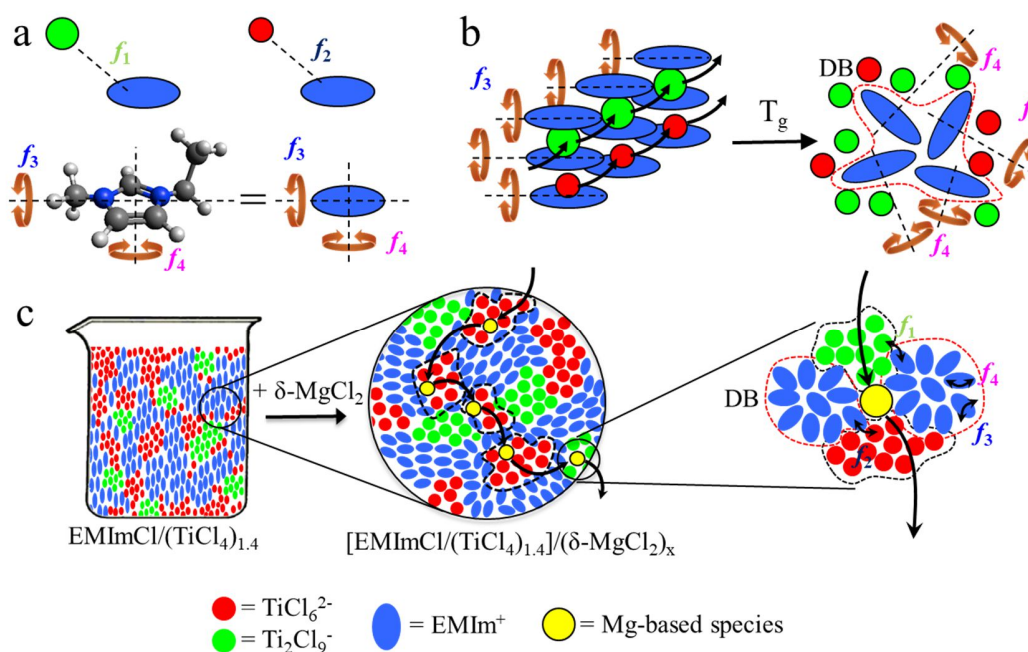


Figure 9.16. Dielectric relaxations (f_j , with $1 \leq j \leq 4$) of EMIm⁺ cations (a). Conductivity mechanisms of the electrolytes below and above the glass transition temperature (b). Conductivity mechanism occurring by exchange events of magnesium-chlorotitanate complexes through different cationic and anionic nanodomains (delocalization bodies, DBs) at room temperature (c).

9.2.5 Electrochemical Studies

Preliminary electrochemical studies are conducted in order to evaluate the applicability of the proposed electrolytes in magnesium-titanium alloy electrodeposition applications. Results are shown in Figure 9.17. Electrochemical experiments are obtained using a three-electrode configuration cell, with two magnesium ribbons are counter and reference electrodes, and Pt as working electrode.

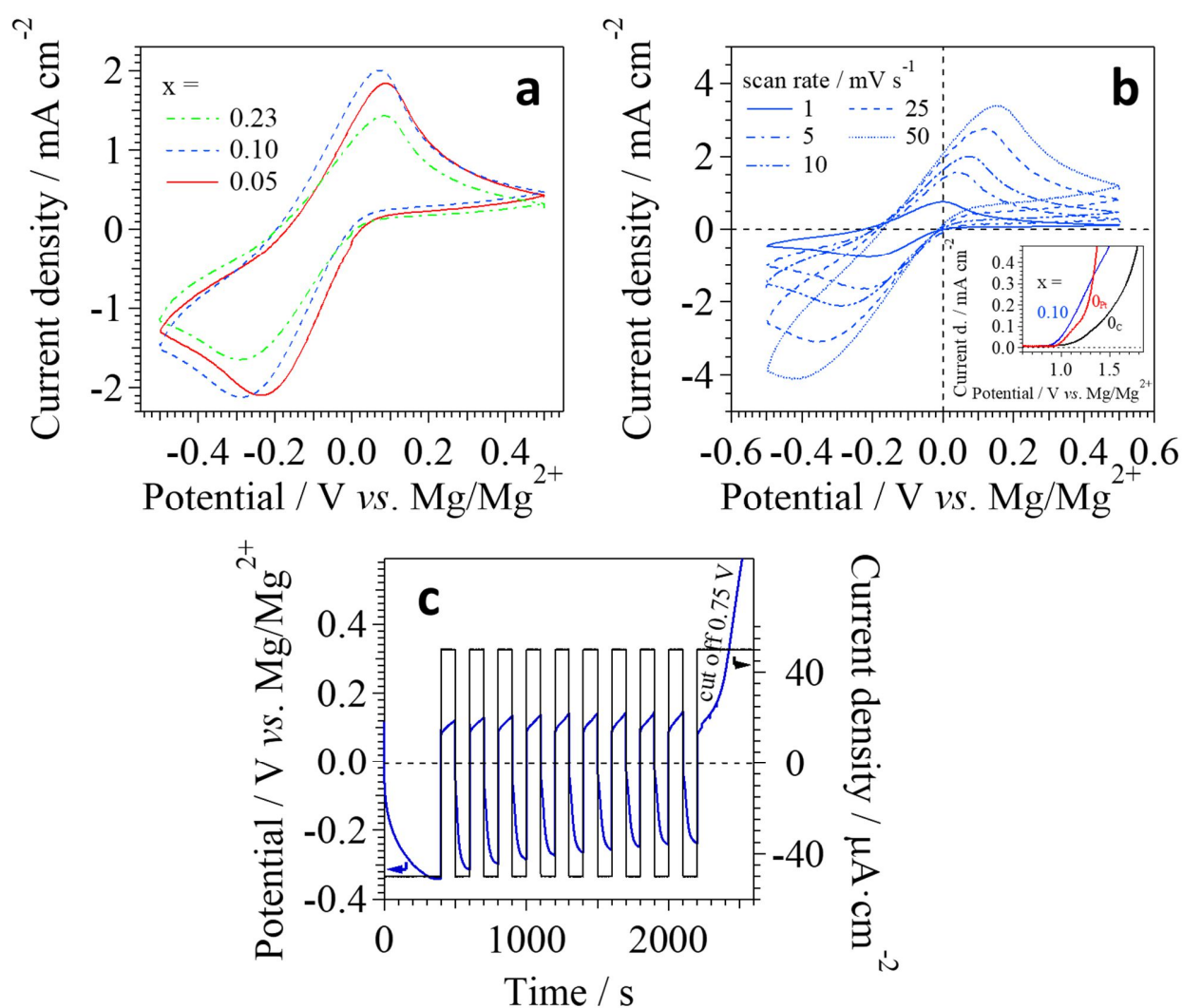


Figure 9.17. Cyclic voltammograms of $[\text{EMImCl}/(\text{TiCl}_4)_{1.4}]/(\delta\text{-MgCl}_2)_x$ on x , with $x \geq 0.05$, at a scan rate of 10 mV s^{-1} (a); at $x = 0.10$ at different scan rates (b). The inset shows the electrochemical stability window of $[\text{EMImCl}/(\text{TiCl}_4)_{1.4}]/(\delta\text{-MgCl}_2)_0$ vs. C we (black line), $[\text{EMImCl}/(\text{TiCl}_4)_{1.4}]/(\delta\text{-MgCl}_2)_0$ vs. Pt we (red line), and $[\text{EMImCl}/(\text{TiCl}_4)_{1.4}]/(\delta\text{-MgCl}_2)_{0.10}$ vs. C we (blue line). Average coulombic efficiency evaluation for $[\text{EMImCl}/(\text{TiCl}_4)_{1.4}]/(\delta\text{-MgCl}_2)_{0.10}$ (c).

Cyclic voltammetry tests prove that all the electrolytes are able to deposit and strip magnesium onto a platinum electrode with a high reversibility. The cathodic peak (Figure 9.17a), that appears in the range from 10 to 100 mV vs. Mg/Mg²⁺, demonstrates that the deposition event occurs with a very low overvoltage. It is shown that, as x is increased in [EMImCl/(TiCl₄)_{1.4}]/(δ -MgCl₂) _{x} , no significant differences in the overvoltage is observed, but the current density of the anodic peak changes substantially. In details, current densities of 1.8, 2.0, and 1.4 mA·cm⁻² are detected, for $x = 0.05$, 0.10, and 0.23, respectively. Indeed, in materials with $x = 0.05$ and 0.10, the electrochemical processes occur thank to the presence of the dimeric halotitanate species, while in the sample with $x = 0.23$ the density of Ti₂Cl₉⁻ species is significantly reduced, decreasing the current density of the obtained voltammograms. It is observed that the high degree of 3D catenation results in an increased viscosity of [EMImCl/(TiCl₄)_{1.4}]/(δ -MgCl₂) _{x} , reducing the conductivity and inhibiting the deposition/stripping kinetic processes. The sample at $x = 0.10$ is also studied at different scan rates (Figure 9.17b). Indeed, this material is the best compromise in terms of the concentration of dimers and size of 3D concatenated anionic domains. The current density is observed to depend linearly on the square root of the scan rate, revealing that the reactions occurring at the electrode are highly reversible and show fast kinetics. The passivation that appears under resting conditions on the working electrode is evaluated by performing a cyclic voltammogram under freshly conditions and after a rest of 6 hours. Both the measurements are conducted at a scan rate of 10 mV·s⁻¹ using [EMImCl/(TiCl₄)_{1.4}]/(δ -MgCl₂)_{0.10} electrolyte material (see Figure 9.18).

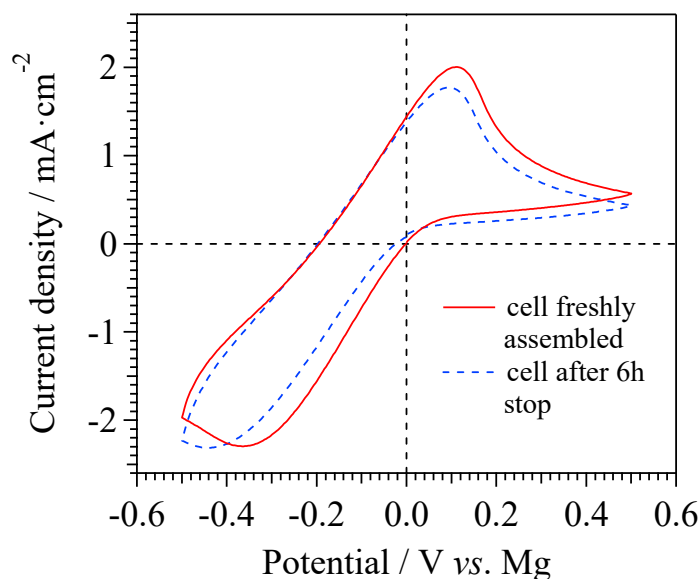


Figure 9.18. Cyclic voltammograms of $[\text{EMImCl}/(\text{TiCl}_4)_{1.4}]/(\delta\text{-MgCl}_2)_{0.10}$ at a scan rate of $10 \text{ mV}\cdot\text{s}^{-1}$ for the freshly assembled cell (red solid line) and after a 6 hours stop (blue dashed line).

The aged cell shows a slight increase in overpotential for the deposition process (20 mV higher) and a reduced intensity of the Mg-Ti alloy stripping peak. These results are a consequence of the formation of a passivation layer on the surface of the working electrode. Nevertheless, even if the passivation occurs, the excellent electrochemical properties of the proposed materials (*e.g.* deposition overpotential) are not only maintained, but they are also greater than those exhibited by several electrolytes used in Mg secondary batteries recently published in the literature [117, 281-283]. The electrochemical stability window (ESW), evaluated by linear sweep voltammetry (inset of Figure 9.17b), demonstrates a value which is higher than 1.0 V vs. Mg/Mg²⁺ for $[\text{EMImCl}/(\text{TiCl}_4)_{1.4}]$ ($x = 0$) and *ca.* 0.9 V vs. Mg/Mg²⁺ for $[\text{EMImCl}/(\text{TiCl}_4)_{1.4}]/(\delta\text{-MgCl}_2)_{0.10}$. This small reduction in the ESW at $x = 0.10$ is the consequence of the presence of a higher concentration of TiCl_6^{2-} in the bulk material. These complexes, as expected, have a lower electrochemical stability with respect to Ti_2Cl_9^- . Indeed, a high concentration of TiCl_6^{2-} species results in a high concentration of “free” Cl^- , which can be easily oxidized to chlorine. Moreover, in accordance with literature [265], it is observed that the ESW of the proposed materials is *ca.* 100 mV higher when a working electrode consisting of glassy carbon is used. On the contrary, no stable stripping and deposition processes can be obtained using a stainless-steel working electrode. The electrochemical performances of the proposed materials during galvanostatic cycling is measured by evaluating their average coulombic efficiency (CE) (Figure 9.17c) following the Aurbach method

[284]. The CE for $[\text{EMImCl}/(\text{TiCl}_4)_{1.4}]/(\delta\text{-MgCl}_2)_{0.10}$ material reaches a value of 99.3%, indicating that, with respect to similar electrolytes, this material is very promising for a series of different electrochemical applications [57, 133]. Finally, the composition of the alloy that can be obtained by electrodeposition for 20 minutes at a current density of $50 \mu\text{A}\cdot\text{cm}^{-2}$ on a Pt electrode, is determined by ICP-AES analysis. Results demonstrate that the obtained layer (*ca.* 2.35 mg) consists of a Mg-Ti alloy with a metal ratio composition of 1:10.5. It has to be highlighted that it should be difficult to reduce Ti^{4+} species to Ti^0 at 0 V vs. Mg/Mg²⁺. However, in accordance with other studies obtained using similar IL-chlorometallate electrolytes [57, 133], the deposition of magnesium is able to promote an efficient co-deposition of the other metal species present in the electrolyte (*i.e.*, in this case, titanium). Moreover, the co-deposition of the alloy, induced by the presence of Mg²⁺, starts at a very low overpotential, less than 10 mV, and the overall deposition and stripping processes take place in a very narrow potential range. To our knowledge, such interesting properties have never been demonstrated before by any other electrolyte [117, 281-283]. In conclusion, in $[\text{EMImCl}/(\text{TiCl}_4)_{1.4}]/(\delta\text{-MgCl}_2)_x$ electrolytes both Mg and Ti are the active species: magnesium is able to shift the titanium electrodeposition at 0 V vs. Mg, while Ti is essential in order to reduce the overpotential of Mg deposition/stripping at the lowest values ever seen in literature for this class of materials.

9.3 Conclusions

A new family of ionic liquid-based electrolytes for reversible magnesium/titanium alloy deposition/stripping processes is proposed. The electrolytes are synthesized by direct reaction of 1-ethyl-3-methylimidazolium chloride (EMImCl) with titanium(IV) chloride (TiCl₄), and with different additions of $\delta\text{-MgCl}_2$. DFT calculations and vibrational spectroscopy studies demonstrate that the electrolytes are composed by aggregates of EMIm⁺ cations interacting with catenated anionic domains based on TiCl₆²⁻ and Ti₂Cl₉⁻ complexes. In these electrolytes Mg²⁺ is coordinated by halotitanate species creating a 3D catenated coordination network. Furthermore, the addition of different amounts of $\delta\text{-MgCl}_2$ salt is able to modulate the equilibrium between the monomeric (TiCl₆²⁻) and dimeric (Ti₂Cl₉⁻) metal complexes forming the anion domains. In details, on x , the concentration of Ti₂Cl₉⁻ species decreases, and the density of monomeric TiCl₆²⁻ units increases. At 40 °C, the proposed electrolyte materials demonstrate conductivities greater than $10^{-4} \text{ S cm}^{-1}$. BES measurements reveal that the conductivity in these electrolytes occurs following a mechanism

which involves the exchange of anion species between different ionic domains (DBs). The long-range charge migration process is facilitated by the local fluctuations of the imidazolium cations and the segmental motion of cation aggregates. Finally, preliminary electrochemical tests demonstrate that reversible deposition and stripping processes of a Mg-Ti alloy, with a coulombic efficiency up to 99.3% and a deposition overvoltage of only 10 mV, can be obtained. Taken all together, these results allow to reveal the Mg and Ti conductivity mechanism occurring in the proposed IL-based electrolytes. Thus, this work opens the door to the application of these materials in the electrodeposition and dissolution of Mg-Ti alloys and to the development of more efficient electrolytes for future magnesium secondary batteries.

10. Beyond Mg Electrolyte Limits: High Performing Ionic Liquid Electrolyte for Magnesium Secondary Batteries Based on Pyr₁₄Cl, AlCl₃, and δ-MgCl₂

In this chapter, we report the synthesis and the study of a novel family of ionic liquid-based electrolytes for secondary magnesium batteries. In these materials we have studied the effect of the change in the cation nature of the IL, substituting the well-known imidazolium [57] with pyrrolidinium. In particular, 1-methyl-1-butylpyrrolidinium (Pyr₁₄) chloride is used, together with AlCl₃ and δ-MgCl₂ compounds like in the previous study [57]. Four different materials are obtained with a general formula [Pyr₁₄Cl/(AlCl₃)_{1.5}]/(δ-MgCl₂)_x, varying the Mg-salt concentration from 0 to 3.55 %_{wt} (0 ≤ x ≤ 0.146). DSC studies show the presence of five thermal transitions that are highly affected by the different magnesium concentrations. Thus, revealing that there is an evolution of the structure and the coordination of the aggregates increasing both the temperature and the Mg content. Vibrational measurements indicate the presence of two different chloroaluminate complexes, the monomer AlCl₄⁻ and the dimer Al₂Cl₇⁻, to which MgCl₂ units are coordinated. Mg-salt concentration can modulate the equilibrium between the two forms. Broadband electrical spectroscopy studies reveal a room-temperature conductivity up to 2.07·10⁻³ S·cm⁻¹ for [Pyr₁₄Cl/(AlCl₃)_{1.5}]/(δ-MgCl₂)_{0.091}. Moreover, this analysis allows us to evaluate and propose a reasonable conductivity mechanism that describes how Mg-active species are exchanged between different aggregates. Electrochemical characterizations show the reversible deposition and stripping of Mg on a platinum electrode, with a very low overpotential (< 50 mV) if compared with other electrolytes proposed for magnesium secondary batteries. The electrochemical stability window of these materials is extended with respect to [EMImCl/(AlCl₃)_{1.5}]/(δ-MgCl₂)_x, shifting the anodic limit by 150 mV (up to *ca.* 2.35 V vs. Mg/Mg²⁺) and the cathodic down to *ca.* -0.25 V vs. Mg/Mg²⁺. The coulombic efficiency exhibited by these electrolytes reaches a value of 99.65 %, that is one of the highest values ever reported in literature for this kind of materials. Finally, Mg-anode cells, coupled with the proposed electrolytes and a vanadium oxide cathode, are cyclically tested at high current rates (up to 350 mA·g⁻¹), revealing an initial capacity of 92 mAh·g⁻¹ and initial steady-state voltage of 2.3 V.

10.1 Experimental Section

10.1.1 Reagents

Pyr₁₄Cl is supplied from io·li·tec. Metallic magnesium (50 mesh), aluminum trichloride, and 1-chlorobutane are Aldrich reagents grade. The ionic liquid is dried under vacuum at 105 °C for 7 days, while 1-chlorobutane is further purified by standard methods and stored under Argon on 4A molecular sieves to prevent moisture contamination. All transfer and handling operations are performed under a strictly argon atmosphere, either inside an argon-filled glove-box or using a Schlenk line.

10.1.2 Synthesis

Anhydrous δ -MgCl₂ is obtained by direct reaction of metallic magnesium with 1-chlorobutane under a strictly anhydrous atmosphere as described elsewhere [17]. The ionic liquid Pyr₁₄Cl/(AlCl₃)_{1.5} is obtained by slow additions of aluminum trichloride on Pyr₁₄Cl. The most concentrated sample ([Pyr₁₄Cl/(AlCl₃)_{1.5}]/(δ -MgCl₂)_{0.146}) is synthesized by dissolving the 3.55 %_{wt} of the magnesium salt into the pure ionic liquid. Further dilutions with Pyr₁₄Cl/(AlCl₃)_{1.5} yield the [Pyr₁₄Cl/(AlCl₃)_{1.5}]/(δ -MgCl₂)_x electrolytes, thus obtaining a family of compounds with x (n_{Mg}/n_{IL}) ranging from 0 to 0.146. The composition of the obtained electrolytes is evaluated by ICP-AES measurements and results are reported in Table 10.1.

Table 10.1. Composition of [Pyr₁₄Cl/(AlCl₃)_{1.5}]/(δ -MgCl₂)_x electrolytes.

Sample	% _{wt} δ -MgCl ₂	x = n _{Mg} /n _{IL} ^a
IL	0	0
1	1.39	0.056
2	2.25	0.091
3	3.55	0.146

^an_{Mg}, and n_{IL} are the moles of δ -MgCl₂ and [Pyr₁₄Cl/(AlCl₃)_{1.5}], respectively, determined by ICP-AES spectroscopy.

10.2 Results and Discussion

10.2.1 Thermal Behavior

Differential scanning calorimetry measurements (Figure 10.1) reveal the presence of a glass transition (T_g) in a temperature range -90 ÷ -80 °C, attributed to an order-disorder event where Pyr₁₄⁺ cation and chloroaluminate anion stacks are reorganizing. Three different solid-state transitions (T_{s3}, T_{s2}, and T_{s1}) appear at ca. -78, -76, and -50 °C, respectively. They are associated

with transitions between phases with different rotational order that are gradually formed during heating [252-255]. Finally, a very broad melting event (T_m) is detected between -20 and 30 °C.

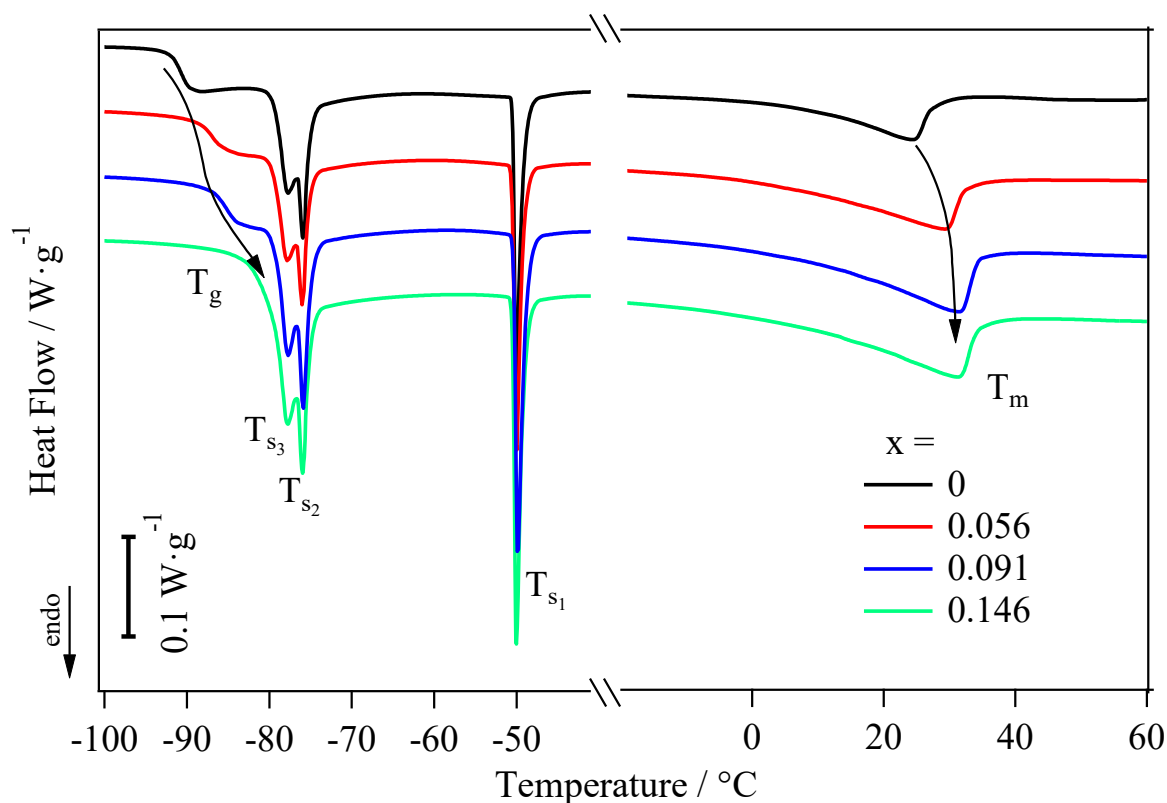


Figure 10.1. DSC profiles for $[\text{Pyr}_{14}\text{Cl}/(\text{AlCl}_3)_{1.5}]/(\delta\text{-MgCl}_2)_x$.

Differently from literature, these compounds do not show any crystallization event, probably as a consequence of the higher disorder given by the presence of the large AlCl_4^- and Al_2Cl_7^- anions. While the solid-state transitions temperatures are not affected by the different concentrations of the Mg-salt, T_g and T_m increase with x . Indeed, the equilibrium between the monomeric (AlCl_4^-) and the dimeric (Al_2Cl_7^-) form of the chloroaluminate complexes, together with their steric hindrance, is modulated by the concentration of $\delta\text{-MgCl}_2$ (see section 10.2.2). Thus, this equilibrium between the two species can vary the flexibility of anion and cation stacks. A phase diagram can be obtained by DSC results, which demonstrates the presence of five different regions (Figure 10.2). In region I, below the glass transition temperature ($T < -90$ °C), a rigid phase is present. In region II ($-90 < T < -80$ °C), ordered Pyr_{14}^+ cations are packed along one-dimensional pillars, with the coordinating chloroaluminates forming anion domains. In region III ($-80 < T < -50$ °C), after the second solid-state transition, these one-dimensional cation pillars reorganize in a more thermodynamically

stable zig-zag stacking structure. At T_{s1} , region IV ($-50 < T < 25$ °C), another cation reorganization occurs toward a phase with a further lower order. Finally, in region V ($T > 25$ °C) the compounds melt, forming a liquid with an increasing viscosity together with the increasing x value. The broadness of the melting event suggests the presence of a large distribution of interacting ordered nanodomains.

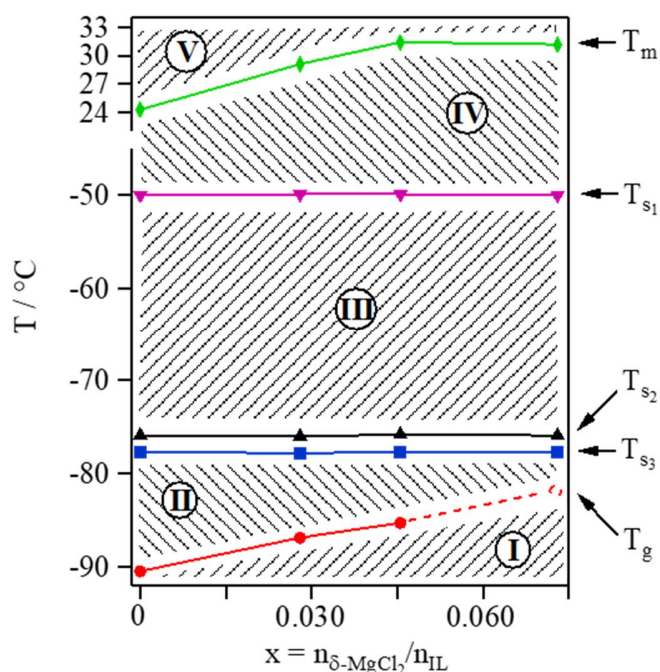


Figure 10.2. Phase diagram of $[\text{Pyr}_{14}\text{Cl}]/(\text{AlCl}_3)_{1.5}/(\delta\text{-MgCl}_2)_x$ electrolytes.

10.2.2 Vibrational Studies

Raman spectra of the proposed materials are reported in Figure 10.3. Curves are normalized on the peak centered at *ca.* 2967 cm^{-1} , attributed to $\nu_a(\text{CH}_2)(\text{Bu})$. In the spectral range above 600 cm^{-1} , all the peaks are attributed to the vibrations of the pyrrolidinium cation. Their intensity and position are not affected by the different concentrations of $\delta\text{-MgCl}_2$. On the contrary, peaks present at a lower Raman Shift ($< 600\text{ cm}^{-1}$) demonstrate a variability in the intensity and, slightly, in the position. In particular, these peaks are attributed to the presence of two different chloroaluminate complexes, AlCl_4^- and Al_2Cl_7^- [57].

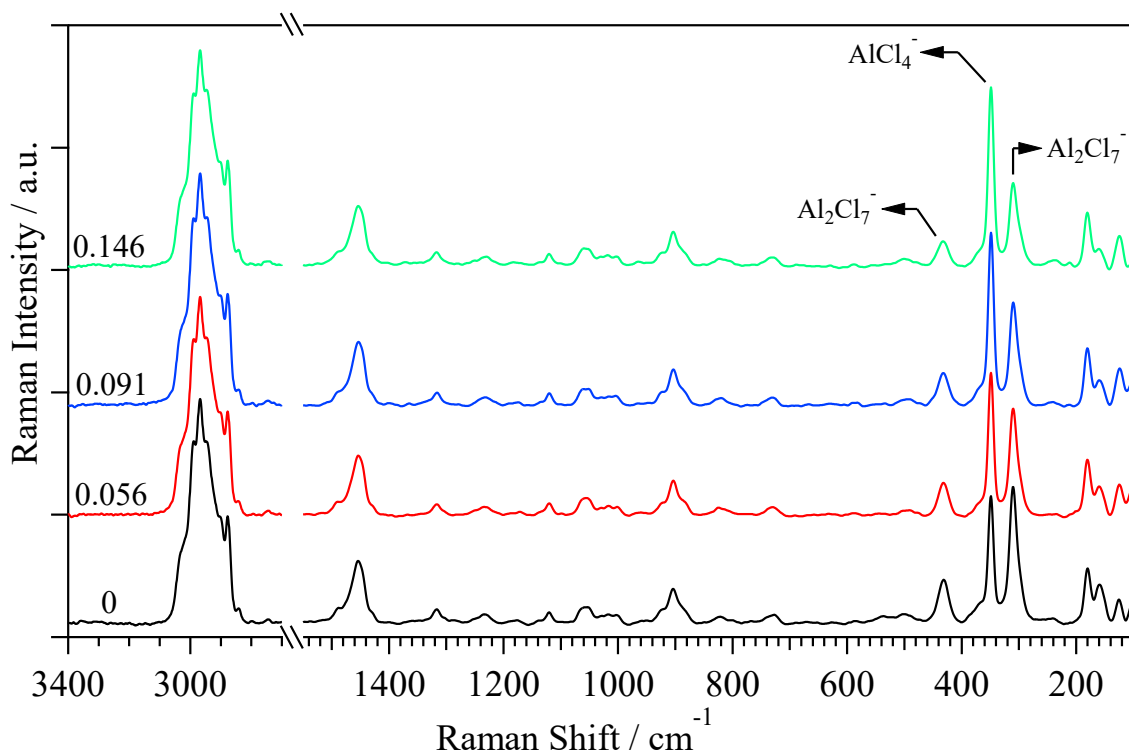


Figure 10.3. Raman spectra of $[\text{Pyr}_{14}\text{Cl}/(\text{AlCl}_3)_{1.5}]/(\delta\text{-MgCl}_2)_x$ electrolytes.

A complete assignment of all the vibrations for all the proposed electrolytes observed in the Raman spectra is summarized in Table 10.2.

Table 10.2. Correlative assignment of [Pyr₁₄Cl/(AlCl₃)_{1.5}]/(δ-MgCl₂)_x electrolytes Raman vibrations.

x = 0 ^a	Experimental Frequencies / cm ⁻¹			Assignment ^b	Ref.
	0.056 ^a	0.091 ^a	0.146 ^a		
3032 (m,sh)	3032 (m,sh)	3032 (m,sh)	3032 (m,sh)	ν(CH)	[this work]
2989 (s,sh)	2989 (s,sh)	2989 (s,sh)	2989 (s,sh)	ν _a (CH ₂)(Bu)	[256-258]
2967 (s)	2967 (s)	2967 (s)	2968 (s)	ν _a (CH ₂)(Bu)	[256-258]
2944 (s,sh)	2944 (s,sh)	2944 (s,sh)	2944 (s,sh)	ν _a (CH ₂)(Bu)	[256-258]
2905 (m,sh)	2905 (m,sh)	2905 (m,sh)	2905 (m,sh)	ν(CH ₂)	[258]
2878 (m)	2878 (m)	2878 (m)	2878 (m)	ν _a (CH ₂)(Bu)	[256-258]
2842 (w,sh)	2842 (w,sh)	2842 (w,sh)	2842 (w,sh)	ν _a (CH ₂)(N)	[260]
2745 (vw)	2745 (vw)	2745 (vw)	2745 (vw)	overtone	[257]
1487 (w,sh)	1487 (w,sh)	1487 (w,sh)	1487 (w,sh)	δ(CH ₂)(ring)	[258]
1454 (m)	1454 (m)	1454 (m)	1454 (m)	δ(CH ₂ ,CH ₃)(Bu)	[258]
1317 (w)	1317 (w)	1317 (w)	1317 (w)	τ(CH ₂)(Bu)	[256-258]
1234 (w)	1234 (w)	1234 (w)	1234 (w)	ω(CH ₂)(ring)	[257]
1176 (vw)	1176 (vw)	1176 (vw)	1176 (vw)	ω(CH ₂)	[257]
1136 (vw,sh)	1136 (vw,sh)	1136 (vw,sh)	1136 (vw,sh)	τ(CH ₂)	[256, 262]
1120 (w)	1120 (w)	1120 (w)	1120 (w)	ν(C-C)	[260]
1053 (w)	1053 (w)	1053 (w)	1053 (w)	τ(CH ₂)	[257]
1014 (w)	1014 (w)	1014 (w)	1014 (w)	ω(CH ₂)(ring)	[258]
959 (vw)	959 (vw)	959 (vw)	959 (vw)	ν _a (C-N)(ring)	[256]
922 (w,sh)	922 (w,sh)	922 (w,sh)	922 (w,sh)	ω(CH ₂)	[256, 257]
904 (m)	904 (m)	904 (m)	904 (m)	ν _a (C-C)	[256]
886 (w,sh)	886 (w,sh)	886 (w,sh)	886 (w,sh)	symmetric ring breath	[256, 257]
822 (vw)	822 (vw)	822 (vw)	822 (vw)	ω(CH ₂) in phase	[259]
727 (vw)	727 (vw)	727 (vw)	727 (vw)	ω(CH ₂) in phase	[259]
587 (vw)	587 (vw)	587 (vw)	587 (vw)	ν(Al ₂ Cl ₇ ⁻) _{term}	[57]
537 (vw)	537 (vw)	537 (vw)	537 (vw)	ν(Al ₂ Cl ₇ ⁻) _{term}	[57]
502 (vw)	502 (vw)	502 (vw)	502 (vw)	ν _{as} (AlCl ₄ ⁻)	[57]
431 (m)	431 (m)	431 (m)	431 (m)	ν(Al ₂ Cl ₇ ⁻) _{term}	[57]
374 (w,sh)	374 (w,sh)	374 (w,sh)	374 (w,sh)	ν(Al ₂ Cl ₇ ⁻)	[57]
349 (s)	349 (s)	349 (s)	349 (s)	ν(AlCl ₄ ⁻)	[57, 285]
310 (s)	310 (s)	310 (m)	310 (m)	ν _s (Al ₂ Cl ₇ ⁻)	[57]
241 (vw)	241 (vw)	241 (vw)	241 (vw)	γ(N-Me)	[57, 266]
180 (m)	180 (m)	180 (m)	180 (m)	δ(AlCl ₄ ⁻)	[57]
160 (m)	160 (m)	160 (m)	160 (m)	δ(Al ₂ Cl ₇ ⁻)+δ(MgCl ₂)	[57]
125 (w)	125 (w)	125 (w)	125 (w)	δ _s (AlCl ₄ ⁻)	[264]

^aIntensities are reported in brackets: s=strong; m=medium; w=weak; vw=very weak; sh=shoulder. ^bν stretching; δ bending; τ twisting; ω wagging; γ out of plane; term terminal; bridg bridging; s symmetric; as antisymmetric.

The principal outcomes of Raman spectroscopy measurements are: i) cation-anion interactions, revealed by the intensity and the position of both the stretching and the deformation modes of the pyrrolidinium ring, are not strongly influenced by the different additions of magnesium salt; ii) proofs of the presence of bimetallic complexes based on Mg and Al centers, bridged together by chloride atoms, are given; and iii) moreover, by fitting Raman spectra of all the sample in the 275÷390 cm^{-1} region, an evaluation of how the equilibrium between the two chloroaluminate complexes behaves on x can be obtained (see Figure 10.4).

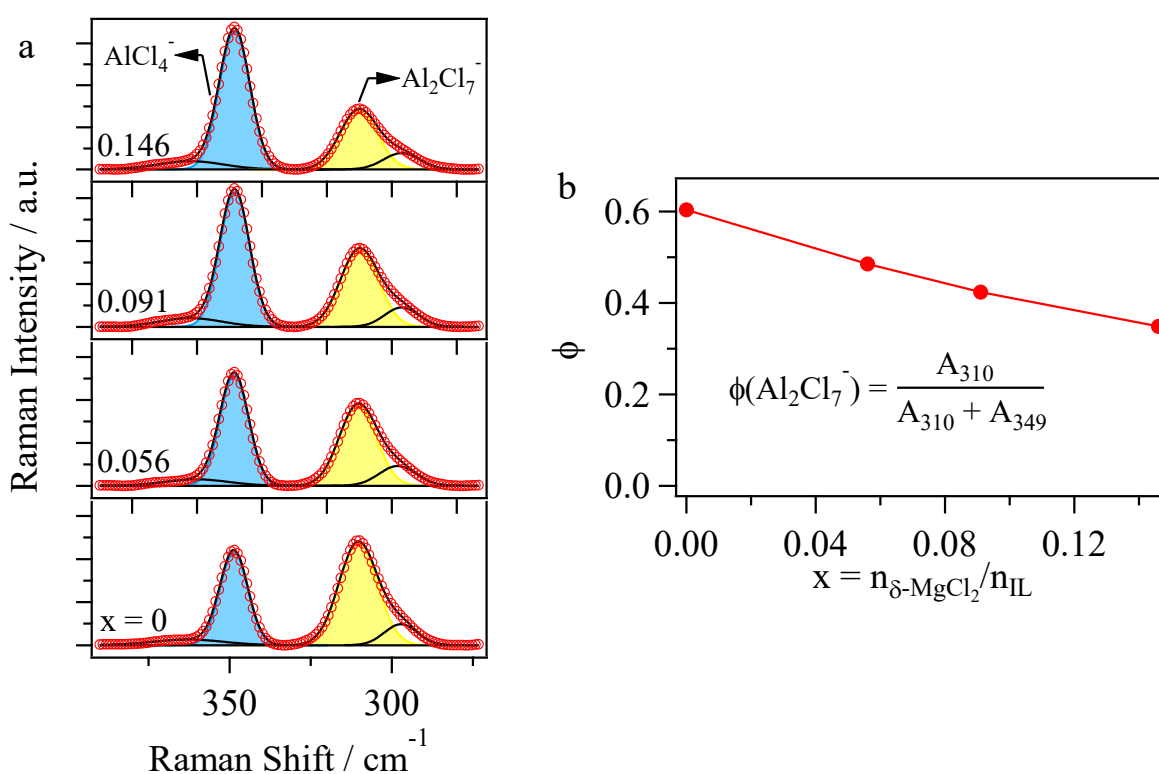
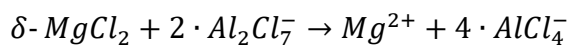


Figure 10.4. Raman spectra decomposition (a) and ratio (Φ) between the area of the Al_2Cl_7^- and AlCl_4^- bands vs. x (b).

It can be observed that the peak associated with the $\nu(\text{AlCl}_4^-)$ vibration (highlighted in light blue) grows in intensity on x, while the area of $\nu(\text{Al}_2\text{Cl}_7^-)$ peak (highlighted in yellow) decreases. The trend of Φ vs. x, evaluated as the ratio between the area of the Al_2Cl_7^- peak and the sum of the areas of both AlCl_4^- and Al_2Cl_7^- peaks, shows a decreasing exponential behavior. Thus, samples at high values of x are richer in the monomer form of chloroaluminate complex, while in IL with low amounts of magnesium salt the dimer is more stable. Indeed, this equilibrium can be expressed considering the following reaction:



A representation of the equilibrium existing between the dimer and the monomer after the addition of $\delta\text{-MgCl}_2$ is reported in Figure 10.5.

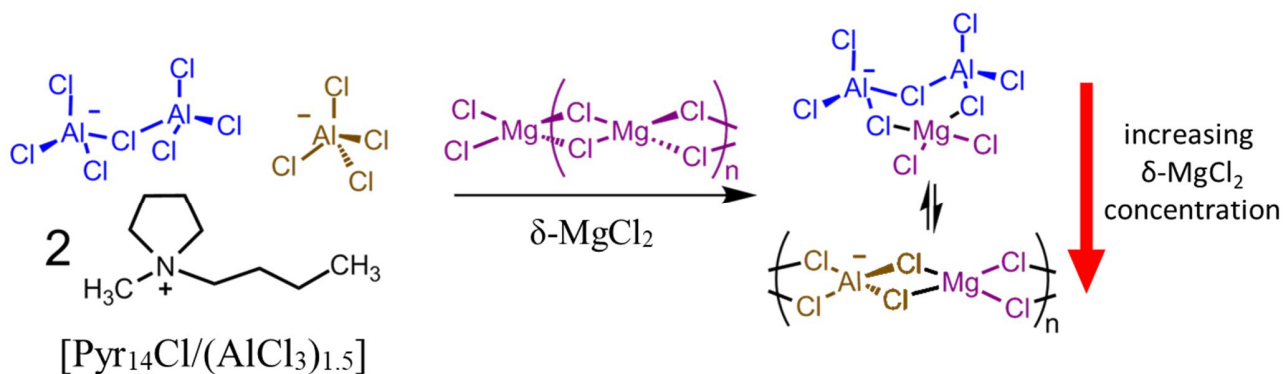


Figure 10.5. Concentration equilibrium of the two forms of chloroaluminate complexes increasing the $\delta\text{-MgCl}_2$ salt concentration.

Figure 10.6 reports the results of FT-FIR measurements for all the proposed electrolyte materials.

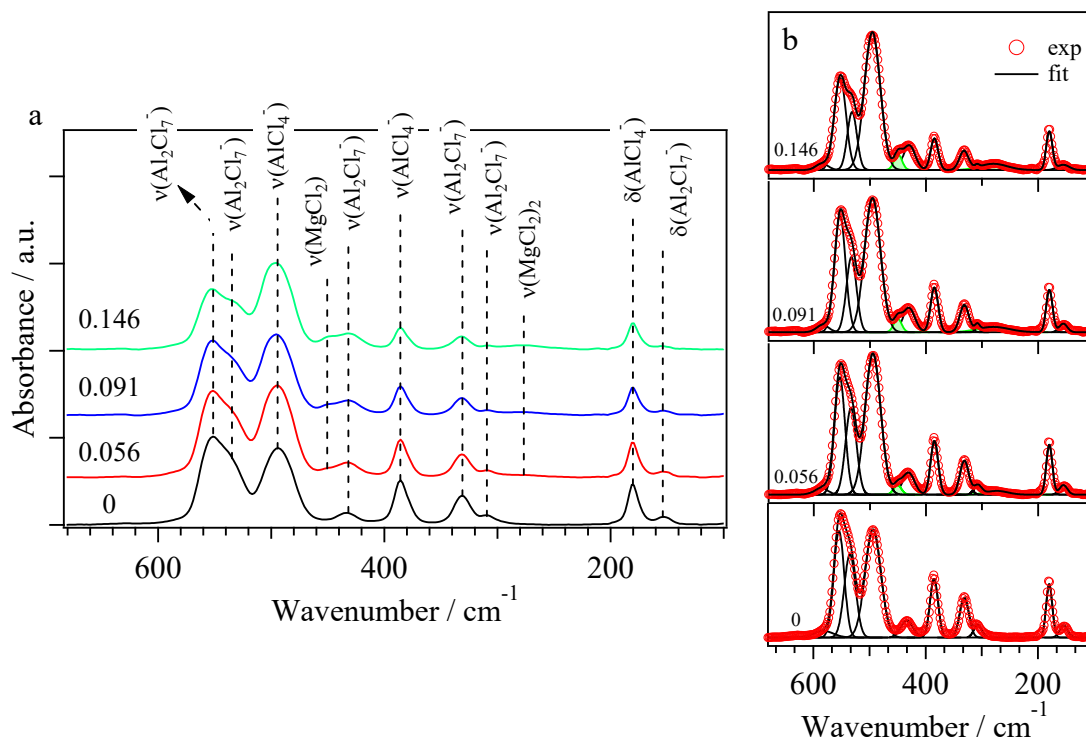


Figure 10.6. FT-FIR spectra (a) and spectral decomposition (b) for $[\text{Pyr}_{14}\text{Cl}/(\text{AlCl}_3)_{1.5}]/(\delta\text{-MgCl}_2)_x$ electrolytes. Peaks attributed to the vibrations of $\delta\text{-MgCl}_2$ are highlighted in green.

FT-FIR vibrational analyses confirm the presence of both the monomer and the dimer Mg-chloroaluminate complexes. The peaks centered at *ca.* 385, 332, 308, and 155 cm⁻¹, attributed to the vibration of the Al₂Cl₇⁻, decrease in intensity increasing the content of magnesium salt, confirming Raman results. Furthermore, at *x* ≥ 0.056, two new peaks appear at *ca.* 451 and 280 cm⁻¹, assigned to the stretching vibrations of Mg-Cl. In accordance with literature, the peak present at *ca.* 280 cm⁻¹ appears in computational calculations only if we consider the presence of more than one magnesium chloride concatenated unit in the anion complex [57]. Thus, in these electrolytes, the typical chain-like structure of δ-MgCl₂ is present. The shift of Al-Cl stretching vibration after Mg addition, observed at *ca.* 430 cm⁻¹, is attributed to the formation of an Al-Cl-Mg coordination, supporting the interpretation of the existence of Mg-chloroaluminate complexes.

The correlative assignment of all the vibrations observed in FT-FIR spectra is given in Table 10.3.

Table 10.3. Correlative assignment of [Pyr₁₄Cl]/(AlCl₃)_{1.5}]/(δ-MgCl₂)_x electrolytes FT-FIR vibrations.

x = 0 ^a	0.056 ^a	0.091 ^a	0.146 ^a	Assignment ^b	Ref
582 (vw,sh)	580 (vw,sh)	585 (vw,sh)	584 (vw,sh)	v(Al ₂ Cl ₇) _{term}	[57]
554 (s)	554 (s)	553 (s)	553 (s)	v(Al ₂ Cl ₇) _{term}	[57]
535 (s,sh)	534 (s,sh)	532 (s,sh)	533 (s,sh)	v(Al ₂ Cl ₇) _{term}	[57]
494 (s)	495 (s)	496 (s)	495 (s)	v _{as} (AlCl ₄) ⁻	[57]
	451 (vw,sh)	450 (w,sh)	451 (w,sh)	v(MgCl ₂)	[57]
434 (w)	431 (w)	430 (w)	430 (w)	v(Al ₂ Cl ₇) _{term}	[57]
385 (m)	385 (m)	385 (m)	385 (m)	v(Al ₂ Cl ₇)	[57]
331 (m)	332 (m)	332 (m)	332 (m)	v _{as} (Al ₂ Cl ₇)	[57, 274]
307 (w)	308 (w)	309 (w)	308 (w)	v _s (Al ₂ Cl ₇)+v(MgCl ₂) ₂	[57]
	274 (vw)	280 (w)	280 (w)	v(MgCl ₂) ₂	[57]
180 (m)	180 (m)	180 (m)	180 (m)	δ(AlCl ₄) ⁻	[57]
154 (w)	155 (w)	155 (w)	155 (w)	δ(Al ₂ Cl ₇)+δ(MgCl ₂)	[57]

^aIntensities are reported in brackets: s=strong; m=medium; w=weak; vw=very weak; sh=shoulder. ^bv stretching; δ bending; term terminal; bridg bridging; as antisymmetric.

Summarizing, adding δ-MgCl₂ salt to the IL leads to: i) a modulation of the relative concentration of AlCl₄⁻/Al₂Cl₇⁻ anions; ii) the formation of two types of concatenated anionic complexes between δ-MgCl₂ and Al₂Cl₇⁻ or AlCl₄⁻ compounds; and iii) the retention of the typical highly reacting chain-like structure of δ-MgCl₂ in [Pyr₁₄Cl]/(AlCl₃)_{1.5}]/(δ-MgCl₂)_x electrolytes.

10.2.3 Broadband Electrical Spectroscopy Studies

[Pyr₁₄Cl]/(AlCl₃)_{1.5}]/(δ-MgCl₂)_x samples are extensively characterized by Broadband Electrical Spectroscopy (BES) technique with the aim of: i) study the conductivity mechanisms responsible for the long-range charge migration process; and ii) highlight the effects of the δ-MgCl₂ addition on the overall conductivity of the IL-based electrolytes. BES measurements are carried out from 30 mHz to 10 MHz, in the temperature range -130÷150 °C. The obtained results for the compound with x = 0.091 are reported, as an example, in Figure 10.7.

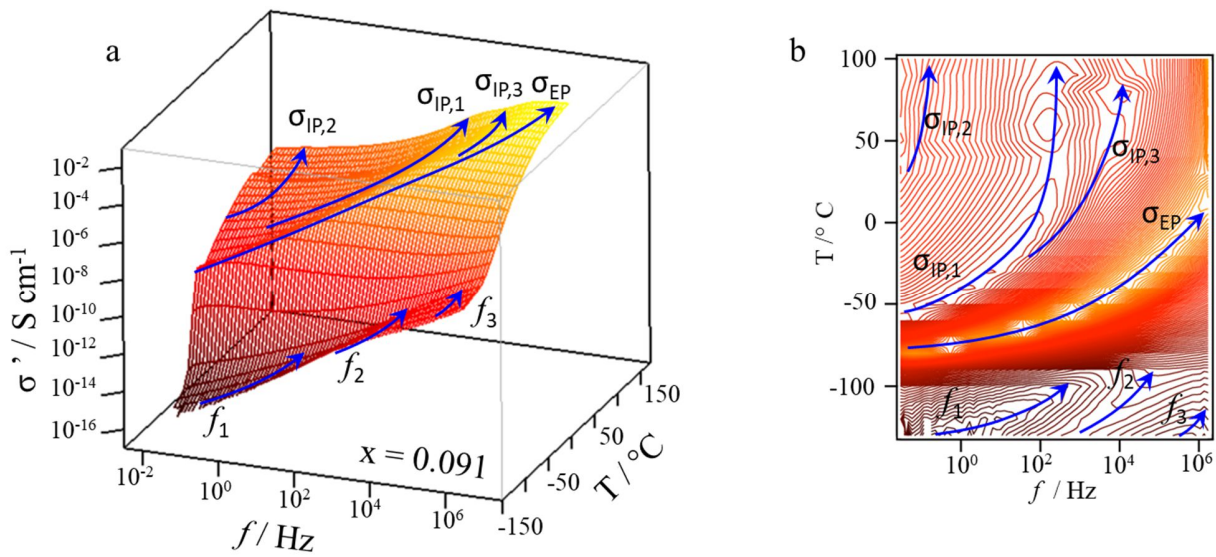


Figure 10.7. 3D conductivity spectra as a function of frequency and temperature (a). Counter plot of the conductivity (b). Both the figures are related to [Pyr₁₄Cl]/(AlCl₃)_{1.5}]/(δ-MgCl₂)_{0.091} sample.

The electric response, in terms of both the imaginary and real components of the conductivity and permittivity, are analysed with a suitable model, described by the following equation [52, 162]:

$$\varepsilon_m^*(\omega) = -i \left(\frac{\sigma_0}{\omega \varepsilon_0} \right)^N + \sum_{k=1}^n \frac{\sigma_k (i\omega \tau_k)^{\gamma_k}}{i\omega \varepsilon_0 [1 + (i\omega \tau_k)^{\gamma_k}]} + \sum_{j=1}^m \frac{\Delta \varepsilon_j}{[1 + (i\omega \tau_j)^{a_j}]^{b_j}} + \varepsilon_\infty \quad (10.1)$$

where $\varepsilon^*(\omega) = \varepsilon'(\omega) - i\varepsilon''(\omega)$, and $\sigma^*(\omega) = i\omega \varepsilon_0 \varepsilon^*(\omega)$. The first term of the equation describes the material conductivity at zero frequency. ε_∞ accounts for the permittivity of the material at infinite frequency (electronic contribution). The second term is associated with the electrode polarization and the interdomain polarizations. σ_k and τ_k are the conductivity and the relaxation times, respectively, associated with the k^{th} electrical event. γ_k is associated with the broadening of the k^{th} polarization peak. The third term accounts for the dielectric relaxation described by the Havriliak-

Negami theory [162, 182]. $\Delta\epsilon$, τ_j , α_j , and β_j are the dielectric strength, relaxation time, symmetric and antisymmetric shape parameter of each j^{th} relaxation event, respectively.

10.2.3.1 Polarization Phenomena

The conductivity values of all the polarization events, obtained by fitting the BES data using Equation 10.1, are plotted vs. T^{-1} . Each curve is fitted with a suitable model, *i.e.* Vogel-Tammann-Fulcher (VTF) [183] or Arrhenius (A) equation [162]. Results are reported in Figure 10.8.

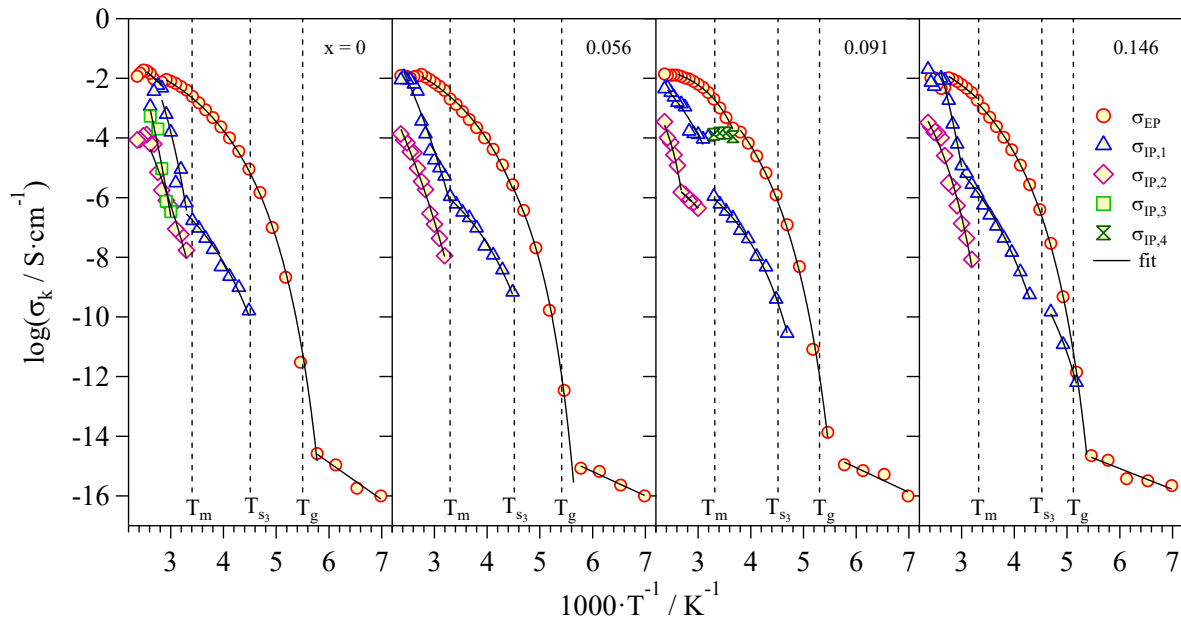


Figure 10.8. Log σ_k vs. T^{-1} curves of each polarization for every sample. Temperature regions are divided by the transition temperatures of each sample detected with MDSC measurements.

Four different temperature regions are detected, which are delimited by the thermal transitions detected by DSC measurements (T_m , T_{s1} , T_g). At temperatures higher than the glass transition temperature five polarization phenomena can be observed (see Figure 10.7): one electrode polarization (σ_{EP}), arising from the accumulation of charge at the interfaces between the sample and the electrodes of the measuring cell [162], and four different interdomain polarizations ($\sigma_{IP,i}$, with $1 \leq i \leq 4$), attributed to the charge accumulation at the interfaces between nano domains with different permittivity [162]. The presence of these latter events allows to confirm that the proposed materials are heterogeneous at the mesoscale, and that they consist of pyrrolidinium-based cation aggregates coordinated to chloroaluminate anion nanodomains, in agreement with vibrational spectroscopy results. At these temperatures all the polarizations reveal a VTF-like

behavior, demonstrating that the conductivity mechanism is assisted by the relaxations of the IL aggregates.

At $T < T_g$ σ_{EP} is the only detectable polarization phenomena, contributing with a very low conductivity ($<10^{-14} \text{ S}\cdot\text{cm}^{-1}$). This is in accordance with the limited mobility of ions at these temperatures, due to a low thermal activation energy available at these conditions for an effective conductivity process. Moreover, it follows an Arrhenius behavior, witnessing that, in this temperature region, charge migration occurs through hopping events between different domains.

The overall conductivity (σ_T) is calculated as the sum of the single conductivities of each polarization occurring in the electrolyte [205]:

$$\sigma_T = \sum_{k=1}^n \sigma_k = \sigma_{EP} + \sigma_{IP,1} + \sigma_{IP,2} + \sigma_{IP,3} + \sigma_{IP,4} \quad (10.2)$$

Figure 10.9 shows the logarithm of the overall conductivity as a function of T^{-1} .

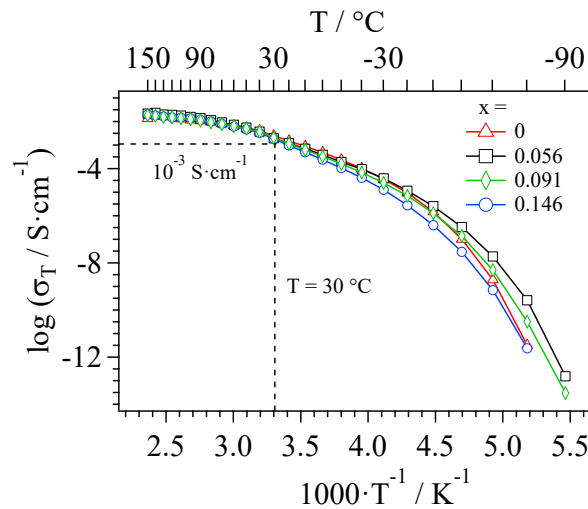


Figure 10.9. Log σ_T vs. T^{-1} curves for the various $[\text{Pyr}_{14}\text{Cl}/(\text{AlCl}_3)_{1.5}]/(\delta\text{-MgCl}_2)_x$ electrolytes.

Below 0 °C, an increase in the overall conductivity after the addition of $\delta\text{-MgCl}_2$ is observed. This indicates that the initial formation of Mg-chloroaluminate species improves the ability of the IL to exchange ionic species. After this initial improvement, further additions of the salt slightly decrease σ_T , thus witnessing that the increasing coordination network created by Mg-chloroaluminate species hinders the overall conductivity at high magnesium concentrations ($x \geq 0.091$). Above 0 °C the conductivity of all the samples seem to not be affected by the different additions of Mg salt, reaching room-temperature values higher than $10^{-3} \text{ S}\cdot\text{cm}^{-1}$. In particular, the

highest room-temperature conductivity value is $2.07 \cdot 10^{-3} \text{ S} \cdot \text{cm}^{-1}$ for $[\text{Pyr}_{14}\text{Cl}/(\text{AlCl}_3)_{1.5}]/(\delta\text{-MgCl}_2)_{0.091}$ sample.

The contribution of each polarization ($\varphi_k = \sigma_k / \sigma_T$) to the total conductivity (σ_T) as a function of temperature is shown in Figure 10.10.

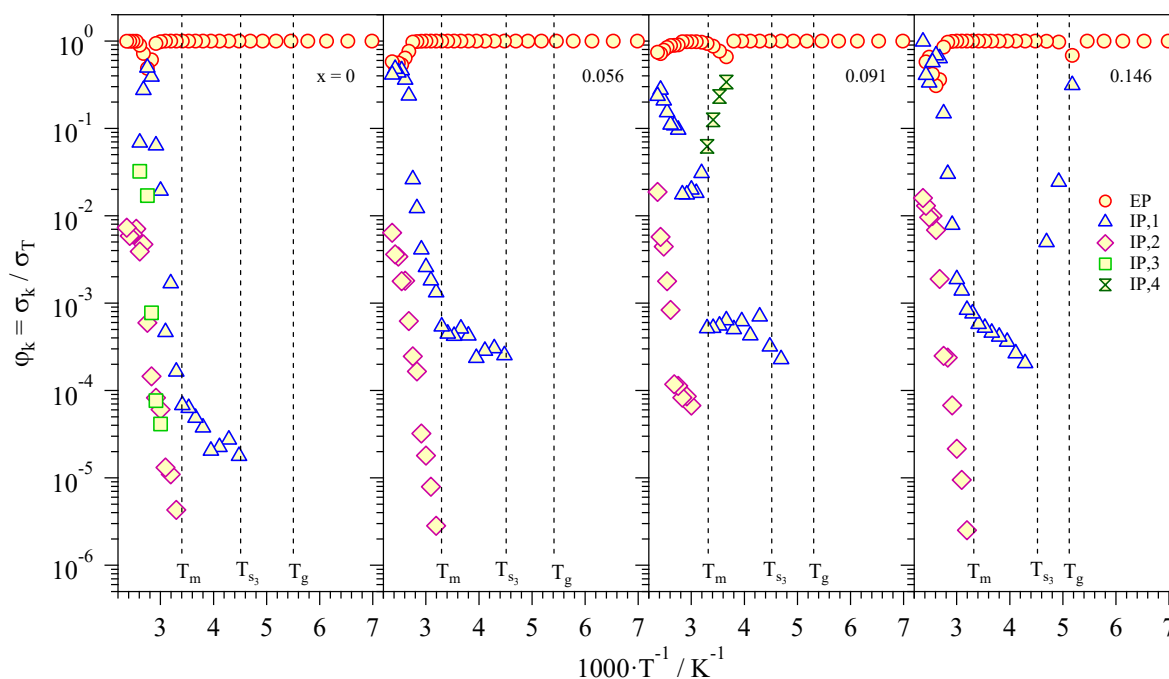


Figure 10.10. Contribution of each polarization (φ_k) to the total conductivity as a function of temperature.

The electrode polarization is the dominant contribution to the overall conductivity for all the samples and in the whole studied temperature range (Figure 10.10). Only $\sigma_{\text{IP},1}$, for some samples ($x=0.056$ and 0.146) and at a high temperature ($T \geq 100 \text{ }^\circ\text{C}$), reaches values comparable to those of σ_{EP} .

10.2.3.2 Dielectric Relaxation Events

The dielectric relaxation frequency (f_j) values, obtained from the fitting of the 3D surfaces of the electric response of the electrolytes, are plotted as a function of temperature (T^{-1}) and reported in Figure 10.11. All the curves are fitted with a Vogel-Tammann-Fulcher-Hesse (VTFH) [183] or an Arrhenius (A) [162] equations.

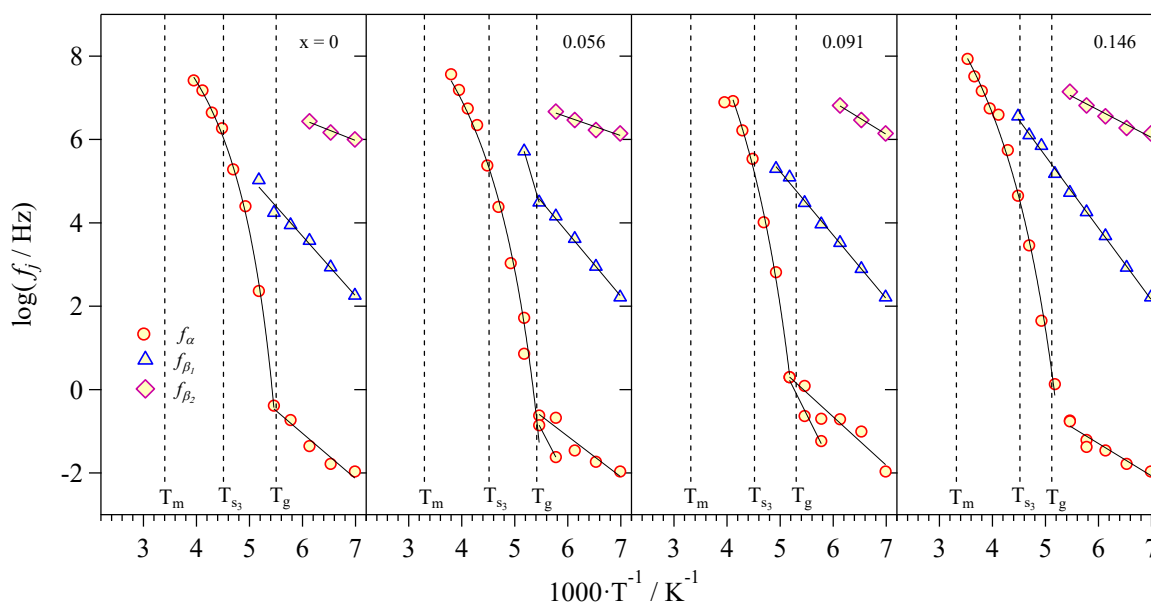


Figure 10.11. $\text{Log } f_j$ vs. T^{-1} curves of each dielectric relaxation event for every sample. Temperature regions are divided by the transition temperatures of each sample detected with MDSC measurements.

At $T < T_g$ three dielectric relaxation events (f_j , with $1 \leq j \leq 3$) are detected: α -, β_1 - and β_2 -modes. The α relaxation is attributed to the diffusion of conformational states along the interacting butyl chains, while β_1 and β_2 are associated with the rotational motion of Pyr_{14}^+ around the short and the long axis, respectively, of rod-like cations. β_1 takes place at a lower frequency with respect to β_2 due to the steric hindrance of the ordered butyl chains.

At $T_g < T < T_m$, the α relaxation follows a VTF behavior and probably is the only event that can modulate the electric response of the electrolytes.

In Figure 10.12 a representative sketch of the dielectric relaxation events detected for $[\text{Pyr}_{14}\text{Cl}/(\text{AlCl}_3)_{1.5}]/(\delta\text{-MgCl}_2)_x$ electrolytes is reported.

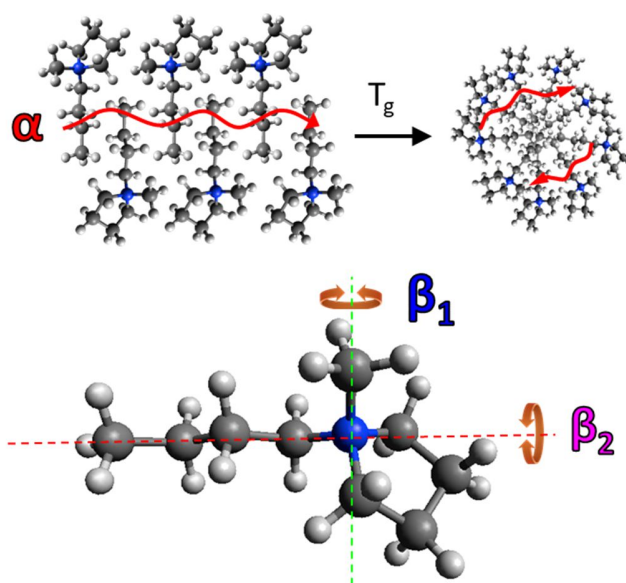


Figure 10.12. Representative cartoon of the dielectric relaxation events detected for these materials.

10.2.3.3 Activation Energies

The values of the activation energy (E_a), associated with the different conductivity pathways and dielectric relaxations, are calculated by fitting the curves reported in Figure 10.8 and Figure 10.11 using an Arrhenius or VTF/VTFH equations [162]. Results are reported in Figure 10.13.

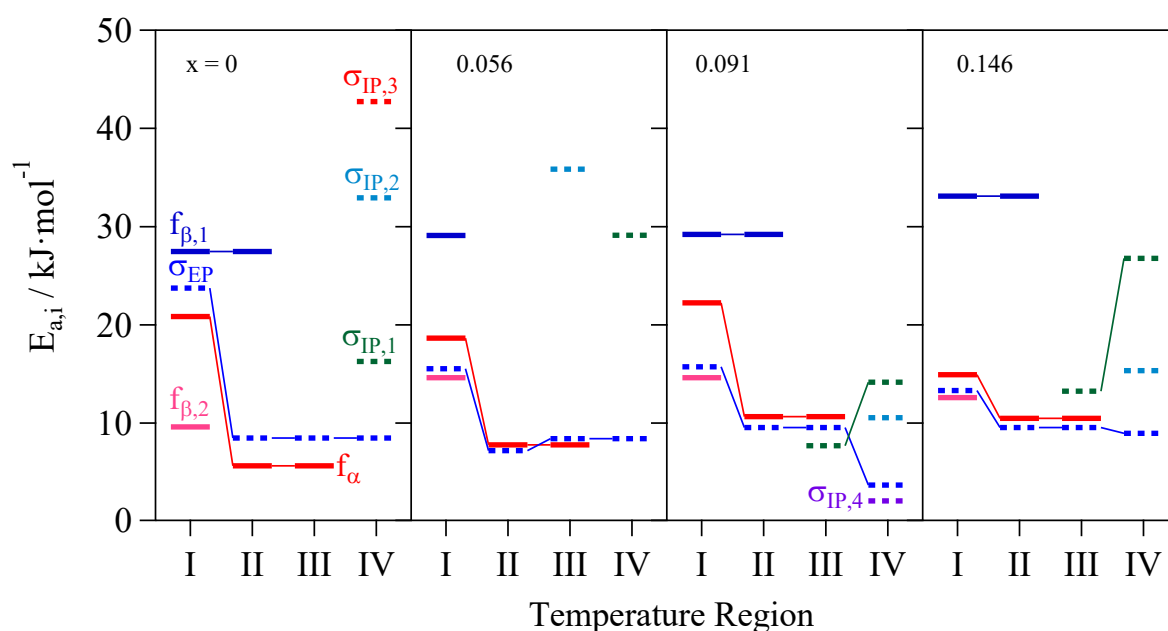


Figure 10.13. Activation energies calculated for each polarization phenomenon and relaxation event of every sample in the various temperature regions.

It can be observed that β_1 , detected only in the low temperature regions, shows the highest activation energy values ($27 < E_{a,\beta1} < 34 \text{ kJ}\cdot\text{mol}^{-1}$) and is not involved in the conductivity mechanism. On the contrary, at these temperatures, β_2 reveals an activation energy value very close to that of σ_{EP} , indicating that the relaxation of piled cations facing anions is modulating the overall conductivity mechanism. At higher temperatures ($T > T_g$) the activation energy of the electrode polarization is more similar to $E_{a,\alpha}$ (*i.e. ca.* $9 \text{ kJ}\cdot\text{mol}^{-1}$). Thus, at high temperature the diffusion of conformational states along the butyl chains enables the fluctuation of the cationic aggregates which actively modulates and activates the charge transfer mechanism.

10.2.3.4 Charge Migration Distances

The temperature dependence of the average charge migration distance ($\langle r_k \rangle$) for the different percolation pathways can be calculated following the Einstein-Smoluchowski equation:

$$\langle r_k \rangle(T_i) = \sqrt{6D_{\sigma_k} \tau_k} = \sqrt{\frac{6RT_i \sigma_k \tau_k}{Z_k^2 C_k F^2}} \quad (10.3)$$

where R is the gas constant, T_i corresponds to the temperature at which R is calculated, σ_k and τ_k are the conductivity and the relaxation time of the k^{th} polarization, Z_k and C_k are the charge and concentration of the k^{th} species exchanged during the σ_k polarization, and F is the Faraday constant. Results are reported in Figure 10.14.

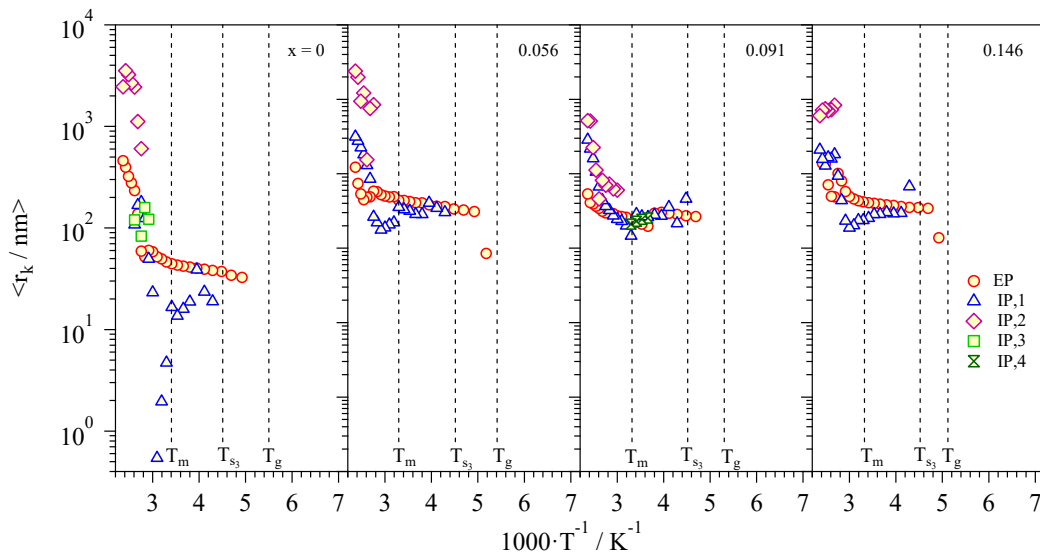


Figure 10.14. Average charge migration distances vs. T^{-1} for $[\text{Pyr}_{14}\text{Cl}/(\text{AlCl}_3)_{1.5}]/(\delta\text{-MgCl}_2)_x$ samples.

Generally, $\langle r_k \rangle$ increases with T, due to a higher thermal energy. Moreover, it grows also with x, indicating that the delocalization bodies (DBs) formed by aggregates of cations with different morphologies are increasing in size and that charge carriers can reach longer distances. In details, a delocalization body is a volume of the bulk electrolyte where the active species are exchanged so fast to be considered delocalized along the percolation pathways.

Concluding, the conductivity mechanism occurs by the long-range charge migration of Mg-coordinated anion species that are exchanged between different DBs, and it is mainly assisted by the effect of the segmental motions of Pyr₁₄⁺ aggregates (α -mode).

10.2.4 Electrochemical Characterization

The ability of the proposed electrolytes to reversibly deposit magnesium is evaluated by cyclic voltammetry tests, using a three-electrode configuration cell, with a Pt working electrode, and Mg reference and counter electrodes. [Pyr₁₄Cl]/(AlCl₃)_{1.5}]/(δ -MgCl₂)_{0.056} electrolyte is selected, because of its optimal mixture of low viscosity, high conductivity, high stability, and low overpotential in the redox processes. In Figure 10.15 the results of the measurements are reported.

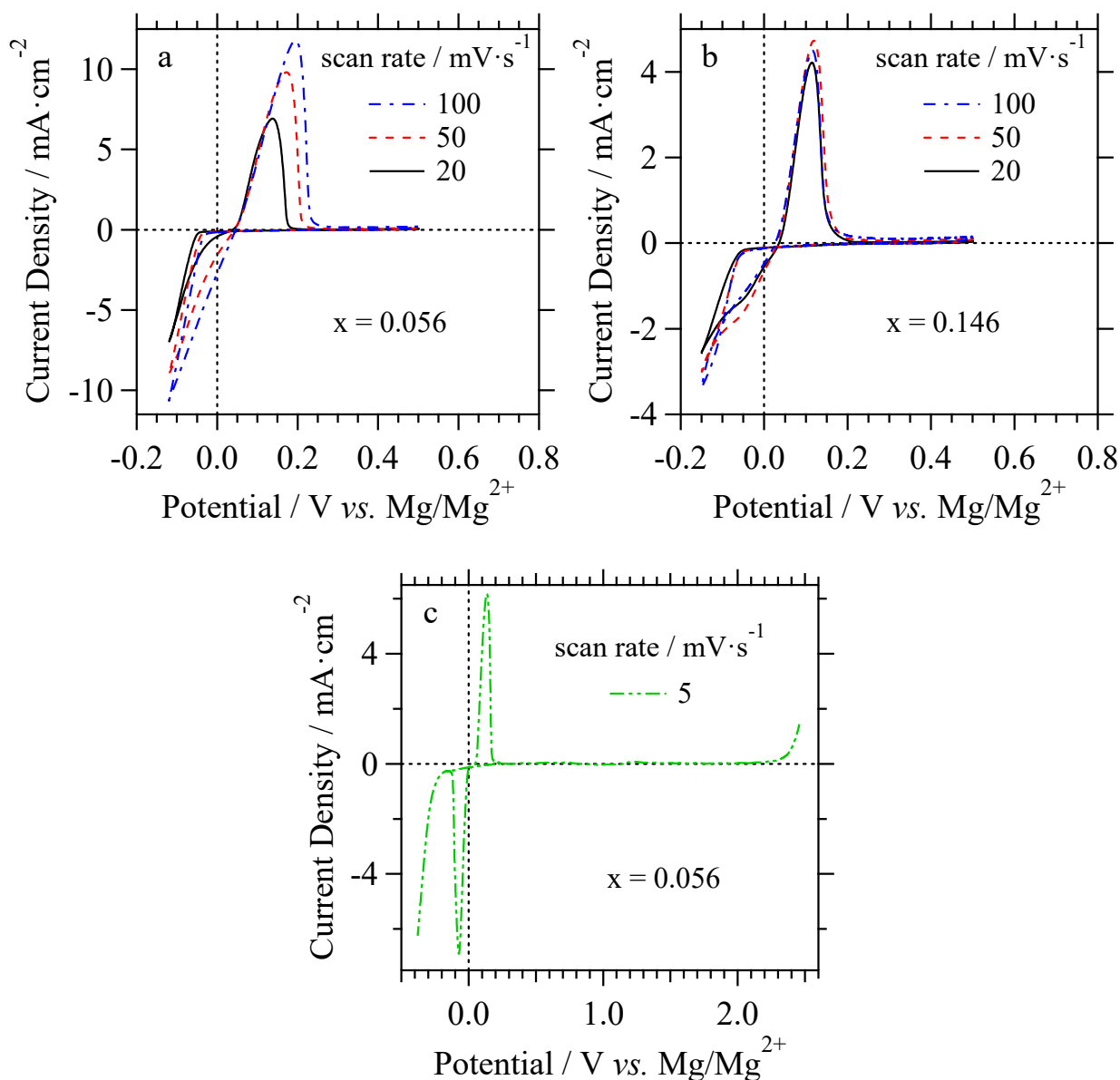


Figure 10.15. CV deposition/stripping measurements of [Py_{r14}Cl]/(AlCl₃)_{1.5}/(δ -MgCl₂)_{0.056} (a) and [Py_{r14}Cl]/(AlCl₃)_{1.5}/(δ -MgCl₂)_{0.146} (b) at different scan rates on a platinum working electrode. ESW of [Py_{r14}Cl]/(AlCl₃)_{1.5}/(δ -MgCl₂)_{0.056} at 5 mV·s⁻¹ (c).

As it can be observed, this electrolyte shows a lower overvoltage in the deposition (only 50 mV vs. Mg/Mg²⁺), and/or higher current densities with respect to similar [23, 133] and competing [117-119, 132, 286] materials. These exceptional results, if compared to the *state of the art* electrolytes materials for rechargeable magnesium batteries, will allow to obtain devices with very high energy efficiencies, due to the low overpotential in the deposition and dissolution of Mg, and high rate capabilities, thanks to the fast kinetics in the redox processes. One interesting feature of the

proposed materials is that even the most concentrated sample ($x = 0.146$) is able to reversibly deposit Mg with a low overpotential and a quite high current density (see Figure 10.15b).

The electrochemical stability window is evaluated by a linear sweep voltammetry. Sweep in the anodic and cathodic direction are docked together in Figure 10.15c. The oxidation limit is restricted by the degradation of aluminum chloride and the consequent formation of chlorine. Nevertheless, a potential of 2.35 V vs. Mg/Mg²⁺ can be reached. On the cathodic side, the use of a pyrrolidinium-based ionic liquid instead of an imidazolium [57], allows to shift the stability limit towards more negative potentials, *i.e.* < -0.2 V vs. Mg/Mg²⁺, thus separating the reduction degradation of the IL from the Mg deposition events. Indeed, from the figure, it is clear that they are not overlapping.

Finally, the average coulombic efficiency is evaluated by using the Aurbach method [284], and results are reported in Figure 10.16.

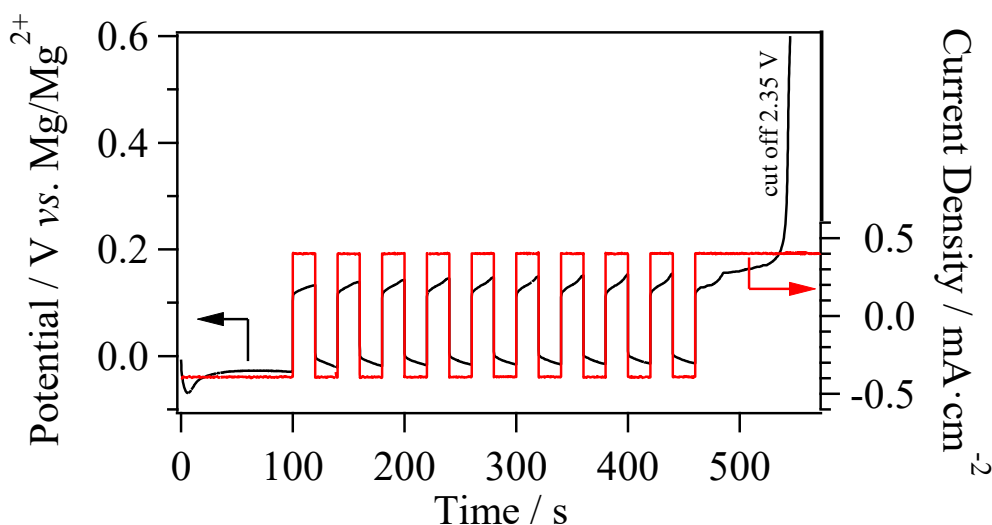


Figure 10.16. Average coulombic efficiency evaluation for [Pyr₁₄Cl]/(AlCl₃)_{1.5}/(δ -MgCl₂)_{0.056} electrolyte.

As expected, the overpotential, especially in the magnesium deposition, is very low (*ca.* 15 mV). This electrolyte exhibits an average coulombic efficiency of 99.65 %, which is one of the best among IL-based electrolytes, improving by more than 1.6 % the analogous [EMImCl]/(AlCl₃)_{1.5}/(δ -MgCl₂)_{0.08} electrolyte [57]. Furthermore, a negligible shift in the overvoltage is detected in the first ten cycles, demonstrating a good stability over cycling.

The electrodeposited layer that can be obtained during a galvanostatic experiment is studied by both ICP-AES and SEM microscopy (Figure 10.17), to evaluate the metal composition of the electrodeposited layer and to determine the homogeneity with which it can be formed.

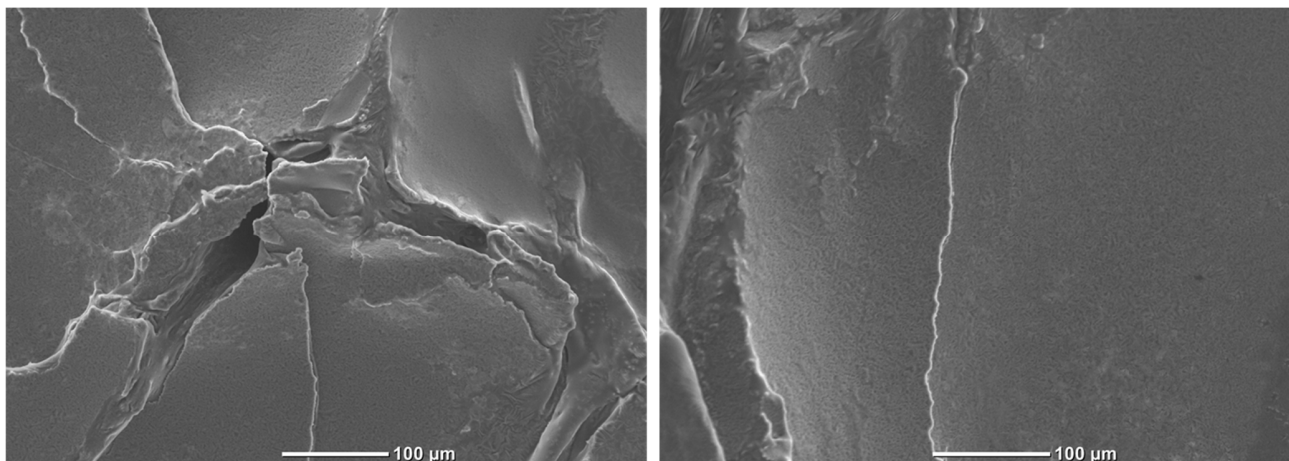


Figure 10.17. SEM images of the electrodeposited layer.

The electrodeposited layer consists of an Al-Mg alloy, as already demonstrated by similar electrolytes [57]. Nevertheless, with respect to $[\text{EMImCl}/(\text{AlCl}_3)_{1.5}]/(\delta\text{-MgCl}_2)_{0.08}$, the magnesium concentration in the alloy is three times richer ($\phi 29.1 \rightarrow 10.5$, with $\phi = n_{\text{Al}}/n_{\text{Mg}}$ in the alloy). SEM images of the electrodeposited alloy revealed a roughness-free layered surface, demonstrating a homogeneity in the electrochemical process and anticipating an efficient magnesium deposition on the anode surface during the battery charge process.

10.2.5 Battery Test

In order to demonstrate the applicability of the proposed electrolytes in a real cycling device, the best material is sandwiched between a Mg metal anode and a vanadium oxide-based cathode in a EL-CELL testing battery. The device is cycled in a potential range $0.5 \div 2.5$ V vs. Mg/Mg²⁺ at different current rates (*ca.* 0.9 and 1.8 C). The battery is then tested for 100 cycles at $350 \text{ mA}\cdot\text{g}^{-1}$ (*ca.* 1.8 C). Preliminary results are shown in Figure 10.18.

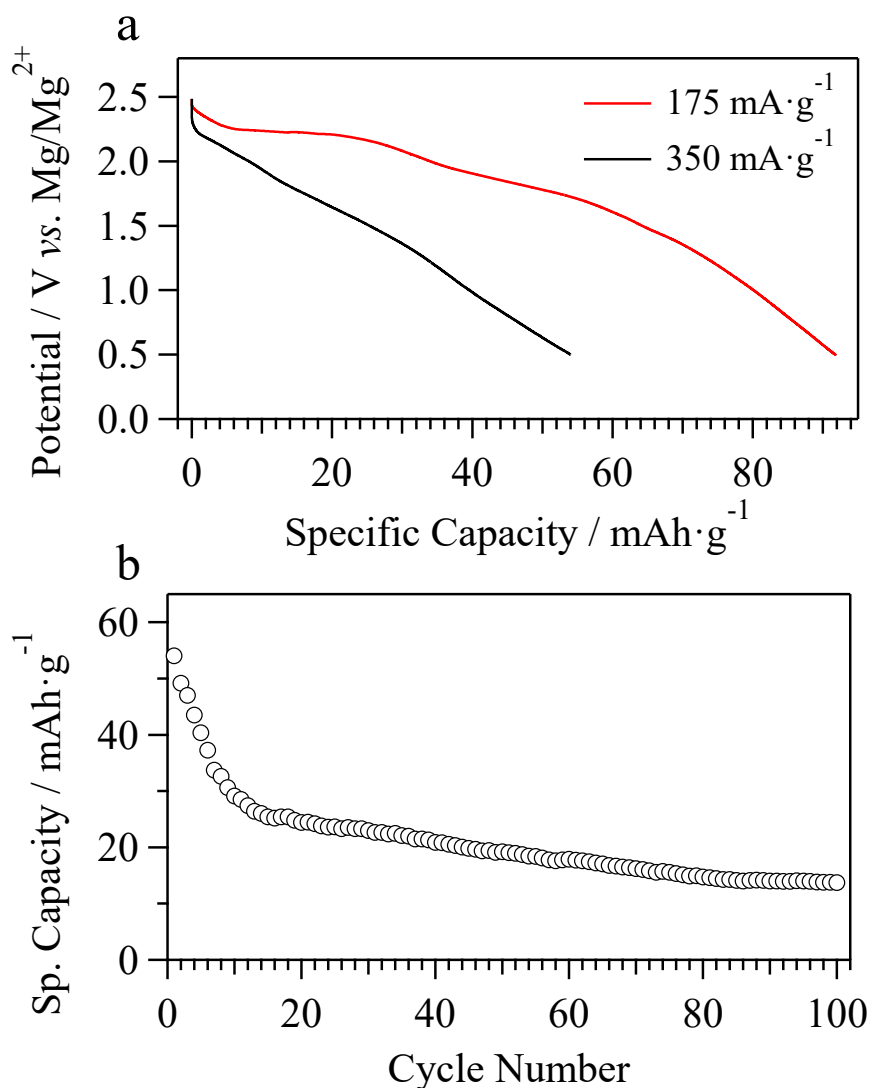


Figure 10.18. Cycling performances of a Mg[Py₁₄Cl]/(AlCl₃)_{1.5}/(δ -MgCl₂)_{0.056}|V₂O₅ battery at different current rates (a) and long-term cycling at 350 mA·g⁻¹ (b).

The good performances demonstrated in CV tests are confirmed by the galvanostatic cycling measurements. The electrolyte is able to sustain remarkable current rates, higher than those at which V₂O₅ is typically cycled in literature (*ca.* 35 mA·g⁻¹ [57]). An initial discharge specific capacity of 92 mA·g⁻¹ is achieved when the battery is cycled at 175 mA·g⁻¹, while it drops at 54 mA·g⁻¹ when cycled at 350 mA·g⁻¹. These values are higher than those reported using the imidazolium-based ionic liquid [57], and also using other type of electrolytes [140, 141]. Only if the architecture of the cathode is optimized, a higher capacity is demonstrated in literature [142]. Nevertheless, in the study reported in literature [142], the current rate at which the battery is tested is five times

lower than the one reported in this work. Even if the capacity drop is not negligible, the device obtained using the proposed electrolyte is able to be charged and discharged for over 100 cycles. After 100 cycles, a residual capacity of *ca.* 15 mAh·g⁻¹ is still obtained, which, for a magnesium secondary battery, it is still a remarkable result. Indeed, in a water-free device, these results are one of the best ever reported in literature for a non-optimized V₂O₅ cathode material, in terms of specific capacity, working potential, and cyclability at elevated current rates [287].

10.3 Conclusions

In this work a new family of four [Pyr₁₄Cl/(AlCl₃)_{1.5}]/(δ-MgCl₂)_x electrolytes with 0 ≤ x ≤ 0.146 is studied. DSC investigations reveal that the thermal transitions of the proposed materials are significantly affected by the different concentrations of δ-MgCl₂ salt, and that they consist of anion and cation nanodomains. Vibrational studies confirm the heterogeneity of the compounds and suggest that: i) two different anionic complexes are present in the electrolytes, the AlCl₄⁻ monomer and the Al₂Cl₇⁻ dimer; ii) after the addition of the salt, magnesium species are coordinated by the halometallate compounds, forming concatenated Mg-chloroaluminate complexes; and iii) on x, the concentration of Al₂Cl₇⁻ decreases, while that of AlCl₄⁻ increases. BES studies reveal that the electric response of [Pyr₁₄Cl/(AlCl₃)_{1.5}]/(δ-MgCl₂)_x electrolytes is modulated by four dielectric events (at T < T_g) and four polarization phenomena (at T > T_g). The long-range charge migration process is mediated by the fluctuations of Pyr₁₄⁺ aggregates, which assist the Mg-ion conductivity mechanism. A room-temperature conductivity of 2.07·10⁻³ S·cm⁻¹ for [Pyr₁₄Cl/(AlCl₃)_{1.5}]/(δ-MgCl₂)_{0.091} sample is demonstrated. Finally, electrochemical investigations prove that the proposed electrolytes are able to deposit and strip magnesium with low overpotentials, high efficiencies, and with fast kinetics. Battery devices assembled with these materials demonstrate remarkable discharge capacities (92 mAh·g⁻¹) and a promising long-term cyclability (> 100 cycles).

11. Graphene Oxide Decorated Vanadium Nanoparticles: a High Power Cathode for Magnesium Batteries

Magnesium secondary batteries have the capability to ensure high volumetric capacity, safety, and cost saving due to Mg abundancy, dendrite-free electrodeposition, and environmentally green properties. Since the main roadblock to the development of this technology is the finding of a suitable electrolyte, great efforts still have to be done in this field. Nevertheless, the research in high performing cathodes able to host magnesium ions with good capacity at high current is very weak. Thus, the research in Mg-batteries should be focused also in this topic. Following this, the synthesis and the characterization of an innovative cathode (GO@V) for secondary magnesium batteries is reported in this work. The novelty of this material is its new architecture: vanadium-based active species are locally covered by a graphene oxide layer, in order to protect it and ensure a high electric conductivity. Thus, the material is able to sustain high current rates, with a low decay in capacity performances. The architecture of this cathode is studied by high-resolution thermogravimetric analysis and vibrational spectroscopies. The electrochemical features are elucidated by cyclic voltammetry experiments and by galvanostatic cycling test. This latter experiment demonstrates that the material is able to deliver a good specific capacity ($72 \text{ mAh}\cdot\text{g}^{-1}$) at a high working potential (*ca.* 1.80 V), even if cycled at extremely high currents ($1000 \text{ mA}\cdot\text{g}^{-1}$). Thus, a specific power of $1.70 \text{ W}\cdot\text{g}^{-1}$ can be reached, that is the highest value ever reported in literature for a cathode in a Mg secondary battery and that makes it competitive with lithium batteries. Nevertheless, further improvements in the cyclability of the device need to be pursued.

11.1 Experimental Section

11.1.1 Reagents

Vanadium(IV) sulfate oxide hydrate (99.9 %) and graphite (type SK6) are obtained from Alfa Aesar and TIMCAL, respectively. Sulfuric acid (98.0 %), barium chloride (99.9 %), ammonium hydroxide solution (30.0 %), polyvinyl difluoride (PVDF), 1-methyl-2-pyrrolidone (NMP, 99.5%, anhydrous), 1-ethyl-3-methylimidazolium chloride-aluminum chloride 1:1.5 (ionic liquid, IL), magnesium powder, magnesium foil, and 1-chlorobutane are purchased from Sigma-Aldrich. Graphene oxide (GO) is home-made produced following the modified Hummers method [288].

11.1.2 Electrochemical Activation of Vanadium Species

In the first step a 1.0 M solution of vanadium sulfate is prepared by dissolving VOSO_4 in 5.0 M H_2SO_4 . Then, the obtained mixture is divided into two bottles with a volume ratio of 1:2, and inserted into a system that provide an ionic interconnection by the interposition of a Nafion 117® proton conducting membrane. A potential of +1.80 V is applied to two carbon paper electrodes that are previously immersed into the two solutions. The electrochemical activation process is considered completed when the oxidation of V(IV) to V(V) species occurring in the negative side of the system yields the 96 %. Concurrently, in the second solution, V(II) species are obtained.

11.1.3 GO@V Synthesis

60 mL of the activated 1.0 M V(V) sulfate solution are diluted with 240 mL of double-distilled water. Then, 75.162 g of barium chloride are added, in order to exchange sulfate anions with chloride ions. Indeed, a white precipitate is formed (BaSO_4). The mixture is stirred for 2 h and then the solid is removed by filtration. 100 mL of this filtered solution are added to 5 mL of a $10 \text{ mg}\cdot\text{mL}^{-1}$ GO suspension and vigorously stirred for 30 minutes. During stirring, 4.5 mL of a 30 % NH_4OH aqueous solution are added dropwise, and stirred for other 1 h. The mixture is finally transferred into a sealed Teflon-lined stainless-steel autoclave and heated at 200 °C for 12 h with a heating ramp of $2 \text{ }^\circ\text{C}\cdot\text{min}^{-1}$. After cooling, the solvent is evaporated under vacuum at 90 °C. The obtained GO@V sample is washed several times with cold methanol and dried again under vacuum at 70 °C for 12 h. The IL-based electrolyte for electrochemical investigations and battery tests is synthesized as reported elsewhere [57]. In particular, the electrolyte is obtained by reacting 1-ethyl-3-methylimidazolium chloride with aluminum trichloride, in a molar ratio 1:1.5. To this novel ionic liquid, 2 wt% of $\delta\text{-MgCl}_2$ salt is added as a source of magnesium ions.

11.2 Results and Discussion

11.2.1 Composition

The weight ratio between vanadium and graphene oxide is determined by ICP-AES and CHNS analyses, and it is equal to *ca.* 20:1. This specific vanadium-carbon composition ratio is decided in order to synthesize the GO@V material with an architecture where graphene oxide flakes are only forming a surface layer on the vanadium-based particles. Thus, the inter-particle electric contact and the contact between particles and the electrode is actively formed. Elemental analysis confirms also the inclusion of nitrogen, validating the hypothesis of the presence of a positive charged

ammonium shell that allows vanadium particles and graphene oxide flakes to be kept in contact through electrostatic interactions. Less than 0.1 %_wt of barium is found, confirming that BaSO₄ is completely removed by the washing process. In Figure 11.1 a cartoon schematically represents the hypothesized architecture of the proposed material.

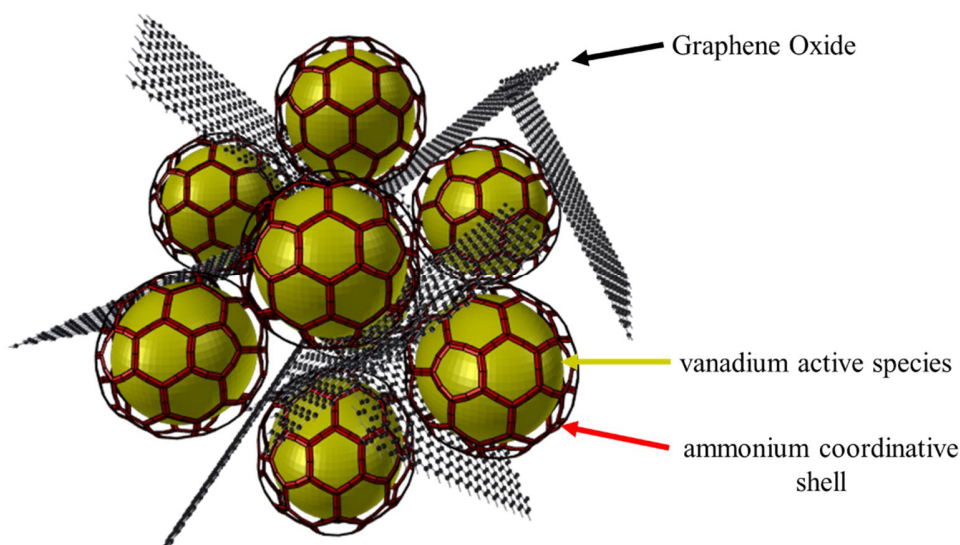


Figure 11.1. Representative sketch of the GO@V architecture. It can be observed how the positively-charged ammonium “shell” is able to coordinate the negatively-charged vanadium active species nanoparticles to the graphene oxide nanoflakes.

11.2.2 Thermal Behavior

The high-resolution thermogravimetric analysis result under a nitrogen atmosphere is reported in Figure 11.2.

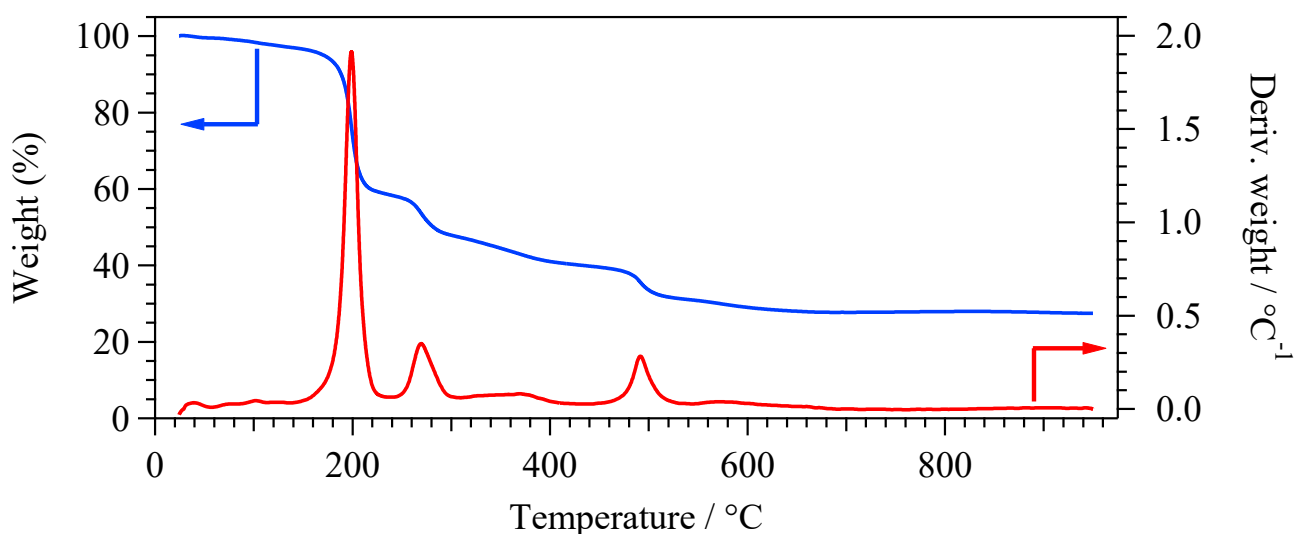


Figure 11.2. HR-TGA profiles of GO@V sample obtained under a N₂ atmosphere.

HR-TGA profiles reveal the presence of three main events at *ca.* 150, 250, and 460 °C, respectively. These thermal decomposition events are assigned to the multi-step degradation of the ammonium shell, that occurs giving rise to the formation of several ammonium-oxyvanadyl species with a gradually lower NH_4^+ content [289]. During these events, the evolution of chloro- and sulphur-based species can also occur with a marginal contribution to the weight loss. At *ca.* 315 °C a partial decomposition is observed, that can be attributed to the degradation of a few amount of ammonium chloride. The residual weight (27.5 %_{wt}) is attributed to the presence of vanadium oxide and graphene oxide compounds.

This measurement is very useful to confirm the architecture of the active material. Indeed, the observed thermal profile is very similar to that of ammonium metavanadate, which occurs in three steps (*i.e.* $\text{NH}_4\text{VO}_3 \rightarrow (\text{NH}_4)_2\text{V}_4\text{O}_{11} \rightarrow \text{NH}_4\text{V}_3\text{O}_8 \rightarrow \text{V}_2\text{O}_5$, at *ca.* 160, 195, and 260 °C) [289]. Thus, we are observing the thermal decomposition of the particles shell where ammonium and vanadium-based species are effectively coordinated. Differently from NH_4VO_3 , the ammonium degradation taking place in the proposed GO@V active materials is shifted towards higher temperatures, demonstrating that: i) a low content of oxygen atoms is present, which hinders the formation of vanadium oxide; ii) the addition of graphene oxide increases the thermal stability of the obtained materials; and iii) the vanadium-based particles, the ammonium shell, and the GO flakes are dynamically interacting, creating a strong coordination network that leads to the proposed architecture.

11.2.3 Morphology and Structure

11.2.3.1 Electron Microscopy

The obtained material is investigated by SEM measurements, and results are reported in Figure 11.3.

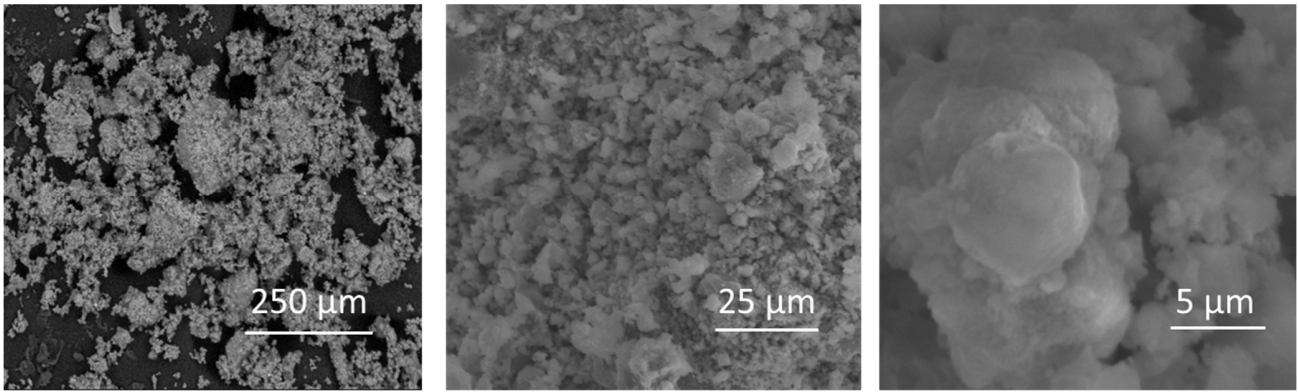


Figure 11.3. SEM micrographs of GO@V material at different magnifications.

Scanning electron microscopy images reveal that graphene oxide flakes are strictly coordinated to vanadium-based particles on their surface. The dimensional distribution of GO@V material is homogeneous, with a bi-modal particle size dispersal: i) large particles with an average diameter of *ca.* 5 μm ; and ii) smaller particles with a diameter lower than 1 μm grown on the surfaces of the larger particles.

11.2.3.2 Vibrational Analyses

The structure and coordination occurring in the here proposed material are studied by ATR-FTIR and micro-Raman spectroscopies, as shown in Figure 11.4.

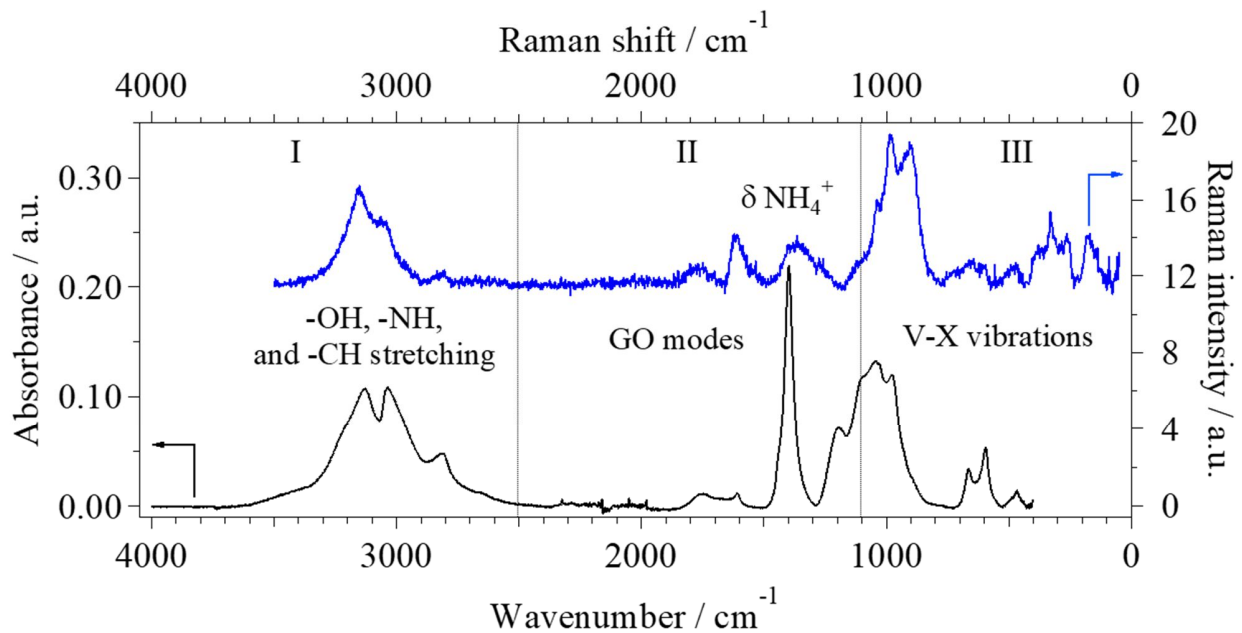


Figure 11.4. Micro-Raman (blue) and ATR-FTIR (black) vibrational spectra of GO@V sample.

The spectra can be divided into three different regions: i) in region I, between 4000 and 2500 cm^{-1} , the typical -OH, -CH, and -NH stretching (ν) vibrations are detected, due to the presence of hydroxyl and alkyl groups of graphene oxide, and amine groups of ammonium bridges [290-295]; ii) region II, 1750÷1100 cm^{-1} , is dominated by the presence of the symmetrical bending of ammonium ions ($\delta_s(\text{NH}_4^+)$) at 1390 cm^{-1} [295, 296] and the peaks attributed to the graphene oxide matrix (*e.g.* $\nu(\text{C}=\text{O})$, $\nu(\text{C}=\text{C})$, $\tau(\text{CH}_2)$) [290, 291, 293, 294, 297-300]; and iii) at low wavenumbers (region III), below 1100 cm^{-1} , the peaks attributed to the vibrational modes of different V-X ($\text{X}=\text{NH}_4^+$, SO_4^{2-} , Cl^-) functional groups are found [289, 295, 296, 301-303]. A complete correlative assignment of vibrational modes of GO@V compound is given in Table 11.1.

Table 11.1. Correlative assignment of FT-FIR and micro-Raman vibrations for GO@V sample.

ATR-FTIR ^a	Micro-Raman ^a	Assignment ^b	Ref
3447 (vw,sh)		$\nu(\text{OH})$	[290-292]
3129 (m)	3151 (m)	$\nu(\text{OH})$	[291-293]
3036 (m)	3060 (m)	$\nu(\text{CH})$	[294]
2813(w)	2835 (w)	$\nu(\text{NH}_4)$	[295]
1749 (vw)	1765 (vw)	$\nu(\text{C}=\text{O})$	[290, 293, 297, 298]
1609 (vw)	1611 (w)	$\nu(\text{C}=\text{C})$, G band	[290, 291, 293, 298]
1398 (s)	1372 (w)	$\delta_s(\text{NH}_4)$	[295, 296]
	1280 (w)	$\nu(\text{C}=\text{C})$, D band	[299]
1192 (w)		$\tau(\text{CH}_2)$	[300]
1096 (m,sh)	1115 (m,sh)	$\nu(\text{C}-\text{O})$	[293, 294]
1044 (m)	1037 (m)	$\nu(\text{V}=\text{O})_{\text{term}}$	[289, 296]
978 (m)	978 (s)	$\nu(\text{V}=\text{O})_{\text{term}}$	[289, 295, 296, 301, 302]
	904 (s)	$\nu(\text{V}=\text{O})$	[301]
663 (w)	660 (vw)	$\nu_{\text{as}}(\text{V}-\text{O}-\text{V}) + \nu_{\text{as}}(\text{V}-\text{O}-\text{S})$	[289, 296, 301]
595 (m)		$\delta_s(\text{SO}_3)$	[301]
467 (w)	465 (vw)	$\nu_{\text{as}}(\text{V}-\text{Cl}) + \delta(\text{V}-\text{O}-\text{S})_{\text{bridg}} + \delta(\text{V}-\text{O}-\text{V})_{\text{bridg}}$	[301-303]
	372 (w,sh)	$\nu_s(\text{V}-\text{Cl})$	[303]
	329 (w)	$\delta_s(\text{Cl}-\text{V}-\text{Cl})$	[303]
	259 (w)	$\delta_s(\text{Cl}-\text{V}-\text{Cl}) + \delta_{\text{as}}(\text{Cl}-\text{V}-\text{Cl}) + \delta(\text{V}-\text{O})$	[302, 303]
	176 (w)	$\delta_s(\text{Cl}-\text{V}-\text{Cl})$	[303]

^aIntensities are reported in brackets: s=strong; m=medium; w=weak; vw=very weak; sh=shoulder. ^b ν stretching; δ bending; τ twisting; term terminal; bridg bridging; s symmetric; as antisymmetric.

The order-disorder relation of the crystal structure in graphene oxide-based material can be evaluated analyzing region II of the here reported spectra. Indeed, the ratio between the intensities

of the D and G bands in Raman spectra is an index of the quantity of defects present into the GO network. The G band is attributed to the *in-phase* vibration of the E_{2g} mode of the sp^2 carbon domains, while the D band arises when a) a disordered structure with a symmetry breaking or b) edges on the flakes are present in the graphene oxide matrix [299]. In the case of GO@V material, the I_D/I_G ratio is equal to *ca.* 0.46, indicating the presence of a very well crystalline graphene-based compound, with a high ordering and a low number of defects. Region III is the fingerprint of the complex metal network existing in vanadium-based particles composing GO@V material. The observed vibrations reveal the presence of: i) $(V-O-V)_n$ chain-like structures; ii) vanadium and sulphur residual atoms interconnected by oxygen ions; iii) oxygen atoms that are coordinating 3 or 4 different vanadium ions; and iv) $(Cl-V-Cl)_n$ functional groups. Moreover, the peak pointing at *ca.* 663 cm^{-1} confirms the hypothesis that the vanadium-based active species are predominately dominated by the presence of a framework-like structure rather than a chain-like structure [296]. Concluding, structural analyses endorse the hypothesis of the successful formation of the complex architecture represented in Figure 11.1.

11.2.4 Electrochemical Characterization

Cyclic voltammetry experiments are conducted using a three-electrodes cell, with a platinum working electrode covered by the cathode ink, and magnesium metal ribbons used as reference and counter electrodes. The redox reactions occurring in GO@V material during the insertion and extraction of Mg^{2+} ions are very well characterized by cyclic voltammetry experiments, as shown in Figure 11.5a.

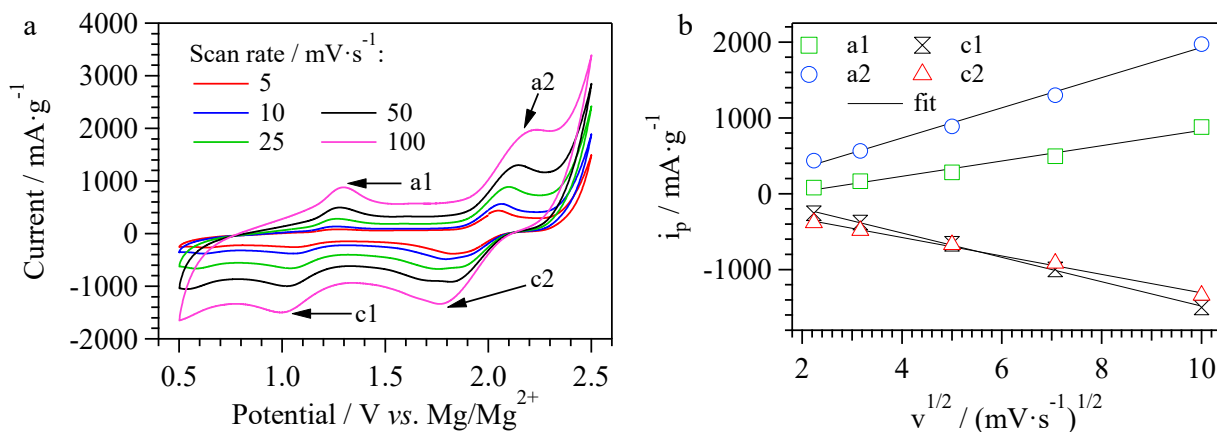


Figure 11.5. CV tests at different scan rates (a); peak current of the different redox events as function of the square root of the scan rate (b).

Cyclic voltammetry tests reveal the presence of two different redox processes, with the appearance of two cathodic peaks at *ca.* 1.0 V (c1), and at *ca.* 1.8 V (c2), and the corresponding anodic peaks at *ca.* 1.3 V (a1), and 2.2 V (a2). They demonstrate a high reversibility with a quite low overpotential. The oxidation of the electrolyte appears at high potential (>2.35 V) [57], which is superimposed to the electrochemical reactions characterizing GO@V cathode material, in particular reaction a2. The events detected by CV experiments seems to be similar to those of pure V₂O₅ [304]: this indicates that, during the reduction of vanadium species, magnesium ions are inserted into the vanadium matrix following two different steps, that occur at 1.0 V and 1.8 V. Thus, a gradual occupancy of two different sites in the crystalline structure is taking place [304]. After the fully insertion of Mg²⁺ in the hosting sites, magnesium ions are then removed in the back scan of the CV, with the formation of two oxidation peaks at *ca.* 2.2 and 1.3 V. The similarity between the GO@V proposed material and pure V₂O₅ could be explained by the presence of the same active species (V(V)) in the both compounds. Furthermore, it is observed that the electrochemical insertion and extraction of magnesium ions is highly stable in time. In Figure 11.5b the correlation between the intensity of peak current vs. the square root of the scan rate is reported for each redox event. It is shown that a very well defined linear trend is present, demonstrating that the kinetics of the electrochemical reactions occurring in this material are very fast (rapid charge transfer) and, again, these events are highly reversible. Thus, the architecture suitably designed following the here reported synthetic protocol, enables the production of a cathode able to insert and extract magnesium ions with a high reversibility and high current.

11.2.5 Battery Test

Finally, the cycling performances of the here proposed cathode material are evaluated assembling a CR2032 coin cell device, using a magnesium metal anode and an ionic liquid-based electrolyte [57]. The battery is cycled between 0.5 and 2.5 V, at a current rate of $1000 \text{ mA}\cdot\text{g}^{-1}$, $4.12 \text{ mA}\cdot\text{cm}^{-2}$, corresponding to *ca.* 12.5 C. Figure 11.6 reports the obtained cycling performances of GO@V, evaluated by amperostatic charge/discharge test over the first five cycles.

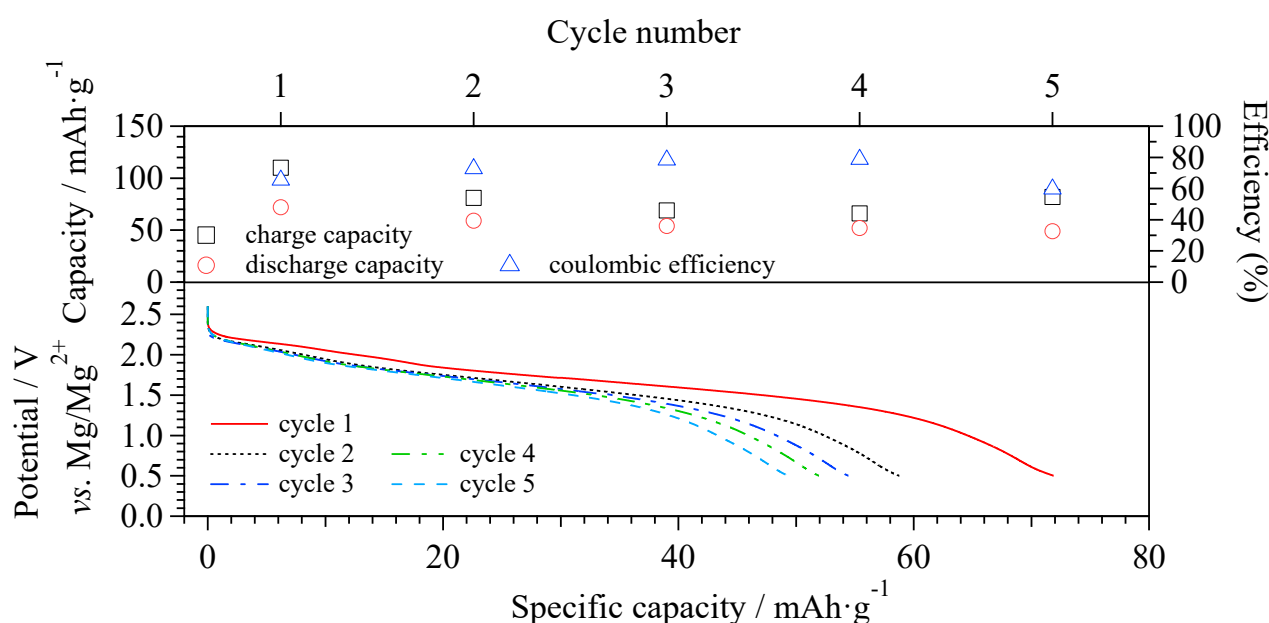


Figure 11.6. Cycling performances of GO@V sample, cycled at a current rate of *ca.* 12.5 C ($1000 \text{ mA}\cdot\text{g}^{-1}$).

The presence of two different plateaus is detected in the discharge profiles, which are occurring at *ca.* 2.20 and 1.70 V. This is consistent with the beginning of the reduction peaks observed by CV tests. The slight discrepancy in the potential between galvanostatic tests and CV experiments could be attributed to the higher proximity between the two electrodes (Mg anode and GO@V cathode) in the coin cell device of the former measurement. During the first discharge, GO@V cathode material exhibits a specific capacity of $72 \text{ mAh}\cdot\text{g}^{-1}$, which is in line with respect to similar systems embedding a vanadium-based cathode [57, 140, 305]. The most interesting feature that allows this material to stand out among the state of the art for Mg secondary battery cathodes is the extremely high current rate at which it can be cycled: typically, in literature Mg batteries are cycled between 0.1 and 1.0 C, without exceeding $200 \text{ mA}\cdot\text{g}^{-1}$. In this report we are able to achieve similar specific capacities at more than ten times of the usual current rate (*ca.* 12.5 C). This cycling conditions

result in high specific power values that GO@V cathode is able to deliver: a value of $1.70 \text{ W}\cdot\text{g}^{-1}$ is achieved, while the Chevrel-phase Mo_6S_8 cathode (reference cathode in Mg batteries) is typically cycled at a maximum power of $0.24 \text{ W}\cdot\text{g}^{-1}$. Moreover, these outcomes are also remarkable if compared to commercially available cathodes for Li-ion batteries: LiCoO_2 is typically cycled at a specific power of $2.50 \div 0.05 \text{ W}\cdot\text{g}^{-1}$, usually $0.52 \text{ W}\cdot\text{g}^{-1}$, while LiFePO_4 is tested between 2.80 and $0.06 \text{ W}\cdot\text{g}^{-1}$, most commonly $0.56 \text{ W}\cdot\text{g}^{-1}$. The high performance in terms of sustained current rates are guaranteed by the appropriate architecture of GO@V. Indeed, the presence of graphene oxide flakes is able to fast supply the electrons to the vanadium-based active material, with very efficient kinetics. The capacity fade and low cyclability in these preliminary tests are reasonably attributed to the electrochemical degradation of the $[\text{EMImCl}/(\text{AlCl}_3)_{1.5}]/(\delta\text{-MgCl}_2)_{0.08}$ electrolyte, which occurs at these currents and voltages. Further studies should be carried out with the new generation ionic liquid electrolytes for Mg secondary batteries, such as the one proposed in chapter 10, which show a higher stability and faster kinetics of the electrochemical reactions.

11.3 Conclusions

In this chapter a high performing cathode material for magnesium secondary batteries is presented. Its exotic architecture consists of vanadium-based microparticles decorated on the surface by graphene oxide flakes. The coordination is ensured by an ammonium inter-layer present between the two compounds. HR-TGA and vibrational analyses are in agreement with the hypothesized design of GO@V material. CV and galvanostatic measurements confirm the high electrochemical reactivity and reversibility of the proposed material. In particular, GO@V cathode exhibits an initial discharge specific capacity of $72 \text{ mAh}\cdot\text{g}^{-1}$. The most outstanding result reached by this material is the high current rate at which it is able to deliver this capacity, *i.e.* $1000 \text{ mA}\cdot\text{g}^{-1}$, $4.12 \text{ mA}\cdot\text{cm}^{-2}$, or $1.70 \text{ W}\cdot\text{g}^{-1}$. Nevertheless, only five charge/discharge cycles have been obtained. Thus, further improvements need to be pursued in order to increase the cycle life of the assembled magnesium secondary battery prototype.

12. Conclusions

This research has been intended to address the problem of the lack in innovative and high-performing materials for electrical energy storage applications in the so called “*beyond Li-ion*” battery technology. In the lithium batteries topic, particular attention has been devoted not only to the development of advanced electrolytes and electrode materials, but also in the unveiling of the Li⁺ conductivity mechanism occurring in the both categories, thus laying the groundwork for the future development of advanced batteries. In the second part of this work, the propensity of magnesium to become a good alternative to lithium, or at least to replace part of its market, has been revealed. Nevertheless, further research on the development of new electrolytes and high capacity cathodes still needs to be pursued.

Two different lithium ion conducting materials have been studied: i) a solid-state polymer electrolyte and ii) a glass-forming electrolyte. The former, in chapter 4, has been obtained by direct lithiation of poly(vinyl alcohol-co-vinyl lithium alkoxide), thus obtaining a single ion conductivity. The effect of the doping with an ionic liquid has been determined. In particular, it has been highlighted that the plasticization and the cation-exchange abilities of the IL have allowed for an increased conductivity, which has reached a value of $1.29 \cdot 10^{-5} \text{ S} \cdot \text{cm}^{-1}$ at room temperature. The latter, in chapter 5, consists by a mixture of glycerol and lithium glycerolate. Thus, because of the similar nature of the two compounds, a high affinity between the salt and the solvent has been obtained. All the conformations assumed by glycerol molecules as a function of lithium content have been determined by vibrational spectroscopies, and the correlation between the glycerol preferential conformation and the lithium conductivity mechanism has been highlighted. Glycerol, as expected, acted as a glass-former, providing discrete conductivities even at low temperatures. With this material, a room temperature conductivity of $1.99 \cdot 10^{-4} \text{ S} \cdot \text{cm}^{-1}$ has been achieved.

Two cathodes for high-voltage lithium batteries have been proposed and deeply analyzed, both belonging to the olivine structure family. In chapter 6, the application of a new characterization technique (BES) has been proposed in order to evaluate the flexibility of the hosting structure. Thus, it has been demonstrated that the ability of the material in the lithium ion insertion and extraction processes can be predicted by this technique, without the need of assembling a device. Moreover, indications in the design of a suitable structure for the most efficient and reversible

hosting capabilities of a cathode material can be drawn by these measurements. The effects of the substitution of part of the transition metal ions composing an olivine-based material with a higher valence metal have been reported in chapter 7. Moreover, performances evolution obtained by increasing the reducing character of the synthesis have been also evaluated. In particular, vanadium(IV), niobium(V), and tantalum(V) doping of a $\text{LiFe}_{0.33}\text{Ni}_{0.07}\text{Co}_{0.61}\text{PO}_4$ cathode material has been done, and structural, morphological, and electrochemical characterizations have been performed. Results have demonstrated that low amounts of high valence ions can be hosted in the olivine matrix, giving rise to the “charge compensation effect”. This effect can be exploited improving the rate capability of the cathodes, because of their enhanced electrical conductivity. The cathode material where niobium ions have been inserted into the structure has exhibited the best battery performances. Indeed, it has been able to provide a specific capacity of $149 \text{ mAh}\cdot\text{g}^{-1}$ at C/5 current rate, between 4.0 and 5.0 V. This specific capacity value is very close to the maximum theoretical specific capacity of a LMPO_4 compound. Furthermore, the excellent specific energy value exhibited by this cathode, *i.e.* $656 \text{ mWh}\cdot\text{g}^{-1}$, has made it one of the most interesting material in the cathode panorama for Li batteries.

In the field of magnesium secondary batteries, three different ionic liquid electrolytes, comprising an innovative magnesium salt, have been taken under consideration to evaluate the modulation of the physicochemical and electrochemical properties by: i) changing the anion of the ionic liquid; ii) changing the metal of the halometallate component of the IL; iii) changing the cation of the IL; and iv) in the all cases, increasing the magnesium salt concentration within the same material. All of these substitutions have been compared to the firstly developed IL-based electrolyte $[\text{EMImCl}/(\text{AlCl}_3)_y]/(\delta\text{-MgCl}_2)_x$ [57]. The first example has been described in chapter 8: the structural probe abilities of the boron tetrachloride anion have been exploited to study the structural and coordination features of a pyrrolidinium-based electrolyte. Indeed, BCl_4^- anion has been able to reveal the interactions and reorganizations of the surrounding environment by modifications of its own structure. The combination of DSC, DFT, MM, and FT-IR studies has revealed which coordination of the ionic species have been preferentially assumed at the different magnesium salt concentrations. BES studies have pointed out that Mg^{2+} conduction occurs by the exchange of anionic species between different domains, named delocalization bodies. This long-range charge migration mechanism is assisted by the ionic liquid dielectric relaxation modes. Conductivities up to $1.43\cdot 10^{-4} \text{ S}\cdot\text{cm}^{-1}$ have been achieved for the sample with

[Pyr₁₄Cl/(BCl₃)_{0.25}]/(δ-MgCl₂)_{0.041} formula. In chapter 9, the results obtained by the aluminum/titanium metal exchange, in the halometallate complex, have been studied. In particular, a [EMImCl/(TiCl₄)_{1.4}]/(δ-MgCl₂)_x family of electrolytes has been proposed. It has been demonstrated by DFT calculations and vibrational spectroscopy studies that the electrolytes are composed by aggregates of EMIm⁺ cations interacting with catenated anionic domains based on TiCl₆²⁻ and Ti₂Cl₉⁻ complexes. The equilibrium between the two halometallate species has been evaluated by Raman spectroscopy, and it has been demonstrated that the addition of δ-MgCl₂ salt results in the shift towards the preferential formation of the monomer species (TiCl₆²⁻). Thanks to the affinity between the chain-like structure of both δ-MgCl₂ and TiCl₄, a complex network has been formed. BES measurements have revealed a total conductivity value higher than 10⁻⁴ S·cm⁻¹ at 40 °C, and that the magnesium conduction occurs by the exchange of anionic species between different delocalization bodies. The fluctuation of ionic aggregates assists the overall charge migration process. Finally, preliminary electrochemical studies have demonstrated the Mg-Ti reversible deposition and stripping processes, with a coulombic efficiency up to 99.3%, and an overvoltage in the alloy deposition of only 10 mV. The last example of IL-based electrolyte for Mg conduction has been described in chapter 10, and consists of a [Pyr₁₄Cl/(AlCl₃)_{1.5}]/(δ-MgCl₂)_x material. Up to date, this material has shown one of the best performances in the field of electrolytes for Mg batteries. Similarities with the other IL-based electrolytes have been demonstrated, such as: i) the formation of cation and anion domains; ii) the equilibrium between the monomeric and dimeric form of the chloroaluminate anion; and iii) the modulation of the conductivity mechanism by the dynamics of the ionic aggregates. Nevertheless, this particular composition of the material has allowed for a greatly improved electrochemical performances. In particular, the Mg enrichment of the deposited alloy, the extension of the electrochemical stability window, the increase of the Coulombic efficiency, the improvement of the room-temperature conductivity, and the reduction of the overpotential in the deposition and stripping processes have been demonstrated. These high electrochemical performances have allowed to obtain a device which has shown an initial specific capacity for the V₂O₅-based cathode of 92 mAh·g⁻¹, and a promising long-term cyclability (> 100 cycles). Further studies need to be done in the limitation of the Al content into the deposited layer, in order to obtain a full magnesium battery. Otherwise, the development of a suitable cathode material able to host both Mg and Al has to be achieved, in order to take advantage of all the electrons exchanged during the redox reactions. Further measurements

on these materials still need to be done, in order to obtain more information about the characteristics and kind of aggregations of ionic species. Indeed, NMR analyses could be very useful in order to confirm BES results in terms of detected relaxations and diffusion coefficients, together with the evaluation of coordination interactions. Furthermore, NMR measurements could allow to determine the Mg^{2+} transference number ($t_{\text{Mg}^{2+}}$) on the basis of the evaluation of the diffusion coefficients, since the Bruce and Vincent method is not suitable to evaluate $t_{\text{Mg}^{2+}}$ in this class of materials. Further insights on the aggregation domains formed in the proposed IL electrolytes could be given by quasielastic and small-angle neutron scattering measurements. Indeed, these techniques are able to reveal the mechanism of aggregation of the different species composing the IL, and the relaxations occurring in the resulting domains.

Finally, in chapter 11, a high-power cathode for secondary magnesium batteries has been described. Its architecture has been designed in order to increase the rate delivery skills, therefore to be able to sustain high current demands maintaining high values of retained capacity. In details, graphene oxide flakes have been coordinated to the surface of vanadium-based particles through the presence of an ammonium shell interposed between the two components. HR-TGA and vibrational analyses have supported the hypothesis of the presence of this coordination, while CV and galvanostatic tests have confirmed the expected high electrochemical reactivity and reversibility of the proposed material. This material has achieved an initial specific capacity of $72 \text{ mAh}\cdot\text{g}^{-1}$ at $1000 \text{ mA}\cdot\text{g}^{-1}$ (more than 12 C), which corresponds to $4.12 \text{ mA}\cdot\text{cm}^{-2}$, or $1.70 \text{ W}\cdot\text{g}^{-1}$.

Taking all together, the materials proposed and studied in this Ph.D. thesis have given a direction in several aspects of the “*beyond Li-ion*” battery field, paving the way to the development of novel and high-performing electrochemically active compounds. Moreover, the power of BES technique has been demonstrated to be a useful tool in its classical applications, such as to reveal the conductivity mechanism of active species in electrolytes, and in exotic applications, like to describe the structural flexibility in cathode materials. A lot of improvements in the electrode and electrolytes materials for Li- and Mg-based batteries still remain to be pursued. Nevertheless, several roadblocks in these technologies have been broken by the materials developed in this Ph.D. project, and a further step towards the realization of a full renewable energy economy has been done.

References

- [1] M. Sawicki, L.L. Shaw, Advances and challenges of sodium ion batteries as post lithium ion batteries, *RSC Advances*, 5 (2015) 53129-53154.
- [2] The European environment — state and outlook 2015: an integrated assessment of the European Environment. Global Megatrends. Increasing environmental pollution (GMT 10), <http://www.eea.europa.eu/soer-2015/global/pollution>.
- [3] J. Liu, J.G. Zhang, Z. Yang, J.P. Lemmon, C. Imhoff, G.L. Graff, L. Li, J. Hu, C. Wang, J. Xiao, G. Xia, V.V. Viswanathan, S. Baskaran, V. Sprenkle, X. Li, Y. Shao, B. Schwenzer, Materials science and materials chemistry for large scale electrochemical energy storage: From transportation to electrical grid, *Adv. Funct. Mater.*, 23 (2013) 929-946.
- [4] Department of Energy - FY 2017 Congressional Budget Request - Volume 3, https://energy.gov/sites/prod/files/2016/02/f29/FY2017BudgetVolume3_2.pdf.
- [5] B. Dunn, H. Kamath, J.M. Tarascon, Electrical energy storage for the grid: A battery of choices, *Science*, 334 (2011) 928-935.
- [6] N.S. Pearre, L.G. Swan, Technoeconomic feasibility of grid storage: Mapping electrical services and energy storage technologies, *Applied Energy*, 137 (2015) 501-510.
- [7] M.S. Whittingham, Materials challenges facing electrical energy storage, *MRS Bull.*, 33 (2008) 411-419.
- [8] P. Saha, M.K. Datta, O.I. Velikokhatnyi, A. Manivannan, D. Alman, P.N. Kumta, Rechargeable magnesium battery: Current status and key challenges for the future, *Prog. Mater. Sci.*, 66 (2014) 1-86.
- [9] B. Dunn, H. Kamath, J.-M. Tarascon, Electrical Energy Storage for the Grid: A Battery of Choices, *Science*, 334 (2011) 928-935.
- [10] History Of Batteries: A Timeline, <https://www.upsbatterycenter.com/blog/history-batteries-timeline>.
- [11] P. Nikolaidis, A. Poullikkas, Cost metrics of electrical energy storage technologies in potential power system operations, *Sustainable Energy Technologies and Assessments*, 25 (2018) 43-59.
- [12] K.E. Aifantis, S.A. Hackney, R.V. Kumar, High Energy Density Lithium Batteries: Materials, Engineering, Applications, Wiley 2010.

- [13] P. Verma, P. Maire, P. Novák, A review of the features and analyses of the solid electrolyte interphase in Li-ion batteries, *Electrochim. Acta*, 55 (2010) 6332-6341.
- [14] Y. Li, M. Gong, Y. Liang, J. Feng, J.E. Kim, H. Wang, G. Hong, B. Zhang, H. Dai, Advanced zinc-air batteries based on high-performance hybrid electrocatalysts, *Nature Communications*, 4 (2013) 1-7.
- [15] L. Cecchetto, M. Salomon, B. Scrosati, F. Croce, Study of a Li-air battery having an electrolyte solution formed by a mixture of an ether-based aprotic solvent and an ionic liquid, *J. Power Sources*, 213 (2012) 233-238.
- [16] M. Agostini, Y. Aihara, T. Yamada, B. Scrosati, J. Hassoun, A lithium-sulfur battery using a solid, glass-type P_2S_5 - Li_2S electrolyte, *Solid State Ion.*, 244 (2013) 48-51.
- [17] V. Di Noto, S. Lavina, D. Longo, M. Vidali, A novel electrolytic complex based on δ - $MgCl_2$ and poly(ethylene glycol) 400, *Electrochim. Acta*, 43 (1998) 1225-1237.
- [18] M.-C. Lin, M. Gong, B. Lu, Y. Wu, D.-Y. Wang, M. Guan, M. Angell, C. Chen, J. Yang, B.-J. Hwang, H. Dai, An ultrafast rechargeable aluminium-ion battery, *Nature*, 520 (2015) 324-328.
- [19] A. Manthiram, Materials Challenges and Opportunities of Lithium Ion Batteries, *The Journal of Physical Chemistry Letters*, 2 (2011) 176-184.
- [20] G. Pagot, F. Bertasi, K. Vezzù, G. Nawn, G. Pace, A. Nale, V. Di Noto, Correlation between Properties and Conductivity Mechanism in Poly(vinyl alcohol)-based Lithium Solid Electrolytes, *Solid State Ion.*, 320 (2018) 177-185.
- [21] G. Pagot, S. Tonello, K. Vezzù, V. Di Noto, A New Glass-Forming Electrolyte Based on Lithium Glycerolate, *Batteries*, 4 (2018) 41.
- [22] G. Pagot, F. Bertasi, G. Nawn, E. Negro, A. Bach Delpeuch, K. Vezzù, D. Cristofori, V. Di Noto, Effect of Graphite and Copper Oxide on the Performance of High Potential $Li[Fe_{1/3}Ni_{1/3}Co_{1/3}]PO_4$ Olivine Cathodes for Lithium Batteries, *Electrochim. Acta*, 225 (2017) 533-542.
- [23] G. Pagot, F. Bertasi, K. Vezzù, F. Seppehr, X. Luo, G. Nawn, E. Negro, S.J. Paddison, V.D. Noto, Three-dimensional Catenated 1-ethyl-3-methylimidazolium Halotitanate Ionic Liquid Electrolytes for Electrochemical Applications, *Electrochim. Acta*, 246 (2017) 914-923.

- [24] C. Mikolajczak, M. Kahn, K. White, R.T. Long, *Lithium-Ion Batteries Hazard and Use Assessment*, 1 ed., Springer-Verlag, New York, 2011.
- [25] K. Xu, Nonaqueous Liquid Electrolytes for Lithium-Based Rechargeable Batteries, *Chem. Rev.*, 104 (2004) 4303-4418.
- [26] P. Knauth, Inorganic solid Li ion conductors: An overview, *Solid State Ion.*, 180 (2009) 911-916.
- [27] J.Y. Seok, O.D. Yang, N.Y. Jin, P.K. Ho, Issues and Challenges for Bulk-Type All-Solid-State Rechargeable Lithium Batteries using Sulfide Solid Electrolytes, *Isr. J. Chem.*, 55 (2015) 472-485.
- [28] A. Manthiram, X. Yu, S. Wang, Lithium battery chemistries enabled by solid-state electrolytes, *Nature Reviews Materials*, 2 (2017) 1-16.
- [29] M.D. Tikekar, S. Choudhury, Z. Tu, L.A. Archer, Design principles for electrolytes and interfaces for stable lithium-metal batteries, *Nature Energy*, 1 (2016) 1-7.
- [30] B. Scrosati, J. Hassoun, Y.K. Sun, Lithium-ion batteries. A look into the future, *Energy Environ. Sci.*, 4 (2011) 3287-3295.
- [31] M. Uitz, V. Epp, P. Bottke, M. Wilkening, Ion dynamics in solid electrolytes for lithium batteries, *J. Electroceram.*, 38 (2017) 142-156.
- [32] J.B. Goodenough, H.Y.P. Hong, J.A. Kafalas, Fast Na⁺-ion transport in skeleton structures, *Mater. Res. Bull.*, 11 (1976) 203-220.
- [33] C.R. Mariappan, C. Yada, F. Rosciano, B. Roling, Correlation between micro-structural properties and ionic conductivity of Li_{1.5}Al_{0.5}Ge_{1.5}(PO₄)₃ ceramics, *J. Power Sources*, 196 (2011) 6456-6464.
- [34] V. Thangadurai, S. Narayanan, D. Pinzaru, Garnet-type solid-state fast Li ion conductors for Li batteries: critical review, *Chem. Soc. Rev.*, 43 (2014) 4714-4727.
- [35] V. Thangadurai, W. Weppner, Investigations on electrical conductivity and chemical compatibility between fast lithium ion conducting garnet-like Li₆BaLa₂Ta₂O₁₂ and lithium battery cathodes, *J. Power Sources*, 142 (2005) 339-344.
- [36] E.J. Cussen, Structure and ionic conductivity in lithium garnets, *J. Mater. Chem.*, 20 (2010) 5167-5173.

- [37] Y.X. Gao, X.P. Wang, W.G. Wang, Z. Zhuang, D.M. Zhang, Q.F. Fang, Synthesis, ionic conductivity, and chemical compatibility of garnet-like lithium ionic conductor $\text{Li}_5\text{La}_3\text{Bi}_2\text{O}_{12}$, *Solid State Ion.*, 181 (2010) 1415-1419.
- [38] S. Yu, R.D. Schmidt, R. Garcia-Mendez, E. Herbert, N.J. Dudney, J.B. Wolfenstine, J. Sakamoto, D.J. Siegel, Elastic Properties of the Solid Electrolyte $\text{Li}_7\text{La}_3\text{Zr}_2\text{O}_{12}$ (LLZO), *Chem. Mater.*, 28 (2016) 197-206.
- [39] N. Kamaya, K. Homma, Y. Yamakawa, M. Hirayama, R. Kanno, M. Yonemura, T. Kamiyama, Y. Kato, S. Hama, K. Kawamoto, A. Mitsui, A lithium superionic conductor, *Nat. Mater.*, 10 (2011) 682-686.
- [40] T. Takahashi, H. Iwahara, Ionic conduction in perovskite-type oxide solid solution and its application to the solid electrolyte fuel cell, *Energy Conversion*, 11 (1971) 105-111.
- [41] S. Stramare, V. Thangadurai, W. Weppner, Lithium Lanthanum Titanates: A Review, *Chem. Mater.*, 15 (2003) 3974-3990.
- [42] B. Huang, X. Yao, Z. Huang, Y. Guan, Y. Jin, X. Xu, Li_3PO_4 -doped $\text{Li}_7\text{P}_3\text{S}_{11}$ glass-ceramic electrolytes with enhanced lithium ion conductivities and application in all-solid-state batteries, *J. Power Sources*, 284 (2015) 206-211.
- [43] H. Muramatsu, A. Hayashi, T. Ohtomo, S. Hama, M. Tatsumisago, Structural change of Li_2S - P_2S_5 sulfide solid electrolytes in the atmosphere, *Solid State Ion.*, 182 (2011) 116-119.
- [44] Z. Deng, B. Radhakrishnan, S.P. Ong, Rational Composition Optimization of the Lithium-Rich $\text{Li}_3\text{OCl}_{1-x}\text{Br}_x$ Anti-Perovskite Superionic Conductors, *Chem. Mater.*, 27 (2015) 3749-3755.
- [45] Y. Zhao, L.L. Daemen, Superionic Conductivity in Lithium-Rich Anti-Perovskites, *J. Am. Chem. Soc.*, 134 (2012) 15042-15047.
- [46] Y. Zhang, Y. Zhao, C. Chen, Ab initio study of the stabilities of and mechanism of superionic transport in lithium-rich antiperovskites, *Physical Review B*, 87 (2013) 1343031-1343038.
- [47] V. Di Noto, S. Lavina, G.A. Giffin, E. Negro, B. Scrosati, Polymer electrolytes: Present, past and future, *Electrochim. Acta*, 57 (2011) 4-13.
- [48] V. Di Noto, E. Negro, S. Lavina, M. Vittadello, Hybrid inorganic-organic polymer electrolytes, *Polymer Electrolytes: Fundamentals and Applications*, Woodhead Publishing Limited 2010, pp. 219-273.

- [49] V. Di Noto, M. Vittadello, K. Yoshida, S. Lavina, E. Negro, T. Furukawa, Broadband dielectric and conductivity spectroscopy of Li-ion conducting three-dimensional hybrid inorganic–organic networks as polymer electrolytes based on poly(ethylene glycol) 400, Zr and Al nodes, *Electrochim. Acta*, 57 (2011) 192-200.
- [50] V. Di Noto, Zeolitic Inorganic–Organic Polymer Electrolyte Based on Oligo(ethylene glycol) 600 K_2PdCl_4 and $K_3Co(CN)_6$, *The Journal of Physical Chemistry B*, 104 (2000) 10116-10125.
- [51] M. Vittadello, S. Suarez, K. Fijimoto, V.D. Noto, S.G. Greenbaum, T. Furukawa, A lithium Z-IOPE ionomer based on PEG600, $(CH_3)_2SnCl_2$, and $Li_3Fe(CN)_6$, *J. Electrochem. Soc.*, 152 (2005) A956-A965.
- [52] V. Di Noto, M. Vittadello, S.G. Greenbaum, S. Suarez, K. Kano, T. Furukawa, A New Class of Lithium Hybrid Gel Electrolyte Systems, *The Journal of Physical Chemistry B*, 108 (2004) 18832-18844.
- [53] W.P. V., Electrical conductivity in ionic complexes of poly(ethylene oxide), *British Polymer Journal*, 7 (1975) 319-327.
- [54] V. Di Noto, D. Longo, V. Münchow, Ion-Oligomer Interactions in Poly(ethylene glycol)400/(LiCl)_x Electrolyte Complexes, *The Journal of Physical Chemistry B*, 103 (1999) 2636-2646.
- [55] R. Meziane, J.-P. Bonnet, M. Courty, K. Djellab, M. Armand, Single-ion polymer electrolytes based on a delocalized polyanion for lithium batteries, *Electrochim. Acta*, 57 (2011) 14-19.
- [56] K. Vezzù, A.M. Maes, F. Bertasi, A.R. Motz, T.-H. Tsai, E.B. Coughlin, A.M. Herring, V. Di Noto, Interplay Between Hydroxyl Density and Relaxations in Poly(vinylbenzyltrimethylammonium)-b-poly(methylbutylene) Membranes for Electrochemical Applications, *J. Am. Chem. Soc.*, 140 (2018) 1372-1384.
- [57] F. Bertasi, C. Hettige, F. Seppehr, X. Bogle, G. Pagot, K. Vezzù, E. Negro, S.J. Paddison, S.G. Greenbaum, M. Vittadello, V. Di Noto, A Key concept in Magnesium Secondary Battery Electrolytes, *ChemSusChem*, 8 (2015) 3069-3076.
- [58] H. Ohno, *Electrochemical Aspects of Ionic Liquids*, 2nd ed., John Wiley & Sons, Inc., Hoboken, New Jersey, 2011.
- [59] M. Armand, F. Endres, D.R. MacFarlane, H. Ohno, B. Scrosati, Ionic-liquid materials for the electrochemical challenges of the future, *Nat. Mater.*, 8 (2009) 621-629.

- [60] M. Yoshizawa, A. Narita, H. Ohno, Design of Ionic Liquids for Electrochemical Applications, *Aust. J. Chem.*, 57 (2004) 139-144.
- [61] M.J. Park, I. Choi, J. Hong, O. Kim, Polymer electrolytes integrated with ionic liquids for future electrochemical devices, *J. Appl. Polym. Sci.*, 129 (2013) 2363-2376.
- [62] M. Armand, F. Endres, D.R. MacFarlane, H. Ohno, B. Scrosati, Ionic-liquid materials for the electrochemical challenges of the future, *Nat. Mater.*, 8 (2009) 621-629.
- [63] M. Watanabe, M.L. Thomas, S. Zhang, K. Ueno, T. Yasuda, K. Dokko, Application of Ionic Liquids to Energy Storage and Conversion Materials and Devices, *Chem. Rev.*, 117 (2017) 7190-7239.
- [64] S. Seki, Y. Kobayashi, H. Miyashiro, Y. Ohno, Y. Mita, A. Usami, N. Terada, M. Watanabe, Reversibility of Lithium Secondary Batteries Using a Room-Temperature Ionic Liquid Mixture and Lithium Metal, *Electrochem. Solid-State Lett.*, 8 (2005) A577-A578.
- [65] S. Seki, Y. Kobayashi, H. Miyashiro, Y. Ohno, Y. Mita, N. Terada, P. Charest, A. Guerfi, K. Zaghib, Compatibility of N-Methyl-N-propylpyrrolidinium Cation Room-Temperature Ionic Liquid Electrolytes and Graphite Electrodes, *The Journal of Physical Chemistry C*, 112 (2008) 16708-16713.
- [66] H. Nakagawa, S. Izuchi, K. Kuwana, T. Nukuda, Y. Aihara, Liquid and Polymer Gel Electrolytes for Lithium Batteries Composed of Room-Temperature Molten Salt Doped by Lithium Salt, *J. Electrochem. Soc.*, 150 (2003) A695-A700.
- [67] H. Sakaebe, H. Matsumoto, N-Methyl-N-propylpiperidinium bis(trifluoromethanesulfonyl)imide (PP13-TFSI) – novel electrolyte base for Li battery, *Electrochem. Commun.*, 5 (2003) 594-598.
- [68] F.R. Gamble, J.H. Osiecki, M. Cais, R. Pisharody, F.J. DiSalvo, T.H. Geballe, Intercalation Complexes of Lewis Bases and Layered Sulfides: A Large Class of New Superconductors, *Science*, 174 (1971) 493-497.
- [69] M.S. Whittingham, Electrical Energy Storage and Intercalation Chemistry, *Science*, 192 (1976) 1126-1127.
- [70] F.A. Trumbore, Niobium triselenide: A unique rechargeable positive electrode material, *J. Power Sources*, 26 (1989) 65-75.

- [71] C. Delmas, H. Cognac-Auradou, J.M. Cocciantelli, M. Ménétrier, J.P. Doumerc, The $\text{Li}_x\text{V}_2\text{O}_5$ system: An overview of the structure modifications induced by the lithium intercalation, *Solid State Ion.*, 69 (1994) 257-264.
- [72] T.L. Kulova, New electrode materials for lithium-ion batteries (Review), *Russ. J. Electrochem.*, 49 (2013) 1-25.
- [73] K. Le Van, H. Groult, A. Mantoux, L. Perrigaud, F. Lantelme, R. Lindström, R. Badour-Hadjean, S. Zanna, D. Lincot, Amorphous vanadium oxide films synthesised by ALCVD for lithium rechargeable batteries, *J. Power Sources*, 160 (2006) 592-601.
- [74] G. Pistoia, M. Pasquali, G. Wang, L. Li, $\text{Li}/\text{Li}_{1+x}\text{V}_3\text{O}_8$ Secondary Batteries - Synthesis and Characterization of an Amorphous Form of the Cathode, *J. Electrochem. Soc.*, 137 (1990) 2365-2370.
- [75] H. Huang, S.C. Yin, T. Kerr, N. Taylor, L.F. Nazar, Nanostructured Composites: A High Capacity, Fast Rate $\text{Li}_3\text{V}_2(\text{PO}_4)_3/\text{Carbon}$ Cathode for Rechargeable Lithium Batteries, *Adv. Mater.*, 14 (2002) 1525-1528.
- [76] M.S. Whittingham, Y. Song, S. Lutta, P.Y. Zavalij, N.A. Chernova, Some transition metal (oxy)phosphates and vanadium oxides for lithium batteries, *J. Mater. Chem.*, 15 (2005) 3362-3379.
- [77] G.G. Amatucci, J.M. Tarascon, L.C. Klein, CoO_2 , The End Member of the Li_xCoO_2 Solid Solution, *J. Electrochem. Soc.*, 143 (1996) 1114-1123.
- [78] K. Mizushima, P.C. Jones, P.J. Wiseman, J.B. Goodenough, Li_xCoO_2 ($0 < x < 1$): A new cathode material for batteries of high energy density, *Mater. Res. Bull.*, 15 (1980) 783-789.
- [79] M.S. Islam, C.A.J. Fisher, Lithium and sodium battery cathode materials: computational insights into voltage, diffusion and nanostructural properties, *Chem. Soc. Rev.*, 43 (2014) 185-204.
- [80] R. Koksang, J. Barker, H. Shi, M.Y. Saïdi, Cathode materials for lithium rocking chair batteries, *Solid State Ion.*, 84 (1996) 1-21.
- [81] K. Zaghib, A. Mauger, H. Groult, J.B. Goodenough, C.M. Julien, Advanced electrodes for high power Li-ion batteries, *Mater.*, 6 (2013) 1028-1049.
- [82] T. Nohma, H. Kurokawa, M. Uehara, M. Takahashi, K. Nishio, T. Saito, Electrochemical characteristics of LiNiO_2 and LiCoO_2 as a positive material for lithium secondary batteries, *J. Power Sources*, 54 (1995) 522-524.

- [83] J. Cho, Y.J. Kim, B. Park, Novel LiCoO_2 cathode material with Al_2O_3 coating for a Li ion cell, *Chem. Mater.*, 12 (2000) 3788-3791.
- [84] M.S. Whittingham, Lithium Batteries and Cathode Materials, *Chem. Rev.*, 104 (2004) 4271-4302.
- [85] K. Zaghib, J. Dubé, A. Dallaire, K. Galoustov, A. Guerfi, M. Ramanathan, A. Benmayza, J. Prakash, A. Mauger, C.M. Julien, Enhanced thermal safety and high power performance of carbon-coated LiFePO_4 olivine cathode for Li-ion batteries, *J. Power Sources*, 219 (2012) 36-44.
- [86] J.R. Dahn, U. von Sacken, C.A. Michal, Structure and electrochemistry of $\text{Li}_{1\pm y}\text{NiO}_2$ and a new Li_2NiO_2 phase with the $\text{Ni}(\text{OH})_2$ structure, *Solid State Ion.*, 44 (1990) 87-97.
- [87] K. Amine, J. Liu, S. Kang, I. Belharouak, Y. Hyung, D. Vissers, G. Henriksen, Improved lithium manganese oxide spinel/graphite Li-ion cells for high-power applications, *J. Power Sources*, 129 (2004) 14-19.
- [88] A.R. Armstrong, P.G. Bruce, Synthesis of layered LiMnO_2 as an electrode for rechargeable lithium batteries, *Nature*, 381 (1996) 499-500.
- [89] R. Chen, M.S. Whittingham, Cathodic Behavior of Alkali Manganese Oxides from Permanganate, *J. Electrochem. Soc.*, 144 (1997) L64-L67.
- [90] R. Chen, P. Zavalij, M.S. Whittingham, Hydrothermal Synthesis and Characterization of $\text{K}_x\text{MnO}_2 \cdot y\text{H}_2\text{O}$, *Chem. Mater.*, 8 (1996) 1275-1280.
- [91] A.R. Armstrong, A.D. Robertson, R. Gitzendanner, P.G. Bruce, The Layered Intercalation Compounds $\text{Li}(\text{Mn}_{1-y}\text{Co}_y)\text{O}_2$: Positive Electrode Materials for Lithium-Ion Batteries, *J. Solid State Chem.*, 145 (1999) 549-556.
- [92] A. Robert Armstrong, R. Gitzendanner, The intercalation compound $\text{Li}(\text{Mn}_{0.9}\text{Co}_{0.1})\text{O}_2$ as a positive electrode for rechargeable lithium batteries, *Chem. Commun.*, (1998) 1833-1834.
- [93] T. Kulova, A. Skundin, High-voltage materials for positive electrodes of lithium ion batteries, *Russian Journal of Electrochemistry*, 52 (2016) 501-524.
- [94] R. Schmich, R. Wagner, G. Hörpel, T. Placke, M. Winter, Performance and cost of materials for lithium-based rechargeable automotive batteries, *Nature Energy*, 3 (2018) 267.

- [95] G. Zubi, R. Dufo-López, M. Carvalho, G. Pasaoglu, The lithium-ion battery: State of the art and future perspectives, *Renewable and Sustainable Energy Reviews*, 89 (2018) 292-308.
- [96] J. Wolfenstine, J. Allen, Ni³⁺/Ni²⁺ redox potential in LiNiPO₄, *J. Power Sources*, 142 (2005) 389-390.
- [97] M. Minakshi, P. Singh, D. Appadoo, D.E. Martin, Synthesis and characterization of olivine LiNiPO₄ for aqueous rechargeable battery, *Electrochim. Acta*, 56 (2011) 4356-4360.
- [98] C.M. Julien, A. Mauger, K. Zaghib, R. Veillette, H. Groult, Structural and electronic properties of the LiNiPO₄ orthophosphate, *Ionics*, 18 (2012) 625-633.
- [99] M. Hu, X. Pang, Z. Zhou, Recent progress in high-voltage lithium ion batteries, *J. Power Sources*, 237 (2013) 229-242.
- [100] A.A. Salah, P. Jozwiak, J. Garbarczyk, K. Benkhrouja, K. Zaghib, F. Gendron, C.M. Julien, Local structure and redox energies of lithium phosphates with olivine- and Nasicon-like structures, *J. Power Sources*, 140 (2005) 370-375.
- [101] N.N. Bramnik, K.G. Bramnik, T. Buhrmester, C. Baetz, H. Ehrenberg, H. Fuess, Electrochemical and structural study of LiCoPO₄-based electrodes, *J. Solid State Electrochem.*, 8 (2004) 558-564.
- [102] J.L. Allen, T.R. Jow, J. Wolfenstine, Improved cycle life of Fe-substituted LiCoPO₄, *J. Power Sources*, 196 (2011) 8656-8661.
- [103] Y. Zhang, Q.Y. Huo, P.P. Du, L.Z. Wang, A.Q. Zhang, Y.H. Song, Y. Lv, G.Y. Li, Advances in new cathode material LiFePO₄ for lithium-ion batteries, *Synth. Met.*, 162 (2012) 1315-1326.
- [104] Y. Wang, J. Wang, J. Yang, Y. Nuli, High-Rate LiFePO₄ Electrode Material Synthesized by a Novel Route from FePO₄·4H₂O, *Advanced Functional Materials*, 16 (2006) 2135-2140.
- [105] V.A. Streltsov, E.L. Belokoneva, V.G. Tsirelson, N.K. Hansen, Multipole analysis of the electron-density in triphylite, LiFePO₄, using X-Ray-Diffraction data, *Acta Crystallogr., Sect. B: Struct. Sci.*, B49 (1993) 147-153.
- [106] D. Aurbach, Y. Gofer, Z. Lu, A. Schechter, O. Chusid, H. Gizbar, Y. Cohen, V. Ashkenazi, M. Moshkovich, R. Turgeman, E. Levi, A short review on the comparison between Li battery systems and rechargeable magnesium battery technology, *J. Power Sources*, 97-98 (2001) 28-32.

- [107] J. Heath, H. Chen, M.S. Islam, MgFeSiO₄ as a potential cathode material for magnesium batteries: ion diffusion rates and voltage trends, *Journal of Materials Chemistry A*, 5 (2017) 13161-13167.
- [108] C. Liebenow, Z. Yang, P. Lobitz, The electrodeposition of magnesium using solutions of organomagnesium halides, amidomagnesium halides and magnesium organoborates, *Electrochem. Commun.*, 2 (2000) 641-645.
- [109] J. P., Formula of the organomagnesium derivative and magnesium hydride, *Comptes Rendus*, 155 (1912) 353-355.
- [110] T.D. Gregory, R.J. Hoffman, R.C. Winterton, Nonaqueous electrochemistry of magnesium. Applications to energy storage, *J. Electrochem. Soc.*, 137 (1990) 775-780.
- [111] K. Soeda, M. Yamagata, M. Ishikawa, Reversible Deposition and Dissolution of Mg Negative in Non-Ethereal Electrolyte, *Meeting Abstracts*, MA2015-01 (2015) 321.
- [112] M. Shiraga, F. Sagane, K. Miyazaki, T. Fukutsuka, T. Abe, K. Nishio, Y. Uchimoto, Electrochemical Behavior of Platinum Electrode in 2-Methyltetrahydrofuran Containing Magnesium Bromide, *Meeting Abstracts*, MA2010-02 (2010) 52.
- [113] E. Sheha, Ion transport properties of magnesium bromide/dimethyl sulfoxide non-aqueous liquid electrolyte, *Journal of Advanced Research*, 7 (2016) 29-36.
- [114] J.H. Connor, W.E. Reid, G.B. Wood, Electrodeposition of Metals from Organic Solutions: V . Electrodeposition of Magnesium and Magnesium Alloys, *J. Electrochem. Soc.*, 104 (1957) 38-41.
- [115] J. Muldoon, C.B. Bucur, A.G. Oliver, J. Zajicek, G.D. Allred, W.C. Boggess, Corrosion of magnesium electrolytes: chlorides – the culprit, *Energy Environ. Sci.*, 6 (2013) 482-487.
- [116] J. Muldoon, C.B. Bucur, T. Gregory, Quest for Nonaqueous Multivalent Secondary Batteries: Magnesium and Beyond, *Chem. Rev.*, 114 (2014) 11683-11720.
- [117] O. Mizrahi, N. Amir, E. Pollak, O. Chusid, V. Marks, H. Gottlieb, L. Larush, E. Zinigrad, D. Aurbach, Electrolyte Solutions with a Wide Electrochemical Window for Rechargeable Magnesium Batteries, *J. Electrochem. Soc.*, 155 (2008) A103-A109.

- [118] R.E. Doe, R. Han, J. Hwang, A.J. Gmitter, I. Shterenberg, H.D. Yoo, N. Pour, D. Aurbach, Novel, electrolyte solutions comprising fully inorganic salts with high anodic stability for rechargeable magnesium batteries, *Chem. Commun.*, 50 (2014) 243-245.
- [119] S. Higashi, K. Miwa, M. Aoki, K. Takechi, A novel inorganic solid state ion conductor for rechargeable Mg batteries, *Chem. Commun.*, 50 (2014) 1320-1322.
- [120] J. Kawamura, K. Morota, N. Kuwata, Y. Nakamura, H. Maekawa, T. Hattori, N. Imanaka, Y. Okazaki, G.-y. Adachi, High temperature ^{31}P NMR study on Mg^{2+} ion conductors, *Solid State Commun.*, 120 (2001) 295-298.
- [121] M.L. Aubrey, R. Ameloot, B.M. Wiers, J.R. Long, Metal-organic frameworks as solid magnesium electrolytes, *Energy Environ. Sci.*, 7 (2014) 667-671.
- [122] A. Patrick, M. Glasse, R. Latham, R. Linford, Novel solid state polymeric batteries, *Solid State Ion.*, 18-19 (1986) 1063-1067.
- [123] L.L. Yang, A.R. McGhie, G.C. Farrington, Ionic Conductivity in Complexes of Poly(ethylene oxide) and MgCl_2 , *J. Electrochem. Soc.*, 133 (1986) 1380-1385.
- [124] V. Di Noto, M. Fauri, G. De Luca, M. Vidali, A new magnesium ion polymer battery (poster), in: 9th, Edinburgh, Scotland, United Kingdom, (1998).
- [125] V. Di Noto, S. Bresadola, New synthesis of a highly active $\delta\text{-MgCl}_2$ for $\text{MgCl}_2/\text{TiCl}_4/\text{AlEt}_3$ catalytic systems, *Macromol. Chem. Phys.*, 197 (1996) 3827-3835.
- [126] S. Ikeda, Y. Mori, Y. Furuhashi, H. Masuda, O. Yamamoto, Quasi-solid polymer electrolytes using photo-cross-linked polymers. Lithium and divalent cation conductors and their applications, *J. Power Sources*, 81-82 (1999) 720-723.
- [127] G.G. Kumar, N. Munichandraiah, Reversibility of Mg/Mg^{2+} couple in a gel polymer electrolyte, *Electrochim. Acta*, 44 (1999) 2663-2666.
- [128] D. Aurbach, O. Chasid, Y. Gofer, C. Gizbar, High-energy, rechargeable electrochemical cells, 9/870707 (2004).
- [129] Y. NuLi, J. Yang, P. Wang, Electrodeposition of magnesium film from BMIMBF_4 ionic liquid, *Appl. Surf. Sci.*, 252 (2006) 8086-8090.

- [130] Y. NuLi, J. Yang, R. Wu, Reversible deposition and dissolution of magnesium from BMIMBF₄ ionic liquid, *Electrochem. Commun.*, 7 (2005) 1105-1110.
- [131] M. Morita, T. Shirai, N. Yoshimoto, M. Ishikawa, Ionic conductance behavior of polymeric gel electrolyte containing ionic liquid mixed with magnesium salt, *J. Power Sources*, 139 (2005) 351-355.
- [132] N. Yoshimoto, M. Matsumoto, M. Egashia, M. Morita, Mixed electrolyte consisting of ethylmagnesiumbromide with ionic liquid for rechargeable magnesium electrode, *J. Power Sources*, 195 (2010) 2096-2098.
- [133] F. Bertasi, F. Sepehr, G. Pagot, S.J. Paddison, V. Di Noto, Toward a Magnesium-Iodine Battery, *Adv. Funct. Mater.*, 26 (2016) 4860-4865.
- [134] F. Bertasi, K. Vezzù, G. Nawn, G. Pagot, V. Di Noto, Interplay Between Structure and Conductivity in 1-Ethyl-3-methylimidazolium tetrafluoroborate/(δ -MgCl₂)_f Electrolytes for Magnesium Batteries, *Electrochim. Acta*, 219 (2016) 152-162.
- [135] M. Kar, Z. Ma, L.M. Azofra, K. Chen, M. Forsyth, D.R. MacFarlane, Ionic liquid electrolytes for reversible magnesium electrochemistry, *Chem. Commun.*, 52 (2016) 4033-4036.
- [136] D. Aurbach, Z. Lu, A. Schechter, Y. Gofer, H. Gizbar, R. Turgeman, Y. Cohen, M. Moshkovich, E. Levi, Prototype systems for rechargeable magnesium batteries, *Nature*, 407 (2000) 724-727.
- [137] L. Yanliang, F. Rujun, Y. Siqi, M. Hua, L. Jing, C. Jun, Rechargeable Mg Batteries with Graphene-like MoS₂ Cathode and Ultrasmall Mg Nanoparticle Anode, *Adv. Mater.*, 23 (2011) 640-643.
- [138] B. Liu, T. Luo, G. Mu, X. Wang, D. Chen, G. Shen, Rechargeable Mg-Ion Batteries Based on WSe₂ Nanowire Cathodes, *ACS Nano*, 7 (2013) 8051-8058.
- [139] R. Zhang, X. Yu, K.-W. Nam, C. Ling, T.S. Arthur, W. Song, A.M. Knapp, S.N. Ehrlich, X.-Q. Yang, M. Matsui, α -MnO₂ as a cathode material for rechargeable Mg batteries, *Electrochemistry Communications*, 23 (2012) 110-113.
- [140] P. Novák, J. Desilvestro, Electrochemical Insertion of Magnesium in Metal Oxides and Sulfides from Aprotic Electrolytes, *J. Electrochem. Soc.*, 140 (1993) 140-144.
- [141] L. Jiao, H. Yuan, Y. Wang, J. Cao, Y. Wang, Mg intercalation properties into open-ended vanadium oxide nanotubes, *Electrochem. Commun.*, 7 (2005) 431-436.

- [142] X. Du, G. Huang, Y. Qin, L. Wang, Solvothermal synthesis of GO/V₂O₅ composites as a cathode material for rechargeable magnesium batteries, *RSC Advances*, 5 (2015) 76352-76355.
- [143] T.E. Sutto, T.T. Duncan, Electrochemical and structural characterization of Mg ion intercalation into Co₃O₄ using ionic liquid electrolytes, *Electrochim. Acta*, 80 (2012) 413-417.
- [144] T.E. Sutto, T.T. Duncan, Electrochemical and structural characterization of Mg ion intercalation into RuO₂ using an ionic liquid electrolyte, *Electrochim. Acta*, 79 (2012) 170-174.
- [145] Z. Feng, J. Yang, Y. NuLi, J. Wang, X. Wang, Z. Wang, Preparation and electrochemical study of a new magnesium intercalation material Mg_{1.03}Mn_{0.97}SiO₄, *Electrochem. Commun.*, 10 (2008) 1291-1294.
- [146] Y. Li, Y. Nuli, J. Yang, T. Yilinuer, J. Wang, MgFeSiO₄ prepared via a molten salt method as a new cathode material for rechargeable magnesium batteries, *Chin. Sci. Bull.*, 56 (2011) 386-390.
- [147] J.-z. Sun, Preparation and characterization of novel positive electrode material for magnesium cells, *Monatshefte für Chemie - Chemical Monthly*, 145 (2014) 103-106.
- [148] Y. NuLi, Y. Zheng, Y. Wang, J. Yang, J. Wang, Electrochemical intercalation of Mg²⁺ in 3D hierarchically porous magnesium cobalt silicate and its application as an advanced cathode material in rechargeable magnesium batteries, *J. Mater. Chem.*, 21 (2011) 12437-12443.
- [149] H.S. Kim, T.S. Arthur, G.D. Allred, J. Zajicek, J.G. Newman, A.E. Rodnyansky, A.G. Oliver, W.C. Boggess, J. Muldoon, Structure and compatibility of a magnesium electrolyte with a sulphur cathode, *Nature Communications*, 2 (2011) 427.
- [150] X. Yu, A. Manthiram, Performance Enhancement and Mechanistic Studies of Magnesium–Sulfur Cells with an Advanced Cathode Structure, *ACS Energy Letters*, 1 (2016) 431-437.
- [151] Z. Zhang, Z. Cui, L. Qiao, J. Guan, H. Xu, X. Wang, P. Hu, H. Du, S. Li, X. Zhou, S. Dong, Z. Liu, G. Cui, L. Chen, Novel Design Concepts of Efficient Mg-Ion Electrolytes toward High-Performance Magnesium–Selenium and Magnesium–Sulfur Batteries, *Advanced Energy Materials*, 7 (2017) 1602055.
- [152] T. Shiga, Y. Hase, Y. Kato, M. Inoue, K. Takechi, A rechargeable non-aqueous Mg–O₂ battery, *Chem. Commun.*, 49 (2013) 9152-9154.
- [153] H. Tian, T. Gao, X. Li, X. Wang, C. Luo, X. Fan, C. Yang, L. Suo, Z. Ma, W. Han, C. Wang, High power rechargeable magnesium/iodine battery chemistry, *Nature Communications*, 8 (2017) 1408301-1408310.

- [154] X. Yao, J. Luo, Q. Dong, D. Wang, A Rechargeable Non-aqueous Mg-Br₂ Battery, *Nano Energy*, 28 (2016) 440-446.
- [155] G. Pagot, F. Bertasi, K. Vezzù, E. Negro, G. Nawn, A. Nale, C. Sun, Y. Bang, A. Zlotorowicz, V. Di Noto, Poly(vinyl alcohol)-based Electrolytes for Lithium Batteries, *21st International Conference on Solid State Ionics*, Padova, Italy, 18-23 June 2017.
- [156] G. Pagot, E. Donà, F. Bertasi, K. Vezzù, A. Nale, E. Negro, V. Di Noto, Structure and Conductivity Mechanism of a Boron-based Ionic Liquid Electrolyte for Magnesium Batteries, *XVI International Symposium on Polymer Electrolytes - ISPE-16*, Yokohama, Japan, 24-29 June 2018.
- [157] G. Pagot, K. Vezzù, A. Nale, E. Negro, V. Di Noto, A Boron-based Ionic Liquid Electrolyte for Magnesium Batteries: Structure and Conductivity Mechanism, *6th International Conference on Ionic Liquids for Electrochemical Devices - ILED-6*, Roma, Italy, 9-11 September 2018.
- [158] G. Pagot, F. Bertasi, E. Negro, F. Sepehr, S.J. Paddison, V. Di Noto, 3D-Catenated EMImCl/(TiCl₄)_{1.4}/(δ -MgCl₂)_x Ionic Liquid Electrolyte for Mg Secondary Batteries, *PRiME 2016 - 230th ECS*, Honolulu, USA, 2-7 October 2016.
- [159] G. Pagot, F. Bertasi, K. Vezzù, G. Nawn, C. Sun, A. Nale, E. Negro, V. Di Noto, [EMImCl/(TiCl₄)_{1.4}]/(δ -MgCl₂)_x Ionic Liquid Electrolyte for Mg-ion Batteries, *XXVI Congresso Nazionale della Società Chimica Italiana*, Paestum, Italy, 10-14 September 2017.
- [160] G. Pagot, F. Bertasi, G. Pace, K. Vezzù, E. Negro, A. Bach Delpuch, G. Nawn, V. Di Noto, Hydrothermal Synthesis of Vanadium Sulfate supported on Graphene Oxide as Novel Cathode for Magnesium Ion Batteries, *6th edition of International Graphene Conference - Graphene 2016*, Genova, Italy, 19-22 April 2016.
- [161] D.F. Shriver, D.F.S. Mark A. Drezdson, M.A. Drezdson, *The Manipulation of Air-Sensitive Compounds*, Wiley 1986.
- [162] V. Di Noto, G.A. Giffin, K. Vezzù, M. Piga, S. Lavina, *Broadband Dielectric Spectroscopy: A Powerful Tool for the Determination of Charge Transfer Mechanisms in Ion Conductors*, *Solid State Proton Conductors: Properties and Applications in Fuel Cells*, John Wiley & Sons, Chichester, U.K., 2012, pp. 109-183.
- [163] M.S. Peresin, Y. Habibi, J.O. Zoppe, J.J. Pawlak, O.J. Rojas, Nanofiber composites of polyvinyl alcohol and cellulose nanocrystals: Manufacture and characterization, *Biomacromolecules*, 11 (2010) 674-681.

- [164] J.W. Gilman, D.L. VanderHart, T. Kashiwagi, Thermal Decomposition Chemistry of Poly(vinyl alcohol), *Fire and Polymers II*, American Chemical Society 1995, pp. 161-185.
- [165] W. Dong, Y. Wang, C. Huang, S. Xiang, P. Ma, Z. Ni, M. Chen, Enhanced thermal stability of poly(vinyl alcohol) in presence of melanin, *J. Therm. Anal. Calorim.*, 115 (2014) 1661-1668.
- [166] S. Krimm, C.Y. Liang, G.B.B.M. Sutherland, Infrared spectra of high polymers. V. Polyvinyl alcohol, *Journal of Polymer Science*, 22 (1956) 227-247.
- [167] K.B. Renuka Devi, R. Madivanane, Normal Coordinate Analysis of Poly Vinyl Acetate, *Engineering Science and Technology: An International Journal*, 2 (2012) 795-799.
- [168] H. Huang, L. Gu, Y. Ozaki, Non-isothermal crystallization and thermal transitions of a biodegradable, partially hydrolyzed poly(vinyl alcohol), *Polymer*, 47 (2006) 3935-3945.
- [169] C. Bergeron, E. Perrier, A. Potier, G. Delmas, A Study of the Deformation, Network, and Aging of Polyethylene Oxide Films by Infrared Spectroscopy and Calorimetric Measurements, *International Journal of Spectroscopy*, 2012 (2012) 1-13.
- [170] A. Ait-Salah, J. Dodd, A. Mauger, R. Yazami, F. Gendron, C.M. Julien, Structural and magnetic properties of LiFePO_4 and lithium extraction effects, *Z. Anorg. Allg. Chem.*, 632 (2006) 1598-1605.
- [171] V. Di Noto, D. Longo, V. Münchow, Ion-Oligomer Interactions in Poly(ethylene glycol)400/(LiCl) Electrolyte Complexes, *J. Phys. Chem. B*, 103 (1999) 2636-2646.
- [172] M. Jeyapandian, S. Lavina, S. Thayumanasundaram, H. Ohno, E. Negro, V. Di Noto, New hybrid inorganic-organic polymer electrolytes based on $\text{Zr}(\text{O}(\text{CH}_2)_3\text{CH}_3)_4$, glycerol and EMIm-TFSI ionic liquid, *J. Power Sources*, 195 (2010) 341-353.
- [173] I. Rey, P. Johansson, J. Lindgren, J.C. Lassègues, J. Grondin, L. Servant, Spectroscopic and theoretical study of $(\text{CF}_3\text{SO}_2)_2\text{N}^-$ (TFSI⁻) and $(\text{CF}_3\text{SO}_2)_2\text{NH}$ (HTFSI), *J. Phys. Chem. A*, 102 (1998) 3249-3258.
- [174] S.J. Lue, J.Y. Chen, J.M. Yang, Crystallinity and stability of poly(vinyl alcohol)-fumed silica mixed matrix membranes, *Journal of Macromolecular Science, Part B: Physics*, 47 (2008) 39-51.
- [175] N.A. Peppas, Infrared spectroscopy of semicrystalline poly(vinyl alcohol) networks, *Die Makromolekulare Chemie*, 178 (1977) 595-601.

- [176] J.C. Lassègues, J. Grondin, C. Aupetit, P. Johansson, Spectroscopic identification of the lithium ion transporting species in LiTFSI-doped ionic liquids, *J. Phys. Chem. A*, 113 (2009) 305-314.
- [177] V. Di Noto, D. Longo, V. Münchow, Ion–Oligomer Interactions in Poly(ethylene glycol)400/(LiCl)_x Electrolyte Complexes, *The Journal of Physical Chemistry B*, 103 (1999) 2636-2646.
- [178] V. Di Noto, M. Bettinelli, M. Furlani, S. Lavina, M. Vidali, Conductivity, luminescence and vibrational studies of the poly(ethylene glycol) 400 electrolyte based on europium trichloride, *Macromol. Chem. Phys.*, 197 (1996) 375-388.
- [179] J. Evans, C.A. Vincent, P.G. Bruce, Electrochemical measurement of transference numbers in polymer electrolytes, *Polymer*, 28 (1987) 2324-2328.
- [180] D. Bansal, F. Cassel, F. Croce, M. Hendrickson, E. Plichta, M. Salomon, Conductivities and transport properties of gelled electrolytes with and without an ionic liquid for Li and Li-Ion batteries, *J. Phys. Chem. B*, 109 (2005) 4492-4496.
- [181] H. Cheng, C. Zhu, B. Huang, M. Lu, Y. Yang, Synthesis and electrochemical characterization of PEO-based polymer electrolytes with room temperature ionic liquids, *Electrochim. Acta*, 52 (2007) 5789-5794.
- [182] S. Kitajima, F. Bertasi, K. Vezzù, E. Negro, Y. Tominaga, V. Di Noto, Dielectric relaxations and conduction mechanisms in polyether-clay composite polymer electrolytes under high carbon dioxide pressure, *PCCP*, 15 (2013) 16626-16633.
- [183] G. Tammann, W. Hesse, Die Abhängigkeit der Viscosität von der Temperatur bei unterkühlten Flüssigkeiten, *Z. Anorg. Allg. Chem.*, 156 (1926) 245-257.
- [184] R. Yu, J.-J. Bao, T.-T. Chen, B.-K. Zou, Z.-Y. Wen, X.-X. Guo, C.-H. Chen, Solid polymer electrolyte based on thermoplastic polyurethane and its application in all-solid-state lithium ion batteries, *Solid State Ion.*, 309 (2017) 15-21.
- [185] E. Ikada, K. Shounaka, M. Ashida, Dielectric properties of oligomers. VIII. The dielectric properties of model molecules for poly(vinyl acetate), *Polym. J.*, 13 (1981) 413-419.
- [186] S. Bhavani, M. Ravi, Y. Pavani, V. Raja, R.S. Karthikeya, V.V.R.N. Rao, Studies on structural, electrical and dielectric properties of nickel ion conducting polyvinyl alcohol based polymer electrolyte films, *Journal of Materials Science: Materials in Electronics*, (2017) 1-6.

- [187] K.P. Singh, P.N. Gupta, Study of dielectric relaxation in polymer electrolytes, *Eur. Polym. J.*, 34 (1998) 1023-1029.
- [188] A. De La Rosa, L. Heux, J.Y. Cavaillé, Secondary relaxations in poly(allyl alcohol), PAA, and poly(vinyl alcohol), PVA. II. Dielectric relaxations compared with dielectric behaviour of amorphous dried and hydrated cellulose and dextran, *Polymer*, 42 (2001) 5371-5379.
- [189] K. Nakamura, T. Shikata, Systematic dielectric and NMR study of the ionic liquid 1-alkyl-3-methylimidazolium, *ChemPhysChem*, 11 (2010) 285-294.
- [190] F.S. Howell, C.T. Moynihan, P.B. Macedo, Electrical Relaxations In Mixtures Of Lithium Chloride And Glycerol, *Bull. Chem. Soc. Jpn.*, 57 (1984) 652-661.
- [191] O. Bastiansen, Intra-Molecular Hydrogen Bonds in Ethylene Glycol, Glycerol, and Ethylene Chlorohydrin, *Acta Chem. Scand.*, 3 (1949) 415-421.
- [192] R. Chelli, P. Procacci, G. Cardini, R.G. Della Valle, S. Califano, Glycerol condensed phases part I. A molecular dynamics study, *PCCP*, 1 (1999) 871-877.
- [193] R. Chelli, P. Procacci, G. Cardini, S. Califano, Glycerol condensed phases Part II. A molecular dynamics study of the conformational structure and hydrogen bonding, *PCCP*, 1 (1999) 879-885.
- [194] R. Chelli, F.L. Gervasio, C. Gellini, P. Procacci, G. Cardini, V. Schettino, Density Functional Calculation of Structural and Vibrational Properties of Glycerol, *The Journal of Physical Chemistry A*, 104 (2000) 5351-5357.
- [195] Y.P. Zhao, J.W. Zhang, C.C. Zhao, Z.Y. Du, Tetrahedrally coordinated lithium(I) and zinc(II) carboxylate-phosphinates based on tetradentate 2-carboxyethyl(phenyl)phosphinate ligand, *Inorg. Chim. Acta*, 414 (2014) 121-126.
- [196] U. Liddel, E.D. Becker, Infra-red spectroscopic studies of hydrogen bonding in methanol, ethanol, and t-butanol, *Spectrochim. Acta*, 10 (1957) 70-84.
- [197] D. Lin-Vien, N.B. Colthup, W.G. Fateley, J.G. Grasselli, *The Handbook of Infrared and Raman Characteristic Frequencies of Organic Molecules*, Academic Press 1991.
- [198] E. Mendelovici, R.L. Frost, T. Kloprogge, Cryogenic Raman spectroscopy of glycerol, *Journal of Raman Spectroscopy*, 31 (2000) 1121-1126.

- [199] T.S. Perova, D.H. Christensen, U. Rasmussen, J.K. Vij, O.F. Nielsen, Far-infrared spectra of highly viscous liquids: glycerol and triacetin (glycerol triacetate), *Vib. Spectrosc*, 18 (1998) 149-156.
- [200] J.P. Zietlow, F.F. Cleveland, A.G. Meister, Substituted methanes. III. Raman spectra, assignments, and force constants for some trichloromethanes, *J. Chem. Phys.*, 18 (1950) 1076-1080.
- [201] B. Dou, V. Dupont, P.T. Williams, H. Chen, Y. Ding, Thermogravimetric kinetics of crude glycerol, *Bioresour. Technol.*, 100 (2009) 2613-2620.
- [202] J.L. Hong, X.H. Zhang, R.J. Wei, Q. Wang, Z.Q. Fan, G.R. Qi, Inhibitory effect of hydrogen bonding on thermal decomposition of the nanocrystalline cellulose/poly(propylene carbonate) nanocomposite, *J. Appl. Polym. Sci.*, 131 (2014) 39847.
- [203] C.A. Angell, Entropy and fragility in supercooling liquids, *Journal of Research of the National Institute of Standards and Technology*, 102 (1997) 171-181.
- [204] P. Claudy, S. Jabrane, J.M. L  toff  , Annealing of a glycerol glass: Enthalpy, fictive temperature and glass transition temperature change with annealing parameters, *Thermochim. Acta*, 293 (1997) 1-11.
- [205] F. Bertasi, K. Vezz  , G.A. Giffin, T. Nosach, P. Sideris, S. Greenbaum, M. Vittadello, V. Di Noto, Single-ion-conducting nanocomposite polymer electrolytes based on PEG400 and anionic nanoparticles: Part 2. Electrical characterization, *Int. J. Hydrogen Energy*, 39 (2014) 2884-2895.
- [206] P. Dhatarwal, S. Choudhary, R.J. Sengwa, Electrochemical performance of Li⁺-ion conducting solid polymer electrolytes based on PEO–PMMA blend matrix incorporated with various inorganic nanoparticles for the lithium ion batteries, *Composites Communications*, 10 (2018) 11-17.
- [207] V. Di Noto, M. Piga, G.A. Giffin, S. Lavina, E.S. Smotkin, J.Y. Sanchez, C. Iojoiu, Influence of anions on proton-conducting membranes based on neutralized nafion 117, triethylammonium methanesulfonate, and triethylammonium perfluorobutanesulfonate. 2. electrical properties, *Journal of Physical Chemistry C*, 116 (2012) 1370-1379.
- [208] P. Lunkenheimer, U. Schneider, R. Brand, A. Loid, Glassy dynamics, *Contemporary Physics*, 41 (2000) 15-36.
- [209] A. Kudlik, S. Benkhof, T. Blochowicz, C. Tschirwitz, E. R  ssler, The dielectric response of simple organic glass formers, *J. Mol. Struct.*, 479 (1999) 201-218.

- [210] C.A.C. Sequeira, D. Santos, *Polymer Electrolytes: Fundamentals and Applications*, Woodhead Publishing Limited 2010.
- [211] N.-S. Cheng, Formula for the Viscosity of a Glycerol–Water Mixture, *Industrial & Engineering Chemistry Research*, 47 (2008) 3285-3288.
- [212] V. Di Noto, M. Piga, G.A. Giffin, K. Vezzù, T.A. Zawodzinski, Interplay between mechanical, electrical, and thermal relaxations in nanocomposite proton conducting membranes based on nafion and a $[(\text{ZrO}_2)\cdot(\text{Ta}_2\text{O}_5)]_{0.119}$ core-shell nanofiller, *J. Am. Chem. Soc.*, 134 (2012) 19099-19107.
- [213] C.F. Smura, D.R. Parker, M. Zbiri, M.R. Johnson, Z.A. Gál, S.J. Clarke, High-Spin Cobalt(II) Ions in Square Planar Coordination: Structures and Magnetism of the Oxysulfides $\text{Sr}_2\text{CoO}_2\text{Cu}_2\text{S}_2$ and $\text{Ba}_2\text{CoO}_2\text{Cu}_2\text{S}_2$ and Their Solid Solution, *J. Am. Chem. Soc.*, 133 (2011) 2691-2705.
- [214] G. Pagot, F. Bertasi, G. Nawn, E. Negro, G. Carraro, D. Barreca, C. Maccato, S. Polizzi, V. Di Noto, High-Performance Olivine for Lithium Batteries: Effects of Ni/Co Doping on the Properties of $\text{LiFe}_\alpha\text{Ni}_\beta\text{Co}_\gamma\text{PO}_4$ Cathodes, *Adv. Funct. Mater.*, 25 (2015) 4032-4037.
- [215] J.F. Moulder, J. Chastain, *Handbook of x-ray photoelectron spectroscopy : a reference book of standard spectra for identification and interpretation of XPS data*, Physical Electronics Division, Perkin-Elmer Corp., Eden Prairie, Minn., 1992.
- [216] J. Ma, B. Li, H. Du, C. Xu, F. Kang, The Effect of Vanadium on Physicochemical and Electrochemical Performances of LiFePO_4 Cathode for Lithium Battery, *J. Electrochem. Soc.*, 158 (2011) A26-A32.
- [217] C. Sun, Z. Zhou, Z. Xu, D. Wang, J. Wei, X. Bian, J. Yan, Improved high-rate charge/discharge performances of LiFePO_4/C via V-doping, *J. Power Sources*, 193 (2009) 841-845.
- [218] T. Yamashita, P. Hayes, Analysis of XPS spectra of Fe^{2+} and Fe^{3+} ions in oxide materials, *Appl. Surf. Sci.*, 254 (2008) 2441-2449.
- [219] A. Mansour, R.A. Brizzolara, Characterization of the surface of FeO powder by XPS, *Surf. Sci. Spectra*, 4 (1996) 345-350.
- [220] L. Tan, Z. Luo, H. Liu, Y. Yu, Synthesis of novel high-voltage cathode material LiCoPO_4 via rheological phase method, *J. Alloys Compd.*, 502 (2010) 407-410.

- [221] M.C. Biesinger, B.P. Payne, A.P. Grosvenor, L.W. Lau, A.R. Gerson, R.S.C. Smart, Resolving surface chemical states in XPS analysis of first row transition metals, oxides and hydroxides: Cr, Mn, Fe, Co and Ni, *Appl. Surf. Sci.*, 257 (2011) 2717-2730.
- [222] S. Nordlinder, A. Augustsson, T. Schmitt, J. Guo, L.C. Duda, J. Nordgren, T. Gustafsson, K. Edström, Redox behavior of vanadium oxide nanotubes as studied by X-ray photoelectron spectroscopy and soft X-ray absorption spectroscopy, *Chem. Mater.*, 15 (2003) 3227-3232.
- [223] G. Silversmit, D. Depla, H. Poelman, G.B. Marin, R. De Gryse, Determination of the V2p XPS binding energies for different vanadium oxidation states (V^{5+} to V^{0+}), *J. Electron. Spectrosc. Relat. Phenom.*, 135 (2004) 167-175.
- [224] P. Zhang, Y. Wang, M. Lin, D. Zhang, X. Ren, Q. Yuan, Doping Effect of Nb^{5+} on the Microstructure and Defects of $LiFePO_4$, *J. Electrochem. Soc.*, 159 (2012) A402-A409.
- [225] E. Atanassova, T. Dimitrova, J. Koprinarova, AES and XPS study of thin RF-sputtered Ta_2O_5 layers, *Appl. Surf. Sci.*, 84 (1995) 193-202.
- [226] MATCH!, Crystal Impact, 2012, 2.0.7.
- [227] L. Lutterotti, Maud, 2018, 2.8.
- [228] T. Kimura, C.K. Chang, F. Kimura, M. Maeyama, The pseudo-single-crystal method: a third approach to crystal structure determination, *J. Appl. Crystallogr.*, 42 (2009) 535-537.
- [229] G. Liang, R.E. Benson, J.Y. Li, D. Vaknin, L.M. Daniels, $LiNi_{0.66}Fe_{0.34}PO_4$, *Acta Crystallographica Section E-Structure Reports Online*, 63 (2007) i73-i74.
- [230] D. Riou, N. Nguyen, R. Benloucif, B. Raveau, $LiFeP_2O_7$: Structure and magnetic properties, *Mater. Res. Bull.*, 25 (1990) 1363-1369.
- [231] Ğ. Vitiřš, Z. Kaņepe, A. Vitiřš, J. Ronis, A. Dindūne, A. Lūsis, Structural and conductivity studies in $LiFeP_2O_7$, $LiScP_2O_7$, and $NaScP_2O_7$, *J. Solid State Electrochem.*, 4 (2000) 146-152.
- [232] L. Pauling, S.B. Hendricks, The Crystal Structures of Hematite And Corundum, *J. Am. Chem. Soc.*, 47 (1925) 781-790.

- [233] R.W.G. Wyckoff, *The Structure of Crystals: Supplement for 1930-1934 to the Second Edition*, Reinhold Publishing Corporation 1935.
- [234] L.A. Aleshina, S.V. Loginova, Rietveld analysis of X-ray diffraction pattern from β -Ta₂O₅ oxide, *Crystallography Reports*, 47 (2002) 415-419.
- [235] B.H. Toby, R factors in Rietveld analysis: How good is good enough?, *Powder diffraction*, 21 (2006) 67-70.
- [236] C.M. Julien, P. Jozwiak, J. Garbarczyk, Vibrational spectroscopy of electrode materials for rechargeable lithium batteries - IV. Lithium metal phosphates, *Advanced Techniques for Energy Sources Investigation and Testing*, Sofia, Bulgaria,
- [237] M.T. Paques-Ledent, P. Tarte, Vibrational studies of olivine-type compounds—II Orthophosphates, -arsenates and -vanadates AIBIXVO₄, *Spectrochim. Acta, Part A*, 30 (1974) 673-689.
- [238] W. Paraguassu, P.T.C. Freire, V. Lemos, S.M. Lala, L.A. Montoro, J.M. Rosolen, Phonon calculation on olivine-like LiMPO₄ (M = Ni, Co, Fe) and Raman scattering of the iron-containing compound, *Journal of Raman Spectroscopy*, 36 (2005) 213-220.
- [239] W.M. Haynes, *CRC Handbook of Chemistry and Physics*, 93rd Edition, Taylor & Francis 2012.
- [240] R.J.H. Clark, D. Brown, J.C. Bailar, H.J. Emeléus, R. Nyholm, *The Chemistry of Vanadium, Niobium and Tantalum: Pergamon Texts in Inorganic Chemistry*, Elsevier Science 2013.
- [241] N. Ravet, M. Gauthier, K. Zaghbi, Goodenough, A. Mauger, F. Gendron, Julien, Mechanism of the Fe³⁺ Reduction at Low Temperature for LiFePO₄ Synthesis from a Polymeric Additive, *Chem. Mater.*, 19 (2007) 2595-2602.
- [242] J. Liu, M.N. Banis, Q. Sun, A. Lushington, R. Li, T.K. Sham, X. Sun, Rational design of atomic-layer-deposited LiFePO₄ as a high-performance cathode for lithium-ion batteries, *Adv. Mater.*, 26 (2014) 6472-6477.
- [243] M. Ren, Z. Zhou, Y. Li, X.P. Gao, J. Yan, Preparation and electrochemical studies of Fe-doped Li₃V₂(PO₄)₃ cathode materials for lithium-ion batteries, *J. Power Sources*, 162 (2006) 1357-1362.
- [244] A.J. Bard, L.R. Faulkner, *Electrochemical Methods: Fundamentals and Applications*, 2nd Edition, 2nd ed., John Wiley & Sons 2000.

- [245] Z.P. Cai, Y. Liang, W.S. Li, L.D. Xing, Y.H. Liao, Preparation and performances of LiFePO_4 cathode in aqueous solvent with polyacrylic acid as a binder, *J. Power Sources*, 189 (2009) 547-551.
- [246] K. Dokko, M. Mohamedi, M. Umeda, I. Uchida, Kinetic Study of Li-Ion Extraction and Insertion at LiMn_2O_4 Single Particle Electrodes Using Potential Step and Impedance Methods, *J. Electrochem. Soc.*, 150 (2003) A425-A429.
- [247] J. Xie, K. Kohno, T. Matsumura, N. Imanishi, A. Hirano, Y. Takeda, O. Yamamoto, Li-ion diffusion kinetics in LiMn_2O_4 thin films prepared by pulsed laser deposition, *Electrochim. Acta*, 54 (2008) 376-381.
- [248] J. Xie, T. Tanaka, N. Imanishi, T. Matsumura, A. Hirano, Y. Takeda, O. Yamamoto, Li-ion transport kinetics in LiMn_2O_4 thin films prepared by radio frequency magnetron sputtering, *J. Power Sources*, 180 (2008) 576-581.
- [249] C. Ho, I.D. Raistrick, R.A. Huggins, Application of A-C Techniques to the Study of Lithium Diffusion in Tungsten Trioxide Thin Films, *J. Electrochem. Soc.*, 127 (1980) 343-350.
- [250] I.D. Johnson, E. Blagovidova, P.A. Dingwall, D.J. Brett, P.R. Shearing, J.A. Darr, High power Nb-doped LiFePO_4 Li-ion battery cathodes; pilot-scale synthesis and electrochemical properties, *J. Power Sources*, 326 (2016) 476-481.
- [251] F. Omenya, N.A. Chernova, S. Upreti, P.Y. Zavalij, K.-W. Nam, X.-Q. Yang, M.S. Whittingham, Can vanadium be substituted into LiFePO_4 ?, *Chem. Mater.*, 23 (2011) 4733-4740.
- [252] C. Stefan, D. Lemordant, P. Biensan, C. Siret, B. Claude-Montigny, Thermal stability and crystallization of N-alkyl-N-alkyl'-pyrrolidinium imides, *J. Therm. Anal. Calorim.*, 102 (2010) 685-693.
- [253] W.A. Henderson, V.G. Young, S. Passerini, P.C. Trulove, H.C. De Long, Plastic Phase Transitions in N-Ethyl-N-methylpyrrolidinium Bis(trifluoromethanesulfonyl)imide, *Chem. Mater.*, 18 (2006) 934-938.
- [254] D.R. MacFarlane, P. Meakin, J. Sun, N. Amini, M. Forsyth, Pyrrolidinium Imides: A New Family of Molten Salts and Conductive Plastic Crystal Phases, *The Journal of Physical Chemistry B*, 103 (1999) 4164-4170.
- [255] W.A. Henderson, S. Passerini, Phase Behavior of Ionic Liquid-LiX Mixtures: Pyrrolidinium Cations and TFSI- Anions, *Chem. Mater.*, 16 (2004) 2881-2885.

- [256] B. Babushkina Olga, Phase Behaviour and FTIR Spectra of Ionic Liquids: The Mixtures of 1-Butyl-1-methylpyrrolidinium Chloride and TaCl₅, *Zeitschrift für Naturforschung A*, 63 (2008) 66-72.
- [257] B. Bednarska-Bolek, R. Jakubas, G. Bator, J. Baran, Vibrational study of the structural phase transition in bis(pyrrolidinium)-chloride-hexachloroantimonate(V) by infrared spectroscopy, *J. Mol. Struct.*, 614 (2002) 151-157.
- [258] J. Evans, W. J., Thermodynamic and Spectroscopic Study of Pyrrolidine. II. Vibrational Spectra and Configuration, *J. Chem. Phys.*, 31 (1959) 655-662.
- [259] J. Adebahr, P. Johansson, P. Jacobsson, D.R. MacFarlane, M. Forsyth, Ab initio calculations, Raman and NMR investigation of the plastic crystal di-methyl pyrrolidinium iodide, *Electrochim. Acta*, 48 (2003) 2283-2289.
- [260] G. Ramis, G. Busca, FTIR spectra of adsorbed n-butylamine, *J. Mol. Struct.*, 193 (1989) 93-100.
- [261] T.C. Waddington, F. Klanberg, The infrared spectra of some new compounds of boron trifluoride, boron trichloride, and sulphur trioxide, *J. Chem. Soc.*, 1 (1960) 2339-2343.
- [262] J.I. Bullock, N.J. Taylor, F.W. Parrett, Some metal halide-phosphorus halide-alkyl halide complexes. Part I. Reactions with boron, aluminium, silicon, germanium, and tin halides, *J. Chem. Soc., Dalton Trans.*, 17 (1972) 1843-1846.
- [263] W. Kynaston, B.E. Larcombe, H.S. Turner, Preparation and infrared spectra of some tetrachloroborates, *Journal of the Chemical Society (Resumed)*, 1 (1960) 1772-1778.
- [264] K. Nakamoto, Infrared and Raman Spectra of Inorganic and Coordination Compounds - Part A: Theory and Applications in Inorganic Chemistry, Sixth ed., John Wiley & Sons, INC., Hoboken, New Jersey, 2009.
- [265] S.D. Williams, J.P. Schoebrechts, J.C. Selkirk, G. Mamantov, A new room temperature molten salt solvent system: Organic cation tetrachloroborates, *J. Am. Chem. Soc.*, 109 (1987) 2218-2219.
- [266] C.J. Dymek, D.A. Grossie, A.V. Fratini, W. Wade Adams, Evidence for the presence of hydrogen-bonded ion-ion interactions in the molten salt precursor, 1-methyl-3-ethylimidazolium chloride, *J. Mol. Struct.*, 213 (1989) 25-34.
- [267] K. Matsumoto, R. Hagiwara, Z. Mazej, P. Benkič, B. Žemva, Crystal structures of frozen room temperature ionic liquids, 1-ethyl-3-methylimidazolium tetrafluoroborate (EMImBF₄), hexafluoronioate

(EMImNbF₆) and hexafluorotantalate (EMImTaF₆), determined by low-temperature X-ray diffraction, *Solid State Sci.*, 8 (2006) 1250-1257.

[268] L. Gao, L. Wang, T. Qi, J. Chu, J. Qu, Preparation and characterization of titanium tetrachloride-based ionic liquids, *J. Electrochem. Soc.*, 156 (2009) P49-P55.

[269] M. Vittadello, P.E. Stallworth, F.M. Alamgir, S. Suarez, S. Abbrent, C.M. Drain, V. Di Noto, S.G. Greenbaum, Polymeric δ -MgCl₂ nanoribbons, *Inorganica Chimica Acta*, 359 (2006) 2513-2518.

[270] S.P. Webb, M.S. Gordon, Intermolecular self-interactions of the titanium tetrahalides TiX₄ (X = F, Cl, Br), *J. Am. Chem. Soc.*, 121 (1999) 2552-2560.

[271] S.A. Katsyuba, P.J. Dyson, E.E. Vandyukova, A.V. Chernova, A. Vidiš, Molecular structure, vibrational spectra, and hydrogen bonding of the ionic liquid 1-ethyl-3-methyl-1H-imidazolium tetrafluoroborate, *Helv. Chim. Acta*, 87 (2004) 2556-2565.

[272] N.E. Heimer, R.E. Del Sesto, Z. Meng, J.S. Wilkes, W.R. Carper, Vibrational spectra of imidazolium tetrafluoroborate ionic liquids, *J. Mol. Liq.*, 124 (2006) 84-95.

[273] K.M. Dieter, C.J. Dymek Jr, N.E. Heimer, J.W. Rovang, J.S. Wilkes, Ionic structure and interactions in 1-methyl-3-ethylimidazolium chloride-AlCl₃ molten salts, *J. Am. Chem. Soc.*, 110 (1988) 2722-2726.

[274] S.A. Katsyuba, E.E. Zvereva, A. Vidiš, P.J. Dyson, Application of density functional theory and vibrational spectroscopy toward the rational design of ionic liquids, *J. Phys. Chem. A*, 111 (2007) 352-370.

[275] J. Shamir, S. Schneider, A. Bino, S. Cohen, New double salt [PCl₄]₃[TiCl₆][PCl₆] and related compounds in the PCl₅TiCl₄ system. Synthesis and structural determination by Raman spectra and X-ray analysis, *Inorg. Chim. Acta*, 111 (1986) 141-147.

[276] V. Di Noto, A. Marigo, M. Viviani, C. Marega, S. Bresadola, R. Zannetti, MgCl₂-supported Ziegler-Natta catalysts: Synthesis and X-ray diffraction characterization of some MgCl₂-Lewis base adducts, *Die Makromolekulare Chemie*, 193 (1992) 123-131.

[277] K. Nakamoto, *Infrared and Raman Spectra of Inorganic and Coordination Compounds, Theory and Applications in Inorganic Chemistry*, Wiley 2008.

[278] J.A. Creighton, J.H.S. Green, The vibrational spectra of some penta- and hexa-halogeno-complexes of tin, titanium, and tellurium, *J. Chem. Soc. A, Inor. Phys. Theor.*, (1968) 808-813.

- [279] W. Van Bronswyk, R.J.H. Clark, L. Maresca, Infrared spectra, laser Raman spectra, and force constants of the metal-hexahalo species R_2MIVX_6 , $RMVX_6$ [$R = (C_2H_5)_4N$ or Cs ; $MIV = Ti, Zr, \text{ or } Hf$; $MV = Nb \text{ or } Ta$; $X = Cl$ or Br], and WCl_6 , *Inorg. Chem.*, 8 (1969) 1395-1401.
- [280] V. Di Noto, M. Vittadello, Mechanism of ionic conductivity in poly(ethylene glycol 400)/(MgCl₂)_x polymer electrolytes: Studies based on electrical spectroscopy, *Solid State Ion.*, 147 (2002) 309-316.
- [281] J.H. Cho, J.H. Ha, S.H. Lee, B.W. Cho, K.Y. Chung, B.K. Na, K.B. Kim, S.H. Oh, Effect of 1-allyl-1-methylpyrrolidinium chloride addition to ethylmagnesium bromide electrolyte on a rechargeable magnesium battery, *Electrochim. Acta*, 231 (2017) 379-385.
- [282] K.A. See, K.W. Chapman, L. Zhu, K.M. Wiaderek, O.J. Borkiewicz, C.J. Barile, P.J. Chupas, A.A. Gewirth, The Interplay of Al and Mg Speciation in Advanced Mg Battery Electrolyte Solutions, *J. Am. Chem. Soc.*, 138 (2016) 328-337.
- [283] I. Shterenberg, M. Salama, H.D. Yoo, Y. Gofer, J.B. Park, Y.K. Sun, D. Aurbach, Evaluation of (CF₃SO₂)₂N-(TFSI) based electrolyte solutions for Mg batteries, *J. Electrochem. Soc.*, 162 (2015) A7118-A7128.
- [284] D. Aurbach, Y. Gofer, The Correlation Between Surface Chemistry, Surface Morphology, and Cycling Efficiency of Lithium Electrodes in a Few Polar Aprotic Systems, *J. Electrochem. Soc.*, 136 (1989) 3198-3205.
- [285] S. Takahashi, L.A. Curtiss, D. Gosztola, N. Koura, M.L. Saboungi, Molecular Orbital Calculations and Raman Measurements for 1-Ethyl-3-methylimidazolium Chloroaluminates, *Inorg. Chem.*, 34 (1995) 2990-2993.
- [286] C.J. Barile, R.G. Nuzzo, A.A. Gewirth, Exploring salt and solvent effects in chloride-based electrolytes for magnesium electrodeposition and dissolution, *Journal of Physical Chemistry C*, 119 (2015) 13524-13534.
- [287] A. Mukherjee, N. Sa, P.J. Phillips, A. Burrell, J. Vaughey, R.F. Klie, Direct Investigation of Mg Intercalation into the Orthorhombic V₂O₅ Cathode Using Atomic-Resolution Transmission Electron Microscopy, *Chem. Mater.*, 29 (2017) 2218-2226.
- [288] G. Zhao, J. Li, X. Ren, C. Chen, X. Wang, Few-Layered Graphene Oxide Nanosheets As Superior Sorbents for Heavy Metal Ion Pollution Management, *Environmental Science & Technology*, 45 (2011) 10454-10462.
- [289] J. Twu, C.-F. Shih, T.-H. Guo, K.-H. Chen, Raman spectroscopic studies of the thermal decomposition mechanism of ammonium metavanadate, *J. Mater. Chem.*, 7 (1997) 2273-2277.

- [290] M. Acik, G. Lee, C. Mattevi, M. Chhowalla, K. Cho, Y.J. Chabal, Unusual infrared-absorption mechanism in thermally reduced graphene oxide, *Nat. Mater.*, 9 (2010) 840-845.
- [291] T. Szabó, O. Berkesi, I. Dékány, DRIFT study of deuterium-exchanged graphite oxide, *Carbon*, 43 (2005) 3186-3189.
- [292] T. Szabó, O. Berkesi, P. Forgó, K. Josepovits, Y. Sanakis, D. Petridis, I. Dékány, Evolution of surface functional groups in a series of progressively oxidized graphite oxides, *Chem. Mater.*, 18 (2006) 2740-2749.
- [293] M. Acik, G. Lee, C. Mattevi, A. Pirkle, R.M. Wallace, M. Chhowalla, K. Cho, Y. Chabal, The role of oxygen during thermal reduction of graphene oxide studied by infrared absorption spectroscopy, *Journal of Physical Chemistry C*, 115 (2011) 19761-19781.
- [294] D. Lin-Vien, N.B. Colthup, W.G. Fateley, J.G. Grasselli, CHAPTER 17 - Aromatic and Heteroaromatic Rings, *The Handbook of Infrared and Raman Characteristic Frequencies of Organic Molecules*, Academic Press, San Diego, 1991, pp. 277-306.
- [295] M.R. Todorović, U.B. Mioč, I. Holclajtner-Antunović, D. Šegan, Synthesis and characterization of ammonium decavanadate (V), *Mater. Sci. Forum*, 2005, pp. 351-356.
- [296] G.S. Zakharova, C. Täschner, T. Kolb, C. Jähne, A. Leonhardt, B. Büchner, R. Klingeler, Morphology controlled $\text{NH}_4\text{V}_3\text{O}_8$ microcrystals by hydrothermal synthesis, *Dalton Transactions*, 42 (2013) 4897-4902.
- [297] H. Zhang, T. Kuila, N.H. Kim, D.S. Yu, J.H. Lee, Simultaneous reduction, exfoliation, and nitrogen doping of graphene oxide via a hydrothermal reaction for energy storage electrode materials, *Carbon*, 69 (2014) 66-78.
- [298] E. Fuente, J.A. Menéndez, M.A. Díez, D. Suárez, M.A. Montes-Morán, Infrared spectroscopy of carbon materials: A quantum chemical study of model compounds, *J. Phys. Chem. B*, 107 (2003) 6350-6359.
- [299] M. Kang, D.H. Lee, J. Yang, Y.M. Kang, H. Jung, Simultaneous reduction and nitrogen doping of graphite oxide by using electron beam irradiation, *RSC Advances*, 5 (2015) 104502-104508.
- [300] R. Bariseviciute, J. Ceponkus, V. Sablinskas, Matrix isolation FTIR spectroscopical study of ethene secondary ozonide, *Central European Journal of Chemistry*, 5 (2006) 71-86.
- [301] N. Kausar, R. Howe, M. Skyllas-Kazacos, Raman spectroscopy studies of concentrated vanadium redox battery positive electrolytes, *J. Appl. Electrochem.*, 31 (2001) 1327-1332.

- [302] L. Mai, C. Han, Reaction-crystallization growth and electrical property of ammonium decavanadate nanorods, *Mater. Lett.*, 62 (2008) 1458-1461.
- [303] S. Mohan, S. Gunasekaran, K. Kumar, Vibrational spectra of vanadium chloride and its normal coordinate analysis, *Proc. Indian Natl. Sci. Acad.*, 3 (1986) 641-646.
- [304] D. Imamura, M. Miyayama, Characterization of magnesium-intercalated V₂O₅/carbon composites, *Solid State Ion.*, 161 (2003) 173-180.
- [305] L. Yu, X. Zhang, Electrochemical insertion of magnesium ions into V₂O₅ from aprotic electrolytes with varied water content, *J. Colloid Interface Sci.*, 278 (2004) 160-165.